UNIVERSITY OF CALIFORNIA, MERCED

Alterations to the PI3K/PTEN/AKT signaling cascade initiate cellular transformation during adult tissue renewal in planarians

A dissertation submitted in stratification of the requirements
for the degree Doctor of Philosophy

in

Quantitative and Systems Biology

by

Paul George Barghouth

Committee in charge:

Professor Ramendra N. Saha, Chair
Professor Clarissa J. Nobile, Member
Professor Laura Beaster-Jones, Member
Professor Néstor J. Oviedo, Advisor

2019

DEDICATION

Primarily, I would like to thank God for helping me through this trying time. This could not have been accomplished without His grace and watchful eye.

Secondly, I would like to thank my family, who have encouraged me to keep pushing through the rough patches during my 6 years in the QSB program.

Third, I would like to thank Dr. Nestor J. Oviedo and Edelweiss Pfister for acting as my science parents during my graduate studies. Moreover, I am thankful for Dr. Oviedo for believing in my ability to become a scientist, when all other paths were closed. Initially, I was a master student and then he identified that I had the capacity to become a PhD student. I enjoyed my time working with him side-by-side writing manuscripts and planning/conducting experiments. I appreciate everything he has done for me and my future advancements.

I would like to thank the current and past lab members of the Oviedo lab. You all made this stressful time bearable and enjoyable. I will miss you all. Special thanks to Melanie LeGro and Ben Ziman for helping me with my PTEN paper by conducting RNAseq analysis and western blots, respectively. Salvador Rojas for conducting *in situ* hybridization experiments for the DMAP1 project. Eli Maciel thank you for your aid with the irradiation and TRAF projects. Devon Davidian, Manish Thiruvalluvan and Peter Karabinis thank you for helping me with troubleshooting and with experimental design questions. Thank you to both of my undergraduates, Andrew Betancourt, Lacey O'dell and Eloise Moua for being amazing individuals and helping me with my many projects. Finally, thank you, T. Harshani Peiris, Natasha Flores, Daniel Ramirez and Udokanma Ofoha for teaching me all the protocols in the lab and setting me up to become a successful graduate student.

Last but not least, I would like to thank my friends who supported me throughout this process. Special thanks to Niral Patel, Tina Kuang, Eddie Aboujudom, Andrew Macias, Morgan Quail, Michael Urner, Jessica Lopez, Erik Lau, Carlos Bejarano, Jordan Mason, Brian Pham, Steven Duval, Cody Canerdy, Marwin Ko, Cassandra Hernandez, Connor Ross, Rolando Romero and, Alan Ramirez, for your frequent phone calls, being great workout partners and/or making sure I was doing well throughout this process.

COPYRIGHT

The Dissertation of Paul George Barghouth is approved, and it is acceptable in quality and form for publication on microfilm and electronically:

_____

Laura Beaster-Jones

_____

Clarissa J. Nobile

_____

Ramendra N. Saha, Chair

University of California, Merced

2019

TABLE OF CONTENTS

LIST OF FIGURES

LIST OF ABBREVIATIONS

SC: Stem cell

Smed: Schmidtea mediterranea

AP: Anteroposterior axis

OTS-DDM: Oncogene/tumor suppressor-induced DNA damage model

RNAi: RNA interference

PTEN: Phosphatase and tensin homologue deleted on chromosome 10

Rb: Retinoblastoma protein

p53: Tumor protein p53

PI3K: Phosphoinositide-3-Kinase

TOR: Mammalian Target of Rapamycin

FACS: Fluorescence-activated cell sorting/ flow cytometry

DSB: DNA double-strand break

SSB: DNA single-strand break

DDR: DNA damage response

ICL: Interstrand and intrastrand crosslinks

ROS: Reactive oxygen species

MRN: MRE11-Rad50-Nbs1 complex

RPA: Replication protein A

Chk1/2: Checkpoint Kinase 1 or 2

CDC: Cell division cycle

ATM: Ataxia telangiectasia mutated

R-point: Restriction point

ATR: Ataxia telangiectasia and Rad3-realted

P21: P21 (RAC1) activated kinase 1

BCL2: BCL2, Apoptosis Regulator

AKT: Protein kinase B (PKB)

CDK: Cyclin-dependent kinase

PCNA: Proliferating cell nuclear antigen

MDM2: Murine double minute 2

NHEJ: Non-homologous end joining

HR: Homologous recombination

Alt_EJ: Alternative end joining

SSA: Single strand annealing

DNA-PKcs: DNA-dependent protein kinase catalytic subunit

MMR: Mismatch repair

Rad51: RAD51 Recombinase

BRCA1/2: Breast Cancer Type 1/2 Susceptibility Protein

HBOC: Hereditary breast and ovarian cancer

Wnt: Wingless-Type MMTV Integration Site Family

PARP: Poly (ADP-Ribose) Polymerase

c/EBPβ: CCAAT/Enhancer Binding Protein (C/EBP), Beta

CtIP: RB Binding Protein 8, Endonuclease

γH2AX: H2A Histone Family Member X

MDC1: Mediator of DNA damage checkpoint 1

53BP1: Tumor protein p53 binding protein 1

BLM: Bloom syndrome RecQ like helicase

Exo1: Exonuclease 1

IR: Ionizing radiation

MMS: Methyl methanesulfonate

BrdU: 5-Bromo-2-Deoxyuridine

WISH: Whole-mount *in situ* hybridization

FISH: Fluorescent *in situ* hybridization

WIHC: Whole-mount immunohistochemistry

TUNEL: Terminal deoxynucleotidyl transferase dUTP nick end labeling

Piwi-1: Piwi like RNA-mediated gene silencing 1

SUMO: Small ubiquitin-like modifier

UBC9: Ubiquitin Conjugating Enzyme E2

DPFI: Days post first injection

RNAseq: RNA sequencing

HPA: Hours post amputation

2xRNAi: Double *Smed-MVP+USP7(RNAi)*

3xRNAi: Triple *Smed-MVP+USP7+NEDD4-1(RNAi)*

HCL: Hydrochloric acid

MqH_2O: MilliQ Water

PBS: Phosphate-Buffered Saline

PBSTx: Phosphate-Buffered Saline + Triton X-100

PBSTxBSA: Phosphate-Buffered Saline + Triton X-100 + Bovine Serum Albumin

BSA: Bovine Serum Albumin

H_2O_2: Hydrogen Peroxide

NAC: N-acetyl-L-cysteine

P-H_2O: Planarian Montjuic Water

DMSO: Dimethyl Sulfoxide

NaCl: Sodium Chloride

SDS: Sodium Dodecyl Sulfate

CMF: Calcium and magnesium phosphate free media

ACKNOWLEDGEMENTS

The text of this dissertation is a reprint of the material as it appears in “DNA damage and tissue repair: What we can learn from planaria.” The co-author listed in this publication directed and supervised research which forms the basis for the dissertation.

The text of this dissertation is a reprint of the material as it appears in “The Akt signaling pathway is required for tissue maintenance and regeneration in planarians.” The co-author listed in this publication directed and supervised research which forms the basis for the dissertation.

CURRICULUM VITAE

PAUL GEORGE BARGHOUTH

EDUCATION

University of California, Merced **August 2013-May 2019**
Ph.D. Candidate: Quantitative and Systems Biology
Dissertation advisor: Dr. Nestor J. Oviedo

University of California, Merced **August 2009-May 2013**
Bachelor of Sciences in Bioengineering

PUBLICATIONS

- Devon Davidian, **Paul G. Barghouth**, Melanie LeGro, Ben Ziman, Salvador Rojas, Eli Maciel and Néstor J. Oviedo. "Electric Stimulation Enhances Cellular Plasticity and Stem Cell Reconstitution." Submitted November 2018
- Eli Maciel, Cen Jiang, **Paul G. Barghouth**, Clarissa Nobile and Néstor J. Oviedo. "The planarian Schmidtea mediterranea is a new model to study host-pathogen interactions during fungal infections." Developmental and Comparative Immunology. December 10, 2018. PMID:30571995
- **Paul G. Barghouth**, Manish Thiruvalluvan, Melanie LeGro and Néstor J. Oviedo. "DNA damage and tissue repair: What we can learn from planaria." Seminars in Cell and Developmental Biology. May 3, 2018. PMID:29727725
- Manish Thiruvalluvan, **Paul G. Barghouth**, Assaf Tsur, Limor Broday and Néstor J. Oviedo. "SUMOylation controls stem cell proliferation and regional cell death through Hedgehog signaling in planarians." Cellular and Molecular Life Sciences. November 2, 2017. PMID: 29098326
- T. Harshani Peiris, Daniel Ramirez, **Paul G. Barghouth**, Udokanma Ofoha, Devon Davidian, Frank Weckerle, and Néstor J. Oviedo. "Regional signals in the planarian body guide stem cell fate in the presence of genomic instability." Development. May 15, 2016. PMID: 27013241
- T. Harshani Peiris[#1], Daniel Ramirez[#1], **Paul G. Barghouth[#1]**, and Néstor J. Oviedo. "The AKT signaling pathway is required for tissue maintenance and regeneration in planarian." BMC Dev Biol. April 11, 2016. PMID: 27068018
- **Paul G. Barghouth**[#1], Manish Thiruvalluvan[#1], and Néstor J. Oviedo. "Bioelectrical regulation of cell cycle and the planarian model system." Biochim Biophys Acta. March 6, 2015. PMID: 25749155

PUBLICATIONS IN PROGRESS

- **Paul G. Barghouth**, Melanie LeGro, Ben Ziman, and Néstor J. Oviedo. "The interplay of PTEN in abnormal cellular hyperproliferation during adult tissue maintenance and regeneration".
- **Paul G. Barghouth**, and Néstor J. Oviedo. "Detecting DNA damage through the COMET assay in the planarian model system".
- **Paul G. Barghouth**, Salvador Rojas and Néstor J. Oviedo. "DMAP1 is an epigenetic regulator of cell fate decision along the anterior-posterior axis during planarian tissue maintenance".
- **Paul G. Barghouth**, Eli Maciel and Néstor J. Oviedo. "Accelerated DNA damage repair result in radioresistant stem cells".
- **Paul G. Barghouth**, Eli Maciel, Ben Ziman and Néstor J. Oviedo. "TRAF proteins regulate tissue integrity and stem cell fate decisions during homeostasis and cancer progression".

- **Paul G. Barghouth**, Peter Karabinis, and Néstor J. Oviedo. "DNA damage response and repair are crucial for large scale tissue and organ regeneration in the planarian adult organism".

PATENTS

- Nadarasa Visveshwara, Stanley Stumpf, **Paul Barghouth**, Kin-Tong Gao, Katarina Short and Michael Urner. "Humidification of Ventilator Gases". February 2, 2017. **(U.S. Patent No. 20140338666)**
- Nadarasa Visveshwara, Stanley Stumpf, **Paul Barghouth**, Kin-Tong Gao, Katarina Short and Michael Urner. "Humidification of Ventilator Circuits". Patent pending, filing January 18, 2017. **(U.S. Patent No. US20170119992 A1)**

RESEARCH EXPERIENCE

Cancer and Tissue Regeneration Laboratory **2013-May 2019**

- Preceptor: Nestor Oviedo, Ph.D.
- Stem cell regulation at a systemic level to provide better therapeutic approaches in correcting cancer or regenerative disorders
- In vivo understanding of precancerous lesions at the subcellular, cellular and epigenetic levels, resulting in tumor progression and onset
- DNA damage repair during large-scale tissue regeneration and stem cell radio-resistance

Genetically Engineered Machine Laboratory **2012-2013**

- Preceptor: Marcos Garcia-Ojeda, Ph.D.
- Exploited the fermentation capabilities of E. coli to produce abundant amounts of hydrogen gas as an alternative fuel source
- Created SOPs and organized experimental design for group
- Presented team results at Stanford University during the iGEM regional meeting

MOLECULAR AND PROGRAMING TOOLSETS

Molecular Biology Tools

- Cloning and Transformation
- COMET Assay (DNA integrity)
- Confocal Microscopy
- Flow Cytometry/FACS
- Gibson Assembly
- Histology/Tissue Sectioning
- Immunohistochemistry (Cells and whole tissue samples)
- Whole mount *in situ* hybridization
- Karyotyping (chromosome Analysis)
- Planarian husbandry
- PCR/Quantitative PCR
- RNA, DNA and Protein Extractions
- RNA Interference (injections and feeding)
- RNA Sequencing (RNA/cDNA preparation)

Bioinformatics Tools

- RNA Sequencing Data Analysis (BLST, Gene Finding, Data Mining and Sequence Alignment)
- Bash Scripting /Command-Line Toolbox (Java and Perl programing)
- Statistical Analysis/ Data Visualization (R programming, Prism, ImageJ, FlowJo, Seaview and Adobe Illustrator /photoshop)

EMPLOYMENT AND PROJECT EXPERIENCE

Tergis Technologies LLC (Cofounder) **2017-Current**

- Medical devise start-up aimed on the abatement of Hospital Acquired Infections (HAIs) through mechanical means and not through radiation or pharmacological approaches
- Facilitating R&D and FDA clearance of medical devises targeting CLABSI and VAP infections
- Funded by National Science Foundation (NSF) I-Corps and UC Merced Venture Lab
- Awards: UC Merced proof of concept award (2018), UC Davis Big Bang (2018), Small business development center (2016), San Juaquin Valley entrepreneur challenge (2016)

Learn B.E.A.T. (Event Coordinator) **2014-2019**

- Nonprofit providing schools in Central Valley with hands on and proactive STEM related curriculum
- In collaboration with the Merced County Office of Education, we aim to immerse students (K-12) with basic STEM through hands-on activities during a five-week summer program (400 students)
- Created time tables, event breakdown sheets and academic curriculum aligned to Common Core State Standards (CCSS)

Children's Hospital Central California (Project Engineer) **2013-2014**

- Managed a diverse team of engineers to create medical grade ventilation devices within the neonatal intensive care unit (NICU)
- Communicated clearly and effectively with nurses and doctors to produce user friendly devices
- Received funds from the CHCC to create, patent and manufacture a fully functional prototype (**US15408852** and **US9561341B2**)
- Award winning prototype design and oral presentation at UC Merced's Annual Innovate to Grow

Oral Pathogen Immunology Laboratory (Lab Technician) **2011-2013**

- Preceptor: David Ojcius, PhD
- Worked in an aseptic and biohazardous environment (BSL2)
- Prepared buffers and solutions for cell culture (chlamydia trachomatis and porphyromonas gingivalis)
- Maintained inventory of lab consumables and cell stocks

Independent Contractor for Bandak Enterprises International **2008-2013**

- Main focus is shipping and handling of AnaNOitch products
- Advertising products, social media marketing, generating press releases and aided in social networking

Exam Proctor for UC Merced Disabilities Services **2010-2013**

- Facilitated and distributed exams to students that have special testing accommodations

TEACHING EXPERIENCE

- Teaching Assistant: Contemporary Biology Lab (1&2), UC Merced. **Fall 2013 – Fall 2018**
- Teaching Assistant: Contemporary Biology Discussion, UC Merced. **Summer 2017**
- Teaching Assistant: Thermodynamics, UC Merced. **Summer 2013**

PRIZES AND AWARDS

- Graduate Dean's Dissertation Fellowship January 2019

- Quantitative and Systems Biology travel award July 2018
- UC Merced Summer Fellowship Award May 2017
- UC Merced's Distinguished Leadership Award May 2013
- Second Place in Prototype Design, UC Merced Annual Innovate to Grow, Merced, CA, May 2013
- Second Place in Oral Presentation, UC Merced Annual Innovate to Grow, Merced, CA, May 2013
- Second Place in Poster Presentation, UC Merced Annual Innovate to Grow, Merced, CA, May 2013
- UC Merced Chancellor's Honor List (Two consecutive semesters with a GPA of 3.5 or higher) Spring 2013
- UC Merced School of Engineering Dean's Honor List (GPA of 3.5 or higher in a specific semester) 2010-2013

ORAL PRESENTATIONS

- **Paul Barghouth** and Néstor J. Oviedo. "Altered DNA repair Mechanism Initiate Cancer Progression During Adult Tissue Renewal" UC Merced QSB retreat, Midpines, CA, April 2019

- **Paul Barghouth** and Néstor J. Oviedo. "Altered DNA repair Mechanism Initiate Cancer Progression During Adult Tissue Renewal" International Planarian Meeting, Madison, WI, July 2018

- **Paul Barghouth** and Néstor J. Oviedo. "Altered DNA repair Mechanism Initiate Cancer Progression During Adult Tissue Renewal" Molecular and Cell Biology Seminar Series, Merced, CA, April 2018

- **Paul Barghouth[#1]**, T. Harshani Peiris[#1], Daniel Ramirez[#1] and Néstor J. Oviedo. "AKT Regulates Stem Cell Behavior During Tissue Renewal and Regeneration in Planarians" North American Planarian Meeting, Chicago, IL, September 2015

- **Paul Barghouth**. "Planarian Tissue Regeneration and Wound Healing". *Society for Advancement of Hispanics/Chicanos and Native Americans in Science (SACNAS) Research Seminar Series*, Merced, CA, February 2014.

- **Paul Barghouth**. "Planarian Tissue Regeneration and Wound Healing". Ingenieros Unidos IU-SHPE's Road to Research Seminar Series, Merced, CA, February 2014.

- **Paul Barghouth** and Daniel Ramirez. "Planarian Tissue Regeneration and Wound Healing". Yosemite Leadership Program S.T.E.M. Outreach Day, Merced, CA, March 2014.

- **Paul Barghouth**, Kin-Tong Gao, Katarina Short and Michael Urner. "Humidification of ventilator gases". University of California, Merced's Annual Innovate to Grow, Merced, CA, May 2013. ***(Judged Winning Presentation).***

- **Paul Barghouth**, John Flicker, Israel Juarez-Contreras, Marwin Ko, Norman Luong, Rumman Razzak, Sunny Seth, Michael Urner, Duc Vo, Catherine Vu, Yale Yuen, Nosherwan Zahid and Marcos E. García-Ojeda. "Streamlining bacterial production of hydrogen gas". International Genetically Engineered Machine Regional Jamboree, Stanford, CA, November 2012.

POSTER PRESENTATIONS

- T. Harshani Peiris, Udoka Ofoha, **Paul Barghouth**, Daniel Ramirez, Katie Wang, Emma Tkachuk, Manish Thiruvalluvan, Alexander Wilson-Fallon, Frank Weckerle, Elyse Ozamoto, and Néstor J. Oviedo. "Molecular regulation of cell proliferation and tissue repair along the anteropostior axis in the adult body". Gordon Science Conferences in Tissue Repair and Regeneration, New London, NH, June 2013.

- T. Harshani Peiris, Udoka Ofoha, **Paul Barghouth**, Daniel Ramirez, Katie Wang, Emma Tkachuk, Manish Thiruvalluvan, Alexander Wilson-Fallon, Frank Weckerle, Elyse Ozamoto, and Néstor J. Oviedo. "Molecular regulation of cell proliferation and tissue repair along the anteropostior axis in the adult body". Stem Cells and Aging Symposium, Santa Cruz, CA, May 2013.

- Daniel Ramirez, T. Harshani Peiris, Emma Tkachuk, **Paul Barghouth,** Manish Thiruvalluvan, Frank Weckerle, Elyse Ozamoto, and Néstor J. Oviedo. "AKT regulates stem cell behavior during tissue renewal and regeneration in planarians". Stem Cells and Aging Symposium, Santa Cruz, CA, May 2013.

- **Paul Barghouth**, Kin-Tong Gao, Katarina Short and Michael Urner. "Humidification of ventilator gases". University of California, Merced's Annual Innovate to Grow, Merced, CA, May 2013. ***(Judged Winning Poster Presentation).***

- Amanda Baijnauth, **Paul Barghouth**, etc and Marcos E. García-Ojeda. "Streamlining bacterial production of hydrogen gas". Merced City Council Funding Meeting, Merced, CA, March 2013.

- **Paul Barghouth**, John Flicker, Israel Juarez-Contreras, Marwin Ko, Norman Luong, Rumman Razzak, Sunny Seth, Michael Urner, Duc Vo, Catherine Vu, Yale Yuen, Nosherwan Zahid and Marcos E. García-Ojeda. "Streamlining bacterial production of hydrogen gas". International Genetically Engineered Machine Regional Jamboree, Stanford, CA, November 2012.

ORGANIZATIONS

BioMedical Engineering Society at UC Merced and National Member **2010-Present**
- Secretary **2013**
- Treasurer **2010-2011**

Phi Delta Epsilon International Medical Fraternity at UC Merced **2010-2013**
- Chapter President **2011-2012**
  - Lead a group of 50 members and coordinated events for charity fundraising and med school support
  - Raised over $8,000 in donations for the Children's Miracle Network Central California

ULISTAC Natural Area Restoration Project in Santa Clara, CA **2006-Present**

ABSTRACT

Continuous cellular division that is essential for the renewal of adult tissues, also provides recurrent opportunities for cancer development. However, it remains poorly understood how systemic tissue renewal leads to cancer formation. Planarians constantly renew their tissues and are susceptible to develop cancer-like phenotypes upon disruption of tumor suppressor genes (e.g. PTEN). PTEN is among the most commonly inactivated genes in human cancers, known to counteract the PI3K/AKT/TOR signaling cascade required for cellular proliferation, anti-apoptosis and growth. PTEN disruption in planarians is characterized by stem cell hyperproliferation and tissue colonization by abnormal cells, which rapidly kills the animal in roughly two weeks. In this study, we have catalogued the process of cellular transformation during tissue renewal and defined early and late stages (e.g. subcellular and cellular, respectively) of the PTEN phenotype in planarians. Our results indicate that early manifestation of cellular transformation in planarians have important similarities with cancer evolution in mammals. Furthermore, we can track pre-malignant abnormalities starting within 24-48 hours after PTEN disruption, which are attributed with DNA double stranded breaks, chromosomal abnormalities and checkpoint override. We have identified new genes and signaling pathways central to the regulation of cell cycle and DNA repair. Specifically, cell cycle checkpoint stability and DNA repair mechanisms; such as Rad54B and Rad51, respectively. Together, these signaling mechanisms facilitate the establishment and evolution of hallmarks of cancer (e.g. genomic instability, sustained proliferation and evasion of death) into the cancer-like phenotype. Our findings support the use of *PTEN(RNAi)* planarian model to obtain critical and new insights about cancer evolution during adult tissue renewal.

CHAPTER ONE

INTRODUCTION

1.1. Dissertation Introduction

The adult human body replaces 50-70 billion cells every day [1]–[6]. Roughly 90% of deaths caused by cancer worldwide originate from abnormalities in tissues that are continuously renewed by stem cells (SCs). Hence, to maintain homeostasis within organs and tissues, a delicate balance must be made between cellular division and programmed cell death. Adult tissue renewal is mediated by small pools of adult SCs, which can self-renew, differentiate and generate cellular progeny that carry out tissue specific functions in renewing, stressed or aged tissues. Thus, SCs regulate tissue repair, maintenance and regeneration throughout an organism's lifespan. However, the frequent renewal of aging and damaged tissues provides recurring opportunities for cancer development. Genomic instability (i.e. higher rates of genomic changes per cell division) is a pervasive trait in almost all cancer types. Nonetheless, the basic mechanisms regulating survival and growth of these cancerous cells during tissue renewal remain a puzzling issue within the biomedical field.

Cells are constantly exposed to DNA damage [7]. DNA integrity is under constant threat caused by multiple sources, including errors during DNA replication, products of intrinsic cellular reactions (e.g. reactive oxygen species) and environmental factors such as UV radiation and chemical exposure [3], [7]–[10]. In humans, DNA damage caused by exogenous and endogenous insults generate 10^5 DNA lesions per cell every 24 hours [11]–[13]. Long lived SCs are prone to harboring DNA damage derived mutations, which can alter their renewal and/or differentiation, providing a selective advantage for mutated SCs survival. If not repaired, DNA damage will be transmitted to SC progenitors and subsequently compromise tissue integrity and function [14]. Thereby, organisms have evolved highly efficient regulatory and surveillance machinery (e.g. cell cycle arrest, apoptosis and DNA repair) to prevent exhaustion and/or cellular transformation of SC pools during cellular turnover [7], [15]–[20].

Identifying genomic instability as a precursor to aging and malignant phenotypes is difficult to monitor during tissue renewal due to limitations with *in vivo*, *in vitro* and organ specific models available. The current techniques (e.g. transgenic or loss-of-function) used to establish genomic instability, aging and/or cancer models yield concerns of capturing relevant genetic or molecular changes during tissue renewal [21]. Thus, simultaneous analysis of DNA damage and SC-mediated tissue renewal at the organismal level would allow better appreciation of cancer evolution *in situ*. Studies merging homeostatic cellular turnover and SC response to DNA damage may provide important insights about intercellular crosstalk regulating cell fate decisions in the adult body. For example, there are patterns of regional differences of cell proliferation along the anteroposterior (AP) body axis that affect the fate of SCs and their progeny during tissue renewal, regeneration and carcinogenesis [22]–[28]. These regional differences are found across different species and recent studies have shown the fate of cells with DNA damage are susceptible to regional signals [16], [17], [29].

Cellular transformation is the process by which cells acquire cancer properties (i.e. transition of a normal cell to malignant). Despite its central role in cancer, it remains poorly

understood how cellular transformation is established during adult tissue renewal. The oncogene/tumor suppressor-induced DNA damage model (OTS-DDM) is the prevailing model outlining the process of cellular transformation [30]–[32]. It suggests a deregulation of genes controlling cellular growth (i.e. tumor suppressor and oncogenes) leads to the accumulation of DNA damage or DNA replication stress (e.g. stalling and collapse of DNA replication forks) within proliferative cells. Therefore, DNA damage is a pervasive feature present at early and initiating stages of almost all cancers [32]–[34]. Constitutively active DNA damage response and repair pathways ignite many hallmarks of cancer. For instance, DNA damage or replication stress can result in genomic instability and the selection of cells to escape apoptosis/senescence. In addition, sustained proliferation of these cells results in shortened telomeres and the establishment of replicative immortality (Fig. 1) [30], [31], [35]–[38]. Thus, proteins involved in the DNA damage response and repair pathways are becoming novel anti-cancer therapeutic targets. Nonetheless, current DNA damage pathway agents lack specificity and a defined mechanism of action [21],

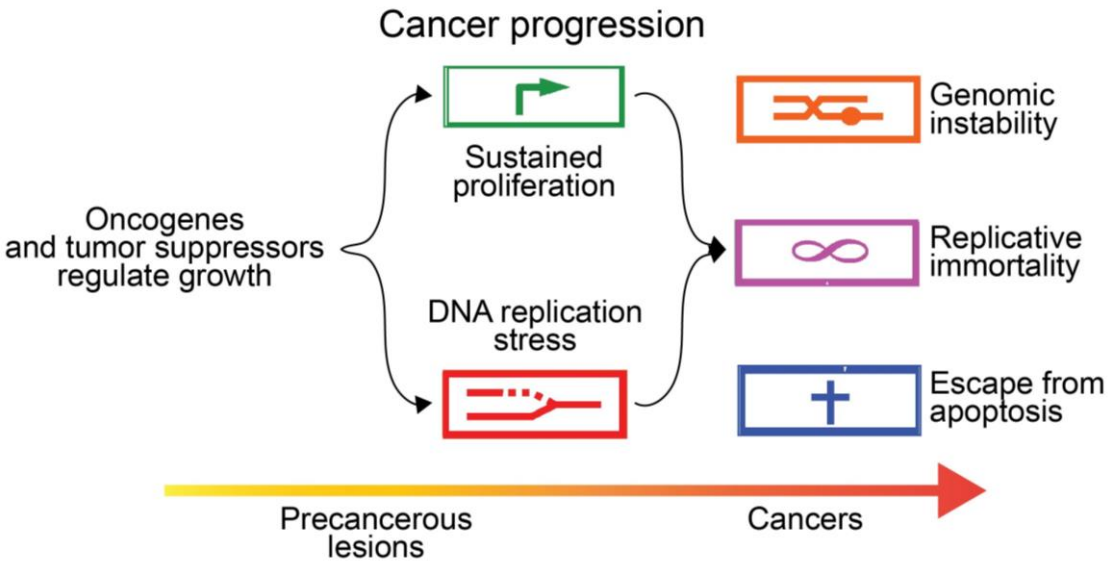

Figure 1. The oncogene-tumor suppressor- induced DNA Damage/replication stress model for cancer development derived from Macheret and Halazonetis 2015. Alterations to growth promotor or suppressor genes create the primary hallmarks of cancer: sustained proliferation and DNA damage/replication stress. As cancer progresses, the latter hallmarks emerge such as replicative immortality, genomic instability and escape form apoptosis/senescence.

[36], [39]–[41].

In this dissertation, we will capitalize on a unique model system, the planarian flatworm, *Schmidtea mediterranea*, as a novel archetype to study OTS-DDM in the adult body. Planarian possess high rates of cellular turnover and tissue regeneration, driven by adult pluripotent SCs called neoblasts [42]. Neoblasts possess clonogenic properties and are the only cells in the organism with the capacity to divide [43]–[49]. Continual proliferation of neoblasts support the renewal of roughly 40 different tissue types in their bodies and facilitate studies about SC-mediated tissue renewal and DNA damage [16], [17], [29], [42]–[44], [50]–[55]. Neoblasts undergo cellular transformation when highly

conserved tumor suppressors (e.g. PTEN, Rb, MLL3/4, SMG-1 and p53) are inactivated or by pharmacological alterations [45], [56]–[63]. Furthermore, PTEN, one of the most commonly inactivated tumor suppressor genes found in cancers can be disabled in planarians through RNA interference (RNAi), resulting in tumor formation and lethality within two weeks [56]. Planarian provide a novel and simplified platform for studies of cancer initiation in the adult body. Here, we will provide new arenas to investigate the role of the OTS-DDM model, *in vivo*, to further elucidate the mechanisms underlying DNA damage and signals contributing to cellular transformation.

1.2. Research Summary

The planarian will be introduced as a novel model to study evolutionary conserved DNA damage response and repair pathways, setting the stage for the use of planarian to study the OTS-DDM model, *in vivo*. We aim to shed light on system wide cell fate decision of SCs harboring genomic instability during adult tissue homeostasis, cellular turnover and regeneration. Thus, we will describe primarily, the response of neoblasts to the induction of DNA damage and the reestablishment of tissue homeostasis. Secondly, we will highlight body-wide signals affecting cellular decisions (e.g. survival, proliferation, and death) in the presence of genomic instability within our genetically induced-DNA damage models. Third, we will discuss transcriptomic changes of DNA damage response and repair signaling pathways during large-scale tissue regeneration. Lastly, we will provide an *in vivo* validation of the transcriptomic analyses conducted during planarian head regeneration. Overall, results indicate that the DNA damage response and repair signaling pathways are central for tissue homeostasis and regeneration in the planarian.

Next, we examine the molecular conservation of the PI3K/PTEN/AKT/TOR signal transduction cascade in the planarian model. A discussion on the signaling pathway will be presented as well as the roles of key components of the cascade (e.g. PTEN, AKT and TOR) during cancer and its progression. The conservation of this pathway within the planarian model will be determined through bioinformatic approaches, focusing on key components of the PI3K/AKT/PTEN signaling cascade. Lastly, a discussion of four key papers involved in characterizing of planarian *Smed-PTEN*, *Smed-AKT* and *Smed-TOR* will be made. Here, we will further elucidate the roles of these signaling molecules by using updated single-cell RNA sequencing data to determine expression levels and neoblast lineage enrichment. The goal of this discussion is to showcase the planarian as a novel cancer model to study cellular transformation in the context of tissue renewal and present unanswered questions within the *Smed-PTEN* cancer model.

The next chapter will discuss the role of the proto-oncogene *Smed-AKT* during planarian tissue homeostasis and regeneration. We find that *Smed-AKT* regulates the balance between cell death and proliferation as results showed an increase in cell death accompanied by a decrease in neoblast division. The reduction of neoblasts results in the decline of differentiated tissue integrity such as the nervous and ciliated structures. In addition, *Smed-AKT(RNAi)* animals exhibited bloating, elongation and edema-like phenotypes because of a decaying filtration and excretory systems. Furthermore, we identify that *Smed-AKT* expression is critical for planarian head regeneration and blastema formation. Lastly, a theoretical discussion of the role of *Smed-AKT* overexpression within the planarian cancer model *Smed-PTEN(RNAi)* will further support the use of the planarian to study the OTS-DDM model *in vivo*.

Succeeding this chapter, we will discuss the functional role of PTEN within the nucleus. Majority of the studies in the field, focus their attention on the cytoplasmic role of

PTEN in counteracting the PI3K/AKT/TOR signaling cascade. However, the role of nuclear PTEN provides a unique opportunity to study the initiation and onset of cancer and its progression into malignancies. As PTEN contains no canonical nuclear shuttling sites, we discuss the role of PTEN-C-terminal segment as a crucial component of its nuclear translocation. Nuclear PTEN is found to regulate centromere stability, cell cycle and the DNA repair process via direct interaction with Rad51 and an indirect role of protecting the tumor suppressor p53 from degradation. We focus on specific roles of PTEN during DNA replication (e.g. firing and restart of replication origins) and mitotic division checkpoints in relation to the fidelity of chromosome segregation. Here, we will propose the planarian model as an amenable alternative to understand the process of cellular transformation during tissue renewal.

Lastly, we will discuss the conserved role of planarian PTEN within the nucleus and its relation to the OTS-DDM model. Primarily, we catalogued the process of cellular transformation during tissue renewal and defined early and late stages of the *PTEN* phenotype. Our results suggest that early manifestation of cellular transformation in planarians involve deregulation of nuclear PTEN, cell cycle checkpoint stability and DNA repair mechanisms. Furthermore, we identified that PTEN is required for the induction of cell death of cells harboring DNA damage. Lastly, we identified that cells carrying DNA damage and DNA replication stress are capable of bypassing cell cycle checkpoints and abnormally divide. Together, these phenotypes facilitated the establishment and progression of genomic instability during tissue renewal. We also add to the OTS-DDM two additional hallmarks (e.g. mitotic stress and evasion of death) as precancerous characteristics, which lead to cancer progression. Collectively, the results presented here introduce a new model to the study of cancer evolution and identify a new paradigm to analyze *in situ* cellular transformation in a time/cost-effectively manner.

CHAPTER TWO

BACKGROUND

Planarian as a model organism to study DNA damage during tissue renewal and regeneration

2.1. Introduction

The lifespan of an organism relies on faithful renewal of aging and damaged tissues [64]–[67]. SCs generate cellular progeny to maintain adult tissues and in humans, this process requires the daily demand of billions of cells that could span over a century [2], [68]–[70]. Tissue renewal is extremely complex and appears to be unsynchronized among tissues. Turnover rates may be based on tissue's physiological conditions and/or SCs response to DNA damage. For instance, the architecture of epithelial tissues within the small intestine and colon are quite similar as their SCs are localized to the base of the crypt and their differentiated cells are near the lumen. However, their rates of cellular turnover are substantially different. Specifically, small intestine epithelial tissues renew every 5 days while colonic tissues turnover approximately every 20 days [71], [72]. Other differences in turnover rates have been identified in skin epidermal cells and cells within blood tissue (e.g. 10-30 days and 1 day-several months, respectively) [73]–[76]. Tissue-specific SC turnover maintains organ functionality; however, it remains poorly understood how coordination and faithful turnover occurs as organisms age.

This chapter addresses critical problems of SC derived DNA damage: (1) during tissue renewal and homeostasis, (2) cellular turnover in the complexity of adult body and (3) systemic cell-fate decisions that maintain genomic integrity. Primarily, we will discuss various DNA lesions and the molecular cascades involved in their repair. Here, we emphasize on double-strand breaks (DSBs), the most hazardous form of DNA damage [11], [15], [77], [78]. Secondly, the proposal of a novel organism, the planarian, *Schmidtea mediterranea* to track the onset of DNA damage mediated aging and degenerative disease. In addition, how planarian can provide insights to DNA damage response (DDR) and repair during adult tissue maintenance and regeneration. Lastly, a discussion on how the DDR is a critical component of the large-scale tissue homeostasis and regeneration in planaria. Overall, this chapter will discuss the use of planarian as a model to address evolutionarily conserved mechanisms of DDR and DNA repair during adult tissue renewal.

2.2. Tissue renewal and stem cell response to DNA damage

Exposure to DNA damaging agents generally lead to lesions that are common throughout all living organisms [7], [12], [18]. The chemical structure of DNA contains regions that are sensitive to both endogenous and exdogenous insults or lesions. Spontaneous endogenous factors such as hydrolysis and chemical reactions (e.g. cellular

metabolism and reactive oxygen species (ROS), respectively) can alter the structure of DNA by creating abasic sites, base deaminations, 8-oxoguanine lesions or base oxidation. In addition, endogenous DNA replication errors can produce nucleotide substitutions, insertions or deletions as one mistake per 100-1000 nucleotides is made during DNA replication [79]. Environmental factors also give rise to DNA alterations, such as UV light and chemical reagents that can induce nucleotide modifications. Moreover, DNA single stranded breaks (SSBs), double strand breaks (DSBs), interstrand and intrastrand crosslinks (ICLs) are exploited by the clinical use of ionizing radiation, X-rays and chemotherapy drugs. These lesions being the most hazardous within the genome, inhibit essential processes such as DNA replication and gene transcription, resulting in highly mutagenic alterations and genomic instability if not repaired (Fig. 1A).

Organisms have formed highly conserved pathways to counteract DNA damage by employing cell-fate decisions to maintain long-term genomic stability and tissue homeostasis. This is known as the DNA damage response (DDR) and it consists of

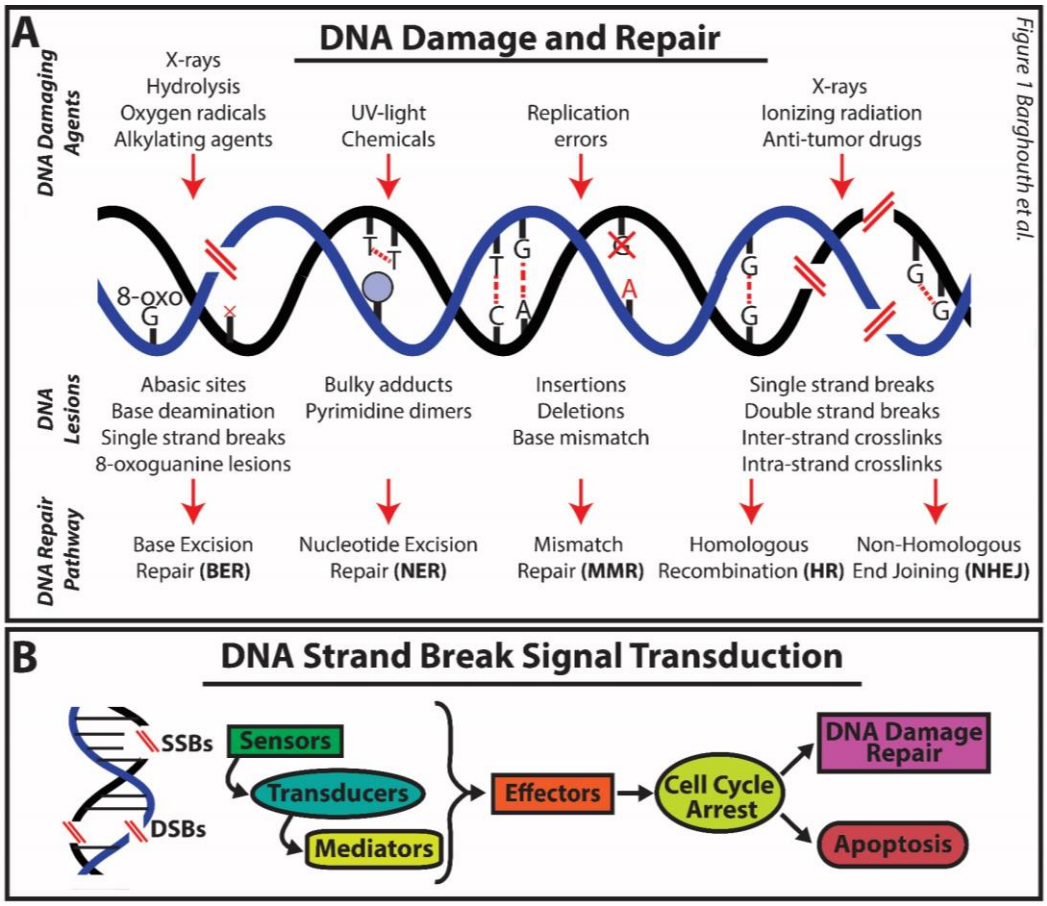

Figure 1. DNA damage responses and stranded break signal transduction. (A) The illustration summarizes different types of DNA damaging agents, the genomic lesions they produce and the specialized DNA repair pathway deployed. For example, exposure to ionizing radiation may lead to DNA single and/or double-stranded breaks and crosslinks that can be repaired through HR or NHEJ (B) Different molecules mediate the repair of DNA strand breaks. Commonly, a signal transduction cascade involving sensors, transducers, mediators, and effector molecules that together influence cellular fate decisions to repair the damage or undergo programmed cell death

sensors, transducer kinases, mediators and effectors that are continuously deployed with the goal of reestablishing genomic integrity [7], [15]–[17], [19] (Fig. 1B). Specifically, in the presence of SSBs, DSBs or ICLs, organisms employ a series of cascades that sense damage such as the MRN complex (MRE11-Rad50-Nbs1), Ku70/80 heterodimer and RPA (replication protein A). Once sensed, signal transduction is established by ATM (ataxia telangiectasia mutated) or ATR (ataxia telangiectasia and Rad3-realted) proteins which mediate this response. Effector kinases and proteins that regulate cell cycle checkpoints (e.g. Chk1, Chk2, p53 and CDC25s) mediate cell-fate outcome. Central to this process are the well-studied tumor suppressors p53 and Rb (retinoblastoma) proteins which work in tandem to mediate effector outcomes, consisting of cell cycle arrest, quiescence, senescence, apoptosis and DNA repair. Overall, these signaling cascades mediate cell-fate decisions in the presence of DNA damage (Fig. 2).

Activation of DNA damage sensing cascade leads to the phosphorylation and stabilization of p53. Nuclear accumulation of p53 and upregulating of its target genes (e.g. p21-cyclin-dependent kinase inhibitor 1), mediates cell cycle arrest to initiate DNA damage repair or induce programmed cell death [7]. The p53-p21 axis arrests cell cycle at G1/S or G2/M checkpoints. The inhibition of CyclinD-CDK4/6 complex via p21 promotes Rb hypo-phosphorylation which inhibits the E2F transcription activity and cells to bypass the G1 restriction point (R-point). Rb activity allows for cell cycle arrest in G1 phase and the maintenance of cells within the G0 quiescent state. Further, in the presence of DNA damage Rb and p53 have been implicated in cellular senescence which blocks cellular renewal giving rise to aging phenotypes and inhibits the rise of cancer cell accumulation. Moreover, the loss of Rb/p53 and the re-expression of telomerase proteins are key steps

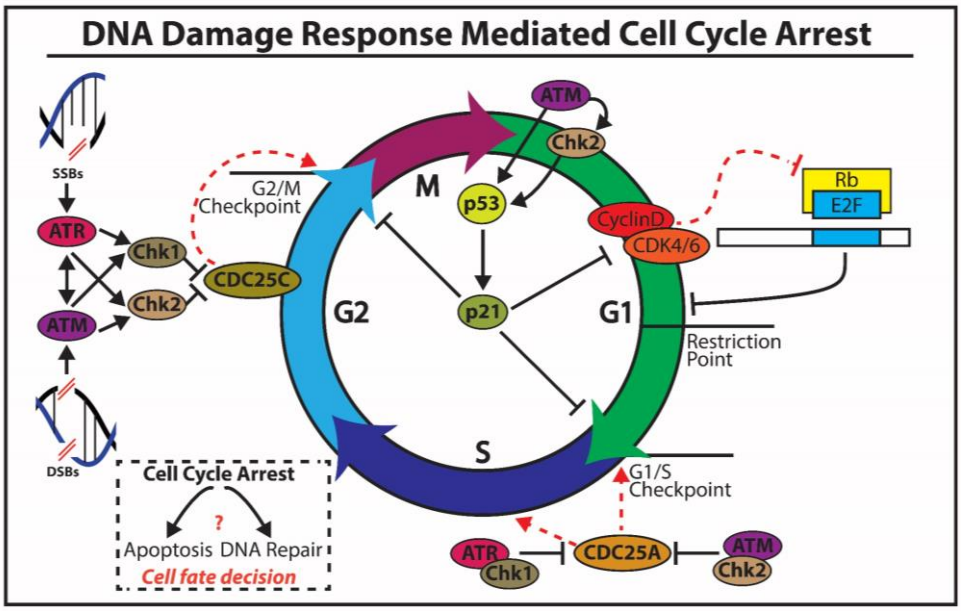

Figure 2: DNA damage response's regulation of cell cycle. The protein p53 is central to the cell cycle and influence cell cycle arrest at all three checkpoints through p21 upon upstream signals. Rb regulates the G1/S transition and counteracts Cyclin D and CDK4/6 preventing cells for passing the restriction point. CDC25A is inhibited by either ATM and/or ATR inhabiting the G1/S transition. Furthermore, ATM and ATR can regulate damage formed in G2/M phases through the regulation of CDC25A thus inhibiting cell division. Once the cycle is in arrest, cell fate decision such as apoptosis or DNA repair will be determined in response to the severity of lesion.

for cancer cells to escape cellular senescence and drive malignant transformation. Thus, further understanding how cell-fate decisions are determined in the presence of DNA damage is crucial in understanding aging and malignant phenotypes.

A positive correlation between DNA repair and lifespan of organisms (e.g. humans and naked mole rates) have been identified [64], [65], [80], [81]. Several lines of evidence imply continued exposure of SCs to DNA damage plays a major role in age-related dysfunctions (e.g. cancer and degenerative diseases) and their inability to repair DNA results in SC attrition, cellular transformation and aberrant differentiation [8], [9], [82]. The mechanistic process by which genome integrity declines with age is not well understood and may be due to different cell-fate decisions in the presence of DNA damage within epithelial tissues. For instance, SC-fate decisions can produce mixed outcomes in the presence of DNA damage, either preserving or deteriorating genomic stability. Epidermal tissues are constantly being exposed to genotoxic stress (e.g. UV radiation and cellular metabolism) and despite their SCs (e.g. melanocyte and bulge SCs) residing within the same hair follicle niche, their cell-fate decisions differ drastically. In the presence of DNA damage, bulge SCs display accelerated DNA repair through the error-prone non-homologous end joining pathway, thus increasing SC maintenance. In contrary, melanocyte SCs do not induce DNA repair but activate irreversible terminal differentiation which depletes the SC pool. Another example can be seen within the intestine. Upon exposure to irradiation, small intestinal SCs undergo massive apoptosis and is attributed to increased activation of p53 tumor suppressor signaling, reduced anti-apoptotic BCL2 expression and lack DNA repair activity [83]. Interestingly, colonic SCs require eight times the amount of irradiation to exhibit apoptosis rates similar to small intestinal SCs. This is attributed to colonic SCs possessing low levels of p53 signaling and high levels of BCL2 expression [84]–[87]. Due to the response to DNA damage, it is well noted that the rise of malignancies, despite cellular turnover rates, are rare in intestinal tissues versus colon cancers which are placed within the top five most common cancers. Overall, SC-fate decisions can eliminate pre-cancerous lesions and promote aging phenotypes or compromise genomic integrity to maintain a mutation enriched SC pool.

2.3. Repair of DNA double stranded breaks

Eukaryotic organisms have adapted highly conserved repair mechanisms that can recognize and repair an array of DNA lesions with varying fidelity and mutagenic consequences. The most severe and less understood form of DNA damage are DSBs and the pathways involved in their repair. DNA insults give rise to roughly ten DNA DBSs per cell per day [77], [88], [89] and occur when both strands of the DNA double helix are broken in close proximity. DSBs can be repaired through the following mechanisms: non-homologous end joining (NHEJ) and homologous recombination (HR) and their alternative pathways: alternative end joining (alt-EJ) and single strand annealing (SSA).

2.3.1. Non-homologous end joining (NHEJ)

NHEJ is active throughout the cell cycle but is pervasive during the G0 and G1 phases. The Ku70-Ku80 heterodimer first recognizes and docs onto the blunt ends of DSBs, thus recruiting, facilitating and improving the binding of proteins needed to join them together. This repair lacks micro-homology (e.g. DNA-dependent protein kinase catalytic subunit (DNA-PKcs)). Interestingly, the two DNA ends may act independently of each other, therefore, the processing of DNA ends is highly error-prone. Thus, NHEJ may alter the original DNA template leading to insertions, deletions, nucleotide change or

chromosomal translocations. Acquired errors through NHEJ are corrected by the high-fidelity mismatch repair (MMR) pathway.

2.3.2. Homologous recombination (HR)

HR repairs DSBs using a template strand and relies on the presence of DNA segments sharing high homology between the donor and acceptor, allowing for HR to conduct error-free repair. Science HR requires undamaged chromosomes to initiate strand invasion, this pathway can only be activated after a cell duplicates its DNA (S and G2/M). Three main phases comprise HR signaling: presynaptic, synaptic and postsynaptic. These stages prepare the DNA through multiple series of end restrictions to contain 3'-end overhangs or 5'-end restrictions to facilitate proper HR repair. Upon DNA damage, the exposed single stranded DNA are coated with RPA, which stabilizes the strand, prevent its degradation and formation of secondary structures. Rad51 recombinase (Rad51) is a key player in stand invasion and homologous search which must replace RPA though Breast Cancer Type 2 Susceptibility Protein (BRCA2) facilitation. In the synaptic phase, Rad51 filaments span over several thousand base pairs of DNA and require ATP hydrolysis to tightly bind Rad51 to DNA. Post binding, Rad51 filament-mediated strand invasion is initiated. Alterations in several HR related proteins have been of high clinical significance as their mutation lead to aging phenotypes or cancer predisposition disorders such as Bloom's syndrome, Cockayne syndrome, Fanconi's anemia and Hereditary breast-ovarian cancer syndrome [39], [90].

2.3.3. Double strand break repair pathway alternatives and choices

Studies are currently reporting that cancer SCs may take advantage of faults within DNA repair mechanisms which are commonly used by tissue-specific SCs to mediate resistance to chemo- and radio- therapies. Regulated DNA damage repair acts as an anticancer barrier inhibiting the progression of DNA damage to malignant transformation [91], [92]. In hereditary breast and ovarian cancer (HBOC) patients the mutations in one of the two BRCA1 or BRCA2 genes result in increased risk for cancer initiation. Mammary gland cancer SCs exhibit increased expression of many DNA damage response and repair genes (e.g. p53 and Rad51) [93], [94]. For instance, in HR deficient BRCA1 or BRCA2 mutant tumors the over expression of p53 is accompanied by an elevation of AKT and Wnt oncogene signaling activity [93], [95]. Further, the elevation of RAD51 protein stabilization is seen to support triple negative breast cancers, genomic instability and the transcription of pro-metastatic CCAAT/Enhancer Binding Protein, Beta (c/EBPβ) signaling [94], [96]–[98]**.** Concurrent inhibition Rad51 and Poly(ADP-Ribose) Polymerase (PARP), a key determinant in alternative end joining DNA repair, have been shown to rescue and sensitize breast cancer SCs [98]. Continual DNA damage response signaling and HR dysregulation in cancer SCs allow for the activation of alternative error-prone DNA repair pathways such as SSA, which is usually suppressed by Rad51 accumulation, thus inhibiting Rad52 activity during DSB repair.

Proper and timely selection of DSBs repair pathways are required for faithful DNA repair. HR induced activity during G0 and G1 phases of the cell cycle is often mutagenic as sister chromatid are needed as a template [99]. The selection of DSB repair pathways is determined by three independent variables: the resection of DNA blunt ends, cell cycle phase and the abundance of regulatory proteins in each cell cycle phase. NHEJ is active throughout the cell cycle but is predominantly activated during the G1 phase, when it relies on alternative homologous sequences (e.g. repetitive elements) with little or no microhomology <20bp (Fig. 3A, B). In G1-phase, HR, Alt-EJ and SSA are limited by the

lower efficiency of MRN and RB binding protein 8, endonuclease (CtIP). Furthermore, the abundance of ATM, H2A Histone family member X, gamma (γH2AX), mediator of DNA damage checkpoint 1 (MDC1) and p53 binding protein 1 (53BP1) regulatory proteins result in an inhibitory activity. Together, these proteins and a high affinity for the Ku70/80 complex; commit the cell to NHEJ repair. NHEJ remains an active player in DSB repair later in the cell cycle however, its efficiency is reduced due to the decreased inhibitory effect of G1 regulatory proteins and increased abundance of MRN and CtIP. In the presence of microhomology, Alt-EJ, SSA and HR repair pathways are employed (e.g. <25bp, >25bp and >50bp, respectively). In the S, G2, M phases, additional series of DNA end restrictions are mediated by regulatory proteins, required to have error-free DSB repair (e.g. PARP1, BLM, Exo1 and RPA).

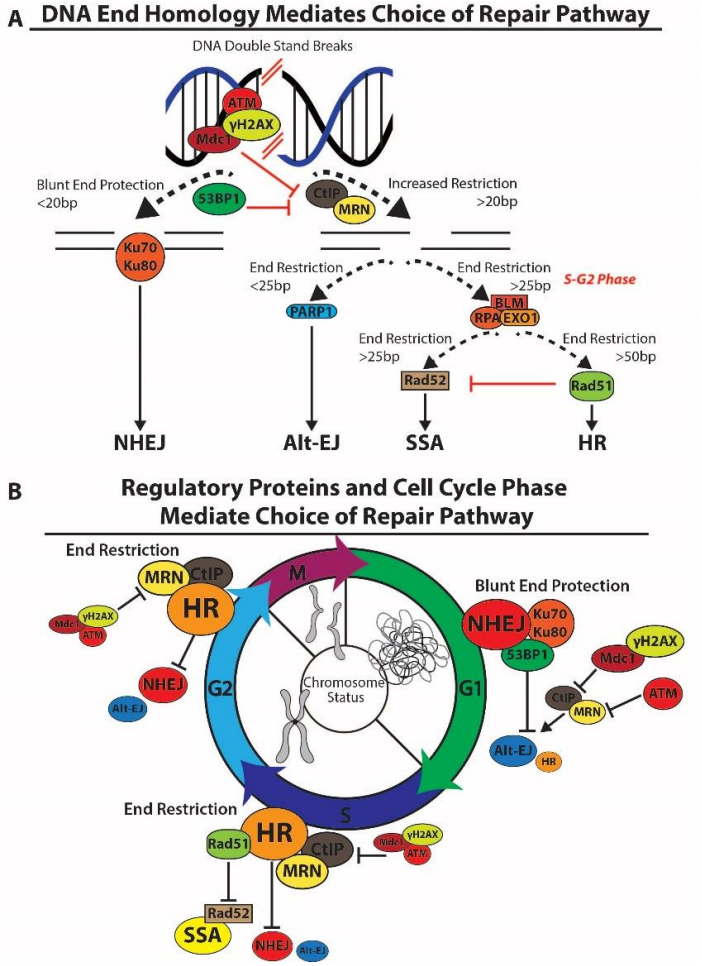

Figure 3. (A) DSB repair is mediated by four different pathways (*e.g*. NHEJ, Alt-EJ, SSA and HR) and these pathways are deployed dependent on blunt end formation or restriction. (B) Moreover, the selection of which pathway is also determined by three mechanisms: (1) the status of chromosome homology which is dependent on what phases of the cell cycle DSBs occur (*e.g*. homology during S-G2-M phases which favors HR). (2) The abundance of regulatory proteins in each cell cycle phase. For example, increased expression of ATM, Mdc1 and 53BP1 have been shown to favor NHEJ in the G0/G1 phase of the cell cycle by suppressing MRN and CtIP expression needed for HR-mediated repair. (3) Lastly, the restriction of DNA blunt ends. The length of DSB nucleotide base pairs give rise to blunt end protection or a series of end restrictions. (*e.g*. <20 bp for NHEJ and >50 bp for HR mediated repair).

2.4. Planarian as a model to study DNA damage and tissue renewal

Planarians are members of the phylum Platyhelminthes (flatworms) and are classically known for their robust regenerative capabilities within seven days (Fig. 4A) [50], [100]. Planarians undergo constant renewal and repair upon injury of their organs and tissues (e.g. digestive, nervous, muscle, etc.) [42], [101]. The planarian *Schmidtea mediterranea*, which is the most common species used worldwide to study aspects of tissue homeostasis, contains a large pool of SCs called neoblasts. Neoblasts are recognized as the only cells with capacity to proliferate in *S. mediterranea* and therefore, serve as the sole source of new cells that support the dozens of different tissues types [42]–[44], [50]–[52], [102]. The neoblast diversity is only beginning to be elucidated and so far, twelve subpopulations have been described (e.g. Nb1-12) support six different lineages and display restricted potential to generate and maintain tissues within the endoderm, mesoderm and ectoderm (Fig. 4B) [43], [44], [103]–[106]. This diversity within planarian neoblasts allows for the integration of local and environmental stimuli throughout

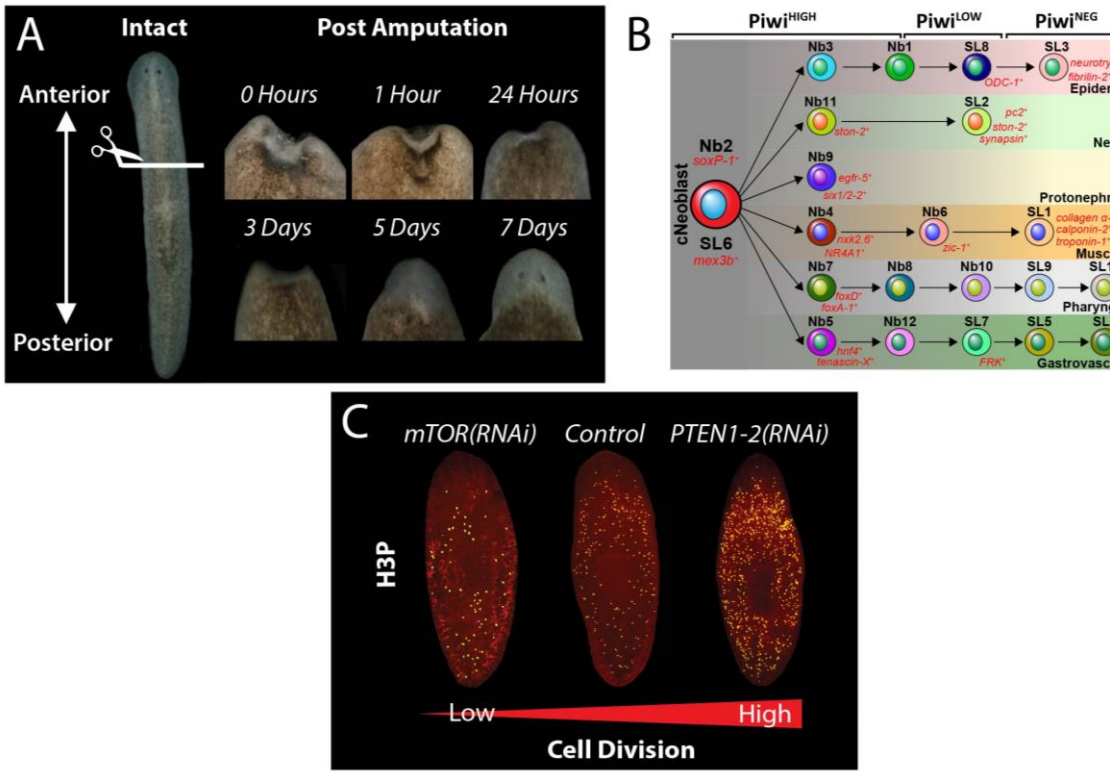

Figure 4. Planarian a novel model organism. (A) Images of a live worm (left) amputated pre-pharyngeal; images on the right show the regeneration of the anterior portion including the head. Time-lapse images depict proper wound healing response and blastema formation in a regenerating planarian. By Day 7, the fragment has regenerated into a completely functional animal. (B) Linage model for planarian neoblasts consists of 12 major classes representing 6 distinct tissue lineages. Image derived from Zeng et al. 2018. (C) Image depicts cell division (yellow dots, H3P immunostaining) after RNAi of TOR and PTEN genes in comparison to control (mock-RNAi). TOR (RNAi) reduces mitotic activity while PTEN (RNAi) induce the opposite effect.

its lifespan to maintain tissue homeostasis. Similar to SCs in other organisms, neoblasts are in constant crosstalk with their surroundings and are influenced by local and systemic signals involving metabolic status, neural inputs, tissue integrity, etc. In the presence of nutrients, planarians increase the body size by incorporation of new cells. Conversely, starvation conditions lead to reduction in animal size by elimination of cells that maintain body proportion [74], [107]–[109]. Neoblasts also sense and respond to tissue injury by mounting a multi-step proliferative response that mediates regrowth of missing and damaged parts[53], [110]–[112].

The capacity to regulate SC division in response to physiological demands and injury has been attributed to the conserved tumor suppressors and oncogenes within the planarian (e.g. PTEN, AKT, p53, Rb) [45], [56], [57], [109]. Planarian cells rarely develop cancer but can be forced to undergo cellular transformation after treatment with carcinogenic compounds or manipulation of tumor suppressor genes (Fig. 4C) [45], [45], [57]–[59]. Thus, preservation of DNA integrity is paramount for tissue regeneration and extended lifespan in planarians. Recent interest in dissecting mechanisms of DNA repair in planarians revealed evolutionary conservation of key regulators such as *Rad51, p53, Ubc9, Brca2,* and *Rad54B* that are activated in response to endogenous and exogenous environmental insults [16], [17], [60], [113]–[115]. Functional studies of DNA repair pathways identified patterns of SC exhaustion and tissue renewal defects similar to those observed in mammals [82]. These planarian features confer unique advantages to analyze critical parameters in response to DNA damage in the context of the whole body. Thus, we propose the use of *S. mediterranea* as a simplified platform to address cell fate decisions in the presence of genomic instability during large-scale SC-mediated cellular turnover and tissue repair.

2.5. Evolutionarily conserved DNA damage repair mechanisms exist in planarian

Older specimens of *S. mediterranea* are phenotypically indistinguishable from younger ones, which highlight the efficient mechanisms of unlimited cellular renewal in planarian [42]. This also implies that planaria contain efficient DNA repair mechanisms to combat endogenous and exogenous insults that normally deplete SCs in adult tissues, thus preventing aging and cancer-like phenotypes [58]. Indeed, high-throughput query on genomic resources [116], [117] have allowed us to identify a wide range of DSB recognition and repair homologs in planaria (Fig. 5). Specifically, we uncovered components of signaling pathways involved in DNA damage recognition, signaling transduction and effector outcome (*e.g*. cell cycle arrest, cell death and DNA repair). Though DNA damage can affect cells in numerous ways, DSBs represent the most severe form of DNA damage as they occur when both strands of the DNA double helix are broken in close proximity. Two DSBs within a cell are capable of forming chromosomal translocations and some estimates establish that 10–50 DSBs occur per cell per cycle [11], [77], [78], [118]. As previously discussed, DSBs can be repaired through: non-homologous end joining (NHEJ), homologous recombination (HR) and their alternative pathways: alternative end joining (alt-EJ) and single strand annealing (SSA).

Detailed evaluation of the planaria genome revealed an important molecular conservation of the DDR mediator γ-H2AX and DSB repair protein RAD51 (*e.g*. ∼65% and ∼81%, respectively) (Fig. 6A, B). Further analysis also showed the presence of key signatures of their phosphorylation sites (*e.g*. S-Q motif the signature for γ-H2AX) or binding domain activity (*e.g*. Rad51′s Walker A/B, L1/2 and BRC domains) (Fig. 6A, B). The molecular conservation of these molecules in planaria also facilitates the possibility

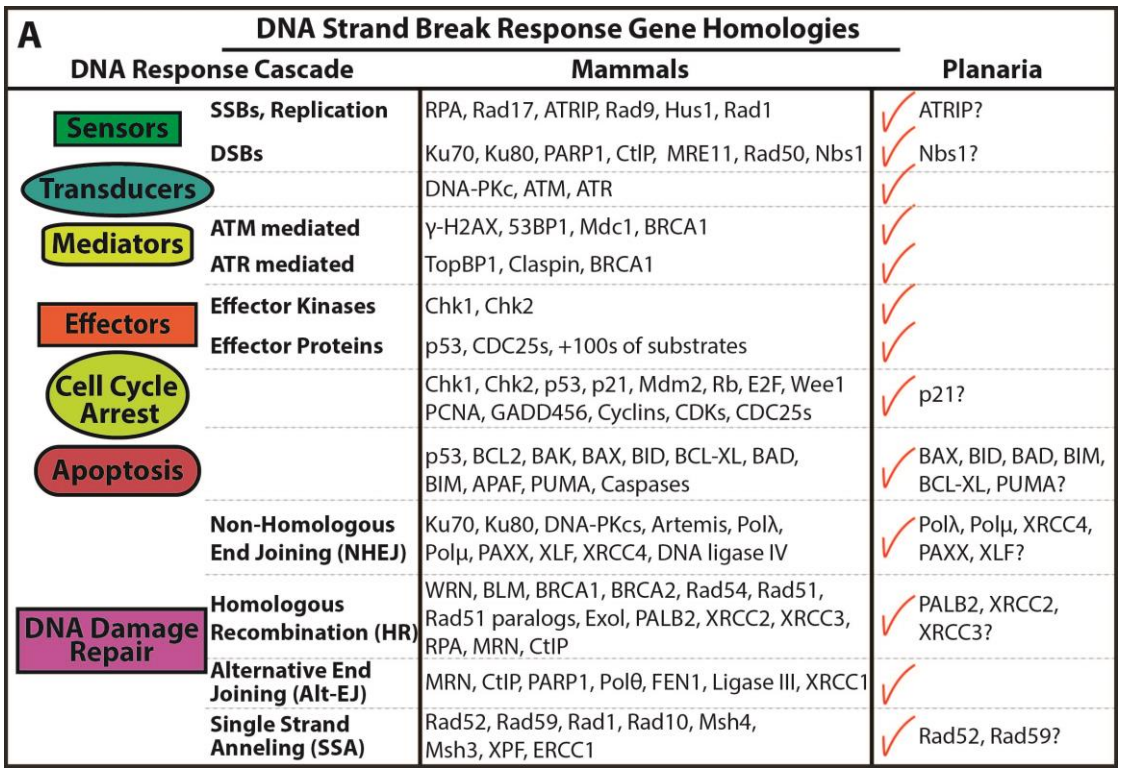

Figure 5. Planarian display evolutionary conservation of the mechanisms involved in DNA double strand break (DSB). (A) Gene homologies for sequences regulating DDR and signal transduction mechanisms are found in planaria. For simplicity the attention is mostly focused on mediators of DSB. Checkmarks indicate conservation between the planarian species S. *mediterranea* and humans. However, some genes remain unfound in the planarian genome indicated by a question mark.

of using commercial antibodies to evaluate the spatial distribution of DDR proteins at cellular and organismal levels (Fig. 6C) [16], [17], [119]. DSBs can be induced in planaria through ionizing radiation (IR), RNA interference (RNAi) and through drug exposure such as methyl methanesulfonate (MMS) [16], [17], [59]. In order to gauge the effects of these DSB inducing strategies, three key strategies have been optimized (*e.g*. TUNEL, COMET assay and karyotyping) [16], [17]. The COMET assay, under alkaline conditions (pH > 13), is commonly used to monitor DNA integrity with focus on DSBs. In addition, karyotyping protocols have been optimized to assay abnormalities found in neoblast-specific chromosomes [16], [17], [120]. FACS protocols have been implemented to monitor neoblast populations, cell cycle progression and cellular apoptosis (Fig. 6D) [46], [101], [121], [122].

Planaria tolerate relatively high doses of IR, far surpassing the thresholds of exposure that are known to be lethal in mammals [123], [124]. Thus, the DDR in planaria can be analyzed by exposing animals to IR. For example, exposing planaria to IR above 3000rad irreversibly eliminates neoblasts, abolishes regeneration, and leads to animal death in about three weeks [50], [105], [113], [125]–[127]. Lethal doses of IR has been traditionally used as a tool to identify neoblast-associated markers and mechanisms of neoblast repopulation during tissue transplantation and irradiation [50], [105], [113], [125]–[127]. However, data mining of recent transcriptional data involving samples from a seven day time course upon lethal IR [54] revealed a persistent upregulation of genes involved in DNA damage sensing and signal transduction of DSBs throughout the time course.

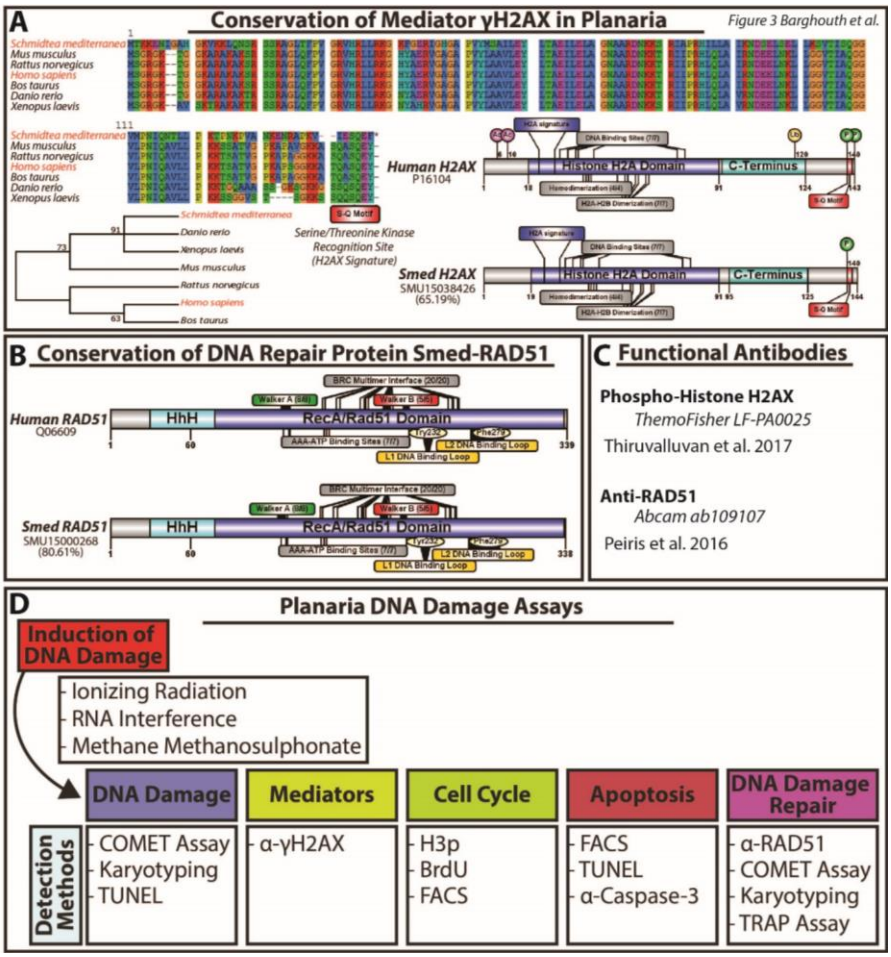

Figure 6. Molecular conservation of key proteins regulating DNA double strand break repair and DNA damage assays in planarian. (A) Protein alignment of planaria γH2AX and homologs indicate conservation of γH2AX 's S-Q motif among species The S. *mediterranea* mediator γH2AX scores 65.19% similar to the human homolog. Sequence alignment was obtained by CLUSTALW. Using Illustrator for biological sequences (IBS version 1.0) we were able to create diagrams for both human and SMED-γH2AX protein sequences. Human protein length is 143 amino acids (aa) *versus* 144aa in SMED-γH2AX. Within this protein both the planaria and human sequences contain Histone H2A domain (dark blue, 73aa long) and a C-terminus (light blue, 30aa long). Within the Histone H2A domain both contain the H2A signature (6aa long), DNA binding sites (7/7 sites) homodimerization sites (4/4 sites) and H2A-H2B dimerization sites (7/7 sites). Importantly, both contain the S-Q motif (red domain) phosphorylation on Ser139 site in the S-Q motif. However, human γH2AX contains acetylation sites (6aa and 10aa), ubiquination site at 120aa and another phosphorylation site at 143aa. (B) The S. *mediterranea* RAD51 sequence shares 80.61% similarity with the human homolog and contains all the documented characteristic binging domains. Both contain a helix-hairpin-helix (HhH) motif (light blue, 48aa long) with a large RecA/Rad51 domain (dark blue, 277aa long). Within the RecA/Rad51 domain there two key features Walker A (green and 8/8 sites) and Walker B (red, 5/5 sites) binding regions. Other features of the protein are the BRC multimer interface (20/20 sites), (AAA-ATP binding sites (7/7 sites), L1/L2 DNA binding loops (yellow) which contain a Tyr232 and Phe279, respectively. (C) Details of commercial antibodies that recognize the S. *mediterranea* RAD51 and γH2AX homologs. (D) General assays and detection methods for inducing and quantifying the response and outcome of DNA damage in native stem cells in the planarian model.

Interestingly, there was high expression of ATM but reduced gene expression of DNA-PKcs, required for NHEJ, throughout the time course (Fig. 7A). Similar effects are observed in primary human fibroblasts cell lines during chronic exposure to IR [128]. Because lethal IR exposure irreversibly eliminates neoblasts, the results confirmed that key regulators of cell cycle progression and markers of proliferating neoblasts were nearly abolished upon IR (*e.g*. *PCNA* and *cyclinB*). Furthermore, the irreversible elimination of neoblasts may also result from a gradual increase in the expression of the inhibitor of growth protein (ING) (Fig. 7A). Members of the ING family have been found to negatively regulate EGFR/PI3K/Akt signaling pathway, which is central to planaria neoblast re-population post IR [113], [129]. Thus, the increased amount of IR-induced DNA damage together with upregulation of ING expression may act together to eliminate neoblast and prevent residual cell proliferation post-IR. These findings also indicate that most components of the DDR are associated with neoblasts.

Exposure to sub-lethal doses of IR (i.e*.* 1000–1750 rad) leads to a partial elimination of neoblasts, which allow for studies of DDR, SC repopulation and recovery during adult tissue renewal [47], [113] (Fig. 7B). The re-establishment of mitotic activity post sub-lethal IR has been attributed to EGF signaling and active DNA repair mechanisms *(*e.g. Rad51 and Rad54B) [16], [113]. Sub-lethal IR depletes neoblast mitotic activity within 24 h, accompanied by a significant spike in apoptosis and DSBs. There is a gradual increase in DSB repair that peaks at five days post IR as determined by RAD51 gene/protein expression and RAD51 nuclear translocation (Fig. 7B). Neoblasts uniquely express the gene *smedwi-1* (*piwi-1,* henceforth) [47], [104], [125]. *piwi-1* expression is currently used as the gold standard to recognize the presence of neoblasts and their distribution. *piwi-1*+ cells clusters are severely reduced during the first 7 days post-irradiation (dpi, 1250 rad) and begin to expand after 9 dpi [47], [113]. However, mitotic activity is detectable after 7 dpi (Fig. 7B). Neoblast repopulation depends on EGF signaling that requires active DNA repair mediated by ATM, Rad51, Ku70 and Rad54B [16], [113]. Interestingly, functional disruption of ATM with RNA-interference (RNAi) leads to an accelerated re-establishment of mitotic activity 7dpi [16] (Fig. 7C).

ATM is an important player of the DDR that influences cellular decisions upon IR through regulation of p53/p21 axis to facilitate cell cycle checkpoint arrest [128], [130]. Thus, we can postulate that *Smed-ATM* may be key to facilitating an appropriate cellular response to DSBs (e.g*.* detection and cell cycle arrest). Further experiments will be required to identify the role of *Smed-ATM* upon IR in cell cycle regulation and determine if *Smed-ATM(RNAi)* hyper-proliferative neoblasts are gnomically stable; altogether validating the conservation of this protein in planaria. The interplay of DNA repair and neoblast repopulation is only beginning to be understood but the recent evidence suggest that mechanisms of HR are the predominant repair pathway in planaria [16], [17], [113]. This is further supported by results demonstrating that RNAi of *Rad51* and *Rad54B* in sub-lethally irradiated animals fail to repopulate *piwi-1*+ cells and mitotic activity, resulting in lethality. Conversely, dynamics of mitotic repopulation in *Ku70(RNAi)* sub-lethally irradiated animals are indistinguishable from untreated control group (Fig. 7C) [16]. All together, these results imply that *Smed-ATM* is a key upstream regulator of cell fate in response to IR-induced DSBs and HR is the dominant pathway used in repairing damaged DNA in planaria.

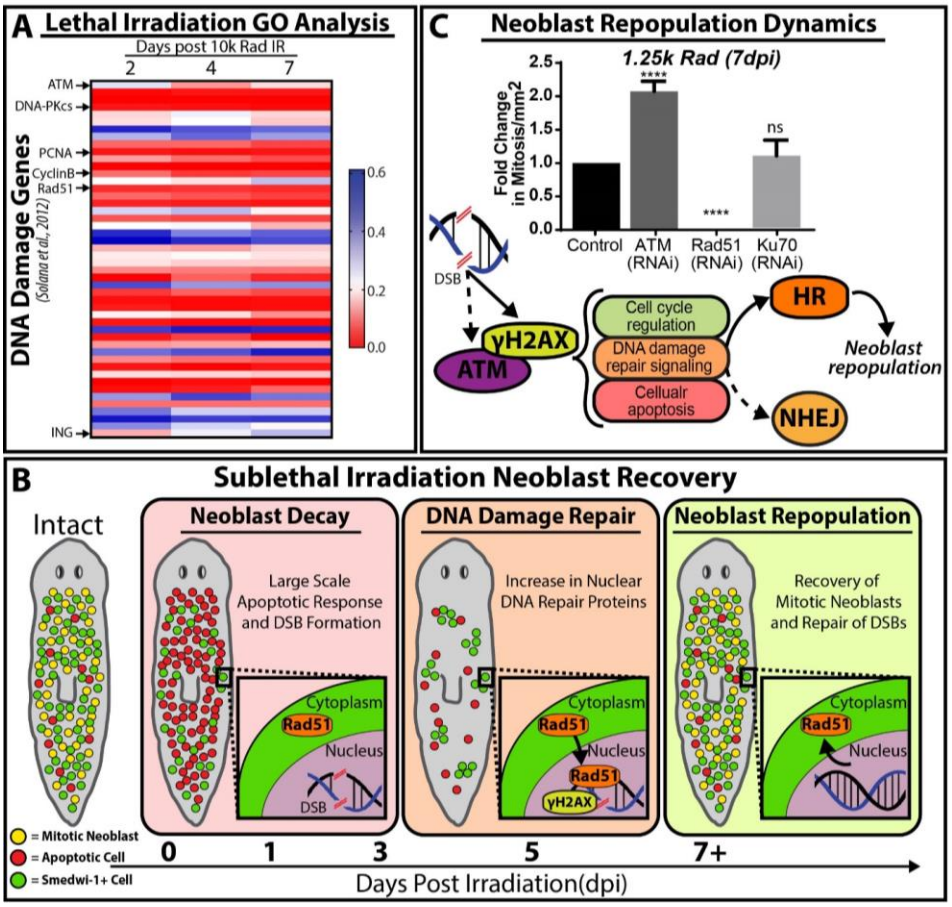

Figure 7. Neoblast response and repopulation post irradiation is attributed to functional DNA damage detection and repair. (A) Lethal irradiation of planarian (10k rad) irreversibly depletes neoblast populations. Upon analysis of GO term annotations published by Solana et al., genes involved in DDR and repair along a 7-day time course were selected. The heat map shows changes in gene expression at different times post-irradiation with color red indicating reduction and blue increase in gene expression (scale bar to the right). DNA damage response triggers upregulation of ATM gene expression accompanied by a decrease in cell cycle and DNA repair gene expression (*e.g*. *PCNA, CyclinB and Rad51*, respectively). Note that the inhibitor of growth (ING) gene expression is upregulated after 2hpi. (B) Cartoon depiction of neoblast response to sublethal irradiation. Upon sublethal irradiation, 1–3 dpi, neoblast decay arises from a large-scale apoptotic response and a lack of RAD51 nuclear translocation accompanies increases of DSBs. Secondly, the remainder of *piwi-1*+ neoblast clusters begin to slowly expand and cells exhibit a peak of DDR and DNA repair proteins at 5dpi (*e.g*. γH2AX and RAD51, respectively); marking the DNA damage repair response. Lastly, neoblast repopulation occurs 7+ dpi with increases of *piwi-1*+ cells, recovery of mitotic neoblasts and a decrease in DSBs. Cellular events are depicted by the following: mitotic neoblasts (yellow), apoptotic cells (red) and *piwi-1*+ cells (green) (C) Fold change in mitosis in RNAi and mock control animals is quantified 7dpi after 1.25k rad (sub-lethal dose). Notice the increase in mitotic events upon *ATM(RNAi)* and the inability for neoblasts to recover post *Rad51(RNAi)*. Underneath, proposed mechanism of neoblast repopulation post sublethal IR show a possible role of *Smed-ATM* functioning as a transducer of DSB signal in tandem with γH2AX phosphorylation. Further, this model implies that HR signaling is a key player in neoblast repopulation as RNAi of NHEJ did not affect neoblast repopulation. Dotted arrows and shaded colors imply uncertainties within the model and further experiments are required to validate these assumptions and interactions. ****$p < 0.0001$; one-way-ANOVA.

2.6. Genomic instability models in planarian

Two independent DNA damage models have been developed in planarian by disrupting gene function via RNAi of *Rad51* and *Ubc9* [1], [2]. Planaria homologs of *Rad51* and *Ubc9* show high evolutionary conservation with higher organisms and their disturbance revealed important patterns of regional defects along the AP axis (Fig. 8A-D). Furthermore, RNAi of *Rad51* and *Ubc9* display loss of genomic integrity, specifically by the accumulation of DSB throughout the planaria body [16], [17]. Rad51 is required for nucleofilament formation and without functional RAD51 protein the HR repair complex cannot form [15], [131], [132]. Full knockout of *Rad51* results in embryonic lethality in mammals [133], [134]. Nonetheless, it is possible to knockdown the HR pathway, but it is challenging to evaluate organismal SC response and track their progeny in an environment of genomic instability. Thus, the planaria model system offers unique opportunities to overcome these limitations by enabling the possibility of disrupting HR while SC attend systemic demands of cellular turnover and repair.

On the other hand, SUMOylation is a dynamic and reversible post-translational modification that requires the cooperation of a host of proteins [135]. Critical to this pathway is UBC9, which determines protein SUMOylation [135]. SUMO attachment regulates protein function as it can affect protein localization, stability, protein–protein interaction, cause conformational changes or act as a hub to form multi-protein complexes [136]. Mounting evidence suggests SUMOylation plays a critical role in the regulation of DSB repair [137]–[140]. It does so in three ways: (1) regulates protein stability, DNA binding ability and localization of sensors and effectors of DSB repair, including both NHEJ and HR; (2) leads to creation of an open chromatin state more amenable to repair by controlling epigenetic modification through modulation of various methylases and acetylases; (3) orchestrates successful DDR response by coordinating multiple types of post-translational modifications, most notably SUMO-targeted ubiquitin ligase-mediated ubiquitination [141]–[150].

The unique feature of the *Rad51* and *Ubc9* knockdown models is the prevalence of DNA damage, especially DSBs that is present throughout the planaria body [16], [17]. Molecular analysis in both models revealed a transient presence of DNA DSBs and chromosomal abnormalities that progressively increased over time. This is consistent with the role *Rad51* plays in DSBs repair through HR. However, the mechanism driving this phenomenon in the *Ubc9* phenotype was less evident. Two observations were critical to relate SUMOylation to DNA damage: (i) the regional defects in animals subjected to *Ubc9 (RNAi)* were similar to those observed in *Rad51* phenotype and (ii) late stages of the *Ubc9* phenotype display increase in RAD51 and γ-H2AX protein expression, which appeared in clusters along the AP axis. Additional analysis revealed that DNA damage in *Ubc9(RNAi)* is due to the inability of RAD51 to translocate from the cytoplasm to the nucleus to repair DSBs [17]. This finding links the two models together and additionally explains phenotypic similarities, which altogether supports the idea that HR is the prominent pathway for repair of DSBs in planaria.

The induction of DNA damage after *Ubc9* and *Rad51(RNAi)* results in a cascade of cell fate decisions led by cell cycle arrest [16], [17]. Cell cycle analysis revealed that while most cells in the *Rad51(RNAi)* were arrested in S phase, cells in *Ubc9 (RNAi)* animals were primarily arrested in the G1 phase (Fig. 8E). p53 and *Rb* commonly regulate neoblast fate decisions (*i.e*. apoptosis, proliferation and cell cycle arrest) during tissue renewal and regeneration. This is also the case in the presence of DNA damage in planaria but intriguingly; we found that *p53* gene expression is downregulated across the

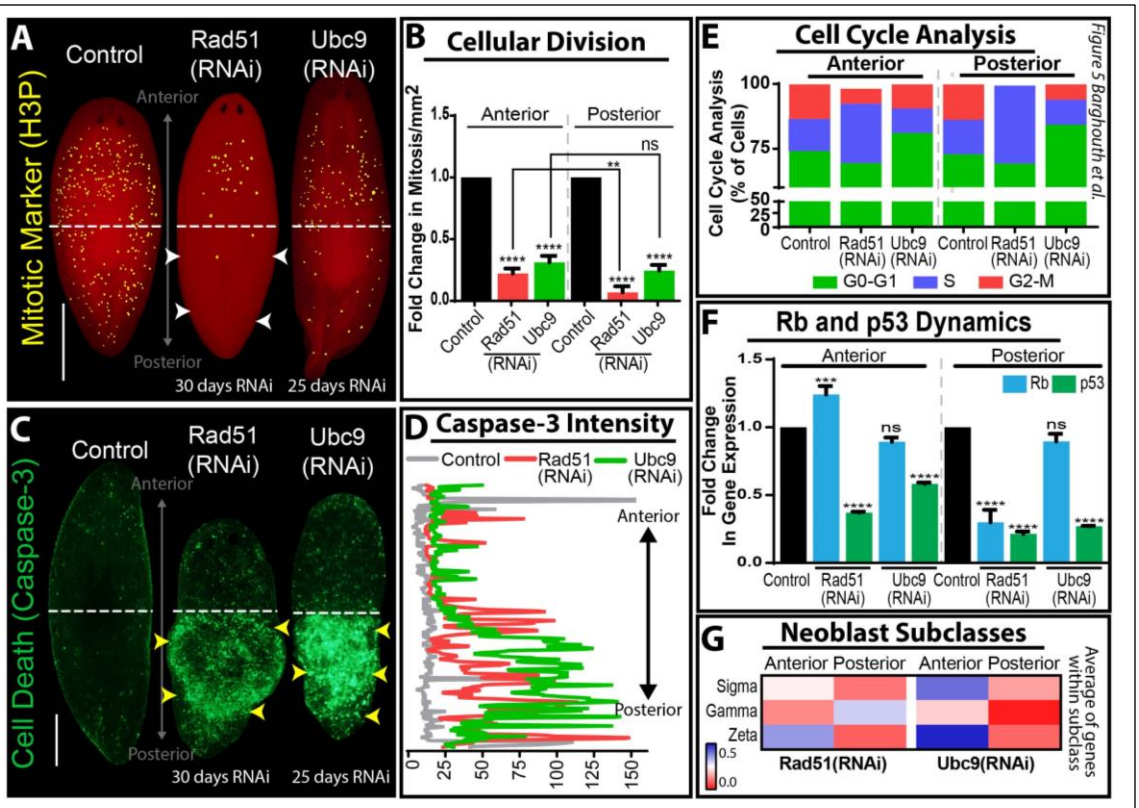

Figure 8. *Rad51* and *Ubc9* inhibition in planaria yields high levels of DSB and region-specific neoblast responses (A) Whole mount immunostaining of mitotic neoblasts marked by Histone3 phosphorylated (H3P) in mock control, *Rad51(RNAi)* and *Ubc9(RNAi)* models. Note the difference in mitotic cells along the anteroposterior axis in the *Rad51(RNAi)* group; white arrow heads indicate a severe decrease in mitosis in the posterior *versus* the anterior. (B) Levels of mitotic cells across the anteroposterior axis, confirms the asymmetric distribution of mitoses is specific to *Rad51(RNAi)* but not to animals subjected to *Ubc9(RNAi)*. (C) Whole mount immunostaining of cell death marked by the Caspase-3 antibody. Note the increase of apoptotic events (green signal) is concentrated in the posterior region of both *Rad51(RNAi)* and *Ubc9(RNAi)*animals (yellow arrowheads). (D) Quantification of the fluorescent intensity signal from caspase-3 stained *Rad51(RNAi)* and *Ubc9(RNAi)* animals confirming the increased cell death in the posterior regions compared to the anterior and control (yellow arrowheads coincide with the increase in cell death). Intensity readings were obtained by tracing a line in the middle of the animal from the anterior to the posterior region using ImageJ software. (E) Cell cycle analysis using flow cytometry in cells dissociated from the anterior and posterior regions in animals subjected to *Rad51(RNAi)* and *Ubc9(RNAi).* Different phases of the cell cycle are color coded and show that *Rad51(RNAi)* and *Ubc9(RNAi)*animals display different effects on cell cycle represented by important reduction in M-phase in the posterior region of *Rad51(RNAi)*, while *Ubc9(RNAi)* animals tend to halt cell cycle in G0/G1 phases but some cells still continue to divide. (F) Fold change in gene expression of *Rb* and *p53* relative to the control. *Rb* expression is asymmetrically upregulated in the anterior of *Rad51(RNAi)* but it does not appear affected in the same manner after *Ubc9(RNAi).* (G) Heat map, representing fold change in the average of gene expression of neoblast subclass (sigma, gamma, zeta) markers in the anterior and posterior regions. Red indicates diminished gene expression and blue increased gene expression. **p < 0.01; ***p < 0.001; ****p < 0.0001; two-way-ANOVA. Scale bars: 200 µm.

AP axis in both RNAi groups (Fig. 8F). However, there were stark differences in *Rb* expression. Specifically, there is an increase in *Rb* expression in the anterior region of *Rad51(RNAi)* animals whereas there is no significant change in *Ubc9(RNAi)* group (Fig. 8F). Although our knowledge of *Rb* dynamics relies on gene expression data, it is tempting to link increased *Rb* expression with cell cycle arrest. Canonically, *Rb* is thought to be an important regulator of the G1/S checkpoint and studies suggest that overexpression of *Rb* can increase rates of cellular survival and predispose cells to become more cancerous [151], [152].

Furthermore, the genomic instability driven cell cycle arrest in both lead to interesting changes in tissue homeostasis and cellular turnover, specifically in terms of cell survival and death [16], [17]. While both models coincide in a significant decrease in the cycling neoblasts, the *Rad51* model reveals a remarkably difference across the AP axis, specifically loss of survival in the posterior region. This is likely due to the differential expression of cell fate regulators *p53* and *Rb*. On the other hand, both models show a massive increase in cell death in the tail region with significantly less cells dying in the anterior. It is possible that *Rb* is acting as switch for allowing cell survival in the anterior but not the posterior. Another explanation as derived from experimentation in the *Ubc9(RNAi)* model, where the cell death is partially attributed to attenuation of Hedgehog signaling, which is known to be an important regulator of posterior polarity in planaria. Whether the same mechanism is driving cellular decisions in the *Rad51*phenotype requires further experimentation.

A remarkable finding from these studies is that some SCs in the anterior region are able to overcome surveillance mechanisms and continue proliferating with genomic instability [16], [17]. In the *Rad51(RNAi)*, this is in part due to increased expression of *Rb* and neural inputs in the anterior region. Ectopic introduction of brain tissue in the posterior region, induce neoblast proliferation with DSB. These findings highlight the possibility of intercellular effects, whereby neural signals alter fate decisions of neoblasts with DSBs. Likewise, these results also prompt future studies about possible neural regulation of *Rb* signaling that facilitate proliferation of neoblasts with DSBs. Alternatively, it is possible that a subset of neoblasts is endowed with proliferative capacity to give rise to cancer-like cells in the anterior. Multiple neoblast subtypes have been characterized [43], [103], [104]. We found that gene expression of markers associated with zeta neoblasts are increased in the anterior for both *Ubc9* and *Rad51 (RNAi)* animals (Fig. 8G). Recent research demonstrates the intriguing possibility that inhibition of Hippo signaling trigger dedifferentiation of postmitotic progenitors in planarians [153].

It is tantalizing to speculate that the increasing load of genomic instability may act as a switch for zeta neoblasts to leave their lineage-restricted state and try to fill the niche left behind by sigma cells that cannot survive increasing DNA damage. It is also possible that persistent demands of cellular turnover override fate decisions to promote exit of cell cycle arrest has been noted in hematopoietic SCs [154]. Some of these cells may have weaker sensors and effectors of the DDR, allowing them to more easily circumvent these checks and balances and ultimately evolve into cancer-like cells. Additional experiments are required to dissect the actual mechanisms driving cells to withstand excessive DNA damage and continue to proliferate. Nonetheless, the results obtained with *Rad51* and *Ubc9* downregulation supports the notion that cellular decisions in the presence of DNA damage are also influenced by regional signals that may involve crosstalk among tissues and organs. This is an important finding as a comprehensive focus on regional signals that supports proliferation of cells with genomic instability may help to understand the mechanisms facilitating cancer formation and progression.

2.7. DNA damage and repair are essential components for tissue regeneration

Cell death and proliferation are not only instrumental during tissue renewal but also in the process of regenerating missing or injured body parts. Upon amputation, planaria undergo an orchestrated series of localized and systemic cascades of cellular proliferation and programmed cell death (*e.g*. ~4–6 h and ~48 h). Recent research has greatly furthered our understanding of the genetic and molecular cascades required for tissue repair and regeneration [53], [110], [155]. The initial peaks of systemic cell division and localized cell death events were found to be accompanied by a genetic response called the generic wound response that happen during the first 24hrs post-injury/amputation (hpa). This is followed by a wave of specific gene expression representing the regeneration response (24–70hpa) that includes the second molecular peak of mitosis and apoptosis. Finally, the differentiation phase is attributed to neoblast progeny mediated differentiation and specialization of the blastema at +70hpa (Fig. 9A) [53], [110].

The ability to adjust cell proliferation during simultaneous demands of tissue renewal and injury highlight the faithful mechanisms used by planaria to regulate cell number. Since injury repair relies on cell proliferation and consequently DNA replication, we argue that the DDR is an active player that preserves genome integrity during regeneration. In other words, an increase in cell division is accompanied by DNA replication that is carefully monitored by DNA repair mechanisms. Indeed, recent studies have demonstrated that key components of DNA replication and repair (*e.g*. *p53*, *Rb, Rad51* and *Ubc9*) are critical for the regenerative process and without them; planaria fail to regenerate [16], [17], [60], [61]. In addition, cell death is necessary for proper regeneration. The TUNEL assay, which detects cellular apoptosis induced by DSB-nicked ends, is commonly used to evaluate cell death in planaria [101]. After amputation, two peaks of cell death are known to happen at ~4hrs and ~48 h. However, it remains unclear whether these stereotypical patterns of TUNEL + cells are derived from the stressful environment of regeneration or actual DNA damage, specifically DSBs.

We were prompted to reanalyze the possible role DNA damage response play during the early and late phases of tissue regeneration based on published transcriptomic data [53], [110]. Transcriptomic changes during the first half of the generic response in planaria offer an interesting resource to discern the role of DDR [110]. This process involves four waves of gene expression found within differentiated tissues (waves 1–3) and neoblasts (wave 4) (Fig. 9B). Using published RNAseq data from Wenemoser et al. [110], we were able to identify genes involved in DNA damage response by GO term analysis. We found that all waves except wave 3 contained genes involved in DDR (Fig. 9C-E). Interestingly, we found PARP-3 as the only DDR gene involved in wave 1 and the only DDR-specific gene with a peak in gene expression within the first hour post amputation. At the decline of PARP-3 expression at 3 h, both wave 2 and wave 4 DDR specific gene expression increased and peaked at 6 h, which coincide with the system wide mitotic response (Fig. 9C). These results suggest that expression of genes in the DDR follow similar transcriptomic changes of the generic wound response except in wave 3. It also implies that PARP family genes may prime the DDR during early regenerative events (Fig. 9C-E). However, the question still remains whether the first peak of TUNEL+ cells starting ~4hrs is linked to DNA damage.

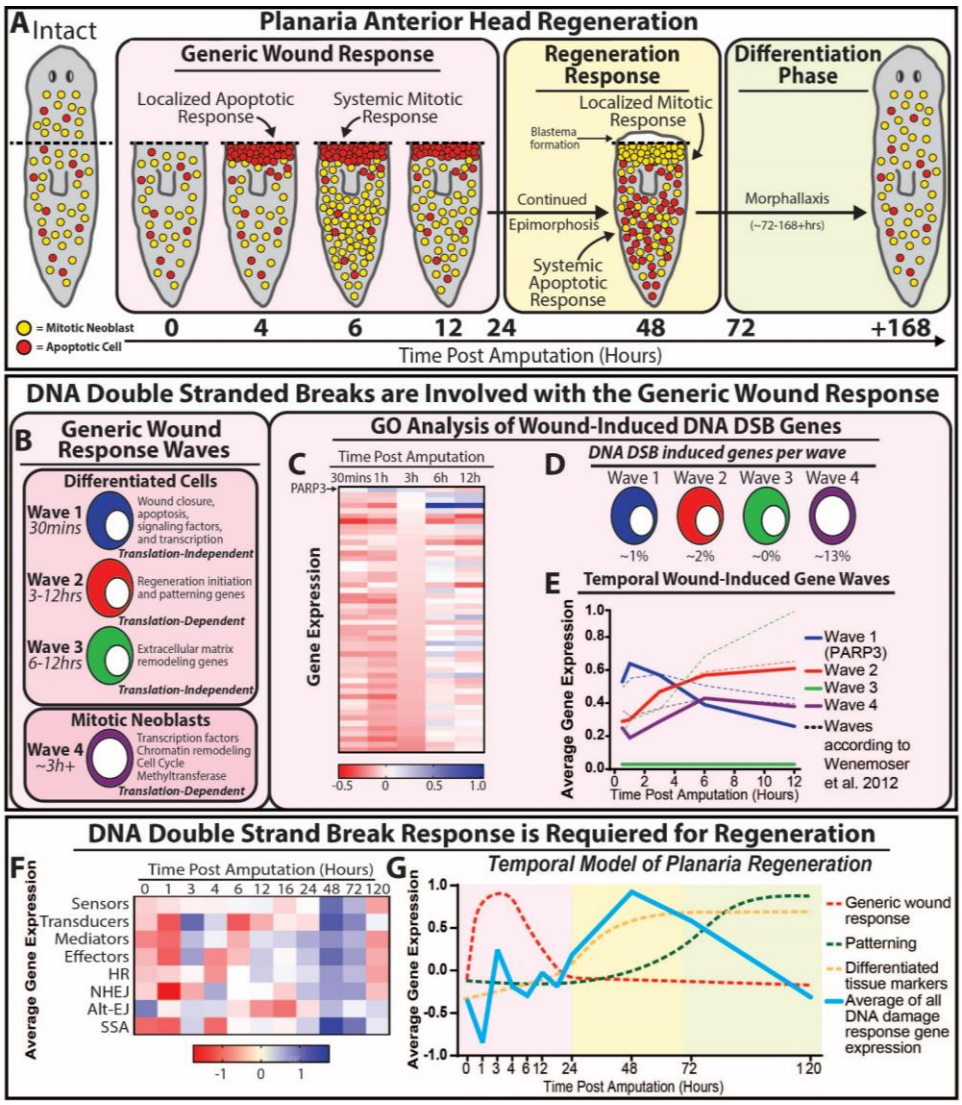

Figure 9. DNA damage repair (DDR) is activated during the initiation of tissue regeneration (A) Schematic representation of the general cellular events taking place during the first week post-amputation (hpa) of the anterior region in planaria (color coded boxes). During the generic wound response, a localized apoptotic response occurs ~4hpa, accompanied by a systemic burst of mitotic neoblasts at 6hpa that gradually reduces ~12hpa. Next, the regeneration response is followed by a localized increase in cell proliferation and a systemic wave of death. After 72hpa the tissue will continue restructuring newly formed tissue through differentiation of stem cells and progenitors. (B) Waves of gene expression found in the generic wound response within the first 12hpa. (C) Heat map representing GO term analysis of wound induced DDR gene expression derived from Wenemoser et al. 2012 (D) Percent of DNA damage genes associated within each wave. (E) Temporal wound-induced gene expression waves. Solid lines indicate averages of DDR specific wave response and dotted lines indicate waves according to Wenemoser et al. 2012. (F) Heat map of average DDR gene expression post amputation. At 48 hpa the average expression of all DDR genes is upregulated following wounding. (G) Graph depicts the temporal model of planaria regeneration including the average expression for genes involved in the DDR. The average of all DNA damage gene expression was obtained from the heat map in (F), (blue line) is plotted against the established temporal model of regeneration (dotted lines) according to Wenemoser et al. 2012 and is color coded as shown in (A).

PARP-3 catalyzes post-translational modifications of proteins involved in transcription silencing, cell death and interacts with PARP-1 during DDR to accelerate NHEJ [156]–[159]. In addition, PARP-3 has been shown to act independently of DNA damage and mediate centrosome stability, G1/S cell cycle progression and telomerase activity [157], [160], [161]. For instance, PARP-3 expression has an inverse relationship with telomerase activity. Lung cancer cells depleted of PARP-3 displayed an increase in telomerase activity [161]. During planaria regeneration, telomerase activity is upregulated and accompanies neoblast proliferation [55]. Thus, the possible role of PARP-3 expression during the first 3 h of regeneration may be to restrict both neoblast cell cycle progression and telomerase activity. The decline in PARP-3 after 3 h may allow the priming of transcription of both cell cycle and DNA repair proteins that are involved during initial mitotic burst at 6h. The data analysis shows that the initial localized peak of TUNEL+ cells may not be in response to DNA damage but to the harsh environment at the amputation site to facilitate wound closure and there is a possibility that PARP-3 may be mediating the post-translational modifications associated with cell death.

Regenerating planaria exhibit a localized mitotic peak and a systemic increase in TUNEL+ cells resulting in the formation of a regenerative blastema starting at 48 h post amputation [101], [110], [111]. Gene expression levels associated with DNA damage response and repair are relatively low within the first 24h of regeneration (Fig. 9F). Strikingly, at 48h, there was a dramatic increase in the expression of genes involved in DNA damage signal transduction and DDR (Fig. 9F). Thus, by plotting the average of DDR gene expression values onto the established temporal model of planaria regeneration [53], we observed that the second wave of DDR is much more significant than that of the generic phase and remains a key feature in the regeneration and early differentiation phases (Fig. 9G). Consistently, our recent work strongly supports the idea that DDR is required for large-scale tissue regeneration. Without key molecules such as *Rad51, BRCA2*, *Ubc9* animals, fail to regenerate and replace lost tissues [16], [17]. Furthermore, according to Wurtzel et al. [53]; expression levels of genes involved in HR (*e.g*. *Rad51-A,-B,-C* and *BRCA2*) were highly active compared to the decrease in NHEJ (*e.g*. *Ku70, Ku80* and *Ligase IV*) related genes. However, gene expression analysis revealed that HR and NHEJ were at their peaks at 48h post amputation. Delving into the molecular dynamics of mitotic events during regeneration in *Rad51* and *Ubc9(RNAi)* animals, we observe that at 6 h post-amputation both groups respond with a slight increase in mitoses but fail to elicit a second mitotic peak at 48 h [16], [17]. These results together provide further evidence that DDR is a crucial component of the overall regenerative response in planaria.

2.8. *In vivo* validation of PARP's role during planarian regeneration

To validate the functional role of PARP3 during tissue regeneration and homeostasis, we began by identifying the planarian homologs and cloning the genes. Human PARP-1, -2 and -3 contain similar domains such as the WGR binding domain and a PARP catalytic domain. Thus, to verify that we are obtaining PARP3, the human sequence for PARP-1, PARP-2 and PARP-3 were BLAST-ed into PlanMine3.0 [162] and obtain three independent hits with PARP1 having a direct target (e.g. E-value zero) (Fig. 10A). Observing domain conservation, *Smed-PARP1* contained zinc fingers and a BRCT domain, a key feature for human PARP1. *Smed-PARP2* contained conserved WGR binding domain and a PARP catalytic domain just as the human counterpart. Lastly, *Smed-PARP3* contained a PARP catalytic domain however, it lacked the PARP3-specific WGR binding domain. Moreover, the percent identity of the planarian PARPs show a large

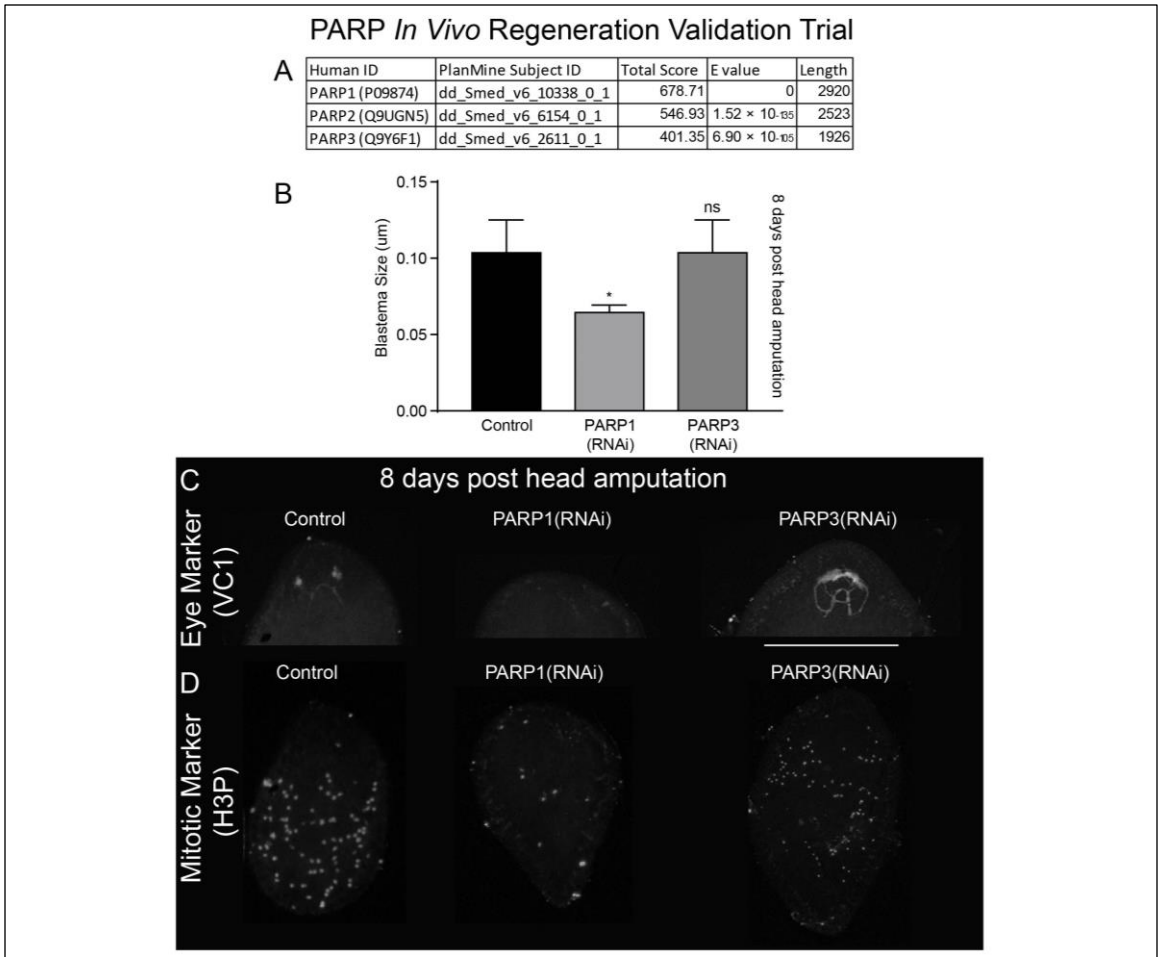

Figure 10. *in vivo* validation of PARPs during larger-scale regeneration. (A) BLAST hits obtained from placing human PARP-1, -2, and -3 into PlanMine3.0. The planarian homologs contained high conservation of PARP-specific domains and percent identity (e.g. 44.20%, 51.92% and 58.29%, respectively). (B) Blastema measurements 8 days post head amputation (μm). (C) Immunostaining using the eye marker VC-1 antibody of the control and RNAi groups. (D) Mitotic neoblasts marked by H3p antibody at 8 days post head amputation. *$p < 0.05$; one-way-ANOVA. Scale bars: 200μm.

homology between the planarian and human PARPs (e.g. 44.20%, 51.92% and 58.29%, respectively). These results imply that PARP pathway proteins are highly conserved in the planarian.

The initial screen consisted of testing both *Smed-PARP1* and *Smed-PARP3* during tissue homeostasis. After a 30-day injection period consisting of five dsRNA microinjections we identified that both *Smed-PARP1* and *Smed-PARP3* did not alter tissue homeostasis and did not alter tissue integrity or mitotic numbers; thus, indistinguishable from the control group. To test the roles of these two genes during regeneration, planarian underwent head amputation at the end of the 30-day injection schedule and monitored animal regeneration over the span of 8 days (8dpa). Relative to the control that formed blastemas, *Smed-PARP1(RNAi)* failed to form regenerative-specific blastemas unlike *Smed-PARP3(RNAi)* (Fig. 10B). Interestingly, *Smed-PARP-1(RNAi)* with the limited blastema that was formed did not produce photoreceptors of eye pigmentation and when observing *Smed-PARP3(RNAi)* we identified that within their regenerative blastemas they

did form cycloptic eyes or were aberrant of eye pigmentation but were photophobic. To further understand this phenomenon, we stained 8dpa animals with the VC-1 antibody which marks the eye structures. Relative to the control, *Smed-PARP1(RNAi)* did not contain any VC-1 signal and that *Smed-PARP3(RNAi)* animals contained signal that was disordered, tangled and showing that both eye cups were connected (Fig. 10C). Further, looking at mitotic activity, marked by Histone 3 phosphorylated (H3P), *Smed-PARP1(RNAi)* displayed a marked reduction and *Smed-PARP3(RNAI)* animals did not show any difference in mitotic activity 8dpa (Fig. 10D).

As *Smed-PARP3(RNAi)* animals are capable of forming blastemas and forming deformed differentiated tissue structures, a hallmark of an intact regeneration response, we can postulate that *Smed-PARP3(RNAi)* may function specifically within the first 3hours post amputation. Thus, the deformities obtained from *Smed-PARP3(RNAi)* can be the result of a defective wave 1 wound response required for apoptosis, signaling factors and transcription. On the other hand, *Smed-PARP1(RNAi)* failed to regenerate differentiated tissues, re-establish basial levels of mitosis and form a regenerative blastema. This finding supports the notion that DNA repair proteins are highly crucial for the regenerative response wave of gene expression found ~48hpa as other DNA repair and DDR proteins exhibited the same phenotypes as discussed above. These findings are intriguing and need further experiments to validate and confirm the roles of *Smed-PARP3* during the early phases of regeneration and *Smed-PARP1* during the late phases as well as their role in maintaining DNA integrity during the regenerative process.

2.9. Discussion

Preserving genomic integrity over recurrent tissue renewal is an important challenge that wanes with age. DNA damage and the cellular responses associated with it are at the center of efficient cellular turnover. Thus, we advocate for studies of SCs in their natural environment as they attend demands of tissue renewal and repair. The analyses integrating SCs, DNA damage and tissue renewal in the complexity of the whole body present fresh opportunities to the field and has the potential to inform about cellular crosstalk and regulation of signaling pathways (*e.g*. tumor suppressors, oncogenes) that control cellular decisions in the face of DNA damage (Fig. 11A). The evolutionary and functional conservation of the DDR and mechanisms of SC function in planarian offers a simplified paradigm, in which pharmacological or genetic screens can be performed rapidly and cost-effectively.

The capacity to induce different levels/types of DNA damage with pharmacological compounds, IR and genetic manipulations paves the way for additional studies aimed at understanding the biology of the DDR and possible alternatives for therapeutic applications (Fig. 11B). The genetic models using loss of function of *Rad51* and *Ubc9*enable *in situ* analysis of tissue renewal in response to DNA damage that uniquely allow us to address the molecular basis controlling regional differences in the adult body (Fig. 11A). Furthermore, the activation of regional cell survival and death in response to the systemic presence of DSBs is a great resource to address mechanisms of SC survival with defective DNA. This example prompts the possibility of studying intrinsic and extrinsic cues that may favor or restrict the growth of cancer initiating cells (Fig. 11C, D).

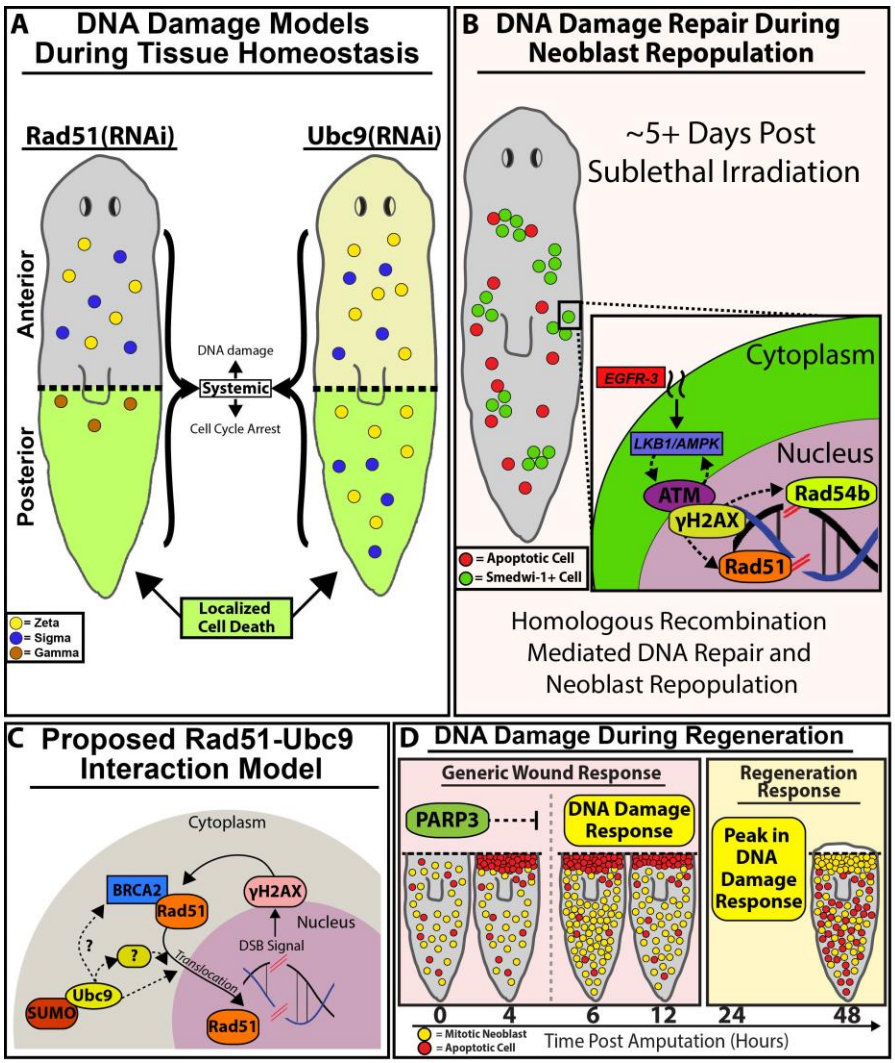

Figure 11. DNA damage repair (DDR) pathways are critical components of the cell proliferation required for tissue regeneration. (A) *Rad51(RNAi) (gray)* and *Ubc9(RNAi)* (light-yellow) planaria share similar increases in DNA damage along the AP axis accompanied by varying levels of cell cycle arrest. Localized cell death (green) is observed in the posterior region of both RNAi conditions. Survival of neoblasts/sub-types were determined from gene expression data from Fig. 8G; neoblast subtypes: zeta (yellow), sigma (blue) and gamma (brown). (B) 5 days post sublethal irradiation, remaining neoblasts will repair DSBs by homologous recombination and neoblasts will repopulate the entire animal. We propose a hypothetical model whereby EGFR signaling integrates with DDR to facilitate neoblast repopulation post-irradiation (indicated with dotted lines). (C) Proposed RAD51-UBC9 interaction model. Presence of DNA DSB breaks triggers upregulation of RAD51 and γ-H2AX that together participate in DNA repair. However, after *Ubc9(RNAi)* the RAD51 protein accumulates in the cytoplasm as SUMOylation is required for RAD51 translocation to the nucleus. We propose that *Ubc9* may interact with intermediate regulators of Rad51 for DDR. (D) Model of DNA damage during large-scale tissue regeneration. PARP3 expression peaks during the first 4 hpa and may be suppressing DDR gene expression within that timeframe. Upon the decline of PARP3 expression, DDR expression at +6 hpa is observed. A substantial peak in DDR observed in parallel with the regeneration responses that begins +24 hpa. The robust responses of DDR pathways during wound repair could be necessary to drive DNA repair during neoblast proliferation that is required in tissue regeneration.

What are the signals facilitating survival of SCs with DSB in the anterior, whereas in the posterior surveillance mechanisms remain active and effectively eliminate damaged cells? Our results suggest that neural inputs may influence dynamics of cell cycle in neoblasts carrying DSBs. Thus, future experiments will address the source and the molecules mediating nervous signals that facilitate cell survival in an environment of genomic instability. Since neoblasts in the anterior region tend to survive with DSBs, it brings interesting opportunities to dissect potential differences among SCs and their susceptibility and advantages to DNA damage. Likewise, future studies will also integrate positional cues along the AP axis [163], [164] with DNA repair to inform about potential interactions that can enhance or reduce the integrity of the genome. Answering these fundamental questions will enable the field to identify early markers of cellular transformation, mechanisms regulating tumor suppressors, and to define means by which transformed cells survive and form tumors. Finally, we believe that planaria traditionally recognized as a model for tissue regeneration, may also represent a fresh alternative to understanding and manipulating DNA damage and its effects in the adult body.

CHAPTER THREE

FINDINGS

The conserved PI3K/AKT/PTEN/TOR signaling transduction cascade is required for tissue maintenance in planarians

3.1 Introduction

Approximately 90% of cancer related deaths in the U.S. result from alterations in tissues often undergoing cellular renewal (e.g. epithelial lining of organs) [165], [166]. Tissue homeostasis and repair requires constant cellular turnover dependent on precise interactions between SCs and differentiated tissues. This process is highly influenced by the balance between oncogene (i.e. growth genes) and tumor suppressors (i.e. growth suppression genes) which are evolutionarily conserved across species [30], [167]–[169]. Tumor suppressor genes can halt the positive influence of oncogenes in cell growth, proliferation, migration, division, differentiation, metabolism and genomic instability. However, cancer cells take advantage of homeostatic signaling pathways and grow beyond normal confines of a cellular niche characterized by the hallmarks of cancer (e.g. angiogenesis, maintaining energetics, overcoming stress and sustaining cellular viability) [169].

Various signaling pathways collaborate at the cellular and systemic levels to maintain tissue repair and regeneration. Disruption of a cellular pathway can result in the onset of cancer and degenerative diseases. For instance, the tumor suppressor PTEN is a lipid phosphatase that is frequently under-expressed in many cancer types due to deletions, mutations or gene silencing [30], [170]–[174]. Its main function is to dephosphorylate PIP3 in the plasma membrane, thereby opposing the activity of Class I oncogene PI3K. Aberrant PI3K results in increases of cellular growth, proliferation and survival factors through its effectors and proto-oncogenes, AKT and mTOR [172]–[175]. The PI3K/AKT/TOR pathway is well studied however, further characterization of how this pathway is regulated at cellular and systemic levels are crucial for therapeutic advances.

Loss or gain of function of key components of the PI3K/PTEN/AKT/mTOR signaling transduction pathway is recognized to be a dominant player in cancer formation and progression [30], [170]–[174]. Importantly, PI3K and PTEN have been identified as the second and third most targeted genes by point mutations. From 3,281 tumor genome data sets representing 12 different cancer types, mutations (e.g. nucleotide substitutions, deletions, amplifications, translocations, etc.) targeted PI3K 17.8% of the time followed by PTEN at a rate of 9.7% [30]. The suppression or balance of PI3K/AKT/mTOR signaling by PTEN during cellular turnover acts as a barrier against oncogene induced DNA damage required for the onset of tumorigenesis [30], [176], [177]. Many of these components have been studied separately or in tandem but lack an understanding on how the balance of PI3K/PTEN/AKT/mTOR signaling cascade regulates SCs during adult tissue maintenance with respect to the OTS-DDM.

This section will introduce the PI3K/PTEN/AKT/mTOR pathway as a conserved and integral player within the planarian, *Schmidtea mediterranea.* Specifically, their roles in SC regulation, tissue homeostasis and regeneration. Primarily, a more in-depth

explanation of PI3K/PTEN/AKT/mTOR signal transduction cascade will be presented. Secondly, the conservation and roles of these signaling molecules within the planarian will be discussed in respect to tumorigenesis. The goal of this section is to identify if the planarian is a viable model to reveal new aspects to the OST-DDM in the context of cellular turnover.

3.2 PI3K/PTEN/AKT pathway signal transduction

3.2.1. PTEN negatively regulates PI3K-AKT signaling

Phosphoinositides have been found to coordinated may components of homeostasis such as cell migration, cell proliferation, membrane transport and cellular turnover [178], [179]**.** Receptor tyrosine kinases (RTK) are cell surface receptors with high-affinity for growth factors ligands, cytokines and hormones [180], [181]. Through their downstream signaling cascades (e.g. PI3K and Ras), they regulate normal cellular processes and are integral regulators of cancer development and progression [182]. Phosphatidylinositol-3 kinase (PI3K) is a heterodimer protein requiring phosphorylation at its regulatory subunit p85 and within its catalytic subunit p110 (i.e. PI3KR and PI3KCA, respectively) [183], [184]. PI3K is directly activated by p85 association with phosphorylated tyrosine kinase and/or insulin receptor substrate 1 (IRS-1). In addition, p110 catalytic subunit can indirectly be activated by Ras signaling. Thereby, allowing the transfer of a phosphate group to membrane phospholipids [183], [185]–[187]. Activated PI3K mediates the phosphorylation of PIP2 (phosphatidylinositol 4,5 bisphosphate) by transferring an ATP-derived phosphate to the D-3 position of the inositol ring therefore forming PIP3 (phosphatidylinositol 3,4,5 trisphosphate).

PTEN (phosphatase and tensin homologue deleted on chromosome 10) a well characterized phosphatase and tumor suppressor counteracts PI3K/AKT/mTOR signaling cascade by dephosphorylating PIP3 into PIP2 (Fig. 1A) [188], [189]. Moreover, this event allows for the suppression of AKT signaling required for cell proliferation, differentiation, transcription and cell migration in both vertebrates and invertebrate [56], [174], [185], [190]. Since its identification in 1997 (Li & Sun 1997, Li et al. 1997, Steck et al. 1997) [191]–[193] PTEN has been of interest to the pharmaceutical realm as a new and promising approach for SC regulation during regeneration and wound healing [56], [172], [173], [190], [194]. Overall, the balanced activation of PI3K and PTEN act as compass molecules essential for systemic homeostasis and the prevention of cancer induction.

3.2.2. AKT signaling

Following PTEN loss, the accumulation of PIP3 at the plasma membrane recruits and activates proteins that contain pleckstrin homology (PH) domains (e.g. AKT and PDK1). Importantly, once bound to PIP3 at the plasma membrane, AKT serine/threonine kinase can undergo a stepwise and dual phosphorylation process. Primarily, the phosphorylation of Thr308 activates AKT by phosphatidylinositol 4,5 bisphosphate-dependent protein kinase-1 (PDK1) within its kinase domain activation loop. Active AKT bound to the membrane is primed for its last phosphorylation event at Ser473 within the regulatory domain HM region by mammalian target of rapamycin complex 2 (mTORC2) [195]–[199]. Furthermore, AKT has been seen to be activated in a PI3K-independent manner through ACK1 or PKA which activate AKT in the presence of increased cAMP/insulin [200], [201]. Once activated at the plasma membrane, phosphorylated AKT can translocate to the cytosol or nucleus to phosphorylate its substrates that promote

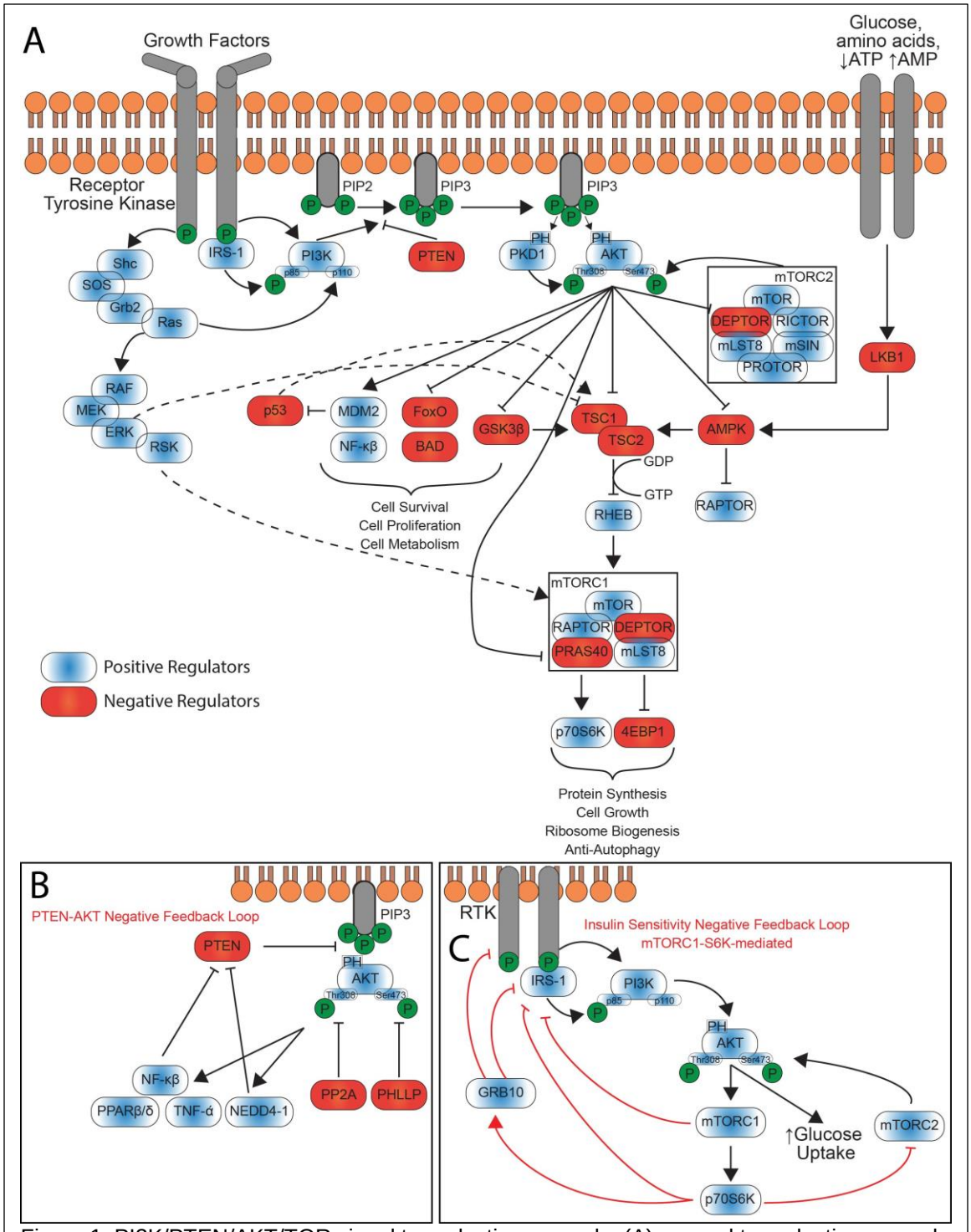

Figure 1. PI3K/PTEN/AKT/TOR signal transduction cascade. (A) general transduction cascade with the downstream effectors. (B) PTEN-AKT negative feedback loop. (C) insulin sensitivity negative feedback loop which is mediated by mTORC1-S6K. Red depicts negative regulators of the pathway (e.g. PTEN) and positive regulators of the pathway in blue (e.g. Akt, TOR).

survival (e.g. NF-κB, BAD, BCL2, FoxO), migration, cell cycle progression (e.g. MDM2), protein synthesis (e.g. mTOR, REHB) and metabolism (e.g. mTOR, REHB, GSK3β, TSC complex, AMPK) [199], [202]–[206].

3.2.2.1. AKT signaling: Cell Cycle Regulation and Cell Survival

AKT works upstream of key regulators required for the suppression of cell survival, proliferation and metabolism (e.g. forkhead box O family transcription factors (FoxO) and glycogen synthase kinase 3 (GSK3β)) [207]–[209]. AKT can altering cell cycle dynamics through FoxO suppression which regulates cell cycle arrest via p21 and p27 [210]–[213]. Furthermore, AKT-dependent phosphorylation of p21 prevents the formation of the p21-PCNA complex and in turn inhibits DNA replication fidelity. Furthermore, allowing for an accelerated rate of cell cycle progression through CDK2 and CDK4 [212]. Interestingly, in the presence of mitogenic signals, AKT can inactivate FoxO3a thus, increasing ROS production, DNA damage and Rb-mediated senescence [214]. Cells harboring DNA damage continue to progress through the cell cycle as a result of AKT-mediated phosphorylation of MDM2 inhibits p53 tumor suppressive activity [215]–[218].

AKT activity mediates cell survival by phosphorylating FoxO and mediates its binding to 14-3-3 [219]. Akt-dependent phosphorylation of FKHRL1, MAP kinase kinase kinase, apoptosis signal-regulating kinase 1 and mixed lineage kinase 3, suppress the transcription of death genes (e.g Fas ligand gene, etc.) and promots cell survival [219], [220]. AKT binds to the pro-apoptotic gene BAD, resulting in the activation of anti-apoptotic BCL2 through enhanced activity of cAMP-response element-binding protein (CREB) [221]. Phosphorylation of AKT is a negative modulator of pro-apoptotic BIM binding to BCL2 and inhibits the Caspase-9 protease activity [199], [222], [223]. Furthermore, AKT's requirement for glucose metabolism has been seen to suppress p53-dependant transcription of PUMA, preventing apoptosis via glucose depravation [224]. Interestingly, PUMA can be activated in a p53-independnat fashion, via FoxO3a and NF-κβ when AKT or PI3K signaling is inhibited [225]–[227].

3.2.2.2. AKT signaling: Cell Metabolism and Growth

AKT kinase activity activates mammalian target of rapamycin (mTOR) to promote protein synthesis, cell growth, biogenesis and anti-autophagy [228]. PTEN loss is attributed to the overexpression of Ras homolog enriched in brain (RHEB) protein leading to mTOR activation [229], [230]. Mechanistically, in the presence of aberrant AKT activity, the mTORC1 inhibitor tuberous sclerosis complex (TSC1 and TSC2) can no longer function to suppress RHEB. In addition, AKT can suppress the GSK3β and the energy sensing liver kinase B1 (LKB1)-AMP-activated protein kinase (AMPK) pathway which also phosphorylates TSC complex. The suppression of TSC complex allows for REHB to convert GDP to GTP and its subsequent activation of mTOR and its complexes (e.g. mTORC1 and mTORC2). mTOR signaling pathway simultaneously couples energy, stress, growth factors and nutrient abundance to execute its functions in cell growth and division [197].

mTOR forms two complexes to execute its function by regulating important kinases (e.g. 70S6 kinase (S6K) and AKT) required for cell growth and cell proliferation/survival, respectively [197]. The mTORC1 complex is composed of mTOR, DEP domain-containing mTOR-interacting protein (DEPTOR), mammalian lethal with SEC13 protein 8 (mLST8), 40 kDa Pro-rich AKT1 substrate 1 (PRAS40) and regulatory associated

protein of mTOR (RAPTOR). Secondly, the mTORC2 complex is composed of: mTOR, DEPTOR, mLST8, stress-activated MAP kinase-interacting protein 1 (mSIN1), Pro-rich protein 5 (PROTOR) and rapamycin insensitive companion of mTOR (RICTOR). Raptor is specific to mTORC1 and facilitates substrate recruitment to mTOR. Furthermore, mTORC1 contains inhibitory subunits PRAS40 and DEPTOR which are inhibited by active AKT. Importantly, mTORC1 not mTORC2 is sensitive to rapamycin pharmacological treatment due to the rapamycin-FKBP12 complex that forms and binds to mTOR [231]. mTORC2 contains Rictor, insensitive to rapamycin, as well as mSin1 and Protor1/2 and together can further phosphorylate AKT. Moreover, both of these complexes contain mLST8 which is crucial for mTOR function and the stimulation of its catalytic activity [232].

3.2.2.3. AKT signaling: Feedback Loops

AKT activation is accompanied by both positive and negative feedback loops. PI3K-AKT signaling can negativity regulate PTEN by activating its downstream target transcription factor NF-κB, peroxisome proliferator-activated receptor delta (PPARβ/δ) and tumor necrosis factor (TNFα), in turn suppressing PTEN activity (Fig. 1B) [233]–[235]. Furthermore, PI3K-AKT signaling activity can upregulate NEDD4-1, which targets PTEN for degradation [236], [237]. Downstream negative regulator of AKT signaling are protein phosphatases PP2A and PHLLP that dephosphorylate AKT [238], [239]. The loss of PHLPP1 and PHLPP2 expression is reduced in many cancers, resulting in AKT hyperphosphorylation [240].

The most prominent negative feedback loop regulating PI3K/AKT pathway is its downstream target mTORC1 complex (Fig. 1C). However, chronic insulin-mediated PI3K stimulation leads to phosphorylation and degradation of IRS-1 by mTORC1/p70S6K; decreasing inding of p85 subunit of PI3K to IRS-1 [241]–[243]. Furthermore, S6K1 and mTORC1 can phosphorylate IRS-1, preventing its recruitment and binding to RTKs [242], [242], [244]–[247]. Interestingly, PTEN loss can override the mTORC1-medaited negative feedback loop by overexpressing RHEB [229], [230]. Together, we see that the PI3K/AKT/mTOR pathway and its regulation by PTEN is crucial for the suppression of age-related disease such as diabetes and cancer. However, the field lacks on how these molecules interact together *in vivo* and systemically during tissue homeostasis.

3.3 Conservation of PI3K/PTEN/AKT pathway signal transduction in planarian

A multitude of updates and advances to the planarian genome and transcriptome have been made since 2013 [61], [106], [116], [117], [162], [248]–[253]. Over the years, genes in this dissertation have been identified and validated countless times. Thus, gene identification has been cross-referenced in SmedGD 2.0 [117], PlanMine1.0 [116], Toronto Transcriptome [106] and lastly in 2019, PlanMine3.0 [162]. Further details can be found in the methods and materials section. Gene identification of molecules found within the PI3K/PTEN/AKT/TOR signaling cascade were obtained by BLAST-ing the human sequence into PlanMine3.0 and cross-referenced using the Toronto Transcriptome. By doing so, many genes of this signaling pathway and downstream targets have been identified (Fig. 2A). For example, PI3K heterodimer protein complex PI3KR and PI3KCA are highly conserved in planarian (e.g. 30% and 38%, respectively). However, *Smed-PI3KR* does not contain SH3 domain, a requirement for biding to PxxP motifs and *Smed-PI3KCA* is missing the RAS biding domain (Fig. 2B,C). Next, we will concentrate on the conservation of PTEN, AKT and mTOR within planarian as these genes will be crucial for

A

		Human ID into PlanMine3.0			Toronto Genome Hit into PlanMine3.0			
			PlanMine3.0				PlanMine3.0	
Name	Human ID	PlanMine3.0	Total Score	E value	Toronto Genome	PlanMine3.0	Total Score	E value
PIK3R1	P27986	dd_Smed_v6_4794_0_1	203.76	1.83x10^-54	SmedASXL_006822	dd_Smed_v6_4794_0_1	5898.3	0
PK3CG	P48736	dd_Smed_v6_8025_0_1	379.41	7.18x10^-113	N/A	dd_Smed_v6_8025_0_1	N/A	N/A
IRS1	P35568	N/A	N/A	N/A	N/A	N/A	N/A	N/A
PTEN	P60484	dd_Smed_v6_8546_0_1	244.97	3.59x10^-74	SmedASXL_006734	dd_Smed_v6_8546_0_1	6754.26	0
PTEN	P60484	dd_Smed_v6_7478_0_1	240.35	1.48x10^-72	SmedASXL_012903	dd_Smed_v6_7478_0_1	7220.28	0
PDPK1	O15530	dd_Smed_v6_9662_0_1	356.3	9.46x10^-115	SmedASXL_010239	dd_Smed_v6_9662_0_1	2857.82	0
AKT1	P31749	dd_Smed_v6_4393_0_1	538.88	0	N/A	N/A	N/A	N/A
AKT2	P31751	dd_Smed_v6_4393_0_1	534.64	0	SmedASXL_006249	dd_Smed_v6_4393_0_1	3662.12	0
AKT3	Q9Y243	dd_Smed_v6_4393_0_1	551.21	0	N/A	N/A	N/A	N/A
TSC1	Q92574	N/A	N/A	N/A	N/A	N/A	N/A	N/A
TSC2	P49815	dd_Smed_v6_6504_0_1	107.07	1.19x10^-22	N/A	N/A	N/A	N/A
mTOR	P42345	dd_Smed_v6_3921_0_1	1518.78	0	SmedASXL_016999	dd_Smed_v6_3921_0_1	15780.8	0
RICTOR	Q6R327	dd_Smed_v6_9324_0_6	296.96	6.04x10^-39	SmedASXL_017866	dd_Smed_v6_9324_0_6	9164.2	0
RPTOR	Q8N122	dd_Smed_v6_4759_0_1	824.68	2.42x10^-127	SmedASXL_013989	dd_Smed_v6_4759_0_1	8552.35	0
MLST8	Q9BVC4	dd_Smed_v6_3174_0_1	252.29	1.45x10^-79	SmedASXL_005234	dd_Smed_v6_3174_0_1	2080.57	0
PRR5	P85299	N/A	N/A	N/A	SmedASXL_008947	dd_Smed_v6_9467_0_1	3029.14	0
PRR5L	Q6MZQ0	dd_Smed_v6_12983_0_1	50.06	1.39x10^-06	SmedASXL_009013	dd_Smed_v6_12983_0_1	1855.15	0
DEPTOR	Q8TB45	N/A	N/A	N/A	N/A	N/A	N/A	N/A
PRAS40	Q96B36	N/A	N/A	N/A	N/A	N/A	N/A	N/A
mSIN1	Q9BPZ7	dd_Smed_v6_11576_0_1	96.67	8.12x10^-21	SmedASXL_013473	dd_Smed_v6_11576_0_1	3425.88	0

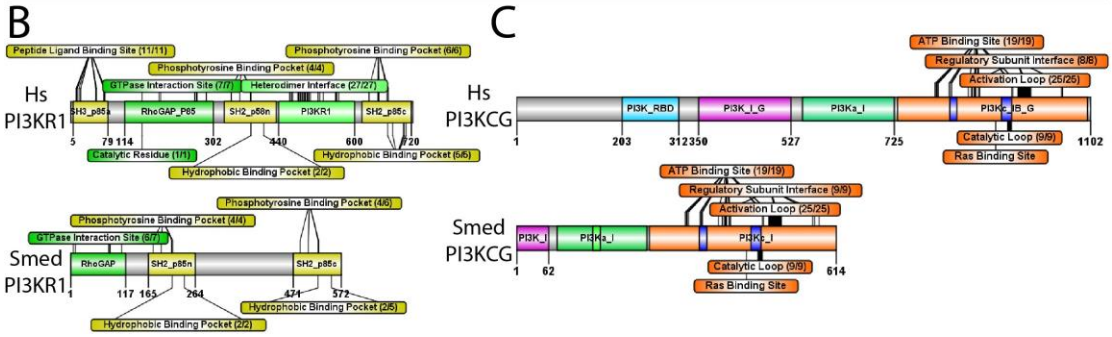

Figure 2. Conservation of the planarian PI3K/PTEN/AKT/TOR signaling cascade. (A) BLAST outcomes of the human genes placed into the various planarian databases such as PlanMine3.0 (left side) and Toronto genome transcripts placed into the PlanMine3.0 (right). Subject IDs, total score and E values were documented. (B, C) Conservation of planarian Smed-PI3K(R1) and Smed-PI3K(CG) protein structure relative to the human counterpart.

RNA interference regimen created to test if the planarian is an exemplary model to test the OTS-DDM.

3.3.1. Identification of *Smed-PTEN*

Human PTEN consists of four main regions that allow for PTEN's phosphatase activity as it migrates from the cytosol to the plasma membrane of a cell. First, the N-terminal of PTEN consists of a phosphoinositide-binding motif (PBM) required for its allosteric binding to PI(4,5)P2 on the plasma membrane [254]–[256]. Second, the phosphate domain of PTEN recognizes and hydrolyzes the substrate PI(3,4,5)P3 [255]. Third, a C2 domain electrostatically attracts and binds phosphatidylserine onto the plasma membrane independently of Ca2+ membrane voltage-gated channels [255], [257], [258]. The end of the PTEN protein contains a C-terminal tail which negativity regulates the phosphatase activity by binding to the C2 and phosphatase domains when phosphorylated [258]. Therefore, the selectivity of PTEN for the plasma membrane is mediated by interactions within the C- and N-terminal ends (Fig. 3A).

The function of PTEN signaling has been identified and characterized in the planarian model over ten years ago [56]. Oviedo et al. 2009 identified two paralogues of human PTEN in the planarian known as *Smed-PTEN-1* and *Smed-PTEN-2*. The

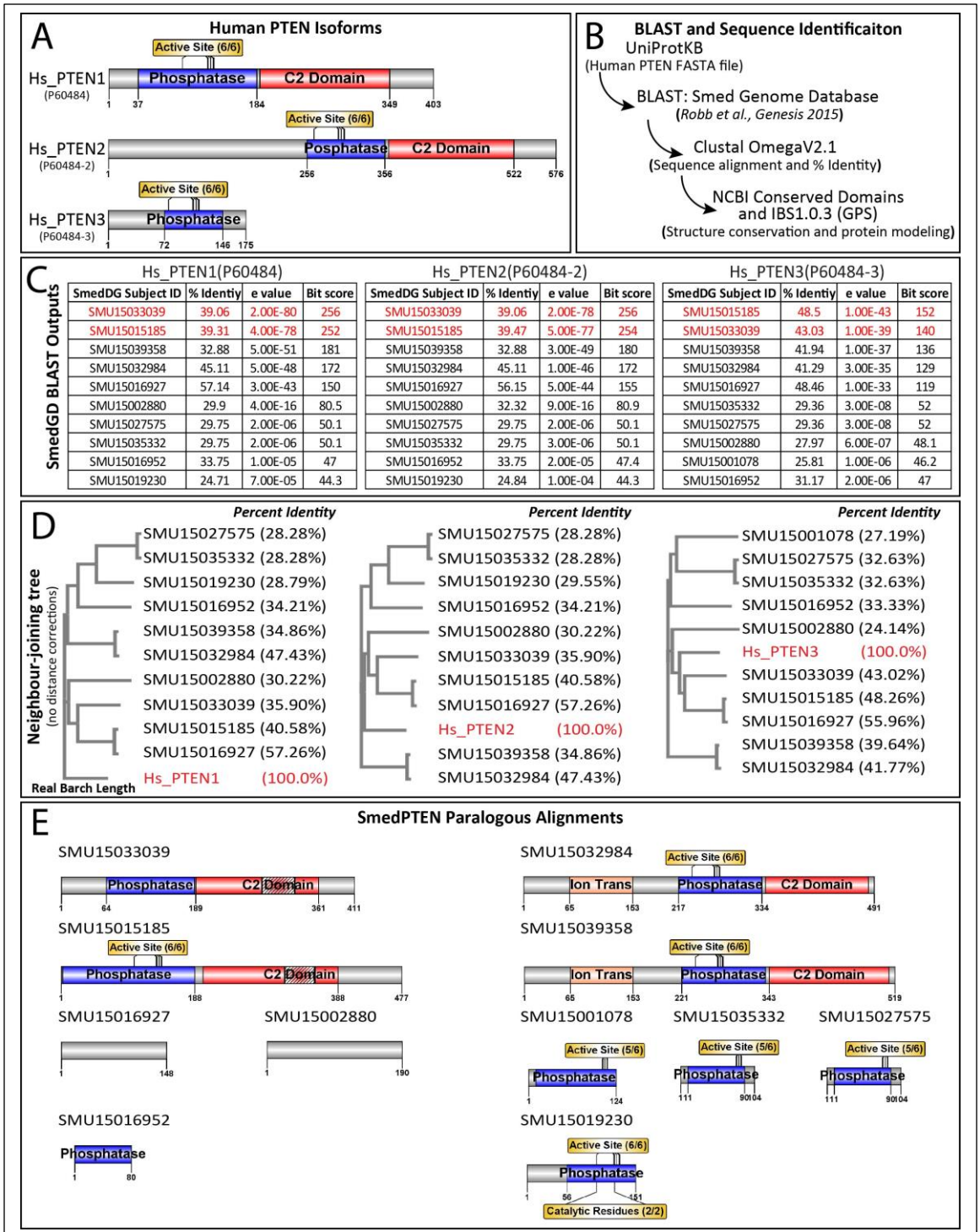

Figure 3. PTEN homologs identification through SmedGD2.0. (A) The three human isoforms of PTEN. (B) BLAST and sequence identification strategy. (C) SmedGD BLAST outputs for each of the three human isoforms. (D) Phylogenetic trees, neighbor-joining tree with real branch length of all SMU ID hits against the three-individual human PTEN isoforms. (E) Protein domain conservation of the eleven *Smed-PTEN* paralogues.

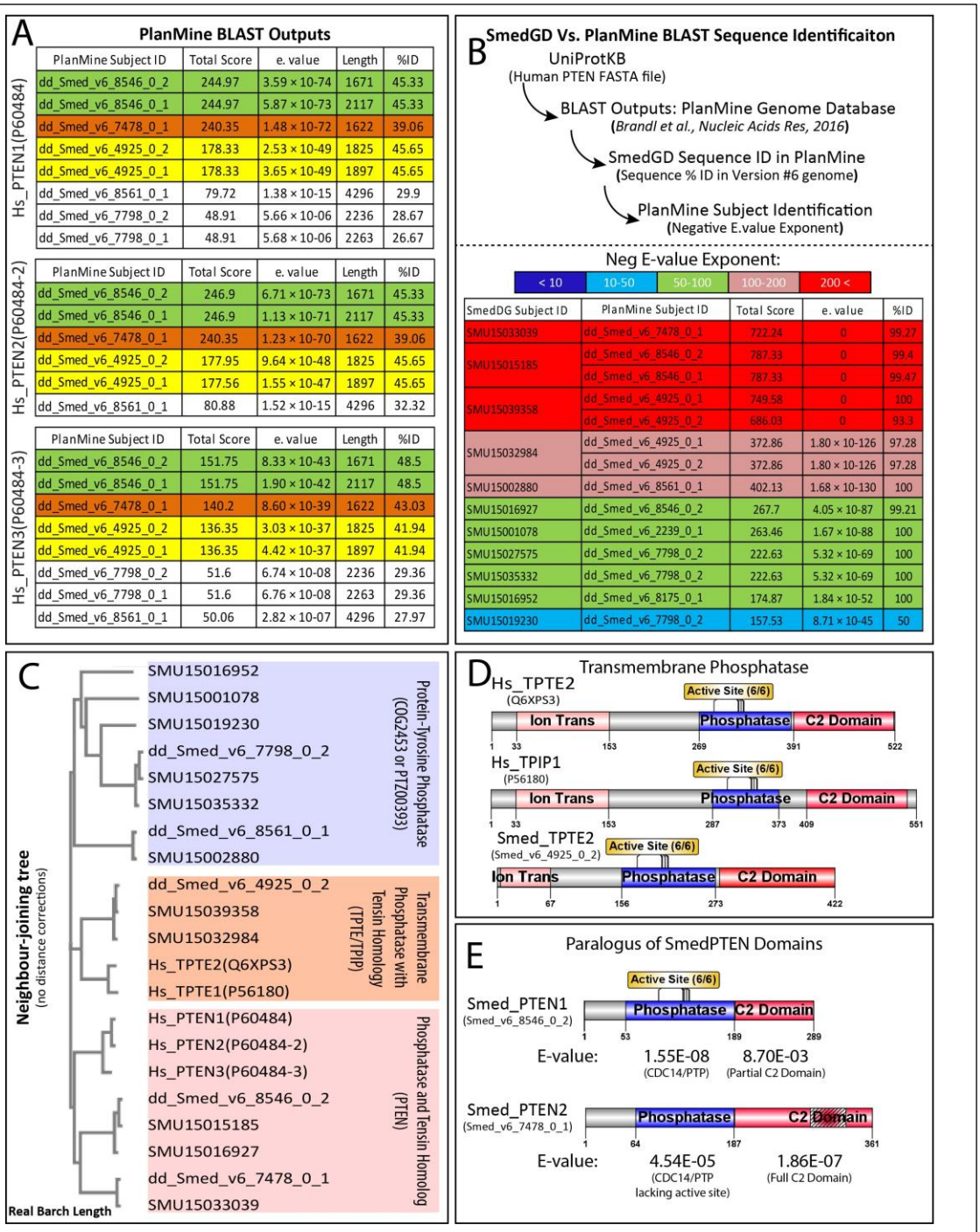

Figure 4. PTEN homologs identification through PlanMine. (A) The three human isoforms were BLAST-ed into PlanMine and V6 IDs were obtained. Green, orange and yellow represent like outputs. (B) BLAST and sequence identification strategy. Bottom: The outputs of SmedGD were placed into PlanMine and were BLAST-ed to obtain the V6 ID. Color represent the E. value of the sequence within PlanMine. (C) Phylogenetic trees, neighbor-joining tree with real branch length of all SMU ID hits, with PlanMine IDs and the three-individual human PTEN isoforms. (D) Identification of the Smed-TPTE2 transmembrane phosphatase protein conservation (E) Protein domain conservation of the two *Smed-PTEN* paralogues.

paralogues were identified in the SmedDb database published in 2002 [252]. However, recent updates to the planarian genome database (e.g. SmedDG 2.0) resulted in additional maker annotations for the three human PTEN (Hs_PTEN-1, -2 and -3). The initial BLAST of the three Hs_PTEN isoforms into SmedDG 2.0 resulted in 10 additional maker annotation without e-values of zero (Fig. 3B, C, D). Maker annotations SMU15033039 and SMU15015185 ranked the highest in terms of bit score and e-value. However, all maker IDs when placed into Clustal Omega V2.1 to identify percent identity and phylogeny, we found that SMU15016927 was relatively closer to Hs_PTEN1. Consistently, this maker ID was clustered around SMU15033039 and SMU15015185 in context to Hs_PTEN1/2/3 on the neighbor-joining trees. In addition, SMU15039358 and SMU15032984 clustered together in all cases. To resolve this issue, the structural conservation of all 10 BLAST hits were investigated (Fig. 3E). We found that the top ranked maker genes SMU15033039 and SMU15015185 both contained a phosphatase domain and a C2 domain with gap a region. The maker annotation with the highest percent identity to Hs_PTEN1, SMU15016927 did not contain any domains as well as SMU15002880. Interestingly, the clustering of SMU15039358 and SMU15032984 was correlated to their resemblance to PTEN transmembrane phosphatase (TPTE/TPIP) as they both contained an ion transmembrane phosphatase domain. Moreover, the rest of the maker IDs consisted of phosphatase domains with a variation of active sites and catalytic residues.

Next, we BLAST-ed Hs_PTEN1/2/3 into PlanMine1.0 database. The results yielded dd_Smed_v6_8546_0_1, dd_Smed_v6_7478_0_1, and dd_Smed_v6_4925_0_1 as top BLAST hits and highest percent identities (e.g. Hs_PTEN1/2: 45%, 39%, 46%, and Hs_PTEN3: 49%, 43% and 42%, respectively) (Fig. 4A). To identify what maker annotation from SmedGD correlated to PlanMine1.0 V6 IDs, we BLAST-ed the SMU sequences into PlanMine1.0. Direct targets for SMU and Smed_v6 were correlated with e-values of zero (Fig. 4B). Using neighbor-joining trees, we identified that dd_Smed_v6_4925_0_1 clustered with SMU15039358 and was identified with as *Smed-TPTE2* (Fig. 4C). Furthermore, dd_Smed_v6_8546_0_1 and dd_Smed_v6_7478_0_1 clustered with SMU15015185 and SMU15033039, respectively. Interestingly, *Smed-PTEN1* (dd_Smed_v6_8546_0_1) contained a phosphatase domain with active sites and a partial C2 domain. On the other hand, *Smed-PTEN2* (dd_Smed_v6_7478_0_1) contained a phosphatase domain lacking active sites and a full C2 domain with a gap region (Fig. 4D, E). Lastly, the remainder of the clustered together, resembling protein-tyrosine phosphatase (COG453 or PTZ00393)

In 2018 and 2019, the Toronto transcriptome and PlanMine3.0 were published. Here we identified bonafide *Smed-PTEN1, Smed-PTEN2* and *Smed-TPTE2.* To validate the Toronto Transcriptome, we BLAST-ed their transcripts in preexisting databases, and the outcomes were consistent with V6 IDs (Fig. 5A). *Smed-PTEN1* and *Smed-PTEN2* are highly conserved across many species. Specifically, 37.7% and 35.6% to human counterpart, respectively (Fig. 5B). Interestingly, *Smed-PTEN1* contains a phosphatase domain with 6/6 active sites and now, unlike PlanMine1.0, a full C2 domain with a gap region 296-351. *Smed-PTEN2* was found to contain a phosphatase domain lacking active sites and a C2 domain with a gap region 302-347 (Fig. 5C).

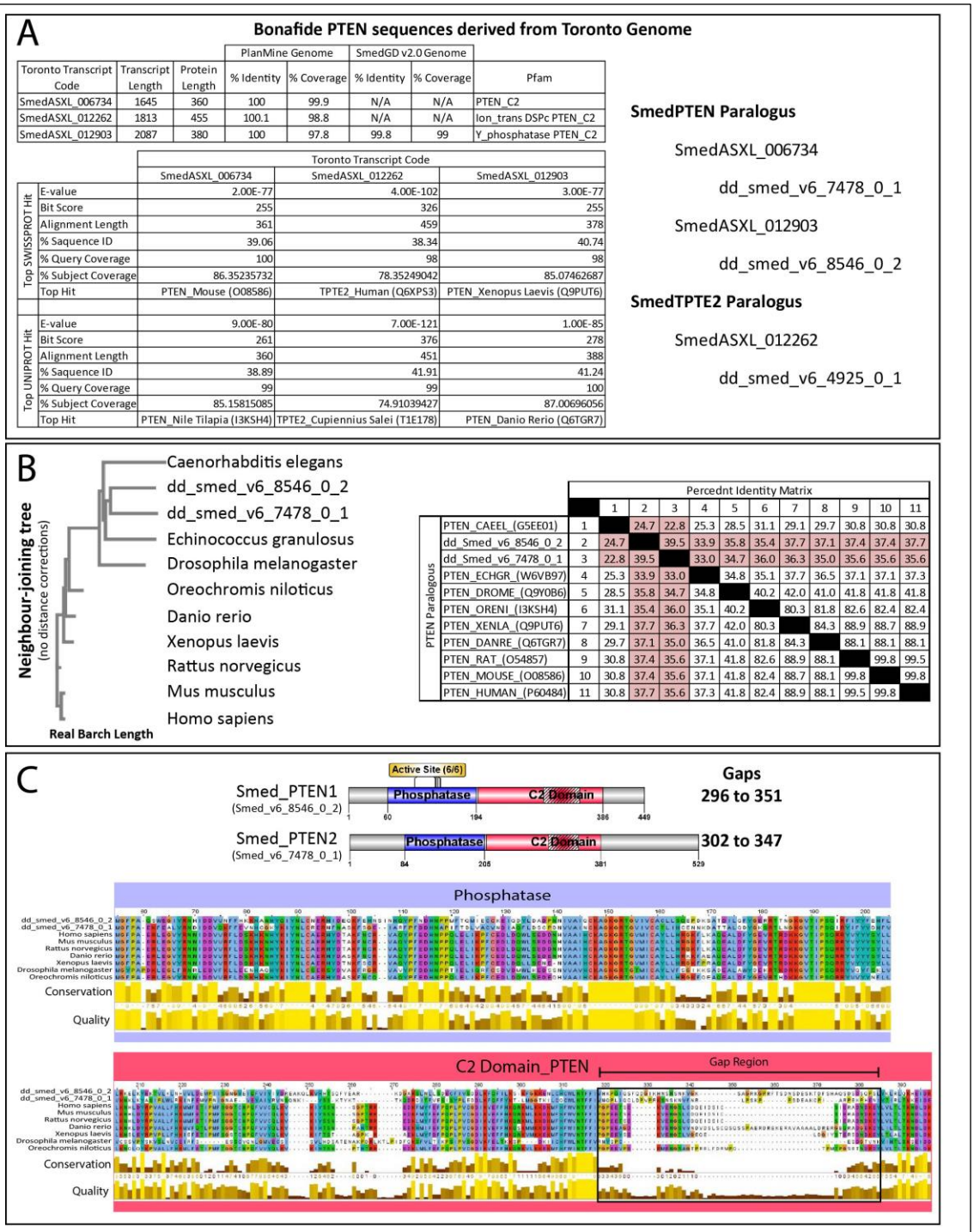

Figure 5. Bonafide PTEN sequences derived from Toronto Genome. (A) The search outputs for PTEN homologs within the database. Transcript code and top UniPort or SwissProt BLAST hits. (B) Phylogenetic trees, neighbor-joining tree with real branch length of transcript codes aligned to other species and to the right the percent identity matrix. (C) Protein domain conservation of the two *Smed-PTEN* paralogues revealing gap regions. The bottom is an up-close view of the sequence alignments for the input species. Sequence regions were isolated to zoom into the phosphatase and C2 domain region of PTEN across species.

3.3.2. Conservation of AKT

Human AKT also known as protein kinase B is an important serine/threonine kinase and consists of three isoforms AKT1, AKT2 and AKT3. These isoforms all contain highly homologous structures but their knockout in mice produce independent outcomes [259]–[262]. Each isoform contains four functional domains: (1) N-terminal pleckstrin homology domain, (2) central catalytic domain, (3) hinge region and (4) C-terminal regulatory domain [262], [263]. Importantly, the pleckstrin homology domain binds to phosphoinositides with high affinity (e.g. PIP3). Disruption of pleckstrin homology domain via somatic mutations results in constitutively activity and oncogenic activation of AKT in human cancers (Fig. 6A) [264].

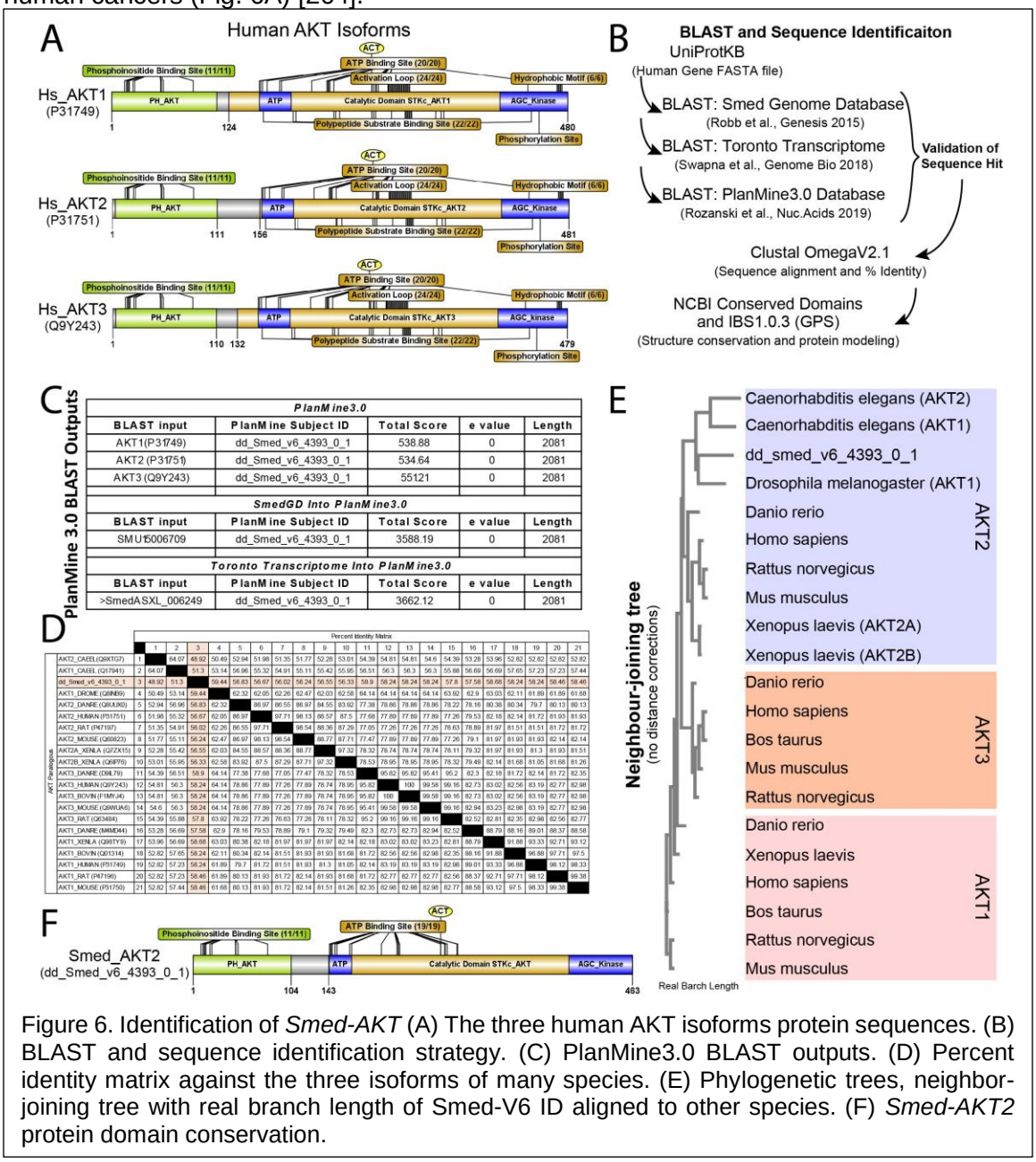

Figure 6. Identification of *Smed-AKT* (A) The three human AKT isoforms protein sequences. (B) BLAST and sequence identification strategy. (C) PlanMine3.0 BLAST outputs. (D) Percent identity matrix against the three isoforms of many species. (E) Phylogenetic trees, neighbor-joining tree with real branch length of Smed-V6 ID aligned to other species. (F) *Smed-AKT2* protein domain conservation.

To find the planarian AKT paralogues, we used the same regimen as previously discussed. BLAST-ing the three human AKT isoforms in SmedGD2.0 resulted in direct hits (e.g. e-values of zero) for all isoforms. However, each hit held the same ID number, SMU15006709 with their percent identify varying depend on isoform (e.g. 57%, 56% and 57%) (Fig. 6B, C). This may indicate that planarian only contain one form of AKT. To validate these findings, all three human isoforms we placed into PlanMine3.0 and again direct hits were obtained for the three isoforms (dd_Smed_v6_4393_0_1). Further conformation was obtained by BLAST-ing both the SMU ID and Toronto transcript into PlanMine3.0. Furthermore, to discern which AKT isoform planarian contain, we placed an array of isoforms from different species into Clustal Omega (Fig. 6D). The percent identity of *Smed-AKT* ranged from 56-60% depending on what species and isoform it correlated to in the matrix. Observing phylogeny, *Smed-AKT* clustered closely with Hs_AKT2 (Fig. 6E). *Smed-AKT* contains a highly conserved pleckstrin homology domain and central catalytic domain with an ATP region and a C-terminal AGC_Kinase region. However, it lacks conserved structures such as an activation loop, polypeptide substrate biding sites, hydrophobic motif and phosphorylation site (Fig. 6F).

3.3.3. Conservation of TOR, RICTOR and RAPTOR

Mechanistic target of rapamycin, Hs_mTOR contains a large FRB domain known as the FKBP12-rapamycin biding domain. This domain is where Rapamycin macrolide antibiotic and the cytosolic protein FKBP12 inhibit the formation of TORC1 complex. Within this domain, there are many HEAT (Huntington elongation factors) repeats, a FAT and a catalytic (PIKKc_TOR) domain, which have intrinsic serine/threonine kinase activity. After this catalytic domain, a small FATC (FRAP, ATM, TRRAP C-terminal) domain is present where redox-dependent structural stability and cellular stability occur. BLAST-ing Hs_TOR in various planarian databases resulting in a direct hit in all cases. Thus, *Smed-TOR* is identified by dd_Smed_v6_3921_0_1 and is 35.70% identical to the human counterpart. *Smed-TOR* contains a conserved FRB domain, HEAT repeats and a FAT domain however, it lacks a PIKKc_TOR catalytic domain (Fig. 7A).

TOR can form complexes mTORC1 and mTORC2 thus, key components of the complexes were identified in the planarian. The first complex is formed with Hs_RAPTOR that contains a Raptor N-terminal that is a CASPase-like domain. Further, it contains multiple HEAT repeats and WD40 repeats (e.g. 4 and 7, respectively). The WD40 repeats are found within RAPTOR's C-terminal and may coordinate interaction with other proteins/ligands. Interestingly, there were a few maker annotations found that resemble Hs_RAPTOR. Through further analysis, we identified that majority of the hits had low or no similarity to the human counterpart. Therefore, *Smed_RAPTOR* (dd_Smed_v6_4759_0_1) was identified to be 55.80% homologous to *Hs_RAPTOR* and contained a highly conserved Raptor N-terminal domain that is CASPase-like (Fig. 7B). The second complex is formed with Hs_RICTOR which contains a Rictor N-terminal, a middle domain, a RasGEF domain, Rictor domain 5 and Rictor phosphorylation-site. Interestingly, BLAST results using Hs_RICTOR in SmedDG2.0 yielded four maker annotations. However, in PlanMine3.0, Hs_RICTOR resulted in a direct hit (dd_Smed_v6_9324_0_6). The other subject IDs clustered within themselves and did not contain conserved domains of RICTOR. Thus, the planarian *Smed_RICTOR* is 33.14% homologous to the human counterpart and contains a middle domain, a RasGEF domain, Rictor domain 5 (Fig. 7C).

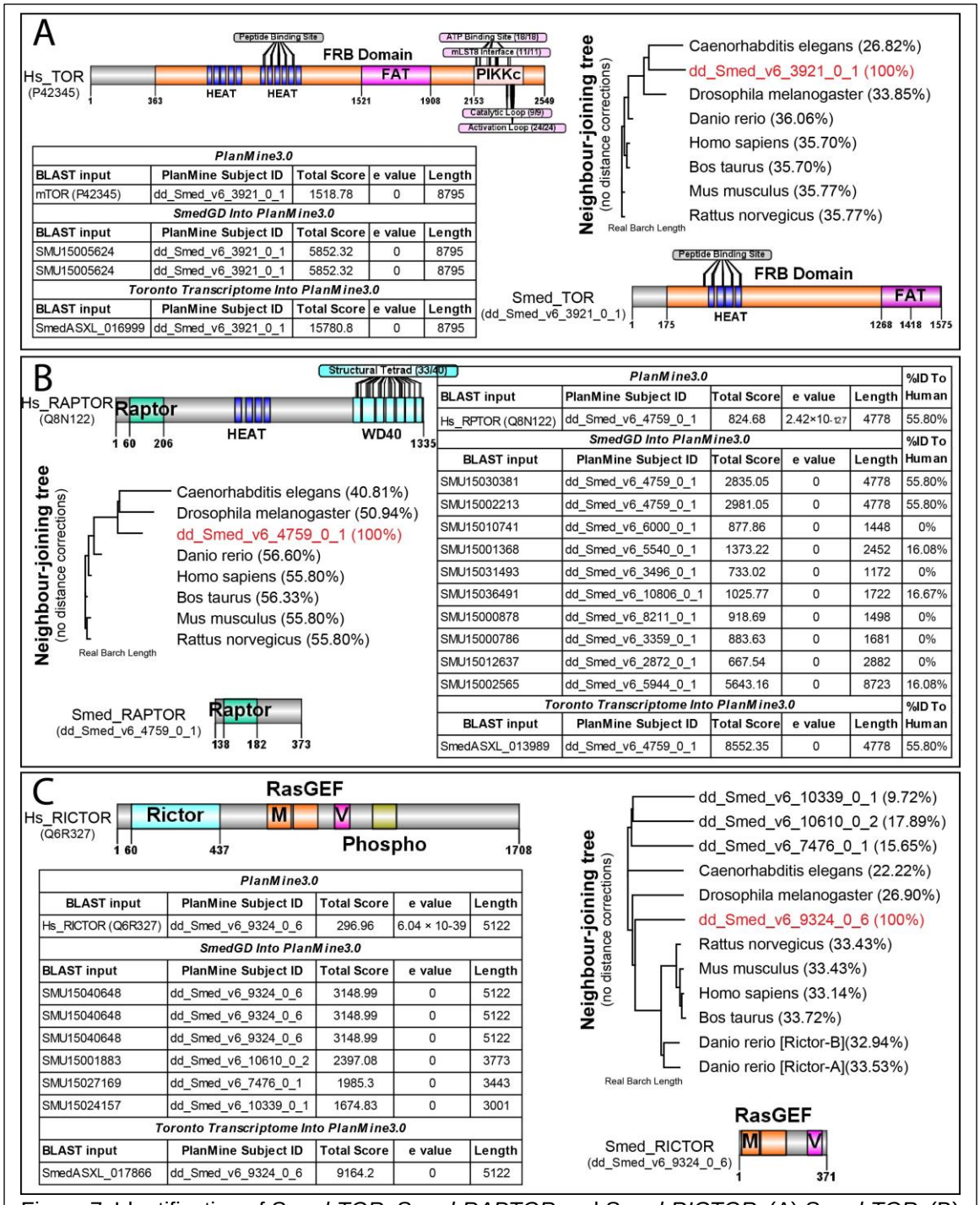

PlanMine3.0

BLAST input	PlanMine Subject ID	Total Score	e value	Length
mTOR (P42345)	dd_Smed_v6_3921_0_1	1518.78	0	8795

SmedGD Into PlanMine3.0

BLAST input	PlanMine Subject ID	Total Score	e value	Length
SMU15005624	dd_Smed_v6_3921_0_1	5852.32	0	8795
SMU15005624	dd_Smed_v6_3921_0_1	5852.32	0	8795

Toronto Transcriptome Into PlanMine3.0

BLAST input	PlanMine Subject ID	Total Score	e value	Length
SmedASXL_016999	dd_Smed_v6_3921_0_1	15780.8	0	8795

PlanMine3.0

BLAST input	PlanMine Subject ID	Total Score	e value	Length	%ID To Human
Hs_RPTOR (Q8N122)	dd_Smed_v6_4759_0_1	824.68	2.42×10-127	4778	55.80%

SmedGD Into PlanMine3.0

BLAST input	PlanMine Subject ID	Total Score	e value	Length	%ID To Human
SMU15030381	dd_Smed_v6_4759_0_1	2835.05	0	4778	55.80%
SMU15002213	dd_Smed_v6_4759_0_1	2981.05	0	4778	55.80%
SMU15010741	dd_Smed_v6_6000_0_1	877.86	0	1448	0%
SMU15001368	dd_Smed_v6_5540_0_1	1373.22	0	2452	16.08%
SMU15031493	dd_Smed_v6_3496_0_1	733.02	0	1172	0%
SMU15036491	dd_Smed_v6_10806_0_1	1025.77	0	1722	16.67%
SMU15000878	dd_Smed_v6_8211_0_1	918.69	0	1498	0%
SMU15000786	dd_Smed_v6_3359_0_1	883.63	0	1681	0%
SMU15012637	dd_Smed_v6_2872_0_1	667.54	0	2882	0%
SMU15002565	dd_Smed_v6_5944_0_1	5643.16	0	8723	16.08%

Toronto Transcriptome Into PlanMine3.0

BLAST input	PlanMine Subject ID	Total Score	e value	Length	%ID To Human
SmedASXL_013989	dd_Smed_v6_4759_0_1	8552.35	0	4778	55.80%

PlanMine3.0

BLAST input	PlanMine Subject ID	Total Score	e value	Length
Hs_RICTOR (Q6R327)	dd_Smed_v6_9324_0_6	296.96	6.04 × 10-39	5122

SmedGD Into PlanMine3.0

BLAST input	PlanMine Subject ID	Total Score	e value	Length
SMU15040648	dd_Smed_v6_9324_0_6	3148.99	0	5122
SMU15040648	dd_Smed_v6_9324_0_6	3148.99	0	5122
SMU15040648	dd_Smed_v6_9324_0_6	3148.99	0	5122
SMU15001883	dd_Smed_v6_10610_0_2	2397.08	0	3773
SMU15027169	dd_Smed_v6_7476_0_1	1985.3	0	3443
SMU15024157	dd_Smed_v6_10339_0_1	1674.83	0	3001

Toronto Transcriptome Into PlanMine3.0

BLAST input	PlanMine Subject ID	Total Score	e value	Length
SmedASXL_017866	dd_Smed_v6_9324_0_6	9164.2	0	5122

Figure 7. Identification of *Smed-TOR, Smed-RAPTOR* and *Smed-RICTOR.* (A) *Smed-TOR.* (B) *Smed-RAPTOR.* (C) *Smed-RICTOR.* (A, B, C) The human protein domain is represented in the top left. The table represent the BLAST outputs for PlanMine3.0, SmedDG IDs and Toronto transcript code. Percent identity is noted in the phylogenetic trees, neighbor-joining tree with real branch length of Smed-V6 ID aligned to other species. Lastly, the smed homolog of the perspective gene.

3.4. *Smed-PTEN* function in planarian

3.4.1. *Smed-PTEN* genes are expressed in neoblasts and differentiated cell populations

Through FACS sorting, cells of the X1 and X2 (i.e. irradiation-sensitive populations) and the irradiation-insensitive Xins population were isolated [56]. Using qPCR, Oviedo et al. 2008 identified that *Smed-PTEN-1* and *Smed-PTEN-2* were found within all three cell populations with elevated expression in the Xins population. Recently, with advances in the planarian field (e.g. annotated genome and single cell sequencing) we are now able to further characterize the expression pattern of *Smed-PTEN-1* and *Smed-PTEN-2*.

Labbe et al. 2012 [250] found through FACS sorted cell populations that the expression index of *Smed-PTEN1* and *Smed-PTEN2* was highly expressed in the differentiated cell compartment with a slight expression in neoblast and their cell progeny compartments (e.g. Xins, X1 and X2, respectively) (Fig. 8A). These findings support Oviedo et al. 2008 findings with FACS sorted cells. In 2015 Wurtzel et al. conducted a single-cell RNAseq and identified many expression values within major cell type clusters (e.g. neoblast, early and late progeny and differentiated tissues) [53]. Examining the violin plots of expression values within different clusters, it is evident that *Smed-PTEN1* and *Smed-PTEN2* are expressed within the neoblast populations sigma, gamma and zeta however, their expression levels are minimal in the early epithelial tissue progeny (e.g. early epithelial) (Fig. 8B). Interestingly, their expression levels increase within the late epithelial and epithelial 1, gut and ciliated neurons with negligible expression in other differentiated tissue sections. The database published by Fincher et al. 2018, further confirm the spatial distribution of *Smed-PTEN1* and *Smed-PTEN2* expression levels (Fig. 8C) [265]. Specifically, *Smed-PTEN1* is identified to be highly expressed in the major cluster 40 of the protonephridia and sub-cluster group 11 of epidermal cells (Fig. 8D, E). *Smed-PTEN2* yielded higher expression levels in main clusters: Cathepsin+ cells (e.g. groups 10, 15, 17, 28, 31, 39 and 41) and group 29 of the protonephridia, as well as minor subclusters: Cathepsin+ cells group 13 and brain group 14 (C2) (Fig. 8D, E).

Single cell transcriptomics conducted by Plass et al, 2018 allowed for lineage tree tracking of cells and greater resolution in gene expression analysis [266]. *Smed-PTEN1* and *Smed-PTEN2* were expressed at low levels in the center of the tree which cluster neoblasts (Fig. 9A). In addition, both genes were expressed in the parenchymal cells and highly enriched in the aqp+ cells. *Smed-PTEN1* had higher coverage throughout many other differentiated tissue compartments (e.g. neural, muscle, secretory and epidermal) when compared to *Smed-PTEN2*, which was additionally expressed in the protonephridia compartment. Normalized gene expression levels allowed for a higher resolution of linage specificity against pseudotime (Fig. 9B). *Smed-PTEN1* and *Smed-PTEN2* were enriched in the epidermis cell population and the phagocytes of the gastrovascular lineage. There expression was found to be elevated in the muscle pharynx, muscle body and pharynx cell types. In terms of the parenchymal lineage both *Smed-PTENs* were expressed in the pgrn+, glia, pigment and aqp+ cell lineages. Interestingly, *Smed-PTEN1* and *Smed-PTEN2* were expressed in the secretory 1 and 3 lineages which filtration is correlated with the protonephridia where their expression levels are elevated. Lastly, *Smed-PTEN1* and *Smed-PTEN2* were slightly expressed in the neural progenitor linage and highly expressed in the differentiated compartments (e.g. cav1+, GABA, ChAT1/2, appp11+ and

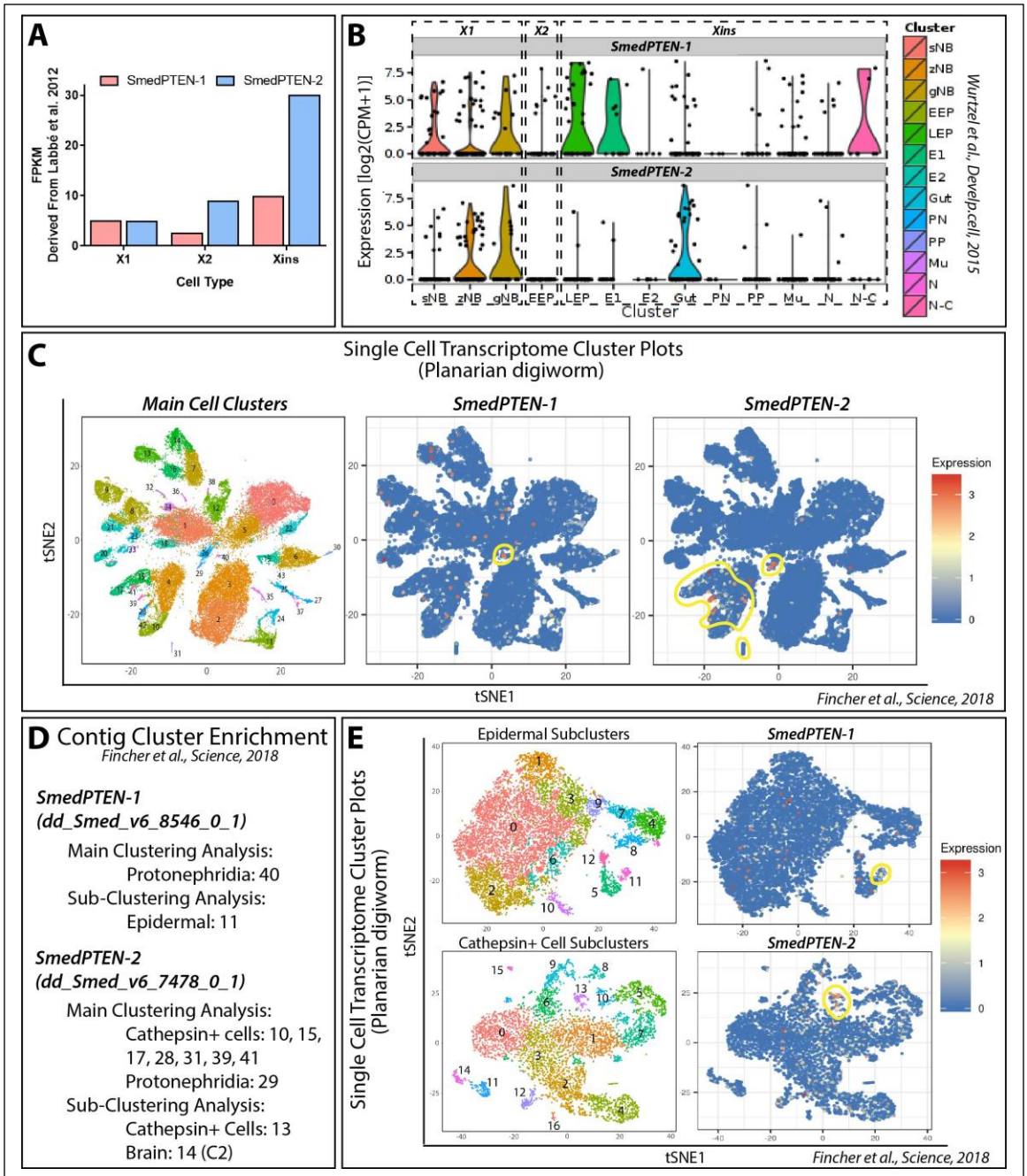

Figure 8. *Smed-PTEN* cluster enrichment. (A) FACS isolated cells published by Lebbe et al. 2012 depicting *Smed-PTEN-1, -2* expression within the various neoblast populations. (B) Violin plots showing expression of *Smed-PTEN-1, -2* clustering within the neoblast and differentiae tissue compartments (e.g. epithelial, gut and neural). (C) Single cell transcriptomic cluster plots showing *Smed-PTEN-1, -2* within protonephridia and cathepsine+ cells, respectively. (D) Contig cluster enrichment summary. (E) Single cell transcriptomic cluster plots showing *Smed-PTEN-1, -2* within sub-clusters such as epidermal 11 and brain 14(C2), respectively.

npp18+ cells). Together, both paralogues of PTEN are highly expressed within the differentiated tissue lineages and slightly expressed in the neoblast and early neoblast progenitors. Noteworthy, *Smed-PTEN1* and *Smed-PTEN2* expression levels were seen to be highly elevated in the neural progenitor linage relative to the other tissue progenitors.

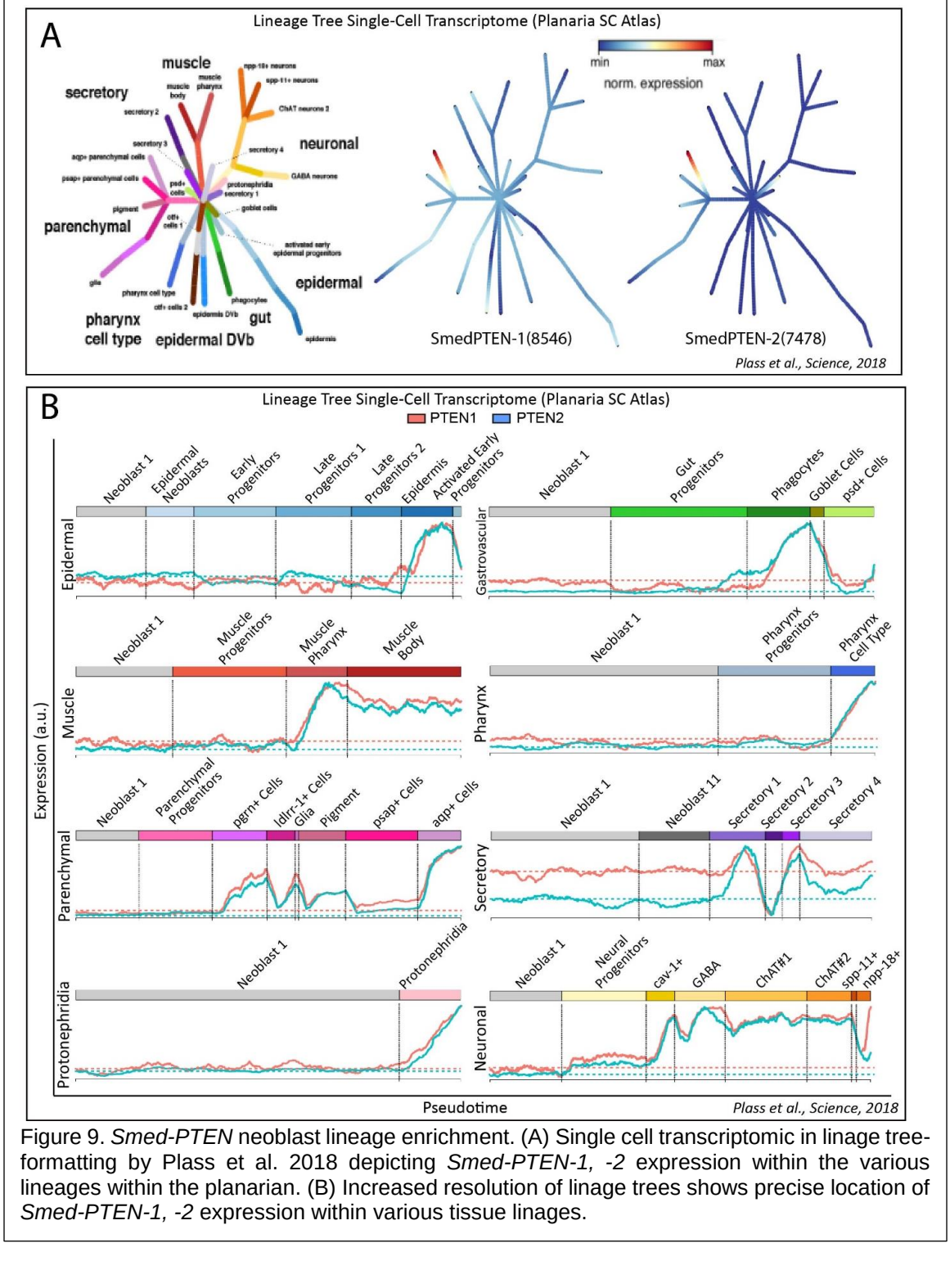

Figure 9. *Smed-PTEN* neoblast lineage enrichment. (A) Single cell transcriptomic in linage tree-formatting by Plass et al. 2018 depicting *Smed-PTEN-1, -2* expression within the various lineages within the planarian. (B) Increased resolution of linage trees shows precise location of *Smed-PTEN-1, -2* expression within various tissue linages.

3.4.2. Silencing of *Smed-PTEN* results in abnormal tissue growth, lethality and cellular transformation

Oviedo et al. 2008 identified that single RNAi of the *Smed-PTEN* paralogues did not result in a phenotype. However, double RNAi of *Smed-PTEN-1* and *Smed-PTEN-2* (*Smed-PTEN*, henceforth) resulted in animals that slowed in movement, lack normal photophobic response and head regression that is attributed to impaired neoblast function. Accompanied to these characteristics, abnormal tissue outgrowth formed and increased in size 12 days post first injection, concluding with full animal lysis and death by day 15. Interestingly, abnormal outgrowths and their severity were correlated to anterior-specific tissues within the head region of the animals. These results suggest that the anterior region of the animals play an important part in the *Smed-PTEN(RNAi)* phenotype.

Smed-PTEN(RNAi) animals displayed evidence of hyperplasia, in which the normal monolayered epidermis and pharynx tissues became multilayered. The basement membrane of the epithelium and pharynx tissues revealed an increase of cell number and was attributed to a significant increase in mitotic cells. Furthermore, differentiated tissues were compromised by RNAi treatment. Specifically, photoreceptors were found to be in disarray above the eyes, musculature displayed areas devoid of myosin positive cells and cilia that covers the dorsal surface area was reduced. Obtaining dissociated cells from the experimental group, Oviedo et al. 2008 found a substantial increase in expression of neoblast markers and a marked reduction in the expression of differentiated cell marker expression (e.g. neuronal, excretory and digestive). These results suggest that defects within neoblast differentiation and their progeny are compromised after silencing of *Smed-PTEN*.

3.4.3. Rapamycin prevents abnormalities produced by *Smed-PTEN(RNAi)*

Smed-PTEN(RNAi) is associated with activated PI3K/AKT/mTOR signaling activity. They found that inhibition of mTOR activity though rapamycin treatment recapitulated the *Smed-PTEN(RNAi)* phenotype. Molecular analysis identified that rapamycin treatment resulted in decreased mitotic activity and gene expression for proliferative neoblast markers. Interestingly, treatment was incapable of restoring gene expression levels of differentiated tissue markers (e.g. neuronal and digestive) and exacerbated their expression levels when compared to *Smed-PTEN(RNAi).*

The oncoprotein AKT was elevated in the *Smed-PTEN(RNAi)* phenotype showing a striking increase in FACS sorted cells. Specifically, *Smed-AKT* expression was increased 1.3-fold change in X1, 4.2-fold in the X2 compartment and in the Xins, 1.6-fold. Moreover, rapamycin treatment was able to downregulate *Smed-AKT* expression to basial levels. Performing double RNAi with *Smed-AKT* and *Smed-PTEN* resulted in no reduction of mitotic events and animals still formed abnormal outgrowth. Interestingly, the head regression phenotype and outgrowths were no longer seen in the anterior region of the animals. Moreover, exposing double RNAi of *Smed-AKT+PTEN* to rapamycin treatment yielded a marked reduction in mitotic activity. Strikingly, abnormal tissue outgrowths still formed within these animals. Together, this data suggests that rapamycin requires functional *Smed-AKT* to prevent the *Smed-PTEN(RNAi)* phenotype.

3.5. *Smed-TOR* function in planarian

The function of TOR signaling has been recently characterized in the planarian model however, its function remains debatable. In 2012, three labs (Oviedo, Sanchez-Alvarado, and Aboobaker) simultaneously characterized and published on *Smed-TOR* and the conservation of all its components (e.g. TOR, Raptor, Rictor, LST8 and SIN1) [57], [109], [267]. Currently, the gaps are as follows: (1) the cell type(s) *Smed-TOR* is found within and functions and (2) its role during tissue homeostasis. Here, we will aim to resolve the current debate on the role of *Smed-TOR.*

3.5.1. *Smed-TOR, Smed-Raptor* and *Smed-Rictor* genes are expressed in neoblasts and differentiated cell populations

All three papers identified that *Smed-TOR, Smed-Raptor* and *Smed-Rictor* expression levels are diffused throughout the planarian body except within the pharyngeal areas. Tu et al. 2012 identified that *Smed-TOR* and *Smed-Raptor* positive cells are associated with the brain and gastrovascular system [267]. However, *Smed-Rictor* expression patter is nonspecific and further diffused throughout the mesenchymal tissues. To identify what cell types these genes are expressed in, irradiation techniques and FACS-cell isolation were used. Through irradiation, Tu et al. 2012 identified that *Smed-TOR* and *Smed-Raptor* were not affected by lethal doses of gamma irradiation (>60 Gy) suggesting their expression to be within the post-mitotic tissues. However, *Smed-Rictor* was diminished by this insult, implying its role in the neoblast compartment. Contradictory, *Smed-TOR* expression through FACS-isolated cells were identified to be highly expressed within the neoblast population, followed by their post-mitotic and differentiated cells (e.g. X1: ~82%, X2: ~69% and Xins: ~76%, respectively) [57], [109]. However, *Smed-Raptor* expression increased stepwise into the differentiated cell population (e.g. X1: ~85%, X2: ~87% and Xins: ~89).

To pinpoint the expression and location patterns of *Smed-TOR, Smed-Raptor* and *Smed-Rictor*, we look within recently published databases. Labbe et al. 2012 [250] found through FACS sorted cell populations that the expression index of *Smed-TOR* was highly expressed in the neoblast compartment and slightly expressed within the neoblast progeny and differentiated cell compartments (e.g. X1, X2 and Xins, respectively) (Fig. 10A). Further, S*med-Rictor* was expressed at extremely low levels with majority of expression in the cell population. Lastly, S*med-Raptor* expression was highly expressed throughout all the cell populations. This supports Tu et al. 2012 finding that S*med-Rictor* expression reduced upon lethal irradiation. Next, we looked at violin plots derived from single-cell RNAseq results (Fig. 10B, C) [53]. We observed *Smed-TOR* and *Smed-Raptor* to be highly expressed in the neoblast populations, progeny (e.g. early epithelial) and differentiated tissues (e.g. epithelial1/2, gut, protonephridia and parapharyngeal). On the other hand, S*med-Rictor's* expression was found within the sigma and zeta neoblast population and mostly in the differentiated tissues (e.g. parapharyngeal, muscle, neural, ciliated neuron). Lastly, two independent labs in 2018 conducted single-cell RNAseq to determine the transcriptome for essentially every cell type of the complete animal [265], [266]. Fincher et al. 2018 database provided further resolution for S*med-Rictor* and *Smed-Raptor* expression pattern but not for *Smed-TOR* (Fig. 10D). Based off contig enrichment in major and minor clusters revealed that *Smed-Raptor* is expressed in the subcluster parenchymal group 11. Surprisingly, S*med-Rictor* was highly expressed in major clusters: muscle (13 and 14), neural (8,9,20,21,23 and 33) pharynx (27 and 37) as well as minor

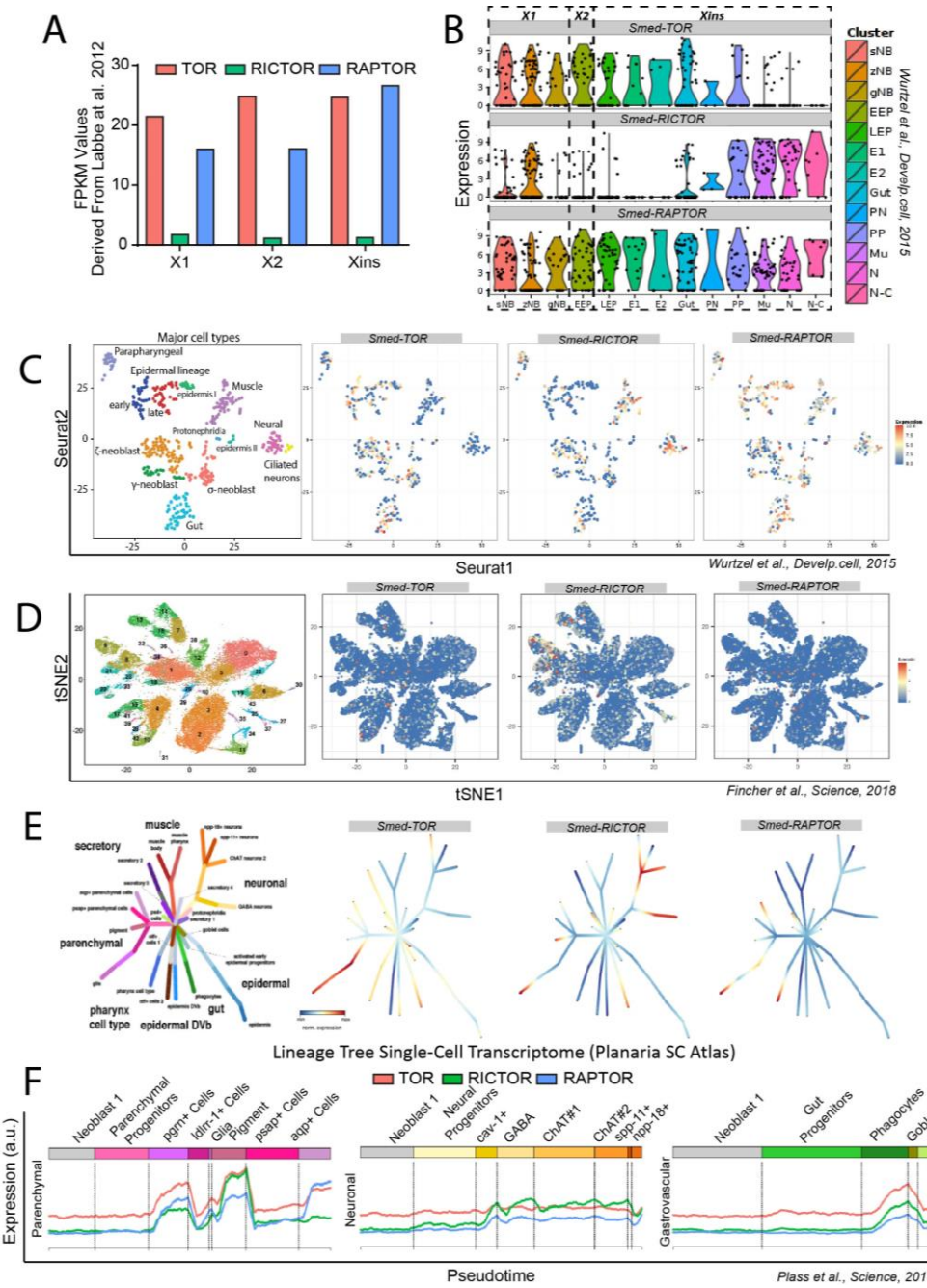

Figure 10. *Smed-TOR*, *Smed-RICTOR* and *Smed-RAPTOR* cluster enrichment. (A) FACS isolated cells published by Lebbe et al. 2012 depicting expression levels within the various neoblast populations. (B) Violin plots showing expression of *Smed-TOR*, *Smed-RICTOR* and *Smed-RAPTOR* clustering within the neoblast and differentiae tissue compartments. (C) Single cell transcriptomic cluster plots showing expression levels Wurtzel et al. 2015. (D) Single cell transcriptomic main and sub-cluster plots Fincher et al. 2018. (E) Single cell transcriptomic in linage tree-formatting by Plass et al. 2018 depicting *Smed-TOR*, *Smed-RICTOR* and *Smed-RAPTOR* expression within the various lineages within the planarian. (F) Increased resolution of linage trees shows precise location of gene expression within parenchymal, neural and gastrovascular linage compartments.

subclusters: intestine group 7, muscle (2,7 and 12) neural (3,5,8 and 18) pharynx group 4 and importantly in the stem cell enriched Smedwi+1 cell group 15.

Single cell transcriptomics conducted by Plass et al, 2018 allowed for lineage tree tracking of gene expression (Fig. 10E). *Smed-TOR* is expressed within the central neoblasts and in the parenchymal, secretory, pharynx, epidermal and gut progenitors. *Smed-Rictor* is slightly expressed in the neoblast populations but enrichment was found in the neural, gut and parenchymal tissues. As for *Smed-Raptor*, its expression mimicked that of *Smed-TOR's* expression within the differentiated cell types. Normalized gene expression levels allowed for a higher resolution of linage specificity against pseudo time (Fig. 10F). Together, these results identify that *Smed-TOR* and *Smed-Raptor* are highly expressed within the neoblast populations and differentiated tissues. This may explain the unapparent reduction in gene expression upon exposure to lethal irradiation. *Smed-Rictor* diffused expression can be attributed to its vast expression pattern within the planarian. Together, advances in single cell transcriptomics have allowed to identify the neoblast population and/or lineage of cells that are enriched with *Smed-TOR, Smed-Raptor and Smed-Rictor.*

3.5.2. *Smed-TOR* and *Smed-Raptor* are required for tissue homeostasis in planarian

Smed-TOR(RNAi) alters tissue homeostasis dependent on the knockdown method (e.g. feeding vs injections with dsRNA) which places the animals in states of nutrient rich or starvation periods. Tu et al. 2012 identified that RNAi of both *Smed-TOR* and *Smed-Raptor* resulted in animals developing pharynx-specific lesions 27 days post first feeding of dsRNA, leading to lethality 30 days RNAi. Despite confirmed gene knockdown, no microscopic lesions were identified for *Smed-TOR* and *Smed-Raptor* animals by Peiris et al. 2012 and Estevez et al. 2012 who used dsRNA microinjections 30-40 starvation period. Moreover, all three reports, despite RNAi method, indicate that planarian maintain tissue homeostasis through the TORC1 complex and not TORC2 (e.g. *Smed-Raptor* and *Smed-Rictor*, respectively). This is consistent with the literate as TORC1 is required for cell growth and TORC2 is required for cytoskeletal organization.

Smed-TOR knockdown by feeding did not alter neoblast division rates or reduce gene expression levels for markers of neoblast and postmitotic-progeny. Moreover, animal lethality was attributed to increased amount of cell death within *Smed-TOR(RNAi)* animals relative to feed controls. However, by injection, Peiris et al. 2012 identified that *Smed-TOR(RNAi)* reduced mitotic division by 50% during a 40-day starvation period. In addition, gene expression for neoblast and progeny markers was reduced and resulted in mild differentiated tissue defects (e.g. head regression and reduced gene expression). The reminder of mitotic cells, void of *Smed-TOR*, were still capable of dividing and contributed to cellular turnover for more than 50 days post first injection. Peiris et al. 2012 did confirm Tu et al. 2012's findings that loss of *Smed-TOR* results in increased amounts of cell death. Overall, suggesting that there is an imbalance between cell death and cellular proliferation in the absence of *Smed-TOR*.

To identify *Smed-TOR's* role of cellular turnover during growth and de-growth periods (e.g. nutrients-rich and starvation, respectively), animal size was documented. In a nutrient poor environment, both control and *Smed-TOR(RNAi)* animals reduced in size equally. However, in a nutrient rich environment, control animals grew and *Smed-TOR(RNAi)* maintained their size over the 40-day period. Interestingly, *Smed-TOR(RNAi)* were able of electing distinguished peaks of proliferation post feeding similar to the control

(e.g. 6hr, 12hr, 24hr post feeding) [268]. These results suggest that the remainder of cells in *Smed-TOR(RNAi)* animals are capable of sensing nutrients, maintain organism size and facilitating some type of cellular turnover to maintain animals for greater than 50 days. Together, these results indicate that *Smed-TOR* is a key regulator in planarian growth and de-growth as it balances cell death and cellular proliferation. Overall, it can be postulated that increases in cell death may attribute to the decrease in animal size during starvation periods. Further, nutrient rich environments may allow for an increase in proliferation that balances the increased amount of cell death.

3.6. Discussion

This section provided context in regards the highly conserved PI3K/PTEN/AKT signal transduction cascade, identified which cellular compartment these genes reside and how these genes function within the adult body of the planarian. To do so, bioinformatics (e.g. BLAST, phylogenetics and protein domain modeling), single-cell RNA sequencing databases (e.g. identification of expression and cell lineage) and RNA interference (e.g. PTEN, AKT and TOR) approaches were used to discern the conservation of the pathway. The planarian contains highly conserved paralogues of the human PTEN. *Smed-PTEN1* and *Smed-PTEN2* both contain a phosphatase and C2 domain. However, their C2 domain contain gap regions with slight overlap. Oviedo et al., 2009 identified that knockdown of both paralogues are required for the formation of the cancer-like phenotype [56]. We can postulate that these two paralogues compensate for each other during single RNAi. In human cancers, truncated forms of PTEN are commonly formed by alterations to the C2 domain[269], [270]. The C2 domain contains many phosphorylation sites needed for PTEN stability, activity and recruitment [271]–[273]. Truncated forms of PTEN re-expressed in cells, fail to suppress the PI3K pathway and are incapable of performing their nuclear function in maintaining genomic stability [274]. Additional studies in the planarian discerning if nuclear PTEN localization is mediated by its C2 domain. Furthermore, it is possible that the individual loss of planarian PTEN paralogues may result in subcellular accumulation of DNA damage and not necessarily hyperproliferation; discussed in the chapter five.

The disruption of *Smed-PTEN* results in a cancer-like phenotype. Specifically, animals exhibit metastasis-like characteristics such as sustained proliferation, invasion by abnormal cells of organs and tissues, abnormal tissue outgrowths and lethality. These phenotypes were credited to over active PI3K/AKT/TOR signaling in the *Smed-PTEN(RNAi)* planarian model. Interestingly, the suppression of TOR signaling through rapamycin treatment resulted in the reduction of hyperproliferation and reduced AKT expression to basal levels. However, rapamycin treatment was incapable of restoring differentiated tissue gene expression correlated to the brain and digestive tissues. Furthermore, the suppression of *Smed-AKT* within the *Smed-PTEN* animals did not reduce cellular division but eliminated head regression and anterior specific abnormal outgrowths. Together, these results imply that *Smed-TOR* and *Smed-AKT* function in different compartments within the phenotype.

Expression levels of *Smed-PTEN* were found to be in the neoblast compartment and highly expressed in the differentiated tissues (e.g. epithelial, protonephridia, gut and nervous system). *Smed-TOR* is highly expressed within the X1 mitotic cells and X2 post mitotic cell populations with expression levels found within differentiated tissues (e.g. epithelial, gut, protonephridia and parenchyma). *Smed-AKT* expression resided somewhat within the neoblast compartment but was highly expressed within the progenitor

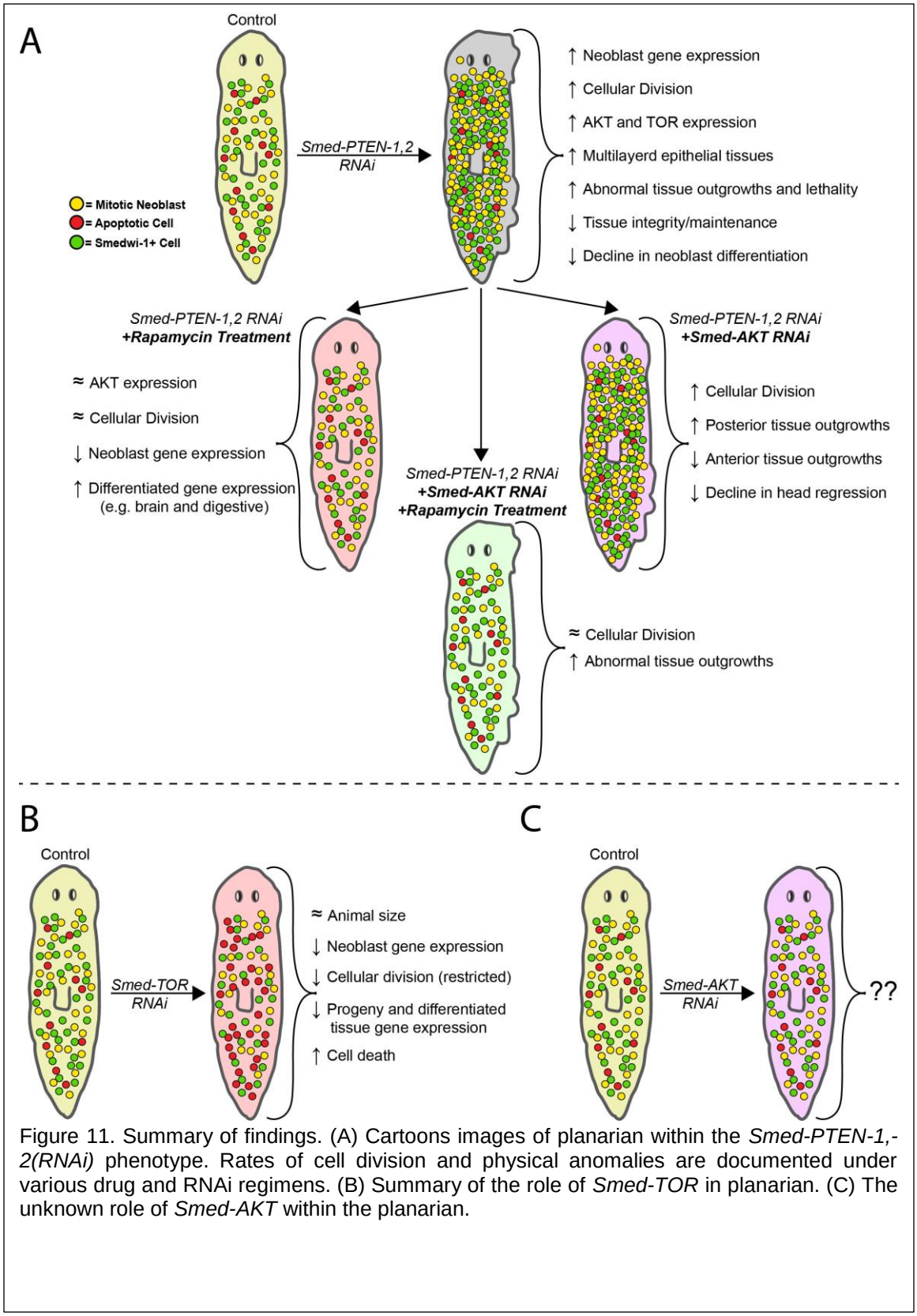

Figure 11. Summary of findings. (A) Cartoons images of planarian within the *Smed-PTEN-1,-2(RNAi)* phenotype. Rates of cell division and physical anomalies are documented under various drug and RNAi regimens. (B) Summary of the role of *Smed-TOR* in planarian. (C) The unknown role of *Smed-AKT* within the planarian.

and differentiated tissues (e.g. epithelial progeny, epidermis, gut and parenchyma) (data shown in chapter 4). Noteworthy, *Smed-AKT* expression levels were found within the neuron and ciliated neuron compartments. These results suggest that rapamycin treatment targets abnormal neoblst division in *Smed-PTEN(RNAi)* as *Smed-TOR* resides highly within the neoblast populations. The phenotype produced by *Smed-TOR(RNAi)* identified that the remaineder of neoblsts within the animal can divide with a restricted capacity to maintain tissue integrity. Noteworthy, haulting rapamycin treatment in *Smed-PTEN(RNAi)* animals resulted in a delayed reestablishment of anterior-specific abnormal outgrowths in a third for the population. Perhaps rapamycin treatment dose not homogenously suppress all abnormal neoblasts and only restricts their capacity to hyperproliferate. The *Smed-TOR(RNAi)* phenotype is attributed to increased amounts of cell death without showing signs of tissue degradation, a common feature of increased cell death. Therefore, we can postulate that the cell death in these animals may be neoblast-type specific. Moreover, the remainder of mitotic cells dividing without functional *Smed-TOR* may be mediated by alternative pathways either upstream or downstream (e.g. AKT and S6K1, respectively) of *Smed-TOR* and needs further elucidation (Fig. 11A, B)

Dual RNAi of *Smed-PTEN+AKT* results in sustained hyperproliferation but eliminates anterior specific abnormalities and tumor outgrowths. These results may be attributed to *Smed-AKT* expression within the nervous system and ciliated neurons found within the anterior region of the planarian. *Smed-TOR* expression is not found within these compartments thus, the ability for *Smed-PTEN(RNAi)* phenotype to persist post rapamycin treatment may be correlated to a small neural population that is incapable of being eliminated. This is a plausible as majority of tissues (e.g. muscle and epithelial tissues) within *Smed-PTEN(RNAi)* animals degraded despite the nervous tissues that were disordered and enlarged. It is tantalizing to attribute the *Smed-PTEN(RNAi)* phenotype to abnormal neural neoblasts that harbor increases susceptibility to Smed-PTEN loss and proto-oncogene activity of aberrant *Smed-AKT* expression. However, further analysis of role of *Smed-AKT* during cellular turnover and tissue homeostasis are required to support these theories (Fig. 11C). Moreover, the ability for animals to form abnormal outgrowths with rapamycin treatment and double RNAi of *Smed-AKT+PTEN* may be explained by alternative signal transduction caused by PI3K (e.g. SGK, CDC42 and PKC) or PDK1 (e.g. PKA, PKC and p70SK6) overactivation which can activate other downstream targets without the aid of AKT or TOR resulting in cell survival, proliferation, cellular reorganization and transformation [275], [276].

Overall, it is evident that the planarian contains highly conserved PI3K/PTEN/AKT signal transduction cascade, which is frequently unbalanced in many human cancer types. Therefore, the planarian may be a novel model to study the OTS-DDM in respect to tissue renewal. However, prior to this, the overexpression *Smed-AKT* within the *Smed-PTEN(RNAi)* phenotype must be deciphered (Fig. 11C).

CHAPTER FOUR

FINDINGS

The Akt signaling pathway is required for tissue maintenance and regeneration in planarians

4.1. Introduction

The protein kinase Akt also known as PKB, regulates multiple cellular functions including proliferation, survival, and growth during embryonic development and adult tissue homeostasis [203], [277]–[280]. In mammals, Akt expression is widely distributed across the body and includes three isoforms, Akt-1-3 (PKBα, ß, and δ, respectively) [277]–[279]. Akt is evolutionary conserved in both its molecular structure and function among vertebrate and invertebrate organisms [203], [280]–[282]. Across metazoans, Akt signaling integrates local and systemic information central to cellular and organismal physiology.

Akt regulates adult stem cell proliferation, migration and apoptosis and its deregulation has been implicated in the progression of cancer, diabetes, and aging [277]–[280], [283]–[285]. Conditional deletions and transgenic approaches have revealed key aspects of Akt signaling in hematopoietic, epithelial, neural and other tissues [278], [279], [286]–[289]. Nonetheless, there is limited understanding of how Akt signaling controls the response of stem cells during cellular turnover and tissue injury in the complexity of the whole organism. This paucity is likely due to the ubiquitous nature of this signaling pathway and the difficulty of analyzing stem cells in their natural environment during physiological cell turnover and regeneration in conventional animal models [48], [290], [291].

Thus, we sought to investigate Akt function during cellular turnover and injury using the planarian flatworm *Schmidtea mediterranea*. This organism is well known for its stem cell-based regenerative capability. Planarians contain an abundant and accessible population of somatic adult stem cells called neoblasts[47], [51], [52], [292]. The neoblasts are the only dividing cells in planarians and constantly proliferate to repair tissues and support systemic cellular turnover [47]. Recently, we described that the genome of *S. mediterranea* contains a single Akt ortholog termed *Smed-Akt*, which affects cell division and impairs planarian locomotion [56]. This study defined the role of *Smed-Akt* in abnormal cell proliferation triggered by the abrogation of the phosphatase PTEN, an upstream component of the Akt signaling pathway, which is highly mutated in human cancers.

Here, we report on an extended RNA-interference (RNAi) strategy that disrupts *Smed-Akt* in the whole organism, to analyze its function on the response of neoblasts during systemic cell turnover and tissue repair. Our results show, *Smed-Akt* abrogation leads to a gradual decline in the number of neoblasts, accompanied by massive cell death that affects cellular turnover and maintenance of adult tissues. We also found that impaired locomotion in the *Smed-Akt* phenotype is due to the disruption of cilia maintenance in the ventral epithelium. Intriguingly, large-scale tissue injury is capable of reducing the high levels of *Smed-Akt(RNAi)*-induced levels of cell death, while increasing neoblast proliferation near the wound site however, animals failed to complete the

formation of the regenerative blastema. Thus, our results reveal novel roles for Akt signaling during systemic cell turnover and large-scale regeneration of adult tissues.

4.2. *Smed-Akt* is required for proper neoblast function

Our previous studies identified in the planarian *Schmidtea mediterranea* genome a single Akt ortholog (*Smed-Akt*) to the mammalian Akt2/PKB-ß, precisely 56.67% identity [56]. *Smed-Akt* contains a highly conserved pleckstrin homology domain and central catalytic domain containing an ATP region and a C-terminal AGC_Kinase region but lack conserved structures such as activation loop, polypeptide substrate biding sites, hydrophobic motif and phosphorylation site when compared to the human counterpart (Fig. 1A). *Smed-Akt* is widely expressed in neoblasts, post-mitotic and differentiated cells (e.g. X1, X2 and Xins) (Fig. 1B). Furthermore, single-cell analysis reveals that *Smed-Akt* expression is present across all neoblast subclasses (e.g. sigma, gamma and zeta) as well as in a subset of differentiated cells compartments (e.g. epithelial, gut, parapharyngeal, neural and ciliated neurons) (Fig. 1C). Previously, its functional downregulation with RNA-interference (*Smed-Akt(RNAi)*) has been identified to reduce of

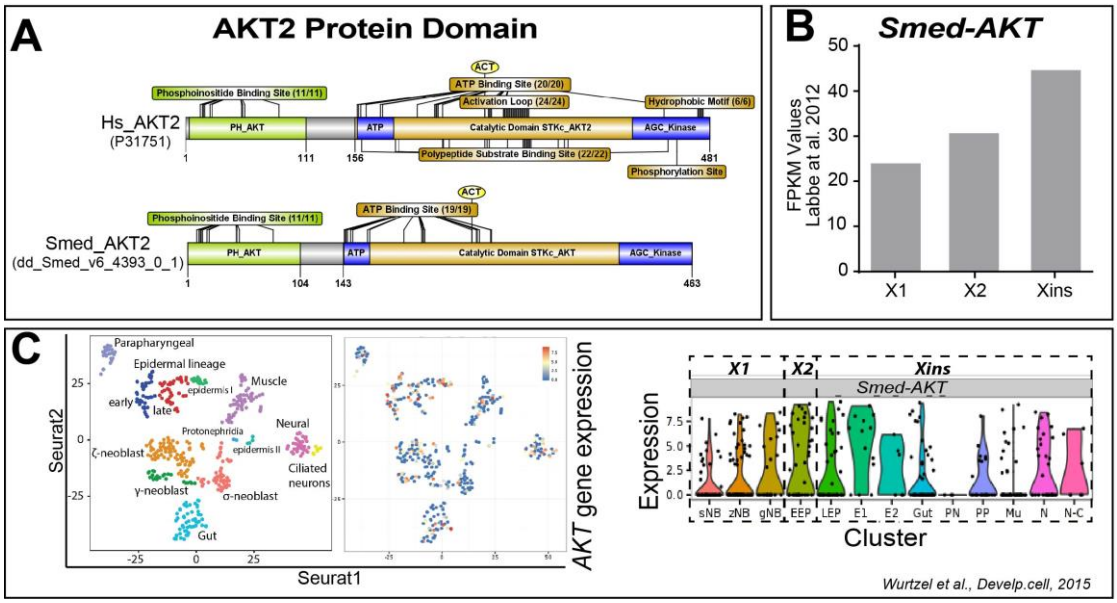

Figure 1. *Smed-Akt* expression cluster enrichment. (A) Conservation of *Smed-Akt* protein domains relative to human counterpart. (B) FACS isolated cells published by Lebbe et al. 2012 depicting expression levels within the various neoblast populations. (C) Single cell seurat and violin plots showing expression of *Smed-Akt* clustering within the neoblast and differentiae tissue compartments.

neoblast numbers and result in loss of planarian locomotion [56]. To test whether Akt signaling plays additional roles in the regulation of cellular turnover and tissue regeneration in the adult body, we designed an RNAi protocol consisting of six dsRNA microinjections that effectively downregulated (8.4 folds) *Smed-Akt* expression over the span of 30 days (Fig. 2A).

Neoblast division was visualized through whole-mount immunostaining against the α–phosphorylated histone-3 (H3P) antibody, which labels cells in G2/M phase of the cell cycle (observed as yellow dots in (Fig. 2B). Animals subjected to *Smed-Akt(RNAi)* initially displayed an important increase in neoblast division (~0.75 fold) 10 days post RNAi

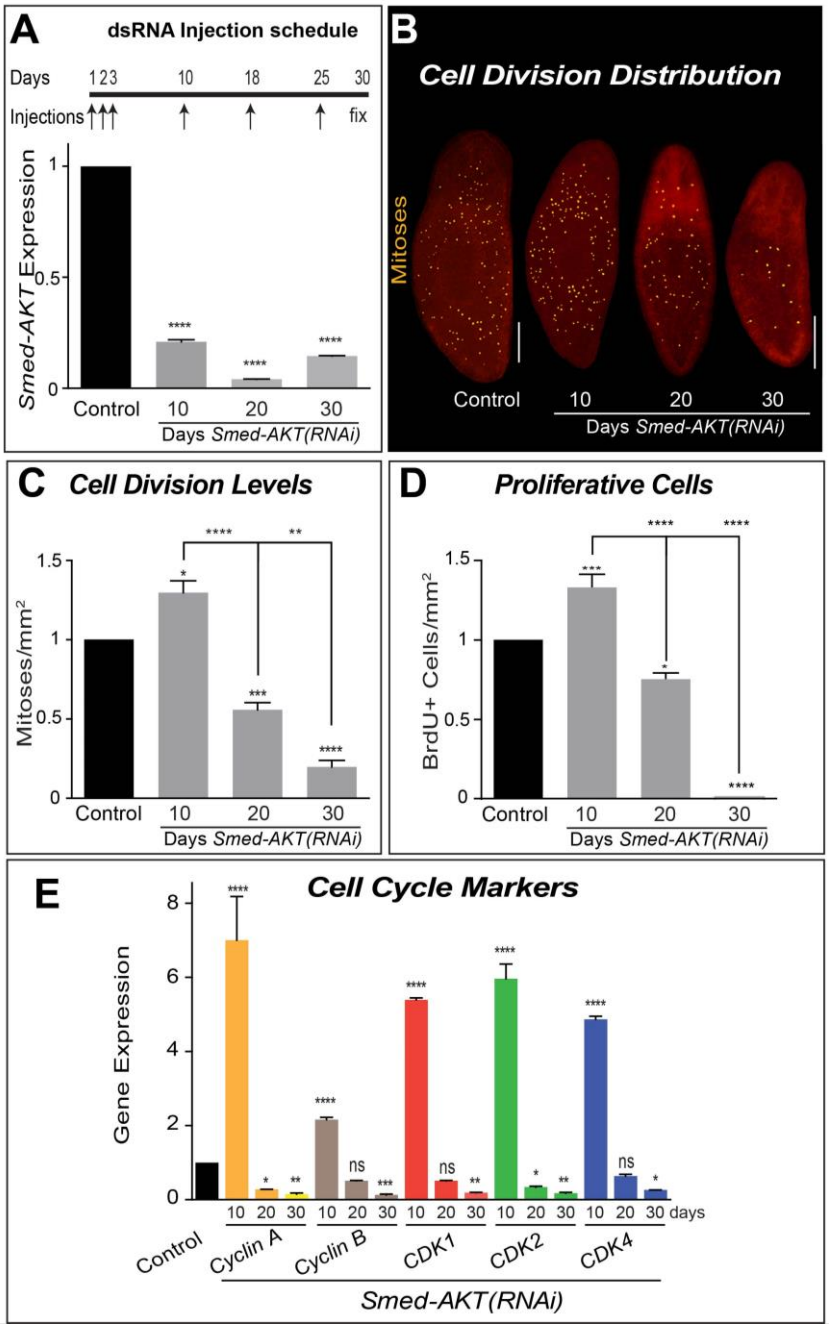

Figure 2. Downregulation of *Smed-AKT(RNAi)* reduces neoblast proliferation. (A) dsRNA microinjection schedule is depicted on top. The RNAi efficiency of the dsRNA microinjections was tested with quantitative PCR (qPCR) on days 10, 20 and 30 after the first dsRNA injection, showing significant down-regulation (B) Whole-mount immunostaining of control and *Smed-AKT(RNAi)* worms, using anti-H3P antibody. Yellow dots represent mitotic cells. Scale bar 200µm. (C) H3P-signal quantification, represents fold change of cell division (mitoses per mm^2) relative to the control. (D) Quantification of fold change in BrdU positive cells relative to the control. (E) Relative levels of gene expression, fold change, of cell cycle markers 10, 20 and 30 days after first *Smed-AKT(RNAi)* injection. *P* values *** < 0.005 and **** < 0.0001, were calculated by two-way ANOVA.

initiation, which was followed by a gradual decline in mitoses, reaching ~ five-fold decrease by day 30, when compared to control (Fig. 2B, C). Importantly, all samples were processed either before or a few days after injection to avoid the possibility of injury-induced increase in mitotic activity. To further characterize the effects of Akt downregulation on the cell cycle dynamics, we evaluated the incorporation of the bromodeoxyuridine analog (BrdU) every ten days for one month (Fig. 2D). BrdU is incorporated during the S phase of the cell cycle and remains in the cell through multiple rounds of cell division, albeit at lower concentrations in each successive cell generation. Control and *Smed-Akt(RNAi)* animals were exposed to a single BrdU pulse at different time points after the first dsRNA injection (i.e. 10, 20, and 30 days) and after 12 h samples were processed as previously described [293]. Consistent with the mitotic counts, BrdU positive cells increased in the first 10 days after *Smed-Akt(RNAi)* and gradually decrease to almost undetectable levels after one month of RNAi treatment (Fig. 2D). We also found a consistent trend in the expression of genes associated with cell cycle regulation (i.e. *cyclin A, cyclin B, CDK1, CDK2,* and *CDK4*), which showed general increase during the first 10 days and dramatically decreases in the successive days, further confirming our observations in mitotic activity and BrdU labeling upon *Smed-Akt(RNAi)* (Fig. 2E). The early increase in gene expression and proliferative cells upon *Smed-Akt* downregulation implies that the phenotype most likely starts before day 10. Our results suggest that *Smed-Akt* is essential to maintain the appropriate number of proliferating neoblast during tissue renewal in adult planarians.

To assess whether the effects of *Smed-Akt(RNAi)* are restricted to cell cycle events, we analyzed the expression of markers associated with neoblasts and the early and late division progeny (e.g. *smedwi-1*, *Prog-1, and Agat-1*, respectively). This analysis revealed a dramatic decrease in the expression of markers associated with neoblasts and their progeny (Fig. 3A). Interestingly, the pattern of expression for *smedwi*-1 and *Agat*-1 were similar to that previous observed in cell cycle genes, while the marker for the early neoblast progeny (*prog-1*) followed a somewhat different pattern, characterized by a strong downregulation from the beginning of *Smed-Akt(RNAi)* time course. Whole mount fluorescent in situ hybridization (FISH) with markers of neoblasts and the post-mitotic progeny one month after *Smed-Akt(RNAi)* further confirmed the quantitative PCR (qPCR) results and showed a generalized reduction in gene expression throughout the body, after *Smed-Akt(RNAi)* (Fig. 3B).

Proliferative neoblasts are contained within the irradiation sensitive X1 population and can be isolated via flow cytometry cell sorting (FACS) [125]. Recently, cells within the X1 population were classified into two functionally distinct subclasses, the sigma- and zeta-neoblasts [104]. Sigma-neoblasts are sought to be clonogenic neoblasts that give rise to progenitor cells of the nephridia, muscle, CNS, eyes and intestine and the sigma class produces the zeta-neoblasts and early/late progenitors (e.g. *Smed-Prog-1* and *Smed-AGAT1*) of the epidermis (Fig. 3C) [104]. FACS was used to isolate equal number of X1 cells from both control and *Smed-Akt(RNAi)* animals after one month of RNAi. We used a larger number of experimental animals to obtain comparable number of FACS-isolated cells between both groups. The total RNA extracted was processed to evaluate levels of expression of markers of the sigma and zeta populations (Fig. 3D). Markers of the sigma neoblast subpopulations tend to increase upon *Smed-Akt(RNAi),* while there little to no change in the zeta subclass, suggesting the effect of *Smed-Akt(RNAi)* is not homogeneously distributed among the neoblasts. Further evidence produced by FACS sorted single-cell RNAseq revealed that *Smed-Akt* expression is found within the neoblast specific *Smedwi-1*+ cell sub-clusters [265]. Noteworthy, *Smed-Akt* resided highly within

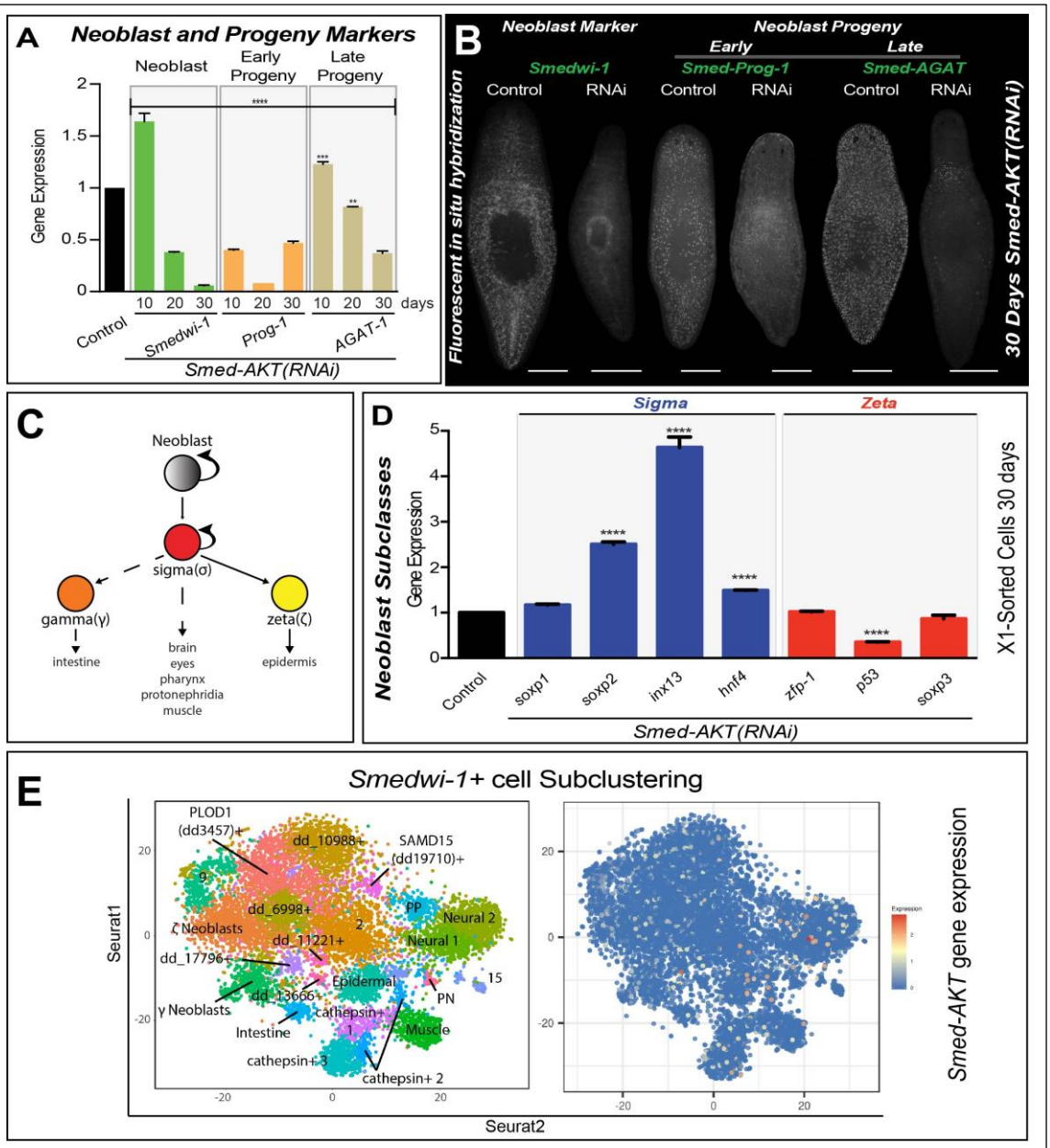

Figure 3. Akt regulates expression of neoblast and progeny markers. (A) Gene expression levels for markers of neoblasts (*smedwi-1)* and neoblast early (*Prog*-1) and late (*AGAT-1*) progeny were evaluated with qPCR. (B) Representative images of fluorescent in situ hybridization of *smedwi*-1, *Smed-Prog-1* and *Smed-AGAT-1* reveals an important reduction upon Smed-*Akt(RNAi)*. (C) Neoblast heterogeneity and the types of progenitors they use to support tissue renewal. (D) Fold change in gene expression levels involving markers of neoblast subpopulations sigma (blue) and zeta (red). The mRNA levels were measured in X1 sorted cells at day 30 after first injection was used to determine gene expression of *Smed-AKT(RNAi)* animals. All values are relative to equal number (~20,000) of X1 cells sorted from control-water injected animals at 30 days. (E) Single cell transcriptomic analysis looking at *Smed-Akt* expression within *smedwi*-1+ cell subcluster. *P* values ** < 0.001, *** < 0.0005 and **** < 0.0001, were calculated by two-way ANOVA. Scale bar 200μm.

the sigma-neoblasts within neoblast populations that give rise to cathepsin-1/2/3+cells, muscle, epidermal, parapharyngeal, protonephridia and neural1/2 sub-clusters. However, *Smed-Akt* expression was minimal within zeta, gamma and other neoblast populations (Fig. 3E). Thus, additional experiments are required to further define the differences between gene expression in the neoblast subclasses and to understand these implications. Altogether, our results indicate that *Smed-Akt* is essential for the appropriate expression of neoblast and progeny markers and suggests that a gradual depletion in the number of neoblasts takes place after *Smed-Akt(RNAi)*.

4.3. *Smed-Akt* is a critical regulator of cell death in planarians

A fine balance between stem cell proliferation and programmed cell death enables physiological cellular turnover that supports maintenance and growth of adult tissues [42]. Over a 40 days starvation period, animals subjected to *Smed-Akt(RNAi)* exhibited a ~3 fold reduction in surface area compared to the control group (0.23 ± 0.08 vs 0.72 ± 0.07 mm^2, respectively) (Fig. 4A). These results together with the reduction in neoblast proliferation suggests that the *Smed-Akt(RNAi)*phenotype may be accompanied by increased levels of cell death, contributing to an accelerated reduction in animal size over time, and death by ~45 days after the first injection.

Akt function has been implicated in cellular pro-survival mechanisms [289], [294]–[296]. Thus, we examined possible roles of *Smed-Akt* as regulator of cell death in planarians by analyzing levels of cell death after RNAi treatment. First, spatial distribution of cell death in the whole body was evaluated using the terminal deoxynucleotidyl transferase dUTP nick end-labeling (TUNEL) assay [101]. These experiments revealed that *Smed-Akt(RNAi)* double the number of TUNEL positive cells, 15 days after the first dsRNA injection and it gradually increase to about threefold by day 30 of the RNAi treatment (Fig. 4B). Despite a slight increase in TUNEL+ cells by day 10 of *Smed-Akt(RNAi)* (data not shown), the predominant increase in cell death was observed around day 15 after the first dsRNA injection. TUNEL+ cells appeared indistinctively scattered along the planarian body at all times, suggesting this is a generalized event, most likely involving both neoblasts and differentiated cells (Fig. 4C). Next, we performed flow cytometry analysis using Annexin V and 7AAD staining [46], [122]. This experiment confirmed the high levels of cell death induced by *Smed-Akt(RNAi)*may involve apoptosis and necrosis (Fig. 4D). The increased levels of cell death in *Smed-Akt(RNAi)* together with the overall animal size reduction indicates that Akt is an important regulator of cellular turnover. The mechanisms are not entirely clear however, it is possible that the impairment in tissue renewal may result from either (1) an initial reduction in neoblast numbers that fail to support homeostasis or (2) generalized cell death events that impact both neoblasts and differentiated cells alike.

4.4. *Smed-Akt* regulates the maintenance of differentiated tissues

A distinctive macroscopic feature of the *Smed-Akt(RNAi)* phenotype is the impairment of locomotion accompanied by the elongation of the whole body, which are initiated as early as day 15 and progress for over 35 days after the first dsRNA injection. Planarian gliding is mediated by synchronized cilia movement on the ventral epithelial surface of the animal [297]. Since locomotion is impaired in *Smed-Akt(RNAi)* animals, we therefore evaluated the status of cilia through the expression levels of genes specifically corresponding to intraflagellar transport machinery and flagellar beating (*IFT88, IC2, LC1,*

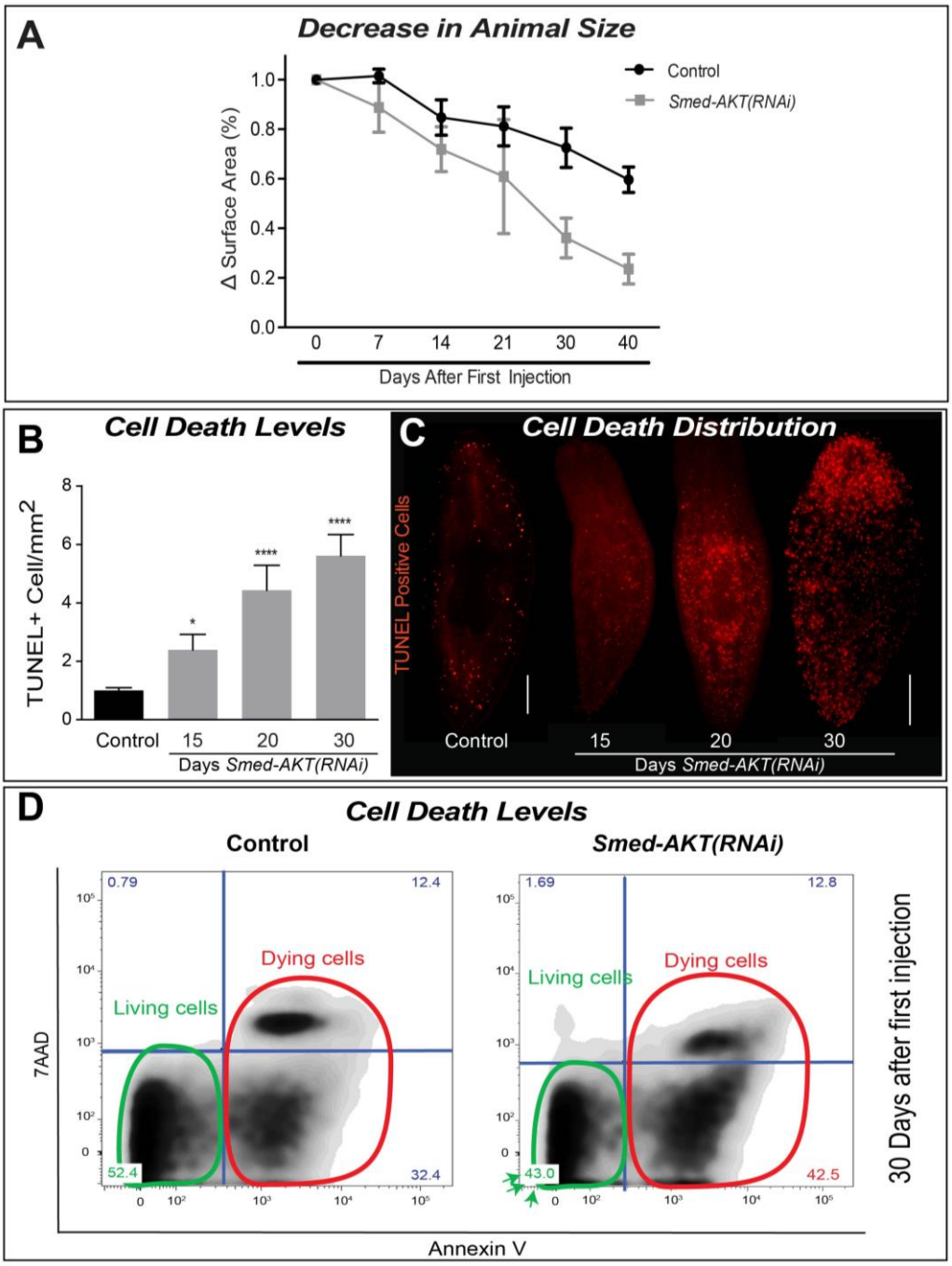

Figure 4. Impairment of Akt leads to increased cell death. (A) Reduction in animal size over time was recorded as the difference in surface area expressed in percentage. (B) Quantification of TUNEL+ nuclei reveal a gradual increase in cell death. *P*-value * <0.05 and **** <0.0001, by one way-ANOVA. (C) Whole-mount immunostaining labeling TUNEL+ nuclei (cell death) with control on the left and *Smed-AKT(RNAi)* on the right. Scale bar 200µm. (D) Flow cytometry analysis of AnnexinV and 7AAD expression, reveals the frequency distribution between living and dead cells. AnnexinV-7AAD quadrant indicates live cells (green circle). AnnexinV + 7AAD and AnnexinV+ 7AAD+ indicates cells that are in early and late stages of cell death, respectively (red circle). The numbers per quadrant indicate the percentage of cells with that staining profile.

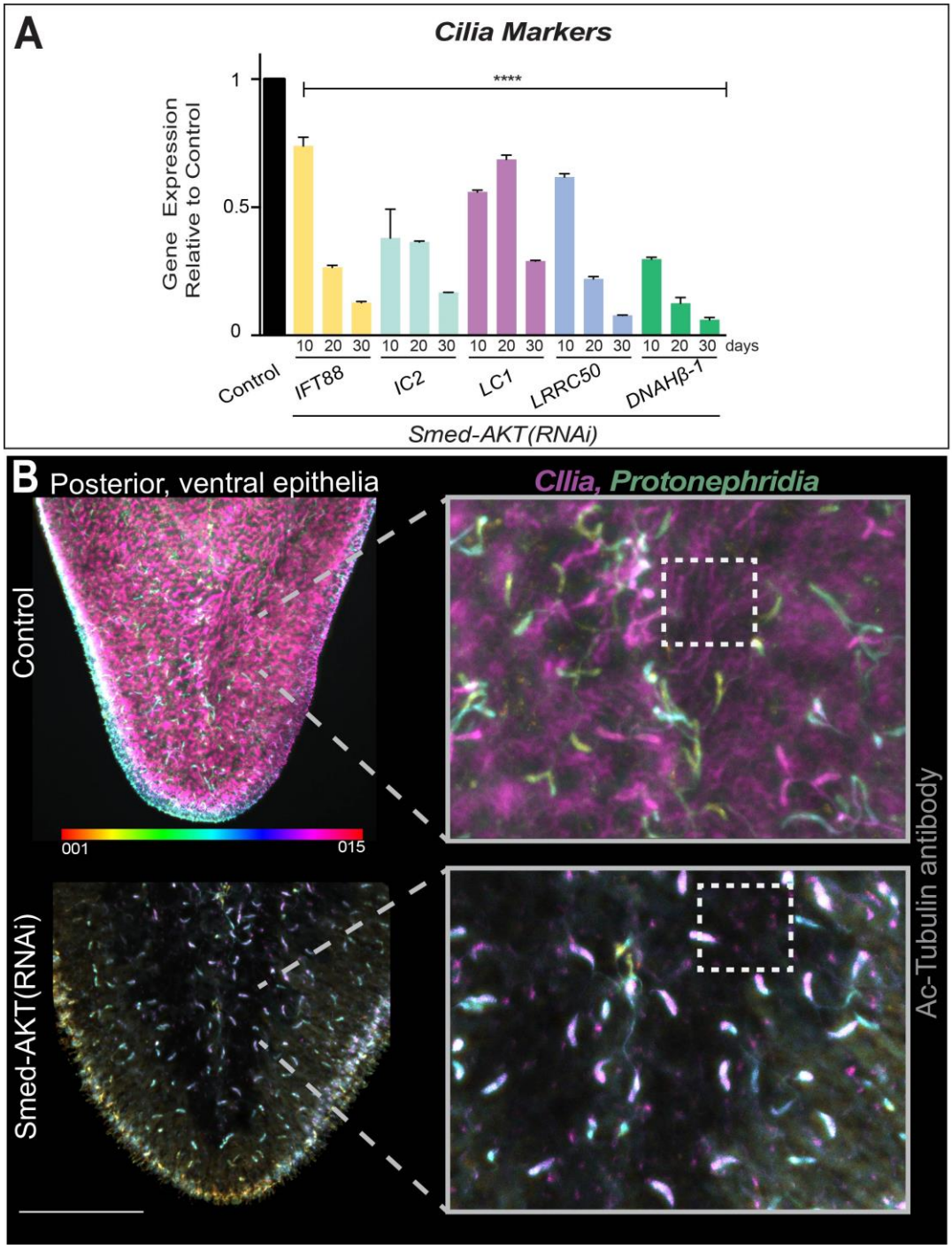

Figure 5. Akt is required for the maintenance of cilia in the ventral epithelia. (A) Gene expression levels of cilia specific markers after *Smed-AKT(RNAi)* relative to the control. Gene expressions are all relative to the internal control, the ubiquitously expressed clone *H.55.12e*. Significance **** <0.0001 is determined through two way-ANOVA. (B) Images show control (top) and *Smed-Akt (RNAi)* (bottom) at day 30. Images represent depth-coded maximum projections of confocal z-sections in the posterior specific ventral cilia and proximal structures stained with Ac-Tubulin antibody. Superficial structures were labeled in magenta and structures near the dorsal epithelial layer appear in orange (color code scale on the left). Scale bar 100µm.

*LRRC50*and *DNAHβ-1*) [297], [298]. First, we observed through qPCR, a dramatic reduction in the expression of cilia markers required for the structural and mechanical integrity of cilia [297], [299] (Fig. 5A). The reduction in gene expression of cilia markers is detected as early as 10 days after *Smed-Akt(RNAi)* and their expression continues to reduce over time. Second, whole-mount staining with anti-α-Ac-tubulin antibody allowed us to visualize the integrity of ciliated structures in the ventral epithelia, including parts of the excretory system (e.g. proximal tubules and flame cells in protonephridia) [56], [297]–[301]. We noted that one month after *Smed-Akt(RNAi),* the anti-α-Ac-tubulin antibody signal is nearly absent in the areas corresponding to ventral cilia, while control animals showed dense coverage by cilia (magenta signal in Fig. 5B). The confocal stacks, 30 days after *Smed-Akt(RNAi),* showed a marked reduction of ventral cilia, making the proximal tubules and flame cells of the excretory system readily evident (Fig. 5B). Together, the results obtained through gene and protein expression demonstrates that *Smed-Akt* is required for the structural integrity of cilia and its maintenance. Additionally, our findings suggest that the impaired locomotion in the Akt phenotype is most likely a consequence of inadequate cilia density in the ventral epithelia.

We next sought to evaluate whether the *Smed-Akt(RNAi)* effects are specific to the ventral epithelia or if they extend to other tissues. The excretory system in planarians consists of protonephridial tubules including both ciliated and non-ciliated structures that could be labeled with anti-α-Ac-tubulin antibody and the *Smed-CAVII-1* gene, respectively [299], [301], [302]. Additional markers to each portion of the protonephridial tubules were recently mapped [299], thus providing better opportunities to analyze effects on the excretory system. Specifically, we evaluated the expression of solute carrier transporters (slc) family of genes expressed along the proximal and distal tubules, and the collecting ducts of the protonephridia and identified a significant reduction throughout all compartments (Fig. 6A) [299]. Interestingly, *Smed-CAVII-1* gene expression as it resides within the distal tubule was significantly reduced compared to the control but remained elevated when compared to the solute carrier transporters within this section of the protonephridia (e.g slc4A-6, slc6A-12 and slc13A-7). FISH experiments confirmed the reduction of excretory marker *Smed-CAVII-1* gene expression, exposing disfigures and diffused distal tubule structures relative to the control (Fig. 6B). Further evidence produced by single-cell RNAseq revealed that *Smed-Akt* expression is found within the protonephridia sub-clusters, specifically within the flame cells, transition state 1/2 and collecting duct (Fig. 6C) [265]. Proximal and distal tubule sub-clusters were nearly void of *Smed-Akt* expression. Thus, the reduction in gene expression of slc may be a cause or an effect of *Smed-Akt(RNAi)* manifesting prior to day 10 and requires further analysis.

Structural disruption of cilia and protonephridia has been documented to result in excretory filtration issues within planarians [299], [301], [302]. Additional single-cell RNAseq allowed for lineage tracking of neoblasts and their progenitors in the complexity of the adult animal [266]. Lineage tracking of *Smed-Akt* expression provided further resolution of its expression within the protonephridia and within the secretory lineage and was expressed within the secretory1/2/3 compartments (Fig. 6D). With this information, we further extended the analysis to include planarian homologs of nephrocystins known to regulate excretory functions and upon their downregulation, lead to cyst-like disease in *S. mediterranea* [299]. The results provided evidence of a generalized reduction in gene expression of nephrocystin markers (e.g. NPHP5, 6 and 8) within *Smed-Akt(RNAi)* animals (Fig. 6E). The striking reduction in gene expression in the protonephridia structures is evident as early as 10 days after *Akt* disruption. However, macroscopic signs of excretory system defects such as edema and clearing of body pigmentation are evident

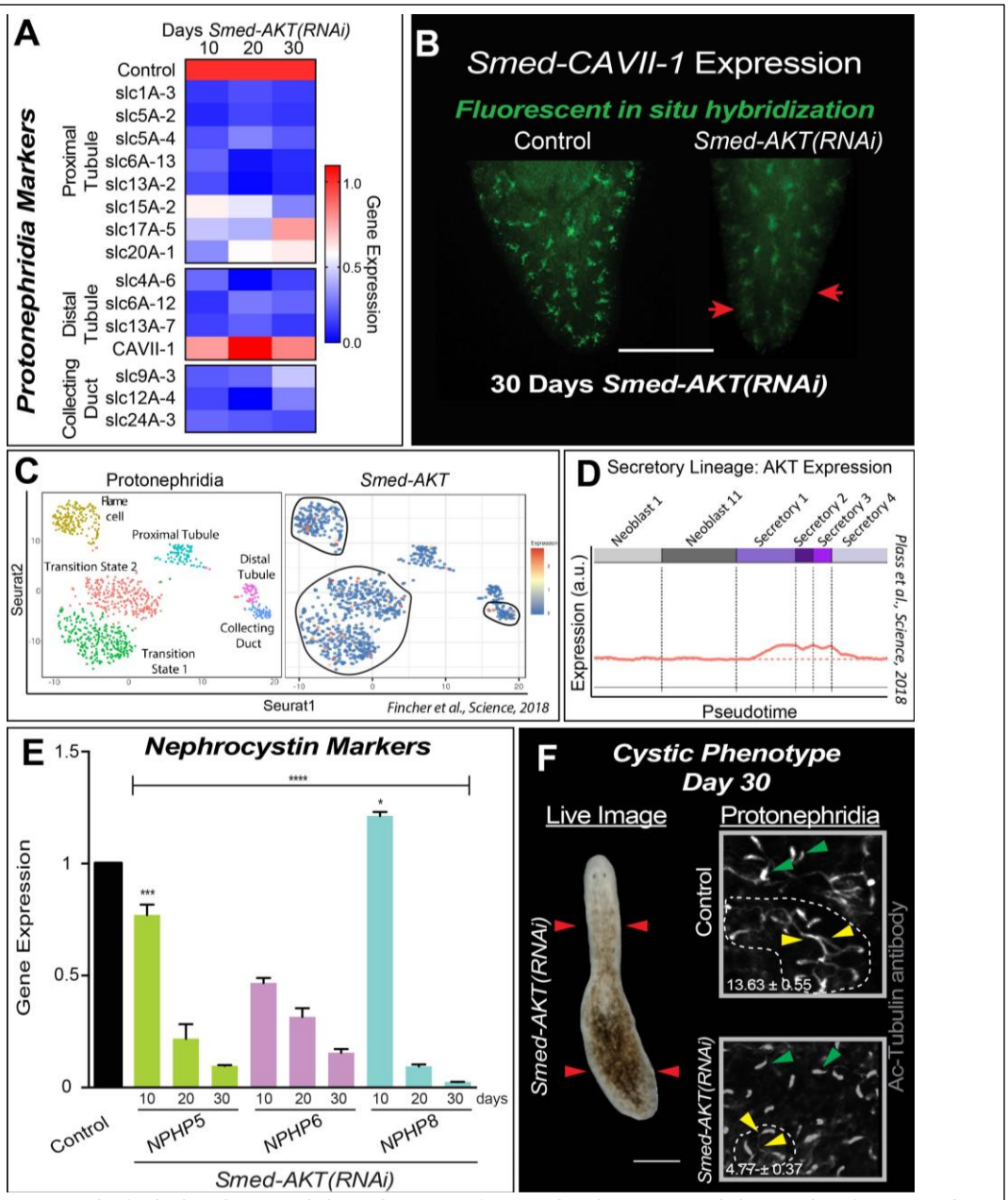

Figure 6. RNAi of Akt leads to a delayed onset of a cystic phenotype. (A) Levels of expression of solute carrier (slc) genes expressed along the planarian protonephridia tubules (proximal and distal) and collecting ducts. (B) Fluorescent in situ hybridization of *Smed-CAVII-1* (excretory system) shows a reduction of signal in the posterior part of the animal. (C) Single-cell RNAseq revealing that *Smed-Akt* is expressed in the flame cells and collecting duct cell clusters. (D) Single-cell linage tracking determines *Smed-Akt* expression is in the secretory lineages-1, -2 and -3. (E) Expression levels of nephrocystin markers (NPHP5, 6 and 8) at different time points after RNAi. (F) Cystic phenotype is seen in *Smed-AKT(RNAi)* animals by day ≥30 ($N = 30/30$). In the live image, seen on the left, show elongation of the head and bloating of the tail. Confocal z-stack images on the right, control (top) and RNAi (bottom), highlight protonephridial clusters (dotted lines) using Ac-Tubulin staining at day 30. Protonephridial clusters contain tubules (yellow arrows) and flame cells (green arrows). The number of flame cells per proximal unit are strongly reduced in *Smed-AKT(RNAi)* animals 4.77 ± 0.72 vs 13.63 ± 0.55 in control.

in *Smed-Akt(RNAi)* animals (30/30) during advanced stages of the phenotype, i.e. ≥ 30 days after the first dsRNA injection. Formation of the edema phenotype is consistent with the markedly downregulation of nephrocystin genes, and structural alterations in the proximal structures of the protonephridia (i.e. flame cells) (Fig. 6F). Particularly, *Smed-Akt(RNAi)* lead to a generalized decrease in proximal tubules per protonephridial unit (13.63 ± 0.55 vs 4.77 ± 0.37) (protonephridial unit is outlined in Fig. 6F), when compared to control. This structural disruption is consistent with the manifestation of edema in planarians [299], [301], [302], further validating the reduced integrity of the excretory system during the advanced stages of the *Smed-Akt(RNAi)* phenotype.

To determine whether *Smed-Akt(RNAi)* also affects other organs within planarians, we set out to explore gene and protein expression of markers in terminally differentiated tissues [47], [111], [293], [303]–[306]. Specifically, mRNA levels of genes associated with the nervous and digestive system, connective and muscle tissues. The results from these experiments demonstrated that most of the genes screened (i.e. 8/10) tend to gradually deplete after *Smed-Akt(RNAi),* but at least two of the markers including the choline acetyltransferase *ChAT* (neurons) and *tropomyosin* (muscle) followed a different pattern characterized by an increase in expression one month after *Smed-Akt* downregulation (Fig. 7A). FISH experiments also confirmed the reduction of the nervous system marked by *Smed-PC2*, resulting in decayed expression throughout the animal (bottom, Fig. 7A). However, the increase in *Smed-ChAT*, another neural marker and *Smed-tropomyosin* remain uncertain. Thus, we looked into the single-cell RNAseq lineage published by Plass and colleagues to track *Smed-AKT* expression within the neurons and muscle branches [266]. The published database uncovered the expression of *Smed-AKT* within *cav-1+, GABA, ChAT-1/-2, spp-11+ and npp-18+* cells of the neural compartment and its expression within the muscle pharynx and muscle body cell populations (Fig. 7B). Staining with the monoclonal antibody Smed-6G10 (6G10) that labels different muscle fibers in the planarian body [307], revealed the disruption of the *Smed-Akt* signaling affects planarian musculature. Specifically, we observed the disorganization of circular and diagonal muscle fibers and the absence of signal in some areas, suggesting alterations in the normal tissue architecture (arrows in head and pharynx, Fig. 7C). The structural changes in musculature may also explain the incapability to ingest food after 20 days of *Smed-Akt(RNAi)* (data not shown) but also the animal's ability to slightly maneuver through peristaltic muscle contractions [300]. Together, these data support the notion that disruption of tissue integrity is not restricted to one tissue in particular but rather a more generalized event after downregulation of *Smed-Akt* function. Further, within the same tissue compartment (i.e. neural), loss if *Smed-Akt* activity may result in mixed outcomes such as overexpression or suppression. Lineage tracing of single-cells adds to the complexity and deepens our understanding of the cell-types within the planarian that are dependent on *Smed-Akt* activity (Fig. 7D). Future experiments are needed to determine whether particular cell types are more susceptible to structural alterations after *Smed-Akt* systemic inhibition. Nonetheless, these results together demonstrate *Smed-Akt* is essential for the maintenance of tissues in planarians.

4.5. *Smed-Akt(RNAi)* leads to regeneration defects

Tissue amputation triggers well-coordinated waves of apoptosis and cellular proliferation aimed at recreating missing tissues and organs within the regenerative blastema. The *Smed-Akt* phenotype is characterized by a reduction in neoblast numbers and increased cell death, affecting the maintenance of differentiated tissues. Thus, we

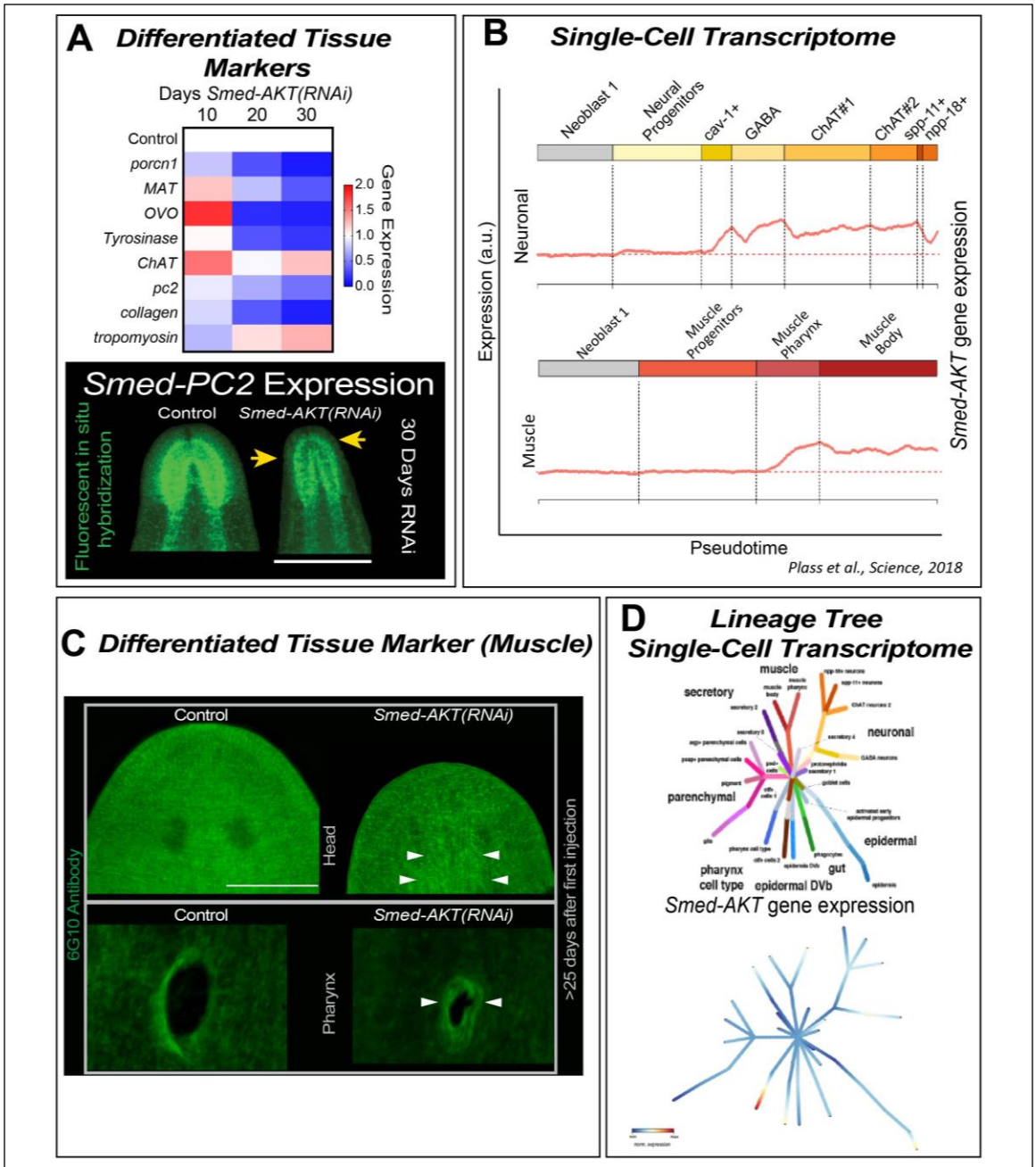

Figure 7. *Smed-AKT(RNAi)* leads to a generalized reduction in the expression of genes in differentiated tissues and alterations in muscle fibers. (A) Gene expression analysis of differentiated tissue markers: intestinal (*porcn-1 & MAT*), photoreceptors (*ovo & tyrosinase*), central nervous system (*ChAT & pc2*), and connective and muscle tissues (*collagen & tropomyosin, respectively*). Bottom, fluorescent in situ hybridization of *Smed-PC2* (central nervous system) expression depicts a reduction (yellow arrows) upon RNAi. (B) Single-cell RNAseq identify *Smed-Akt* expression in nervous and muscular linages. (C) Whole-mount immunostaining of intact control and *Smed-AKT(RNAi)* planarians at >day 25 post RNAi initiation with SMED-6G10 (muscle tissue) antibody. SMED-6G10 antibody specifically labels the circular and diagonal muscle fibers throughout the animal. Images show disarray in muscle fibers in the head (top images) and pharyngeal (bottom images) (arrowheads). (D) Lineage tree single-cell RNAseq tracking of *Smed-Akt* expression. Scale bar 200 µm.

assessed how an unbalance in cell death and proliferation affects large-scale injury-induced regeneration in *S. mediterranea*. We performed planarian head decapitations after 30 days post-RNAi initiation and followed macroscopic and microscopic responses in regenerative body trunks (Fig. 8). One week after amputation control animals formed head blastemas with photoreceptor pigmentation, whereas *Smed-Akt(RNAi)* animals only formed a marginal blastema with limited eye pigmentation (Fig. 8A). Further experiments with antibodies that recognize brain structures and visual neurons (i.e. anti-SYNORF1, anti-VC1), revealed *Smed-Akt(RNAi)* animals failed to regenerate brain and visual neuronal connections (Fig. 8B, C). Likewise, animals with tail amputation also fail to regenerate during the advanced phenotype, suggesting that the reduced number of neoblasts may affect both anterior and posterior regeneration in *Smed-Akt(RNAi)* animals (data not shown). These results also imply that injury-mediated cell differentiation is active despite the initial high levels of cell death and low levels of cellular proliferation.

Previous studies in *S. mediterranea* have shown that localized waves of cell death concentrate to the injury site and a systemic spike of neoblast division take place within the first six hours post-amputation [101], [111]. We followed both cell death and the mitotic response post amputation for seven days and observed cell death is suppressed over time, whereas cell division is increased in *Smed-Akt(RNAi)*animals when compared to the initial time point (Fig. 8D-G). Moreover, cell death not only reduced in *Smed-Akt(RNAi)* animals but it also failed to localize to the injury site as is expected in the first six hours post-amputation (Fig. 8D, E). The system wide cell death expected was also absent even after more than 2 days of amputation. Instead, TUNEL positive cells were slightly accumulated to the uninjured, opposite end of the regenerating trunk (n = 10/10). Intriguingly, amputation in the *Smed-Akt(RNAi)*group elicited a system-wide increase in cell division that peaked at six hours post-amputation and was sustained during the first week post-amputation (Fig. 8F, G). Additionally, the experimental group was incapable of producing a timely and localized mitotic response at the injury site, as seen in the control animals 2 days post amputation. However, *Smed-Akt(RNAi)* animals exhibited a delayed localization of cell division (i.e. 4 days post amputation), which persisted through 7 days post amputation. We propose *Smed-Akt* functions as regulator of cell death and proliferation, during large-scale tissue regeneration in planarians.

4.6. Discussion

Maintenance of adult tissues proceeds through a fine balance between cell death and cell division. Our results implicate *Smed-Akt* as a critical regulator of cellular turnover, adult tissue maintenance, and regeneration. Disrupting *Smed-Akt* signaling affects the number of proliferative neoblasts during cellular turnover and alters integrity and function of differentiated tissues. Strikingly, tissue injury is capable of altering patterns of cell death and cell proliferation after Akt downregulation.

The *Smed-Akt* phenotype is characterized by an initial increase in cell division that is followed by a gradual depletion in the number of proliferative neoblasts. The nature of the signals triggering cell proliferation in the first 10 days of the phenotype are not clear, but it might involve a compensatory response to overcome deficiencies in cellular turnover due to abnormalities in ciliogenesis [308]–[311]. Interestingly, even at late stages of the Akt phenotype some neoblasts continue dividing probably to self-renew and/or to continue supporting tissue turnover to some extent as animals subjected to *Smed-Akt(RNAi)* survive for over one month. Two non-exclusive scenarios may explain the presence of dividing neoblasts after *Smed-Akt(RNAi):* (1) residual Akt expression after

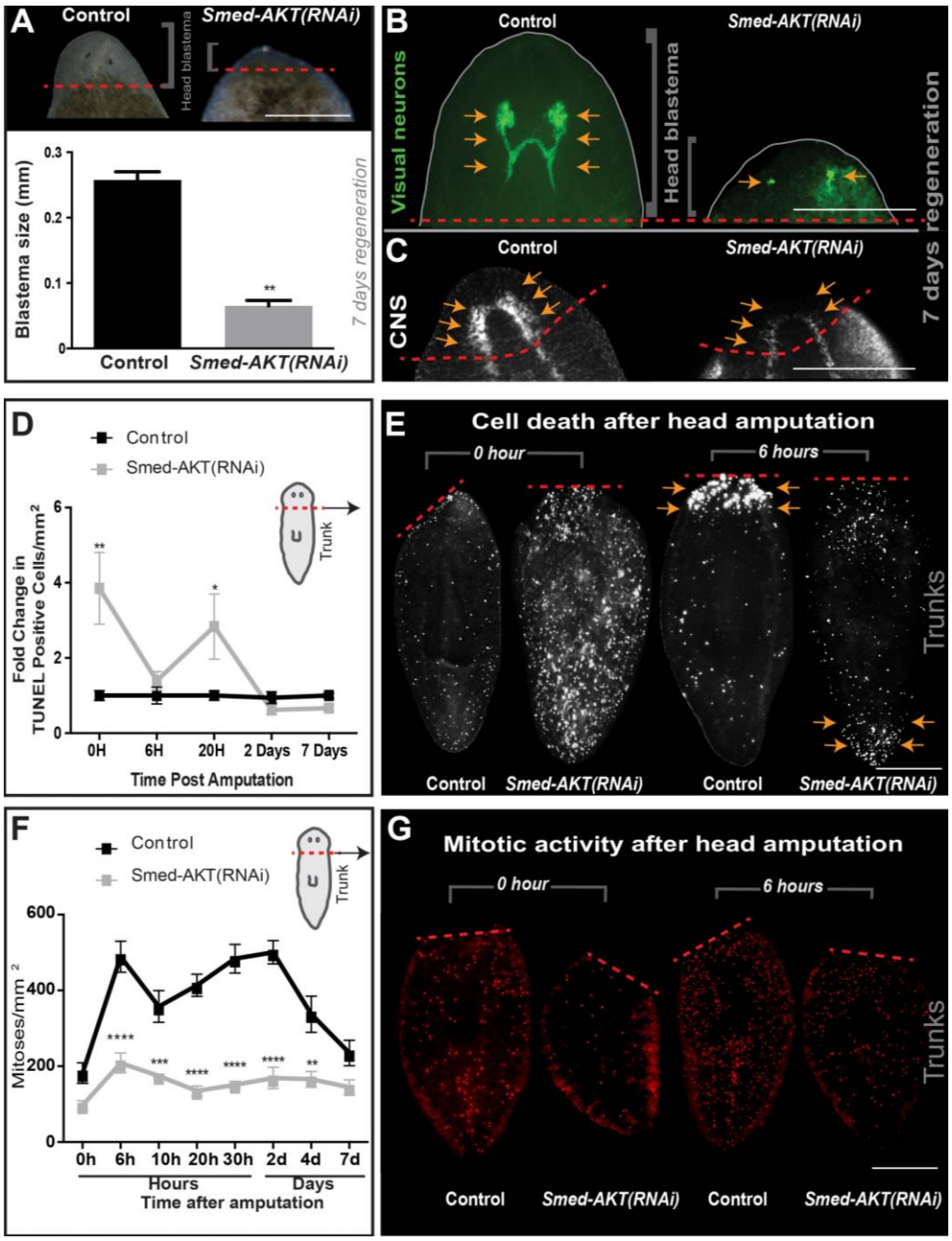

Figure 8. Akt is required for tissue regeneration. (A) Live images of control and *Smed-Akt (RNAi)* head blastema formation seven days post amputation. Dashed red line represents the amputation plane. (B) Immunostaining labeling the visual neurons (anti-VC-1 antibody) and (C) central nervous system (anti-SYNORF1 antibody) seven days post amputation. (D) TUNEL+ nuclei post amputation, represented in fold change compared to the control. (E) Immunostaining of TUNEL+ nuclei of trunk fragments 0 and 6h post amputation. Scale bar 200µm. (F) Levels of H3P+ cells over time post amputation in control and *Smed-Akt (RNAi)*. (G) Representative images showing mitotic activity (red dots) after head amputation at 0 and 6h in trunk fragments. Scale bar 200 µm. Graphs represent mean ± s.e.m. of two or more biological replicates and *P* values *<0.01, **<0.001, ***<0.0005 and ****<0.0001 were obtained with Wilcoxon test or two-way ANOVA.

RNAi, due to incomplete abrogation. Our qPCR analyses demonstrated that *Smed-Akt* expression is strongly downregulated after RNAi, however, additional experiments involving specific antibody against SMED-AKT protein may be needed to rule out whether AKT protein is still present and active, and (2) intrinsic differences among neoblast populations may confer survival properties to a select group of stem cells when Akt is downregulated. This possibility is supported by the differential expression displayed by neoblast subclasses after *Smed-Akt(RNAi)* (Fig. 3B). Recent progress to unravel the diversity of neoblast sub-populations suggest planarian stem cells are more complex than previously anticipated [104], [302]. Therefore, we envision future experiments would evaluate individual neoblast subpopulations to identify whether some neoblast subtypes are more susceptible to Akt downregulation [279], [284], [285], [312], [313].

The increased amount of cell death in *Smed-Akt(RNAi)* suggests this is a rather generalized event involving both neoblasts and differentiated cells. Our findings implicate decisions of cellular survival greatly depend on *Akt* signaling, but future experiments are required to discern whether apoptosis and/or necrosis initially target neoblasts. This possibility may, in fact, reduce the number of neoblasts making them unable to efficiently support demands of cellular turnover, leading to generic tissue defects. We did not address the mechanism of cell death in the *Smed-Akt* phenotype but since the mitochondrial pathway of apoptosis is remarkably conserved in planarians; it may serve, as in vertebrates, as the favored mechanism for *Akt*-mediated cell death [101], [122], [221], [278], [288], [314].

Studies in mammals show that not all tissues respond homogeneously in response to Akt deficiency, while some do not show measurable changes (e.g. bone marrow and pancreas), others undergo apoptosis (e.g. testes and thymus) [314]. A fine balance between stem cell proliferation and programmed cell death enables physiological cellular turnover to support adult tissue maintenance. Tissue renewal is seen to be altered in *Smed-Akt(RNAi)* animals, most likely due to the increased levels of cell death, which reduce the number of proliferating neoblasts. Our findings indicate that *Smed-Akt(RNAi)* lead to a heterogeneous gene expression response and mixed effects on the architecture of differentiated tissues. This differential sensitivity to *Smed-Akt* deficiency is observed early with alteration of cilia-mediated locomotion and the late onset of a cystic phenotype defined by a malfunctioning excretory system. The effects of abrogated *Smed-Akt* in differentiated tissues may depend on tissue-specific turnover rates but more experiments are needed to better understand the phenotype at systemic level.

The mechanisms by which cilia is strongly reduced after *Smed-Akt(RNAi)* is unclear but our findings indicating severe downregulation in IFT88 may suggest, as in other systems [308]–[310], [315], [316], that phosphorylated Akt fail to localize to the cilium at the cilliary base leading to disruption of the apical cellular projections. An intriguing finding of the *Smed-Akt(RNAi)* phenotype is the disruption of ciliated structures within the epithelium and excretory system (e.g. flame cells and proximal tubules), which is being recently introduced as an alternative model for cystic kidney disease [299]. Our results showed a significant reduction in gene expression correlating to ciliated structures, protonephridia and nephrocystins within the first 10 days of RNAi initiation that persisted to decrease by day 30. Interestingly, impaired locomotion in *Smed-Akt(RNAi)* animals became slightly evident by day 15 after RNAi treatment, which was exacerbated over time, and the delayed onset of the edema phenotype that correlated with a dysfunctional excretory system. Planarian studies have shown functional downregulation of genes correlating to ciliated structures and nephrocystins led to a rapid edema phenotype by 9–15 days post RNAi treatment [299], [301], [302]. These results imply that Akt activity may

facilitate the assembly of ciliated structures by regulating gene and protein expression required for maintenance of these structures (e.g. IFT88, NPHPs and SCL family of genes). It is also possible that during the initial part of the Akt phenotype, functional protonephridial units balance electrolyte and carry on waste excretion to compensate the reduction in the number of flame cells and proximal tubules. However, as the phenotype progresses it become unsustainable deriving in extensive damage, leading to the collapse of the excretory system. Further experiments will be required to discriminate how Akt signaling regulates the delayed onset of cyst-like formations. Nonetheless, these results are also significant because Akt signaling and cilia are emerging as possible therapeutic target in leukemia and polycystic disease [317]–[320]. Altogether, these findings highlight the convenience of the planarian model for analyzing Akt signaling dysfunction in the whole adult organism.

Akt has been studied extensively in the context of cancer and as a regulator of cellular functions, but its participation in large-scale regeneration remains poorly understood. Our findings reveal that Akt plays critical roles during planarian regeneration. Specifically, disruption of Akt impairs the process of blastema formation but does not prevent the initial peaks of cell proliferation upon amputation. In response to amputation, some cells migrate and differentiate to form an incipient blastema, which is discontinued probably due to the lack of timely localization of cell death near the wounded area. The mechanisms by which cell death regulates the process of regeneration still remains poorly understood [321]. Nonetheless, the Akt phenotype presents unique opportunities to address whether a particular signaling pathway and/or cell type that plays major role in guiding injury-induced apoptosis. We propose that Akt signaling serves as mediator of localized cell death events during planarian regeneration.

The intriguing finding that injury-induced repair signals in *Smed-Akt(RNAi)* is capable of reducing cell death is exciting and it reveals a novel role for Akt in large-scale tissue regeneration. Uninjured animals subjected to *Smed-Akt(RNAi)* show high levels of cell death and restricted neoblast division, but within a few hours after amputation, levels of apoptosis dramatically reduce while cellular proliferation increase in the absence of functional Akt. While future experiments will be required to investigate the mechanisms contributing to injury-mediated cellular death, these results imply tissue damage and repair may alter cellular decisions imposed by a dysfunctional Akt pathway.

4.7. Discussion: Overexpressed *Smed-Akt* hypothetical role in *Smed-PTEN(RNAi)* phenotype

The PI3K/Akt/TOR signaling pathway has been identified to be upregulated in the planarian cancer model produced by the knockdown of *Smed-PTEN* [56]. Oviedo et al., 2008 identified that knockdown of *Smed-Akt* within the cancer-like model rescued physical phenotypes such as anterior specific tumors and head regression. As a consequence of *Smed-Akt(RNAi),* the *Smed-PTEN(RNAi)* animals gained further phenotypes such as elongation, posterior bloating and accelerated locomotion issues (Fig. 9A). Moreover, the double RNAi animals were incapable of reducing cellular hyperproliferation and posterior-specific tissue outgrowths. This study also identified that treatment of *Smed-PTEN(RNAi)* animals with rapamycin (i.e. inhibitor of TOR signaling) restored cellular proliferation to basial levels despite the functionality of *Smed-Akt* (e.g. overexpressed or knockdown). Noteworthy, a small population of *Smed-PTEN(RNAi)* animals undergoing rapamycin treatment were able to recapitulate the cancer-like phenotype and lethality a few weeks after treatment termination. Lastly, *Smed-PTEN(RNAi)* animals with the addition of *Smed-*

Akt(RNAi) and rapamycin treatment were able to reduce cellular proliferation to basial levels. However, abnormal outgrowths within the animals persevered and resulted in lethality. Together, these results support the notion that *Smed-TOR* is a key mediator of cellular hyperproliferation within the cancer-like phenotype. However, the role of *Smed-Akt* in the phenotype may be correlated with its ability to drive a subset of neoblasts and/or progenitors within the animal to progress or restore the phenotype (e.g. anterior outgrowths or post rapamycin treatment, respectively).

Treatment of planarian with *Smed-Akt(RNAi)* resulted in the deterioration of structural tissues (e.g. nervous and muscular) unlike the *Smed-TOR(RNAi)* phenotype which restricted the capacity for neoblasts to divide. Through single-cell RNAseq, *Smed-Akt* expressed was determined to be within the neoblast sub-clusters (e.g. sigma population, epidermal, muscle, protonephridia and neural-1 and -2). As previously described, *Smed-TOR* expression was found to be highly expressed throughout the majority of neoblast sub-clusters with exception to neural-2 and epidermal neoblasts. With the treatment of rapamycin, *Smed-PTEN(RNAi)* animals reduce cellular division and subsequently exacerbated the expression of differentiated markers (e.g. nervous, excretory and digestive). We postulate that the reoccurrence of the cancer-like phenotype may be attributed to the inability for rapamycin to fully suppress aberrant *Smed-Akt* expression. Specifically, *Smed-Akt* expression within certain neoblast population (e.g. neural-2 and epidermal) that can provide the means for these cells to gradually expanded post treatment.

Analysis of single-cell RNAseq support to the notion that *Smed-Akt* may regulate subsets of neoblast and their progenitors independently of *Smed-TOR.* Results showed *Smed-Akt(RNAi)* reduced expression of the nervous system marker *Smed-PC2*. Moreover, simultaneous RNAi of *Smed-Akt+PTEN* inhibited the formation of abnormal tissue outgrowths in the anterior of the animals. These results suggest that neoblasts or progenitors within the nervous system, mediated by *Smed-Akt*, may play an essential role in the cancer model. Analyzing single-cell sequencing data published by Plass and colleagues in 2018 [266], it is evident the normalized expression of *Smed-Akt* increases in conjunction with both homologs of *Smed-PTEN* in the neural and epidermal linages. However, *Smed-TOR* expression levels did not change within these linages (Fig. 9B). The comparable expression levels of the genes could be attributed to PTEN's conserved function in counteracting Akt activity. Therefore, the loss of *Smed-PTEN* could allow the neural compartment to expand in a *Smed-Akt*-dependent fashion. It is enticing to suggest that neural progenitors may have an increased susceptibility to loss of *Smed-PTEN* and drive the phenotype, but further experiments are required.

Not all tissues respond homogeneously to *Smed-Akt* deficiency. Oviedo and colleagues identified that *Smed-Akt+PTEN(RNAi)* animals treated with rapamycin eliminated cellular hyperproliferation but abnormal tissue outgrowth still formed and may be attributed to *Smed-Akt(RNAi)*. In this chapter, we identified that *Smed-Akt* is highly expressed within the epidermis. However, despite extremely high levels of cell death within the animal, epithelial tissues do not produce apoptosis-mediated tissue lesions. The only physical abnormalities observed were elongation and bloating of animals because of a defective secretory system. Thus, we can postulate that in *Smed-PTEN(RNAi)* animals epidermal cell populations my expand with loss of *Smed-Akt* and result in the abnormal outgrowths despite rapamycin treatment. An alternative theory can be because of compensatory activity of PI3KR1, PI3KCG and/or PDPK1 which can activate downstream targets independent of Akt activity. Interestingly, PI3KCG and PDPK1 are expressed in the protonephridia, neural and ciliated neuron cell types and can drive the phenotype (Fig.

9D). Further experiments will be required to elucidate the role of aberrant neoblast progenitors and *Smed-Akt* within the *Smed-PTEN(RNAi)* phenotype.

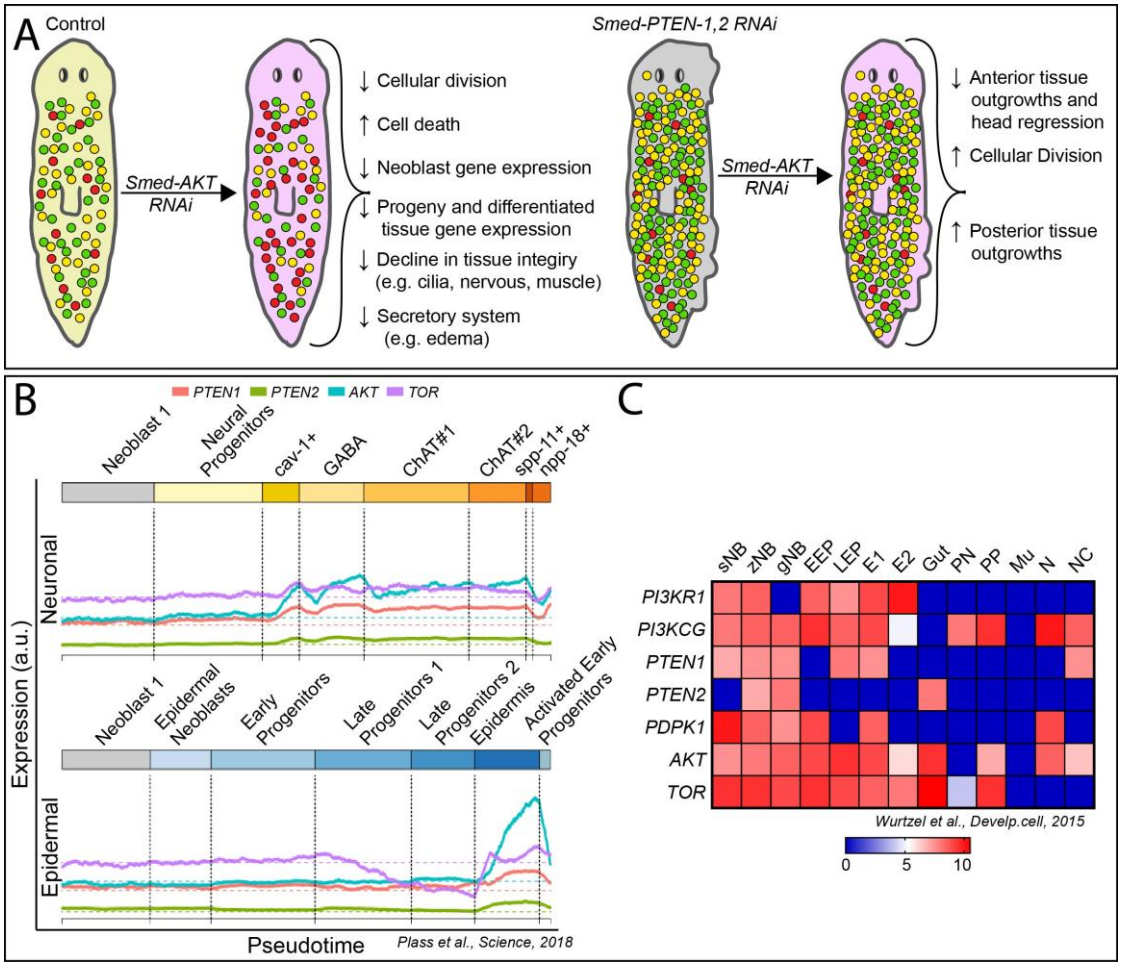

Figure 9. Theoretical role of *Smed-Akt* in the *Smed-PTEN(RNAi)* phenotype. (A) Concluding remarks on the *Smed-Akt(RNAi)* phenotype 30 days RNAi. (B) Summary of results obtained with double knockdown of *Smed-PTEN* and *Smed-Ak*t RNAi. (C)Expression patterns of Smed-*PTEN-1, -2, Smed-Akt* and *Smed-TOR* within the neural and epidermal lineage tree compartments. (D) Expression patterns of genes per neoblast sub-cluster involved in the PI3K/PTEN/AKT/TOR signaling pathway.

CHAPTER FIVE

BACKGROUND

Functional role of nuclear PTEN during cellular transformation

5.1. Introduction

Despite decades of research the mechanism of adult tissue transformation into malignancies remain poorly understood. Intriguingly, early detection of malignant transformation in epithelial tissues attribute to a 90% patient survival rate versus 10% in late stage detection [322]–[330]. Early diagnosis of malignant cells/tissues are made by morphological identification and often results in a high false-negative detection rate [331]. Clinicians must be able to distinguish precancerous and early malignant lesions from more common benign inflammatory conditions. Therefore, creating methods allowing accurate diagnosis of precancerous events in real-time would increase the efficiency of early patient intervention. However, we have yet to identify common and ubiquitous features within all precancerous cells/tissues due to the complex heterogeneity found within all cancer types. The analysis of cancer cells in tissue culture is highly informative however it may not accurately represent stages of cellular transformation within the complexity of an adult organism.

PTEN's dual functionality within the cytoplasm and nucleus provides a unique opportunity to understand the onset and progression of cancer. Interestingly, histological analysis of early and advances stage cancer tissue samples has identified inappropriate subcellular compartmentalization of PTEN (e.g. nuclear and cytoplasmic) dictates cancer progression. PTEN mutations have been identified in 80% of Cowden and 60% of Bannayan-Riley-Ruvalaba Syndrome patients and is attributed to aberrant nuclear exclusion of PTEN resulting in noncancerous hamartomas tumors and increased risk of developing cancer [269], [271], [332]. It is established that PTEN's N-terminal containing its phosphatase domain is responsible for antagonizing the PI3K/AKT pathways and therefore inhibiting cell survival and proliferation [188], [191]–[193]. However, a large number of PTEN mutations occur in the C-terminus of its catalytic domain. The C-terminal of PTEN has a less defined mechanism but studies have shown it is important in PTEN nuclear localization and in preserving chromosomal integrity [271], [333], [334]. Thus, the C-terminal PTEN plays a significant role in suppressing neoplasm and requires further elucidation.

In the previous sections, we have discussed the conservation of DNA damage response and repair proteins in the planarian and its requirement for tissue homeostasis and regeneration. In addition, we have already discussed the planarian cancer model created by *Smed-PTEN(RNAi)* results in hallmarks of cancer and is driven by the upregulation of oncogenic signaling cascades such as the PI3K/AKT/TOR pathway. However, we have yet to test the hypothesis that with the loss of tumor suppressors, in an oncogenic environment, DNA damage or replication stress is a pervasive feature of cancer initiation. In this section we capitalize on the less understood function of the PTEN tumor suppressor within the nucleus which, is active in a phosphatase-independent fashion. To further learn about the nuclear role of PTEN, we will address its potential function in

preserving genomic stability, DNA replication and cell cycle checkpoint stability. This literature review will provide the background of the field so that we can aim to address the OTS-DDM using the planarian model organism to understand cancer and its initiation.

5.2. Genetic alterations of PTEN tumor suppressor gene

There are many mechanisms were tumor suppressor genes can be inactivated. For example, PTEN function can be compromised by alterations to its promoter region (e.g. epigenetic silencing, transcriptional repression/activation), microRNA regulation, post-translational modifications and protein-protein interactions resulting in aberrant localization of PTEN [178], [270], [335]–[351]. Importantly, genetic alterations of PTEN resulting in allelic or complete deletion of PTEN is frequently observed in cancers (Fig. 1A, B). Continual onslaught from endogenous or exogenous stimuli produces DNA damage and the subsequent accumulation of genetic alterations within hot spot regions in genomes [30], [32], [33], [352], [353]. Alterations within genome hot spots arise from point mutations (e.g. single nucleotide substitutions) and/or copy number alterations (CNAs), which are two common features found in tumor suppressor inactivated-mediated cancer progression.

A study by Macheret and Halazonetis in 2015 [30] identified that out of 3,281 tumor genome data sets representing 12 different cancer types, PTEN tumor suppressor gene is targeted by point mutations in 9.7% of all cancers [30]. Further, using the Sanger Institute Catalogue of Somatic Mutation in Cancer (COSMIC) [354] we confirmed that PTEN mutations are mainly comprised of point mutations (e.g. nonsense, missense and synonymous substitutions) yielding 61.08% mutations found within 4,778 different cancer samples (Fig. 1C, D, E). Deletions (e.g. frameshift and inframe) are a distant second accounting for 21.51% mutations followed by insertions and other mutations types (e.g. 10.11% and 8.69%, respectively). The distribution of mutation types (e.g. substitutions, deletions and insertion) per sample with respect to the amino acid site within the PTEN sequence, reveals that exons 5-8 harbor high rate of mutational loads (Fig. 1F, G) Specifically, two-thirds of PTEN mutations are found within these exons in Cowden disease [269], [270]. These results suggest that high mutational loads within the phosphatase core motif (exon 5) and the catalytic terminal (exon 6-8) are pervasive features of many cancer types.

PTEN being a quite large gene on chromosome 10 (105,338bps), is also highly susceptible to CNAs. CNAs are somatic changes to chromosome structures and result in gain or loss (e.g. loss of heterozygosity) of specific DNA fragments; commonly found in many cancer types [355]. In terms of PTEN, it has been noted that most recurrent cancer CNAs reside in common fragile sites (CFS) or hot spots found in large genes [353], [356]. PTEN consists of many hot spot mutation sites (e.g. Arg130, Arg173 and Arg233) where point mutations and CNAs target frequently [178]. For instance, Arg233 is located in PTEN's nuclear localization sequences and may alter its nuclear tumor suppressor activity (discussed in detail in the next section). With the mutational load on exons 6-8 and hot spot targets of its nuclear transport, PTEN C-terminal region is more than likely a crucial component of neoplasia. Together, its role in nucleocytoplasmic shuttling requires further investigation.

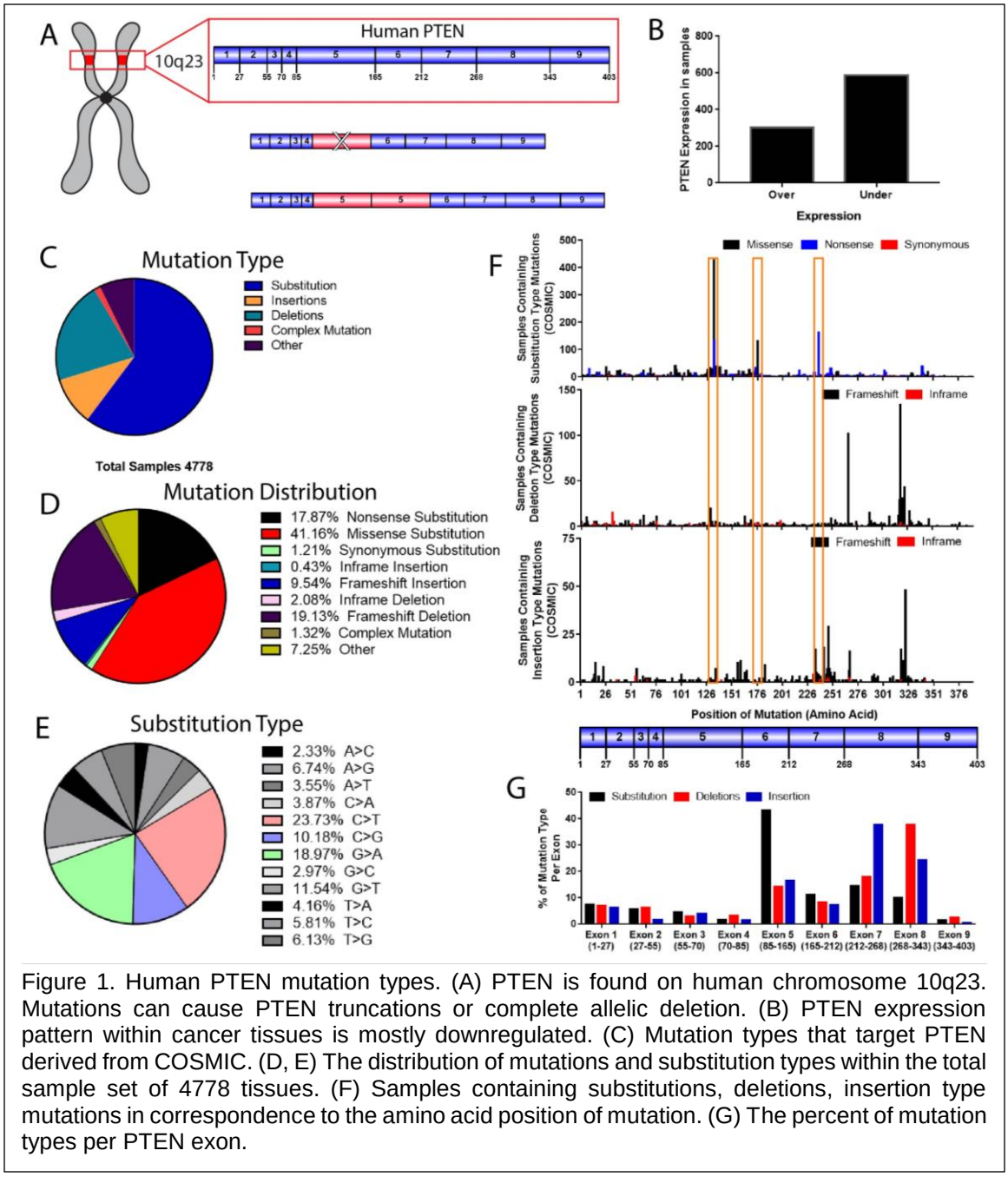

Figure 1. Human PTEN mutation types. (A) PTEN is found on human chromosome 10q23. Mutations can cause PTEN truncations or complete allelic deletion. (B) PTEN expression pattern within cancer tissues is mostly downregulated. (C) Mutation types that target PTEN derived from COSMIC. (D, E) The distribution of mutations and substitution types within the total sample set of 4778 tissues. (F) Samples containing substitutions, deletions, insertion type mutations in correspondence to the amino acid position of mutation. (G) The percent of mutation types per PTEN exon.

5.3. Nuclear PTEN, a guardian of the genome

PTEN zygosity has been shown to dictate prostate cancer progression and prognosis outcomes [357], [358]. For instance, in prostate cancer progression heterozygous PTEN deletions (50%) are associated with hyperplasia and dysplasia lesions [359], [360] and homozygous deletions (100%) are frequent found in primary tumors and metastatic prostate cancer [361], [362]. It is postulated that prostate transformation is attributed to the progressive reduction of nuclear PTEN which precedes

prostate adenocarcinoma followed by complete loss of cytoplasmic PTEN in most invasive cancers [363], [364]. Histological analysis has shown progressive loss of nuclear PTEN accompanies cancer progression in various tumors including gastrointestinal stromal, melanoma, esophageal, thyroid and breast [365]–[370]. Overall, genetic alterations and spatiotemporal distribution of PTEN within a cell give rise to distinct cancer phenotypes. PTEN tumor suppressor provides us with a robust gene to analyze cancer progression in both its earliest and latest stages.

Recent reports have shown PTEN functions beyond its lipid phosphatase activity, residing in small pools localized to and functions within the nucleus [178], [371], [372]. Interestingly, nuclear PTEN is thought to act as a guardian of genome stability as its disruption induces chromosomal abnormalities and spontaneous DNA double stranded breaks[171], [271], [373], [374]. PTEN is seen to maintain cell cycle progression centromere stability, chromatin condensation and the mitotic checkpoint. In this section, we will discuss how PTEN enters the nucleus and its functions within the nucleus.

5.3.1. PTEN translocation and presence in the nucleus

Nuclear localization and proper nuclear-cytoplasm shuttling are crucial for PTEN's tumor suppressive function. PTEN lacks traditional nuclear localization sequences (NLS) required for the tagging of its import into the nucleus by nuclear transport. However, it can enter the nucleus through passive diffusion via nuclear pore complex (NPC) and major vault protein (MVP)-mediated import. Furthermore, PTEN mono-ubiquitination (Ub) or sumoylation have been identified to regulate its nuclear and cytoplasmic localization. Recent reports on PTEN nuclear translocation mechanisms show conflicting results and have not yet been clearly identified.

5.3.1.1. PTEN translocation into the nucleus: MVP-mediated import

PTEN contains four non-traditional nuclear localization signal (NLS) sequences that contain lysine-rich sequences. They are NLSM1 (aa 10-14 RNKRR), NLSM2 (aa 160-164 RTRDKK), NLSM3 (aa 233-237 RREDK) and lastly, NLSM4 (aa 265-269 KKDK) found within the C2 domain active site. Importantly, a combination of NLS2+NLS4 or NLS3+NLS4 are required for nuclear localization [375]. Importantly, the C2 domain of PTEN, containing both NLSM2 and NLSM3, mediates a highly stable interaction between PTEN and MVP. Therefore, the nuclear import of PTEN requires two NLS sequences to facilitate this process.

The interaction between PTEN+MVP is mediated by binding of Ca^{2+} within the C2 domain of PTEN and the two EF hands of MVP [376]. Furthermore, concentrations of Ca^{2+} and Mg^{2+} regulate the PTEN+MVP interaction by antagonizing each other (i.e. binding of Mg^{2+} to MVP inhibits its conformational change) [377]. Minaguchi et al. 2006 attributed increased PTEN nuclear localization to its downstream effects of p44/p42 MAPK downregulation. In conjunction with their previous work [378], it is postulated that the increase Ca^{2+} signaling, known to regulate G1-S transition of the cell cycle may be a result of increased PTEN nuclear entry. Nuclear PTEN has been shown to induce G0/G1 cell cycle arrest and the downregulation of CyclinD1 [377].

5.3.1.2. PTEN translocation into the nucleus: passive diffusion or active transport

PTEN's import into the nucleus can occur independently of NLS sequences through passive diffusion or active transport. Liu et al. 2005 identified that PTEN enters into the nucleus through passive diffusion by nuclear pores [379]. To validate this finding, they identified that RAN-mediated nuclear transport occurred despite mutations in NLS sequences. Secondly, that large GFP-PTEN fusion proteins did not enter the nucleus (e.g. ~60,000 Da or less can diffuse through nuclear pores) and require active transport. Lastly, mutations in K13 and R14 residues decreased nuclear localization of PTEN and are not considered to be classical NLS. The last finding identified other possibilities of PTEN nuclear inclusion or exclusion that resided in the N-terminal of PTEN.

To further uncover the role of PTEN nuclear transport, in 2006, Gil and colleges identified multiple nuclear exclusion motifs (NEM) in PTEN's structure residues. Specifically, at 159-164 (PTP region/N-terminal), 233-237 (C2 region), 263-269 (CBR3 region) and 327-335 (Cα2 region) that are required to keep PTEN in the cytoplasm [380]. They identified that peak nuclear accumulation of PTEN was achieved in the following mutation order: Cα2 region ranked highest, followed by PTP and CBR3, and C2 region had moderate levels of nuclear PTEN. Interestingly, the NEMs overlap with the NLS sequences [375]. Despite these findings, they identified that RAN-dependent GTPase activity at residues 8-32 in the N-terminal results in PTEN nuclear localization. Recent report in 2017 Chen and colleagues identified that the importin-11 and RAN-GTPase complex mediates PTEN nuclear localization through active transport [381]–[384]. Interestingly, they identified both residues at Lys13 and Lys289 are required for nuclear import and PTEN poly-ubiquitination (poly-Ub) mediated degradation (will be discussed in the next section) [384].

5.3.1.3. Post-translational modification of PTEN mediated nucleocytoplasmic localization: ubiquitination of PTEN

PTEN inactivation is attributed to alterations in proteasome degradation within the cytoplasm [237], [269]. The ability of the neural precursor expressed, developmentally down-regulated protein 4-1 (NEDD4-1) to poly-Ub and mono-Ub PTEN has been reported to regulate its stability and subcellular compartmentalization *in vitro* and *in vivo* [385], [386]. Ub of target proteins on lysine rich regions is achieved by the action of an E1 enzyme that transfers activated ubiquitin to an E2 ligase and the addition of E3 ligase. It has been found that K13E and K289E are target lysines for PTEN ubiquitination (found in the N-terminal and C2-terminal, respectively) [386]. Cytoplasmic mono-Ub of PTEN positively influences nuclear shuttling and de-Ub maintains its nuclear localization, protecting PTEN from cytoplasmic degradation. Furthermore, poly-Ub of PTEN results in cytoplasmic retention, resulting in proteasome degradation [237], [387]. Thus, NEDD4-1 modification on PTEN attributes to both an oncogenic and tumor suppressive potential (e.g. PTEN degradation and shuttling, respectively).

NEDD4-1-mediated PTEN downregulation is associated with poor prognosis and drug/chemo-resistance in an array of tumor specimens [385], [387]–[391][387], [389]. NEDD4-1 expression levels are minimal in normal tissues but overexpressed within the cytoplasm of many cancer types [385], [387]. NEDD4-1 knockdown decreases proliferation, migration, invasion and improved chemo-sensitivity in cells through the stabilization of PTEN and reduction of PI3K/AKT signaling [392]–[394]. Upregulation of NEDD4-1 activity promotes cellular transformation in a PTEN-heterozygous background more effectively than its complete loss; triggering p53-dependent senescence [237], [395]. Moreover, Cowden Syndrom (CS) patients harbor germline mutation in PTEN and are

more susceptible to cancer onset. Specifically, mutation of PTEN's codon 307 (E307K) in the C2 loop results in NEDD4-1-mediated PTEN cytoplasmic accumulation and PTEN-mediated hyper-suppression of Akt activity [396]. Furthermore, truncated PTEN C-terminal fragments bind with greater affinity to NEDD4-1 than full-length PTEN, resulting in their poly-Ub and degradation [397]. Interestingly, the anticancer drug indole-3-carbinol (I3C) cannot antagonize NEDD4-1 under PTEN RNA interference or in PTEN null genotypes [388], [398], [399]. Overall, we see that the interaction between NEDD4-1 and PTEN is contingent on PTEN's mutation location (e.g. C- terminal) and genotype during cancer progression.

NEDD4-1 binds to PTEN thought its N-terminal region containing both the C2-domain and HECT domain [397]. NEDD4-1 contains a HECT domain mediating Ub ligation activity,4 WW substrate binding sites and C2-domain which regulates E3 targeting to intracellular membranes [400]. The WW1 domain of NEDD4-1 is required for p34 binding and their interaction degrades PTEN though its poly-Ub [401]. Knockdown of p34 in cancer models results in PTEN mono-Ub and suppression of cellular hyperproliferation [401]–[403]. p34 affects subcellular localization of PTEN and contributes to the PTEN-dependent oncogenic activity of NEDD4-1. Furthermore, overexpression of FoxM1B transcription factor results in the upregulation of NEDD4-1 poly-Ub of PTEN [399]. FoxM1B overexpression is correlated with increased expression of Cyclin-D1/-E accompanied by decreased levels of p53 and pRb in normal human astrocytes promoting their transformation. In certain instances, nuclear exclusion of PTEN is beneficial. For instance in keratinocyte proliferation, ΔNp63α eliminates PTEN Ub entirely by binding to NEDD4-1's promoter and represses its E3 ligase activity [404]. Overall, the balance between PTEN and NEDD4-1 allows for inhibition of cancer progression and regulates cell cycle progression (discussed in depth in next section).

De-ubiquitination is predominantly cytoplasmic and facilitates PTEN nuclear localization. Counteracting the E3 ligase Ub properties, USP7 and USP13 de-Ub PTEN. PTEN mono-Ub is reversed by USP7 leading to its nuclear export and USP13 is identified to increase PTEN stability by reversing PTEN poly-Ub preventing its degradation [405], [406]. Further, scaffolding proteins that aid in cellular trafficking of PTEN such as β-arrestins and Ndfip1-Rab5-GTPase [407]–[409]. Specifically, Ndfip1-Rab5 complex is involved in cytoplasmic Ub-modifications of PTEN, acting as a molecular scaffold on early endosomes to mediate the Ub of PTEN by NEED4-1 [409]. Further regulation of PTEN Ub by regulator inputs converge on USP7 to regulate PTEN nucleocytoplasmic shuttling such as PML, nucleophosmin interactions (NPM1) and BCR-ABL mediate phosphorylation [410], [411]. PML opposes USP7 though a mechanism involving the adaptor protein death domain-associated protein (DAXX) thus nuclear PTEN function and accumulation is possible [405], [411], [412]. Further, BCR-ABL acts in opposition to PML resulting in PTEN cytoplasmic retention however, in the case of chronic myeloid leukemia stem cells, BCR-ABL inactivation by tyrosine kinase inhibitor (e.g imatinib) had no effect [411]. The PML/USP7/PTEN pathway is critical in cancer therapies as USP7 can act as an oncogene. Specifically, its inhibition through inhibitor P5091, activates PTEN allowing for an apoptotic and cell growth arrest response which occurs by-passing *TP53* genetic loss [413].

5.3.1.4. Post-translational modification of PTEN mediated nucleocytoplasmic localization: phosphorylation of PTEN

Nucleocytoplasmic localization of PTEN by post-translational modifications are known to increase or decrease PTEN stability through its phosphorylation. PTEN

phosphorylation mediates three distinctive conformation forms: open-open (active), open-closed (PTEN-phosphatase) and closed-closed (inactive) thus its conformation facilitates its localization [336], [414], [415]. The closed-closed inactive conformation of PTEN results in its cytoplasmic retention and stabilization in contrary to its open-open conformation that is active at the plasma membrane and capable of entering nucleus [414], [416], [417]. The N-terminal of PTEN facilitates its phosphatase properties by counteracting Akt activity and the C-terminal of PTEN is important for its nuclear localization [188], [271], [334]. The phosphorylation status of PTEN's C-terminal facilitates this conformational change which is mediated by many proteins (e.g. RAK, CK2, ROCK and GSK3β) [178]. Phosphorylation of PTEN at levels of high stoichiometry of the main residues in the C-terminal ~354-403, specifically on the cluster of four Ser/Thr residues (380, 382, 383, 385) results in PTEN increase protein stability but less active [272], [273], [418]–[420]. Whereas, its dephosphorylation activates PTEN allowing for its C-tail to become susceptible to Ub-mediated proteasome degradation or promote nuclear shuttling.

PTEN regulation relies on a well-orchestrated balance between its open- and closed- conformation to prevent its degradation. RAK tyrosine kinase interacts with PTEN in the cytoplasm to mediate its phosphorylation on Tyr336 [394], [421]. RAK-mediated PTEN phosphorylation aids in its tumor suppressing potential against Akt signaling and inhibits cancer formation/progression. Knockdown of RAK results in PTEN poly-Ub through enhanced interaction with NEDD4-1, leading to PTEN proteasome degradation [422], [423]. In addition, avian reovirus (ARV) protein p17 can stabilize PTEN though phosphorylation by elevating RAK+PTEN association preventing cytoplasmic degradation by NEDD4-1 [424]. More recently, studies have identified that E3 ligase and PTEN interaction is based on Ub and phosphorylation status of PTEN [425]. Chen et al. 2016 found WWP2 to be more active than NEDD4-1 in ubiquitinating non-phosphorylated PTEN as WWP2-PTEN interaction was weakened by tetra-phosphorylated PTEN. Whereas NEDD4-1 is more capable of achieving PTEN Ub despite phosphorylation status in its C2 domain. Aberrant overexpression of NEDD4-1 can drastically reduce PTEN protein levels and is correlated with neoplasia [237]. Cai et al. in 2018 identified that CK1α binds to C-terminal tail of PTEN promoting (1) stabilization, (2) competitively antagonizing NEDD4-1 induced PTEN poly-Ub and (3) inhibiting the phosphorylation of PTEN therefore, stopping AKT activity in NSCLC cells [393]. Thus, the intricate balance between PTEN ubiquitination and phosphorylation is quite complicated needing further elucidation to enhance cancer treatments and therapies (Fig. 2).

5.3.2. Nuclear PTEN function within the nucleus

Prior to the clear identification of PTEN's nuclear localization sites (NLSs), required for its nuclear transport, immunohistochemical studies implying nuclear localization of PTEN were thought to be artifacts [367]–[369], [426]. However, these studies, conducted in an array of cancer tissues and cell lines, identified that PTEN’s shift from the nucleus to the cytoplasm was correlated to increased cancer susceptibility/progression [367]–[369], [426]. Nuclear localization of PTEN has been identified to regulate cell cycle progression and checkpoint stability. Furthermore, its nuclear activity is capable to eliciting G1 arrest, promoting a response to DNA damage, cell size control and cell fate determination; independently of AKT signaling [427]. Thus, in the following sections we will further elaborate on PTEN's roles in the nucleus.

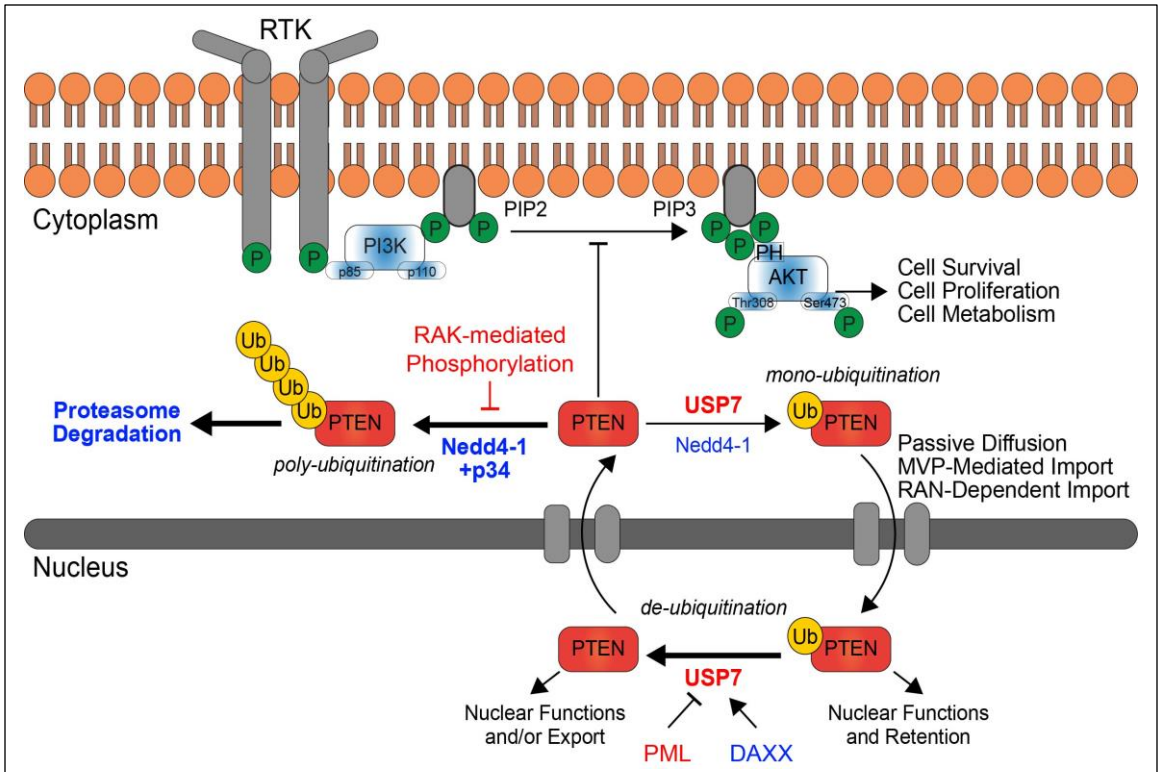

Figure 2. Nucleocytoplasmic shuttling of PTEN through balanced post-translational modification of phosphorylation and ubiquitination allows for PTEN nuclear function.

5.3.2.1. Nuclear PTEN is associated with G0/G1 phase transition

PTEN peeks inside of nucleus during G0/G1 phase of the cell cycle [370]. Key studies in an array of cancer cell lines, in the late 90s and early 2000s, revealed that PTEN expression is capable of inducing G0/G1-S cell cycle arrest, growth inhibition and apoptosis. Since then, nucleocytoplasmic partitioning of PTEN has been identified to regulate different function of cell cycle progression. In the nucleus, PTEN is capable of mediating cell growth suppression by downregulating p70S6K activation thought AMPK and electing cell cycle arrest by reducing both the expression of CyclinD1 and MAPK phosphorylation [378], [428]. Mechanistically, nuclear PTEN reduces growth factor-stimulated MAPK activation and inhibits the phosphorylation of its signaling molecules (e.g. ERK1/2, Raf, MEK1/2, EST2). Thus, in turn leading to the down regulation of CyclinD1 transcription levels and cell cycle arrest [378]. Cytoplasmic PTEN, on the other hand, regulates PI3K/Akt signaling, apoptosis, p18Ink4c, p21(Waf1/Cip1) and upregulate p27Kip1 [378], [429]–[435]. Importantly, cytoplasmic PTEN-mediates cell growth and cell cycle arrest in G1 phase by the increased accumulation of cyclin-dependent kinas (CDK) inhibitor p27Kip1 [359], [433], [436]–[440]. Together, nucleocytoplasmic shuttling of PTEN simultaneously induces expression of p27Kip1 and reduces the activity of Cyclin-A/-D1/-D3/-E, CDK2 and CDK4; inhibiting tumor development [377], [433], [435], [437]–[443].

PTEN-induced cell cycle arrest is facilitated by inhibiting oncogene or proto-oncogene signaling transduction cascades (e.g. PI3K, Akt, PDK1, RAC1, SKP2 and CDC42) [441], [444]. For instance, SKP2 expression in concatenation PI3K/Akt pathway is required to reverse cell cycle arrest mediated by p27Kip1 and therefore restoring levels

of Cyclins and CDKs [440]. Nucleocytoplasmic PTEN overexpression inhibits PI3K meditated Rb gene degradation and Rb protein (hyper)phosphorylation via CyclinD1/CDK4. This allows for PTEN prevented the increase and nuclear localization of CyclinD1 during G1-S progression [437], [441], [442], [445]. Noteworthy, PTEN is not capable of inducing G1 cell cycle arrest in Rb deficient cell lines resulting in accelerated malignant development [441], [445]. Furthermore, the interaction of PTEN-p27Kip1-Rb induces G1 cell cycle arrest independent of p53 inactivation [438].

Interestingly, PI3K/Akt and RAS/ERK pathways are frequently activated in cancers to promote primary tumor cells to bypass PTEN-induced growth arrest and senescence [446], [447]. PTEN was seen to support malignant potential of different cell populations dependent on the progression of tumorigenesis [448]. Yao and colleagues identified that PTEN mutant during early papillomatogenesis initially elevated RAS(Ha)/ERK/Akt activity. However, in PTEN null keratinocytes (i.e. late phase of papillomatogenesis) early phase phenotypes were eliminated and CyclinE2 expression was elevated and correlated with increased malignant potential. More recently, PTEN functions in the tumor suppressor network SPRY2/PP2A/GSK3β which counteracts PI3K and RAS pathways and is an important determinant of prostate cancer progression [449]. SRPY2 inactivation resulted in elevated levels of reactive oxygen species (ROS), the activation of PP2A and GSK3β which then phosphorylates and transports PTEN into the nucleus. Lastly, SRPY2 inactivation resulted in TP53-mediated G1 cell cycle and growth arrest of the prostate primary tumor cells. However, simultaneous loss of PTEN and SRPY2 resulted in PI3K/Akt and RAS/ERK pathway activation, enhanced proliferation and invasive tumors. Together, these findings support the notion that PTEN facilitates cell fate decisions at two different levels (1) in the cytoplasm and (2) in the nucleus. Overall, nucleocytoplasmic partitioning of PTEN mediates different phases of cancer initiation and tumor progression.

5.3.2.2. Symbiotic relationship between nuclear PTEN and p53 regulates G0/G1 and S cell cycle phases

In early phases of carcinogenesis, decreased PTEN protein levels are found to be associated with increased p53 levels [277], [450], [451]. For example, in endometrial carcinogenesis loss of PTEN protein staining was related to grade 1 and grade 2 adenocarcinoma. Furthermore, p53 protein levels were elevated in grade 3 adenocarcinoma and other late phenotype of endometrial carcinogenesis [450]. Similar results are found in hepatocellular carcinoma (HCC) patient samples. Interestingly, increase p53 expression was correlated with the upregulation of cell cycle protein proliferating cell nuclear antigen (PCNA) and resulted in increased HCC dedifferentiation, advanced cancer stages, shorter survival and higher recurrence rates [452]–[454]. These findings are supported as p53 regulates PCNA which is required for cell cycle regulation through its activity with DNA polymerase-delta [455]. Further, in PTEN-knockout skin showed a delayed p53 protein accumulation and down-regulation of its downstream targets (e.g. p21, 14-3-3 and Reprimo) [456]. PTEN cues the accumulation of p53 after DNA damage and without PTEN, p53-mediated cell cycle checkpoint stability is lost, initiating early phases of tumor progression [456], [457].

p53 tumor suppressor gene is frequently targeted by point mutations in 42% of all cancers [30], [458]. Shockingly, PTEN can also promote tumor formation by enhancing the stability of gain-of-function p53 mutants leading to increased cell proliferation and inhibition of cell death [459]. Human cancers contain low frequency of simulations loss of both alleles of PTEN and p53 and their combined loss accelerates tumorigenesis [460]–

[464]. There is a strong symbiotic connection between the two tumor suppressors PTEN and p53 and they function in concert to mediate stress responses, DNA damage repair, apoptosis and cancer inhibition through a positive feedback loop.

PTEN promoter contains approximately seven p53 binding element sites all of which are in intron 1 within PTEN's point mutation hot spots (discussed above) [465], [466]. p53 is an activator of PTEN gene transcription, regulating cellular survival. However, p53-mediated apoptosis and cell cycle regulation requires functional PTEN despite p53 status [456], [465], [467]. PTEN is capable of inducing p53-independent DNA damage-mediated apoptosis with p73, a component of p53-dependant network to induce apoptosis [468]. The PTEN-p73 protein complex is correlated with increased PARP cleavage and apoptotic mediators (e.g. PUMA and Bax) in genotoxic environments [468], [469]. Despite its nuclear role of transcriptionally activating PTEN expression, increased levels of p53 can in turn lead to degradation of PTEN by activating caspase-3 [465], [470].

PTEN controls p53 protein stability in both the cytoplasm and nucleus in a phosphatase dependent and independent manner, respectively [457], [471]. Phosphatase-dependent PTEN activity antagonizes PI3K/Akt signaling thus reducing nuclear entry of Mdm2 required for p53 ubiquitination/degradation. In a phosphatase-independent fashion, PTEN directly interacts with p53 promoting its activity and transcription [218], [467], [472]–[474]. Nuclear PTEN initiates an auto-regulatory feedback loop leading to: (1) PTEN-dependent nuclear localization of p53, (2) PTEN-p53 physically association and (3) PTEN-p53 complex recruitment to PTEN promoter and p53 trans-activation of PTEN promoter activity [475]. Mechanistically, nuclear PTEN forms a complex with p300 promoting nuclear PTEN-mediate cell cycle arrest and acetylation-mediated tetramerization of p53. Acetylation of p53 further promotes PTEN-p53 association thereby sustaining high levels of p53 acetylation in a positive feedback loop [473]. The interaction between PTEN-p53 further enhances p53 DNA binding to p21 promoters, decreased levels of CyclinD1 and induced cell cycle arrest [457], [475].

In the presence of DNA damage or cellular stress the PTEN-p53 complex is formed. For instance, in the presence of oxidative stress, PTEN is phosphorylated on S380 and accumulates in the nucleus. Subsequently, resulting in cell cycle arrest in a PTEN-p53 fashion and reduce reactive oxygen species (ROS) through a p53-dependent mechanism [476]. Interestingly, PTEN-containing mutations in either of its 3 ATP-binding motifs are unable to inhibit ROS-induced DNA damage through decreased nuclear p53 protein and transcription levels [469]. These observations may be due to increased nuclear shuttling of Mdm2 thus inhibiting acetylation of p53. Under hypoxic conditions the nuclear PTEN-p53 complex is established and increases the production of Maspin tumor suppressing activity in a PTEN-dependent manner [471]. In response to UV radiation, loss of p53 decreases PTEN protein expression and enhances PI3K/Akt signaling, subsequently leading to activation of AP1 and NF-κβ [477]. Overall, the interplay between PTEN and p53 aids in the preservation of genomic stability.

5.3.2.3. Nuclear PTEN is involved in maintenance of chromatin structure to DNA replication during interphase of the cell cycle

PTEN mutations in C-terminal are associated with common fragile site instabilities that most likely arise from oncogenic-induced DNA replication stress [30], [271], [478]. Mass spectrometry studies have indicated that PTEN is associated with many DNA replication fork factors [479]. DNA replication is a well-coordinated and timely process requiring replisome assembly, helicase-mediated DNA unwinding and polymerase-

mediated DNA synthesis. In this section, we will discuss how PTEN's C-terminal mediates the integrity of chromatin and regulates DNA replication.

5.3.2.3.1. PTEN maintains chromatin structural integrity and the fidelity of DNA replication

The regulation of histones in the maintenance of chromatin condensation is essential in the process of DNA replication initiation, progression and recovery. The interplay of PTEN's C-terminal and histone HP1α promotes chromatin condensation and PTEN tumor suppression activity [480]–[482]. Loss of PTEN impairs heterochromatic distribution of HP1α leading to relaxation of chromatin (e.g. de-condensation), increased H4K16 hyperacetylation and amplified chromatin association of MOF acetyl-transferase. This together results in an open structure of active chromatin and transcription activation. More recently, Gong et al. 2015, found that PTEN maintains heterochromatin by forming a complex with HP1α and histone H1, stabilizing HP1α form degradation [482].

Studies in 2018 using patient-derived glioma xenografts identified that PTEN suppresses oncogene expression and tumor growth through chromatin-associated complexes of DAXX and histone H3.3 [483]. This study showed a complex interplay between PTEN-DAXX-H3.3: (1) DAXX physically interacts with PTEN and (2) PTEN regulate H3.3 loading on chromatin. Together, PTEN limits DAXX's interaction with H3.3; thereby, controlling oncogene expression. Furthermore, chromatin de-condensation in PTEN-null cells resulted in a dramatic reduction of key replication factors on chromatin (e.g. Rad51, PCNA and CHK1) [374]. The decline in replication factors inhibit baseline levels of DNA replication by slowed DNA replication forks, increased fork stalling and delayed fork recovery. Overall, PTEN is essential to mainlining chromatin dynamics, regulating epigenetic modifications of chromatin and maintaining the fidelity of DNA replication.

5.3.2.3.2. PTEN maintains intra-S checkpoint integrity and activity

In the presence of endogenous or exogenous DNA replication stress, PTEN-null cells are incapable of arresting cells in S phase [374]. The exogenous accumulation of DNA replication stress can be induced by the application of the DNA polymerase inhibitor aphidicolin (APH) and ribonucleotide reductase inhibitor hydroxyurea (HU) [484]. He et al. 2015, identified that PTEN-null cells were unresponsive to drug (i.e. APH and HU) treatment versus wild-type cells, which were arrested in S-phase. PTEN-null cells were able to escape replication stress barrier in a checkpoint-independent manner, leading to an accumulation of cells in G2/M phases. Importantly, these cells prematurely entered M phase with replication-derived mitotic errors (e.g. anaphase bridges and lagging chromosomes).

During DNA replication, stalling of the replicating fork results in a DNA damage response, igniting the intra-S checkpoint which facilitates cell cycle arrest and DNA repair. Intra-S phase checkpoint occurs because of DNA lesions which block DNA polymerases. Thereafter, the DNA helicase (e.g. MCM2-7 helicase) unwinds the damaged strand, creating single stranded DNA, which is coated by replication protein A (RPA). These steps prime the start ATR-ATRIP complex-mediated DNA repair [485]–[487]. PTEN has been attributed to the temporal and spatial coordination of replication licensing to maintain the intra-S checkpoint by facilitating key proteins of this process (e.g. RPA1, MCM2, Rad51, PCNA and CHK1) [374], [488], [489]. The application of DNA replication inhibitor drugs in

PTEN null cells results in uncontrolled fork progression [374], [488]. During DNA replication origin licensing and firing, PTEN physically interacts and dephosphorylates minichromosome maintenance protein 2 (MCM2), a key component of the pre-replication MCM2-7 complex [488]. PTEN-mediated MCM2 dephosphorylation halts replication forks therefore, preventing unrestrained DNA synthesis and maintaining genomic stability [488].

PTEN promotes RPA1 protein stability through regulating its de-ubiquitination by OTUB1 [489]. Specifically, Wang et al. 2015 through DNA fiber assay, found PTEN acts upstream of RPA1 and is necessary to recruit RPA1 at replication fork [489]. In the absence of PTEN, RPA1 association with chromatin and replication forks is diminished. Thus, preventing the initiation of intra-S checkpoint activity and recruitment of PCNA replisome and CHK1 checkpoint protein. More importantly, the PTEN-Rad51 axis is compromised in PTEN-deficient cells, which fail to restart stalled forks, leading to a detrimental accumulation of stalled and collapsed forks [374]. Interestingly, PTEN-Rad51 axis functions in two different pathways in the presence of DNA lesions [490]: (1) PTEN-mediated genomic stability facilitated through homologous recombination (HR) in which Rad51 filamentous-like foci formation and repair of double strand breaks (DSBs) [333], [491], [492]. (2) PTEN-dependent replication fork restart by recruiting Rad51 to ssDNA at the site of stalled forks without creating filamentous-like foci formations [374]. Furthermore, He et al. 2015 though western blot in cytoplasmic, nuclear and chromatin fractions identified that RAD51 in PTEN-null cells was expressed in both the cytoplasmic and nuclear fractions [484]. However, absence of RAD51 was found in the chromatin fraction, resulting in accumulation of stalled forks. Together, PTEN facilitates the recruitment of RPA1 to break-induced ssDNA and allowing for Rad51 loading, mediating replication fork restart [489], [493].

5.3.2.4. PTEN is a key regulator of G2-M transition checkpoint and mitotic fidelity in the presence of DNA damage

In the presence of DNA damage and replication stress, PTEN is capable of inducing G2-specific cell cycle arrest through the inhibition of the AKT, FAK and MAPK pathways [494]–[496]. AKT signaling normally peaks during G2/M phase of the cell cycle [496]. However, cells harboring DNA damage or replication stress in constitutively active AKT backgrounds result in reduced activation of CHK1 and DNA-damaged induced arrest in G2 [496]. CHK1 is an important kinase that regulates DNA damage-induced cell cycle arrest in S and G2/M checkpoints and mediates DDR and repair proteins (e.g. CDC25, p53 and Tousled-like kinase) [497]–[504]. Mechanistically, loss of PTEN and activation of AKT leads to unresolved DNA damage repair by: (1) AKT-mediated phosphorylation of CHK1 at amino acid 280, (2) reduced CHK1 ubiquitination, (3) inhibition of ATM/ATR-mediated CHK1 phosphorylation and (4) the inability for CHK1 to localize into the nucleus [497], [505], [506]. Together, aberrant AKT signaling in cells harboring DNA damage results in continual cellular proliferation, evasion of G2/M induced apoptosis, increased CyclinB activation and promotes unfaithful mitotic division [494], [496].

Inability to halt PTEN-null cells at the G2 checkpoint results in abnormal progression into mitosis of cells containing DNA damage, metaphase chromosome breaks and aneuploidy [374], [497], [505], [506]. The phosphorylation status of nuclear PTEN can dictate G2 phase checkpoint stability. Dephosphorylation of nuclear PTEN results in prometaphase arrest through its interaction with CyclinB1/CDK1 complex, leading to cellular apoptosis [507], [508]. Moreover, PTEN-CHK1 interaction can result in a positive and negative feedback loop to regulate genomic stability/instability. PTEN positively

influences CHK1 activity however, CHK1 can also negatively regulate PTEN in a phosphorylation-dependent manner [509]. The phosphorylation of PTEN by CHK1 allows for cells containing replication stress to bypass G2/M checkpoint and subsequently re-enter the cell cycle [509]. Furthermore, Notch1 and TOPK (lymphokine-activated killer T-cell-originated protein kinase) signaling are capable of phosphorylating PTEN leading to its cytoplasmic retention, reversed mitotic arrest and tumorigenesis [508], [510], [511]. Interestingly, TOPK overexpression in many cancers is equated to oncogene activity as it regulates AKT activation. Consequently, AKT phosphorylates CHFR (checkpoint protein with FHA and RING domains) leading to the inhibition of checkpoint stability by promoting its downstream substrates required for mitotic transition (e.g. CyclinB, Aurora A, Plk1, Kif22 and PARP1) [510], [512]–[519]. Together, PTEN phosphorylation status contributes to checkpoint bypass promoting mitotic cell division cells containing DNA replication stress and DNA damage.

Additionally, PTEN maintains genomic stability through its function in the G2 phase decatenation checkpoint required to resolve chromatin entanglement prior to mitosis [520]. Decatenation is regulated by DNA topoisomerase IIα (TOP2A) and DNA topoisomerase II-binding protein 1 (TOPBP1), which facilitate the separation of intertwined and catenated sister chromatids [521], [522]. Chromatin entanglement naturally occurs during DNA replication and decatenation inhibits the formation of anaphase bridges during mitosis [521], [522]. PTEN-null cells form ultrafine anaphase bridges during mitosis and exacerbates polo-like kinase-interacting checkpoint helicase (PICH) bridges [374], [520]. In all, PTEN is required for both G2 checkpoint activity and decatenation checkpoint to prevent premature entry of cells into mitosis.

Attenuation of PTEN activity impairs Rad51-mediated homologous recombination and activates AKT signaling (e.g. genomic instability and cell survival signal, respectively) [271], [333], [374], [492], [523]. Chromosomal translocations in PTEN null cells are attributed to defects in repair mechanisms for DSBs via Rad51 transcription suppression [333]. Thus, PTEN maintains genomic stability by slowing cells at the G2/M checkpoint, promoting DNA DSB repair via Rad51-mediated HR post irradiation [524]. However, PTEN-depleted cells exhibit CHK1 cytoplasmic sequestration by AKT resulting in cells which failed to resect DSBs through HR [525]. PTEN's C-terminal has been implicated to work with many DDR and repair proteins (e.g. γH2AX, ATM, BRCA1, Rad52, Rad51 and XPC) [171], [373], [526]–[533]. Consequently, PTEN loss confer radioresistance and DNA damage hypersensitivity in cells as alternative and error prone forms of DNA repair take place [171], [373], [526]–[534]. Specifically, PARP inhibitors are becoming an important anti-cancer therapeutic drug as cancer cells thrive via PARPylation in a HR deficient background due to PTEN loss. Moreover, 80% of endometrial cancer lack PTEN and these cancers can be reverted by simulations inhibition of PI3K and PARP [491], [535]–[537].

5.3.2.5. PTEN's C-terminal is essential for faithful chromosome segregation and spindle alignment

The spindle assembly checkpoint is tightly regulated and overexpression of its proteins results in chromosomal abnormalities, aneuploidy and the development of cancer [538]–[540]. Mitotic catastrophe is a mechanism for avoiding mitotic-derived missegregation of chromosomes resulting in apoptosis, necrosis or senescence [539]. PTEN accumulates in the nucleus during mitosis and act as a negative regulator of both the mitotic checkpoint complex (MCC) and the interaction of CDC20 and MAD2 with

BubR1 and Bub3 [541]–[543]. Further, the spindle assembly checkpoint inhibits the recognition of CyclinB by catalyzing the incorporation of the anaphase promoting complex/cyclosome (APC/C) to CDC20 [543]. Critically, nuclear PTEN directly enhances the activity of APC/C and its interaction with CDH1, resulting in its tumor suppressive functions [542], [544]. Impairment of the APC-CDH1 tumor-suppressive complex results in overexpression of their substrates (e.g. CyclinA, AuroraA, CDC20 and SKP2), chromosomal abnormalities and poor prognosis [545], [546]. Choi et al. 2014 identified that PTEN's C-terminal tail region mediates the physically interact with CDH1 at the chromatin level [542]. Lastly, CDH1 promotes poly-Ub of PTEN and its removal form chromatin during the mitotic exit [542].

The timely formation of the spindle assembly checkpoint is crucial to ensure proper attachment of chromosome to spindle fibers of kinetochore-microtubule. PTEN has been attributed to the timely formation of the spindle assembly checkpoint by integrating with MAD1 and promotes its dimerization and localization into the nuclear pore [547]. PTEN+MAD1 interaction is mediated by PTEN's C-terminal tail and seen to peak during interphase [547]. Liu et al. 2017 found that PTEN+MAD1 interaction during interphase prevents chromosome missegregation, formation of aneuploidy and lagging chromosomes. Moreover, PTEN-null prostate cancer cells in a mouse xenograft model show that Polo-like kinase 1 (PLK1) confers tumor formation [548]. This is interesting as PTEN localizes at mitotic centrosomes in parallel with PLK1 and gamma-tubulin during centrosome maturation [549]. PTEN knockdown results in increased PLK1 and gamma-tubulin in an AKT-dependent manner and reduced pericentrin levels in an AKT-independent manner. Furthermore, dual knockdown of PTEN and AKT can rescue the integrity and composition of mitotic centrosomes [549]. More recently, Van Ree et al. 2016 identified that PTEN is recruited to pre-mitotic centrosomes in a PLK1-dependant fashion [550]. This action primes a docking sites for Dlg1 and Eg5/Kif11 required for centrosome movement and spindle formation [550]. Further, evident supports the essential role for nuclear PTEN in maintaining chromosomal integrity by its physically associating with CENP-C in the inner kinetochore plate [333].

5.4. Planarian as a novel model to understand nucleocytoplasmic shuttling of PTEN during cancer progression

Early detection of malignant transformation is crucial to enhanced patient outcome. Despite decades of research the mechanisms of which adult tissues transform into malignancies remain poorly understood. Intriguingly, early detection of malignant transformation in epithelial tissues attribute to a 90% patient survival rate versus 10% in late stage detection [322], [323], [325]–[330], [551]. Early diagnosis of malignant cells and tissues are made by morphological identification and often results in a high false-negative detection rate [331]. Clinicians must be able to distinguish precancerous and early malignant lesions from more common benign inflammatory conditions. Therefore, creating methods allowing accurate diagnosis of precancerous events in real-time would increase the efficiency of early patient intervention. However, we have yet to identify common and ubiquitous features within all precancerous cells and tissues. This may be attributed to the complex heterogeneity found within the array of cancer types. Thus, identifying universal features in early cellular transformation during tissue maintenance may lead to the generation of novel and effective cancer therapies.

DNA damage occurs early during tumorigenesis and promotes tumor progression and heterogeneity [30], [32]–[35], [352]. Misregulation of genes involved in DDR, cell cycle

checkpoints or proper chromosome transmission is associated with cancer development [552]–[556]. Precancerous and cancerous cells exhibit altered cell architecture, abnormal centrosomes and multipolar spindles, resulting in genomic instability (i.e. higher rate of genomic changes per cell division) [553]. Despite its central role in cancer development and heterogeneity, it remains poorly understood whether DNA damage reflects cause or effect of altered cell dynamics. Evidence suggests that in precancerous lesions DNA damage occurs before signs of telomere attrition, hypoxia or reactive oxygen species (ROS), stimulating a strong DDR [34], [35], [557]–[561]. DDR activity acts as an anticancer barrier, which slows or inhibits the progression of precancerous lesions toward metastasis [91], [92]. The OTS-DDM integrates cancer phenotypes and molecular changes to explain the initiation of cancer and evolution of heterogeneous cancer cell populations. However, the progression of early DNA damage into genomic instability found in late stage cancers remains elusive. Therefore, understanding the development and survival of (pre)cancerous cells containing DNA damage will allow us to identify vulnerabilities exhibited within heterogeneous cell populations during their transformation from normal to malignant.

Studies primarily focus on PTEN's phosphatase function within the plasma membrane however, recent studies indicate the presence of nuclear PTEN, the function of which remains to be further understood during cancer initiation. Histological analysis identify that loss of nuclear PTEN accompanies cancer initiation and its progression [365]–[370], [562]. However, these studies do not correlate the loss of nuclear PTEN to altered cell architecture, abnormal centrosomes and genomic instability. As reviewed above, nuclear PTEN is involved in many aspects of cell cycle regulation and genomic stability. Therefore, we lack the mechanistic role of nuclear PTEN loss within a precancerous environment. Understanding how the accumulation of abnormalities within cells and their transformation into malignancies will be crucial for advancements in biomedicine. To better understand the mechanism(s) that allow cellular transformation we use the planarian, *Schmidtea mediterranea*, a model organism to determine how precancerous lesions provide a selective advantage for cells to transform into metastasis. The planarian provides novel yet simplified grounds for studies of cancer initiation in the adult body. These experiments consider cells in their natural environment and the influence of physiological signals on their behavior. We expect to identify crucial markers of cancer initiation and distinctive molecular features in SCs that drive cancer during tissue renewal.

Nuclear PTEN is critical for genomic integrity through regulation of Rad51, an integral protein for DNA damage repair and replication fork stability [374], [491], [524]. Interestingly, cells with the loss of nuclear PTEN contain DNA damage, DNA replication stress and chromosomal abnormalities despite elevated nuclear accumulation of Rad51 expression [484]. Overexpression of DNA damage repair proteins are found in highly metastatic cancers and correlates with poor patient prognosis [39]–[41], [563]. For instance, Rad51 expression is not observed in most normal differentiated tissues but is elevated in immortalized cancer SCs, mediating evasion of apoptosis, radio-resistance and altered cell cycle checkpoints dynamics [38], [564]–[567]. Therefore, anticancer therapeutics have led to targeting proteins involved in DNA damage response and repair however, current DDR agents lack specificity and a defined mechanism of action to combat cellular transformation [69]. Nevertheless, it remains unknown whether the function of PTEN and Rad51 in DNA damage is a general characteristic resulting from increased susceptibility of cells to undergo malignant transformation or is a specific feature of specific cells.

We hypothesize that upon the loss of planarian nuclear PTEN, distinct neoblast progenitors are increasingly prone to fostering DNA damage and undergo cellular transformation. PTEN tumor suppressor function is conserved in planarian [56], [58]. The *Smed-PTEN(RNAi)* phenotype resembles many features observed in human cancers including: cellular hyperproliferation, aberrant cell migration, tissue invasion, and outgrowths that all together are lethal. To better understand the evolution of the *Smed-PTEN* phenotype in planarians, we performed RNA sequencing during a stringent RNAi time course (e.g. 2-, 3-, 4-, 6- and 12- days RNAi) to determine the genetic landscape required for cellular transformation. Noteworthy, molecular results (shown in next chapter) identified two distinct phases of the *Smed-PTEN(RNAi)* phenotype: (1) subcellular events that occur in the first three days and (2) cellular events that occur day four and onward. Therefore, through RNAseq, we aim to identify the following: (1) a chronological list of day specific genetic modifications throughout the time course and (2) candidate genes postulated to drive the early phenotype. Lastly, these results will allow us to determine if specific and/or all neoblast subpopulations hold increased risk of accumulating DNA damage, driving the hyperproliferative phenotype. Furthermore, GO term enrichment will allow us to identify enriched biological processes, molecular functions and cellular components involved with the loss of *Smed-PTEN*. If the nuclear PTEN is conserved in the planarian we speculate to see GO term enrichment in DNA repair, spindle pole, transcription, replication and cell cycle within the first three days of the phenotype (Fig. 3)

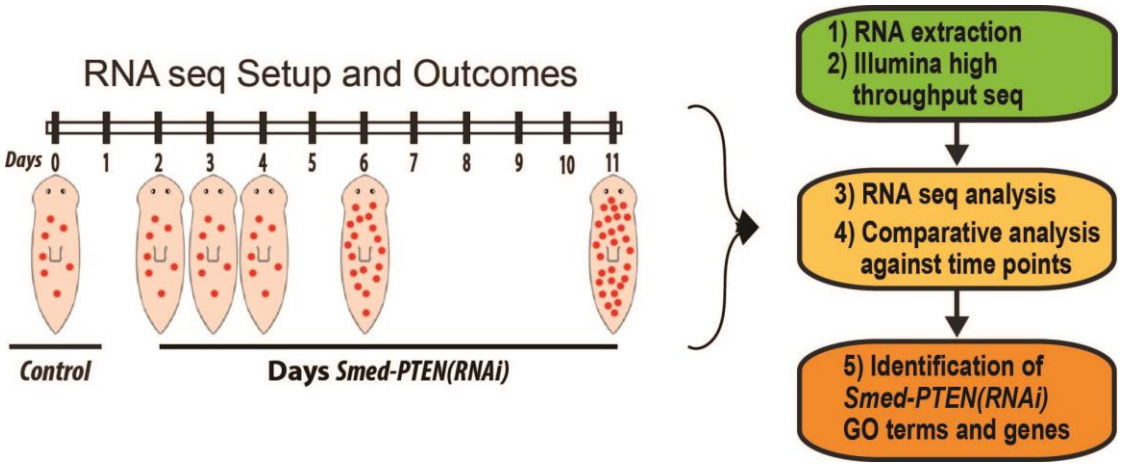

Figure 3. Smed-PTEN(RNAi) RNAseq design. Schematic diagram detailing how the RNAseq analysis was performed.

CHAPTER SIX

FINDINGS

DNA damage underlies cellular transformation in planarian

6.1. Introduction

The constant renewal of aging and damaged cells provides recurrent opportunities for cancer development and other age-related diseases. Approximately 90% of cancer related deaths in the U.S. result from alterations in tissues often undergoing cellular renewal (e.g. epithelial lining of organs) [6], [165], [166], [574]. Despite its central role in cancer, the establishment of cellular transformation during adult tissue renewal remains poorly understood. Studies have shown stem cells (SC) harboring DNA damage display a selective advantage to acquire cancerous properties [552], [575], [576]. In particular, cancer arising from SCs often evade apoptosis and bypass surveillance mechanisms as they undergo malignant transformation (e.g. acquisition of cancer properties). Evidence support that deregulation in genes controlling growth (i.e. oncogenes and tumor suppressors) lead to hallmarks of cancer including DNA replication stress (e.g. collapse or stalling of DNA replication forks), sustained proliferation, replicative immortality, escape from apoptosis/senescence, and genomic instability (i.e. higher rate of genomic changers per cell division). Thus, the oncogene/tumor suppressor-induced DNA replication stress model provides unique opportunities to understand cancer initiation and its progression. DNA replication stress is a pervasive feature present at earliest stages of almost all cancers, however, its establishment and evolution into genomic instability is elusive [32]–[34]. Our project addresses early manifestations of cellular transformation to identify mechanisms underlying DNA damage and signals contributing to the expansion of cells carrying genomic instability.

The tumor suppressor PTEN is one of the most frequently inactivated genes in human cancers. PTEN is a well characterized lipid phosphatase, which dephosphorylates PIP3 at the plasma membrane and negatively counteracts PI3K-mediated signals for cell proliferation, differentiation and survival in both vertebrates and invertebrates [56], [170], [171], [174]. Recent studies indicate the presence of nuclear PTEN which acts independently of its phosphatase activity. Noteworthy, histological analysis of early and advanced stage cancer tissue samples have identified inappropriate subcellular compartmentalization of PTEN (e.g. nuclear and cytoplasmic) which have been attributed to point mutations within the C-terminal (e.g. codon 307 and 289) [365]–[370], [386], [396]. Germline PTEN mutations are present in 80% of Cowden and 60% of Bannayan-Riley-Ruvalaba Syndrome patients and is attributed to aberrant nuclear exclusion of PTEN. However, these PTEN mutants retain functional phosphatase activity, resulting in noncancerous hamartomas tumors and increased risk of developing cancer [269], [386]. Small pools of nuclear PTEN have phosphatase independent roles for maintaining heterochromatin structures, cell cycle regulation, mitotic spindle pole movement replication and centromere stability. Moreover, PTEN regulates Rad51, an integral player in the repair of DNA double started breaks (DSB). Together, this interaction creates the PTEN-Rad51 axis, guarding against genomic instability [374].

Monitoring cellular transformation during epithelial tissue renewal is challenging and current experimental models are restricted to organ-specific tissues (e.g. pancreatic and colon) [358], [577]. The following study presents an innovative approach to monitor the transition from normal to malignant cells during tissue maintenance in the entire adult body. This study utilizes the planarian, *Schmidtea mediterranea.* This model organism constantly renews tissues, a process driven by SCs (neoblasts). Neoblasts undergo cellular transformation when tumor suppressors are inactivated [56], [60], [61]. Previously shown, disturbance of *Smed-PTEN* function with RNA interference (RNAi) leads to neoblast-induced tumorigenesis and aberrant tissue colonization that kill planarians in less than two weeks [56]. Using the planarian PTEN cancer model, we created a novel archetype to study the subcellular and cellular events that result in tumorigenesis in the adult body. Here, we found that within 48hrs post first PTEN injection, neoblasts harbored chromosomal abnormalities and high rates of DNA damage. Neoblast-specific transformation were found as a result of G2/M checkpoint adaptation, evasion of cell death and the dysregulation of the DDR pathway, specifically Rad51. Our findings support the idea that DNA damage and replication stress underline precancerous lesions that result in molecular and genetic alterations crucial for cancer evolution in the adult body.

6.2. *Smed-PTEN* is required for proper regulation of cell proliferation during cellular turnover

PTEN homologs were identified in the planarian by Oviedo et al. 2009 (e.g. *Smed-PTEN1* and *Smed-PTEN2*) [56]. With recent advances in creating a nearly fully annotated genome, *Smed-PTEN1* and *Smed-PTEN2* remain the most conserved candidates with both a phosphatase and C2 domains (previously discussed in chapter 3). The *Smed-PTEN(RNAi)* phenotype was produced by simultaneous RNAi of both homologs as single RNAi did not produce a phenotype [56]. The planarian cancer-like phenotype resembles many features observed in human cancers including: cellular hyperproliferation, aberrant cell migration, tissue invasion and abnormal outgrowths that all together result in lethality within <15 days RNAi (Fig. 1A). To determine if the *Smed-PTEN(RNAi)* phenotype is an accurate model to study cancer progression, we performed RNA sequencing (RNAseq) at the 12-day timepoint. GO term enrichment for biological processes (KS < 0.3 cut-off) revealed a substantial number of genes involved in cellular energetics (e.g. metabolic, catabolic and biosynthetic processes), evading cell death, DNA damage and/or replication stress and lastly mitotic stress (e.g. microtubule organization) (Fig. 1B, C). When looking at the hallmarks of cancers found to produce mammalian malignant tumors, the *in-silico* and published *in-vivo* results prove that the planarian cancer model is both a valid and novel architype to study the onset of cellular transformation and cancer progression (Fig. 1D). Lastly, the *in-silico* results provide us with a basis to explore the oncogene and tumor suppressor induce replication stress model (Fig. 1E).

To better understand the progression of the PTEN phenotype in planarians, we performed a time course to evaluate cell division of neoblasts, the only proliferative cell within the animal. Thus, we used the established *Smed-PTEN(RNAi)* microinjection schedule, consisting of five injection over the span of twelve days (Fig. 2A) [56]. Whole-mount immunostaining (WIHC) against phosphorylated histone-3 Ser10 (H3P) and its quantification revealed a significant increase of cellular division six days post first injection (dpfi) and progressively increased stepwise to the day 12 phenotype (Fig. 2B, C). These

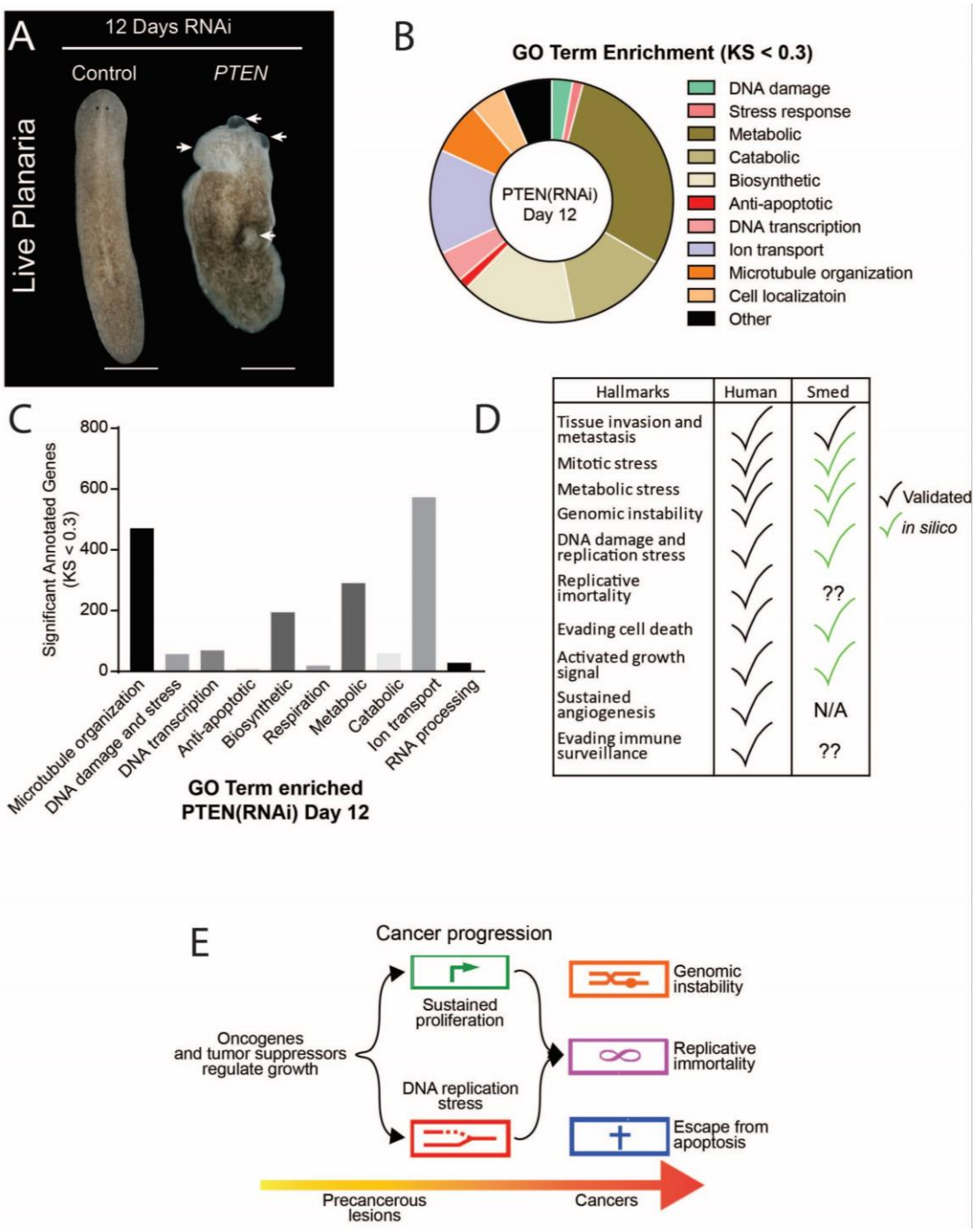

Figure 1. *Smed-PTEN(RNAi)* a novel cancer model. (A) Live planarian images 12 days after RNAi. Arrows indicate abnormal tissue outgrowths. (B) Pie chart representing the percent of biological processes-related GO terms enriched at day 12 *Smed-PTEN(RNAi).* (C) The amount of significantly annotated genes found within the phenotype organized by category. (D) Summary of the hallmarks of cancer determined by *in silico* and *in vivo* studies in human and planarian cancer models. (E) The tumor suppressor-oncogene induced DNA damage/replication stress model depicting sustained proliferation and DNA replication stress as precancerous lesions that evolve into cancer and its many hallmarks.

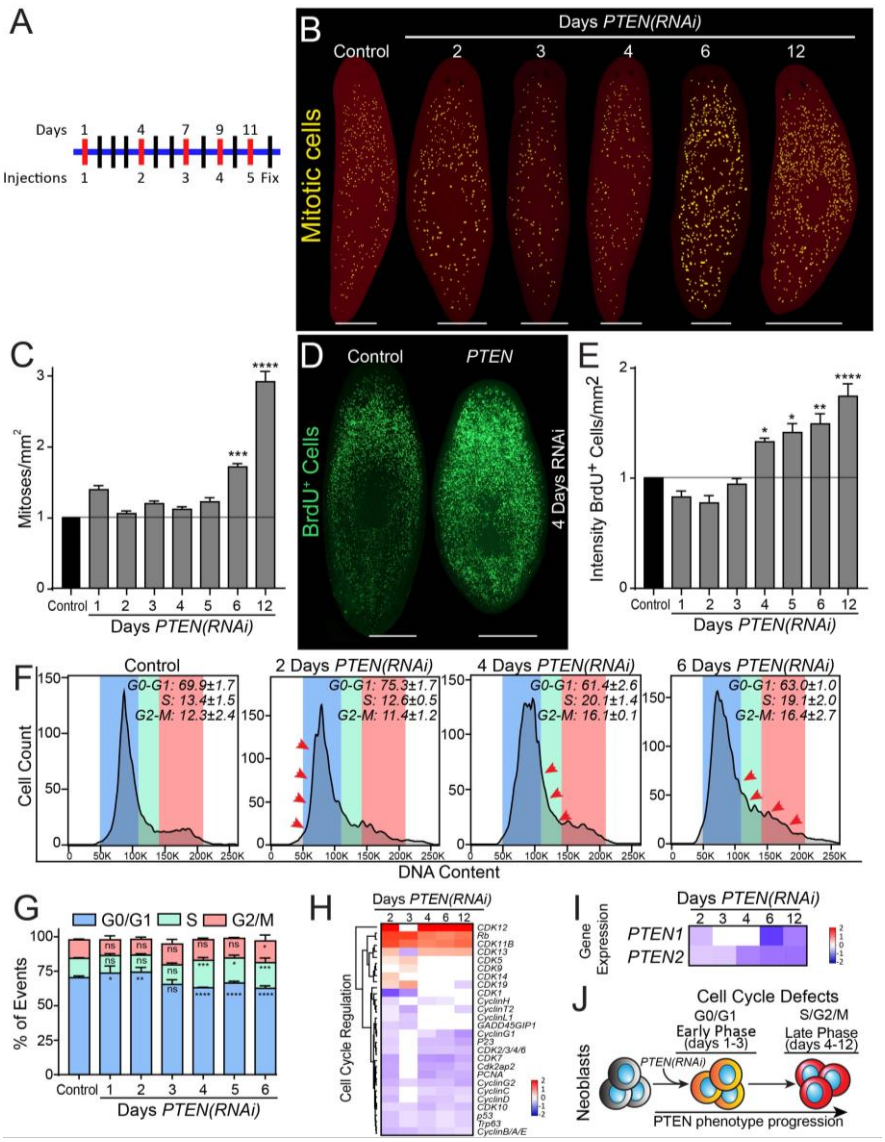

Figure 2. The *Smed-PTEN(RNAi)* results in cell cycle alteration prior to formation of physical abnormalities. (A) PTEN injection schedule consisting of 5 dsRNA microinjections spanning a 12 period. (B) Tracking of mitotic activity using whole-mount immunostaining with α-H3P (yellow dots). (C) Quantification of changes in mitotic (H3P) neoblasts over the time course. (D) immunostaining for proliferative neoblasts using α-BrdU at day 4 RNAi. (E) BrdU positive foci quantification over the 12-day period. (F, G) Cell cycle analysis using flow cytometry at days -2, -4, and -6 into the phenotype and its quantification throughout the initial 6 days of the phenotype. G0/G1 in blue, green represents S-phase and G2/M-phase is depicted in red. (H) Differentially expressed genes involved in cell cycle regulation, red being highly expressed. (I) RNAseq validation of RNAi gene silencing strategy. (J) Experimental design. Using cellular proliferation as an indicator of the onset of the phenotype, two phases are created: (1) early phase consisting of the first three days where alterations to G0/G1 are events and (2) cellular events with alterations to S/G2/M-phases of the cell cycle. Fold change values represent mean±s.e.m. of individual PTEN(RNAi) time points with respect to each time point's mock RNAi. Experiments consisted of at least three biological replicates, n>30 animals per time point. *P<0.01, **P<0.005, ***P<0.0005, ****P<0.0001; NS, no significance; two-way ANOVA. Scale bars 250um.

results imply the *Smed-PTEN(RNAi)* phenotype is initiated earlier than anticipated. Therefore, we sought to identify if proliferation began before the six days mitotic burst. The thymidine analogue bromodeoxyuridine (BrdU) was used to determine S-phase specific increases in proliferation. Shockingly, we identified that 4dpfi, experimental animals experienced an increase of BrdU incorporation relative to the control that gradualy increased as the *PTEN(RNAi)* phenotype progressed (Fig.2D, E). Together, these results suggest that the *PTEN(RNAi)* phenotype begins prior to the onset of macroscopic abnormalities and results with alterations within the S/G2/M phases of the cell cycle producing cellular effects (e.g. increases in proliferation and division).

To assess if sub-cellular alterations are present prior to the increase in proliferative neoblasts, we sought to use flow cytometry (FACS) and RNAseq to further elucidate the role of *Smed-PTEN* in controlling cell cycle dynamics. Staining dissociated cells with Draq5 and Calcein AM (i.e. DNA and live cell marker, respectively) we identified that within 24 and 48 hours post RNAi, *Smed-PTEN(RNAi)* cells exhibited a significant accumulation of cells within the G0/G1 phase (69.9±1.7 vs. 75.3±1.7) (Fig.2F, G). Interestingly, cell cycle dynamics 3dpfi were reestablished relative to the control. FACS analysis further corroborate increases in cellular proliferation and cellular division found with WIHC by an increase of cells within the S-phase at both 4- and 5-dpfi (13.4±1.5 vs. 20.1±1.4) and further a significant increase of cells within G2/M-phase by 6dpf (12.3±2.4 vs. 16.4±2.7). Results obtained from RNAseq throughout the *Smed-PTEN(RNAi)* time course revealed a profound amount of alterations to differentially expressed cell cycle regulatory genes within the first three days post RNAi that persisted well into the phenotype (Fig. 2H). Notebly, genes involved in tumor and cell cycle suppression were altered (e.g. Rb and p53), transcription regulatory cyclin-dependent kinases were overexpressed (e.g. CDK 9, 11B, 12, 13, 19) and CDK5 expression required for mitotic and post-mitotic regulation of neuronal growth was elevated [578]–[580]. To discern if these events are anomalies induced by injection-mediated wound response or *Smed-PTEN* gene knockdown, we examined the RNAseq data. We identified that both homologs of *Smed-PTEN-1, -2* mRNA expression were significantly reduced within 2dpfi and remained suppressed throughout the progression of the phenotype (Fig. 2I). These results suggest the overall effects of *Smed-PTEN* abrogation alters cell cycle dynamics within 24hrs leading to cellular hyper-proliferation and the cancer-like phenotype. Together, two distinct phases of the *Smed-PTEN(RNAi)* phenotype can be established: (1) subcellular events in the first three days and (2) cellular events day four and onward (Fig. 2J).

6.3. *Smed-PTEN* loss results in the accumulation of DSBs and chromosomal abnormalities

Nuclear PTEN acts on DNA replication forks to recruit Rad51 for the repair of DSBs which forms the PTEN-Rad51 axis to guard against genomic instability [484]. To assess if the initial 48 hours of the phenotype consisted of subcellular events related to DNA damage, we subjected animals to WIHC against markers required for the detection and repair of DSBs (e.g. α-γH2AX and α-RAD51, respectively).WIHC revealed a significant increase in γH2AX foci dispersed throughout *Smed-PTEN(RNAi)* animals within just 48 hpfi (Fig. 3A, B). Dissociated cells collected from whole planarian 2dpfi showed a significant increase in nuclear γ-H2AX foci relative to the control (70% vs. 45%, respectively) (Fig. 3C). Together, upon *Smed-PTEN* loss*,* DSBs alongside cell cycle alterations are pervasive features of the early phenotype. Moreover, planarian primarily repair DSBs by Rad51-mediated HR [16], [17], [29]. Thus, by staining both control and *Smed-PTEN(RNAi)* animals with α-RAD51, shows a stricking increase of RAD51 signal

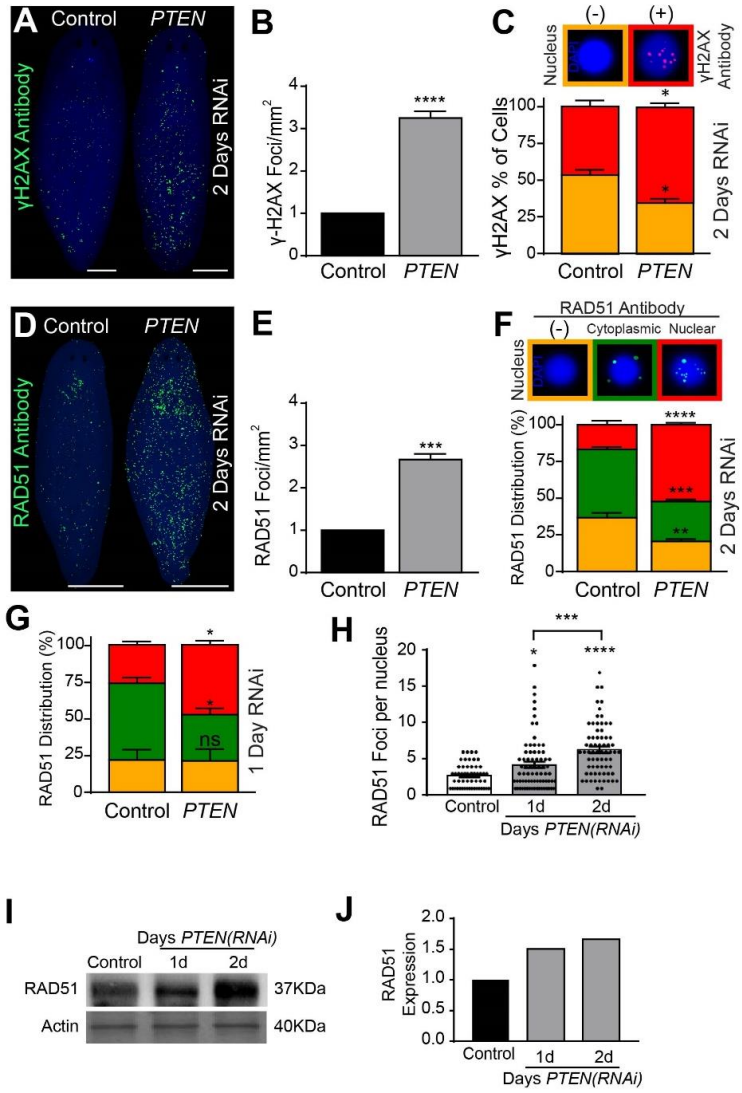

Figure 3. RNAi of Smed-PTEN induces the accumulation of DSBs. (A, B) Whole mount immunostianing against α-γH2AX, a mediator of the DNA damage response and its quantification 2 days RNAi. (C) Dissocaited cells collected from 2 days RNAi animals. Staining α-γH2AX antibody and its quantification reveals a significant increase in γH2AX+ signal. (D, E) Day 2 RNAi animals stained with α-RAD51, indicator of active DSB repair and its foci quantification. (F) Quantification of α-RAD51 on dissociated cells 2 days into the phentoypes reveales a significant increase in cells expressing RAD51. Increase in RAD51 signal is accomanied by an increase in nuclear compartamentilzation of the signal, implying active DNA repair. (G) Quantification of the translocation of RAD51 into the nucleus 24hrs post first injection showing a slight shift in nuclear versus cytoplasmic RAD51. (H) The amount of nuclear RAD51 foci per cell at days 1 and 2 into the phenotype. Both days show a significant increase in the amount of RAD51+ foci nuclei however, there is a significant increase at 2 days *PTEN(RNAi)*. (I, J) Western blotting against α-RAD51 at days 1 and 2 into the phenotyp and its quantification. Actin was used to ensure equal loading per well. Fold change values represent mean±s.e.m. of individual PTEN(RNAi) time points with respect to each time point's mock RNAi. Experiments consisted of at least three biological replicates, n>30 animals per time point. *P<0.01, **P<0.005, ***P<0.0005, ****P<0.0001; NS, no significance; two-way ANOVA. Scale bars 250um.

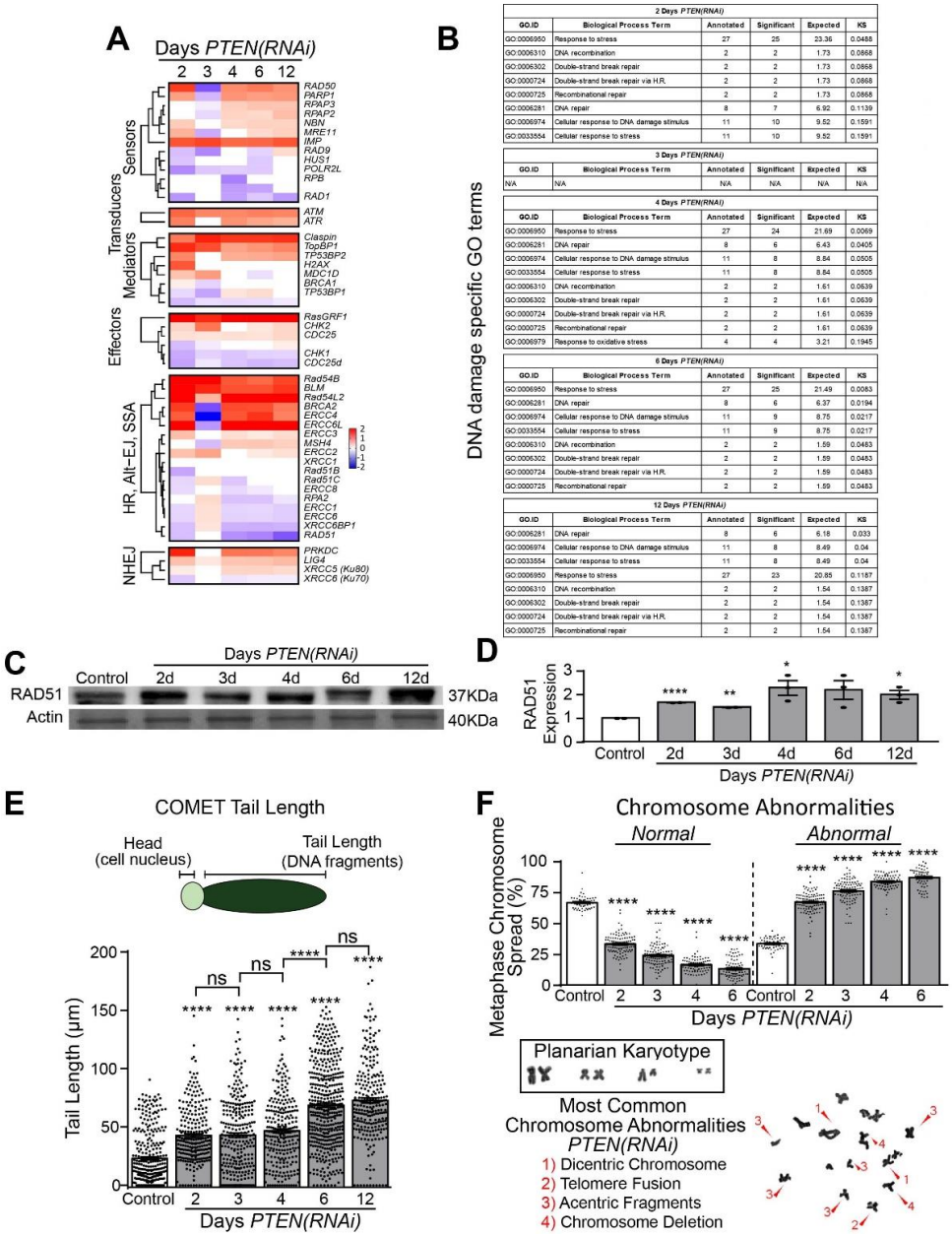

Figure 4. DNA damage and chromosomal abnormalities persist throughout the progression of the phenotype. (A) Differentially expressed genes related to DNA damage response signaling and repair pathways throughout the time course. (B) Biological processes-specific GO terms related to DNA damage, stress and repair. Notice, 3 days PTEN(RNAi) contains no hits. (C, D) Western blotting against α-RAD51 and its quantification throughout various timepoints during the phenotype. (E) COMET assay under alkaline conditions monitoring DNA integrity and the quantification of tail length (µm) per individual cell. (F) Quantification of chromosomal abnormalities within the first 6 days of the phenotype. The planarian chromosomes and their abnormalities found at day 12 are depicted below. Fold change values represent mean±s.e.m. of individual PTEN(RNAi) time points with respect to each time point's mock RNAi. Experiments consisted of at least three biological replicates, n>30 animals per time point. *P<0.01, **P<0.005, ***P<0.0005, ****P<0.0001; NS, no significance; two-way ANOVA. Scale bars 250um.

dispersed throughout the animal 2dpfi (Fig. 3D, E). Additionally, dissociated cells were collected, fixed and subjected to immunostaining. This confirmed a significant increase in RAD51 expression upon *Smed-PTEN(RNAi)* (e.g. 80% vs. 63%, respectively) that was accompanied by an increase in nuclear RAD51, implying active DSB repair (Fig. 3F). Furthermore, we identified that within 24hrs of the phenotype, collected cells exhibited an increase in nuclear localization of RAD51 (Fig. 3G). Interestingly, when compared to the control, cells extracted from the experimental group at 1- and 2-dpfi, expressed higher rates of RAD51 foci per nucleus (e.g. 2.7 foci vs. 4.3 and 7.1 foci, respectively) (Fig. 3H). These findings imply that the severity of DSBs increase as the phenotype progresses. Furthermore, analysis by western blot, revealed a step-wise increase in RAD51 expression (Fig. 3I, J). *Smed-PTEN(RNAi)* animals within the first 48 hpfi accumulate high rates of DSBs and trigger DDR and repair.

To evaluate the repair process of DSBs and its outcomes throughout the *Smed-PTEN(RNAi)* phenotype, we collected animals at various timepoints to perform (1) western blot (2) COMET assay and (3) karyotyping. Primarily, sequencing results identified a striking upregulation of genes involved in sensing both DSBs and SSBs (e.g. Rad50, RPA, MRE11) signal transduction (e.g. ATM and ATR), mediator and effector outcomes (e.g. TopBP1, TP53BP, Claspin). Lastly an increase in DNA damage repair pathways (e.g. HR, NHEJ, Alt-EJ and SSA) throughout the 12-day time course (Fig. 4A). Interestingly, the DDR seemed to dampen by day three post first injection and reverted to elevated expression levels by 4-days and onward. Further, GO term enrichment (strict cut-off, KS <0.2) for biological processes involved in DDR and repair, confirmed the dampening effect observed 3dpfi (Fig. 4B). Western blot determined that RAD51 protein expression was elevated throughout the time course with increased expression at 2-, 4- and 12-dpfi. However, both 3- and 6-dpfi exhibited a slight decay in expression but remained elevated relative to the control (Fig. 4C, D).

To discern if DSBs are actively undergoing repair, suggested by data obtained from RNAseq and western blot, we performed the COMET assay under alkaline conditions to monitor DNA integrity. Our results confirmed a significant increase in COMET tail length 2 dpfi, implying elevated rates of DNA damage (Fig. 4E). However, DNA integrity was not reestablished by day 3 or 4 despite the increase in DDR and repair protein activity. Accumulation of DSBs were found to be significantly exacerbated by 6 dpfi and on forth during the *Smed-PTEN(RNAi)* time course. Furthermore, increases in COMET tail length were accompanied by significant increases in chromosomal abnormalities detected by whole animal metaphase chromosome squashing (Fig. 4F). Over 1000 chromosomes counted per timepoint, allowing us to identify an array of abnormalities (e.g. dicentric chromosomes, telomere fusion, acentric fragments and chromosome deletions) which targeted the four pairs of dicentric planarian chromosomes. Noteworthy, these abnormalities were observed within 24 hpfi and persisted throughout the twelve-day time course (Fig. 5A, B). These findings are consistent with other studies elucidating the role of nuclear PTEN [333], [581], [582]. Together, these results imply that *Smed-PTEN(RNAi)* harbor DSBs early within the time course and deploy signal transduction cascades to produce a repair outcome. Despite the nuclear accumulation of DNA repair machinery (e.g. RAD51), DSBs are incapable of repairing without *Smed-PTEN*.

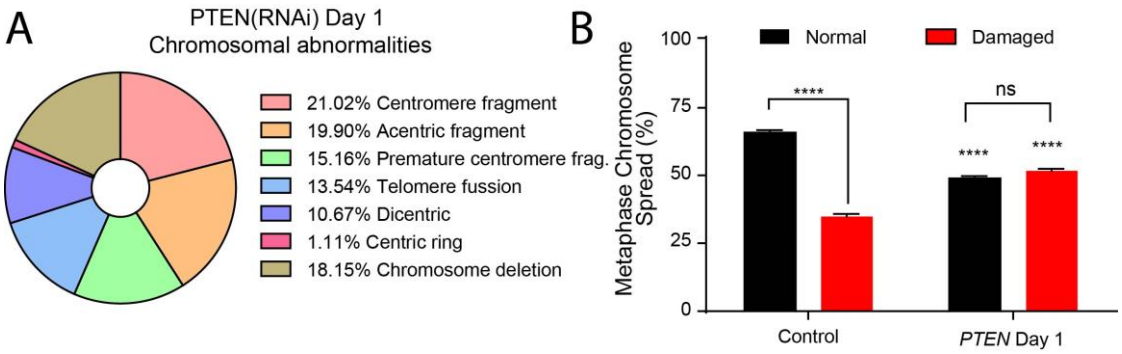

Figure 5. Chromosomal abnormalities are detected 24hours into the phenotype. (A) Pie chart showing the percent of specific types of chromosomal abnormalities day 1 RNAi. (B) Percent of metaphase chromosomes. Black represents normal karyotype and red represent damage karyotype. Experiments consisted of at least three biological replicates, n>30 animals per time point. ****P<0.0001; NS, no significance; two-way ANOVA.

6.4. Nuclear PTEN plays a role in the early phase of the phenotype

PTEN functions within the nucleus to facilitate cell cycle dynamics and genomic stability. However, its nuclear role is underappreciated relative to its cytoplasmic function in cancer development. PTEN does not contain canonical nuclear translocation sites and is reliant on a vast array of proteins to facilitate its nuclear tethering, which is conserved within the planarian (Fig. 6A). The ubiquitination status of PTEN, mediated by NEDD4-1 and USP7, is a crucial component of its nucleocytoplasmic shuttling through the membrane vault protein MVP (Fig. 6B). The planarian contains highly conserved protein domains and interaction sites for *Smed-NEDD4-1, Smed-USP7* and *Smed-MVP* relative to the human counterpart (e.g. 65%, 47% and 59% identity, respectively) (Fig. 6C). To determine if major components of the nucleocytoplasmic shuttling of *Smed-PTEN* are active within the early and late phases of the *Smed-PTEN(RNAi)* phenotype, we examined our RNAseq results (Fig. 6D). To our surprise, components of the PTEN import by ubiquitination (i.e. NEDD4-1, USP7, USP13), sumoylation (i.e. PIASxa) and phosphorylation (i.e. ATM and RAK) were upregulated throughout the time course. However, elements to physically separate PTEN from degradation machinery (i.e. IPO11 and UBE2E1), import it into the nucleus (i.e. MVP and RAN) and nuclear retention signals (i.e. PML and DAXX) had mixed expression in the early versus the late phase. Together, these results imply that planarian *Smed-PTEN* may function within the nucleus and its function may be a critical component to slowing the progression of the phenotype within the early phase.

To address the functionality of nuclear *Smed-PTEN*, we created a stringent RNAi strategy to eliminate components of the nucleocytoplasmic shuttling machinery such as NEDD4-1, USP7 and MVP. Animals were primarily injected with transporter dsRNA 30 days prior to the start of the *Smed-PTEN(RNAi)* injection schedule. This approach was taken to assure that expression of these genes and their protein levels were entirely eradicated in the animal. Five dsRNA micro-injections spanning 30 days of *Smed-NEDD4-1*, *Smed-USP7*, *Smed-MVP, Smed-MVP+USP7* and *Smed-MVP+USP7+NEDD4-1* did not produce any physical abnormalities either in intact or regenerating animals (for simplicity, *Smed-MVP+USP7* will be *2xRNAi* and *Smed-MVP+USP7+NEDD4-1* will be 3xRNAi, henceforth). Interestingly, 6 days into the *Smed-PTEN(RNAi)* time course, 10% of *Smed-MVP+PTEN(RNAi)* animals exhibited head loss, 30% of *Smed-PTEN+2x(RNAi)*

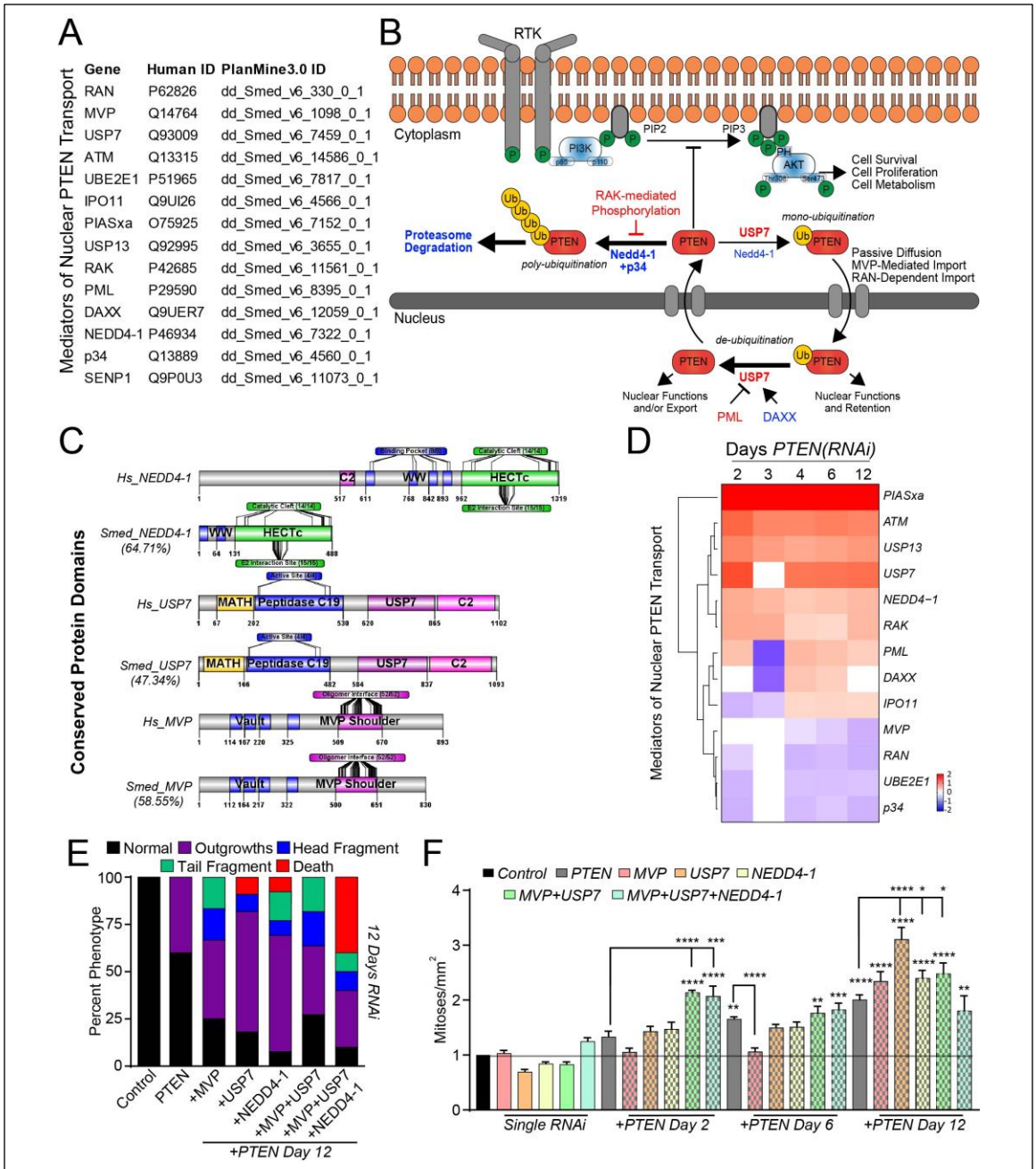

Figure 6. Nucleocytoplasmic PTEN shuttling is active early within the phenotype. (A) Genes involved in nucleocytoplasmic shuttling of PTEN are conserved within the planarian. (B) Ubiquitination and phosphorylation involved in the shuttling of PTEN in/out of nucleus. (C) Protein domain conservation of NEDD4-1, USP7 and MVP; key components to the shuttling system. (D) Differentially expressed genes involved with nucleocytoplasmic shuttling of PTEN throughout the PTEN(RNAi) time course. (E) Quantification of animal phenotypes with single, double, triple and quadruple RNAi of PTEN and its transporters. (F) Quantification of mitotic events of RNAi of transporters at days -2, -6 and -12 into the PTEN(RNAi) phenotype. Fold change values represent mean±s.e.m. of individual PTEN(RNAi) time points with respect to each time point's mock RNAi. Experiments consisted of at least three biological replicates, n>30 animals per time point. *P<0.01, **P<0.005, ***P<0.0005, ****P<0.0001; NS, no significance; two-way ANOVA. Scale bars 250um.

animals lost tail tissue and 40% of *Smed-PTEN+3x(RNAi)* resulted in abnormal outgrowths or loss of tail tissue (data not shown). Moreover, 12 days into the RNAi phenotype, 40% of the animals in *Smed-PTEN(RNAi)* alone exhibited abnormal tissue outgrowths whereas the addition of the transporter RNAi resulted in 60% of the animals experiencing abnormal phenotypes (e.g. tissue outgrowths, loss of tissues, animal fragmentation or premature lethality) (Fig. 6E). Noteworthy, *Smed-USP7+PTEN(RNAi)*, *Smed-NEDD4-1+PTEN(RNAi)* and *Smed-PTEN+3x(RNAi)* resulted in early lethality, compared to *Smed-MVP+PTEN(RNAi)* and *Smed- PTEN+2x(RNAi)* which experienced fragmentation. The onset of lethality mimicked the *Smed-PTEN(RNAi)* alone, suggesting loss of *Smed-MVP* can partially rescue the lethality phenotype imposed by loss of *Smed-USP7* but is overpowered by the loss of *Smed-NEDD4-1.*

To determine if nuclear *Smed-PTEN* plays a role in suppressing hyperproliferation early in the phenotype, we examined rates of cellular division. We monitored the rates of cellular division within animals at 2-, 6- and 12-days post Smed-*PTEN(RNAi)*. Shockingly, 2 dpfi both the *Smed-PTEN+2x(RNAi)* and *Smed-PTEN+3x(RNAi)* animals exhibited significant increases in cell division relative to the control and *Smed-PTEN(RNAi)* alone (Fig. 6F). Different dynamics were observed at 6 dpfi as the double RNAi groups (e.g. *Smed-PTEN* plus +MVP, +USP7 or +MVP) exhibited no significant increase in proliferation relative to the control. Furthermore, a marked reduction in cellular division in *Smed-MVP+PTEN(RNAi)* animals was observed relative to the *Smed-PTEN(RNAi)* on day 6 alone. However, 12 dpfi all RNAi groups experienced hyperproliferation relative to the control. Additionally, *Smed-USP7+PTEN(RNAi), Smed-NEDD4-1+PTEN(RNAi)* and *Smed-PTEN+2x(RNAi)* experienced a significant increase in proliferation relative to *Smed-PTEN(RNAi)* alone animals. Interestingly, *Smed-PTEN+3x(RNAi)* at the 12-day timepoint resulted in increased proliferation however with no significant difference compared to the *Smed-PTEN(RNAi)* animals alone. These results may be due to its accelerated phenotype of animal death and fragmentation. Together, these results support the notion that nuclear *Smed-PTEN* is a crucial component within the phenotype. Further, that compensatory mechanisms within the nucleocytoplasmic shuttling machinery act to slow the progression of the cancer-like phenotype.

6.5. Neoblasts harboring DSBs bypass cellular apoptosis early in the phenotype

Cells containing DNA damage either undergo DNA repair or cell death [583], [584]. The early phase of the *Smed-PTEN(RNAi)* phenotype is attributed to neoblasts harboring high rates of DSBs that persist throughout the phenotype. Thus, we assessed the effects of *Smed-PTEN(RNAi)* on programed cell death throughout the time course using: (1) TUNEL assay, (2) WIHC and (3) FACS analysis. TUNEL assay *in situ* apoptosis tagging has been optimized in the planarian to detect DSB-induced apoptosis [16], [29], [113], [585]. Subjecting both control and treated animals 2dpfi to the TUNEL assay revealed no detectable increase in TUNEL+ foci throughout the animals (Fig. 7A). This phenomenon persisted throughout the first 4 dpfi however, a marked increase in cellular apoptosis was detected 6 dpfiand gradually increased by 12 dpfi (Fig. 7B, C). Alternatively, we subjected animals to WIHC against Caspase3 antibody. Similar results were observed 2- to 4- dpfi with no noticiable increase in Caspase3 intensity between the control and RNAi groups (Fig. 7D). Consistently, a significant increase of cellular apoptosis marked by Caspse3 was detected 6 dpfi and onward (Fig. 7E, F). These results imply that cellular apoptosis does not occur in the early phases of the phenotype. However, cell death accompanies the increases in cellular division at 6 post *Smed-PTEN(RNAi)*.

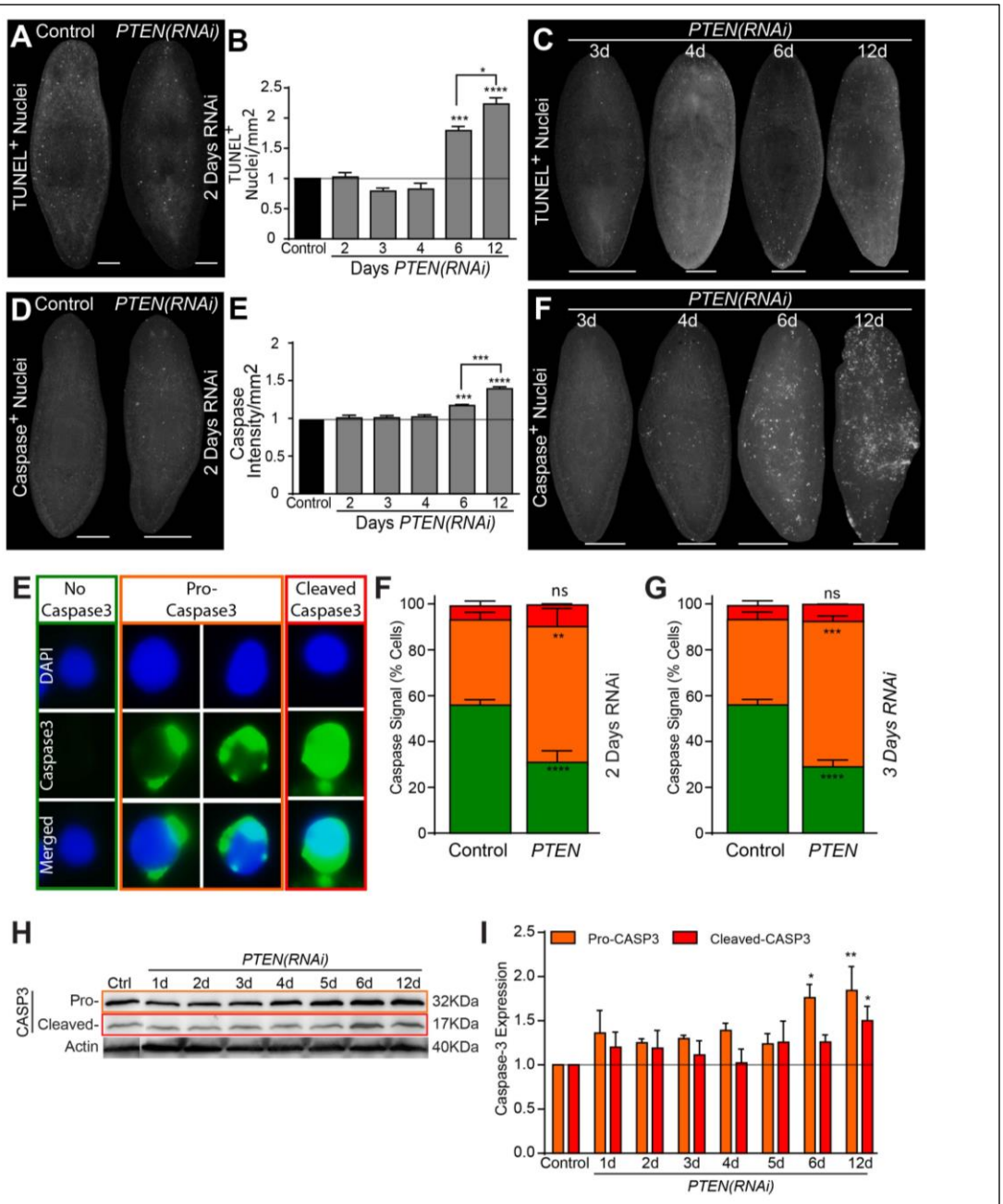

Figure 7. Cells containing DSBs bypass apoptotic signaling. (A, B, C) Whole mount immunostaining for the TUNEL assay at various timepoints throughout the phenotype and the quantification of TUNEL+ foci per animal. (D, E, F) Whole mount immunostaining against Caspase3 antibody at various timepoints throughout the phenotype and the quantification Caspase3 signal via intensity readings. (G, H, I) Immunohistochemistry of Caspase3 on dissociated cells extracted from the day 2 and 3 *PTEN(RNAi)* timepoints. Cleaved-Caspase3 seen in red and pro-Caspase3 seen in orange, cells that did not express Caspase3 are depicted in green. (J, K) Western blotting and its quantification probing for both forms of Caspase3 along the PTEN(RNAi) time course. Fold change values represent mean±s.e.m. of individual PTEN(RNAi) time points with respect to each time point's mock RNAi. Experiments consisted of at least three biological replicates, n>30 animals per time point. *P<0.01, **P<0.005, ***P<0.0005, ****P<0.0001; NS, no significance; two-way ANOVA. Scale bars 250um.

To determine if *Smed-PTEN(RNAi)* cells are activating a cell death response we capitalized on the Caspase3 antibody that can be recognized in two forms, pro- and cleaved-Caspase (i.e. proenzyme and active form, respectively). These forms are distinguishable through immunoassaying on cells and by western blot. Pro-Caspase3 surrounds the nucleus unlike cleaved-Caspase which engulfs the entire cell (Fig. 7G). We observed a significant increase in cells with Caspase3+ signal (i.e. 44% vs 73%) 2 dpfi. Importantly, the increase in expression was attributed to an increase of cells expressing pro-Caspase3 without exhibiting an increase in cleaved form of Caspase3 (Fig. 7H). At days 2 and 3 into the phenotype, we observed an increase in cells expressing pro-Caspase3+ (Fig. 7I). Through western blot, a stepwise increase in pro-Caspase3 was observed starting 2 dpfi, followed by a substantial increase 4 days RNAi (Fig. 7J). Furthermore, the cleaved form of Caspase3 was only observed to peak 6 dpfi and decrease slightly 12 dpfi The decay in signal is likely due to tissue loss and deterioration of animal integrity imposed by the RNAi treatment (Fig. 7K). For a more sensitive approach to detect cellular apoptosis, FACS analysis using AnnexinV and 7AAD (i.e. markers for apoptosis and viability, respectively) were deployed throughout the first 6 post *Smed-PTEN(RNAi)*. Relative to the control, the RNAi group shows a progressive increase in AnnexinV+ cells towards the pre-apoptotic quadrant within the first 5 dpfi (Fig. 8A, B). FACS analysis 6 days *Smed-PTEN(RNAi)* identified a significant shift of cells towards the apoptotic quadrant, supporting our prevous findings with TUENL and Caspase3 staining (Fig. 8B).

To understand the genetic composition of different cell death cascades, we examined RNAseq data. Genes involved in DNA damage induced pro-apoptotic cascade (e.g. *PIDD, APAF1, CRADD*) decrease within the first 3 dpfi and gradually increase starting 4 dpfi (Fig. 8C). Interestingly, genes involved in anti-apoptotic signaling (e.g. *HIAP* and *BCL*) were consistently upregulated throughout the progression of the phenotype followed by an increase in *BAG4*, *CDC37* and *Livin* starting at day four (Fig. 8D). Genes involved in cell death receptor activation were suppressed days 2- to 4-dpfi and later increased > 6 dpfi (Fig. 8E). Surprisingly, genes involved in the Caspase cascade were suppressed except for Caspase3 which returned to basal levels by 4dpfi. Notably, GO terms (strict cut-off of <0.2) involved in negative regulation of apoptotic process were enriched at both 3- and 12-dpfi. Interestingly, at 4 dpfi GO terms (cut-off of <0.23) for apoptosis and autophagy were present (Fig. 8F). To validate the *in-silico* results, we performed quantitive PCR probing for the anti-apoptotic gene BCL2 and found a significant increase in expression 12 days post *Smed-PTEN(RNAi)* (Fig. 8G). These results imply that *Smed-PTEN(RNAi)* cells can initiate pro-apoptotic signals but are unable to mount an apoptotic response within the early stages of the phenotype.

Currently, there are no methods of upregulating genes within the planarian. To determine if *Smed-PTEN* is required for the apoptotic response, we capitalize on the ability for planarian to regenerate lost tissues. A recently published transcriptome annotates the generic wound response preceding head regeneration [53]. We identified that both homologs of *Smed-PTEN* are required for regeneration and expression levels increase at specific timepoints corresponding to the well-established waves of cell death during regeneration (e.g. 4 and 24 hours post amputation (hpa)) [53], [56] (Fig. 8H). To ensure that the day two phenotype was in full effect, all animals were amputated at various time points (e.g. 4, 6, 8, 12 and 24hpa) and fixed exactly at the 48-hour mark of the intact phenotype. Both the control and *Smed-PTEN(RNAi)* animals were subjected head amputation and underwent TUNEL assay staining. Interestingly, *Smed-PTEN(RNAi)* animals failed to produce the cell death peaks at both 4hpa and 24hpa, relative to the

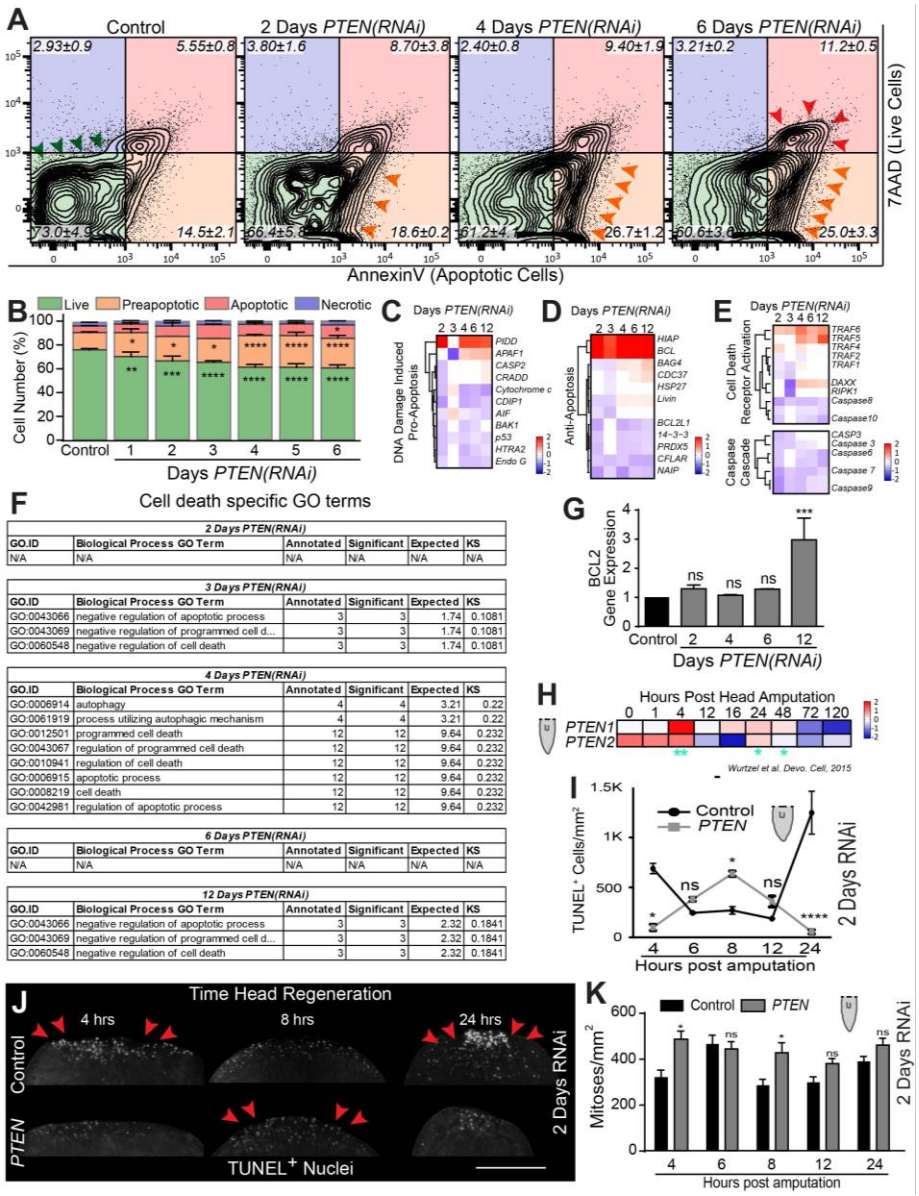

Figure 8. *Smed-PTEN* is required for initiating cell death. (A) FACS plots using Annexin V cell death stain shows a progressive increase in the pro-apoptotic quadrant (Q3) and a reduction of live cells (Q4) with an increase in cell death (Q1) at days 6 *PTEN(RNAi).* (B) Quantification of cell death rates determined by FACS analysis. (C, D, E) Differentially expressed genes involved in the DNA damage induced pro-apoptotic cascade, anti-apoptotic cascade and cell death receptor activation/Caspase cascade, respectively. (F) Biological processes GO terms specific for cell death mediated terms. (G) QPCR validation of RNAseq data monitoring mRNA levels of BCL2 anti-apoptotic gene throughout the *PTEN(RNAi)* time course. (H) PTEN gene expression after 120hours post head amputation; notice the increase in expression at 4 and 24 hours. (I, J) Quantification and visualization of TUNEL+ foci of *PTEN(RNAi)* day 2 animals undergoing regeneration. Red arrows show a shift in apoptotic events after head regeneration within the 24hr time frame. (K) Quantification of mitotic events of *PTEN(RNAi)* day 2 animals undergoing regeneration within a 24hr time period. Experiments consisted of at least three biological replicates, n>30 animals per time point. *P<0.01, **P<0.005, ***P<0.0005, ****P<0.0001; NS, no significance; two-way ANOVA. Scale bars 250um.

control (Fig. 8I, J). However, when *Smed-PTEN* gene expression is not required during regeneration, *Smed-PTEN(RNAi)* animals were able to elect a peak in cell death. The amount of death corresponded to cell death rates found in the control animals 4hpa. Curiously, mitotic division during regeneration was also altered in the treated group when compared to the control. Mitotic division is not substantially elevated 4hpa in control animals however, *Smed-PTEN(RNAi)* animals exhibited increase in proliferation. The increase in mitosis 4hpa resembled the systemic peak of cellular proliferation known to occur in control animals 6hpa. Further, *Smed-PTEN(RNAi)* exhibited a delayed response to suppress cell division at 8hpa but reverted to basial levels (Fig. 8K). Overall, these results show that *Smed-PTEN* expression is required for cell death and cell cycle regulation during regeneration. Moreover, alternative signaling mechanisms within the planarian can produce an apoptotic response upon loss of *Smed-PTEN* expression.

6.6. *Smed-PTEN* depletion impairs mitotic spindle geometry

PTEN regulates the timely expression of genes involved in the spindle checkpoint, architecture and chromosome congression during mitosis [538]–[541], [550], [586]. Overexpression of these components may result in chromosomal instability, aneuploidy and tumor development [538]–[541], [550], [586]. We have previously identified that *Smed-PTEN(RNAi)* animals exhibit alterations in cell cycle dynamics, DNA damage and mitotic cells chromosomal abnormalities. To understand the role of *Smed-PTEN* during chromosome segregation, we examined the organization of the mitotic spindle and chromosomes in cells derived *Smed-PTEN(RNAi)* animals at 1- and 2-dpfi. Through double immunostaining with anti-α-tubulin and anti-H3P antibodies (e.g. spindles and chromosomes, repspectively) we observed an array of abnormalities throughout the different phases of mitosis. Specifically, in microtubule organization of spindles and

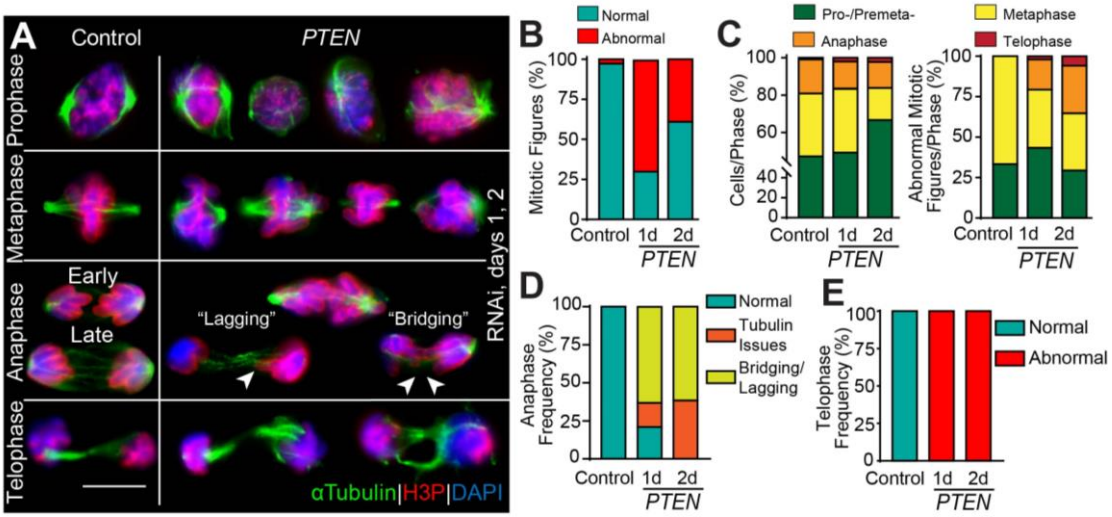

Figure 9. *Smed-PTEN(RNAi)* disrupts mitotic spindle pole architecture. (A) An array of dissociated cells stained with Histone 3, α-Tubulin and DAPI to depict the phases pf mitosis and the subsequent abnormalities obtained through RNAi of PTEN at days 1 and 2. (B) Percent of mitotic figures that a normal versus abnormal. (C) Quantification of cells per phase of mitosis and the abnormal mitotic figure counts per phase at days 1 and 2 RNAi. (D) Quantification of anaphase mitotic figures that are normal blue, experiencing tubulin issues (orange) or bridging/ lagging issues (yellow). (E) The frequency of telophase mitotic figure that are normal or abnormal.

spindle poles throughout all phase of mitosis (e.g. prophase/prometaphase, metaphase, anaphase and telophase) (Fig. 9A, B). Notably, 24 hpfi cells contained most of the abnormalities as errors within the mitotic figures seem to alleviate 48 hpfi (Fig. 9A, B). Importantly, cells in anaphase exhibited characteristics of lagging and bridging chromosomes known to rise from unrepaired DSBs formed in S-phase. Cells from day one *Smed-PTEN(RNAi)* animals exhibited a slight increase in the number of cells in metaphase and telophase relative to the control. However, cells 2 dpfi showed an increase of mitotic cells accumulating in prophase and prometaphase (Fig. 9C). Moreover, the 5% of abnormalities found within control group were restricted to prophase, prometaphase and metaphase. However, cells of the treated group exhibiting abnormalities within anaphase and telophase at both 1- and 2-dpfi (e.g. 21% vs. 35%). Abnormalities in anaphase (e.g. tubulin architecture and bridging/lagging chromosomes) increased as the phenotype progressed (Fig. 9D). Cells within telophase contained abnormalities with tubulin organization and equal segregation of DNA per cell at both 1- and 2-days RNAi (Fig. 9E). These results support an essential role of *Smed-PTEN* in preserving the integrity of cells undergoing mitosis and its role to inhibit the progression of abnormal cells past the metaphase spindle checkpoint.

An increase in lagging chromosomes in anaphase are symptomatic of defects in kinetochore-microtubule attachment dynamics resulting in defective chromosome congression and segregation [587]. To discern the cause of segregation issues, we examined RNAseq data and identified that genes involved in prophase, prometaphase and telophase are upregulated. However, the average gene expression for both metaphase and anaphase are downregulated (Fig. 10A). Notably, proteasome (PSM)-specific subunits and subcomponents were dramatically decreased by *Smed-PTEN(RNAi)* (Fig. 10B). Together, *in silico* results imply that *Smed-PTEN(RNAi)* cells

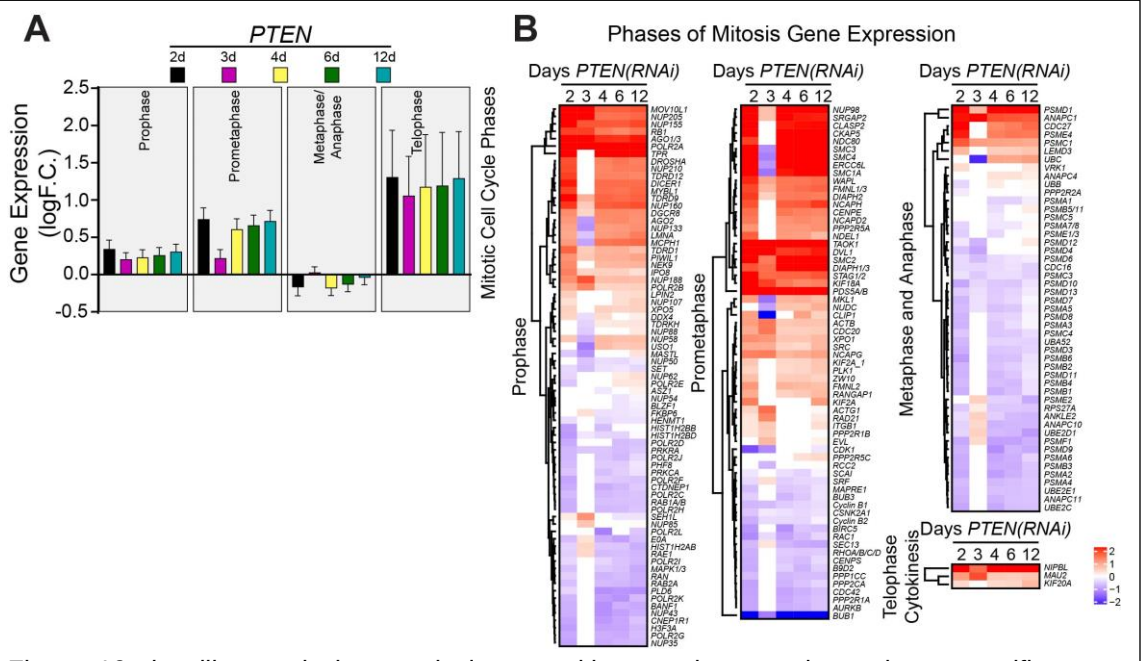

Figure 10. *in silico* analysis reveals issues with metaphase and anaphase specific gene expression upon *Smed-PTEN* loss. (A) average in gene expression (log fold change) of a large array of genes differently expressed throughout the different phases of mitosis. (B) Heat maps of genes categorized by mitotic phase at days 2 to 12 of the *PTEN(RNAi)* phenotype.

within metaphase may undergo defective chromosome congression and segregation resulting in anaphase defects.

To assess chromosome condensation issues within the *Smed-PTEN(RNAi)* phenotype, we examined the geometry of metaphase cells. Within the first two days of the phenotype, metaphase cells showed disorganized spindle microtubules and chromosome alignment defects (Fig. 11A). Noteworthy, phosphorylated Histone H3 accumulated and surrounded centrosomes within the treated group. *Smed-PTEN(RNAi)* cells did not increase in surface area (e.g. bright field cell area) relative to the control (Fig. 11B). Interestingly, significant increases in DNA area per cell were observed within the first 48 hours of the phenotype accompanied by an increase in DNA congression index (e.g. length versus width of DNA) (Fig. 11C, D). These results imply that *Smed-PTEN(RNAi)* cells harbor reduced chromatin packaging and loss of cohesion capabilities. Further, analysis of spindle pole length per cell area portrayed a significant reduction in the treatment group (Fig. 11E). Disorganized spindles arrays were attributed to a significant increase in spindle angle of both astral and polar microtubules (i.e. 30º versus +46º) resulting in an overall increase in spindle arc angle in respect to centrosome (i.e. 60º versus +93º) (Fig. 11F, G). Alterations to chromosome condensation and spindle dynamics play roles in the acquisition of DNA damage during mitosis [588]. These results imply a mechanism for the rise to chromosomal abnormalities found within the *Smed-PTEN(RNAi)* phenotype.

Defects in mitotic spindle geometry due to loss of PTEN have been attributed to overexpression of PTEN-regulated Dlg1-Eg5 complexes and the unscheduled formation of mitotic checkpoint complex [541], [550], [586]. Exploring the RNAseq results, we identified crucial components involved in the phosphorylation of Dlg1-Eg5 complexes were upregulated (e.g. *NEK9, NEK2* and *MST2*) (Fig. 12A). Interestingly, within the inner kinetochore gene expression of the centromere specific variants (e.g. *CENP-A, -H* and *-S*) found in the nucleosome were significantly downregulated. Genes involve in outer kinetochore function are in general overexpressed within the treated group (e.g. *PLK1* and

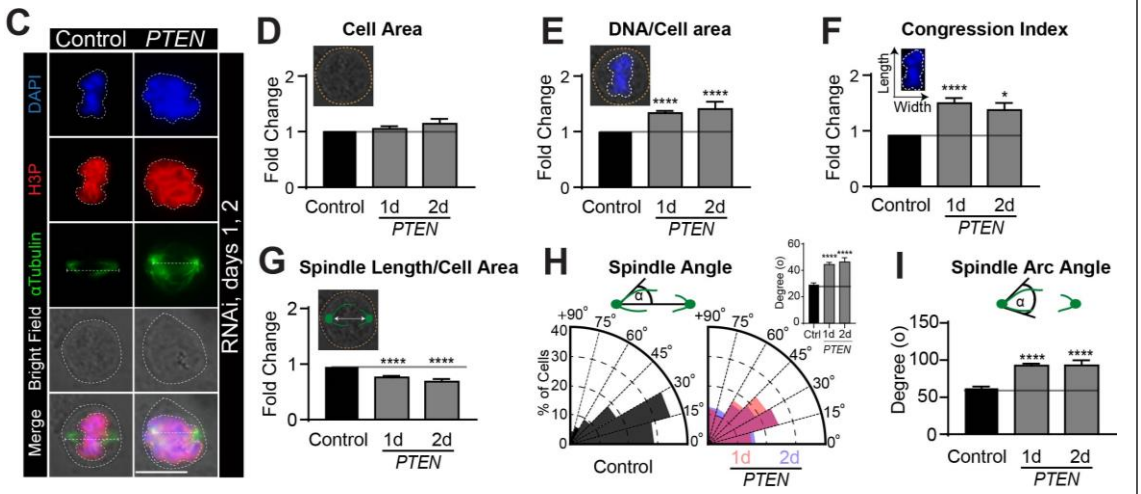

Figure 11. *Smed-PTEN* loss impairs metaphase geometry of planarian neoblasts. (A) Representative control and RNAi neoblasts undergoing cell division. H3P is marking mitotic neoblasts, DAPI the DNA and tubulin in green. (B) Quantification of cell surface area determined by bright field images. (C) Fold change in DNA surface area in relation to cell surface area. (D) Congression index measuring the length and width of metaphase neoblasts. (E) Quantification of spindle pole length relative to surface area of cell. (F, G) Spindle angle and arc angle with respect to the centromere.

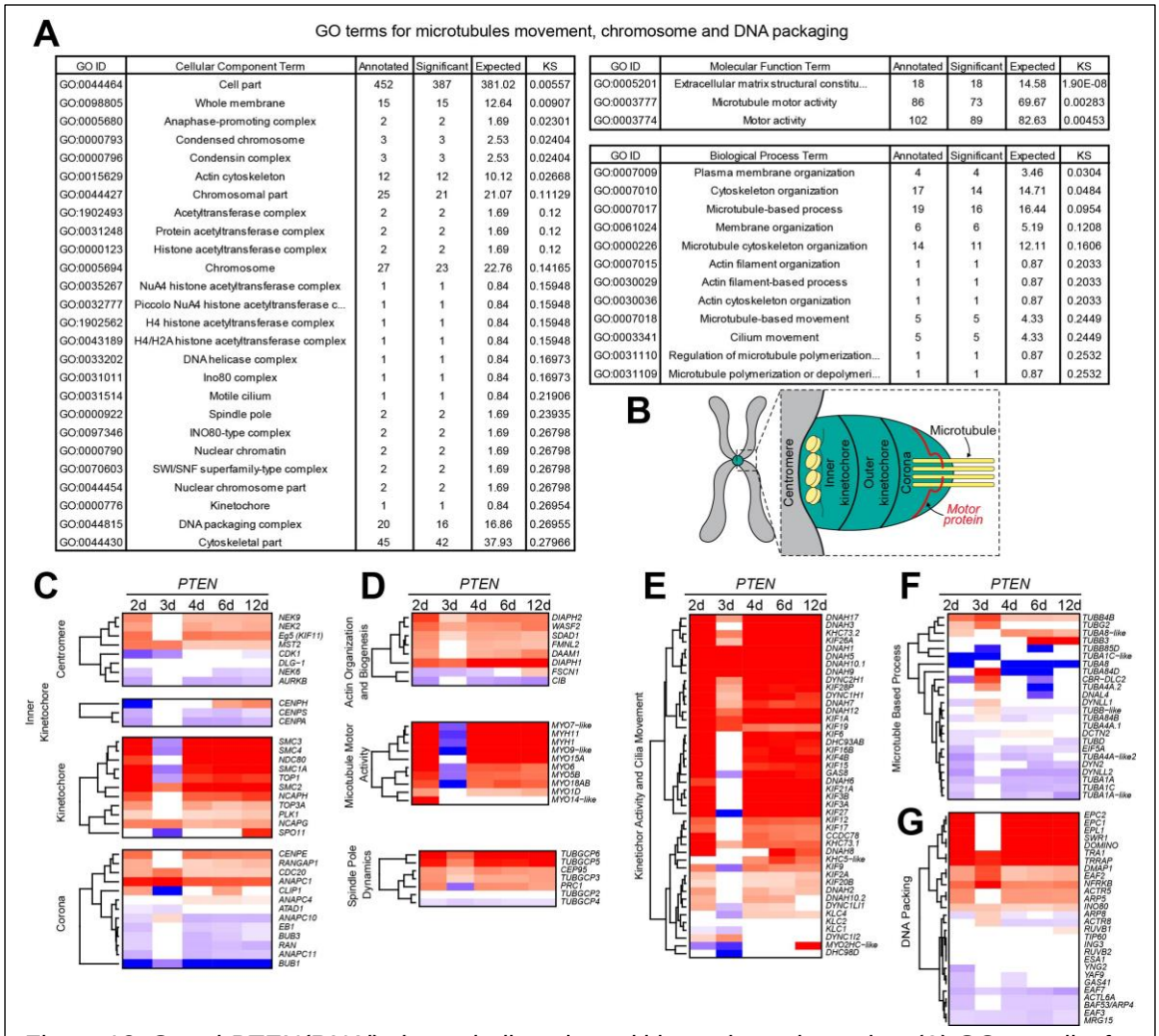

GO ID	Cellular Component Term	Annotated	Significant	Expected	KS
GO:0044464	Cell part	452	387	381.02	0.00557
GO:0098805	Whole membrane	15	15	12.64	0.00907
GO:0005680	Anaphase-promoting complex	2	2	1.69	0.02301
GO:0000793	Condensed chromosome	3	3	2.53	0.02404
GO:0000796	Condensin complex	3	3	2.53	0.02404
GO:0015629	Actin cytoskeleton	12	12	10.12	0.02668
GO:0044427	Chromosomal part	25	21	21.07	0.11129
GO:1902493	Acetyltransferase complex	2	2	1.69	0.12
GO:0031248	Protein acetyltransferase complex	2	2	1.69	0.12
GO:0000123	Histone acetyltransferase complex	2	2	1.69	0.12
GO:0005694	Chromosome	27	23	22.76	0.14165
GO:0035267	NuA4 histone acetyltransferase complex	1	1	0.84	0.15948
GO:0032777	Piccolo NuA4 histone acetyltransferase c...	1	1	0.84	0.15948
GO:1902562	H4 histone acetyltransferase complex	1	1	0.84	0.15948
GO:0043189	H4/H2A histone acetyltransferase complex	1	1	0.84	0.15948
GO:0033202	DNA helicase complex	1	1	0.84	0.16973
GO:0031011	Ino80 complex	1	1	0.84	0.16973
GO:0031514	Motile cilium	1	1	0.84	0.21906
GO:0000922	Spindle pole	2	2	1.69	0.23935
GO:0097346	INO80-type complex	2	2	1.69	0.26798
GO:0000790	Nuclear chromatin	2	2	1.69	0.26798
GO:0070603	SWI/SNF superfamily-type complex	2	2	1.69	0.26798
GO:0044454	Nuclear chromosome part	2	2	1.69	0.26798
GO:0000776	Kinetochore	1	1	0.84	0.26954
GO:0044815	DNA packaging complex	20	16	16.86	0.26955
GO:0044430	Cytoskeletal part	45	42	37.93	0.27966

GO ID	Molecular Function Term	Annotated	Significant	Expected	KS
GO:0005201	Extracellular matrix structural constitu...	18	18	14.58	1.90E-08
GO:0003777	Microtubule motor activity	86	73	69.67	0.00283
GO:0003774	Motor activity	102	89	82.63	0.00453

GO ID	Biological Process Term	Annotated	Significant	Expected	KS
GO:0007009	Plasma membrane organization	4	4	3.46	0.0304
GO:0007010	Cytoskeleton organization	17	14	14.71	0.0484
GO:0007017	Microtubule-based process	19	16	16.44	0.0954
GO:0061024	Membrane organization	6	6	5.19	0.1208
GO:0000226	Microtubule cytoskeleton organization	14	11	12.11	0.1606
GO:0007015	Actin filament organization	1	1	0.87	0.2033
GO:0030029	Actin filament-based process	1	1	0.87	0.2033
GO:0030036	Actin cytoskeleton organization	1	1	0.87	0.2033
GO:0007018	Microtubule-based movement	5	5	4.33	0.2449
GO:0003341	Cilium movement	5	5	4.33	0.2449
GO:0031110	Regulation of microtubule polymerization...	1	1	0.87	0.2532
GO:0031109	Microtubule polymerization or depolymeri...	1	1	0.87	0.2532

Figure 12. *Smed-PTEN(RNAi)* alter spindle pole and kinetochore dynamics. (A) GO term list for enrichment of terms involved in microtubule movement, chromosome and DNA packaging. (B) Representative image of the kinetochore and corona of the chromosome. (C) Heat map representing gene expression levels of genes involved with the specific regions of the kinetochore and corona. (D) Differentially expressed genes involved in actin organization and biogenesis, microtubule motor activity and lastly, spindle pole dynamics. (E) Expression levels of genes involved in kinetochore activity and cilia movement. (F) Gene expression for genes involved in microtubule-based processes. (G) Heatmap of genes involved in DNA packaging.

NDC80). Gene expression found within the corona (i.e. interface between chromosome and spindle) contained mixed expression values. Specifically, underexpression of genes involved in spindle checkpoint complex (e.g. *BUB1* and *BUB3*) with the exception for *CDC20* which was overexpressed throughout the time course. Lastly, we identified alterations to components of the anaphase promoting complex (e.g. *ANAPC-1, -4, -10* and *-11*). Together, these results suggest that loss of *Smed-PTEN* promotes unregulated expression of genes required for spindle geometry.

Suppressed *Smed-PTEN* expression can aid in abnormal motor protein activity for spindle pole movement during mitosis. The most enriched cellular components, molecular function and biological processes were genes involved in microtubule dynamics, chromosome condensation and DNA packaging (Fig. 12B). Analysis of enriched genes

identified the upregulation of actin filament organization/biogenesis (e.g. *DIAPH-1* and -*2*), microtubule motor activity (e.g. *MYO* and *MYH*) and spindle pole dynamics (e.g. γ-tubulin complex) (Fig. 12C). Interestingly, genes involved in kinetochore activity and cilia movement were severely elevated throughout the phenotype (e.g. kinesin and dynein specific) (Fig. 12D). However, genes involved with microtubule-based process such as many members of the tubulin superfamily (e.g. alpha, beta, gamma and delta) were highly downregulated (Fig. 12E). Further, key components within the DNA packaging SWI/SNF, TIP60 and INO80 complexes were altered with mixed expression profiles (Fig. 12F). Together, the *in-silico* results point to a dysregulation for genes involved in DNA packaging and kinetochore-microtubule attachment dynamics, may result in the observed metaphase segregation issues.

6.7. *Smed-PTEN(RNAi)* neoblasts enter metaphase harboring DNA damage generated during synthesis phase

PTEN is required for Rad51 recruitment onto chromatin structures, mediating faithful DNA replication forks progression, restart and recovery [484]. To determine if *Smed-PTEN(RNAi)* neoblasts harboring DSBs can enter mitosis, we subjected both the control and treated group with exogenous exposure to DNA damaging agents. Specifically, (1) DNA polymerase inhibitor aphidicolin (APH) causing replication stress and (2) sublethal γ-irradiation to induce large-scale and repairable DSBs. The calibration of APH drug exposure accounted for animal survival, optimal concentration and time of treatment to produce an effect. We identified that soaking control animas in 0.2mM APH can suppress cell division by 50% within 6 hours post treatment (hpt) relative to DMSO soaked controls (Fig. 13A, B). Exposing *Smed-PTEN(RNAi)* animals to APH within the first 48 hours RNAi resulted in increased amounts of neoblasts entering G2/M relative to APH soaked controls. Moreover, the increase of mitotic cells within the APH soaked *Smed-PTEN(RNAi)* groups were indistinguishable to DMSO controls. However, experimental animals 3 days RNAi responded to APH treatment and significantly reduced the number of neoblasts entering G2/M relative to the DMSO controls. Noteworthy, 4 days RNAi animals subjected to 6 hour soak in APH were incapable of suppressing neoblast entry into G2/M (Fig. 13B). These results suggest that *Smed-PTEN(RNAi)* neoblasts containing DNA replication stress can bypass regulatory mechanisms within the first 2 dpfi. Furthermore, at 3 days RNAi, animals can suppress premature entry of damaged cells into G2/M phase.

To corroborate our findings, we exposed planarian to sub-lethal doses of γ-irradiation to induce systemic accumulation of DSBs. The exposure of planarian to γ-irradiation was calibrated to ensure mitotic division was suppressed within the first 6 hours post exposure and capable of being re-established within 12 hours. 200rad of γ-irradiation resulted in a near complete elimination of mitotic activity by 6 hours post exposure when compared to nonexposed animal, approximately 5.33±3.68 versus 175.25±15 mitotic cells/mm^2. Strikingly, experimental animals 6-hours post 200rad resulted in the inability to suppress mitotic activity at both 1- and 2-dpfi (Fig. 13C, D). However, cell division was suppressed 3dpfi. In addition, when animals were exposed to a higher dose of γ-irradiation at 400rad, increases in cell division were only observed at 2 days *Smed-PTEN(RNAi)*. Lastly, in all cases, mitotic activity was reestablished by 12 hours post-exposure and the amount of events were indistinguishable between the control and RNAi groups (Fig. 13D). These results imply that cells within the first 2 dpfi can bypass regulator mechanisms and that these neoblasts have a higher tolerance to exogenous DNA insults. Moreover, the inability to distinguish between the control and treated groups 12 hours post γ-irradiation

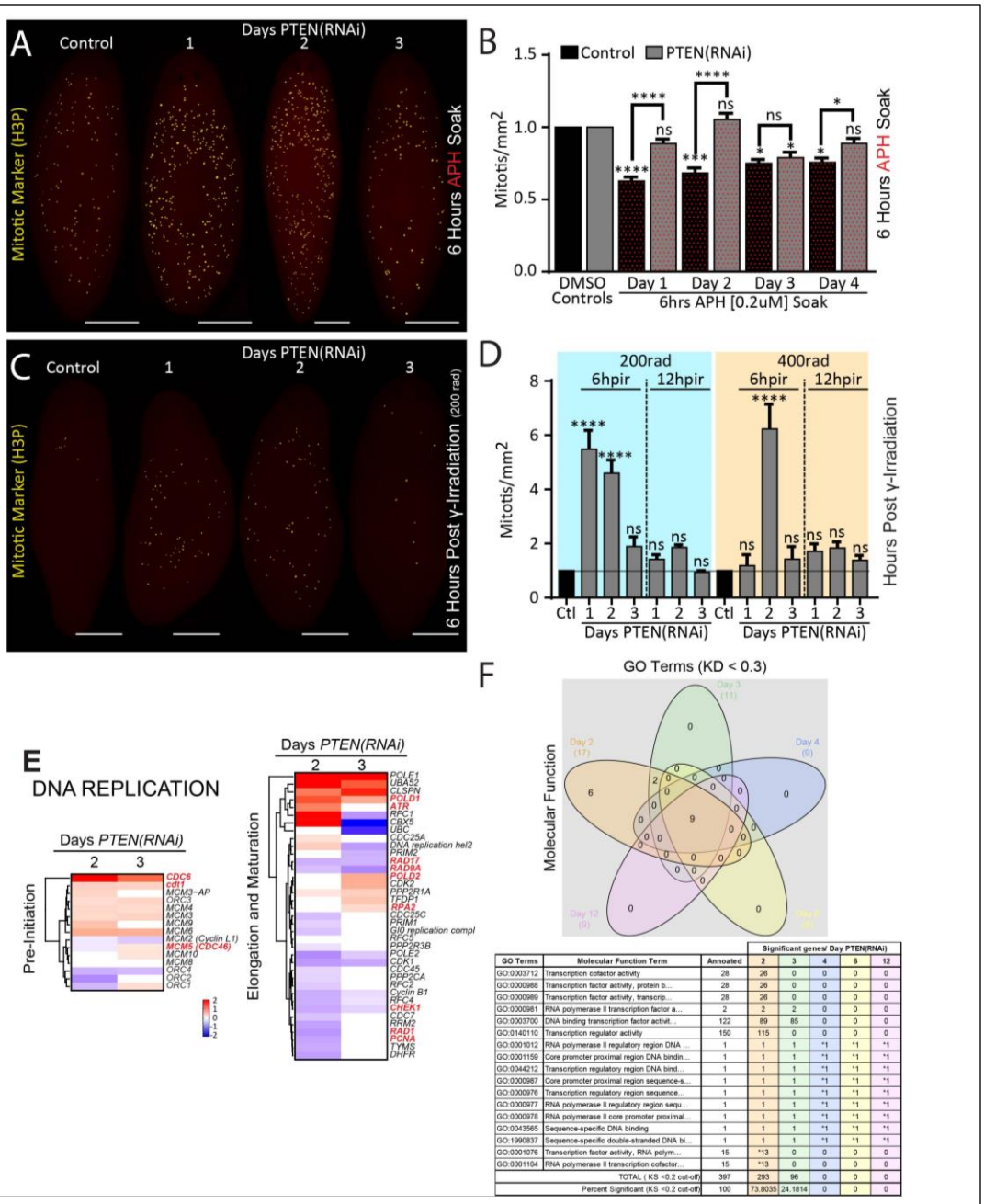

GO Terms	Molecular Function Term	Annoated	Significant genes/ Day PTEN(RNAi)				
			2	3	4	6	12
GO:0003712	Transcription cofactor activity	28	26	0	0	0	0
GO:0000988	Transcription factor activity, protein b...	28	26	0	0	0	0
GO:0000989	Transcription factor activity, transcrip...	28	26	0	0	0	0
GO:0000981	RNA polymerase II transcription factor a...	2	2	2	0	0	0
GO:0003700	DNA binding transcription factor activit...	122	89	85	0	0	0
GO:0140110	Transcription regulator activity	150	115	0	0	0	0
GO:0001012	RNA polymerase II regulatory region DNA ...	1	1	1	*1	*1	*1
GO:0001159	Core promoter proximal region DNA bindin...	1	1	1	*1	*1	*1
GO:0044212	Transcription regulatory region DNA bind...	1	1	1	*1	*1	*1
GO:0000987	Core promoter proximal region sequence-s...	1	1	1	*1	*1	*1
GO:0000976	Transcription regulatory region sequence...	1	1	1	*1	*1	*1
GO:0000977	RNA polymerase II regulatory region sequ...	1	1	1	*1	*1	*1
GO:0000978	RNA polymerase II core promoter proximal...	1	1	1	*1	*1	*1
GO:0043565	Sequence-specific DNA binding	1	1	1	*1	*1	*1
GO:1990837	Sequence-specific double-stranded DNA bi...	1	1	1	*1	*1	*1
GO:0001076	Transcription factor activity, RNA polym...	15	*13	0	0	0	0
GO:0001104	RNA polymerase II transcription cofactor...	15	*13	0	0	0	0
	TOTAL (KS <0.2 cut-off)	397	293	96	0	0	0
	Percent Significant (KS <0.2 cut-off)	100	73.8035	24.1814	0	0	0

Figure 13. Neoblasts harboring DNA damage can bypass G2/M checkpoint two days into the phenotype. (A) Whole mount immunostaining against H3P for both control and experimental groups after 6 hours soak in [0.2mM] APH. (B) Quantification of mitotic events 6 hours post APH soak. Both control and experimental groups were accompanied with day specific DMSO soaked animals and fold change were determined off the days and RNAi specific DMSO controls. (C) Tracking of mitotic events through immunostaining against H3P 6 hours after exposure to 200rad sublethal dose if ionizing irradiation. (D) Quantification of mitotic events at both 6hr and 12hr after exposure to either 200rad or 400rad irradiation. (E) Heat maps containing gene expression levels for marker involved in pre-replication initiation and the elongation and maturation phases of replication. (F) Veen diagram molecular function GO terms throughout the time course. Table represents the significant gene enrichment per *PTEN(RNAi)* days. * indicated inability to make cut-off.

may imply that certain neoblast types harboring DSBs are capable of bypassing regulatory mechanisms.

Many cancers overexpress genes involved in the licensing of DNA replication, which result in the accumulation of DNA damage before division. To identify if *Smed-PTEN(RNAi)* animals exhibit endogenous forms of DNA replication stress, we isolated differentially expressed genes involved in preinitiation, elongation and maturation of replication origins. Results identified a continual overexpression of preinitiation related genes (e.g. *CDC6, cdt1*, and *MCM* complex) throughout the 12-day time course (Fig. 13E). Furthermore, many genes involved in the repair and maintenance of Okazaki fragments formed during DNA replication, were mostly downregulated throughout the phenotype (Fig. 13E). We also identified a significant downregulation of genes involved DDR and DNA repair required for efficient DNA replication (e.g. *RPA, PCNA, RFC1-5, Rad-9, -1, -17* and *CHEK1*). Overall, RNAseq analysis shows a reduction of genes required for DNA replication 2 dpfi and a relative reestablishment by day 3 RNAi. Together, these results imply that early signs of endogenous DNA replication stress are caused by under-replication, over-replication or altered maturation within replicasome.

Accumulation of endogenous DNA replication stress can be attributed to conflicts between transcription and replication. To explore the option of transcription-replication mediated DNA replication stress, we examined GO term ontology related to molecular function during the RNAi schedule. Using a KS cut-off of <0.3, we identified that each timepoint contained nine central GO terms involved in transcription activity, regulation and promotion (Fig. 13F). Strikingly, 2 dpfi was highly enriched with six specific GO terms and shared two terms with 3-day RNAi. Using a more stringent KS cut-off of <0.2, we observed that GO term enrichment for transcription was isolated to the first 3 dpfi. Relative to the annotated genes per transcription-specific GO term, the 2dpfi timepoint contained 74% of significant genes and 3 dpfi contained 24% (i.e. 293 versus 96 genes, respectively) (Fig. 13F). These results imply that the first three days of the phenotype contain highly active roles in transcription. Furthermore, there may be a possible role in transcription-replication mediated replication stress which needs further exploration.

The phenomenon of *Smed-PTEN(RNAi)* neoblasts entering mitosis containing DNA damage has not been described. To address this, we utilized the well-established drug colchicine to terminally freeze cells within mitosis as it targets the disruption of tubulin. Colchicine is usually utilized to view metaphase chromosome spreads. We have adapted the soaking protocol to monitor the rate of neoblasts entering metaphase by fixing animals to stain against α-H3P. To calibrate this experiment, animals were soaked in colchicine during an 8-hour period and when compared to unsoaked animals, mitotic rates increased stepwise (Fig. 14A). Astonishingly, *Smed-PTEN(RNAi)* neoblasts 2 dpfi entered metaphase at an accelerated rate throughout the colchicine soak time course relative to the control (i.e. 1.45- and 1.61-fold change) (Fig. 14B, C). Moreover, prolonged pausing in metaphase through colchicine treatment has been attributed to mitotic catastrophe-mediated apoptosis and the acquisition of DNA damage [589], [590]. Both cell death and DNA repair rates were monitored in control worms during an 8-hours incubation period. A significant peak in Caspase3 and RAD51 signal were observed after 8-hours of colchicine treatment (Fig. 14D). Now calibrated, we examined the effects of cell death and DNA repair of 2-day RNAi neoblasts experiencing prolonged metaphase pausing. Results identified a significant elevation of RAD51 and animals exhibited a significant decrease in cell death by the conclusion of the 8-hour colchicine soaked (Fig. 14E, F, G, H). These results imply that despite drug treatment, *Smed-PTEN(RNAi)* animals still exhibit an inability to induce cellular apoptosis and survive with increased amounts of DNA damage.

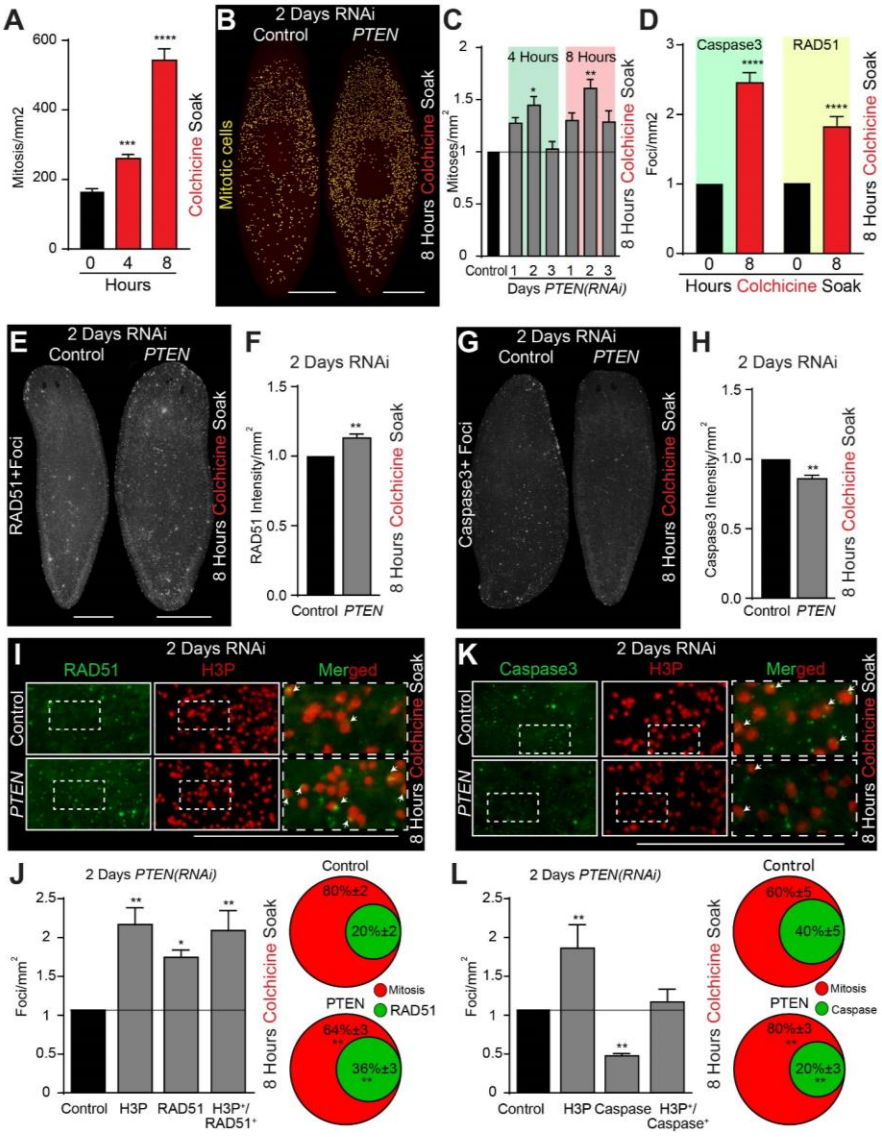

Figure 14. *Smed-PTEN(RNAi)* neoblasts evade mitotic catastrophe. (A) Calibration experiment to determine the increase in mitotic cells halting in metaphase under a 4hr and 8hr soak in colchicine. (B) Immunohistochemistry against H3P for both the control and experimental group day 2 RNAi after an 8hr soak in colchicine. (C) Quantification of mitotic events after a 4hr and 8hr colchicine soak. (D) Standardization of the amount of cell death (Caspase3) and DNA repair (RAD51), foci per mm^2, after soaking control animals in colchicine for 8hrs relative to an untreated animal. (E) Whole-mount immunostaining of control and PTEN(RNAi) animals 2 days into the phenotype stained with RAD51 8 hours after treatment. (F) Quantification of RAD51 intensity post 8hr exposure to treatment. (G) Immunostaining of control and PTEN(RNAi) animals, 2 days RNAi, against Caspase3 antibody 8hrs after soaking. (H) Caspase3 intensity reading for both the control and RNA group after drug soaking. (I) Magnified zoom of H3P+ foci merged with RAD51+ foci 2 days into the phenotype. (J) Analysis of individual and co-expressed foci in relation to animal surface area. Circle graphs depict the percent of cells in the control and RNAi group co-expressing H3P+RAD51. (K) Magnified zoom of H3P+ foci merged with Caspase3+ foci 2 days into the phenotype. (L) Quantification of individual and co-expressed foci in relation to animal surface area. Circle graphs depict the percent of cells in the control and RNAi group co-expressing H3P+Caspase3.

However, these results do not provide a resolution to distinguish between treatment effects on differentiated cells vs. mitotic neoblasts.

Next, we performed double WIHC of H3P+RAD51 and H3P+Caspase3 in both the control and treated groups 2 dpfi, exposed to an 8-hour colchicine soak. With regards to the DNA damage rate within mitotic neoblast, a significant increase in H3P+RAD51 double positive neoblasts relative to the area of the animals was observed in the RNAi group (e.g. 20% vs 36%) (Fig. 14I, J). Moreover, looking at cell death rates of mitotic neoblasts under 8-hour colchicine treatment we observe an increase in H3P+ foci and decline in Caspase3+ foci in *Smed-PTEN(RNAi)* animals. Interestingly, this did not produce a significant increase in double positive H3P+Caspase3 mitotic neoblasts normalized to the surface area of the animals (Fig. 14H, K). Therefore, we quantified co-expression in terms of mitotic neoblasts with disreguard to animal surface area. In doing so, we identified that the control cells harbor 40% double positive mitotic neoblasts relative to *Smed-PTEN(RNAi)* animals that contained 20% double positive signal. Together these results imply a greater amount of mitotic neoblasts contain DNA damage and are capable of bypassing mitotic catastrophe driving the phenotype.

6.8. Discussion

Monitoring cellular transformation quite challenging and current experimental models are restricted to organ-specific tissues or cell culture [358], [577]. The following study presents an innovative approach by using the planarian, *Schmidtea mediterranea* to monitor the transition of normal to malignant cells during adult tissue turnover. Our results provide critical insight on pervasive precancerous lesions that give rise to the planarian cancer-like phenotype. Specifically, we demonstrate that *Smed-PTEN* controls cell cycle checkpoint stability, cellular apoptosis and DNA integrity. In addition, *Smed-PTEN* function is critical for the DDR and DNA repair response through homologous recombination. Finally, we establish that loss of *Smed-PTEN* results in the accumulation of DNA replication stress, which results in abnormal mitotic chromosome segregation.

Despite the central role of DNA damage in cancer development, it remains poorly understood whether DNA damage reflects the cause or effect of altered cell dynamics. The OTS-DDM model identifies that the imbalance between oncogene and tumor suppressor activity results in precancerous lesions of DNA replication that drive cancer progression [30], [32], [33]. Moreover, the dual functionality of PTEN within the nucleus and cytoplasm provides an exemplary protein to study OTS-DDM during tissue renewal. Histological analysis of many tumor types identifies that a progressive loss of nuclear PTEN accompanies cancer initiation and its progression [365]–[370]. However, its nuclear role is less understood in the context of cancer and its progression. We establish that *Smed-PTEN* does function within the nucleus of planarian neoblasts. Further, we attributed subcellular alterations to cell cycle dynamics and DNA integrity to loss of *Smed-PTEN* nuclear function. Studies in *Schmidtea mediterranea* will provide unique opportunities to analyze the OTS-DDM during simultaneous renewal of many tissues in the context of the adult body.

Nuclear PTEN is seen to maintain many facets of cell cycle progression, centromere stability, chromatin condensation and the mitotic checkpoint [171], [484], [488], [489], [538], [547], [549], [550], [586]. *Smed-PTEN(RNAi)* led to rapid alterations to cell cycle dynamics prior to the onset of hyperproliferation. Alterations to cell cycle dynamics resulted in two distinct phases of the phenotype: (1) accumulation of cells in G0/G1 in the first three days and (2) increase of S/G2/M cellular events day four and

onward. The accumulation of cells within G0/G1 at 2-days RNAi is consistent with nuclear PTEN tumor suppressive activity and its function with Rb cell cycle inhibition [429], [442]. Furthermore, alterations to cell cycle 2 days *Smed-PTEN(RNAi)* were accompanied by a strong DDR and damage repair signaling response. Despite the detection of DNA damage, *Smed-PTEN(RNAi)* fail to repair DSBs and neoblasts harbored chromosomal abnormalities. These results provide us with evidence that *Smed-PTEN* functions within the nucleus to preserve genomic stability and prevent DSBs accumulation, as seen in other models.

PTEN lacks traditional nuclear localization sequences required for the tagging of its import into the nucleus by nuclear transport. PTEN can conduct its nuclear functions through nucleocytoplasmic shuttling mediated by post-translational modification of phosphorylation and ubiquitination. Human cancers share properties referred to as hallmarks, among which sustained proliferation, escape from apoptosis, and genomic instability are the most pervasive. The sustained proliferation hallmark can be explained by mutations in oncogenes and tumor suppressors that regulate cell growth, whereas the escape from apoptosis hallmark can be explained by mutations in the TP53, ATM, or MDM2 genes. A model to explain the presence of the three hallmarks listed above, as well as the patterns of genomic instability observed in human cancers, proposes that the genes driving cell proliferation induce DNA replication stress, which, in turn, generates genomic instability and selects for escape from apoptosis. Here, we review the data that support this model, as well as the mechanisms by which oncogenes induce replication stress. Further, we argue that DNA replication stress should be considered as a hallmark of cancer because it likely drives cancer development and is very prevalent [237] [393] [425]. The planarian contains highly conserved proteins that regulate PTEN nucleocytoplasmic shuttling. Our analysis identified that suppression of this network results in an early onset of hyperproliferation 2 days RNAi and lead to premature tissues outgrowths and lethality. These results imply that (1) *Smed-PTEN* functions within the planarian, (2) nuclear *Smed-PTEN* plays an active role in the early stages of the phenotype to prevent premature onset of cellular hyperproliferation and (3) that the accumulation of chromosomal abnormalities and DSBs may result from loss of nuclear PTEN. However, the correlation between nuclear PTEN shuttling and accumulation of DSBs will need to be further investigated. Taken together, with loss of *Smed-PTEN*, cell cycle alterations, DNA damage and chromosomal abnormalities are pervasive feature of the early phase of the PTEN phenotype and may be due to loss of *Smed-PTEN* within the nucleus. Our findings are consistent with other studies that show the exclusion of nuclear PTEN results in increased accumulation of genomic instability and predisposition to cancer onset (e.g. Cowden and Bannayan-Riley-Ruvalaba Syndrome) [365]–[370], [386], [396].

Downregulation of *Smed-PTEN* leads to an increase of neoblasts exhibiting abnormal chromosome segregation. Specifically, we identified an increase in metaphase and anaphase defects that was correlated to suppressed gene expression of specific to these two phases. We also noted that relative to the control *Smed-PTEN* downregulation resulted in mitotic deformities that persisted past the spindle assembly checkpoint. These results are consistent with the role of PTEN in regulating the timely formation of the spindle assembly checkpoint; preventing chromosomal abnormalities, aneuploidy and the development of cancer [538]–[540], [547]. *Smed-PTEN(RNAi)* neoblasts harboring DSBs were found to evade programed cell death early within the phenotype. Moreover, assessing metaphase specific congression and segregation allowed us to identify that neoblasts contained abnormal spindle geometry, overexpressed Histone 3 and enlarged congressional index. RNAseq results identified that proteasome activity was severely

suppressed throughout the phenotype. Proteasome activity is required for faithful centromere separation and the removal of excess non chromatin-bound histone H3 during mitosis [591], [592]. The removal of histone H3 from the centromere allows for the incorporation of the centromere specific variants such as CNEP-A to the nucleosome [593]. Hyper-phosphorylation of H3 leads to mitotic defects including alterations in spindle attachment, delayed cytokinesis, reduced chromatin packaging, cohesion loss, cohesion and condensin I loss [591]. Interestingly, *Smed-PTEN(RNAi)* animals exhibited reduced gene expression of centromere specific variants (e.g. *CENP-A, -H* and *-S*) found in the nucleosome. Together, the loss of proteasome activity may result aberrant Histone H3 expression surrounding the centrosomes subsequentluy resulting in an enlarged congressional index. Overall, with the loss *Smed-PTEN,* abnormal neoblasts circumvent cell death and bypass the spindle assembly checkpoint; providing the basis for neoblast transformation.

Defects found within anaphase have been attributed to cells incapable of repairing DNA damage or DNA replication stress acquired in S-phase [484]. Therefore, by using DNA damaging agents (e.g. APH and γ-irradiation) we identified that *Smed-PTEN(RNAi)* neoblasts can enter mitosis despite the acquisition of damage. Furthermore, increased rates of neoblsats entering G2/M were identified to be day 2 RNAi specific. This may be due to impairment of both the G2/M and M-phase checkpoints and DNA decatenation process, known to result from PTEN loss of function [508], [520], [524], [541]. Furthermore, prolonged pausing in metaphase increases mitotic catastrophe-mediated apoptosis or the activation of DNA damage repair. We identified that relative to the control, *Smed-PTEN(RNAi)* animals under metaphase hault exhibited an increase in neoblasts harboring RAD51 foci and no alterations to the rate of Caspase3+ foci. It is tantalizing to source the increase in RAD51+ foci found in mitotic neoblasts to S-phase, but further experiments will be needed to distinguish the source (e.g. M-phase, S-phase or both). Together, these results suggest one of two things: (1) prolonged halting of RNAi neoblasts in metaphase results in cell death by alterantive methods and (2) that not all neoblasts at day 2 RNAi have a heterogenous outcome to metaphase pausing. Lastly, these results suggest that approximately 20% of neoblasts at day 2 RNAi have abnormal characteristics.

Here, we propose that upon the first injection, small pools of *Smed-PTEN* that reside in the nucleus are abrogated resulting in the initial formation of DSBs and chromosomal abnormalities. However, with the aid of nucleocytoplasmic shuttling proteins, cytoplasmic *Smed-PTEN* is transported into the nucleus. Restoration of nuclear *Smed-PTEN* may be the cause of the reestablishment of checkpoint stability and mild recovery of DNA integrity found at day 3 RNAi. Furthermore, with the addition of the second dsRNA injection of *Smed-PTEN*, both nuclear and cytoplasmic pools of *Smed-PTEN* are lost resulting in the onset of cellular hyperproliferation 4 days RNAi. Together, our results identify the that planarian cancer model provides new insight to study the OTS-DDM model. *Smed-PTEN(RNAi)* neoblasts contain DNA damage and DNA replication stress early within the phenotype accompanied by sustain cellular proliferation. However, with our model we identified that mitotic stress (i.e. disordered mitotic spindles and segregation) and evasion of cell death are pre-cancerous characteristics that promote cancer progression. Gene expression of oncogenes are shown to be elevated 2 days into the phenotype, but the combination of RNAi and protein level experiments will be required to rule out if these events are *Smed-PTEN(RNAi)* specific or oncogene induced. Furthermore, we were unable to prove whether DNA replication stress or DNA damage occurred first and whether these outcomes were a result of the loss of PTEN tumor

suppressor activity or an increase in oncogenic activity. Experiments with DNA fiber assay with COMET assay will aid in which DNA alteration event occurs first.

CHAPTER SEVEN

METHODS

Planarian Cultivation

The clonal asexual strain CIW4 of *Schmidtea mediterranea* was used in all experiments. Animals were kept and maintained as previously described [56], [108], [594]. Planarian were raised in large Ziploc Tupperware container held at a constant temperature of 20ºC in an incubator void of light. Planarians were maintained in 1x Montjuic salt water. P-H_2O was stored in sterilized (30min 15lb/sq in dry cycle) carboys (Nalgene/VWR:16117-977) and P-H_2O was made at a 10X concentration of 1.5L and diluted in 13.5L of MqH_2O. The 10X P-H_2O was made as followed: 2.33g NaCl, 3.68g $CaCl_2$, 3.0g $MgSO_4$, 0.24g $MgCl_2$, 0.19g KCl and 2.53g $NaHCO_3$; diluted in 1.5L MqH_2O (18mΩ) (NaCl; Sigma, Cat# S3014) ($CaCl_2$; Sigma, Cat# C5080) ($MgSO_4$; Sigma, Cat# M7506) ($MgCl_2$; Sigma, Cat# M8266) (KCl; Sigma, Cat# P9541) ($NaHCO_3$; Sigma, Cat# S5761). Importantly, pH was adjusted to 7.0 with 2N HCL (HCl; Fisher, Cat# A144-500). Planarian were feed once a week in a regimented schedule, with organic bovine liver for 1-2hours. Animals were cleaned twice a week, once post feeding and another 2 days later by removing all P-H_2O from the containers, rinsing all animals to one corner and discarding the rise P-H_2O and lastly, the containers surface is wiped down to void any liver residue and mucous build up using natural/untreated hand towels.

Gene Selection Tools

Identification of Gene Homologs

There have been many updates and advances to the planarian genome and transcriptome since 2013 [61], [106], [116], [117], [162], [248]–[253]. Over the years genes in my dissertation have been identified and validated countless times with the various genome/transcriptome updates. Thus, gene identification has been cross-referenced in SmedGD 2.0 (Robb et al. 2015), PlanMine1.0 (Brandl et al. 2016), Toronto Transcriptome (Swapna et al. 2018) and PlanMine3.0 (Rozanski et al. 2019) [106], [116], [117], [162]. Briefly, the gene of interest was found in UniProtKB [595] for the human counterpart and FASTA file was obtained. The human sequence was BLASTed in the various planarian genomes/transcriptomes and the top BLAST outputs were selected for their percent identity, e-value and bit score. To validate top BLAST hit, the planarian protein sequence was placed into NCBI (https://blast.ncbi.nlm.nih.gov) and sequence identity was further confirmed by Blastn, Blastx, Blastp and alignment tools. Other sites to confirm protein domain conservation, NCBI Conserved Domain (https://www.ncbi.nlm.nih.gov/Structure/cdd/wrpsb.cgi), Prosite database to identify protein domains, families and functional sites within the sequence (https://prosite.expasy.org/prosite.html) and Pfam (http://pfam.xfam.org/) yielded a six-frame translation of the identified sequence.

Protein Alignments and Protein Modeling

The identified sequence was aligned to various species by using Clustal OmegaV2.1 (https://www.ebi.ac.uk/Tools/msa/clustalo/) with sequences obtained using HomoloGene (http://www.ncbi.nlm.nih.gov/homologene) and/or UniProtKB. Clustal OmegaV2.1 provided neighbor-joining tree, percent identity matrices and sequence alignments of the multiple sequence inputs. Further, the output sequence alignment code was placed into SeaViewV4.7 (http://doua.prabi.fr/software/seaview) to produce a color-coded protein sequence alignment. Protein modeling of conserved structures, domains and active sites were created by IBS1.0.3 (GPS) (http://ibs.biocuckoo.org/download.php) with results derived from NCBI Conserved Domain, Prosite, Pfam and Jalview2.10.5 (http://www.jalview.org/).

Primer Identification and Selection

The protein sequence for the identified gene of interest is placed into NCBI Primer-BLAST (https://www.ncbi.nlm.nih.gov/tools/primer-blast/). Cloning primers were chosen to amplify a 400–700bps region of the gene of interest. Primers aimed to be cloned for RNA interference by feeding have an addition attB flanking sequence and is discussed in detail in a subsequent section. As for quantitate RT-PCR, primers are chosen to amplify a 75-150bps region of the target sequence. Forward and reverse primer pair selection was based off GC content (~50%), melting temperature (~60ºC) and sequence length (~20pbs).

RNA Extraction and DNA Amplification Tools

RNA Extractions from Whole Planarian

Isolating high-quality RNA from whole planarian is a well-established technique, requiring tissue homogenization in trizol and subsequent purification steps [596]. Whole planarians, 15-20 animals per condition, are placed into a 2mL tube and all residual P-H_2O is removed from the tube. To stabilize RNA, 1mL of trizol (Trizol; Life Tech, Cat# 15596026) is added to the tube, vortexed and allowed several minutes to sit on ice before starting the extraction or samples are stored in the -80˚C until extraction is to take place. Samples are homogenized one of two ways: (1) upright tissue homogenizer (THb; OMNI, Cat# THB2081) for 1min with a stringent cleaning procedure of the probe (e.g. 1min per solution: MqH_2O, 1%SDS, MqH_2O, MqH_2O, 3N NaOH, MqH_2O); probe homogenization can be conducted in 2mL graduated flat cap tube (Microcentrifuge tubes; Fisher, Cat# 02-681-332) or (2) tissue is homogenized by bead mill homogenizer (Bead Ruptor24; OMNI, Cat# 19-040E) with disruptor beads (Beads; CLS, Cat# CLS-1835-BG5) for 30-60 seconds; bead mill must be conducted in 2mL screw cap tubes (Microcentrifuge tubes; Fisher, Cat# 02-707-355).

After Homogenization, 266.6µL of chloroform (200µL chloroform/750µL Trizol) (Chloroform; Fisher, Cat# C606-4) is added to each sample and vortexed for 10-15sec and allow samples to sit for 3mins at room temperature. Samples are then spun down at 11000rpm at 4˚C for 15minutes to allow for separation of digested RNA and trizol. Place top layer void of pink trizol in a fresh 1.5mL Eppendorf tube. Add 666µL of isopropanol (500µL chloroform/750µL Trizol) (Isopropanol; Fisher, Cat# A516-500) and samples are mixed by inversion for 10-20sec and samples rest at room temperature for 10mins.

Thereafter, samples are spun down at 11000rpm for 10mins at 4˚C. RNA is pelleted, and supernatant is decanted. Subsequently, pellet is washed with 1mL of chilled 75% 200 proof ethanol (Ethanol 200; ACROS, Cat#61509-5000) diluted in MqH_2O and spun down at 7500rpm for 5mins at 4˚C. Ethanol is decanted and all traces of ethanol are removed by table top centrifugation. Depending on RNA pellet size, it is dissolved in 10-15µL of nuclease free water (Water; Fisher, Cat# BP2484-100); avoid oversaturation with water. Extracted RNA is kept on ice and assed for purity and concentration using a NanoDrop (NanoDrop Spectrophotometer; Thermo, Cat# ND-1000). Samples are stored in -80˚C, longer term.

Complementary DNA Synthesis

The synthesis of cDNA requires genomic RNA obtained from RNA extractions of a control asexual strain CIW4 of *Schmidtea mediterranea* and using VERSO cDNA synthesis kit (VERSO; Thermo, Cat# AB-1453/B). Set up a master mix, in PCR tube, for a 20µL reaction: 4µL of 5x cDNA synthesis buffer, 2µL of dNTPs mix, 1µL of Anchored Olgio dT, 1µL RT enhancer and 1µL VERSO enzyme mix. The master mix was brought up to a 20µL reaction by adding nuclease free water that is dependent on the volume needed to obtain 1µg/µL concentration of template RNA determined by Nanodrop. Resuspend mixture and set samples in the thermocycler and set the following parameters: 1 cycle of 30mins incubating at 42°C followed by 1 cycle of 2mins at 95°C and hold at 4°C. Samples are stored at -20°C, long term.

Polymerase Chain Reaction and Gel Imaging

PCR reactions are used to amplify target genes for cloning or amplify flanking sequences for dsRNA and riboprobe production. PCR reactions are conducted using Taq DNA polymerase dNTPack (PCR pack; Sigma, Cat# 04738225001) Set up a master mix, in a PCR tube, for a 50µL reaction by adding 1µL of PCR grade nucleotide mix, 5µL of PCR reaction buffer with MgCl and 0.5µL of Taq DNA Polymerase into a tube. Next, add 41.74µL nuclease free water, 0.5-1µL of genomic cDNA or purified target DNA and add 0.625µL of both forward and reverse primer to amplify the target or flanking region sequence; mix all components. Set samples in the thermocycler and choose the following parameters: 1 cycle of 5mins incubating at 94°C, 30-32 cycles of 30sec at 94°C for denaturing, 30sec at 56.5°C for annealing and 45sec at 72°C for elongation temperatures and end with 1 cycle of a 10min incubation at 72°C and hold at 4°C.

Make a 1% agarose gel (0.4g agarose in 40mL 1xTBE) (10x TBE: 108g Tris Base, 55g Boric Acid, 10mM EDTA in 1L MqH_2O) (Agarose; Sigma, Cat# A9539-500G) (Trizma base; Sigma, Cat# T1503-1KG) (EDTA; Fisher, Cat# BP120-500) (Boric Acid; Fisher, Cat# A73-1). Heat in microwave to dissolve mixture and once dissolved add 5µL of ethidium bromide 1% solution (EtBr; Fisher, Cat# BP1302-10). Pour mixture into gel electrophoresis system cast chamber and allow for 1 hours to solidify. Add 1xTBE into the electrophoresis system, to fill line, and load the wells with 3µL of 1kB Plus DNA ladder (DNA ladder; Fisher, Cat# BP2579100) and 5µL of PCR product diluted in 2µL of 6x DNA loading dye (Loading Dye; Thermo, Cat# R0631). Run the gel at 100V 0.05A for 40-60mins. Once complete, gel was imaged a gel documentation system (Enduro GDS; Labnet; Cat# GDS-1302) under an UV transilluminator filter.

Cloning and Transformation Tools

Cloning for T3 and T7 promoter regions

With the end goal of synthesizing dsRNA or ISH probes, amplified cDNA fragment of interest was TA cloned into pCR2.1-TOPO TA Vector (TOPO TA Cloning Kit; Invitrogen, Cat # 45-0030). Master mix was created: 2µL of amplified DNA from fresh PCR product, 1µL salts (NaCl (1.5M), $MgCl_2$ (0.06M)), 2µL sterile water and 1µL of TOPO-activated TA vector (10ng/µL). The liquid was gently mixed and incubated at room temperature for 30mins. Place on ice and proceed to transformation.

Cloning for attb flanked feeding vectors

attB primer flanks were added to primer sequence for the gene of interest. These flanks are required for cloning of feeding vectors used to induce dsRNA by INPG. Primers flanks are: forward 5'-GGGGACAAGTTTGTACAAAAAAGCAGGCTT-3' and reverse 5'-GGGACCACTTTGTACAAGAAAGCTGGGTT-3'. The gene was cloned into the pPR244 vector using Gateway BP Clonase II kit (Gateway Clonase II Kit; Invitrogen, Cat# 11789-020). Master mix was created: 1µL of amplified attB-primer DNA from fresh PCR product, 1µL of pPR244 plasmid, 4µL 5xBP clonase reaction buffer and 10µL of EB buffer. Lastly, add 4µL of enzyme to the reaction and mix well by vortexing and incubate the reaction 25°C overnight. To complete the reaction, add 2µL of Proteinase K (Proteinase K; Invitrogen, Cat# 25530049) to terminate the reaction, vortex and incubate samples at 37°C for 10mins. Place on ice and proceed to transformation.

Cellular Transformation

The newly generated vector is transformed into NEB5α competent bacteria (NEB5α; NEBL, Cat# C2987H). Place 25µL of NEB5α competent bacteria into a 1.5mL tube and depending on what cloning method was used add the following vector amount to the bacteria: 10µL for Gateway Clonase II Kit or 5µL for TOPO TA Cloning. Reaction incubated on ice for 30mins and subsequently, the reaction underwent heat shock at 42°C in a water bath for 30sec and immediately returned to ice for 2mins. Add 450µL of SOC outgrowth medium (SOC medium; NEBL, Cat# B9020S) per reaction and incubate for 1 hour at 37°C at 225rpm. The medium was then plated using sterile technique. Thus, 300µL of the sample was added to a pre-warmed LB agar plates contacting antibiotics (LB recipe: 7.5g LB Agar, 5g Bacto-tryptone, 2.5g Bacto yeast extract and 5g NaCl in 500mL MqH_2O; pH 7) (LB Agar; Fisher, Cat# BP1425-500) (Bacto-Tryptone; BD, Cat# 211705) (Bacto Yeast Extract; BD, Cat# 212750). Importantly, kanamycin (Kanamycin Sulfate; Fisher, Cat# BP906-5) plates were used for pPR244 vectors and carbenicillin (Ampicillin sodium salt; Sigma, Cat# A-9518) plates were used for TOPO vector. Plates were allotted 30mins to incubate face-up at room temperature and then incubated face down overnight (16-20 hours) at 37°C in an incubator. Once several colonies have grown, pick one independent colony with a 10µL pipette tip and validate that the colony contains the gene of interest by running a PCR in a 24µL using your colony as the DNA in the reaction and cloning/flanking primers. After amplification is confirmed, place colony into a 15mL round bottom tube containing 5mL 2XYT media (2XYT media: 16g Bacto-tryptone, 10g Bacto yeast extract and 5g NaCl in 1L MqH_2O; pH 7). Before incubation add 10µL of your vector specific antibiotic at 100µg/mL concentration. Incubate tube overnight (16-20 hours) at 37°C at

225rpm. Importantly, pPR244-NEB5α will be further transformed into HT115 competent bacteria as it has specific sights for IPTG induced dsRNA production. This will take place with purified pPR244-NEB5α plasmid DNA created through Miniprep purification.

DNA Purification

Before purifying DNA, glycerol stocks were made for each gene using a 1:1 dilution of glycerol (Glycerol, ACROS, Cat# 41098-5000) and cultured bacteria and stored at -80°C. Ligated vectors were then isolated using Miniprep kit (Miniprep Kit; QIAGEN, cat# 27104). Overnight liquid cultures were spun down for 5mins at 5000rpm at 4°C. The media was decanted and pellet containing bacteria cells was resuspended in 250µL of Buffer P1/RNAse. Resuspended solution was then transferred into a 2mL tube and 250uL of P2 was added per tube, mixed by inverting 4-6 times and allowed to incubate for 5mins. 350uL of N3 Buffer was added per tube, invert gently ten times and spun down for 10mins at room temperature at 13000rpm. Supernatant is decanted into a QIA Prep spin column and pellet is tossed. Spin samples for 1min room temperature at 13000rpm and discard flow through by pipetting. Add 500uL PB Buffer to the columns and spin for 1min room temperature at 13000rpm. Remove flow through by pipetting. Add 750uL PE/Ethanol (wash buffer) per column and spin for 1min room temperature at 13000rpm. Remove wash buffer and then spin again for 1min room temperature at 13000rpm to remove residual buffer. Place columns into a freshly labeled 1.5mL tube and then add 50uL nuclease free water to the center of the column, let sit for 2mins and spin samples for 1min room temperature at 13000rpm. Repeat with eluted liquid. The concertation and purity of the DNA was established using NanoDrop. Isolated vectors were diluted 1:10 and used to generate PCR products using T3/T7 flanking primers. At this point dsRNA or riboprobes were produced as described in Oviedo et al. 2008 [56]. As for the feeding vector, this purified DNA will be used in the transformation process and placed into HT115 competent bacteria.

Restriction Digest, Gel Extraction and Ligation

Placing TOPO vector into pBlueScript plasmid to ensure stability of the vector, once complete will be used for dsRNA and riboprobe synthesis. Restriction enzyme digestion by creating a 25µL digest by adding 0.5-1µL of Not1, BamHI, XhoI or Pst1, add 2.5µL of NEB2.1 in MqH_2O determined by the concentration of DNA needed to obtain 1µg. Incubate reaction at 37°C for 2 hours (Not1; Thermo, Cat# ER0595) (BamHI; NEBL, Cat# R0136S) (Xhol; NEBL, Cat# R0146S) (Pst1; NEBL, Cat# R0140S).

Samples are run on a 2% agarose gel at 120 volts for 1 hour. Get was then used to begin the gel extraction using a kit (Gel Extraction Kit; QIAGEN, cat# 28704). Gel bands with appropriate weight as placed with 3x volume of QG buffer and incubates at 50°C for 15mins or until gel slice was dissipated. If the color of the solution is not yellow, proceed to add 10µL 3M Sodium Acetate. Relative to the initial volume of gel added to the reaction, add isopropanol to the reaction and mix by inversion. Add 750µL of mixture to spin column, spin samples for 1min room temperature at 13000rpm and decant liquid; repeat if liquid still remains. To remove agarose, add 500µL of QG buffer and spin column for 1min room temperature at 13000rpm. Wash with 750µL PE buffer contacting ethanol and spin column for 1min room temperature at 13000rpm. Decant liquid and spin again for 1min room temperature at 13000rpm. Place columns into a freshly labeled 1.5mL tube and then add 25uL nuclease free water, let sit for 2mins and spin samples for 1min room temperature

at 13000rpm. Repeat with eluted liquid. The concertation and purity of the DNA was established using NanoDrop.

Now ligation of purified DNA into pBlueScript plasmid using DNA Ligation Kit (Rapid DNA Ligation Kit; Thermo, Cat# K1422). To do so, create the following reaction: 4µL of 5xRapid ligation mix, 5µL of T4 DNA ligase, 25ng of pBlueScript vector DNA (16.1ng/µL), 75ng of DNA and complete the reaction up to 20µL with nuclease freed water. At this point, the DNA fragment which was T4 ligated between the T3 and T7 promoter region of the pBlueScript plasmid (pBlueScriptII(+); Agilent Tech, Cat# 212207). With the reaction, transformation into NEB5α competent bacteria of plasmid DNA containing the ligated pBlueScript can take place, isolated using carbenicillin (100 µg/mL), cultured, obtain purified DNA and T3/T7 flanking PCR can be conducted.

RNA Interference Tools

In Vitro Double Stranded RNA Preparation

To being dsRNA synthesis, cDNA of the cloned target gene PCR primers are crated to amplify the gene of interest by flanking T3 and T7 promoter sequences onto it [298], [597]. Primer sequences are T3: 5'-AATTAACCCTCACTAAAGGG-3' and T7: 5'-GTAATACGACTCACTATAGGGC-3'. Amplified T3 and T7 fragment (T3/T7 DNA) of the cloned gene was used to synthesize single stranded T3 and T7 separately. Begin by making a master mix of synthesis solution in a DNAse/RNAse 1.5mL tube. The mixture is as follows: 4µL of nuclease free water, 4µL of 5xTrans Buffer (Trans Buffer; Fisher, Cat#P118B), 4µL of equal mixture of 5xrNTPs (rNTPs; Promega, Cat# P114A, P113A, P115A, P116A), 2µL of 100mM DTT (DTT; Promega, Cat# P117B) and 1µL of Recombinant RNAsin Ribonuclease Inhibitor (RNasin; Promega, Cat# N251B). Mixture was resuspended several times to ensure homogeneity and was split into two separate tubes to synthesize T3 and T7 ssRNA alone thereby, adding 1µL T3 RNA polymerase (T3 Pol; Promega, Cat# P208C) or 1µL of T7 RNA polymerase (T7 Pol; Promega, Cat# P207B). Lastly, 4µL of T3/T7 PCR product was placed in each tube, resuspended and incubated at 37°C for 2 hours or overnight for no more than 16 hours.

Thereafter, 1µL of RQ1 RNase-Free DNase (DNAse; Promega, Cat# M6101) was added and incubated at 37°C for a minimum of 15mins to 1 hour. 1 µL of the synthesized T3 and T7 mixtures were separately stored in -20°C; this will be run in the gene to ensure synthesis worked. Both T3 and T7 mixtures were combined into one tube and 380µL of STOP solution (1mL 10% SDS filtered, 0.1471g EDTA, 5mL ammonium acetate and fill to 50mL with MqH_2O) (1M ammonium acetate, 10mM EDTA, 0.2% SDS) (Ammonium acetate; Fisher, Cat# A637-500) is added and incubated at room temperature for 10mins. Next, adding 200µL of Phenol-chloroform (Phenol-chloroform; Fisher, Cat# BP17521-400), samples were vortexed for 15sec each and centrifuged 2mins at 14000rpm. Place the top aqueous layer into a new tube and add 200µL of chloroform. Samples were vortexed for 15sec and centrifuged for 2mins at 14000rpm. Transfer aqueous phase to a fresh tube. Samples were incubated at 68-72°C for 10mins and the annealing process occurring by allowing the samples to cool within the heat source until reaching room temperature (1-2 hours or overnight) or a 30min incubation at 37°C is sufficient if timing is an issue. Samples were ethanol purified as follows: 1mL of 100% ethanol was added and centrifuged for 10mins at 13000rpm, 4°C. The ethanol was carefully decanted and 1mL of 80% ethanol was added and centrifuged for 10mins at 13000rpm, 4°C. All traces of ethanol were removed by using a table top centrifuge and dsRNA pellet was resuspended

10µL of nuclease free water. The previously stored single stranded T3 and T7 sample and the synthesized double stranded samples were run on a 1% agarose gel and 0.5µL sample was used per well mixed with loading dye. dsRNA is stored long term in -20°C

RNA Interference by Injecting *In Vitro* dsRNA

Consecutive injections with dsRNA has been a well-established protocol in the planarian field to disrupt gene expression allowing analysis of gene during tissues homeostasis and regeneration [112], [125], [298], [594], [597]. Planaria were then placed dorsal side up, atop peltier cooler covered with parafilm, a chilled KimWipe folded into a square with white or black Whatman paper (Whatman paper; Sigma, Cat# WHA1001325) atop it and all excess planaria water was removed using a pasture pipette. Glass microelectrodes were made with a Flaming/Brown micropipette puller (Puller; Sutter, Cat# P-97) by pulling 100mm; 1/0.58 OD/ID (mm) glass capillaries (Capillaries; World Precision Instruments, Cat# 1B100F-4) stretched under the following parameters: heat 800, pull 55, velocity 35, time 1 for approximately 7-8sec. Microelectrodes are filled with mineral oil (Oil; Fisher, Cat# BP2629-1). A Drummond Nanoject II Auto-Nanoliter Injector (Injector; Drummond; Cat# 3-000-204) was used to administered 2-3 pulses containing 32nL of dsRNA each injection. To rule out the possibility of local neoblast depletion, microinjections targeted the pre-pharyngeal area to assure effective dsRNA incorporation as well as homogeneous distribution throughout the body, visualized by gastro-vascular system bloating and expansion. Both control and treated animals received equal amount of injections, controls were injected with nuclease free water and a protocol for each gene downregulation was optimized for each gene. Experimental animals were stored in polystyrene petri dish 100mmx25mm (Petri Dish; Fisher, Cat# FB0875711) and cleaned weekly during the duration of the injection time course.

RNA Interference by Feeding *In Vitro* dsRNA

Induction of bacterially expressed dsRNA inhibits gene expression in planarian and is a robust method for high-throughput studies [598], [599]. Briefly, primers with attB flanking sites were generated for the gene of interest. PCR products were generated using cDNA synthesized from RNA of asexual *S. mediterranea* animals. The gene was cloned into the pPR244 vector using BP Clonase II kit. The newly generated vector was transformed into NEB5α competent bacteria and then into HT115 competent bacteria. Therefore, before starting RNA interference by feeding, create an overnight liquid stock culture by inoculating a 10µL pipette tip with glycerol stock containing the HT115 bacteria with the vector containing target gene. Place the pipette tip into 5mL of 2XYT media contacting kanamycin (50mg/mL) and tetracycline (10mg/mL) and grow overnight (16-20 hours) at 37°C at 225rpm. This stock liquid culture can be stored 4°C. To start the dsRNA synthesis for RNA interference, generate a feeding tube by obtain 500µL of stock liquid culture bacteria and add it to a 15mL round bottom tube containing 4.5mL of 2XYT media contacting antibiotics. Rock culture at 37°C at 225rpm until the optical density of the culture reaches an OD595 of 0.400. Once the desired absorbance is reached, add 50µL of 0.1M IPTG (IPTG; Fisher, Cat# DP1755-1) was added and incubated for an additional 4 hours. The media was pelleted at 5000rpm at 4°C for 5mins, liquid then was decanted, and the pellet was mixed with 25µL of calf liver. Planarian are housed in polystyrene petri dish 100mmx25mm and fed for 1-2 hour or overnight. Once feeding period is over, dishes are cleaned, and P-H_2O is added once feed period is complete. The duration of RNA interference by feeding were optimized per gene and feeding schedule was optimized to

maintain worms at a relatively small size (<4mm) so molecular experiments can be conducted with ease.

Planarian Fixations Methods

Carnoys Fixation

Carnoys fixation has been used in planarian to penetrate the mucus barrier and is used to fix animals for BrdU and Immunohistochemistry protocols [56], [600]–[603]. However, depending on antibody penetrance other fixatives may be required [307]. Place control and treated animals in designated 20mL glass scintillation vials (Fisher, Cat# 03-337-14). Before starting, all reagents must be ice cold before use (e.g. HCl and Carnoys fixative) or from -20ºC freezer (100% Methanol). Remove P-H_2O and simultaneously, kill animals and remove mucous layer by submerging them in 5.7% HCl (570µL of 12.1N HCL and filled to 10mL with MqH_2O) on ice for 5mins sharp. Completely remove HCl solution and fix animals for 2 hours on ice with gentle agitation, using Carnoys fixation solution (6:3:1 ethanol, chloroform, acetic acid) (Ethyl Alcohol Denatured; Fisher, Cat# A407-4) (Acetic Acid; Fisher, Cat# A38-500). Lastly, remove Carnoys solution, rinse with cold (-20ºC) 100% Methanol (Methanol; Fisher, Cat# 177145) and add fresh 100% Methanol onto animals and place in -20ºC for a minimum of 1 hour and this is a stopping point for long-term storage.

NAC Fixation: *in situ* Hybridization

5% NAC fixation removes planarians of their mucous, as it is a mucolytic, and kill animals to be best used in WISH/FISH experiments [604]–[606]. Remove P-H_2O from 20mL glass scintillation vials and submerge animals in 5% NAC solution (0.5g NAC in 10mL 1xPBS) (NAC; Sigma, Cat# A7250-100G) (10xPBS; Fisher, Cat#7647-14-5). Animals should be rocking at room temperature for 10mins in 5% NAC. After 5mins, NAC solution is replaced with 4% formaldehyde (1.1mL 36.5% formaldehyde in 10mL 0.3%PBSTx) (0.3%PBSTx solution preparation is in subsequent section) (Formaldehyde solution; Sigma, Cat# F8775-500ML) for 20mins at room temperature and rocking. Fixative is immediately removed, and animals were quickly rinsed twice with 0.3%PBSTx. Animals are now placed in preheated reduction solution (50mM DTT, 1% Tergitol, 0.5% SDS, in 1XPBS) (Dithiothreitol; Sigma, Cat# 3483-12-3) (Tergitol NP-40; Sigma, Cat# NP40S-100ML) (20% SDS; Fisher, Cat# BP1311-200) for 10mins at 37ºC water bath occasionally agitating to aid in animal permeabilization. Following reduction, samples were rinsed twice with 0.3%PBSTx and then dehydrated to 100% methanol using serial dilutions of 50% Methanol in 0.3%PBSTx and 100% Methanol, both for 5mins and rocking. Rinse with 100% methanol and place animals in fresh 100% Methanol; store in -20ºC for long term.

NAC Fixation: TUNEL Assay

10% NAC fixation yields optimal signal and reproducibility TUNEL assay [101]. Thus, animals are placed in 20mL glass scintillation vials and incubated and rocked at room temperature, for 5mins in 10% NAC (0.8g NAC in 8mL 1xPBS). NAC solution is removed, and animals are fixed in 4% formaldehyde (1.1mL formaldehyde in 10mL 0.3%PBSTx) for 20mins at room temperature and rocking. Fixative is immediately

removed, and animals were quickly rinsed twice with 1xPBS. Lastly, animals were permeabilized for 20mins at room temperature and rocking, in 1% SDS (0.5mL of 20% SDS in 10mL 1xPBS). Animals are quickly rinsed twice with 1xPBS and placed in 0.3%PBSTx. Importantly, at this point, animals are hydrated, 6% bleaching should occur in 0.3%PBSTx (2mL of 30% H_2O_2 in 8mL 0.3%PBSTx) (30% H_2O_2; GR ACS, Cat# HX0635-3) not Methanol. Once bleaching is complete, animals are rinsed in 0.3%PBSTx and TUNEL assay can commence. Usually, TUNEL assay is done on bleached animals immediately however, short term of animals in in 0.3%PBSTx cannot exceed 1 week. Not favorable, however, long term storage of animals is possible, and animals can be dehydrated to 100% methanol using serial dilutions of Methanol in 0.3%PBSTx from 0% to 50% Methanol and from 50% to 100% Methanol at 5mins intervals and rocking. Store in -20ºC.

Animal Bleaching and Rehydration

Remove 100% Methanol and add 6% bleaching solution (2mL of 30% H_2O_2 in 8mL Methanol) and place vials under a light source overnight or until completely bleached. Remove bleaching solution and rinse with room temperature 100% methanol and place back into the -20ºC for at least 1 hour. This is a stopping point for long-term storage. To begin experiments, rehydrate animals by removing 100% Methanol and replacing the solution with 50% Methanol in 0.3%PBSTx (50mL 10xPBS, 1.5mL Triton X-100 and fill to 500mL with MqH_2O) (Triton X-100; Sigma, Cat# T8787-100mL) for 5mins circulating. Remove the 50% Methanol solution and at 100% PBSTx (0.3%) for 5mins circulating. At this point animals are ready for blocking or animals can be stored at 4ºC for short term, no longer than 1 week. To block animals, 0.2% BSA in 0.3% PBSTx (0.125g BSA in 50mL of 0.3% PBSTx and filtered before use) (BSA; Sigma, Cat# A2153-100G) for IHC based experiments and 0.4% BSA in 0.3% PBSTx for BrdU experiments is made and animals are submerged in blocking for 4 hours circulating at room temperature. Now proceed to antibody incubation.

Gene Expression Tools

Riboprobe Synthesis for *In Situ* Hybridization

Riboprobes were synthesized as previously described [56], [298], [604]. Amplified T3 and T7 flanks through PCR (T3/T7 DNA) of the cloned gene was used to synthesize single stranded T3 and T7 separately. Begin by making a master mix of synthesis solution for a 25µL reaction: 4µL of target PCR product, 11µL of nuclease free water, 5µL of 5xTrans Buffer, and 1.5µL of Recombinant RNAsin Ribonuclease Inhibitor. In addition, 2.5µL of RNA labeling mix is added. Note that 10xDIG specific (10xDIG RNA Labeling Mix; Sigma, Cat# 11277073910) riboprobes can be used for both colorimetric or fluorescent *in situ* hybridization. However, for a double fluorescent *in situ* hybridization one riboprobe will have to be DIG specific and the other 10xFluorescien specific (10xFluorescien RNA labeling Mix; Sigma, Cat# 11-685-619-910). Lastly, for each gene T3 or T7 riboprobe must be made to determine sense or antisense. Therefore, add 1µL of T3 RNA polymerase or 1µL of T7 RNA polymerase. Now that the reaction has been made, incubate samples at 37°C in a water bath for 1 hour. After this hour, add an additional 1µL of T3 or T7 RNA polymerase to the corresponding tube and incubate again at 37°C for 1 hour. 1µL of RQ1 RNase-Free DNase is then added and incubated for 15mins at 37°C.

Subsequently, for ethanol precipitation, add 2.7µL 5M Lithium Chloride (LiCl; Fisher, Cat# L121-500) and 54µL of ice cold 100% 200 proof ethanol to each tube. These tubes were then placed in the -80°C for 15mins and centrifuged for 20mins at 14000rpm at 4°C. Post removal of supernatant and any residual ethanol by table top centrifugation, the pellet was resuspended in 50µL of deionized formamide. Make a 1% agarose gel and 2µL of reaction is loaded. The result should yield double bands per sample.

Planarian Whole Mount *In Situ* Hybridization

Protocol was adapted from previously established literature [604], [605]. NAC fixed worms need to be rehydrated thus, in the glass vials, remove 100% Methanol and add 50/50 Methanol/0.3%PBSTx and incubate samples for 7mins. Replace solution and incubate animals with 100% 0.3%PBSTx for an additional 7mins. Remove 0.3%PBSTx and treat animals for 10mins with Proteinase K solution (1mL 10xPBS, 100µL 10% SDS, 1µL Proteinase K and fill to 10mL with MqH_2O). Fix animals for 10mins in 4% Formaldehyde fixative (1.1mL 36.5% formaldehyde and 8.9mL 0.3%PBSTx). Remove fixative and rinse twice with 0.3%PBSTx. Incubate samples for 15mins in 1:1 0.3%PBSTx: Wash-Hybe (5mL Deionized formamide, 2.5mL 20XSSC, 200µL 50xDenhardts and fill to 10mL with MqH_2O) (20XSSC; Sigma, Cat# S6639-1L) (Deionized Formamide; Sigma, Cat# S4117) (Denhardt's solution; Sigma, Cat# 30915). Remove solution and rock for 2 hours at 56°C in hybridization oven with Pre-Hybe solution (5mL deionized formamide, 2.5mL 20XSSC, 200µL 50xDenhardts, 0.010g Yeast RNA, 100µL Heparin, 50µL 10%Triton, 50µL 10%Tween, 50µL 1M-DTT and 2mL MqH_2O) (Tween-20; Sigma, Cat# P9416) (Yeast RNA; Roche, Cat#10-109-223-001) (Heparin; Sigma, Cat# 84020). During the 2-hour incubation, prepare the riboprobe mix by adding riboprobe into Ultra-Hybe solution (5mL deionized formamide, 2.5mL 20XSSC, 200µL 50xDenhardts, 0.010g Yeast RNA, 100µL Heparin, 50µL 10%Triton, 50µL 10%Tween, 50µL 1M-DTT, 1mL 50%Dextran Sulfate and 1mL MqH_2O) (Dextran Sulfate; Sigma, Cat# D8906). Riboprobe mix is then denatured at 72°C for 5mins and then brought to 56°C. After the 2-hour incubation and riboprobe mix has reached temperature, apply 1mL of riboprobe mix to each well and seal the well plate with aluminum sealing tape (Tape; Fisher, Cat# 07-200-684). Allow for hybridization to occur for ~16hrs at 56°C rocking in a hybridization oven.

Remove riboprobes and store at -20°C for future use. Perform each of the following washes three times for the duration of 30mins, with preheated solutions at 56°C and rocking in hybridization oven. Solutions are placed in this order: (1) Wash-Hybe, (2) 1:1 ratio of Wash-Hybe:2xSSC(0.1%Tx) (3) 2xSSC(0.1%Tx) (4) 0.2xSSC(0.1%Tx). Importantly, the last wash of 0.2xSSC(0.1%Tx) is done at room temperature. Remove solution and wash twice for 10mins at room temperature with MABT (11.6g Maleic Acid, 8.76g NaCl, 10mL 10%Tween, fill to 1L with MqH_2O and pH to 7.5 with NaOH) (Malic Acid; Sigma, Cat# M0375). Block animals for 1 hour in 1mL per well of MABT-B (9mL MABT, 1mL Horse serum and 0.1g BSA) (HyClone; GE, Cat# SH30074.03). For colorimetric reaction, dilute 0.5µL of Anti-DIG-AP (1:2000) (Anti-DIG-AP; Roche, Cat#11-093-274-910) per well contacting 1mL blocking solution and incubate samples overnight rocking at 4°C. For a fluorescent reaction, dilute 1µL of Anti-DIG-POD (1:1000) (Anti-DIG-POD; Roche, Cat# 11-207-733-910) in 1mL blocking solution.

Remove antibody and rinse twice with MABT. Subsequently, rinse six times for 10min intervals with MABT. For Tyramide Amplification Fluorescent development follow the protocol in the TSA section below. For NBT/BCIP Colorimetric development: Equilibrate with two 5min washes in AP Buffer (2mL 1M Tris pH 9.5, 1mL 1M $MgCl_2$, 400µL

5M NaCl and fill to 20mL with MqH_2O). Followed by one 5min washes in 5% PVA-AP Buffer (1mL 1M Tris pH 9.5, 500µL 1M $MgCl_2$, 200µL 5M NaCl, 5mL 10%PVA and fill to 10mL with MqH_2O) (Polyvinyl alcohol; Sigma, Cat# P8136). Place NBT/BCIP tablet (NBT/BCIP; Roche, Cat# 11697471001) in 10mL of 10%PVA and add to wells to initiate development for more than 30mins. When fully developed, rise twice with 0.3%PBSTx, followed by a 30min 4% paraformaldehyde fix (Paraformaldehyde; Sigma, Cat# P6148) and ending with two rinses with 0.3%PBSTx. If desired, wash animals with 100% Ethanol for 10mins at room temperature to remove background and incubate samples in 80% glycerol overnight in 4°C and mount.

Planarian Whole Mount Fluorescent *In Situ* Hybridization

Fluorescent *in situ* hybridization was adapted from previously established literature [605]. Samples stored in 100% methanol should be removed from -20°C and given 15mins to reach room temperature. Animals are rehydrated and introduced to 1x SSC in by rocking animals for 10mins in 50% methanol diluted in 0.1%PBSTx, then for 5mins in 0.1%PBSTx and lastly 1xSSC for 10mins. Now, animals placed into *in situ* baskets that are secured in a 24 well plate (Medium incubation baskets; Intavis, Cat# 12.440). Animals must be placed under a light source for 1.5 hours in bleaching solution (8.85mL MqH_2O, 250µL 20XSSC, 500µL Formamide and 400µL 30% H_2O_2) (Formamide; Fisher, Cat# BP227-500). Once bleached, replace solution with 1xSSC for 10mins followed by two washes with 0.1%PBSTx one for 5mins and another for 10mins. Samples are ready to be permeabilized for 10mins in Proteinase K solution (9.9mL 0.1%PBSTx, 100µL 10% SDS and 1µL Proteinase K). Solution is replaced and rocked for 10mins in 4% Formaldehyde solution (8.9mL 0.1%PBSTx and 1.1mL 37% Formaldehyde). Solution is replaced and animals are washed twice with 0.1%PBSTx, one for 5mins and another for 10mins. Animals are moved towards hybridization with an initial incubation of 10mins in 1mL of 1:1 ratio of 0.1%PBSTx:PreHybe solution (25mL Deionized Formamide, 10mL MqH_2O, 12.5mL 20XSSC, 2.5mL 20% Tween-20 and 1mL Yeast RNA). Replace the 1:1 solution with 100% PreHybe, 1mL per well, for 2 hours rotating at 56°C. During the 2-hour incubation, prepare the riboprobe mix by adding riboprobe into Hybe solution at a typical 1:800 concentration. Hybe solution (25mL Deionized Formamide, 5mL MqH_2O, 12.5mL 20XSSC, 2.5mL 20% Tween-20, 1mL Yeast RNA and 5mL 50% Dextran Sulfate). Hybe solution can be stored in -20°C if it does not contain dextran sulfate. Riboprobe mix is then denatured at 72°C for 5mins and then brought to 56°C. After the 2-hour incubation and riboprobe mix has reached temperature, move baskets contacting animals into 1mL of riboprobe mix and seal the well plate with aluminum sealing tape. Allow for hybridization to occur for ~16hrs at 56°C rocking in a hybridization oven.

Remove riboprobes and store them -20°C to be used again. Perform each of the following washes two times for the duration of 30mins, with preheated solution at 56°C and rocking in hybridization oven. Solutions are placed in this order: (1) PreHybe, (2) 1:1 ratio of PreHybe:2xSSC(0.1%Tx) (3) 2xSSC(0.1%Tx) (4) 0.2xSSC(0.1%Tx). Remove the plate from oven and allow it to cool to room temperature ~10-15mins. Solution is replaced and animals are washed twice with 0.1%PBSTx at 10min intervals. Animals are blocked for 1 hour at room temperature or overnight at 4°C in filtered 5% 10xCasein blocking buffer (10xCasein Buffer; Sigma, Cat# B62429) and 5% heat inactivated horse serum. Remove blocking and dilute antibody with fresh blocking buffer and rock at room temperature for 4 hours or overnight at 4°C. The following antibody mixtures are used: Anti-DIG-POD (1:1000) diluted in 0.1%PBSTx + 5% Horse Serum + 5% 10x Casein block or Anti-Fluor-

POD (1:1500) diluted in 0.1%PBSTx + 10% 10x Casein block (Anti-Fluor-POD; Roche, Cat#11-426-346-910)

Antibody is removed and seven washes in 0.1%PBSTx rocking at 15min intervals will commence. During this time, Tyramide stock buffer should be prepared (58.44g NaCl, 3.09g Boric Acid, fill to 500mL with MqH_2O, pH to 8.5 with NaOH and filter) and as well as 4-IPBA stock solution (20mg/mL in dimethyformamide) that can be stored at -20°C (4-IPBA; Sigma, Cat# SML0309) (dimethyformamide; Sigma, Cat# 227056). The working tyramide solution should be made fresh per reaction. Place 1mL of tyramide buffer per well; add 1:1000 of 4-IPBA and 1:10,000 30%H_2O_2 into this solution. Dependent on the color needed add tyramide conjugated to Rhodamine 1:1500, FITC 1:1000 or Cy5 1:300. Incubate the final tyramide solution at room temperature for 10-12mins followed by two washes in 0.1%PBSTx at 5min intervals. At this point single FISH is competed and can be mounted. However, for double or triple FISH proceed with tyramide inactivation by incubating animals for 1.5 hours at room temperature or overnight at 4°C in 1% Sodium Azide (NaN_3; Sigma, Cat# S2002) followed by two washes in 0.1%PBSTx at 5min intervals. To add the second antibody, wash seven more times with 0.1%PBSTx in 20min intervals, block and add secondary antibody at room temperature for 4 hours or overnight at 4°C. Proceed to antibody removal and tyramide amplification.

Quantitative RT-PCR

Quantitative RT-PCR (qPCR) was performed as previously described [16], [109]. Again, RNA was extracted from whole tissue of >20 animals per condition using trizol and cDNA was generated from 1µg of total RNA. The clone H.55.12e “UDP Glucose” (accession number: AY068123) was selected as an internal control as a constitutively expressed gene [125]. Specific target primers for qPCR we designed to be 50-150 base pairs in length and were used to evaluate gene expression and the efficiency of gene knockdown by RNA interference. qPCR reactions were placed in a fast optical 96-well reaction plate (Plate; AB, Cat# 4346906). A 20µL reaction per well: 10µL of SYBR Green Master Mix (SYBER Green; AB, Cat# A25741), 1µL of reverse and forward primer mix (20pmol), 1µL of cDNA and 8µL nuclease free water. To reduce pipetting error and materials used, create two mater mixes: (1) SYBR Green Master Mix + Primer Mix and (2) cDNA + nuclease free water. The control and treated samples receiving target primers will all receive 1 concentration of cDNA. Further, a gradient of different cDNA concentration (e.g. 1, 0.5 and 0.25) will be made per sample receiving internal control H.55.12e primers. Therefore, when loading the plate primarily add the cDNA + nuclease free water starting with the cDNA made for the gradient followed by the wells receiving concentration of 1 cDNA for target primers. Once all sample cDNA (e.g. control and treated) are in the plate, add the SYBR Green Master Mix + Primer Mix; this mix should stay in dark until in use.

Once complete, seal the plate (PCR film, Eppendorf, Cat# 951023019), then spin down for 5mins at 1500rpm at 4ºC and qPCR is performed using a StepOnePlus Real-Time PCR System (qPCR Machine; AB, Cat# 4376600). Data were analyzed using Applied Biosystems StepOne Software V2.0. Additional analysis (e.g. normalization and fold change) was computed using Microsoft Excel. Ct values for different target genes were normalized to expression of the internal control H.55.12e by obtaining a standard curve of H.55.12e expression levels at various concentrations of cDNA (e.g. 1, 0.5 and 0.25) that was specific to that sample (e.g. control or treated). Further, gene expression levels of the experimental group were then made relative to the control extract and

presented in terms of fold change. Reactions were run in triplicate per target primer and at least two different experiments per condition were performed.

RNA Sequencing Tools

Library Preparation and RNA Sequencing

10 large planarians, starved for 7 days, were treated with RNA interference of PTEN (1&2) at various timepoints post first injection (e.g. days 2,3,4,6 and 12) and control planarians were injected with nuclease free water at various timepoints post first injection (e.g. 2,6 and 12). Injection schedule as previously described [56]. All RNA interference regimens ended on the same day to eliminate sample preparation issues. Briefly, samples were treated with trizol, stored at -80°C and RNA was extracted for each sample on the same day. Triplicated analysis was performed for each data point that consisted of pooled samples from 10 animals each. RNA library was prepared and sequenced on the Illumina HiSeq 4000 platform at the DNA Technologies Core at the UC Davis Genome Center. Samples were indexed and pooled for multiplexing. All samples were analyzed by a Bioanalyzer for quality control before sequencing.

Differential Expression Analysis

Trimmed fastq files were assessed for quality control and mapped to the recently published complete *Schmidtea mediterranea* genome dd_Smes_g4_1 from the PlanMine database [249]. The Bioconductor package Rsubread [607] was used to map reads to the reference genome using a robust and efficient seed-and-vote algorithm followed by the featureCounts algorithm to assign counts. The raw counts data were normalized and filtered for genes with log2 counts-per-million (CPM) greater than 0.5. Sample variation was assessed for quality. A customized pipeline using the limma package and voom transformation for precision weights was developed [568]–[570]. Test statistics were produced using empirical Bayes moderation and subsequent heatmaps were made using the ComplexHeatmap Bioconductor package.

Gene Enrichment Analysis

Gene enrichment analysis was performed using the Bioconductor topGO package. Enrichment was computed by ranking gene scores using the conservative Kolmogorov-Smirnov test. Subsequent tables were coded using LaTeX.

Immunoassaying and Fluorescent Tools

Planarian Whole Mount Immunohistochemistry

Antibodies in the planarian have been optimized to track neoblast division, differentiation and their progeny (e.g. gut, central nervous system, cilia, protonephridia, etc.) during tissue homeostasis and regeneration [252], [298], [307], [602], [608]–[614]. After blocking for 4 hours in 0.2% BSA in 0.3% PBSTx (0.125g BSA in 50mL of 0.3% PBSTx and filtered before use), primary antibodies diluted in 0.2% BSA in 0.3% PBSTx are incubated overnight at 4ºC with gentle agitation. Remove antibody and store. Rinse

quickly three times with 0.3%PBSTx and afterward 8 times at 40min intervals, rocking and at room temperature. Block for 1 hour with 0.2% PBSTx-BSA. Remove blocking and add secondary diluted in 0.2% BSA in 0.3% PBSTx overnight with gentle agitation at 4ºC. Remove antibody and store. Rinse quickly three times with 0.3%PBSTx and afterward 8 times at 40min intervals, rocking and at room temperature. If antibody requires HRP substrate amplification, follow instructions in tyramide signal amplification section. Primary and secondary antibodies are as followed:

Primary antibodies: α-Phospho-Histone H3 (Ser10) 1:250 (Millipore Cat# 05-817R), α-Caspase-3, 1:500 (Abcam ab13847), α-Phospho-Histone H2A.X (Ser139) 1:500 (Thermo, Cat# LF-PA0025), α-RAD51 1:500 (Abcam, Cat# ab109107), α-synapsin 1:100 (Developmental Studies Hybridoma Bank), α -VC1 1:10000 (Kind gift of K. Watanabe), α-SYNORF1 1:100 (Developmental Studies Hybridoma Bank), anti-α-Ac-Tubulin 1:500 (Sigma, 6-11B-1) and Smed-6G10 1:1000 (Developmental Studies Hybridoma Bank).

Secondary antibodies: for α-H3p Alexa568 1:800 goat anti-rabbit (Invitrogen Cat# 11036). HRP-conjugated goat anti-rabbit antibody (Millipore, Cat# 12-348) was used at 1:500 for both anti-Rad51 and anti-H2A.X and 1:2000 for anti-Caspase3; all with TSA-Alexa Fluor 488 (Thermo, Cat# A21370). For α-synapsin, α-VC1, α-SYNORF1, anti-α-Ac-Tubulin and Smed-6G10 both Alexa488 1:400 goat anti-mouse (Invitrogen Cat# 673781) or goat-anti-mouse HRP IgG (H+L) 1:1000 (Thermo, Cat# G-21040) can be used.

BrdU Pulse-Chase Analysis

BrdU incorporation is used to monitor planarian neoblasts, their migration and differentiation [602], [603]. Rinse animals in a 24 well plate three times with P-H_2O to remove excess mucus and debris in well. Remove liquid and treat Planarians with freshly made 0.0625% NAC dissolved in P-H_2O (625µL 1% NAC and 9.375mL P-H_2O) for 1min sharp; this will remove mucus layer of the epithelium. Note that 0.0625% NAC is difficult to make thus, prepare a 1% NAC stock solution in P-H_2O and dilute down to 0.0625% NAC. Stock solution can be stored at -20ºC in aliquots. Make in use solution fresh every time before use. Immediately, after 1min, remove NAC and rinse three times with fresh P-H_2O. To begin the BrdU pulse segment, incubate animals for 1 hour in the dark at room temperate in 25mg/mL BrdU in 3%DMSO/0.1x P-H_2O (0.025g BrdU in 1mL P-H_2O and add 30µL DMSO). Note that 25mg/mL BrdU Labeling Reagent in 3%DMSO/0.1x P-H_2O is difficult to dissolve. Therefore, prepare by add P-H_2O into a 1.5mL tube containing desired BrdU labeling reagent (BrdU Labeling Reagent; Sigma, Cat# B5002-5G) and dissolve by mixing at 1000rpm in a Thermomixer-R at 50ºC for approximately 5-10mins. Once dissolved add 3%DMSO (DMSO; DriSolv, Cat# MX1457-7). Allow solution to cool before placing onto animals. Make solution fresh every time before use. Once the pulse is complete, immediately remove BrdU and rinse three times with fresh P-H_2O. Place animals in the dark at room temperature to chase for +8hrs; do not exceed 15hrs chase.

Once BrdU chase is complete, fix animals using the Carnoys fixation and animal bleaching and rehydration protocols. Before blocking, the DNA must be denatured thus, remove 0.3%PBSTx and replace with 2N HCl (1.322mL of 12.1N HCL and add 6.678mL MqH_2O) for 45mins at room temperature rocking. Rinse quickly with 0.1M borax (3.8g sodium tetraborate in 100mL MqH_2O and adjust pH to 8.5 with NaOH) (Sodium tetraborate decahydrate; Fisher, Cat# BP175-500) and to neutralize the animals, incubate animals in fresh 0.1M borax for 2mins and sharply remove. Rinse animals quickly with 0.3%PBSTx and thereafter two times at 5min intervals, shaking. At this point animals are ready for blocking. Again, block animals for 4hrs rotating at room temperature using 0.4% BSA in

0.3% PBSTx (0.25g BSA in 50mL of 0.3% PBSTx and filtered before use). Transfer animals to 24 well plate, remove blocking solution and add 1:50 Anti-BrdU Mouse diluted in 0.4% PBSTx-BSA (20µL Anti-BrdU in 1mL 0.4% PBSTx-BSA) (Anti-BrdU Mouse (BALB/c $IgG_{1,}$ κ); BD, Cat# 347580) and rock overnight at 4ºC. Cheng et al. 2018 identified that incubations up to 48hrs in primary will yield increased signal in hard to probe region in the animal [603]. Rinse quickly three times with 0.3%PBSTx and afterward 8 times at 40min intervals, rocking and at room temperature. Block for 1 hour with 0.4% PBSTx-BSA. Remove blocking and add secondary overnight with gentle agitation at 4ºC. Secondary antibody is 1:200 HRP Goat Anti-Mouse (IgG(H+L)) diluted in 0.4% PBSTx-BSA (5µL HRP-GαM in 1mL 0.4% PBSTx-BSA) (HRP-GαM; Thermo, Cat# G-21040). Rinse quickly three times with 0.3%PBSTx and afterward 8 times at 40min intervals, rocking and at room temperature. To amplify HRP substrate, follow instructions in tyramide signal amplification section.

Tyramide Signal Amplification

Tyramide signal amplification has been identified to enhance detection of gene and protein expression in the planarian [307], [605]. Tyramide substrate was diluted 1:1000 TSA-Alexa Fluor 488 (Thermo, Cat# A21370) or 1:2000 Rhodamine (Rhodamine; Sigma, Cat# R6626-100G) in PBSTxI (500µL 1M Imidazole in 50mL 0.3%PBSTx) (1M Imidazole: 68.1g Imidazole in 1L MqH_2O) (Imidazole; Sigma, Cat# I5513-100G). Animals were presoaked in 300µL tyramide substrate solution for 30mins and activated the reaction by adding 6µL of 0.15%H_2O_2 (1µL 30%H_2O_2 diluted in 199µL PBSTxI) directly into the well contacting tyramide substrate solution. Allow an incubation of 45min at room temperature, rocking and in the dark. Afterward, remove substrate and quickly rinse twice with PBSTxI. Stop the reaction by incubating worms for 45mins in peroxide quench (400µL 30%H_2O_2 and fill to 6mL with PBSTxI). Samples were then rinsed quickly three times with 0.3%PBSTx and afterward rocked for three 5min intervals. Animals were stored overnight in 4ºC with gentle agitation or washed 8 times at 40min intervals, rocking and at room temperature before mounting the animals in VECTASHIELD Mounting Medium (VECTASHIELD; Vector Lab, Cat# H-1000).

TUNEL Assay

TUNEL assay, terminal deoxynucleotidyl transferase dUTP nick end labeling, is a method for detecting DNA double stranded breaks generated during apoptosis in planarian model system [101]. After animals are fixed for TUNEL and bleached, worms are placed in a 96 well plate, no more than 4-5 small animals per well and rinsed with 1xPBS. TUNEL assay ApopTag Red *in situ* Apoptosis Detection Kit is used for all experiments (TUNEL Kit; Millipore, Cat# S7165). To begin the assay, preheat a hybridization oven to 37ºC and create working strength TdT enzyme reaction buffer mix (70% reaction buffer with 30% TdT enzyme) (Reaction Buffer; Millipore, Cat# 90417) (TdT Enzyme; Millipore, Cat# 90418). Remove all 1xPBS and place exactly 20µL of reaction buffer mix per well, tightly cover the 96 well plate with parafilm to avoid evaporation and place into hybridization oven for a minimum of 4 hours at 37ºC and rocking. After the 4-hour incubation, place stop/wash buffer directly into the wells, remove solution and rinse again with fresh stop/wash buffer. This buffer can be prepared (1mL stop/wash buffer and 34mL MqH_2O) (Stop/Wash Buffer; Millipore, Cat# 90419) and stored at 4ºC for up to 1 year. Rinse wells once with 0.2% BSA in 0.3% PBSTx. Binding antibody conjugate with

Rhodamine antibody solution (53% blocking solution with 47% anti-digoxigenin conjugate) (Blocking Solution; Millipore, Cat# 90425) (Anti-Digoxigenin Rhodamine; Millipore, Cat# 90429) in the dark with slight agitation, either overnight at 4ºC for no more than 12 hours or room temperature for no longer than 4-5 hours. Flood wells with 0.2% BSA in 0.3% PBSTx, then rinse three times and wash four times for 10min intervals at room temperature, rocking with 0.2% BSA in 0.3% PBSTx. Mount animals with mounting medium.

Protein Extractions and Quantification for Western Blotting

Animals were dissociated until no tissue fragments were visible with a razor blade, as discussed previously. However, dissociated tissue was not paced into CMF but in a protein extract cocktail. Tissue extracts were incubated for 45-60mins on ice in 1×RIPA buffer (10xRIPA Buffer; Cell Signaling Technologies, Cat# 9806), protease inhibitor cocktail (Complete Mini Protease Inhibitor Cocktail, Sigma, 04693124001), 1mM PMSF (PMSF; Sigma, Cat# P7626) and 1mM DTT (DTT; Sigma, Cat# D0632). Thus, to make 1mL of RIPA-Cocktail buffer: 100µL of 10xRIPA buffer, 800µL MqH_2O, 10µL PMSF (100mM stock) (0.17g PMSF dissolved in 10mL isopropanol), 10µL DTT (100mM stock), 100µL of 10x protease inhibitor cocktail (dissolve 1 tablet into 800µL MqH_2O). Volume-to-mass ratio for this was as follows: 10-20 large dissociated planaria were incubated in 300µL of 1×RIPA+protease cocktail mixture. Samples were spun at 14000rpm for 20 min at 4°C. The supernatant was transferred to a new tube and immediately placed on ice while concentration was being calculated by Bradford Assay.

A Bio-Rad protein assay was used to determine protein concentration. Thus, to calculate protein concentration of protein samples, a standard curve will be created using the quick start bovine serum albumin standard (2mg/mL) (BSA standard; Bio Rad, Cat# 5000206). The BSA standard at concentrations ranging from 0-12 will be made in 1.5mL tubes as follows: 0µL BSA standard, 800µL MqH_2O and 200µLof protein assay dye reagent concentrate (Protein assay; Bio Rad, Cat# 500-0006). To crate standard curve, BSA standard levels will increase by 0.5µL and MqH_2O levels will reduce by 0.5µL; protein assay has a fixed amount. Each protein extract will have its own reaction by placing 1µL of protein extract into 799µL of MqH_2O and 200µL of protein assay. Importantly, mix water and protein for standard and samples before adding the protein assay reagent as samples should incubate no longer than 15mins once reagent is added. Vortex each tube before reading taking protein concentration readings in a spectrophotometer (Genesys 20; Thermo, Cat# 14-385-445). To calculate protein concentration of samples, compare to BSA standard curve. Briefly, (standard value/standard wavelength) x sample extract wavelength). Protein lysates can be stored at −20°C or can be diluted with equal parts per volume of extract:2xLamily Buffer (4% SDS, 10% 2-mercaptoethanol, 20% glycerol, 0.004% bromophenol blue, 0.125 M Tris-HCl) (2-mercaptoethanol; Fisher, Cat# 60-24-2) (Bromophenol blue; Fisher, Cat# SI12-500). Samples in 2x Lamily Buffer are incubated at 95°C for 5min to denature and reduce. Start loading samples at this point or store lysates at −20°C.

Western Blotting or Protein Immunoblotting

Creating a 12% or 15% acrylamide concentration gel dependent on molecular weight range of target protein (e.g. 14-60kD or 12-45kD, respectively). SDS-PAGE gels were made using Bio-Rad Tetra cell casting stand with clap system was use (Casting

Module; Bio-Rad, Cat# 1658052). Set up casting module by clamping down glass spacer plates with 0.75-1.0mm integrated space and atop a short plate (Spacer Plate 0.75mm; Bio-Rad, Cat# 1653310) (Spacer Plate 1.0mm; Bio-Rad, Cat# 1653311) (Short Plate; Bio-Rad, Cat# 1653308). Now test for leaks by placing MqH_2O into the cases and wait for 30-60mins. Make 10mL of separating gel solution, for a 12% gel (4mL 30% Acrylamide, 2.5mL 1.5M Tris-HCL pH8.8, 3.4mL MqH_2O, 100µL 10% SDS, 50µL of freshly made 10% ammonium persulfate (0.05g APS in 500µL MqH_2O)) and for a 15% gel, use 5mL 30% Acrylamide and 2.4mL MqH_2O (30% Acrylamide/Bis Solution; Bio-Rad, Cat# 1610159) (1.5M Tris pH8.8; Bio-Rad, Cat# 161-0798) (Ammonium persulfate; Bio-Rad, Cat# 161-0700). Lastly, add 5µL of TEMED (TEMED; Bio-Rad, Cat# 161-0800) into the separating gel mixture, should be last solution added to mixture as solidification will being, then vortex mixture thoroughly and pour (3/4) up the space plate. The remainder of the spacer plate will be filled with MqH_2O to aid in compressing acrylamide and solidification of gel. Allow gel to solidify for 1-2 hours. To crate the stacking gel, 4mL of solution is needed (670µL 30% Acrylamide, 500µL 0.5M Tris-HCL pH6.8, 2.4mL MqH_2O, 40µL 10% SDS, 30µL of freshly made 10% ammonium persulfate (0.5M Tris pH6.8; Bio-Rad, Cat# 161-0799). Lastly, add 3µL of TEMED into the staking gel mixture and vortex thoroughly. Remove water with a KimWipe, pour staking gel to fill the reminder (1/4) of the space plate and add 10 or 15-well comb dependent on spacer plate size. Allow gel to solidify for 1-2 hours.

Once solidified, move gel cassettes to a vertical electrophoresis chamber (Mini-protean electrophoresis cell; Bio-Rad, Cat# 1658005). If only one gel is being used, place a buffer dam into the electrode assembly module (Buffer dams; Bio-Rad, Cat# 1653130). Fill chamber with 1x running buffer (10X running buffer: 144g Glycine, 30.3g Tris base, 10g SDS and bring to 1L with MqH_2O) (Glycine; Sigma, Cat# G8898) and make sure the internal compartment in completely full. Protein lysate aliquots of 40-50µg were heated at 95°C for 5min and loaded along with 5µL of protein standard marker (Protein Standard; Bio-Rad, Cat# 1610375) (MultiFlex pipet tips; RPI, Cat# 148010). Gels were ran at 80V until the protein reach the interface between stacking/separating gels were the voltage was increased to 100V.

Samples were transferred using a transfer blot module (Mini Trans-Blot Module; Bio-Rad, Cat# 1703935). The transfer cassette contained one a 30sec methanol-activated PVDF membrane, the electrophorese gel, 4 blotting pads (2 on either side of membrane) and 2 transfer sponges (1 on either side of blotting pads) (PVDF; Bio-Rad, Cat# 162-0175) (Blotting Pad; VWR, Cat# 28298-030). Transfer chamber contained an ice block, stir bar and 1x transfer buffer mixed with freshly added 10% (v/v) methanol with adjusted pH to 8.3 (10X Transfer Buffer: 144g Glycine, 30.3g Tris Base and bring up to 1L with MqH_2O). Transfer was conducted either overnight for 16hrs at 40V at 4ºC or for 1 hour at 100V at room temperature covered in ice.

The membrane was blocked for 2 hours at room temperature with 5% milk in 0.1%TBSTween (10X TBS: 24.23g Tris HCL, 80.06g NaCl, bring up to 1L with MqH_2O and pH 7.6 with HCL) (Tris HCL; Sigma, Cat# T5941). Lastly, primary antibody diluted in blocking solution was either incubated on a rocker overnight at 4°C or at room temperature for 2 hours. Retrieve primary antibody, rinse three times with 1xTBSTween followed by six subsequent washes for 5-10min intervals. The secondary antibody was diluted in 1xTBSTween and either incubated on a rocker overnight at 4°C or at room temperature for 2 hours. Retrieve secondary antibody, rinse three times with 1xTBSTween followed by six subsequent washes for 5-10min intervals. Specifically, target protein primary antibodies α-Caspase-3 (Abcam, Cat# ab13847) and α-RAD51 (Abcam, Cat# ab109107) at 1:5000 and secondary antibody HRP-conjugated goat anti-rabbit IgG antibody 1:2000

(Millipore Cat# 12-348). Loading control primary antibody Anti-α-Tubulin 1:750 (Sigma, Cat# T9026) or α-Actin 1:3000 (Developmental Studies Hybridoma Bank, Cat# 224-236-1) and both received secondary antibody HRP-conjugated goat-anti-mouse IgG(H+L) (Thermo, Cat# G-21040) at 1:2000 for Anti-α-Tubulin and 1:10,000 for α-Actin.

Luminata Forte Western HRP substrate (HRP substrate; Millipore, Cat# WBLUF0100) was used to develop the membrane and incubated for 5-10mins prior to exposure on a ChemiDoc using a White Epi filter (ChemiDoc Touch Gel Imaging System; Bio-Rad, Cat# 1708370). After exposure of target protein, membranes were stripped so that the membrane can be probed for the loading control anti-tubulin. Thus, membranes were incubated in 1xTBS for two 5mins washes. Stripping occurred for 10mins rocking at room temperature with Western Blot Stripping Buffer (Restore Stripping Buffer; Thermo, Cat# 21062). Followed by three quick rinses in 1xTBS and two washes for 5mins. Now membrane is ready to be blocked and probed for another target protein.

Target protein levels were normalized to the internal loading control to correct for unavoidable sample-to-sample and lane-to-lane variations using NIH ImageJ. In addition to Anti-α-Tubulin or α-Actin loading control, blots were stained with Ponceau-S solution (Ponceau-S solution; Sigma, Cat# P7170) for 5min and washed with MqH_2O and this provided another parameter to validate loading. Moreover, band intensities are quantified by drawing boxes with the same areas over each band; box overlapping was avoided. The area under the curve was obtained for both the target protein and internal control and protein levels were normalized to internal control.

Dissociated Cells Molecular Tools

Planarian Dissociation and Cell Collection

Planarian dissociation was performed as established in the field with slight modification [46], [121], [125]. Prepare calcium and magnesium phosphate free media (CMF): 0.1g NaH_2PO_4 (NaH_2PO_4; Sigma, Cat# S5011), 0.2g NaCl, 0.3g KCl, 0.2g $NaHCO_3$, 0.06g Dextrose (Dextrose; Fisher, Cat# S73418), 2.5g BSA and 0.69g HEPES (HEPES; Sigma, Cat# H3375) in a total volume of 250mL MqH_2O. Adjust pH to 7.3 with 2N NaOH and 2N HCl. Filter with sterile 0.22µm stericup (Stericup; Millipore, Cat# SCGVU05RE) and refrigerate at 4ºC.

To begin maceration of planarian, place worms onto a chilled polystyrene petri dish via peltier cooler and all excess $P\text{-}H_2O$ is removed using a KimWipe. Dissociate worms with a carbon steel razor blade (Razor Blade; EMS, Cat# 72004) until the homogenate is void of visible tissues. Rinse homogenate, razor blade and petri dish with ice cold CMF and place suspension into a 15mL conical tube; repeat washes until conical tube is filled to 10mL of suspension. Cell suspensions are then rocked at 4ºC for 25-45mins; timing is adjusted depending on sample preparation time (e.g. more samples the longer it will take to macerate worms thus, less rocking time). Note: for FACS analysis, this step is avoided due to the length of sample prep and overall viability of cells in this protocol. Once rocking is complete, cells are filtered using a 70µm filter (Filter; BD, Cat# 9308448) and centrifuged at 1500rpm for 5mins at 4ºC followed by resuspension in 1-2mL of CMF media. Cell density at a 1:1 ratio with Trypan Blue solution (Trypan Blue; Thermo, Cat# SV30084) was quantified using a hemocytometer.

Fixation and Immunoassaying of Dissociated Cells

Cell fixation and IHC on cells was performed as previously described with modification [16], [109], [112]. Cell homogenate were plated at 1mill/cm^2 onto circular glass coverslips that were secured in a 24 well plate. Cells were given 1 hour to adhere to the surface. Coverslips were transferred to glass pitri dish and fixed with Carnoys solution for 2hours on ice. Cells were permeabilized by placing 100% methanol for 1hr at -20°C. Thereafter, allow for the temperature to equilibrate to room temperature and rehydrate the cells with mixtures of 75%, 50% and 25% Methanol:0.3%PBSTx at 5mins intervals and a final wash with 100% 0.3%PBSTx at 5mins. Once cells are in 0.3%PBSTx, coverslips can be transferred to 24 well plate and cells are blocked in 0.3%PBSTx-0.2%BSA for 2hrs rocking at room temperature. Primary antibodies diluted in 0.2% BSA in 0.3% PBSTx are incubated overnight at 4ºC with gentle agitation or at room temperature for 2-3 hours. Remove primary antibody and store. Rinse quickly three times with 0.3%PBSTx-0.2%BSA and afterward six times at 10min intervals, rocking and at room temperature. Add secondary diluted in 0.3%PBSTx-0.2%BSA overnight with gentle agitation at 4ºC with gentle agitation or at room temperature for 2-3 hours. Remove antibody and store. Rinse quickly three times with 0.3%PBSTx-0.2%BSA and afterward six times at 10min intervals, rocking and at room temperature. Tyramide substrate was diluted 1:1000 TSA-Alexa Fluor 488 in PBSTxI with 0.0015% H_2O_2 for 20-30mins, followed by a 2-5min quench of 2% H_2O_2 diluted in fresh PBSTxI. Remove, rinse and wash six times at 10min intervals with 0.3%PBSTx-0.2%BSA. After the final wash, cells were incubated with DAPI (0.1µg/1mL) (DAPI; Thermo, Cat# 62248) for 15 min and mounted. Primary and secondary antibodies are as followed:

Primary antibodies: α-Caspase-3, 1:500 (Abcam ab13847), α-Phospho-Histone H2A.X (Ser139) 1:500 (Thermo, Cat# LF-PA0025) and α-RAD51 1:500 (Abcam, Cat# ab109107).

Secondary antibodies: For all primaries, HRP-conjugated goat anti-rabbit antibody (Millipore, Cat# 12-348) was used but at 1:500 for anti-Rad51 and anti-H2A.X and 1:1000 for anti-Caspase3; all with TSA-Alexa Fluor 488 (Thermo, Cat# A21370).

Fixation and Immunostaining of Dissociated Cells to Obtain Mitotic Figures

Protocol for obtaining mitotic figure for individual cells in planarian was provided by the Adell Lab in Barcelona, Spain and modification were made to their published protocol [153]. Control and RNAi animals were placed in 1.5mL conical tubes and ride of residual P-H_2O. Animals were macerated in a solution containing glacial acetic acid: glycerol: methanol: MqH_2O (1:2:3:14) for 16hrs at 4°C. Approximately 800-1000µL of fixative should be placed onto +6 worms for optimal plaiting density as counting is not feasible in fixative. Cell suspension was gently resuspended until homogenous solution was obtained and plated onto circular glass coverslips that were secured in a 24 well plate. Cells were given 1 hour to adhere to the surface. Cells were rinsed with 100% methanol and rehydrated with mixtures of 75%, 50% and 25% Methanol:0.3%PBSTx at 5mins intervals and a final wash with 100% 0.3%PBSTx at 5mins. Cells can be stored at this point in 0.3%PBSTx for approximately 2 weeks in 4ºC. Cells are blocked in 0.3%PBSTx-1.0%BSA for 2hrs rocking at room temperature. Primary antibodies diluted in 0.3%PBSTx-1.0%BSA are incubated overnight at 4ºC with gentle agitation or at room temperature for 2-3 hours. Remove primary antibody and store. Rinse quickly three times with 0.3%PBSTx-1.0%BSA and afterward six times at 10min intervals, rocking and at room temperature. Add secondary diluted in 0.3%PBSTx-1.0%BSA overnight with gentle agitation at 4ºC with gentle agitation or at room temperature for 2-3 hours. Remove

antibody and store. Rinse quickly three times with 0.3%PBSTx-1.0%BSA and afterward six times at 10min intervals, rocking and at room temperature. After the final wash, cells were incubated with DAPI (0.1µg/1mL) (DAPI; Thermo, Cat# 62248) for 15 min and mounted. Primary and secondary antibodies are as followed:

Primary antibodies: α-Phospho-Histone H3 (Ser10) 1:250 (Millipore Cat# 05-817R) and Anti-α-Tubulin 1:750 (Sigma, Cat# T9026).

Secondary antibodies: Alexa568 1:1000 goat anti-rabbit (Invitrogen Cat# 11036) and Alexa488 1:400 goat anti-mouse (Invitrogen Cat# 673781).

Single Cell COMET Assay

COMET assay under alkaline conditions allow for DNA integrity to be analyzed in individual planarian cells [16], [17], [29]. Cells should be dissociated as discussed in Planarian Dissociation and Cell Collection section. Briefly, decant supernatant after centrifugation and use CMF to break pellet. Aliquot ~40,000-50,000 cells into 1.5mL centrifuge tube and allow cells to incubate in a 37°C water bath for two hours prior to treatment. This step allows for cells to relax after stressful maceration and filtration steps. After incubation period, spin down cells at 2500rpm for 2mins. Aspirate supernatant leaving 40uL and add 100uL of 0.5% Low Melting Point Agarose (0.5% LMPA) (LMPA; Promega, Cat# V2111) made in 10XPBS. Quickly pipette mixture onto coated 1%NMPA dried slides, cover mixture with a cover slip (24x50mm) and let dry at 4°C for 30-40mins until agarose solidifies. 1% Normal Melting Point Agarose (1%NMPA) coated frosted plus blue 25x75x1mm microscope slides are made with 1% Normal Melting Point Agarose (1%NMPA) diluted in 10xPBS prior to the start of the experiment. Gently removing 24x50mm cover slip and place slides overnight in coplin jar at 4°C in 89% of Lysing solution (2.5M NaCl, 100mM EDTA, 10mM Trizma base, 8g pelletized NaOH in MqH2O, filter and pH 10.0), 10% DMSO and 1% Triton X-100 (NaOH pelletized; Fisher, Cat# S318-500).

The morning after, discard lysing solution and add neutralization buffer (0.4M Tris base in MqH2O and adjust pH to 7.5) for 5mins at 4°C. Remove neutralization buffer and place slides into electrophoresis chamber at 4°C and fill chamber with 1x electrophoresis buffer (10N NaOH and 200mM EDTA in MqH2O and adjust pH to 13) (10N NaOH; RICCA, Cat# 7470-32) and let sample equilibrate for 15mins without electrical current. Then, at 4°C, run the chamber at 12V at 300mA for 30mins. Upon completion, place slides back into coplin jar and let samples sit in neutralization buffer for 5mins at 4°C. Sharply remove and fix samples with cold 100% ethanol for 5mins in -20°C (Ethanol; Fisher, Cat# A407-4). Once slides are dry, stain samples with 1:10 ratio of SYBR gold (SYBR Gold; Invitrogen, Cat# S11494) into 1xTE buffer (10mM Tris-HCl, 1mM EDTA in MqH_2O and adjust pH to 7.5) by placing 130µL of solution onto sample and covering with a cover slip (24x50mm). Scoring scheme is based off a rank based on tail length from 0-2, where a score of 0 showed little DNA damage and 2 is a disbursed tail with no nucleus visible (e.g. 0-10µm and 40-60+µm, respectively) [615]. Further, COMET tail lengths can be measured and plotted.

Flow Cytometry/Fluorescence-Activated Cell Sorting

Flow cytometry or FACS allows for the visualization of stem cells and their progeny (e.g. X1, X2 and Xins) as well as cellular apoptosis [16], [17], [46], [49], [121]. Cells should be dissociated as discussed in Planarian Dissociation and Cell Collection section

however, the incubation period after maceration should be omitted and immediately proceed to filtering cell suspension.

To monitor cell cycle dynamics and stem cell populations: 1×10^6 cells from dissociated planaria were incubated with 500µL of DNA marker Draq5 (Draq5; eBioscience, Cat# 65-0880-92) diluted in CMF media (1µL Draq5 in 1mL CMF media) for 30 min on ice in the dark. After 20mins of Draq5 incubation, 500µL Calcein-AM (Calcein; Invitrogen, Cat# C3100MP) dissolved in DMSO (250µL DMSO and vortex powder) and diluted in CMF media (2µL Calcein-AM in 1mL CMF media) is added for the remainder of the 10min incubation. Calcein-AM+CMF solution must be at room temperature before being added to cell suspension and once mixed in, the suspension contacting both Draq5 and Calcein-AM remain at room temperature for the remainder of the incubation.

To monitor apoptotic rates in planarian: 1×10^4 cells from dissociated planaria were stained with apoptotic stain Annexin V (Pacific Blue Annexin V; BioLegend, Cat# 640918) and live marker stain 7-AAD (7-AAD Viability Staining; BioLegend, Cat# 420404). To do so, 100µL of Annexin V binding buffer (Annexin V binding buffer; BioLegend, Cat# 422201) is added to the cells, followed by 5µL of Annexin V and 3µL of 7-AAD. This mixture is incubated in the dark on ice for 15mins and then analyzed.

BD FACSDiva software was used for initial gating and samples were either analyzed using a LSRII flow cytometer (BD Biosciences) or sorted using an ARIAII flow cytometer (BD Biosciences). To calibrate the gates and light emission of instrument, non-experimental control cell suspensions were subjected to no stain, single and double stains and processed through the flow cytometer (e.g. control, control+Draq5, control+Calcein and control+Draq5+Calcein). In addition, lethally irradiated planarians were used to validate and/or approximate gates for X1 and X2 populations [49]. Publication quality images and final flow cytometry analyses were performed with FlowJo software, Version 10 (www.flowjo.com). Gate parameters should follow Peiris et al. 2016 [46].

Other Molecular Tools

Karyotyping: Whole Planarian Chromosome Squash

Planarian karyotype monitoring have been used to detect chromosomal abnormalities and/or their recovery [16], [17], [29], [108], [120], [616]. One day prior to chromosome squash, soak animals in 0.05% colchicine (0.005g 97% colchicine in 10mL P-H_2O) (Colchicine; ACROS, Cat# 227120010) overnight but no greater than 16 hours. Place one animal per 1.5mL tube and remove colchicine solution. Then add 3:1 Ethanol: Acetic Acid Solution to each tube and rotate for 15mins at room temperature. Remove the solution and place 1N HCl solution diluted in MqH_2O and incubate for 2mins at room temperature and immediately incubate at 60°C in a Thermomixer for 6mins. Quickly remove the HCl solution and add Orcein solution (1g Orcein, 45mL acetic acid and 55mL MqH_2O; heated until dissolved) (Orcein; Sigma, Cat# O7380) to each tube for 15mins. Carefully remove orcein solution and replace with 60% acetic acid solution diluted in MqH_2O and incubate for 5mins. Place animals on a 24x60mm cover slips as 25x75mm slides are too thick to view chromosomes at 100x. Nest, add a 10-20µL of (1:1:1) Lactic acid: acetic acid: MqH_2O (Lactic acid; Fisher, Cat# A159-500) on top of each worm and incubate for 5mins. Remove excess liquid and add 1µL of orcein to each animal. With a small 22x22mm cover slip, quickly place it on top of the treated animal. With slight pressure, use your thumb to squash or spread the whole animal throughout the slide. View

chromosomes with 100x objective. Take 10-20 representative fields per animal and score chromosomes as damage or undamaged.

Ionizing Irradiation

Sublethal irradiation of animals at <1250-1750rad will allow neoblasts to recover overtime [16], [17], [29], [113]. Lethal irradiation >6000rad results in complete ablation of neoblasts [50], [54], [125]–[127]. A Cesium source was used in both cases to subject animals to ionizing irradiation. Animals were exposed to the source and were monitored for physical abnormalities and fixed at various time points post irradiation (e.g. 1,3,5 and 7 days post irradiation).

Planarian Amputation and Regeneration

Planarians are masters or regeneration and have this ability due to their large pool of neoblasts [53], [101], [110], [127], [155]. To amputate animals, place worms onto a chilled KimWipe via peltier cooler and amputate worms in three fragments (e.g. head, trunk and tail). The different fragments were placed in different petri dishes, monitored and fixed at various time points during the duration of the regeneration period (e.g. hours post amputation and up to seven days post amputation).

Imaging and Data Analysis Tools

Imaging and Data Processing

Nikon AZ-100 multi-zoom (e.g. Az Plan: Apo 1x, Fluor 2x, and Fluor 5x) upright microscope equipped with NIS Elements AR 3.2 software was used to record animal behavior and acquire digital images of planarian and/or cellular events within the animal. All fluorescence whole mount or cell images consisted of multiple images at different focal planes (*z*-axis) and stacked together into a single image to represent the whole animal or individual cells. Cellular counts or fluorescence intensity signal from images at different magnifications were corrected by area to determine the specific number/mm^2. Foci or intensity were counted either with NIH ImageJ (https://imagej.nih.gov) or with Nikon NIS Elements. Whole animal measurements were calculated using the number of cellular events (e.g. α-H3P, α-RAD51, αH2A.X or $TUNEL^+$ foci) per mm^2 and/or average intensity (e.g. α-Caspase3 and $BrdU^+$ foci) per mm^2. Normalization of foci or intensity per mm^2 was processed in Microsoft Excel.

Area measurement of planarian surface area and physical phenotype changes were conducted by using 6 or more independent experiment containing 20 or more animals per experiment. Both the control and experimental animals were photographed using the same magnification and area measurements (per mm) were calculated along the injection time course. All areas were averaged across experiments.

For antibodies targeting differentiated tissues (e.g. cilia, protonephridia and muscle) a Nikon Eclipse Ti confocal microscope and E Z-C1 software were used to obtain Z-stack images using 20X objective. Z-stacks containing 20 sections at 2-1μm intervals were processed using Image J (1.48v). To image fluorescent signal on dissociated cells and bright field of chromosomal spreads, a Nikon Eclipse TE2000-U inverted microscope and NIS Elements AR 3.2 software were used to obtain Z-stack images using 100X

objective. In all cases, publication quality images were altered with Adobe Photoshop and Adobe Illustrator CC 2015.

Statistical Analysis

Data are expressed as mean ± standard error of the mean (SEM) or fold change ± SEM. Fold change was determined by dividing each individual experimental animal by the mean of the pooled control population for that timepoint (e.g. RNAi/mean of control). Each time point contained >30 injected animals for control and treated groups. Power analysis was used to determine adequate sample size. Statistical analyses were performed using Prism v7, GraphPad software Inc. (http://www.graphpad.com). Two-way ANOVA was used to determine significance and *P*-values less than 0.05 were considered statistically significant.

BIBLIOGRAPHY

[1] J. C. Reed, “Dysregulation of apoptosis in cancer,” *J Clin Oncol*, vol. 17, no. 9, pp. 2941–53, Sep. 1999.

[2] J. C. Reed, “Dysregulation of apoptosis in cancer,” *Cancer J Sci Am*, vol. 4 Suppl 1, pp. S8-14, May 1998.

[3] C. J. Lord and A. Ashworth, “The DNA damage response and cancer therapy,” *Nature*, vol. 481, no. 7381, pp. 287–294, Jan. 2012.

[4] J. Ferlay, H.-R. Shin, F. Bray, D. Forman, C. Mathers, and D. M. Parkin, “Estimates of worldwide burden of cancer in 2008: GLOBOCAN 2008,” *Int. J. Cancer*, vol. 127, no. 12, pp. 2893–2917, 2010.

[5] “Cancer Facts and Statistics | American Cancer Society.” [Online]. Available: https://www.cancer.org/research/cancer-facts-statistics.html. [Accessed: 18-Mar-2019].

[6] C. Tomasetti, B. Vogelstein, and G. Parmigiani, “Half or more of the somatic mutations in cancers of self-renewing tissues originate prior to tumor initiation,” *Proc Natl Acad Sci U A*, vol. 110, no. 6, pp. 1999–2004, Feb. 2013.

[7] A. Sancar, L. A. Lindsey-Boltz, K. Unsal-Kacmaz, and S. Linn, “Molecular mechanisms of mammalian DNA repair and the DNA damage checkpoints,” *Annu Rev Biochem*, vol. 73, pp. 39–85, 2004.

[8] S. P. Jackson and J. Bartek, “The DNA-damage response in human biology and disease,” *Nature*, vol. 461, no. 7267, pp. 1071–8, Oct. 2009.

[9] I. Vitale, G. Manic, R. De Maria, G. Kroemer, and L. Galluzzi, “DNA Damage in Stem Cells,” *Mol Cell*, vol. 66, no. 3, pp. 306–319, May 2017.

[10] J. E. Haber, “DNA recombination: the replication connection,” *Trends Biochem. Sci.*, vol. 24, no. 7, pp. 271–275, Jul. 1999.

[11] R. L. Saul and B. N. Ames, “Background levels of DNA damage in the population,” *Basic Life Sci*, vol. 38, pp. 529–35, 1986.

[12] T. Lindahl, “Instability and decay of the primary structure of DNA,” *Nature*, vol. 362, no. 6422, pp. 709–15, Apr. 1993.

[13] J. Nakamura, V. E. Walker, P. B. Upton, S.-Y. Chiang, Y. W. Kow, and J. A. Swenberg, “Highly Sensitive Apurinic/Apyrimidinic Site Assay Can Detect Spontaneous and Chemically Induced Depurination under Physiological Conditions,” *Cancer Res.*, vol. 58, no. 2, pp. 222–225, Jan. 1998.

[14] C. G. Broustas and H. B. Lieberman, “DNA damage response genes and the development of cancer metastasis,” *Radiat Res*, vol. 181, no. 2, pp. 111–30, Feb. 2014.

[15] J. E. Haber, “A Life Investigating Pathways That Repair Broken Chromosomes,” *Annu Rev Genet*, vol. 50, pp. 1–28, Nov. 2016.

[16] T. H. Peiris *et al.*, “Regional signals in the planarian body guide stem cell fate in the presence of genomic instability,” *Development*, vol. 143, no. 10, pp. 1697–709, May 2016.

[17] M. Thiruvalluvan, P. G. Barghouth, A. Tsur, L. Broday, and N. J. Oviedo, “SUMOylation controls stem cell proliferation and regional cell death through Hedgehog signaling in planarians,” *Cell Mol Life Sci*, vol. 75, no. 7, pp. 1285–1301, Apr. 2018.

[18] T. Iyama and D. M. Wilson 3rd, “DNA repair mechanisms in dividing and non-dividing cells,” *DNA Repair Amst*, vol. 12, no. 8, pp. 620–36, Aug. 2013.

[19] D. B. Lombard, K. F. Chua, R. Mostoslavsky, S. Franco, M. Gostissa, and F. W. Alt, “DNA repair, genome stability, and aging,” *Cell*, vol. 120, no. 4, pp. 497–512, Feb. 2005.

[20] W. K. Kaufmann, “Cell cycle checkpoints and DNA repair preserve the stability of the human genome,” *Cancer Metastasis Rev.*, vol. 14, no. 1, pp. 31–41, Mar. 1995.

[21] C. Le Magnen, A. Dutta, and C. Abate-Shen, “Optimizing mouse models for precision cancer prevention,” *Nat Rev Cancer*, vol. 16, no. 3, pp. 187–96, Mar. 2016.

[22] R. Auerbach and W. Auerbach, “Regional differences in the growth of normal and neoplastic cells,” *Science*, vol. 215, no. 4529, pp. 127–134, Jan. 1982.

[23] R. Auerbach, L. W. Morrissey, L. Kubai, and Y. A. Sidky, “Regional differences in tumor growth: Studies of the vascular system,” *Int. J. Cancer*, vol. 22, no. 1, pp. 40–46, 1978.
[24] R. Auerbach, L. W. Morrissey, and Y. A. Sidky, “Regional Differences in the Incidence and Growth of Mouse Tumors following Intradermal or Subcutaneous Inoculation,” *Cancer Res.*, vol. 38, no. 6, pp. 1739–1744, Jun. 1978.
[25] R. Auerbach, L. W. Morrissey, and Y. A. Sidky, “Gradients in tumour growth,” *Nature*, vol. 274, no. 5672, p. 697, Aug. 1978.
[26] “Regional growth differences of human tumour xenografts in nude mice,” *Lab. Anim.*, vol. 15, no. 2, pp. 179–180, Apr. 1981.
[27] L. Kubai and R. Auerbach, “REGIONAL DIFFERENCES IN THE GROWTH OF SKIN TRANSPLANTS,” *Transplantation*, vol. 30, no. 2, pp. 128–131, Aug. 1980.
[28] R. T. Prehn and V. Karnik, “Differential susceptibility of the axilla and groin of the mouse to chemical oncogenesis,” *Nature*, vol. 279, no. 5712, p. 431, May 1979.
[29] P. G. Barghouth, M. Thiruvalluvan, M. LeGro, and N. J. Oviedo, “DNA damage and tissue repair: What we can learn from planaria,” *Semin. Cell Dev. Biol.*, vol. 87, pp. 145–159, Mar. 2019.
[30] M. Macheret and T. D. Halazonetis, “DNA replication stress as a hallmark of cancer,” *Annu Rev Pathol*, vol. 10, pp. 425–48, 2015.
[31] S. A. Hills and J. F. Diffley, “DNA replication and oncogene-induced replicative stress,” *Curr Biol*, vol. 24, no. 10, pp. R435-44, May 2014.
[32] T. D. Halazonetis, V. G. Gorgoulis, and J. Bartek, “An oncogene-induced DNA damage model for cancer development,” *Science*, vol. 319, no. 5868, pp. 1352–5, Mar. 2008.
[33] C. Da-Rè and T. D. Halazonetis, “DNA replication stress as an Achilles’ heel of cancer,” *Oncotarget*, vol. 6, no. 1, pp. 1–2, Jan. 2015.
[34] V. G. Gorgoulis *et al.*, “Activation of the DNA damage checkpoint and genomic instability in human precancerous lesions,” *Nature*, vol. 434, no. 7035, pp. 907–13, Apr. 2005.
[35] T. D. Halazonetis, “Constitutively active DNA damage checkpoint pathways as the driving force for the high frequency of p53 mutations in human cancer,” *DNA Repair Amst*, vol. 3, no. 8–9, pp. 1057–62, Aug. 2004.
[36] E. Derenzini *et al.*, “Constitutive activation of the DNA damage response pathway as a novel therapeutic target in diffuse large B-cell lymphoma,” *Oncotarget*, vol. 6, no. 9, pp. 6553–6569, Mar. 2015.
[37] D. Hanahan and R. A. Weinberg, “Hallmarks of cancer: the next generation,” *Cell*, vol. 144, no. 5, pp. 646–674, Mar. 2011.
[38] H. L. Klein, “The consequences of Rad51 overexpression for normal and tumor cells,” *DNA Repair Amst*, vol. 7, no. 5, pp. 686–93, May 2008.
[39] A. J. Bishop and R. H. Schiestl, “Role of homologous recombination in carcinogenesis,” *Exp Mol Pathol*, vol. 74, no. 2, pp. 94–105, Apr. 2003.
[40] J. Zhu *et al.*, “A novel small molecule RAD51 inactivator overcomes imatinib-resistance in chronic myeloid leukaemia,” *Embo Mol. Med.*, vol. 5, no. 3, pp. 353–65, Mar. 2013.
[41] A. J. Bishop and R. H. Schiestl, “Homologous Recombination and Its Role in Carcinogenesis,” *J Biomed Biotechnol*, vol. 2, no. 2, pp. 75–85, 2002.
[42] J. Pellettieri and A. Sanchez Alvarado, “Cell turnover and adult tissue homeostasis: from humans to planarians,” *Annu Rev Genet*, vol. 41, pp. 83–105, 2007.
[43] S. J. Zhu and B. J. Pearson, “(Neo)blast from the past: new insights into planarian stem cell lineages,” *Curr Opin Genet Dev*, vol. 40, pp. 74–80, Oct. 2016.
[44] A. Zeng *et al.*, “Prospectively Isolated Tetraspanin(+) Neoblasts Are Adult Pluripotent Stem Cells Underlying Planaria Regeneration,” *Cell*, vol. 173, no. 7, pp. 1593-1608 e20, Jun. 2018.
[45] B. J. Pearson and A. Sanchez Alvarado, “Regeneration, stem cells, and the evolution of tumor suppression,” *Cold Spring Harb Symp Quant Biol*, vol. 73, pp. 565–72, 2008.
[46] T. H. Peiris, M. E. Garcia-Ojeda, and N. J. Oviedo, “Alternative flow cytometry strategies to analyze stem cells and cell death in planarians,” *Regen. Oxf*, vol. 3, no. 2, pp. 123–35, Apr. 2016.

[47] D. E. Wagner, I. E. Wang, and P. W. Reddien, “Clonogenic neoblasts are pluripotent adult stem cells that underlie planarian regeneration,” *Science*, vol. 332, no. 6031, pp. 811–6, May 2011.
[48] A. Sánchez Alvarado and P. A. Tsonis, “Bridging the regeneration gap: genetic insights from diverse animal models,” *Nat. Rev. Genet.*, vol. 7, no. 11, pp. 873–884, Nov. 2006.
[49] G. T. Eisenhoffer, H. Kang, and A. Sanchez Alvarado, “Molecular analysis of stem cells and their descendants during cell turnover and regeneration in the planarian Schmidtea mediterranea,” *Cell Stem Cell*, vol. 3, no. 3, pp. 327–39, Sep. 2008.
[50] P. W. Reddien and A. Sanchez Alvarado, “Fundamentals of planarian regeneration,” *Annu Rev Cell Dev Biol*, vol. 20, pp. 725–57, 2004.
[51] A. A. Aboobaker, “Planarian stem cells: a simple paradigm for regeneration,” *Trends Cell Biol*, vol. 21, no. 5, pp. 304–11, May 2011.
[52] J. C. Rink, “Stem cell systems and regeneration in planaria,” *Dev Genes Evol*, vol. 223, no. 1–2, pp. 67–84, Mar. 2013.
[53] O. Wurtzel, L. E. Cote, A. Poirier, R. Satija, A. Regev, and P. W. Reddien, “A Generic and Cell-Type-Specific Wound Response Precedes Regeneration in Planarians,” *Dev Cell*, vol. 35, no. 5, pp. 632–645, Dec. 2015.
[54] J. Solana *et al.*, “Defining the molecular profile of planarian pluripotent stem cells using a combinatorial RNAseq, RNA interference and irradiation approach,” *Genome Biol*, vol. 13, no. 3, p. R19, 2012.
[55] T. C. J. Tan *et al.*, “Telomere maintenance and telomerase activity are differentially regulated in asexual and sexual worms,” *Proc. Natl. Acad. Sci.*, vol. 109, no. 11, pp. 4209–4214, Mar. 2012.
[56] N. J. Oviedo, B. J. Pearson, M. Levin, and A. Sanchez Alvarado, “Planarian PTEN homologs regulate stem cells and regeneration through TOR signaling,” *Model Mech*, vol. 1, no. 2–3, pp. 131–43; discussion 141, Sep. 2008.
[57] C. Gonzalez-Estevez *et al.*, “SMG-1 and mTORC1 act antagonistically to regulate response to injury and growth in planarians,” *PLoS Genet*, vol. 8, no. 3, p. e1002619, 2012.
[58] N. J. Oviedo and W. S. Beane, “Regeneration: The origin of cancer or a possible cure?,” *Semin Cell Dev Biol*, vol. 20, no. 5, pp. 557–64, Jul. 2009.
[59] A. S. Stevens *et al.*, “Planarians Customize Their Stem Cell Responses Following Genotoxic Stress as a Function of Exposure Time and Regenerative State,” *Toxicol Sci*, vol. 162, no. 1, pp. 251–263, Mar. 2018.
[60] B. J. Pearson and A. Sanchez Alvarado, “A planarian p53 homolog regulates proliferation and self-renewal in adult stem cell lineages,” *Development*, vol. 137, no. 2, pp. 213–21, Jan. 2010.
[61] S. J. Zhu and B. J. Pearson, “The Retinoblastoma pathway regulates stem cell proliferation in freshwater planarians,” *Dev Biol*, vol. 373, no. 2, pp. 442–52, Jan. 2013.
[62] Y. Mihaylova *et al.*, “Conservation of epigenetic regulation by the MLL3/4 tumour suppressor in planarian pluripotent stem cells,” *Nat. Commun.*, vol. 9, no. 1, p. 3633, Sep. 2018.
[63] A. Van Roten *et al.*, “A carcinogenic trigger to study the function of tumor suppressor genes in Schmidtea mediterranea,” *Dis. Model. Mech.*, vol. 11, no. 9, 16 2018.
[64] R. W. Hart and R. B. Setlow, “Correlation between deoxyribonucleic acid excision-repair and life-span in a number of mammalian species,” *Proc Natl Acad Sci U A*, vol. 71, no. 6, pp. 2169–73, Jun. 1974.
[65] S. L. MacRae *et al.*, “DNA repair in species with extreme lifespan differences,” *Aging*, vol. 7, no. 12, pp. 1171–84, Dec. 2015.
[66] N. A. Bishop, T. Lu, and B. A. Yankner, “Neural mechanisms of ageing and cognitive decline,” *Nature*, vol. 464, no. 7288, pp. 529–35, Mar. 2010.
[67] E. K. Nishimura, S. R. Granter, and D. E. Fisher, “Mechanisms of hair graying: incomplete melanocyte stem cell maintenance in the niche,” *Science*, vol. 307, no. 5710, pp. 720–4, Feb. 2005.
[68] B. D. Simons and H. Clevers, “Strategies for homeostatic stem cell self-renewal in adult tissues,” *Cell*, vol. 145, no. 6, pp. 851–62, Jun. 2011.

[69] K. W. Orford and D. T. Scadden, “Deconstructing stem cell self-renewal: genetic insights into cell-cycle regulation,” *Nat Rev Genet*, vol. 9, no. 2, pp. 115–28, Feb. 2008.
[70] C. H. Hsu *et al.*, “Framework analysis for the carcinogenic mode of action of nitrobenzene,” *J Env. Sci Health C Env. Carcinog Ecotoxicol Rev*, vol. 25, no. 2, pp. 155–84, Apr. 2007.
[71] S. M. Karam, “Lineage commitment and maturation of epithelial cells in the gut,” *Front Biosci*, vol. 4, pp. D286-98, Mar. 1999.
[72] C. Blanpain, V. Horsley, and E. Fuchs, “Epithelial stem cells: turning over new leaves,” *Cell*, vol. 128, no. 3, pp. 445–58, Feb. 2007.
[73] L. G. van der Flier and H. Clevers, “Stem cells, self-renewal, and differentiation in the intestinal epithelium,” *Annu Rev Physiol*, vol. 71, pp. 241–60, 2009.
[74] C. Gonzalez-Estevez, D. A. Felix, G. Rodriguez-Esteban, and A. A. Aboobaker, “Decreased neoblast progeny and increased cell death during starvation-induced planarian degrowth,” *Int J Dev Biol*, vol. 56, no. 1–3, pp. 83–91, 2012.
[75] E. Fuchs, “Epithelial Skin Biology: Three Decades of Developmental Biology, a Hundred Questions Answered and a Thousand New Ones to Address,” *Curr Top Dev Biol*, vol. 116, pp. 357–74, 2016.
[76] W. W. Pang, S. L. Schrier, and I. L. Weissman, “Age-associated changes in human hematopoietic stem cells,” *Semin Hematol*, vol. 54, no. 1, pp. 39–42, Jan. 2017.
[77] M. R. Lieber, “The mechanism of double-strand DNA break repair by the nonhomologous DNA end-joining pathway,” *Annu Rev Biochem*, vol. 79, pp. 181–211, 2010.
[78] C. Richardson and M. Jasin, “Frequent chromosomal translocations induced by DNA double-strand breaks,” *Nature*, vol. 405, no. 6787, pp. 697–700, Jun. 2000.
[79] R. E. Johnson, M. T. Washington, S. Prakash, and L. Prakash, “Fidelity of human DNA polymerase eta,” *J Biol Chem*, vol. 275, no. 11, pp. 7447–50, Mar. 2000.
[80] M. Hyun, J. Lee, K. Lee, A. May, V. A. Bohr, and B. Ahn, “Longevity and resistance to stress correlate with DNA repair capacity in Caenorhabditis elegans,” *Nucleic Acids Res*, vol. 36, no. 4, pp. 1380–9, Mar. 2008.
[81] H. Lans *et al.*, “DNA damage leads to progressive replicative decline but extends the life span of long-lived mutant animals,” *Cell Death Differ*, vol. 20, no. 12, pp. 1709–18, Dec. 2013.
[82] N. E. Sharpless and R. A. DePinho, “How stem cells age and why this makes us grow old,” *Nat Rev Mol Cell Biol*, vol. 8, no. 9, pp. 703–13, Sep. 2007.
[83] C. Blanpain, M. Mohrin, P. A. Sotiropoulou, and E. Passegue, “DNA-damage response in tissue-specific and cancer stem cells,” *Cell Stem Cell*, vol. 8, no. 1, pp. 16–29, Jan. 2011.
[84] J. H. Hendry, W. B. Cai, S. A. Roberts, and C. S. Potten, “p53 Deficiency Sensitizes Clonogenic Cells to Irradiation in the Large but Not the Small Intestine,” *Radiat. Res.*, vol. 148, no. 3, pp. 254–259, 1997.
[85] A. J. Merritt *et al.*, “The Role of p53 in Spontaneous and Radiation-induced Apoptosis in the Gastrointestinal Tract of Normal and p53-deficient Mice,” *Cancer Res.*, vol. 54, no. 3, pp. 614–617, Feb. 1994.
[86] A. J. Merritt *et al.*, “Differential expression of bcl-2 in intestinal epithelia. Correlation with attenuation of apoptosis in colonic crypts and the incidence of colonic neoplasia,” *J. Cell Sci.*, vol. 108, no. 6, pp. 2261–2271, Jun. 1995.
[87] W. Qiu *et al.*, “PUMA Regulates Intestinal Progenitor Cell Radiosensitivity and Gastrointestinal Syndrome,” *Cell Stem Cell*, vol. 2, no. 6, pp. 576–583, Jun. 2008.
[88] M. R. Lieber and Z. E. Karanjawala, “Ageing, repetitive genomes and DNA damage,” *Nat Rev Mol Cell Biol*, vol. 5, no. 1, pp. 69–75, Jan. 2004.
[89] G. M. Martin, A. C. Smith, D. J. Ketterer, C. E. Ogburn, and C. M. Disteche, “Increased chromosomal aberrations in first metaphases of cells isolated from the kidneys of aged mice,” *Isr J Med Sci*, vol. 21, no. 3, pp. 296–301, Mar. 1985.
[90] A. Torgovnick and B. Schumacher, “DNA repair mechanisms in cancer development and therapy,” *Front Genet*, vol. 6, p. 157, 2015.

[91] J. Bartek, J. Lukas, and J. Bartkova, “DNA damage response as an anti-cancer barrier: damage threshold and the concept of ‘conditional haploinsufficiency,’” *Cell Cycle*, vol. 6, no. 19, pp. 2344–7, Oct. 2007.
[92] J. Bartkova *et al.*, “DNA damage response as a candidate anti-cancer barrier in early human tumorigenesis,” *Nature*, vol. 434, no. 7035, pp. 864–70, Apr. 2005.
[93] L. Peng, T. Xu, T. Long, and H. Zuo, “Association Between BRCA Status and P53 Status in Breast Cancer: A Meta-Analysis,” *Med Sci Monit*, vol. 22, pp. 1939–45, Jun. 2016.
[94] A. P. Wiegmans *et al.*, “Rad51 supports triple negative breast cancer metastasis,” *Oncotarget*, vol. 5, no. 10, pp. 3261–72, May 2014.
[95] M. Zhang, R. L. Atkinson, and J. M. Rosen, “Selective targeting of radiation-resistant tumor-initiating cells,” *Proc Natl Acad Sci U A*, vol. 107, no. 8, pp. 3522–7, Feb. 2010.
[96] “Correction for Gasparini et al., Protective role of miR-155 in breast cancer through RAD51 targeting impairs homologous recombination after irradiation,” *Proc Natl Acad Sci U A*, vol. 114, no. 10, p. E2065, Mar. 2017.
[97] T. Meissner *et al.*, “Metastatic triple-negative breast cancer patient with TP53 tumor mutation experienced 11 months progression-free survival on bortezomib monotherapy without adverse events after ending standard treatments with grade 3 adverse events,” *Cold Spring Harb Mol Case Stud*, vol. 3, no. 4, Jul. 2017.
[98] D. Wang, R. Du, and S. Liu, “Rad51 inhibition sensitizes breast cancer stem cells to PARP inhibitor in triple-negative breast cancer,” *Chin J Cancer*, vol. 36, no. 1, p. 37, Mar. 2017.
[99] F. Delacote and B. S. Lopez, “Importance of the cell cycle phase for the choice of the appropriate DSB repair pathway, for genome stability maintenance: the trans-S double-strand break repair model,” *Cell Cycle*, vol. 7, no. 1, pp. 33–8, Jan. 2008.
[100] P. G. Barghouth, M. Thiruvalluvan, and N. J. Oviedo, “Bioelectrical regulation of cell cycle and the planarian model system,” *Biochim Biophys Acta*, vol. 1848, no. 10 Pt B, pp. 2629–37, Oct. 2015.
[101] J. Pellettieri, P. Fitzgerald, S. Watanabe, J. Mancuso, D. R. Green, and A. Sanchez Alvarado, “Cell death and tissue remodeling in planarian regeneration,” *Dev Biol*, vol. 338, no. 1, pp. 76–85, Feb. 2010.
[102] A. Sanchez Alvarado, “Planarian regeneration: its end is its beginning,” *Cell*, vol. 124, no. 2, pp. 241–5, Jan. 2006.
[103] A. M. Molinaro and B. J. Pearson, “In silico lineage tracing through single cell transcriptomics identifies a neural stem cell population in planarians,” *Genome Biol*, vol. 17, p. 87, Apr. 2016.
[104] J. C. van Wolfswinkel, D. E. Wagner, and P. W. Reddien, “Single-cell analysis reveals functionally distinct classes within the planarian stem cell compartment,” *Cell Stem Cell*, vol. 15, no. 3, pp. 326–339, Sep. 2014.
[105] P. Abnave, E. Aboukhatwa, N. Kosaka, J. Thompson, M. A. Hill, and A. A. Aboobaker, “Epithelial-mesenchymal transition transcription factors control pluripotent adult stem cell migration in vivo in planarians,” *Development*, vol. 144, no. 19, pp. 3440–3453, Oct. 2017.
[106] L. S. Swapna, A. M. Molinaro, N. Lindsay-Mosher, B. J. Pearson, and J. Parkinson, “Comparative transcriptomic analyses and single-cell RNA sequencing of the freshwater planarian Schmidtea mediterranea identify major cell types and pathway conservation,” *Genome Biol*, vol. 19, no. 1, p. 124, Aug. 2018.
[107] N. J. Oviedo, P. A. Newmark, and A. Sanchez Alvarado, “Allometric scaling and proportion regulation in the freshwater planarian Schmidtea mediterranea,” *Dev Dyn*, vol. 226, no. 2, pp. 326–33, Feb. 2003.
[108] P. A. Newmark and A. Sanchez Alvarado, “Not your father’s planarian: a classic model enters the era of functional genomics,” *Nat Rev Genet*, vol. 3, no. 3, pp. 210–9, Mar. 2002.
[109] T. H. Peiris *et al.*, “TOR signaling regulates planarian stem cells and controls localized and organismal growth,” *J Cell Sci*, vol. 125, no. Pt 7, pp. 1657–65, Apr. 2012.
[110] D. Wenemoser, S. W. Lapan, A. W. Wilkinson, G. W. Bell, and P. W. Reddien, “A molecular wound response program associated with regeneration initiation in planarians,” *Genes Dev*, vol. 26, no. 9, pp. 988–1002, May 2012.

[111] D. Wenemoser and P. W. Reddien, “Planarian regeneration involves distinct stem cell responses to wounds and tissue absence,” *Dev Biol*, vol. 344, no. 2, pp. 979–91, Aug. 2010.
[112] N. J. Oviedo and M. Levin, “smedinx-11 is a planarian stem cell gap junction gene required for regeneration and homeostasis,” *Development*, vol. 134, no. 17, pp. 3121–31, Sep. 2007.
[113] K. Lei *et al.*, “Egf Signaling Directs Neoblast Repopulation by Regulating Asymmetric Cell Division in Planarians,” *Dev Cell*, vol. 38, no. 4, pp. 413–29, Aug. 2016.
[114] A. Chinone and M. Matsumoto, “DrRad51 is required for chiasmata formation in meiosis in planarian Dugesia ryukyuensis,” *Mol Reprod Dev*, vol. 81, no. 5, pp. 409–21, May 2014.
[115] Y. Xiang, D. E. Miller, E. J. Ross, A. Sanchez Alvarado, and R. S. Hawley, “Synaptonemal complex extension from clustered telomeres mediates full-length chromosome pairing in Schmidtea mediterranea,” *Proc Natl Acad Sci U A*, vol. 111, no. 48, pp. E5159-68, Dec. 2014.
[116] H. Brandl, H. Moon, M. Vila-Farre, S. Y. Liu, I. Henry, and J. C. Rink, “PlanMine--a mineable resource of planarian biology and biodiversity,” *Nucleic Acids Res*, vol. 44, no. D1, pp. D764-73, Jan. 2016.
[117] S. M. Robb, K. Gotting, E. Ross, and A. Sanchez Alvarado, “SmedGD 2.0: The Schmidtea mediterranea genome database,” *Genesis*, vol. 53, no. 8, pp. 535–46, Aug. 2015.
[118] M. M. Vilenchik and A. G. Knudson, “Endogenous DNA double-strand breaks: production, fidelity of repair, and induction of cancer,” *Proc Natl Acad Sci U A*, vol. 100, no. 22, pp. 12871–6, Oct. 2003.
[119] S. Yin *et al.*, “SmedOB1 is Required for Planarian Homeostasis and Regeneration,” *Sci Rep*, vol. 6, p. 34013, Sep. 2016.
[120] L. Guo *et al.*, “An adaptable chromosome preparation methodology for use in invertebrate research organisms,” *BMC Biol*, vol. 16, no. 1, p. 25, Feb. 2018.
[121] T. Hayashi, M. Asami, S. Higuchi, N. Shibata, and K. Agata, “Isolation of planarian X-ray-sensitive stem cells by fluorescence-activated cell sorting,” *Dev Growth Differ*, vol. 48, no. 6, pp. 371–80, Aug. 2006.
[122] C. E. Bender *et al.*, “Mitochondrial pathway of apoptosis is ancestral in metazoans,” *Proc Natl Acad Sci U A*, vol. 109, no. 13, pp. 4904–9, Mar. 2012.
[123] E. Seung *et al.*, “Allogeneic hematopoietic chimerism in mice treated with sublethal myeloablation and anti-CD154 antibody: absence of graft-versus-host disease, induction of skin allograft tolerance, and prevention of recurrent autoimmunity in islet-allografted NOD/Lt mice,” *Blood*, vol. 95, no. 6, pp. 2175–82, Mar. 2000.
[124] R. H. Mole, “The LD50 for uniform low LET irradiation of man,” *Br J Radiol*, vol. 57, no. 677, pp. 355–69, May 1984.
[125] P. W. Reddien, N. J. Oviedo, J. R. Jennings, J. C. Jenkin, and A. Sanchez Alvarado, “SMEDWI-2 is a PIWI-like protein that regulates planarian stem cells,” *Science*, vol. 310, no. 5752, pp. 1327–30, Nov. 2005.
[126] C. R. Bardeen and F. H. Baetjer, “The inhibitive action of the Roentgen rays on regeneration in planarians,” *J. Exp. Zool.*, vol. 1, no. 1, pp. 191–195, May 1904.
[127] O. C. th Guedelhoefer and A. Sanchez Alvarado, “Amputation induces stem cell mobilization to sites of injury during planarian regeneration,” *Development*, vol. 139, no. 19, pp. 3510–20, Oct. 2012.
[128] L. Cao *et al.*, “A novel ATM/TP53/p21-mediated checkpoint only activated by chronic gamma-irradiation,” *PLoS One*, vol. 9, no. 8, p. e104279, 2014.
[129] X. L. Liu *et al.*, “ING5 knockdown enhances migration and invasion of lung cancer cells by inducing EMT via EGFR/PI3K/Akt and IL-6/STAT3 signaling pathways,” *Oncotarget*, vol. 8, no. 33, pp. 54265–54276, Aug. 2017.
[130] K. H. Herzog, M. J. Chong, M. Kapsetaki, J. I. Morgan, and P. J. McKinnon, “Requirement for Atm in ionizing radiation-induced cell death in the developing central nervous system,” *Science*, vol. 280, no. 5366, pp. 1089–91, May 1998.
[131] M. R. G. Taylor *et al.*, “Rad51 Paralogs Remodel Pre-synaptic Rad51 Filaments to Stimulate Homologous Recombination,” *Cell*, vol. 162, no. 2, pp. 271–286, Jul. 2015.

[132] J. Liu, T. Doty, B. Gibson, and W.-D. Heyer, “Human BRCA2 protein promotes RAD51 filament formation on RPA-covered single-stranded DNA,” *Nat. Struct. Mol. Biol.*, vol. 17, no. 10, pp. 1260–1262, Oct. 2010.
[133] T. Tsuzuki *et al.*, “Targeted disruption of the Rad51 gene leads to lethality in embryonic mice,” *Proc. Natl. Acad. Sci.*, vol. 93, no. 13, pp. 6236–6240, Jun. 1996.
[134] D. S. Lim and P. Hasty, “A mutation in mouse rad51 results in an early embryonic lethal that is suppressed by a mutation in p53.,” *Mol. Cell. Biol.*, vol. 16, no. 12, pp. 7133–7143, Dec. 1996.
[135] A. Flotho and F. Melchior, “Sumoylation: A Regulatory Protein Modification in Health and Disease,” *Annu. Rev. Biochem.*, vol. 82, no. 1, pp. 357–385, 2013.
[136] A. Pichler, C. Fatouros, H. Lee, and N. Eisenhardt, “SUMO conjugation – a mechanistic view,” *Biomol. Concepts*, vol. 8, no. 1, pp. 13–36, 2017.
[137] Garvin Alexander J. and Morris Joanna R., “SUMO, a small, but powerful, regulator of double-strand break repair,” *Philos. Trans. R. Soc. B Biol. Sci.*, vol. 372, no. 1731, p. 20160281, Oct. 2017.
[138] J. R. Morris and A. J. Garvin, “SUMO in the DNA Double-Stranded Break Response: Similarities, Differences, and Cooperation with Ubiquitin,” *J. Mol. Biol.*, vol. 429, no. 22, pp. 3376–3387, Nov. 2017.
[139] P. Sarangi and X. Zhao, “SUMO-mediated regulation of DNA damage repair and responses,” *Trends Biochem. Sci.*, vol. 40, no. 4, pp. 233–242, Apr. 2015.
[140] Z. Wang, W.-G. Zhu, and X. Xu, “Ubiquitin-like modifications in the DNA damage response,” *Mutat. Res. Mol. Mech. Mutagen.*, vol. 803–805, pp. 56–75, Oct. 2017.
[141] S. Bologna *et al.*, “Sumoylation regulates EXO1 stability and processing of DNA damage,” *Cell Cycle*, vol. 14, no. 15, pp. 2439–2450, Aug. 2015.
[142] I. A. Hendriks, L. W. Treffers, M. Verlaan-de Vries, J. V. Olsen, and A. C. O. Vertegaal, “SUMO-2 Orchestrates Chromatin Modifiers in Response to DNA Damage,” *Cell Rep.*, vol. 10, no. 10, pp. 1778–1791, Mar. 2015.
[143] I. A. Hendriks and A. C. O. Vertegaal, “SUMO in the DNA damage response,” *Oncotarget*, vol. 6, no. 18, pp. 15734–15735, Jun. 2015.
[144] C. Huang, J. Cheng, T. Bawa-Khalfe, X. Yao, Y. E. Chin, and E. T. H. Yeh, “SUMOylated ORC2 Recruits a Histone Demethylase to Regulate Centromeric Histone Modification and Genomic Stability,” *Cell Rep.*, vol. 15, no. 1, pp. 147–157, Apr. 2016.
[145] C.-S. Wu *et al.*, “SUMOylation of ATRIP potentiates DNA damage signaling by boosting multiple protein interactions in the ATR pathway,” *Genes Dev.*, vol. 28, no. 13, pp. 1472–1484, Jul. 2014.
[146] S. P. Jackson and D. Durocher, “Regulation of DNA damage responses by ubiquitin and SUMO,” *Mol. Cell*, vol. 49, no. 5, pp. 795–807, Mar. 2013.
[147] B. Lee and M. T. Muller, “SUMOylation enhances DNA methyltransferase 1 activity,” *Biochem. J.*, vol. 421, no. 3, pp. 449–461, Aug. 2009.
[148] Y. Qin *et al.*, “Ubc9 mediates nuclear localization and growth suppression of BRCA1 and BRCA1a proteins,” *J. Cell. Physiol.*, vol. 226, no. 12, pp. 3355–3367, 2011.
[149] H. Shima *et al.*, “Activation of the SUMO modification system is required for the accumulation of RAD51 at sites of DNA damage,” *J Cell Sci*, vol. 126, no. 22, pp. 5284–5292, Nov. 2013.
[150] R. Vyas *et al.*, “RNF4 is required for DNA double-strand break repair *in vivo*,” *Cell Death Differ.*, vol. 20, no. 3, pp. 490–502, Mar. 2013.
[151] J. N. Davis, M. T. McCabe, S. W. Hayward, J. M. Park, and M. L. Day, “Disruption of Rb/E2F Pathway Results in Increased Cyclooxygenase-2 Expression and Activity in Prostate Epithelial Cells,” *Cancer Res.*, vol. 65, no. 9, pp. 3633–3642, May 2005.
[152] S. Thomas, A. Balan, and P. Balaram, “The expression of retinoblastoma tumor suppressor protein in oral cancers and precancers: A clinicopathological study,” *Dent. Res. J.*, vol. 12, no. 4, p. 307, Jul. 2015.

[153] N. de Sousa, G. Rodriguez-Esteban, J. I. Rojo-Laguna, E. Salo, and T. Adell, “Hippo signaling controls cell cycle and restricts cell plasticity in planarians,” *PLoS Biol*, vol. 16, no. 1, p. e2002399, Jan. 2018.
[154] D. Walter *et al.*, “Exit from dormancy provokes DNA-damage-induced attrition in haematopoietic stem cells,” *Nature*, vol. 520, no. 7548, pp. 549–552, Apr. 2015.
[155] S. Owlarn *et al.*, “Generic wound signals initiate regeneration in missing-tissue contexts,” *Nat. Commun.*, vol. 8, Dec. 2017.
[156] M. Altmeyer, S. Messner, P. O. Hassa, M. Fey, and M. O. Hottiger, “Molecular mechanism of poly(ADP-ribosyl)ation by PARP1 and identification of lysine residues as ADP-ribose acceptor sites,” *Nucleic Acids Res.*, vol. 37, no. 11, pp. 3723–3738, Jun. 2009.
[157] C. Boehler *et al.*, “Poly(ADP-ribose) polymerase 3 (PARP3), a newcomer in cellular response to DNA damage and mitotic progression,” *Proc. Natl. Acad. Sci.*, vol. 108, no. 7, pp. 2783–2788, Feb. 2011.
[158] M. Rouleau *et al.*, “PARP-3 associates with polycomb group bodies and with components of the DNA damage repair machinery,” *J. Cell. Biochem.*, vol. 100, no. 2, pp. 385–401, 2007.
[159] S. L. Rulten *et al.*, “PARP-3 and APLF Function Together to Accelerate Nonhomologous End-Joining,” *Mol. Cell*, vol. 41, no. 1, pp. 33–45, Jan. 2011.
[160] A. Augustin *et al.*, “PARP-3 localizes preferentially to the daughter centriole and interferes with the G1/S cell cycle progression,” *J. Cell Sci.*, vol. 116, no. 8, pp. 1551–1562, Apr. 2003.
[161] T. Fernández-Marcelo *et al.*, “Poly (ADP-ribose) polymerase 3 (PARP3), a potential repressor of telomerase activity,” *J. Exp. Clin. Cancer Res.*, vol. 33, no. 1, p. 19, Feb. 2014.
[162] A. Rozanski *et al.*, “PlanMine 3.0-improvements to a mineable resource of flatworm biology and biodiversity,” *Nucleic Acids Res*, vol. 47, no. D1, pp. D812–D820, Jan. 2019.
[163] T. Stückemann *et al.*, “Antagonistic Self-Organizing Patterning Systems Control Maintenance and Regeneration of the Anteroposterior Axis in Planarians,” *Dev. Cell*, vol. 40, no. 3, pp. 248-263.e4, Feb. 2017.
[164] O. Wurtzel, I. M. Oderberg, and P. W. Reddien, “Planarian Epidermal Stem Cells Respond to Positional Cues to Promote Cell-Type Diversity,” *Dev. Cell*, vol. 40, no. 5, pp. 491-504.e5, Mar. 2017.
[165] J. Cairns, “Mutation selection and the natural history of cancer,” *Nature*, vol. 255, no. 5505, pp. 197–200, May 1975.
[166] C. Tomasetti, L. Li, and B. Vogelstein, “Stem cell divisions, somatic mutations, cancer etiology, and cancer prevention,” *Science*, vol. 355, no. 6331, pp. 1330–1334, Mar. 2017.
[167] J. H. Pomerantz and H. M. Blau, “Tumor suppressors: enhancers or suppressors of regeneration?,” *Dev. Camb. Engl.*, vol. 140, no. 12, pp. 2502–2512, Jun. 2013.
[168] C. J. Sherr, “Principles of tumor suppression,” *Cell*, vol. 116, no. 2, pp. 235–246, Jan. 2004.
[169] B. Qiu and M. C. Simon, “Oncogenes strike a balance between cellular growth and homeostasis,” *Semin. Cell Dev. Biol.*, vol. 43, pp. 3–10, Jul. 2015.
[170] R. Hill and H. Wu, “PTEN, stem cells, and cancer stem cells,” *J Biol Chem*, vol. 284, no. 18, pp. 11755–9, May 2009.
[171] M. Ming and Y. Y. He, “PTEN in DNA damage repair,” *Cancer Lett*, vol. 319, no. 2, pp. 125–9, Jun. 2012.
[172] B. Stiles, M. Groszer, S. Wang, J. Jiao, and H. Wu, “PTENless means more,” *Dev. Biol.*, vol. 273, no. 2, pp. 175–184, Sep. 2004.
[173] I. Sansal and W. R. Sellers, “The biology and clinical relevance of the PTEN tumor suppressor pathway,” *J Clin Oncol*, vol. 22, no. 14, pp. 2954–63, Jul. 2004.
[174] M. L. Sulis and R. Parsons, “PTEN: from pathology to biology,” *Trends Cell Biol*, vol. 13, no. 9, pp. 478–83, Sep. 2003.
[175] C. Miething *et al.*, “PTEN action in leukaemia dictated by the tissue microenvironment,” *Nature*, vol. 510, no. 7505, pp. 402–406, Jun. 2014.

[176] V. Nogueira *et al.*, “Akt determines replicative senescence and oxidative or oncogenic premature senescence and sensitizes cells to oxidative apoptosis,” *Cancer Cell*, vol. 14, no. 6, pp. 458–470, Dec. 2008.
[177] A. Bhardwaj *et al.*, “Suppression of Akt-mTOR pathway-a novel component of oncogene induced DNA damage response barrier in breast tumorigenesis,” *PloS One*, vol. 9, no. 5, p. e97076, 2014.
[178] M. S. Song, L. Salmena, and P. P. Pandolfi, “The functions and regulation of the PTEN tumour suppressor,” *Nat. Rev. Mol. Cell Biol.*, vol. 13, no. 5, pp. 283–296, Apr. 2012.
[179] T. Kurokawa *et al.*, “3’ Phosphatase activity toward phosphatidylinositol 3,4-bisphosphate [PI(3,4)P2] by voltage-sensing phosphatase (VSP),” *Proc Natl Acad Sci U A*, vol. 109, no. 25, pp. 10089–94, Jun. 2012.
[180] M. A. Lemmon and J. Schlessinger, “Cell signaling by receptor tyrosine kinases,” *Cell*, vol. 141, no. 7, pp. 1117–1134, Jun. 2010.
[181] D. R. Robinson, Y. M. Wu, and S. F. Lin, “The protein tyrosine kinase family of the human genome,” *Oncogene*, vol. 19, no. 49, pp. 5548–5557, Nov. 2000.
[182] E. Zwick, J. Bange, and A. Ullrich, “Receptor tyrosine kinase signalling as a target for cancer intervention strategies,” *Endocr. Relat. Cancer*, vol. 8, no. 3, pp. 161–173, Sep. 2001.
[183] L. Zhao and P. K. Vogt, “Hot-spot mutations in p110alpha of phosphatidylinositol 3-kinase (pI3K): differential interactions with the regulatory subunit p85 and with RAS,” *Cell Cycle Georget. Tex*, vol. 9, no. 3, pp. 596–600, Feb. 2010.
[184] T. F. Franke, D. R. Kaplan, L. C. Cantley, and A. Toker, “Direct regulation of the Akt proto-oncogene product by phosphatidylinositol-3,4-bisphosphate,” *Science*, vol. 275, no. 5300, pp. 665–668, Jan. 1997.
[185] J. A. Engelman, J. Luo, and L. C. Cantley, “The evolution of phosphatidylinositol 3-kinases as regulators of growth and metabolism,” *Nat. Rev. Genet.*, vol. 7, no. 8, pp. 606–619, Aug. 2006.
[186] A. M. Martelli *et al.*, “The emerging role of the phosphatidylinositol 3-kinase/Akt/mammalian target of rapamycin signaling network in normal myelopoiesis and leukemogenesis,” *Biochim. Biophys. Acta*, vol. 1803, no. 9, pp. 991–1002, Sep. 2010.
[187] A. M. Martelli, C. Evangelisti, F. Chiarini, and J. A. McCubrey, “The phosphatidylinositol 3-kinase/Akt/mTOR signaling network as a therapeutic target in acute myelogenous leukemia patients,” *Oncotarget*, vol. 1, no. 2, pp. 89–103, Jun. 2010.
[188] T. Maehama and J. E. Dixon, “The tumor suppressor, PTEN/MMAC1, dephosphorylates the lipid second messenger, phosphatidylinositol 3,4,5-trisphosphate,” *J. Biol. Chem.*, vol. 273, no. 22, pp. 13375–13378, May 1998.
[189] A. Carnero, C. Blanco-Aparicio, O. Renner, W. Link, and J. F. M. Leal, “The PTEN/PI3K/AKT signalling pathway in cancer, therapeutic implications,” *Curr. Cancer Drug Targets*, vol. 8, no. 3, pp. 187–198, May 2008.
[190] M. Zhao, “PTEN: a promising pharmacological target to enhance epithelial wound healing,” *Br J Pharmacol*, vol. 152, no. 8, pp. 1141–4, Dec. 2007.
[191] D. M. Li and H. Sun, “TEP1, encoded by a candidate tumor suppressor locus, is a novel protein tyrosine phosphatase regulated by transforming growth factor beta,” *Cancer Res.*, vol. 57, no. 11, pp. 2124–2129, Jun. 1997.
[192] J. Li *et al.*, “PTEN, a putative protein tyrosine phosphatase gene mutated in human brain, breast, and prostate cancer,” *Science*, vol. 275, no. 5308, pp. 1943–1947, Mar. 1997.
[193] P. A. Steck *et al.*, “Identification of a candidate tumour suppressor gene, MMAC1, at chromosome 10q23.3 that is mutated in multiple advanced cancers,” *Nat. Genet.*, vol. 15, no. 4, pp. 356–362, Apr. 1997.
[194] M. Zhao, “Electrical fields in wound healing-An overriding signal that directs cell migration,” *Semin. Cell Dev. Biol.*, vol. 20, no. 6, pp. 674–682, Aug. 2009.
[195] D. R. Alessi *et al.*, “Mechanism of activation of protein kinase B by insulin and IGF-1,” *EMBO J.*, vol. 15, no. 23, pp. 6541–6551, Dec. 1996.

[196] D. D. Sarbassov, D. A. Guertin, S. M. Ali, and D. M. Sabatini, “Phosphorylation and regulation of Akt/PKB by the rictor-mTOR complex,” *Science*, vol. 307, no. 5712, pp. 1098–1101, Feb. 2005.
[197] R. Zoncu, A. Efeyan, and D. M. Sabatini, “mTOR: from growth signal integration to cancer, diabetes and ageing,” *Nat. Rev. Mol. Cell Biol.*, vol. 12, no. 1, pp. 21–35, Jan. 2011.
[198] D. R. Alessi *et al.*, “Characterization of a 3-phosphoinositide-dependent protein kinase which phosphorylates and activates protein kinase Balpha,” *Curr. Biol. CB*, vol. 7, no. 4, pp. 261–269, Apr. 1997.
[199] B. D. Manning and L. C. Cantley, “AKT/PKB signaling: navigating downstream,” *Cell*, vol. 129, no. 7, pp. 1261–1274, Jun. 2007.
[200] J. T. Stuenaes *et al.*, “Beta-adrenoceptor stimulation potentiates insulin-stimulated PKB phosphorylation in rat cardiomyocytes via cAMP and PKA,” *Br. J. Pharmacol.*, vol. 160, no. 1, pp. 116–129, May 2010.
[201] K. Mahajan *et al.*, “Ack1 mediated AKT/PKB tyrosine 176 phosphorylation regulates its activation,” *PloS One*, vol. 5, no. 3, p. e9646, Mar. 2010.
[202] D. R. Plas and C. B. Thompson, “Akt-dependent transformation: there is more to growth than just surviving,” *Oncogene*, vol. 24, no. 50, pp. 7435–7442, Nov. 2005.
[203] E. S. Kandel and N. Hay, “The regulation and activities of the multifunctional serine/threonine kinase Akt/PKB,” *Exp. Cell Res.*, vol. 253, no. 1, pp. 210–229, Nov. 1999.
[204] J. Downward, “PI 3-kinase, Akt and cell survival,” *Semin. Cell Dev. Biol.*, vol. 15, no. 2, pp. 177–182, Apr. 2004.
[205] P. L. Dahia, “PTEN, a unique tumor suppressor gene,” *Endocr. Relat. Cancer*, vol. 7, no. 2, pp. 115–129, Jun. 2000.
[206] I. Vivanco and C. L. Sawyers, “The phosphatidylinositol 3-Kinase AKT pathway in human cancer,” *Nat. Rev. Cancer*, vol. 2, no. 7, pp. 489–501, Jul. 2002.
[207] K. E. van der Vos and P. J. Coffer, “The extending network of FOXO transcriptional target genes,” *Antioxid. Redox Signal.*, vol. 14, no. 4, pp. 579–592, Feb. 2011.
[208] A. E. Webb and A. Brunet, “FOXO transcription factors: key regulators of cellular quality control,” *Trends Biochem. Sci.*, vol. 39, no. 4, pp. 159–169, Apr. 2014.
[209] O. Kaidanovich-Beilin and J. R. Woodgett, “GSK-3: Functional Insights from Cell Biology and Animal Models,” *Front. Mol. Neurosci.*, vol. 4, p. 40, 2011.
[210] L. Hauck *et al.*, “Critical role for FoxO3a-dependent regulation of p21CIP1/WAF1 in response to statin signaling in cardiac myocytes,” *Circ. Res.*, vol. 100, no. 1, pp. 50–60, Jan. 2007.
[211] C.-J. Li, J.-K. Chang, C.-H. Chou, G.-J. Wang, and M.-L. Ho, “The PI3K/Akt/FOXO3a/p27Kip1 signaling contributes to anti-inflammatory drug-suppressed proliferation of human osteoblasts,” *Biochem. Pharmacol.*, vol. 79, no. 6, pp. 926–937, Mar. 2010.
[212] L. Rössig, A. S. Jadidi, C. Urbich, C. Badorff, A. M. Zeiher, and S. Dimmeler, “Akt-dependent phosphorylation of p21(Cip1) regulates PCNA binding and proliferation of endothelial cells,” *Mol. Cell. Biol.*, vol. 21, no. 16, pp. 5644–5657, Aug. 2001.
[213] J. Liang *et al.*, “PKB/Akt phosphorylates p27, impairs nuclear import of p27 and opposes p27-mediated G1 arrest,” *Nat. Med.*, vol. 8, no. 10, pp. 1153–1160, Oct. 2002.
[214] Y. Imai *et al.*, “Crosstalk between the Rb pathway and AKT signaling forms a quiescence-senescence switch,” *Cell Rep.*, vol. 7, no. 1, pp. 194–207, Apr. 2014.
[215] K. H. Limesand, K. L. Schwertfeger, and S. M. Anderson, “MDM2 is required for suppression of apoptosis by activated Akt1 in salivary acinar cells,” *Mol. Cell. Biol.*, vol. 26, no. 23, pp. 8840–8856, Dec. 2006.
[216] A. G. Abraham and E. O’Neill, “PI3K/Akt-mediated regulation of p53 in cancer,” *Biochem. Soc. Trans.*, vol. 42, no. 4, pp. 798–803, Aug. 2014.
[217] T. M. Gottlieb, J. F. M. Leal, R. Seger, Y. Taya, and M. Oren, “Cross-talk between Akt, p53 and Mdm2: possible implications for the regulation of apoptosis,” *Oncogene*, vol. 21, no. 8, pp. 1299–1303, Feb. 2002.

[218] Y. Ogawara *et al.*, “Akt enhances Mdm2-mediated ubiquitination and degradation of p53,” *J. Biol. Chem.*, vol. 277, no. 24, pp. 21843–21850, Jun. 2002.
[219] A. Brunet *et al.*, “Akt promotes cell survival by phosphorylating and inhibiting a Forkhead transcription factor,” *Cell*, vol. 96, no. 6, pp. 857–868, Mar. 1999.
[220] G. Song, G. Ouyang, and S. Bao, “The activation of Akt/PKB signaling pathway and cell survival,” *J. Cell. Mol. Med.*, vol. 9, no. 1, pp. 59–71, Mar. 2005.
[221] S. Pugazhenthi *et al.*, “Akt/protein kinase B up-regulates Bcl-2 expression through cAMP-response element-binding protein,” *J. Biol. Chem.*, vol. 275, no. 15, pp. 10761–10766, Apr. 2000.
[222] B. Vanhaesebroeck and D. R. Alessi, “The PI3K-PDK1 connection: more than just a road to PKB,” *Biochem. J.*, vol. 346 Pt 3, pp. 561–576, Mar. 2000.
[223] Z. Yuan *et al.*, “BIM-mediated AKT phosphorylation is a key modulator of arsenic trioxide-induced apoptosis in cisplatin-sensitive and -resistant ovarian cancer cells,” *PloS One*, vol. 6, no. 5, p. e20586, 2011.
[224] J. L. Coloff *et al.*, “Akt requires glucose metabolism to suppress puma expression and prevent apoptosis of leukemic T cells,” *J. Biol. Chem.*, vol. 286, no. 7, pp. 5921–5933, Feb. 2011.
[225] S. Yang, Z. Zhu, X. Zhang, N. Zhang, and Z. Yao, “Idelalisib induces PUMA-dependent apoptosis in colon cancer cells,” *Oncotarget*, vol. 8, no. 4, pp. 6102–6113, Jan. 2017.
[226] J. Sun *et al.*, “Aurora kinase inhibition induces PUMA via NF-κB to kill colon cancer cells,” *Mol. Cancer Ther.*, vol. 13, no. 5, pp. 1298–1308, May 2014.
[227] L. Sun *et al.*, “Ipatasertib, a novel Akt inhibitor, induces transcription factor FoxO3a and NF-κB directly regulates PUMA-dependent apoptosis,” *Cell Death Dis.*, vol. 9, no. 9, p. 911, Sep. 2018.
[228] R. A. Saxton and D. M. Sabatini, “mTOR Signaling in Growth, Metabolism, and Disease,” *Cell*, vol. 168, no. 6, pp. 960–976, 09 2017.
[229] C. Nardella *et al.*, “Aberrant Rheb-mediated mTORC1 activation and Pten haploinsufficiency are cooperative oncogenic events,” *Genes Dev.*, vol. 22, no. 16, pp. 2172–2177, Aug. 2008.
[230] B. D. Manning, M. N. Logsdon, A. I. Lipovsky, D. Abbott, D. J. Kwiatkowski, and L. C. Cantley, “Feedback inhibition of Akt signaling limits the growth of tumors lacking Tsc2,” *Genes Dev.*, vol. 19, no. 15, pp. 1773–1778, Aug. 2005.
[231] H. Yang, D. G. Rudge, J. D. Koos, B. Vaidialingam, H. J. Yang, and N. P. Pavletich, “mTOR kinase structure, mechanism and regulation,” *Nature*, vol. 497, no. 7448, pp. 217–223, May 2013.
[232] D.-H. Kim *et al.*, “GbetaL, a positive regulator of the rapamycin-sensitive pathway required for the nutrient-sensitive interaction between raptor and mTOR,” *Mol. Cell*, vol. 11, no. 4, pp. 895–904, Apr. 2003.
[233] S. Han, J. D. Ritzenthaler, Y. Zheng, and J. Roman, “PPARβ/δ agonist stimulates human lung carcinoma cell growth through inhibition of PTEN expression: the involvement of PI3K and NF-κB signals,” *Am. J. Physiol.-Lung Cell. Mol. Physiol.*, vol. 294, no. 6, pp. L1238–L1249, Jun. 2008.
[234] S. Kim, C. Domon-Dell, J. Kang, D. H. Chung, J.-N. Freund, and B. M. Evers, “Down-regulation of the tumor suppressor PTEN by the tumor necrosis factor-alpha/nuclear factor-kappaB (NF-kappaB)-inducing kinase/NF-kappaB pathway is linked to a default IkappaB-alpha autoregulatory loop,” *J. Biol. Chem.*, vol. 279, no. 6, pp. 4285–4291, Feb. 2004.
[235] K. M. Vasudevan, S. Gurumurthy, and V. M. Rangnekar, “Suppression of PTEN expression by NF-kappa B prevents apoptosis,” *Mol. Cell. Biol.*, vol. 24, no. 3, pp. 1007–1021, Feb. 2004.
[236] Y. Ahn, C. Y. Hwang, S.-R. Lee, K.-S. Kwon, and C. Lee, “The tumour suppressor PTEN mediates a negative regulation of the E3 ubiquitin-protein ligase Nedd4,” *Biochem. J.*, vol. 412, no. 2, pp. 331–338, Jun. 2008.
[237] X. Wang *et al.*, “NEDD4-1 is a proto-oncogenic ubiquitin ligase for PTEN,” *Cell*, vol. 128, no. 1, pp. 129–139, Jan. 2007.

[238] T. Gao, F. Furnari, and A. C. Newton, “PHLPP: a phosphatase that directly dephosphorylates Akt, promotes apoptosis, and suppresses tumor growth,” *Mol. Cell*, vol. 18, no. 1, pp. 13–24, Apr. 2005.
[239] J. R. Bayascas and D. R. Alessi, “Regulation of Akt/PKB Ser473 phosphorylation,” *Mol. Cell*, vol. 18, no. 2, pp. 143–145, Apr. 2005.
[240] M. Chen *et al.*, “Identification of PHLPP1 as a tumor suppressor reveals the role of feedback activation in PTEN-mutant prostate cancer progression,” *Cancer Cell*, vol. 20, no. 2, pp. 173–186, Aug. 2011.
[241] C. E. Berg, B. E. Lavan, and C. M. Rondinone, “Rapamycin partially prevents insulin resistance induced by chronic insulin treatment,” *Biochem. Biophys. Res. Commun.*, vol. 293, no. 3, pp. 1021–1027, May 2002.
[242] F. Tremblay and A. Marette, “Amino acid and insulin signaling via the mTOR/p70 S6 kinase pathway. A negative feedback mechanism leading to insulin resistance in skeletal muscle cells,” *J. Biol. Chem.*, vol. 276, no. 41, pp. 38052–38060, Oct. 2001.
[243] T. Haruta *et al.*, “A rapamycin-sensitive pathway down-regulates insulin signaling via phosphorylation and proteasomal degradation of insulin receptor substrate-1,” *Mol. Endocrinol. Baltim. Md*, vol. 14, no. 6, pp. 783–794, Jun. 2000.
[244] S. N. Jakobsen, D. G. Hardie, N. Morrice, and H. E. Tornqvist, “5’-AMP-activated protein kinase phosphorylates IRS-1 on Ser-789 in mouse C2C12 myotubes in response to 5-aminoimidazole-4-carboxamide riboside,” *J. Biol. Chem.*, vol. 276, no. 50, pp. 46912–46916, Dec. 2001.
[245] A. Tzatsos and K. V. Kandror, “Nutrients suppress phosphatidylinositol 3-kinase/Akt signaling via raptor-dependent mTOR-mediated insulin receptor substrate 1 phosphorylation,” *Mol. Cell. Biol.*, vol. 26, no. 1, pp. 63–76, Jan. 2006.
[246] O. N. Ozes *et al.*, “A phosphatidylinositol 3-kinase/Akt/mTOR pathway mediates and PTEN antagonizes tumor necrosis factor inhibition of insulin signaling through insulin receptor substrate-1,” *Proc. Natl. Acad. Sci. U. S. A.*, vol. 98, no. 8, pp. 4640–4645, Apr. 2001.
[247] L. S. Harrington *et al.*, “The TSC1-2 tumor suppressor controls insulin-PI3K signaling via regulation of IRS proteins,” *J. Cell Biol.*, vol. 166, no. 2, pp. 213–223, Jul. 2004.
[248] C. Adamidi *et al.*, “De novo assembly and validation of planaria transcriptome by massive parallel sequencing and shotgun proteomics,” *Genome Res*, vol. 21, no. 7, pp. 1193–200, Jul. 2011.
[249] M. A. Grohme *et al.*, “The genome of Schmidtea mediterranea and the evolution of core cellular mechanisms,” *Nature*, vol. 554, no. 7690, pp. 56–61, Feb. 2018.
[250] R. M. Labbe *et al.*, “A comparative transcriptomic analysis reveals conserved features of stem cell pluripotency in planarians and mammals,” *Stem Cells*, vol. 30, no. 8, pp. 1734–45, Aug. 2012.
[251] S. M. Robb, E. Ross, and A. Sanchez Alvarado, “SmedGD: the Schmidtea mediterranea genome database,” *Nucleic Acids Res*, vol. 36, no. Database issue, pp. D599-606, Jan. 2008.
[252] A. Sanchez Alvarado, P. A. Newmark, S. M. Robb, and R. Juste, “The Schmidtea mediterranea database as a molecular resource for studying platyhelminthes, stem cells and regeneration,” *Development*, vol. 129, no. 24, pp. 5659–65, Dec. 2002.
[253] T. Sandmann, M. C. Vogg, S. Owlarn, M. Boutros, and K. Bartscherer, “The head-regeneration transcriptome of the planarian Schmidtea mediterranea,” *Genome Biol*, vol. 12, no. 8, p. R76, Aug. 2011.
[254] K. Hobiger, T. Utesch, M. A. Mroginski, and T. Friedrich, “Coupling of Ci-VSP modules requires a combination of structure and electrostatics within the linker,” *Biophys. J.*, vol. 102, no. 6, pp. 1313–1322, Mar. 2012.
[255] S. Shenoy *et al.*, “Membrane association of the PTEN tumor suppressor: molecular details of the protein-membrane complex from SPR binding studies and neutron reflection,” *PloS One*, vol. 7, no. 4, p. e32591, 2012.

[256] C. A. Villalba-Galea, “New insights in the activity of voltage sensitive phosphatases,” *Cell. Signal.*, vol. 24, no. 8, pp. 1541–1547, Aug. 2012.
[257] G. Li *et al.*, “Conditional loss of PTEN leads to precocious development and neoplasia in the mammary gland,” *Dev. Camb. Engl.*, vol. 129, no. 17, pp. 4159–4170, Sep. 2002.
[258] A. Gericke, N. R. Leslie, M. Lösche, and A. H. Ross, “PtdIns(4,5)P2-mediated cell signaling: emerging principles and PTEN as a paradigm for regulatory mechanism,” *Adv. Exp. Med. Biol.*, vol. 991, pp. 85–104, 2013.
[259] L. Héron-Milhavet *et al.*, “Only Akt1 is required for proliferation, while Akt2 promotes cell cycle exit through p21 binding,” *Mol. Cell. Biol.*, vol. 26, no. 22, pp. 8267–8280, Nov. 2006.
[260] B. Dummler and B. A. Hemmings, “Physiological roles of PKB/Akt isoforms in development and disease,” *Biochem. Soc. Trans.*, vol. 35, no. Pt 2, pp. 231–235, Apr. 2007.
[261] S. Masure *et al.*, “Molecular cloning, expression and characterization of the human serine/threonine kinase Akt-3,” *Eur. J. Biochem.*, vol. 265, no. 1, pp. 353–360, Oct. 1999.
[262] G.-L. Zhou, D. F. Tucker, S. S. Bae, K. Bhatheja, M. J. Birnbaum, and J. Field, “Opposing roles for Akt1 and Akt2 in Rac/Pak signaling and cell migration,” *J. Biol. Chem.*, vol. 281, no. 47, pp. 36443–36453, Nov. 2006.
[263] S. F. Barnett *et al.*, “Identification and characterization of pleckstrin-homology-domain-dependent and isoenzyme-specific Akt inhibitors,” *Biochem. J.*, vol. 385, no. Pt 2, pp. 399–408, Jan. 2005.
[264] C. Parikh *et al.*, “Disruption of PH-kinase domain interactions leads to oncogenic activation of AKT in human cancers,” *Proc. Natl. Acad. Sci. U. S. A.*, vol. 109, no. 47, pp. 19368–19373, Nov. 2012.
[265] C. T. Fincher, O. Wurtzel, T. de Hoog, K. M. Kravarik, and P. W. Reddien, “Cell type transcriptome atlas for the planarian Schmidtea mediterranea,” *Science*, vol. 360, no. 6391, p. eaaq1736, May 2018.
[266] M. Plass *et al.*, “Cell type atlas and lineage tree of a whole complex animal by single-cell transcriptomics,” *Science*, vol. 360, no. 6391, 25 2018.
[267] K. C. Tu, B. J. Pearson, and A. Sanchez Alvarado, “TORC1 is required to balance cell proliferation and cell death in planarians,” *Dev Biol*, vol. 365, no. 2, pp. 458–69, May 2012.
[268] H. Kang and A. Sánchez Alvarado, “Flow cytometry methods for the study of cell-cycle parameters of planarian stem cells,” *Dev. Dyn. Off. Publ. Am. Assoc. Anat.*, vol. 238, no. 5, pp. 1111–1117, May 2009.
[269] C. Eng, “PTEN: one gene, many syndromes,” *Hum. Mutat.*, vol. 22, no. 3, pp. 183–198, Sep. 2003.
[270] M. C. Hollander, G. M. Blumenthal, and P. A. Dennis, “PTEN loss in the continuum of common cancers, rare syndromes and mouse models,” *Nat. Rev. Cancer*, vol. 11, no. 4, pp. 289–301, Apr. 2011.
[271] Z. Sun *et al.*, “PTEN C-terminal deletion causes genomic instability and tumor development,” *Cell Rep.*, vol. 6, no. 5, pp. 844–854, Mar. 2014.
[272] J. Torres and R. Pulido, “The tumor suppressor PTEN is phosphorylated by the protein kinase CK2 at its C terminus. Implications for PTEN stability to proteasome-mediated degradation,” *J. Biol. Chem.*, vol. 276, no. 2, pp. 993–998, Jan. 2001.
[273] M. M. Georgescu, K. H. Kirsch, T. Akagi, T. Shishido, and H. Hanafusa, “The tumor-suppressor activity of PTEN is regulated by its carboxyl-terminal region,” *Proc. Natl. Acad. Sci. U. S. A.*, vol. 96, no. 18, pp. 10182–10187, Aug. 1999.
[274] N. Chalhoub and S. J. Baker, “PTEN and the PI3-kinase pathway in cancer,” *Annu. Rev. Pathol.*, vol. 4, pp. 127–150, 2009.
[275] D. Voskas, L. S. Ling, and J. R. Woodgett, “Signals controlling un-differentiated states in embryonic stem and cancer cells: role of the phosphatidylinositol 3’ kinase pathway,” *J. Cell. Physiol.*, vol. 229, no. 10, pp. 1312–1322, Oct. 2014.
[276] B. T. Hennessy, D. L. Smith, P. T. Ram, Y. Lu, and G. B. Mills, “Exploiting the PI3K/AKT pathway for cancer drug discovery,” *Nat. Rev. Drug Discov.*, vol. 4, no. 12, pp. 988–1004, Dec. 2005.

[277] Y. Liao and M.-C. Hung, “Physiological regulation of Akt activity and stability,” *Am. J. Transl. Res.*, vol. 2, no. 1, pp. 19–42, Jan. 2010.
[278] H. R. Luo *et al.*, “Akt as a mediator of cell death,” *Proc. Natl. Acad. Sci. U. S. A.*, vol. 100, no. 20, pp. 11712–11717, Sep. 2003.
[279] M. Hanada, J. Feng, and B. A. Hemmings, “Structure, regulation and function of PKB/AKT--a major therapeutic target,” *Biochim. Biophys. Acta*, vol. 1697, no. 1–2, pp. 3–16, Mar. 2004.
[280] C.-L. Chuang, Y.-N. Lu, H.-C. Wang, and H.-Y. Chang, “Genetic dissection reveals that Akt is the critical kinase downstream of LRRK2 to phosphorylate and inhibit FOXO1, and promotes neuron survival,” *Hum. Mol. Genet.*, vol. 23, no. 21, pp. 5649–5658, Nov. 2014.
[281] X. Gao, T. P. Neufeld, and D. Pan, “Drosophila PTEN regulates cell growth and proliferation through PI3K-dependent and -independent pathways,” *Dev. Biol.*, vol. 221, no. 2, pp. 404–418, May 2000.
[282] D. C. Goberdhan, N. Paricio, E. C. Goodman, M. Mlodzik, and C. Wilson, “Drosophila tumor suppressor PTEN controls cell size and number by antagonizing the Chico/PI3-kinase signaling pathway,” *Genes Dev.*, vol. 13, no. 24, pp. 3244–3258, Dec. 1999.
[283] M. P. Scheid and J. R. Woodgett, “Unravelling the activation mechanisms of protein kinase B/Akt,” *FEBS Lett.*, vol. 546, no. 1, pp. 108–112, Jul. 2003.
[284] C. Segrelles *et al.*, “Akt signaling leads to stem cell activation and promotes tumor development in epidermis,” *Stem Cells Dayt. Ohio*, vol. 32, no. 7, pp. 1917–1928, Jul. 2014.
[285] J. R. Woodgett, “Recent advances in the protein kinase B signaling pathway,” *Curr. Opin. Cell Biol.*, vol. 17, no. 2, pp. 150–157, Apr. 2005.
[286] A. P. Bhatt and B. Damania, “AKTivation of PI3K/AKT/mTOR signaling pathway by KSHV,” *Front. Immunol.*, vol. 3, Jan. 2013.
[287] Y. L. Chen, P. Y. Law, and H. H. Loh, “Inhibition of akt/protein kinase B signaling by naltrindole in small cell lung cancer cells,” *Cancer Res.*, vol. 64, no. 23, pp. 8723–8730, Dec. 2004.
[288] Q.-W. Fan *et al.*, “Akt and Autophagy Cooperate to Promote Survival of Drug-Resistant Glioma,” *Sci Signal*, vol. 3, no. 147, pp. ra81–ra81, Nov. 2010.
[289] A. Parcellier, L. A. Tintignac, E. Zhuravleva, and B. A. Hemmings, “PKB and the mitochondria: AKTing on apoptosis,” *Cell. Signal.*, vol. 20, no. 1, pp. 21–30, Jan. 2008.
[290] E. M. Tanaka and P. W. Reddien, “The cellular basis for animal regeneration,” *Dev. Cell*, vol. 21, no. 1, pp. 172–185, Jul. 2011.
[291] K. D. Poss, “Advances in understanding tissue regenerative capacity and mechanisms in animals,” *Nat. Rev. Genet.*, vol. 11, no. 10, pp. 710–722, Oct. 2010.
[292] P. W. Reddien, “Specialized progenitors and regeneration,” *Development*, vol. 140, no. 5, pp. 951–7, Mar. 2013.
[293] M. W. Cowles, D. D. R. Brown, S. V. Nisperos, B. N. Stanley, B. J. Pearson, and R. M. Zayas, “Genome-wide analysis of the bHLH gene family in planarians identifies factors required for adult neurogenesis and neuronal regeneration,” *Dev. Camb. Engl.*, vol. 140, no. 23, pp. 4691–4702, Dec. 2013.
[294] D. M. Benbrook and C. P. Masamha, “The pro-survival function of Akt kinase can be overridden or altered to contribute to induction of apoptosis,” *Curr. Cancer Drug Targets*, vol. 11, no. 5, pp. 586–599, Jun. 2011.
[295] K. C. Zimmermann, C. Bonzon, and D. R. Green, “The machinery of programmed cell death,” *Pharmacol. Ther.*, vol. 92, no. 1, pp. 57–70, Oct. 2001.
[296] M. Rane J., “Regulation of neutrophil apoptosis by modulation of PKB/Akt activation,” *Front. Biosci.*, vol. Volume, no. 14, p. 2400, 2009.
[297] P. Rompolas, J. Azimzadeh, W. F. Marshall, and S. M. King, “Analysis of ciliary assembly and function in planaria,” *Methods Enzymol.*, vol. 525, pp. 245–264, 2013.
[298] A. Sanchez Alvarado and P. A. Newmark, “Double-stranded RNA specifically disrupts gene expression during planarian regeneration,” *Proc Natl Acad Sci U A*, vol. 96, no. 9, pp. 5049–54, Apr. 1999.

[299] H. Thi-Kim Vu *et al.*, “Stem cells and fluid flow drive cyst formation in an invertebrate excretory organ,” *eLife*, vol. 4, Jun. 2015.
[300] P. Rompolas, R. S. Patel-King, and S. M. King, “An outer arm Dynein conformational switch is required for metachronal synchrony of motile cilia in planaria,” *Mol. Biol. Cell*, vol. 21, no. 21, pp. 3669–3679, Nov. 2010.
[301] J. C. Rink, H. T.-K. Vu, and A. Sánchez Alvarado, “The maintenance and regeneration of the planarian excretory system are regulated by EGFR signaling,” *Dev. Camb. Engl.*, vol. 138, no. 17, pp. 3769–3780, Sep. 2011.
[302] M. L. Scimone, M. Srivastava, G. W. Bell, and P. W. Reddien, “A regulatory program for excretory system regeneration in planarians,” *Dev. Camb. Engl.*, vol. 138, no. 20, pp. 4387–4398, Oct. 2011.
[303] S. W. Lapan and P. W. Reddien, “Transcriptome analysis of the planarian eye identifies ovo as a specific regulator of eye regeneration,” *Cell Rep.*, vol. 2, no. 2, pp. 294–307, Aug. 2012.
[304] J. N. Witchley, M. Mayer, D. E. Wagner, J. H. Owen, and P. W. Reddien, “Muscle cells provide instructions for planarian regeneration,” *Cell Rep.*, vol. 4, no. 4, pp. 633–641, Aug. 2013.
[305] K. A. Gurley, J. C. Rink, and A. Sánchez Alvarado, “Beta-catenin defines head versus tail identity during planarian regeneration and homeostasis,” *Science*, vol. 319, no. 5861, pp. 323–327, Jan. 2008.
[306] S. W. Lapan and P. W. Reddien, “dlx and sp6-9 Control optic cup regeneration in a prototypic eye,” *PLoS Genet.*, vol. 7, no. 8, p. e1002226, Aug. 2011.
[307] K. G. Ross *et al.*, “Novel monoclonal antibodies to study tissue regeneration in planarians,” *BMC Dev. Biol.*, vol. 15, p. 2, Jan. 2015.
[308] D. L. Clement *et al.*, “PDGFRα signaling in the primary cilium regulates NHE1-dependent fibroblast migration via coordinated differential activity of MEK1/2-ERK1/2-p90RSK and AKT signaling pathways,” *J. Cell Sci.*, vol. 126, no. Pt 4, pp. 953–965, Feb. 2013.
[309] H. Higginbotham *et al.*, “Arl13b-regulated cilia activities are essential for polarized radial glial scaffold formation,” *Nat. Neurosci.*, vol. 16, no. 8, pp. 1000–1007, Aug. 2013.
[310] S. T. Christensen, C. A. Clement, P. Satir, and L. B. Pedersen, “Primary cilia and coordination of receptor tyrosine kinase (RTK) signalling,” *J. Pathol.*, vol. 226, no. 2, pp. 172–184, Jan. 2012.
[311] M. Jacoby *et al.*, “*INPP5E* mutations cause primary cilium signaling defects, ciliary instability and ciliopathies in human and mouse,” *Nat. Genet.*, vol. 41, no. 9, pp. 1027–1031, Sep. 2009.
[312] R. Bernards, “A missing link in genotype-directed cancer therapy,” *Cell*, vol. 151, no. 3, pp. 465–468, Oct. 2012.
[313] S. K. Pal, K. Reckamp, H. Yu, and R. A. Figlin, “Akt inhibitors in clinical development for the treatment of cancer,” *Expert Opin. Investig. Drugs*, vol. 19, no. 11, pp. 1355–1366, Nov. 2010.
[314] W. S. Chen *et al.*, “Growth retardation and increased apoptosis in mice with homozygous disruption of the Akt1 gene,” *Genes Dev.*, vol. 15, no. 17, pp. 2203–2208, Sep. 2001.
[315] L. Schneider *et al.*, “PDGFRalphaalpha signaling is regulated through the primary cilium in fibroblasts,” *Curr. Biol. CB*, vol. 15, no. 20, pp. 1861–1866, Oct. 2005.
[316] D. Zhu, S. Shi, H. Wang, and K. Liao, “Growth arrest induces primary-cilium formation and sensitizes IGF-1-receptor signaling during differentiation induction of 3T3-L1 preadipocytes,” *J. Cell Sci.*, vol. 122, no. Pt 15, pp. 2760–2768, Aug. 2009.
[317] C. Boehlke *et al.*, “Primary cilia regulate mTORC1 activity and cell size through Lkb1,” *Nat. Cell Biol.*, vol. 12, no. 11, pp. 1115–1122, Nov. 2010.
[318] A. Boletta, “Emerging evidence of a link between the polycystins and the mTOR pathways,” *PathoGenetics*, vol. 2, no. 1, p. 6, Oct. 2009.
[319] R. Dere, P. D. Wilson, R. N. Sandford, and C. L. Walker, “Carboxy terminal tail of polycystin-1 regulates localization of TSC2 to repress mTOR,” *PloS One*, vol. 5, no. 2, p. e9239, Feb. 2010.

[320] D.-C. Fischer *et al.*, “Activation of the AKT/mTOR pathway in autosomal recessive polycystic kidney disease (ARPKD),” *Nephrol. Dial. Transplant. Off. Publ. Eur. Dial. Transpl. Assoc. - Eur. Ren. Assoc.*, vol. 24, no. 6, pp. 1819–1827, Jun. 2009.
[321] S. Vriz, S. Reiter, and B. Galliot, “Cell death: a program to regenerate,” *Curr. Top. Dev. Biol.*, vol. 108, pp. 121–151, 2014.
[322] A. M. Aravanis, M. Lee, and R. D. Klausner, “Next-Generation Sequencing of Circulating Tumor DNA for Early Cancer Detection,” *Cell*, vol. 168, no. 4, pp. 571–574, Feb. 2017.
[323] H. Cho, A. B. Mariotto, L. M. Schwartz, J. Luo, and S. Woloshin, “When do changes in cancer survival mean progress? The insight from population incidence and mortality,” *J Natl Cancer Inst Monogr*, vol. 2014, no. 49, pp. 187–97, Nov. 2014.
[324] R. L. Siegel *et al.*, “Colorectal cancer statistics, 2017,” *CA Cancer J Clin*, vol. 67, no. 3, pp. 177–193, May 2017.
[325] M. J. Hayat, N. Howlader, M. E. Reichman, and B. K. Edwards, “Cancer statistics, trends, and multiple primary cancer analyses from the Surveillance, Epidemiology, and End Results (SEER) Program,” *Oncologist*, vol. 12, no. 1, pp. 20–37, Jan. 2007.
[326] C. Piazza, O. Dessouky, G. Peretti, D. Cocco, L. De Benedetto, and P. Nicolai, “Narrow-band imaging: a new tool for evaluation of head and neck squamous cell carcinomas. Review of the literature,” *Acta Otorhinolaryngol Ital*, vol. 28, no. 2, pp. 49–54, Apr. 2008.
[327] A. Watanabe, M. Taniguchi, H. Tsujie, M. Hosokawa, M. Fujita, and S. Sasaki, “The value of narrow band imaging endoscope for early head and neck cancers,” *Otolaryngol Head Neck Surg*, vol. 138, no. 4, pp. 446–51, Apr. 2008.
[328] S. Fujii, M. Yamazaki, M. Muto, and A. Ochiai, “Microvascular irregularities are associated with composition of squamous epithelial lesions and correlate with subepithelial invasion of superficial-type pharyngeal squamous cell carcinoma,” *Histopathology*, vol. 56, no. 4, pp. 510–22, Mar. 2010.
[329] J. J. Jacobson *et al.*, “The cost burden of oral, oral pharyngeal, and salivary gland cancers in three groups: commercial insurance, Medicare, and Medicaid,” *Head Neck Oncol*, vol. 4, p. 15, 2012.
[330] B. Wang, S. Zhang, K. Yue, and X. D. Wang, “The recurrence and survival of oral squamous cell carcinoma: a report of 275 cases,” *Chin J Cancer*, vol. 32, no. 11, pp. 614–8, Nov. 2013.
[331] E. Bogomolny, S. Mordechai, A. Zwielly, and M. Huleihel, “Early detection of premalignant changes in cell cultures using light-induced fluorescence spectroscopy,” *Eur Biophys J*, vol. 38, no. 7, pp. 971–80, Sep. 2009.
[332] L. C. Trotman *et al.*, “Ubiquitination regulates PTEN nuclear import and tumor suppression,” *Cell*, vol. 128, no. 1, pp. 141–56, Jan. 2007.
[333] W. H. Shen *et al.*, “Essential role for nuclear PTEN in maintaining chromosomal integrity,” *Cell*, vol. 128, no. 1, pp. 157–70, Jan. 2007.
[334] E. Terrien *et al.*, “Interference with the PTEN-MAST2 Interaction by a Viral Protein Leads to Cellular Relocalization of PTEN,” *Sci Signal*, vol. 5, no. 237, pp. ra58–ra58, Aug. 2012.
[335] S. R. Shinde and S. Maddika, “PTEN modulates EGFR late endocytic trafficking and degradation by dephosphorylating Rab7,” *Nat. Commun.*, vol. 7, p. 10689, Feb. 2016.
[336] P. Malaney, R. R. Pathak, B. Xue, V. N. Uversky, and V. Davé, “Intrinsic disorder in PTEN and its interactome confers structural plasticity and functional versatility,” *Sci. Rep.*, vol. 3, p. 2035, 2013.
[337] J.-C. Soria *et al.*, “Lack of PTEN expression in non-small cell lung cancer could be related to promoter methylation,” *Clin. Cancer Res. Off. J. Am. Assoc. Cancer Res.*, vol. 8, no. 5, pp. 1178–1184, May 2002.
[338] T. Tamguney and D. Stokoe, “New insights into PTEN,” *J. Cell Sci.*, vol. 120, no. 23, pp. 4071–4079, Dec. 2007.
[339] N. I. Noguera *et al.*, “PML/RARa inhibits PTEN expression in hematopoietic cells by competing with PU.1 transcriptional activity,” *Oncotarget*, vol. 7, no. 41, pp. 66386–66397, 2016.

[340] H. T. Chou *et al.*, “HES-Mediated Repression of Pten in Caenorhabditis elegans,” *G3 GenesGenomesGenetics*, vol. 5, no. 12, pp. 2619–2628, Oct. 2015.
[341] B. Uygur, K. Abramo, E. Leikina, C. Vary, L. Liaw, and W.-S. Wu, “SLUG is a direct transcriptional repressor of PTEN tumor suppressor,” *The Prostate*, vol. 75, no. 9, pp. 907–916, Jun. 2015.
[342] S. Wang *et al.*, “SOX2, a predictor of survival in gastric cancer, inhibits cell proliferation and metastasis by regulating PTEN,” *Cancer Lett.*, vol. 358, no. 2, pp. 210–219, Mar. 2015.
[343] Y. Lin, T. Kang, and B. P. Zhou, “Doxorubicin enhances Snail/LSD1-mediated PTEN suppression in a PARP1-dependent manner,” *Cell Cycle Georget. Tex*, vol. 13, no. 11, pp. 1708–1716, 2014.
[344] M. Escrivà *et al.*, “Repression of PTEN phosphatase by Snail1 transcriptional factor during gamma radiation-induced apoptosis,” *Mol. Cell. Biol.*, vol. 28, no. 5, pp. 1528–1540, Mar. 2008.
[345] A. Yoshimi *et al.*, “Evi1 represses PTEN expression and activates PI3K/AKT/mTOR via interactions with polycomb proteins,” *Blood*, vol. 117, no. 13, pp. 3617–3628, Mar. 2011.
[346] J. Lu *et al.*, “Stem cell factor SALL4 represses the transcriptions of PTEN and SALL1 through an epigenetic repressor complex,” *PloS One*, vol. 4, no. 5, p. e5577, 2009.
[347] J.-Y. Lee *et al.*, “Id-1 activates Akt-mediated Wnt signaling and p27(Kip1) phosphorylation through PTEN inhibition,” *Oncogene*, vol. 28, no. 6, pp. 824–831, Feb. 2009.
[348] P. Zhang, J. H. Chen, and X. L. Guo, “New insights into PTEN regulation mechanisms and its potential function in targeted therapies.,” *Biomed. Pharmacother. Biomedecine Pharmacother.*, vol. 66, no. 7, pp. 485–490, Oct. 2012.
[349] D. Xia *et al.*, “Mitogen-activated protein kinase kinase-4 promotes cell survival by decreasing PTEN expression through an NF kappa B-dependent pathway,” *J. Biol. Chem.*, vol. 282, no. 6, pp. 3507–3519, Feb. 2007.
[350] Y. H. Shen *et al.*, “Up-regulation of PTEN (phosphatase and tensin homolog deleted on chromosome ten) mediates p38 MAPK stress signal-induced inhibition of insulin signaling. A cross-talk between stress signaling and insulin signaling in resistin-treated human endothelial cells,” *J. Biol. Chem.*, vol. 281, no. 12, pp. 7727–7736, Mar. 2006.
[351] T. Virolle *et al.*, “The Egr-1 transcription factor directly activates PTEN during irradiation-induced signalling,” *Nat. Cell Biol.*, vol. 3, no. 12, pp. 1124–1128, Dec. 2001.
[352] A. Dereli-Öz, G. Versini, and T. D. Halazonetis, “Studies of genomic copy number changes in human cancers reveal signatures of DNA replication stress.,” *Mol. Oncol.*, vol. 5, no. 4, pp. 308–314, Aug. 2011.
[353] I. Hazan, T. G. Hofmann, and R. I. Aqeilan, “Tumor Suppressor Genes within Common Fragile Sites Are Active Players in the DNA Damage Response,” *PLOS Genet.*, vol. 12, no. 12, p. e1006436, Dec. 2016.
[354] J. G. Tate *et al.*, “COSMIC: the Catalogue Of Somatic Mutations In Cancer,” *Nucleic Acids Res.*, vol. 47, no. D1, pp. D941–D947, Jan. 2019.
[355] R. Beroukhim *et al.*, “The landscape of somatic copy-number alteration across human cancers,” *Nature*, vol. 463, no. 7283, pp. 899–905, Feb. 2010.
[356] A. Franchitto, “Genome Instability at Common Fragile Sites: Searching for the Cause of Their Instability,” *BioMed Research International*, 2013. [Online]. Available: https://www.hindawi.com/journals/bmri/2013/730714/. [Accessed: 19-Mar-2019].
[357] C. Abate-Shen and M. M. Shen, “Molecular genetics of prostate cancer,” *Genes Dev*, vol. 14, no. 19, pp. 2410–34, Oct. 2000.
[358] R. L. Vinall *et al.*, “Initiation of prostate cancer in mice by Tp53R270H: evidence for an alternative molecular progression,” *Model Mech*, vol. 5, no. 6, pp. 914–20, Nov. 2012.
[359] A. Di Cristofano, B. Pesce, C. Cordon-Cardo, and P. P. Pandolfi, “Pten is essential for embryonic development and tumour suppression,” *Nat. Genet.*, vol. 19, no. 4, pp. 348–355, Aug. 1998.
[360] K. Podsypanina *et al.*, “Mutation of Pten/Mmac1 in mice causes neoplasia in multiple organ systems,” *Proc. Natl. Acad. Sci. U. S. A.*, vol. 96, no. 4, pp. 1563–1568, Feb. 1999.

[361] S. I. Wang, R. Parsons, and M. Ittmann, “Homozygous deletion of the PTEN tumor suppressor gene in a subset of prostate adenocarcinomas,” *Clin. Cancer Res. Off. J. Am. Assoc. Cancer Res.*, vol. 4, no. 3, pp. 811–815, Mar. 1998.
[362] H. Suzuki *et al.*, “Interfocal heterogeneity of PTEN/MMAC1 gene alterations in multiple metastatic prostate cancer tissues,” *Cancer Res.*, vol. 58, no. 2, pp. 204–209, Jan. 1998.
[363] M. Szabolcs *et al.*, “Irs2 inactivation suppresses tumor progression in Pten+/- mice,” *Am. J. Pathol.*, vol. 174, no. 1, pp. 276–86, Jan. 2009.
[364] T. H. Beckham, J. C. Cheng, P. Lu, S. T. Marrison, J. S. Norris, and X. Liu, “Acid ceramidase promotes nuclear export of PTEN through sphingosine 1-phosphate mediated Akt signaling,” *PLoS One*, vol. 8, no. 10, p. e76593, 2013.
[365] R. Ricci *et al.*, “Role of PTEN in gastrointestinal stromal tumor progression,” *Arch. Pathol. Lab. Med.*, vol. 128, no. 4, pp. 421–5, Apr. 2004.
[366] Y. Zhang, D. Yu, X. Li, J. Hu, and J. Gong, “Reduced expression of PTEN protein and its prognostic significance in the gastrointestinal stromal tumor,” *J. Huazhong Univ. Sci. Technol. Med. Sci. Hua Zhong Ke Ji Xue Xue Bao Yi Xue Ying Wen Ban Huazhong Keji Daxue Xuebao Yixue Yingdewen Ban*, vol. 30, no. 2, pp. 165–169, Apr. 2010.
[367] D. C. Whiteman, X. P. Zhou, M. C. Cummings, S. Pavey, N. K. Hayward, and C. Eng, “Nuclear PTEN expression and clinicopathologic features in a population-based series of primary cutaneous melanoma,” *Int J Cancer*, vol. 99, no. 1, pp. 63–7, May 2002.
[368] M. Tachibana *et al.*, “Expression and prognostic significance of PTEN product protein in patients with esophageal squamous cell carcinoma,” *Cancer*, vol. 94, no. 7, pp. 1955–60, Apr. 2002.
[369] O. Gimm *et al.*, “Differential nuclear and cytoplasmic expression of PTEN in normal thyroid tissue, and benign and malignant epithelial thyroid tumors,” *Am. J. Pathol.*, vol. 156, no. 5, pp. 1693–1700, May 2000.
[370] M. E. Ginn-Pease and C. Eng, “Increased nuclear phosphatase and tensin homologue deleted on chromosome 10 is associated with G0-G1 in MCF-7 cells,” *Cancer Res*, vol. 63, no. 2, pp. 282–6, Jan. 2003.
[371] Y.-R. Lee, M. Chen, and P. P. Pandolfi, “The functions and regulation of the PTEN tumour suppressor: new modes and prospects,” *Nat. Rev. Mol. Cell Biol.*, vol. 19, no. 9, pp. 547–562, Sep. 2018.
[372] N. R. Leslie and C. P. Downes, “PTEN function: how normal cells control it and tumour cells lose it,” *Biochem. J.*, vol. 382, no. Pt 1, pp. 1–11, Aug. 2004.
[373] C. Bassi *et al.*, “Nuclear PTEN controls DNA repair and sensitivity to genotoxic stress,” *Science*, vol. 341, no. 6144, pp. 395–9, Jul. 2013.
[374] J. X. He, X. Kang, Y. X. Yin, K. S. C. Chao, and W. H. Shen, “PTEN regulates DNA replication progression and stalled fork recovery,” *Nat. Commun.*, vol. 6, Jul. 2015.
[375] J.-H. Chung, M. E. Ginn-Pease, and C. Eng, “Phosphatase and tensin homologue deleted on chromosome 10 (PTEN) has nuclear localization signal-like sequences for nuclear import mediated by major vault protein,” *Cancer Res.*, vol. 65, no. 10, pp. 4108–4116, May 2005.
[376] Z. Yu *et al.*, “PTEN associates with the vault particles in HeLa cells,” *J. Biol. Chem.*, vol. 277, no. 43, pp. 40247–40252, Oct. 2002.
[377] T. Minaguchi, K. A. Waite, and C. Eng, “Nuclear localization of PTEN is regulated by Ca(2+) through a tyrosil phosphorylation-independent conformational modification in major vault protein,” *Cancer Res.*, vol. 66, no. 24, pp. 11677–11682, Dec. 2006.
[378] J.-H. Chung and C. Eng, “Nuclear-cytoplasmic partitioning of phosphatase and tensin homologue deleted on chromosome 10 (PTEN) differentially regulates the cell cycle and apoptosis,” *Cancer Res.*, vol. 65, no. 18, pp. 8096–8100, Sep. 2005.
[379] F. Liu, S. Wagner, R. B. Campbell, J. A. Nickerson, C. A. Schiffer, and A. H. Ross, “PTEN enters the nucleus by diffusion,” *J. Cell. Biochem.*, vol. 96, no. 2, pp. 221–234, Oct. 2005.

[380] A. Gil *et al.*, “Nuclear localization of PTEN by a Ran-dependent mechanism enhances apoptosis: Involvement of an N-terminal nuclear localization domain and multiple nuclear exclusion motifs,” *Mol. Biol. Cell*, vol. 17, no. 9, pp. 4002–4013, Sep. 2006.
[381] D. Görlich and U. Kutay, “Transport between the cell nucleus and the cytoplasm,” *Annu. Rev. Cell Dev. Biol.*, vol. 15, pp. 607–660, 1999.
[382] Y. M. Chook and G. Blobel, “Karyopherins and nuclear import,” *Curr. Opin. Struct. Biol.*, vol. 11, no. 6, pp. 703–715, Dec. 2001.
[383] F. Melchior, B. Paschal, J. Evans, and L. Gerace, “Inhibition of nuclear protein import by nonhydrolyzable analogues of GTP and identification of the small GTPase Ran/TC4 as an essential transport factor,” *J. Cell Biol.*, vol. 123, no. 6 Pt 2, pp. 1649–1659, Dec. 1993.
[384] M. Chen *et al.*, “The nuclear transport receptor Importin-11 is a tumor suppressor that maintains PTEN protein,” *J. Cell Biol.*, vol. 216, no. 3, pp. 641–656, 06 2017.
[385] N. Amodio *et al.*, “Oncogenic Role of the E3 Ubiquitin Ligase NEDD4-1, a PTEN Negative Regulator, in Non-Small-Cell Lung Carcinomas,” *Am. J. Pathol.*, vol. 177, no. 5, pp. 2622–2634, Nov. 2010.
[386] L. C. Trotman *et al.*, “Ubiquitination regulates PTEN nuclear import and tumor suppression,” *Cell*, vol. 128, no. 1, pp. 141–156, Jan. 2007.
[387] S. S. Kim, N. J. Yoo, E. G. Jeong, M. S. Kim, and S. H. Lee, “Expression of NEDD4-1, a PTEN regulator, in gastric and colorectal carcinomas,” *APMIS Acta Pathol. Microbiol. Immunol. Scand.*, vol. 116, no. 9, pp. 779–784, Sep. 2008.
[388] H. Sun *et al.*, “Phosphatase and tensin homolog deleted on chromosome 10 degradation induced by NEDD4 promotes acquired erlotinib resistance in non-small-cell lung cancer,” *Tumour Biol. J. Int. Soc. Oncodevelopmental Biol. Med.*, vol. 39, no. 7, p. 1010428317709639, Jul. 2017.
[389] Y. Chen, M. J. van de Vijver, H. Hibshoosh, R. Parsons, and L. H. Saal, “PTEN and NEDD4 in Human Breast Carcinoma,” *Pathol. Oncol. Res. POR*, vol. 22, no. 1, pp. 41–47, Jan. 2016.
[390] X.-P. Song *et al.*, “Global land change from 1982 to 2016,” *Nature*, vol. 560, no. 7720, pp. 639–643, 2018.
[391] J. Zhang, X. Li, and Y. Zhang, “Correlation of NEDD4-1 and PTEN expression with the invasive capacity of pituitary adenomas,” *Mol. Clin. Oncol.*, vol. 6, no. 1, pp. 96–100, Jan. 2017.
[392] Y.-H. Song, C.-Q. Zhang, F.-F. Chen, and X.-Y. Lin, “Upregulation of Neural Precursor Cell Expressed Developmentally Downregulated 4-1 is Associated with Poor Prognosis and Chemoresistance in Lung Adenocarcinoma,” *Chin. Med. J. (Engl.)*, vol. 131, no. 1, pp. 16–24, Jan. 2018.
[393] J. Cai *et al.*, “CK1α suppresses lung tumour growth by stabilizing PTEN and inducing autophagy,” *Nat. Cell Biol.*, vol. 20, no. 4, pp. 465–478, Apr. 2018.
[394] P. M. Brauer and A. L. Tyner, “RAKing in AKT: a tumor suppressor function for the intracellular tyrosine kinase FRK,” *Cell Cycle Georget. Tex*, vol. 8, no. 17, pp. 2728–2732, Sep. 2009.
[395] Z. Chen *et al.*, “Crucial role of p53-dependent cellular senescence in suppression of Pten-deficient tumorigenesis,” *Nature*, vol. 436, no. 7051, pp. 725–730, Aug. 2005.
[396] G. Singh, L. Odriozola, H. Guan, C. R. Kennedy, and A. M. Chan, “Characterization of a novel PTEN mutation in MDA-MB-453 breast carcinoma cell line,” *BMC Cancer*, vol. 11, p. 490, Nov. 2011.
[397] X. Wang, Y. Shi, J. Wang, G. Huang, and X. Jiang, “Crucial role of the C-terminus of PTEN in antagonizing NEDD4-1-mediated PTEN ubiquitination and degradation,” *Biochem. J.*, vol. 414, no. 2, pp. 221–229, Sep. 2008.
[398] I. Aronchik, A. Kundu, J. G. Quirit, and G. L. Firestone, “The antiproliferative response of indole-3-carbinol in human melanoma cells is triggered by an interaction with NEDD4-1 and disruption of wild-type PTEN degradation,” *Mol. Cancer Res. MCR*, vol. 12, no. 11, pp. 1621–1634, Nov. 2014.

[399] B. Dai *et al.*, “FoxM1B regulates NEDD4-1 expression, leading to cellular transformation and full malignant phenotype in immortalized human astrocytes,” *Cancer Res.*, vol. 70, no. 7, pp. 2951–2961, Apr. 2010.
[400] H. An, D. T. Krist, and A. V. Statsyuk, “Crosstalk between kinases and Nedd4 family ubiquitin ligases,” *Mol. Biosyst.*, vol. 10, no. 7, pp. 1643–1657, Jul. 2014.
[401] P. Shrestha *et al.*, “NMR uncovers direct interaction between human NEDD4-1 and p34SEI-1,” *Biochem. Biophys. Res. Commun.*, vol. 490, no. 3, pp. 984–990, 26 2017.
[402] S.-W. Hong *et al.*, “p34 is a novel regulator of the oncogenic behavior of NEDD4-1 and PTEN,” *Cell Death Differ.*, vol. 21, no. 1, pp. 146–160, Jan. 2014.
[403] S. Jung *et al.*, “Oncogenic function of p34SEI-1 via NEDD4-1-mediated PTEN ubiquitination/degradation and activation of the PI3K/AKT pathway,” *Int. J. Oncol.*, vol. 43, no. 5, pp. 1587–1595, Nov. 2013.
[404] M. K. Leonard, N. T. Hill, E. D. Grant, and M. P. Kadakia, “ΔNp63α represses nuclear translocation of PTEN by inhibition of NEDD4-1 in keratinocytes,” *Arch. Dermatol. Res.*, vol. 305, no. 8, pp. 733–739, Oct. 2013.
[405] M. S. Song *et al.*, “The deubiquitinylation and localization of PTEN are regulated by a HAUSP-PML network,” *Nature*, vol. 455, no. 7214, pp. 813–817, Oct. 2008.
[406] J. Zhang *et al.*, “Deubiquitylation and stabilization of PTEN by USP13,” *Nat. Cell Biol.*, vol. 15, no. 12, pp. 1486–1494, Dec. 2013.
[407] A. Palmitessa and J. L. Benovic, “Arrestin and the multi-PDZ domain-containing protein MPZ-1 interact with phosphatase and tensin homolog (PTEN) and regulate Caenorhabditis elegans longevity,” *J. Biol. Chem.*, vol. 285, no. 20, pp. 15187–15200, May 2010.
[408] E. Lima-Fernandes *et al.*, “Distinct functional outputs of PTEN signalling are controlled by dynamic association with β-arrestins,” *EMBO J.*, vol. 30, no. 13, pp. 2557–2568, Jun. 2011.
[409] Y. Li, L.-H. Low, U. Putz, C.-P. Goh, S.-S. Tan, and J. Howitt, “Rab5 and Ndfip1 are involved in Pten ubiquitination and nuclear trafficking,” *Traffic Cph. Den.*, vol. 15, no. 7, pp. 749–761, Jul. 2014.
[410] N. I. Noguera *et al.*, “Nucleophosmin/B26 regulates PTEN through interaction with HAUSP in acute myeloid leukemia,” *Leukemia*, vol. 27, no. 5, pp. 1037–1043, Apr. 2013.
[411] A. Morotti *et al.*, “BCR-ABL disrupts PTEN nuclear-cytoplasmic shuttling through phosphorylation-dependent activation of HAUSP,” *Leukemia*, vol. 28, no. 6, pp. 1326–1333, Jun. 2014.
[412] B. Nicholson and K. G. Suresh Kumar, “The multifaceted roles of USP7: new therapeutic opportunities,” *Cell Biochem. Biophys.*, vol. 60, no. 1–2, pp. 61–68, Jun. 2011.
[413] G. Carrà *et al.*, “Therapeutic inhibition of USP7-PTEN network in chronic lymphocytic leukemia: a strategy to overcome TP53 mutated/deleted clones,” *Oncotarget*, vol. 8, no. 22, pp. 35508–35522, May 2017.
[414] A. Gil, J. I. López, and R. Pulido, “Assessing PTEN Subcellular Localization.,” *Methods Mol. Biol. Clifton NJ*, vol. 1388, pp. 169–186, 2016.
[415] M. Rahdar, T. Inoue, T. Meyer, J. Zhang, F. Vazquez, and P. N. Devreotes, “A phosphorylation-dependent intramolecular interaction regulates the membrane association and activity of the tumor suppressor PTEN,” *Proc. Natl. Acad. Sci. U. S. A.*, vol. 106, no. 2, pp. 480–485, Jan. 2009.
[416] F. Vazquez and P. Devreotes, “Regulation of PTEN function as a PIP3 gatekeeper through membrane interaction,” *Cell Cycle Georget. Tex*, vol. 5, no. 14, pp. 1523–1527, Jul. 2006.
[417] A. Gil, A. Andrés-Pons, and R. Pulido, “Nuclear PTEN: a tale of many tails,” *Cell Death Differ.*, vol. 14, no. 3, pp. 395–399, Mar. 2007.
[418] S. J. Miller, D. Y. Lou, D. C. Seldin, W. S. Lane, and B. G. Neel, “Direct identification of PTEN phosphorylation sites,” *FEBS Lett.*, vol. 528, no. 1–3, pp. 145–153, Sep. 2002.
[419] F. Vazquez, S. Ramaswamy, N. Nakamura, and W. R. Sellers, “Phosphorylation of the PTEN tail regulates protein stability and function,” *Mol. Cell. Biol.*, vol. 20, no. 14, pp. 5010–5018, Jul. 2000.

[420] T. Tolkacheva, M. Boddapati, A. Sanfiz, K. Tsuchida, A. C. Kimmelman, and A. M. Chan, “Regulation of PTEN binding to MAGI-2 by two putative phosphorylation sites at threonine 382 and 383,” *Cancer Res.*, vol. 61, no. 13, pp. 4985–4989, Jul. 2001.
[421] E.-K. Yim *et al.*, “Rak functions as a tumor suppressor by regulating PTEN protein stability and function,” *Cancer Cell*, vol. 15, no. 4, pp. 304–314, Apr. 2009.
[422] P. M. Brauer and A. L. Tyner, “RAKing in AKT: A Tumor Suppressor Function for the Intracellular Tyrosine Kinase FRK,” *Cell Cycle Georget. Tex*, vol. 8, no. 17, pp. 2728–2732, Sep. 2009.
[423] E.-K. Yim *et al.*, “Rak functions as a tumor suppressor by regulating PTEN protein stability and function,” *Cancer Cell*, vol. 15, no. 4, pp. 304–314, Apr. 2009.
[424] W.-R. Huang, H.-C. Chiu, T.-L. Liao, K.-P. Chuang, W.-L. Shih, and H.-J. Liu, “Avian Reovirus Protein p17 Functions as a Nucleoporin Tpr Suppressor Leading to Activation of p53, p21 and PTEN and Inactivation of PI3K/AKT/mTOR and ERK Signaling Pathways,” *PloS One*, vol. 10, no. 8, p. e0133699, 2015.
[425] Z. Chen *et al.*, “Enzymatic Analysis of PTEN Ubiquitylation by WWP2 and NEDD4-1 E3 Ligases,” *Biochemistry*, vol. 55, no. 26, pp. 3658–3666, 05 2016.
[426] A. Perren *et al.*, “Mutation and expression analyses reveal differential subcellular compartmentalization of PTEN in endocrine pancreatic tumors compared to normal islet cells,” *Am. J. Pathol.*, vol. 157, no. 4, pp. 1097–1103, Oct. 2000.
[427] A. Brandmaier, S.-Q. Hou, and W. H. Shen, “Cell Cycle Control by PTEN,” *J. Mol. Biol.*, vol. 429, no. 15, pp. 2265–2277, Jul. 2017.
[428] J.-L. Liu, X. Sheng, Z. K. Hortobagyi, Z. Mao, G. E. Gallick, and W. K. A. Yung, “Nuclear PTEN-mediated growth suppression is independent of Akt down-regulation,” *Mol. Cell. Biol.*, vol. 25, no. 14, pp. 6211–6224, Jul. 2005.
[429] S. Ramaswamy *et al.*, “Regulation of G1 progression by the PTEN tumor suppressor protein is linked to inhibition of the phosphatidylinositol 3-kinase/Akt pathway,” *Proc. Natl. Acad. Sci. U. S. A.*, vol. 96, no. 5, pp. 2110–2115, Mar. 1999.
[430] H. Sun *et al.*, “PTEN modulates cell cycle progression and cell survival by regulating phosphatidylinositol 3,4,5,-trisphosphate and Akt/protein kinase B signaling pathway,” *Proc. Natl. Acad. Sci. U. S. A.*, vol. 96, no. 11, pp. 6199–6204, May 1999.
[431] S. Persad *et al.*, “Inhibition of integrin-linked kinase (ILK) suppresses activation of protein kinase B/Akt and induces cell cycle arrest and apoptosis of PTEN-mutant prostate cancer cells,” *Proc. Natl. Acad. Sci. U. S. A.*, vol. 97, no. 7, pp. 3207–3212, Mar. 2000.
[432] F. B. Furnari, H. J. Huang, and W. K. Cavenee, “The phosphoinositol phosphatase activity of PTEN mediates a serum-sensitive G1 growth arrest in glioma cells,” *Cancer Res.*, vol. 58, no. 22, pp. 5002–5008, Nov. 1998.
[433] L. P. Weng, J. L. Brown, and C. Eng, “PTEN coordinates G(1) arrest by down-regulating cyclin D1 via its protein phosphatase activity and up-regulating p27 via its lipid phosphatase activity in a breast cancer model,” *Hum. Mol. Genet.*, vol. 10, no. 6, pp. 599–604, Mar. 2001.
[434] F. Bai, X.-H. Pei, P. P. Pandolfi, and Y. Xiong, “p18 Ink4c and Pten constrain a positive regulatory loop between cell growth and cell cycle control,” *Mol. Cell. Biol.*, vol. 26, no. 12, pp. 4564–4576, Jun. 2006.
[435] A. Hlobilkova, J. Knillova, M. Svachova, P. Skypalova, V. Krystof, and Z. Kolar, “Tumour suppressor PTEN regulates cell cycle and protein kinase B/Akt pathway in breast cancer cells,” *Anticancer Res.*, vol. 26, no. 2A, pp. 1015–1022, Apr. 2006.
[436] D. M. Li and H. Sun, “PTEN/MMAC1/TEP1 suppresses the tumorigenicity and induces G1 cell cycle arrest in human glioblastoma cells,” *Proc. Natl. Acad. Sci. U. S. A.*, vol. 95, no. 26, pp. 15406–15411, Dec. 1998.
[437] I. W. Cheney, S. T. Neuteboom, M. T. Vaillancourt, M. Ramachandra, and R. Bookstein, “Adenovirus-mediated gene transfer of MMAC1/PTEN to glioblastoma cells inhibits S phase entry by the recruitment of p27Kip1 into cyclin E/CDK2 complexes,” *Cancer Res.*, vol. 59, no. 10, pp. 2318–2323, May 1999.
[438] A. R. Gottschalk *et al.*, “p27Kip1 is required for PTEN-induced G1 growth arrest,” *Cancer Res.*, vol. 61, no. 5, pp. 2105–2111, Mar. 2001.

[439] X. Zhu, C. H. Kwon, P. W. Schlosshauer, L. H. Ellenson, and S. J. Baker, “PTEN induces G(1) cell cycle arrest and decreases cyclin D3 levels in endometrial carcinoma cells,” *Cancer Res.*, vol. 61, no. 11, pp. 4569–4575, Jun. 2001.
[440] R. Mamillapalli *et al.*, “PTEN regulates the ubiquitin-dependent degradation of the CDK inhibitor p27(KIP1) through the ubiquitin E3 ligase SCF(SKP2),” *Curr. Biol. CB*, vol. 11, no. 4, pp. 263–267, Feb. 2001.
[441] J. M. Paramio, M. Navarro, C. Segrelles, E. Gómez-Casero, and J. L. Jorcano, “PTEN tumour suppressor is linked to the cell cycle control through the retinoblastoma protein,” *Oncogene*, vol. 18, no. 52, pp. 7462–7468, Dec. 1999.
[442] A. Radu, V. Neubauer, T. Akagi, H. Hanafusa, and M.-M. Georgescu, “PTEN induces cell cycle arrest by decreasing the level and nuclear localization of cyclin D1,” *Mol. Cell. Biol.*, vol. 23, no. 17, pp. 6139–6149, Sep. 2003.
[443] S. Persad, A. A. Troussard, T. R. McPhee, D. J. Mulholland, and S. Dedhar, “Tumor suppressor PTEN inhibits nuclear accumulation of beta-catenin and T cell/lymphoid enhancer factor 1-mediated transcriptional activation,” *J. Cell Biol.*, vol. 153, no. 6, pp. 1161–1174, Jun. 2001.
[444] J.-L. Liu *et al.*, “Cell cycle-dependent nuclear export of phosphatase and tensin homologue tumor suppressor is regulated by the phosphoinositide-3-kinase signaling cascade,” *Cancer Res.*, vol. 67, no. 22, pp. 11054–11063, Nov. 2007.
[445] A. Xiao, H. Wu, P. P. Pandolfi, D. N. Louis, and T. Van Dyke, “Astrocyte inactivation of the pRb pathway predisposes mice to malignant astrocytoma development that is accelerated by PTEN mutation,” *Cancer Cell*, vol. 1, no. 2, pp. 157–168, Mar. 2002.
[446] I. Ahmad *et al.*, “HER2 overcomes PTEN (loss)-induced senescence to cause aggressive prostate cancer,” *Proc. Natl. Acad. Sci. U. S. A.*, vol. 108, no. 39, pp. 16392–16397, Sep. 2011.
[447] A. L. Kennedy *et al.*, “Activation of the PIK3CA/AKT pathway suppresses senescence induced by an activated RAS oncogene to promote tumorigenesis,” *Mol. Cell*, vol. 42, no. 1, pp. 36–49, Apr. 2011.
[448] D. Yao, C. L. Alexander, J. A. Quinn, M. J. Porter, H. Wu, and D. A. Greenhalgh, “PTEN loss promotes rasHa-mediated papillomatogenesis via dual up-regulation of AKT activity and cell cycle deregulation but malignant conversion proceeds via PTEN-associated pathways,” *Cancer Res.*, vol. 66, no. 3, pp. 1302–1312, Feb. 2006.
[449] R. Patel *et al.*, “Sprouty2, PTEN, and PP2A interact to regulate prostate cancer progression,” *J. Clin. Invest.*, vol. 123, no. 3, pp. 1157–1175, Mar. 2013.
[450] F. Inaba, H. Kawamata, T. Teramoto, I. Fukasawa, N. Inaba, and T. Fujimori, “PTEN and p53 abnormalities are indicative and predictive factors for endometrial carcinoma,” *Oncol. Rep.*, vol. 13, no. 1, pp. 17–24, Jan. 2005.
[451] N. Macwhinnie and H. Monaghan, “The use of P53, PTEN, and C-erbB-2 to differentiate uterine serous papillary carcinoma from endometrioid endometrial carcinoma,” *Int. J. Gynecol. Cancer Off. J. Int. Gynecol. Cancer Soc.*, vol. 14, no. 5, pp. 938–946, Oct. 2004.
[452] T.-H. Hu *et al.*, “Down-regulation of tumor suppressor gene PTEN, overexpression of p53, plus high proliferating cell nuclear antigen index predict poor patient outcome of hepatocellular carcinoma after resection,” *Oncol. Rep.*, vol. 18, no. 6, pp. 1417–1426, Dec. 2007.
[453] L. Nakopoulou, J. Janinis, I. Giannopoulou, A. C. Lazaris, A. Koureas, and D. Zacharoulis, “Immunohistochemical expression of p53 protein and proliferating cell nuclear antigen in hepatocellular carcinoma,” *Pathol. Res. Pract.*, vol. 191, no. 12, pp. 1208–1213, Dec. 1995.
[454] T. Itoh *et al.*, “Relationship between p53 overexpression and the proliferative activity in hepatocellular carcinoma,” *Int. J. Mol. Med.*, vol. 6, no. 2, pp. 137–142, Aug. 2000.
[455] R. Bravo, R. Frank, P. A. Blundell, and H. Macdonald-Bravo, “Cyclin/PCNA is the auxiliary protein of DNA polymerase-delta,” *Nature*, vol. 326, no. 6112, pp. 515–517, Apr. 1987.

[456] N. Komazawa *et al.*, “Tumorigenesis facilitated by Pten deficiency in the skin: evidence of p53-Pten complex formation on the initiation phase,” *Cancer Sci.*, vol. 95, no. 8, pp. 639–643, Aug. 2004.
[457] D. J. Freeman *et al.*, “PTEN tumor suppressor regulates p53 protein levels and activity through phosphatase-dependent and -independent mechanisms,” *Cancer Cell*, vol. 3, no. 2, pp. 117–130, Feb. 2003.
[458] C. Kandoth *et al.*, “Mutational landscape and significance across 12 major cancer types,” *Nature*, vol. 502, no. 7471, pp. 333–339, Oct. 2013.
[459] Y. Li *et al.*, “PTEN has tumor-promoting properties in the setting of gain-of-function p53 mutations,” *Cancer Res.*, vol. 68, no. 6, pp. 1723–1731, Mar. 2008.
[460] L. C. Trotman and P. P. Pandolfi, “PTEN and p53: who will get the upper hand?,” *Cancer Cell*, vol. 3, no. 2, pp. 97–99, Feb. 2003.
[461] S. S. Couto *et al.*, “Simultaneous haploinsufficiency of Pten and Trp53 tumor suppressor genes accelerates tumorigenesis in a mouse model of prostate cancer,” *Differ. Res. Biol. Divers.*, vol. 77, no. 1, pp. 103–111, Jan. 2009.
[462] J. C. Liu *et al.*, “Combined deletion of Pten and p53 in mammary epithelium accelerates triple-negative breast cancer with dependency on eEF2K,” *EMBO Mol. Med.*, vol. 6, no. 12, pp. 1542–1560, Dec. 2014.
[463] J. Kim, D. M. Coffey, L. Ma, and M. M. Matzuk, “The ovary is an alternative site of origin for high-grade serous ovarian cancer in mice,” *Endocrinology*, vol. 156, no. 6, pp. 1975–1981, Jun. 2015.
[464] Y. Liu *et al.*, “CRISPR/Cas9-mediated p53 and Pten dual mutation accelerates hepatocarcinogenesis in adult hepatitis B virus transgenic mice,” *Sci. Rep.*, vol. 7, no. 1, p. 2796, 05 2017.
[465] V. Stambolic *et al.*, “Regulation of PTEN transcription by p53,” *Mol. Cell*, vol. 8, no. 2, pp. 317–325, Aug. 2001.
[466] X. Sheng, D. Koul, J.-L. Liu, T.-J. Liu, and W. K. A. Yung, “Promoter analysis of tumor suppressor gene PTEN: identification of minimum promoter region,” *Biochem. Biophys. Res. Commun.*, vol. 292, no. 2, pp. 422–426, Mar. 2002.
[467] L. D. Mayo, J. E. Dixon, D. L. Durden, N. K. Tonks, and D. B. Donner, “PTEN protects p53 from Mdm2 and sensitizes cancer cells to chemotherapy,” *J. Biol. Chem.*, vol. 277, no. 7, pp. 5484–5489, Feb. 2002.
[468] J. A. Lehman, D. L. Waning, C. N. Batuello, R. Cipriano, M. P. Kadakia, and L. D. Mayo, “Induction of apoptotic genes by a p73-phosphatase and tensin homolog (p73-PTEN) protein complex in response to genotoxic stress,” *J. Biol. Chem.*, vol. 286, no. 42, pp. 36631–36640, Oct. 2011.
[469] X. He, Y. Ni, Y. Wang, T. Romigh, and C. Eng, “Naturally occurring germline and tumor-associated mutations within the ATP-binding motifs of PTEN lead to oxidative damage of DNA associated with decreased nuclear p53,” *Hum. Mol. Genet.*, vol. 20, no. 1, pp. 80–89, Jan. 2011.
[470] Y. Tang and C. Eng, “p53 down-regulates phosphatase and tensin homologue deleted on chromosome 10 protein stability partially through caspase-mediated degradation in cells with proteasome dysfunction,” *Cancer Res.*, vol. 66, no. 12, pp. 6139–6148, Jun. 2006.
[471] J. A. Eitel *et al.*, “PTEN and p53 are required for hypoxia induced expression of maspin in glioblastoma cells,” *Cell Cycle Georget. Tex*, vol. 8, no. 6, pp. 896–901, Mar. 2009.
[472] L. D. Mayo and D. B. Donner, “A phosphatidylinositol 3-kinase/Akt pathway promotes translocation of Mdm2 from the cytoplasm to the nucleus,” *Proc. Natl. Acad. Sci. U. S. A.*, vol. 98, no. 20, pp. 11598–11603, Sep. 2001.
[473] A. G. Li, L. G. Piluso, X. Cai, G. Wei, W. R. Sellers, and X. Liu, “Mechanistic insights into maintenance of high p53 acetylation by PTEN,” *Mol. Cell*, vol. 23, no. 4, pp. 575–587, Aug. 2006.
[474] B. P. Zhou, Y. Liao, W. Xia, Y. Zou, B. Spohn, and M. C. Hung, “HER-2/neu induces p53 ubiquitination via Akt-mediated MDM2 phosphorylation,” *Nat. Cell Biol.*, vol. 3, no. 11, pp. 973–982, Nov. 2001.

[475] O. M. Rahal and R. C. M. Simmen, “PTEN and p53 cross-regulation induced by soy isoflavone genistein promotes mammary epithelial cell cycle arrest and lobuloalveolar differentiation,” *Carcinogenesis*, vol. 31, no. 8, pp. 1491–1500, Aug. 2010.
[476] C. J. Chang, D. J. Mulholland, B. Valamehr, S. Mosessian, W. R. Sellers, and H. Wu, “PTEN nuclear localization is regulated by oxidative stress and mediates p53-dependent tumor suppression,” *Mol. Cell. Biol.*, vol. 28, no. 10, pp. 3281–3289, May 2008.
[477] J. Wang *et al.*, “Loss of tumor suppressor p53 decreases PTEN expression and enhances signaling pathways leading to activation of activator protein 1 and nuclear factor kappaB induced by UV radiation,” *Cancer Res.*, vol. 65, no. 15, pp. 6601–6611, Aug. 2005.
[478] A. Franchitto and P. Pichierri, “Replication fork recovery and regulation of common fragile sites stability,” *Cell. Mol. Life Sci. CMLS*, vol. 71, no. 23, pp. 4507–4517, Dec. 2014.
[479] C. Alabert *et al.*, “Nascent chromatin capture proteomics determines chromatin dynamics during DNA replication and identifies unknown fork components,” *Nat. Cell Biol.*, vol. 16, no. 3, pp. 281–293, Mar. 2014.
[480] Z. H. Chen *et al.*, “PTEN Interacts with Histone H1 and Controls Chromatin Condensation,” *Cell Rep.*, vol. 8, no. 6, pp. 2003–2014, Sep. 2014.
[481] K. H. Wrighton, “Chromatin: Interplay of PTEN with histone H1,” *Nat. Rev. Mol. Cell Biol.*, vol. 15, no. 10, p. 630, Oct. 2014.
[482] L. Gong *et al.*, “Nuclear PTEN tumor-suppressor functions through maintaining heterochromatin structure,” *Cell Cycle Georget. Tex*, vol. 14, no. 14, pp. 2323–2332, 2015.
[483] J. A. Benitez *et al.*, “Publisher Correction: PTEN regulates glioblastoma oncogenesis through chromatin-associated complexes of DAXX and histone H3.3,” *Nat. Commun.*, vol. 9, p. 16217, 25 2018.
[484] J. X. He, X. Kang, Y. X. Yin, K. S. C. Chao, and W. H. Shen, “PTEN regulates DNA replication progression and stalled fork recovery,” *Nat. Commun.*, vol. 6, Jul. 2015.
[485] D. Cortez, “Unwind and slow down: checkpoint activation by helicase and polymerase uncoupling,” *Genes Dev.*, vol. 19, no. 9, pp. 1007–1012, May 2005.
[486] L. Zou and S. J. Elledge, “Sensing DNA damage through ATRIP recognition of RPA-ssDNA complexes,” *Science*, vol. 300, no. 5625, pp. 1542–1548, Jun. 2003.
[487] T. S. Byun, M. Pacek, M. Yee, J. C. Walter, and K. A. Cimprich, “Functional uncoupling of MCM helicase and DNA polymerase activities activates the ATR-dependent checkpoint,” *Genes Dev.*, vol. 19, no. 9, pp. 1040–1052, May 2005.
[488] J. Feng *et al.*, “PTEN Controls the DNA Replication Process through MCM2 in Response to Replicative Stress,” *Cell Rep.*, vol. 13, no. 7, pp. 1295–1303, Nov. 2015.
[489] G. Wang *et al.*, “PTEN regulates RPA1 and protects DNA replication forks,” *Cell Res.*, vol. 25, no. 11, pp. 1189–1204, Nov. 2015.
[490] E. Petermann, M. L. Orta, N. Issaeva, N. Schultz, and T. Helleday, “Hydroxyurea-stalled replication forks become progressively inactivated and require two different RAD51-mediated pathways for restart and repair,” *Mol. Cell*, vol. 37, no. 4, pp. 492–502, Feb. 2010.
[491] B. McEllin *et al.*, “PTEN loss compromises homologous recombination repair in astrocytes: implications for glioblastoma therapy with temozolomide or poly(ADP-ribose) polymerase inhibitors,” *Cancer Res.*, vol. 70, no. 13, pp. 5457–5464, Jul. 2010.
[492] A. Mukherjee and P. Karmakar, “Attenuation of PTEN perturbs genomic stability via activation of Akt and down-regulation of Rad51 in human embryonic kidney cells,” *Mol. Carcinog.*, vol. 52, no. 8, pp. 611–618, Aug. 2013.
[493] P. Ruff, R. A. Donnianni, E. Glancy, J. Oh, and L. S. Symington, “RPA Stabilization of Single-Stranded DNA Is Critical for Break-Induced Replication,” *Cell Rep.*, vol. 17, no. 12, pp. 3359–3368, 20 2016.
[494] E. S. Kandel *et al.*, “Activation of Akt/protein kinase B overcomes a G(2)/m cell cycle checkpoint induced by DNA damage,” *Mol. Cell. Biol.*, vol. 22, no. 22, pp. 7831–7841, Nov. 2002.
[495] Y. Saito *et al.*, “Adenovirus-mediated transfer of the PTEN gene inhibits human colorectal cancer growth in vitro and in vivo,” *Gene Ther.*, vol. 10, no. 23, pp. 1961–1969, Nov. 2003.

[496] E. Shtivelman, J. Sussman, and D. Stokoe, “A role for PI 3-kinase and PKB activity in the G2/M phase of the cell cycle,” *Curr. Biol. CB*, vol. 12, no. 11, pp. 919–924, Jun. 2002.
[497] F. W. King, J. Skeen, N. Hay, and E. Shtivelman, “Inhibition of Chk1 by activated PKB/Akt,” *Cell Cycle Georget. Tex*, vol. 3, no. 5, pp. 634–637, May 2004.
[498] B. B. Zhou and S. J. Elledge, “The DNA damage response: putting checkpoints in perspective,” *Nature*, vol. 408, no. 6811, pp. 433–439, Nov. 2000.
[499] J. Bartek and J. Lukas, “Chk1 and Chk2 kinases in checkpoint control and cancer,” *Cancer Cell*, vol. 3, no. 5, pp. 421–429, May 2003.
[500] A. Kumagai and W. G. Dunphy, “Claspin, a novel protein required for the activation of Chk1 during a DNA replication checkpoint response in Xenopus egg extracts,” *Mol. Cell*, vol. 6, no. 4, pp. 839–849, Oct. 2000.
[501] C. C. S. Chini and J. Chen, “Human claspin is required for replication checkpoint control,” *J. Biol. Chem.*, vol. 278, no. 32, pp. 30057–30062, Aug. 2003.
[502] R. I. Yarden, S. Pardo-Reoyo, M. Sgagias, K. H. Cowan, and L. C. Brody, “BRCA1 regulates the G2/M checkpoint by activating Chk1 kinase upon DNA damage,” *Nat. Genet.*, vol. 30, no. 3, pp. 285–289, Mar. 2002.
[503] S. Y. Shieh, J. Ahn, K. Tamai, Y. Taya, and C. Prives, “The human homologs of checkpoint kinases Chk1 and Cds1 (Chk2) phosphorylate p53 at multiple DNA damage-inducible sites,” *Genes Dev.*, vol. 14, no. 3, pp. 289–300, Feb. 2000.
[504] A. Groth *et al.*, “Human Tousled like kinases are targeted by an ATM- and Chk1-dependent DNA damage checkpoint,” *EMBO J.*, vol. 22, no. 7, pp. 1676–1687, Apr. 2003.
[505] J. Puc and R. Parsons, “PTEN loss inhibits CHK1 to cause double stranded-DNA breaks in cells,” *Cell Cycle Georget. Tex*, vol. 4, no. 7, pp. 927–929, Jul. 2005.
[506] J. Puc *et al.*, “Lack of PTEN sequesters CHK1 and initiates genetic instability,” *Cancer Cell*, vol. 7, no. 2, pp. 193–204, Feb. 2005.
[507] A. I. Jacob, T. Romigh, K. A. Waite, and C. Eng, “Nuclear PTEN levels and G2 progression in melanoma cells,” *Melanoma Res.*, vol. 19, no. 4, pp. 203–210, Aug. 2009.
[508] S.-J. Kim *et al.*, “Activation of nuclear PTEN by inhibition of Notch signaling induces G2/M cell cycle arrest in gastric cancer,” *Oncogene*, vol. 35, no. 2, pp. 251–260, Jan. 2016.
[509] S. A. Martin and T. Ouchi, “Cellular commitment to reentry into the cell cycle after stalled DNA is determined by site-specific phosphorylation of Chk1 and PTEN,” *Mol. Cancer Ther.*, vol. 7, no. 8, pp. 2509–2516, Aug. 2008.
[510] Y. Abe *et al.*, “A mitotic kinase TOPK enhances Cdk1/cyclin B1-dependent phosphorylation of PRC1 and promotes cytokinesis,” *J. Mol. Biol.*, vol. 370, no. 2, pp. 231–245, Jul. 2007.
[511] S. R. Shinde, N. R. Gangula, S. Kavela, V. Pandey, and S. Maddika, “TOPK and PTEN participate in CHFR mediated mitotic checkpoint,” *Cell. Signal.*, vol. 25, no. 12, pp. 2511–2517, Dec. 2013.
[512] E. Shtivelman, “Promotion of mitosis by activated protein kinase B after DNA damage involves polo-like kinase 1 and checkpoint protein CHFR,” *Mol. Cancer Res. MCR*, vol. 1, no. 13, pp. 959–969, Nov. 2003.
[513] M. K. Summers, J. Bothos, and T. D. Halazonetis, “The CHFR mitotic checkpoint protein delays cell cycle progression by excluding Cyclin B1 from the nucleus,” *Oncogene*, vol. 24, no. 16, pp. 2589–2598, Apr. 2005.
[514] V. Ayllón and R. O’connor, “PBK/TOPK promotes tumour cell proliferation through p38 MAPK activity and regulation of the DNA damage response,” *Oncogene*, vol. 26, no. 24, pp. 3451–3461, May 2007.
[515] J.-H. Park, M.-L. Lin, T. Nishidate, Y. Nakamura, and T. Katagiri, “PDZ-binding kinase/T-LAK cell-originated protein kinase, a putative cancer/testis antigen with an oncogenic activity in breast cancer,” *Cancer Res.*, vol. 66, no. 18, pp. 9186–9195, Sep. 2006.
[516] M.-C. Shih *et al.*, “TOPK/PBK promotes cell migration via modulation of the PI3K/PTEN/AKT pathway and is associated with poor prognosis in lung cancer,” *Oncogene*, vol. 31, no. 19, pp. 2389–2400, May 2012.

[517] M. Simons-Evelyn *et al.*, “PBK/TOPK is a novel mitotic kinase which is upregulated in Burkitt’s lymphoma and other highly proliferative malignant cells,” *Blood Cells. Mol. Dis.*, vol. 27, no. 5, pp. 825–829, Oct. 2001.
[518] D. M. Scolnick and T. D. Halazonetis, “Chfr defines a mitotic stress checkpoint that delays entry into metaphase,” *Nature*, vol. 406, no. 6794, pp. 430–435, Jul. 2000.
[519] J. Bothos, M. K. Summers, M. Venere, D. M. Scolnick, and T. D. Halazonetis, “The Chfr mitotic checkpoint protein functions with Ubc13-Mms2 to form Lys63-linked polyubiquitin chains,” *Oncogene*, vol. 22, no. 46, pp. 7101–7107, Oct. 2003.
[520] X. Kang *et al.*, “PTEN stabilizes TOP2A and regulates the DNA decatenation,” *Sci. Rep.*, vol. 5, p. 17873, Dec. 2015.
[521] R. Broderick and W. Niedzwiedz, “Sister chromatid decatenation: bridging the gaps in our knowledge,” *Cell Cycle Georget. Tex*, vol. 14, no. 19, pp. 3040–3044, 2015.
[522] G. Witz and A. Stasiak, “DNA supercoiling and its role in DNA decatenation and unknotting,” *Nucleic Acids Res.*, vol. 38, no. 7, pp. 2119–2133, Apr. 2010.
[523] A. Gupta *et al.*, “Cell cycle checkpoint defects contribute to genomic instability in PTEN deficient cells independent of DNA DSB repair,” *Cell Cycle Georget. Tex*, vol. 8, no. 14, pp. 2198–2210, Jul. 2009.
[524] W. Y. Mansour *et al.*, “Loss of PTEN-assisted G2/M checkpoint impedes homologous recombination repair and enhances radio-curability and PARP inhibitor treatment response in prostate cancer,” *Sci. Rep.*, vol. 8, no. 1, p. 3947, Mar. 2018.
[525] D. Piscitello *et al.*, “AKT overactivation can suppress DNA repair via p70S6 kinase-dependent downregulation of MRE11.,” *Oncogene*, vol. 37, no. 4, pp. 427–438, Jan. 2018.
[526] J.-H. Chen *et al.*, “ATM-mediated PTEN phosphorylation promotes PTEN nuclear translocation and autophagy in response to DNA-damaging agents in cancer cells,” *Autophagy*, vol. 11, no. 2, pp. 239–252, 2015.
[527] B. H. Choi, Y. Chen, and W. Dai, “Chromatin PTEN is involved in DNA damage response partly through regulating Rad52 sumoylation,” *Cell Cycle Georget. Tex*, vol. 12, no. 21, pp. 3442–3447, Nov. 2013.
[528] M. Fraser *et al.*, “PTEN deletion in prostate cancer cells does not associate with loss of RAD51 function: implications for radiotherapy and chemotherapy,” *Clin. Cancer Res. Off. J. Am. Assoc. Cancer Res.*, vol. 18, no. 4, pp. 1015–1027, Feb. 2012.
[529] M. Ming *et al.*, “PTEN Positively Regulates UVB-Induced DNA Damage Repair,” *Cancer Res*, vol. 71, no. 15, pp. 5287–5295, Aug. 2011.
[530] C. J. Rosser *et al.*, “Adenoviral-mediated PTEN transgene expression sensitizes Bcl-2-expressing prostate cancer cells to radiation,” *Cancer Gene Ther.*, vol. 11, no. 4, pp. 273–279, Apr. 2004.
[531] G. Pappas, L. A. Zumstein, A. Munshi, M. Hobbs, and R. E. Meyn, “Adenoviral-mediated PTEN expression radiosensitizes non-small cell lung cancer cells by suppressing DNA repair capacity,” *Cancer Gene Ther.*, vol. 14, no. 6, pp. 543–549, Jun. 2007.
[532] M. Ming, C. R. Shea, L. Feng, K. Soltani, and Y.-Y. He, “UVA induces lesions resembling seborrheic keratoses in mice with keratinocyte-specific PTEN downregulation,” *J. Invest. Dermatol.*, vol. 131, no. 7, pp. 1583–1586, Jul. 2011.
[533] A. Minami, A. Nakanishi, Y. Ogura, Y. Kitagishi, and S. Matsuda, “Connection between Tumor Suppressor BRCA1 and PTEN in Damaged DNA Repair,” *Front. Oncol.*, vol. 4, p. 318, 2014.
[534] Q. Zhao *et al.*, “Inhibition of Rad51 sensitizes breast cancer cells with wild-type PTEN to olaparib,” *Biomed. Pharmacother. Biomedecine Pharmacother.*, vol. 94, pp. 165–168, Oct. 2017.
[535] X. Bian *et al.*, “PTEN deficiency sensitizes endometrioid endometrial cancer to compound PARP-PI3K inhibition but not PARP inhibition as monotherapy,” *Oncogene*, vol. 37, no. 3, pp. 341–351, Jan. 2018.
[536] A. M. Mendes-Pereira *et al.*, “Synthetic lethal targeting of PTEN mutant cells with PARP inhibitors,” *Embo Mol. Med.*, vol. 1, no. 6–7, pp. 315–322, Sep. 2009.

[537] K. J. Dedes *et al.*, “PTEN Deficiency in Endometrioid Endometrial Adenocarcinomas Predicts Sensitivity to PARP Inhibitors,” *Sci. Transl. Med.*, vol. 2, no. 53, pp. 53ra75-53ra75, Oct. 2010.
[538] Y. Yin and W. H. Shen, “PTEN: a new guardian of the genome,” *Oncogene*, vol. 27, no. 41, pp. 5443–5453, Sep. 2008.
[539] I. Vitale, L. Galluzzi, M. Castedo, and G. Kroemer, “Mitotic catastrophe: a mechanism for avoiding genomic instability,” *Nat. Rev. Mol. Cell Biol.*, vol. 12, no. 6, pp. 385–392, 2011.
[540] H.-Y. Li, K. Cao, and Y. Zheng, “Ran in the spindle checkpoint: a new function for a versatile GTPase,” *Trends Cell Biol.*, vol. 13, no. 11, pp. 553–557, Nov. 2003.
[541] B. H. Choi, S. Xie, and W. Dai, “PTEN is a negative regulator of mitotic checkpoint complex during the cell cycle,” *Exp. Hematol. Oncol.*, vol. 6, Jun. 2017.
[542] B. H. Choi, M. Pagano, C. Huang, and W. Dai, “Cdh1, a substrate-recruiting component of anaphase-promoting complex/cyclosome (APC/C) ubiquitin E3 ligase, specifically interacts with phosphatase and tensin homolog (PTEN) and promotes its removal from chromatin,” *J. Biol. Chem.*, vol. 289, no. 25, pp. 17951–17959, Jun. 2014.
[543] D. Izawa and J. Pines, “The mitotic checkpoint complex binds a second CDC20 to inhibit active APC/C,” *Nature*, vol. 517, no. 7536, pp. 631–634, Jan. 2015.
[544] M. S. Song *et al.*, “Nuclear PTEN regulates the APC-CDH1 tumor-suppressive complex in a phosphatase-independent manner,” *Cell*, vol. 144, no. 2, pp. 187–99, Jan. 2011.
[545] S. L. Carter, A. C. Eklund, I. S. Kohane, L. N. Harris, and Z. Szallasi, “A signature of chromosomal instability inferred from gene expression profiles predicts clinical outcome in multiple human cancers,” *Nat. Genet.*, vol. 38, no. 9, pp. 1043–1048, Sep. 2006.
[546] Y.-W. Kwon *et al.*, “Pten regulates Aurora-A and cooperates with Fbxw7 in modulating radiation-induced tumor development,” *Mol. Cancer Res. MCR*, vol. 10, no. 6, pp. 834–844, Jun. 2012.
[547] Y. Liu *et al.*, “PTEN regulates spindle assembly checkpoint timing through MAD1 in interphase,” *Oncotarget*, vol. 8, no. 58, pp. 98040–98050, Aug. 2017.
[548] X. S. Liu *et al.*, “Polo-like Kinase 1 Facilitates Loss of Pten Tumor Suppressor-induced Prostate Cancer Formation,” *J. Biol. Chem.*, vol. 286, no. 41, pp. 35795–35800, Oct. 2011.
[549] M. K. Leonard, N. T. Hill, P. A. Bubulya, and M. P. Kadakia, “The PTEN-Akt pathway impacts the integrity and composition of mitotic centrosomes,” *Cell Cycle Georget. Tex*, vol. 12, no. 9, pp. 1406–1415, May 2013.
[550] J. H. van Ree, H.-J. Nam, K. B. Jeganathan, A. Kanakkanthara, and J. M. van Deursen, “Pten regulates spindle pole movement through Dlg1-mediated recruitment of Eg5 to centrosomes,” *Nat. Cell Biol.*, vol. 18, no. 7, pp. 814–821, 2016.
[551] R. L. Siegel, K. D. Miller, and A. Jemal, “Cancer Statistics, 2017,” *CA Cancer J Clin*, vol. 67, no. 1, pp. 7–30, Jan. 2017.
[552] E. J. Fox, M. J. Prindle, and L. A. Loeb, “Do mutator mutations fuel tumorigenesis?,” *Cancer Metastasis Rev*, vol. 32, no. 3–4, pp. 353–61, Dec. 2013.
[553] K. W. Yuen, C. D. Warren, O. Chen, T. Kwok, P. Hieter, and F. A. Spencer, “Systematic genome instability screens in yeast and their potential relevance to cancer,” *Proc Natl Acad Sci U A*, vol. 104, no. 10, pp. 3925–30, Mar. 2007.
[554] L. S. Michel *et al.*, “MAD2 haplo-insufficiency causes premature anaphase and chromosome instability in mammalian cells,” *Nature*, vol. 409, no. 6818, pp. 355–9, Jan. 2001.
[555] H. Rajagopalan *et al.*, “Inactivation of hCDC4 can cause chromosomal instability,” *Nature*, vol. 428, no. 6978, pp. 77–81, Mar. 2004.
[556] W. Dove, “Aurora and the hunt for cancer-modifying genes,” *Nat Genet*, vol. 34, no. 4, pp. 353–4, Aug. 2003.
[557] F. d’Adda di Fagagna *et al.*, “A DNA damage checkpoint response in telomere-initiated senescence,” *Nature*, vol. 426, no. 6963, pp. 194–8, Nov. 2003.
[558] T. G. Graeber, J. F. Peterson, M. Tsai, K. Monica, A. J. Fornace Jr., and A. J. Giaccia, “Hypoxia induces accumulation of p53 protein, but activation of a G1-phase checkpoint by

low-oxygen conditions is independent of p53 status," *Mol. Cell. Biol.*, vol. 14, no. 9, pp. 6264–77, Sep. 1994.
[559] H. Takai, A. Smogorzewska, and T. de Lange, "DNA damage foci at dysfunctional telomeres," *Curr Biol*, vol. 13, no. 17, pp. 1549–56, Sep. 2003.
[560] A. C. Lee *et al.*, "Ras proteins induce senescence by altering the intracellular levels of reactive oxygen species," *J Biol Chem*, vol. 274, no. 12, pp. 7936–40, Mar. 1999.
[561] O. Vafa *et al.*, "c-Myc can induce DNA damage, increase reactive oxygen species, and mitigate p53 function: a mechanism for oncogene-induced genetic instability," *Mol Cell*, vol. 9, no. 5, pp. 1031–44, May 2002.
[562] L. Wang, C. Wang, S. Jin, D. Qu, and H. Ying, "Expression of NF-κB and PTEN in primary epithelial ovarian carcinoma and the correlation with chemoresistance," *Int. J. Clin. Exp. Pathol.*, vol. 8, no. 9, pp. 10953–10963, Sep. 2015.
[563] M. A. Shammas, R. J. Shmookler Reis, H. Koley, R. B. Batchu, C. Li, and N. C. Munshi, "Dysfunctional homologous recombination mediates genomic instability and progression in myeloma," *Blood*, vol. 113, no. 10, pp. 2290–7, Mar. 2009.
[564] A. Slupianek *et al.*, "BCR/ABL regulates mammalian RecA homologs, resulting in drug resistance," *Mol Cell*, vol. 8, no. 4, pp. 795–806, Oct. 2001.
[565] S. Vispe, C. Cazaux, C. Lesca, and M. Defais, "Overexpression of Rad51 protein stimulates homologous recombination and increases resistance of mammalian cells to ionizing radiation," *Nucleic Acids Res*, vol. 26, no. 12, pp. 2859–64, Jun. 1998.
[566] M. S. Tsai, Y. H. Kuo, Y. F. Chiu, Y. C. Su, and Y. W. Lin, "Down-regulation of Rad51 expression overcomes drug resistance to gemcitabine in human non-small-cell lung cancer cells," *J Pharmacol Exp Ther*, vol. 335, no. 3, pp. 830–40, Dec. 2010.
[567] P. Tennstedt *et al.*, "RAD51 overexpression is a negative prognostic marker for colorectal adenocarcinoma," *Int J Cancer*, vol. 132, no. 9, pp. 2118–26, May 2013.
[568] M. E. Ritchie *et al.*, "limma powers differential expression analyses for RNA-sequencing and microarray studies," *Nucleic Acids Res*, vol. 43, no. 7, p. e47, Apr. 2015.
[569] B. Phipson, S. Lee, I. J. Majewski, W. S. Alexander, and G. K. Smyth, "Robust Hyperparameter Estimation Protects against Hypervariable Genes and Improves Power to Detect Differential Expression," *Ann Appl Stat*, vol. 10, no. 2, pp. 946–963, Jun. 2016.
[570] C. W. Law, Y. Chen, W. Shi, and G. K. Smyth, "voom: Precision weights unlock linear model analysis tools for RNA-seq read counts," *Genome Biol*, vol. 15, no. 2, p. R29, Feb. 2014.
[571] F. Supek, M. Bošnjak, N. Škunca, and T. Šmuc, "REVIGO Summarizes and Visualizes Long Lists of Gene Ontology Terms," *PLOS ONE*, vol. 6, no. 7, p. e21800, Jul. 2011.
[572] R. P. Huntley *et al.*, "The GOA database: gene Ontology annotation updates for 2015," *Nucleic Acids Res.*, vol. 43, no. Database issue, pp. D1057-1063, Jan. 2015.
[573] H. Heberle, G. V. Meirelles, F. R. da Silva, G. P. Telles, and R. Minghim, "InteractiVenn: a web-based tool for the analysis of sets through Venn diagrams," *BMC Bioinformatics*, vol. 16, no. 1, p. 169, May 2015.
[574] P. R., "Epidemiology, multistage models, and short-term mutagenicity tests," in *The Origins of Human Cancer.*, vol. 4, W. J. In: Hiatt HH Winsten JA, editors., Ed. NY: Cold Spring Harbor Conferences on Cell Proliferation: Cold Spring Harbor Laboratory, 1977, pp. 1403–1428.
[575] R. G. Fox, F. D. Park, C. S. Koechlein, M. Kritzik, and T. Reya, "Musashi signaling in stem cells and cancer," *Annu Rev Cell Dev Biol*, vol. 31, pp. 249–67, 2015.
[576] P. A. Jeggo and M. Lobrich, "How cancer cells hijack DNA double-strand break repair pathways to gain genomic instability," *Biochem J*, vol. 471, no. 1, pp. 1–11, Oct. 2015.
[577] M. De Robertis *et al.*, "The AOM/DSS murine model for the study of colon carcinogenesis: From pathways to diagnosis and therapy studies," *J Carcinog*, vol. 10, p. 9, Mar. 2011.
[578] Z. H. Cheung and N. Y. Ip, "Cdk5: a multifaceted kinase in neurodegenerative diseases," *Trends Cell Biol.*, vol. 22, no. 3, pp. 169–175, Mar. 2012.

[579] F. Graf, F. Wuest, and J. Pietzsch, “Cyclin-Dependent Kinases (Cdk) as Targets for Cancer Therapy and Imaging,” *Adv. Cancer Ther.*, Nov. 2011.
[580] C. J. Sherr and F. McCormick, “The RB and p53 pathways in cancer,” *Cancer Cell*, vol. 2, no. 2, pp. 103–112, Aug. 2002.
[581] Z. Zhang, S.-Q. Hou, J. He, T. Gu, Y. Yin, and W. H. Shen, “PTEN regulates PLK1 and controls chromosomal stability during cell division,” *Cell Cycle Georget. Tex*, vol. 15, no. 18, pp. 2476–2485, Sep. 2016.
[582] E. A. Vuono *et al.*, “The PTEN phosphatase functions cooperatively with the Fanconi anemia proteins in DNA crosslink repair,” *Sci. Rep.*, vol. 6, p. 36439, 07 2016.
[583] H. L. Borges, R. Linden, and J. Y. Wang, “DNA damage-induced cell death,” *Cell Res.*, vol. 18, no. 1, pp. 17–26, Jan. 2008.
[584] S. Nowsheen and E. S. Yang, “THE INTERSECTION BETWEEN DNA DAMAGE RESPONSE AND CELL DEATH PATHWAYS,” *Exp. Oncol.*, vol. 34, no. 3, pp. 243–254, Oct. 2012.
[585] J. Pellettieri, P. Fitzgerald, S. Watanabe, J. Mancuso, D. R. Green, and A. Sanchez Alvarado, “Cell death and tissue remodeling in planarian regeneration,” *Dev Biol*, vol. 338, no. 1, pp. 76–85, Feb. 2010.
[586] J. He *et al.*, “PTEN regulates EG5 to control spindle architecture and chromosome congression during mitosis,” *Nat. Commun.*, vol. 7, p. 12355, 05 2016.
[587] S. L. Thompson and D. A. Compton, “Chromosome missegregation in human cells arises through specific types of kinetochore-microtubule attachment errors,” *Proc. Natl. Acad. Sci. U. S. A.*, vol. 108, no. 44, pp. 17974–17978, Nov. 2011.
[588] N. J. Ganem and D. Pellman, “Linking abnormal mitosis to the acquisition of DNA damage,” *J. Cell Biol.*, vol. 199, no. 6, pp. 871–881, Dec. 2012.
[589] N. J. Ganem and D. Pellman, “Linking abnormal mitosis to the acquisition of DNA damage,” *J. Cell Biol.*, vol. 199, no. 6, pp. 871–881, Dec. 2012.
[590] B. A. Chromy, M. P. Lambert, and W. L. Klein, “Increased Protein Tyrosine Phosphorylation in Apoptotic Neural Cell Death Due to Microtubule Perturbations,” *Neurotox. Res.*, vol. 2, no. 4, pp. 357–372, Dec. 2000.
[591] C. L. Wike *et al.*, “Excess free histone H3 localizes to centrosomes for proteasome-mediated degradation during mitosis in metazoans,” *Cell Cycle Georget. Tex*, vol. 15, no. 16, pp. 2216–2225, Aug. 2016.
[592] J. F. Giménez-Abián, L. A. Díaz-Martínez, K. G. Wirth, C. De la Torre, and D. J. Clarke, “Proteasome activity is required for centromere separation independently of securin degradation in human cells,” *Cell Cycle Georget. Tex*, vol. 4, no. 11, pp. 1558–1560, Nov. 2005.
[593] E. M. Dunleavy, G. Almouzni, and G. H. Karpen, “H3.3 is deposited at centromeres in S phase as a placeholder for newly assembled CENP-A in G_1 phase,” *Nucl. Austin Tex*, vol. 2, no. 2, pp. 146–157, Apr. 2011.
[594] N. J. Oviedo, C. L. Nicolas, D. S. Adams, and M. Levin, “Establishing and maintaining a colony of planarians,” *CSH Protoc*, vol. 2008, p. pdb prot5053, Oct. 2008.
[595] A. Renaux and U. Consortium, “UniProt: the universal protein knowledgebase (vol 45, pg D158, 2017),” *Nucleic Acids Res*, vol. 46, no. 5, pp. 2699–2699, Mar. 2018.
[596] S. Y. Liu and J. C. Rink, “Total RNA Isolation from Planarian Tissues,” *Methods Mol Biol*, vol. 1774, pp. 259–265, 2018.
[597] N. Shibata and K. Agata, “RNA Interference in Planarians: Feeding and Injection of Synthetic dsRNA,” *Methods Mol Biol*, vol. 1774, pp. 455–466, 2018.
[598] P. A. Newmark, P. W. Reddien, F. Cebria, and A. Sanchez Alvarado, “Ingestion of bacterially expressed double-stranded RNA inhibits gene expression in planarians,” *Proc Natl Acad Sci U A*, vol. 100 Suppl 1, pp. 11861–5, Sep. 2003.
[599] L. Rouhana *et al.*, “RNA interference by feeding in vitro-synthesized double-stranded RNA to planarians: methodology and dynamics,” *Dev Dyn*, vol. 242, no. 6, pp. 718–30, Jun. 2013.

[600] Y. Umesono, K. Watanabe, and K. Agata, “A planarian orthopedia homolog is specifically expressed in the branch region of both the mature and regenerating brain,” *Dev Growth Differ*, vol. 39, no. 6, pp. 723–7, Dec. 1997.
[601] K. J. Pedersen, “Morphogenetic activities during planarian regeneration as influenced by triethylene melamine,” *J Embryol Exp Morphol*, vol. 6, no. 2, pp. 308–34, Jun. 1958.
[602] P. A. Newmark and A. Sanchez Alvarado, “Bromodeoxyuridine specifically labels the regenerative stem cells of planarians,” *Dev Biol*, vol. 220, no. 2, pp. 142–53, Apr. 2000.
[603] L. C. Cheng and A. S. Alvarado, “Whole-Mount BrdU Staining with Fluorescence In Situ Hybridization in Planarians,” *Methods Mol Biol*, vol. 1774, pp. 423–434, 2018.
[604] B. J. Pearson, G. T. Eisenhoffer, K. A. Gurley, J. C. Rink, D. E. Miller, and A. Sanchez Alvarado, “Formaldehyde-based whole-mount in situ hybridization method for planarians,” *Dev Dyn*, vol. 238, no. 2, pp. 443–50, Feb. 2009.
[605] R. S. King and P. A. Newmark, “In situ hybridization protocol for enhanced detection of gene expression in the planarian Schmidtea mediterranea,” *BMC Dev Biol*, vol. 13, p. 8, Mar. 2013.
[606] K. W. Currie *et al.*, “HOX gene complement and expression in the planarian Schmidtea mediterranea,” *Evodevo*, vol. 7, p. 7, 2016.
[607] Y. Liao, G. K. Smyth, and W. Shi, “The Subread aligner: fast, accurate and scalable read mapping by seed-and-vote,” *Nucleic Acids Res*, vol. 41, no. 10, p. e108, May 2013.
[608] F. Cebria and P. A. Newmark, “Planarian homologs of netrin and netrin receptor are required for proper regeneration of the central nervous system and the maintenance of nervous system architecture,” *Development*, vol. 132, no. 16, pp. 3691–703, Aug. 2005.
[609] T. Guo, A. H. Peters, and P. A. Newmark, “A Bruno-like gene is required for stem cell maintenance in planarians,” *Dev Cell*, vol. 11, no. 2, pp. 159–69, Aug. 2006.
[610] A. M. Glazer *et al.*, “The Zn finger protein Iguana impacts Hedgehog signaling by promoting ciliogenesis,” *Dev Biol*, vol. 337, no. 1, pp. 148–56, Jan. 2010.
[611] F. Cebria, “Organization of the nervous system in the model planarian Schmidtea mediterranea: an immunocytochemical study,” *Neurosci Res*, vol. 61, no. 4, pp. 375–84, Aug. 2008.
[612] S. Moritz *et al.*, “Heterogeneity of planarian stem cells in the S/G2/M phase,” *Int J Dev Biol*, vol. 56, no. 1–3, pp. 117–25, 2012.
[613] D. J. Forsthoefel, F. A. Waters, and P. A. Newmark, “Generation of cell type-specific monoclonal antibodies for the planarian and optimization of sample processing for immunolabeling,” *BMC Dev Biol*, vol. 14, p. 45, Dec. 2014.
[614] A. Tazaki, S. Gaudieri, K. Ikeo, T. Gojobori, K. Watanabe, and K. Agata, “Neural network in planarian revealed by an antibody against planarian synaptotagmin homologue,” *Biochem Biophys Res Commun*, vol. 260, no. 2, pp. 426–32, Jul. 1999.
[615] M. Sinha *et al.*, “Restoring systemic GDF11 levels reverses age-related dysfunction in mouse skeletal muscle,” *Science*, vol. 344, no. 6184, pp. 649–52, May 2014.
[616] T. Knakievicz, A. H. Lau, D. Pra, and B. Erdtmann, “Biogeography and karyotypes of freshwater planarians (Platyhelminthes, Tricladida, Paludicola) in southern Brazil,” *Zool. Sci*, vol. 24, no. 2, pp. 123–9, Feb. 2007.

Appendix I

Biochimica et Biophysica Acta 1848 (2015) 2629–2637

Contents lists available at ScienceDirect

Biochimica et Biophysica Acta

journal homepage: www.elsevier.com/locate/bbamem

Review

Bioelectrical regulation of cell cycle and the planarian model system☆

Paul G. Barghouth [a,b,1], Manish Thiruvalluvan [a,b,1], Néstor J. Oviedo [a,b,c,*]

[a] Department of Molecular and Cell Biology, School of Natural Sciences, University of California at Merced, 5200 North Lake Road, Merced, CA 95343, USA
[b] Quantitative and Systems Biology Graduate Program, University of California at Merced, 5200 North Lake Road, Merced, CA 95343, USA
[c] Health Sciences Research Institute, University of California at Merced, 5200 North Lake Road, Merced, CA 95343, USA

ARTICLE INFO

Article history:
Received 13 October 2014
Received in revised form 13 February 2015
Accepted 23 February 2015
Available online 6 March 2015

Keywords:
Membrane potential
Cell cycle
Cancer
Stem cell
Planarian

ABSTRACT

Cell cycle regulation through the manipulation of endogenous membrane potentials offers tremendous opportunities to control cellular processes during tissue repair and cancer formation. However, the molecular mechanisms by which biophysical signals modulate the cell cycle remain underappreciated and poorly understood. Cells in complex organisms generate and maintain a constant voltage gradient across the plasma membrane known as the transmembrane potential. This potential, generated through the combined efforts of various ion transporters, pumps and channels, is known to drive a wide range of cellular processes such as cellular proliferation, migration and tissue regeneration while its deregulation can lead to tumorigenesis. These cellular regulatory events, coordinated by ionic flow, correspond to a new and exciting field termed molecular bioelectricity. We aim to present a brief discussion on the biophysical machinery involving membrane potential and the mechanisms mediating cell cycle progression and cancer transformation. Furthermore, we present the planarian *Schmidtea mediterranea* as a tractable model system for understanding principles behind molecular bioelectricity at both the cellular and organismal level. This article is part of a Special Issue entitled: Membrane channels and transporters in cancers.

Contents

☆ This article is part of a Special Issue entitled: Membrane channels and transporters in cancers.

* Corresponding author at: Department of Molecular and Cell Biology, School of Natural Sciences, University of California at Merced, 5200 North Lake Road, Merced, CA 95343, USA. Tel.: +1 209 228 4541; fax: +1 209 228 4053.
E-mail address: noviedo2@ucmerced.edu (N.J. Oviedo).

[1] Equal contribution.

http://dx.doi.org/10.1016/j.bbamem.2015.02.024
0005-2736/

1. Introduction

Efficient cellular communication is critical for the survival and perpetuation of multicellular organisms. However, the mechanism by which crosstalk among cells is translated into coordinated behavior at both the cellular and organismal levels remains poorly understood. A primitive mode of cellular communication relies on the exchange of ions between the intracellular and extracellular environment. Membrane proteins facilitate the transport of ions from one side of the plasma membrane to the other. The transport of ions is essential for the establishment of electrochemical gradients which influence the behavior of both local and distant cells in the body. For instance, the manipulation of endogenous ionic flows is able to alter patterns of cell division, migration and differentiation in a wide range of embryonic and adult stem cells of vertebrate and invertebrate models [1–4]. Although the characterization of such bioelectrical phenomena is well established, very little is known about how endogenous electric fields actually affect biological functions and the mechanism through which cells respond to their influence. Nonetheless, recent findings provide compelling evidence regarding the potential of controlling this powerful ionic flow communication system to induce regeneration of missing tissues and to stimulate, or control abnormal cell behavior observed in cancer [5–9]. This new field of research, defined as "Molecular Bioelectricity", aims to understand how voltage gradients in nonexcitable cells coordinate morphogenesis, tissue development, repair, and cancer formation [10].

Pharmacological manipulation of ionic flow provides relatively easy access to regulatory properties of cell cycle parameters [9,11,12]. We aim to offer information on the different ionic and voltage dependent variables that modulate the cell cycle during tissue regeneration, cellular turnover and cancer formation from previous research. These voltage gradients are not limited to cells, but also exist at the tissue/organ level, where they provide instructive information for specifying organ identity and large-scale anatomical order [1,10,13]. Therefore, it is essential to address the role of endogenous currents in the context of the whole organism. We propose the extremely versatile planarian model system *Schmidtea mediterranea* as a venue for exploring bioelectrical regulation at both the cellular and the organismal level to better understand the role of voltage gradients in adult tissue maintenance, repair and tumorigenesis.

2. The transmembrane potential (TMP)

All cells generate long-term, steady-state voltage gradients known as transmembrane potentials (TMPs) [3,8,14]. TMP is an ancient and evolutionarily conserved system that can be found in a variety of organisms, ranging from plants to higher vertebrates, and has been reviewed extensively [1–3,10,15,16]. It is generated by a separation of charge across the plasma membrane, leading to a negative voltage difference in respect to the extracellular environment [11,15]. However, gradient changes involved in generating TMPs are much slower and vastly different than the rapid membrane depolarizations observed in both nervous and muscle tissues [3,8]. However, similar to action potentials, TMP changes in a single cell can be transmitted over long distances via gap junction linkages [14,17–19]. TMPs are primarily maintained by the constant activity of various ion channels, pumps and transporters, collectively known as ion transport mechanisms (ITMs). These ITMs segregate charges across the plasma membrane and produce necessary current needed to generate a voltage potential [20]. An ITM of extreme importance to living systems is the sodium/potassium ATPase (Na^+/K^+ ATPase), which is essential for maintaining the transmembrane potential between 10 and −90 mV, depending on the tissue type [15]. The cell invests substantial amounts of energy to maintain TMP as changes in membrane polarity are used to drive alterations in cell behavior [14,15]. We will now explore the role bioelectric regulation of one such aspect, proliferation.

3. TMP and cell cycle regulation

The cell cycle is regulated by a complex array of signals stemming from the microenvironment as well as from intracellular signals such as cyclins, cyclin-dependent kinases (CDKs), CDK inhibitors and the retinoblastoma (Rb) protein. Factors associated with ionic flow (i.e. ITMs), membrane potential, and membrane composition are known to be involved in regulating these cell cycle components [21–25]. Exciting new results in this area unveil powerful strategies to control the cell cycle, that may enhance genetic and biochemical interventions in regenerative medicine and cancer therapy [11,12]. We will discuss some of the bioelectrical mechanisms and properties known to modulate the cell cycle in vertebrates and invertebrates.

3.1. TMP and membrane polarization

Eukaryotic vacuolar-type H+-ATPases (V-ATPase) are electrogenic proton pumps that energize both the intracellular and plasma membranes by expelling H+, changing pH levels in the extracellular environment, which contribute to the maintenance of the TMP [26,27]. As intracellular pH recovers, membrane potential becomes more negative in charge, causing plasma membrane to hyperpolarize [28]. These fluctuations in TMP are particularly evident during cell cycle progression, as demonstrated in Chinese hamster lung cells [29]. During the G0/G1 transition checkpoint, there is a gradual transition of TMP from a state of intermediate depolarization to intermediate hyperpolarization. As the cell passes through the G1/S phase transition checkpoint, the TMP becomes more negative, marking the hyperpolarization of the cell membrane. During the transition through the S phase, S/G2 checkpoint and G2 phase the membrane potential is at a maximum negative voltage and remains hyperpolarized. Entering mitosis, TMP rapidly depolarizes to the lowest minimum voltage, indicating the completion of cell division (Fig. 1A) [29]. Furthermore, these fluctuations in TMP are well documented in other cell types [21–25]. These findings support the notion that TMP fluctuations through V-ATPase are an important regulatory component for ionic flow during the cell cycle and its deregulation may be associated with abnormal cell behavior.

3.2. Generation of TMP and ionic flow

Transient depolarization and hyperpolarization of the plasma membrane is mediated by the constant exchange of charged ions between the cytoplasm and extracellular environments. The V-ATPase proton pump is seen to energize the membrane through ionic gradients whereas Na+/K+ ATPases participate in maintaining the chemical gradient [30]. However, the flow of potassium ions via K+ channels eventually aids in the establishment of TMP. Inhibition of the V-ATPase reduces the proton gradient within the cell, leading to impairment of both the ionic driving force and ionic homeostasis needed for cell proliferation [31]. As intracellular concentrations of Na+ decrease, a concurrent influx of K+ ions is seen, promoting an increase in TMP. Though low in concentration, Cl− ions also play an important role throughout the cell cycle. This interplay between fluctuating states of membrane polarization and ionic flows serves as a regulator of cell cycle and cellular proliferation (Fig. 1B) [5,11,22,32]

3.2.1. Chloride dynamics

Due to nature of electrogenic V-ATPases, a parallel ion conductance must occur to aid in pH regulation and driving membrane potentials. The flux of Cl− occurs in parallel to H+ flux via V-ATPase activity and is required to maintain cellular electroneutrality [33,34]. In yeast cells, inhibition of V-ATPase strongly reduces Cl− concentration in both the vacuolar and plasma membrane [35].

Compression and swelling of a cell during the cell cycle has been attributed to a Cl−/K+ relationship, required to gather essential amino acids, metabolic substrates and materials for the synthesis of proteins

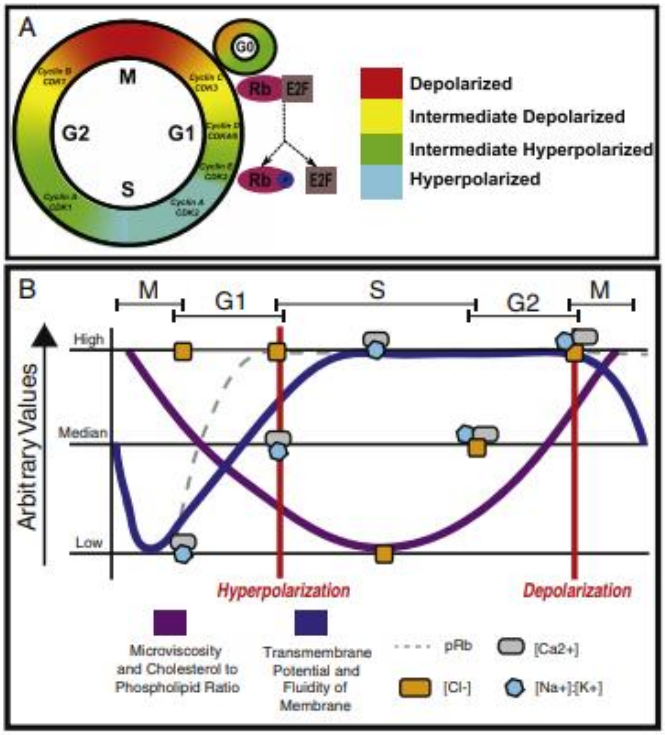

Fig. 1. a. Cell cycle modulation via transmembrane potentials, ionic gradients and gene expression. (A) Depicts the phases of cellular polarization and the regulatory checkpoints in gene expression throughout the cell cycle. M phase is a depolarized state (red), S phase is a hyperpolarized state (teal) and G0,G1 and G2 states oscillate through intermediated phases of depolarization and hyperpolarization (yellow and green). (B) Shows physical characteristics of the cell membrane and oscillation of both gene expression and ionic concentrations during cell cycle progression. The fluctuations in microviscosity/cholesterol to phospholipids ratio (purple). Transmembrane potential/membrane fluidity (blue), pRb gene expression (–) and ionic concentrations of Cl− (yellow square). Ca2+ (gray rectangle) and Na+:K+ ratio (blue hexagon) are seen to fluctuate in terms of arbitrary values throughout the cell cycle.

[36,37]. Isotonic Cl− currents in the cell cycle have been found to regulate cell volume and membrane potential [38–40]. Studies in cancer cells indicate that volume activated Cl− channels can act as regulators of cell cycle progression [41]. They show that although there is low expression of Cl− currents in the G0 phase [37], it reaches a maximum threshold in the G0/G1 and G1/S transition phases [36], reduce in the S phase and back up during the G2/M transition [42,43]. These fluctuations of Cl− currents are not isolated events, but rather correlate with the concentrations of cyclin/CDKs and CDK inhibitors throughout the cell cycle [44]. In various cell types, a decrease in intracellular Cl− concentrations during the cell cycle reduces the rate of cellular proliferation through the upregulation of p21 and CDK inhibitors; therefore, causing a downstream effect on Cdk2 and Rb expression, halting cells in the G0/G1 transition phase [37,41,45–49]. Inducing expression of a hyperpolarizing anion channel such as CLIC1 in normal cells, in the vicinity of tumors, inhibits their growth. This process occurs through the upregulation of HDAC1, an acetylating protein that in *Xenopus* embryos, is critical for cell cycle progression and rate of cellular proliferation [5,6]. This further supports that the precise maintenance of TMP and the voltage gradient via charged ions is key for cell cycle regulation.

3.2.2. Sodium and potassium dynamics

The efflux of H+ by the Na+/H+ transporter into the extracellular environment of the cell generates a driving force for the influx of Na+ into the cytoplasm [30,50–52]. This influx of Na+ into the cell by the Na+/H+ transporter is then counterbalanced by the Na+/K+ ATPase pump to maintain the electrochemical gradient. The ratio [K+]i/[Na+]i created by the interplay between Na+, the most abundant inorganic cation and K+, the second most abundant cation in the intracellular fluid attributes to a heavily regulated electrochemical gradient, as they run parallel in concentration [53]. However, K+ ions and TMP play important roles as they are responsible for creating the driving force needed for the release of intracellular Ca2+ [54,55]. Through the inhibition of membrane bound K+ channels (e.g. Kv), cell cycle progression has been seen to halt during the early and late Gl phase, G1/S transition and G2/M [56,57]. It has been shown in mouse neuroblastoma cells, Na+/K+ ATPase pumping oscillates during cell cycle progression [58]. Membrane permeabilities to K+ and Na+ are reported to be high in M phase (membrane is in depolarized state), decreases by threefold in G1 phase (membrane is in hyperpolarized state) and rises through the G1/S transition into S phase [58]. As the cell progresses into G2 phase, K+ and Na+ permeabilities decrease and rapidly increase through the G2/M transition phase [58]. Studies in several cancer cell lines provide support for the ability of potassium channels to modulate cellular proliferation [59–62]. For example, the overexpression of K+ channels in Glioma cells maintains a depolarized membrane potential, resulting in high rates of cellular proliferation [63,64]. These findings highlight the direct relationship

between TMP, ionic gradients and cellular proliferation through cell cycle.

3.2.3. Calcium dynamics

Cell volume oscillations and K+ influxes during the cell cycle regulates cellular proliferation by modulating the release of intracellular Ca2+ ions [65,66]. The rate of K+ ion permeability through the membrane provides a driving force for Ca2+ influx activating calmodulin. This protein is known to activate crucial proteins such as Rb and cyclin/CDK complexes, necessary for the cell cycle progression. Rb activation is closely regulated by Cyclin D and Cdk4/6 release in early and mid G1 phase [57]. Rb is increasingly phosphorylated through the G1 to S phases, at which point it remains hyperphosphorylated until the completion of M phase [67,68]. It is known that Ca2+ influx is required for the initiation of S phase and the completion of M phase, possibly through its contribution to a more negative TMP [67–69]. Ca2+/calmodulin mediates the activation of Cdk1 and Cdk2, which are known to be upregulated through the S to M phases [70,71]. The activated Cdk2 hyperphosphorylates Rb, releasing E2F allowing the cell to progress through the cell cycle. Inhibition of Ca2+ binding protein calmodulin prevents Rb hyperphosphorylation and ultimately leads to cell cycle arrest in G1 phase with subsequent down regulation of Cyclin-D expression and loss of Cdk4/6 and Cdk2 [72]. These results strongly support a direct role of Ca2+ currents and TMPs in the regulation of protein activity throughout the cell cycle.

3.3. Plasma membrane dynamics

TMP regulation of lipid–protein interactions in the cellular membrane becomes another point of interest in cellular proliferation. Microviscosity, the physical state describing the degree of membrane fluidity, is a key regulator of membrane protein mobility. It is thought to do so by modulating microtubules, microfilaments, and membrane bound enzymes [58,73,74]. TMP has been shown to regulate microviscosity by influencing the conformation of transmembrane ionic channels and activity of enzymes within the phospholipid matrix [23,24,75]. Microviscosity of the membrane lipids varies throughout the cell cycle and is highest during mitosis, rapidly decreases through G1 phase, reaching a minimum during S phase and finally increases during G2 phase as the cell enters mitosis (Fig. 1B) [23].

Membrane microviscosity and fluidity also regulate cellular proliferation through the modulation of membrane binding phospholipids, ionic headgroups, hydrophobic acyl chains and/or the binding of cholesterol [73,76,77]. Expression and accessibility of surface antigens/receptors of a membrane are mediated through fluctuations between membrane microviscosity and membrane fluidity, which are reciprocals of one another [78]. A key relationship between microviscosity and membrane lipids is the ratio of cholesterol to phospholipids that affects internal membrane viscosity, lipid motion and regulates cellular behavior (e.g. cell migration) [24]. As a cell reaches maximum microviscosity, the fluidity of surface membrane lipids are at a minimum while the ratio of cholesterol to phospholipids is at its highest peak [24]. Furthermore, during this microviscosity state, surface antigens and receptors increase in expression, exposure and accessibility, leading to membrane saturation [23]. The reduction of membrane surface area happens concurrently with a decrease in TMP (Fig. 1B) [75]. As a consequence of oscillatory microviscosity levels, the cell surface proteins that are indirectly recruited to the membrane play a key role in the regulation of the cell cycle.

4. TMP and cancer

Since TMP is known to control key cellular processes such as proliferation, migration, and growth, its proper maintenance is crucial to body homeostasis [12,79]. Deregulation of membrane potential can induce drastic changes in cells, and in some cases, cause them to become tumorigenic. In the same virtue, TMP may also be manipulated to prevent tumor progression [5–7,20,62].

4.1. Cancer progression

Numerous studies have shown that deregulation of TMP can lead to tumorigenesis [20,40,80–82]. There is a general correlation between the proliferative capacity of a cell and it's TMP, which cancer cells often use to their advantage [1,22]. A common trait among tumor cells is that they are more depolarized at any given time, comparable to the TMP excitable cells discussed previously [11,79]. A panel of breast cancer cells shows an increase in depolarization as compared to controls [83]. For example, MCF-7 cells exhibit lower TMP values in both the G1 and S phases as compared to normal breast cells [25]. In addition, a K+ channel, hERG1, normally expressed in differentiated cardiac myocytes is upregulated in various types of cancer cells [62,65,84]. Lastly, elevated expression of Kv10.1. and Kv11.1 channels are correlated with an increased probability of relapse and a lower survival rate in human patients [9,12]. Intracellular Na+ levels are usually elevated in cancerous tissue, supporting the notion that a state of depolarization is critical for cancer transformation [9,20,40].

Deregulation of V-ATPase pumps can often lead to excessive cellular proliferation. For example, in many breast cancer cell lines, there is an upregulation in the expression of V-ATPases in the cell membrane whereas overexpression in normal cells confers a neoplastic phenotype [85,86]. Another voltage-gated proton pump Hv1, critical for proton transfer, is overexpressed in high-grade metastatic human breast cancer cell lines such as MCF-7, but shows minimal expression in low-grade metastatic breast tumors [87]. Overall, these studies suggest that proper ionic flow in cells is critical for the proper cellular maintenance.

4.2. Escaping cell death

TMPs not only play an important role in the proliferation required for tissue homeostasis but also maintains constant cellular turnover. It does so through the activation of pathways that results in cellular degeneration via the inhibition of the cell cycle machinery or through both the intrinsic and extrinsic components of the apoptotic pathway [62]. Cells unresponsive to environmental cues may be forced to enter a stage known as senescence, mediated by TMP [88], which results in permanent cell cycle arrest, through secretion of antigrowth signals that prevent oncogene related growth [89]. This change in the TMP may lead to an upregulation of p16-pRb and p53, the primary mediators of senescence [88].

Proper maintenance of TMP by ITMs is critical for determining cellular fate. For instance, downregulation the Na,K-ATPase has been shown to markedly increase apoptosis in normal and tumor cells [90,91] K+ channels are critical modulators of cell fate decisions, such as controlling the onset of apoptosis [62,65,84]. For example, expression of apoptosis-related KCNA1 channel is significantly reduced in human cancers [92]. Blocking hERG1 channels can stop the flow of K+ into the cell, leading to apoptosis [88]. Similarly, efflux of K+ ions is seen to be a major perquisite behind caspase-3 activated apoptosis in HeLa cells [93]. On the other hand, upregulation of hERG1 results in G0/G1 arrest without undergoing apoptosis, consistent with the state of replicative senescence [20,94]. These findings suggest that TMP plays an important role in the maintenance of cellular homeostasis and the deregulation can lead to excessive activation of apoptotic pathways leading to massive cell death.

4.3. Cancer cell migration

Stages of invasive cancer progression begins with the loss of cell adhesion from the primary tumor site, followed by the invasion of cells into the circulatory system and lastly seeding of distant tissues to form secondary tumors [95]. Although TMP is important in abnormal cellular proliferation, it also plays an indirect role in cell migration by modulating intracellular Ca2+ ion concentrations [9,40]. For example, overexpression of Kca2.3, key for maintaining a hyperpolarized

membrane potential, increases the cell's ability to migrate through the release of intracellular Ca2+ [96]. Deregulation of K+ channel GIRK1 is correlated with higher incidence of lymph node metastasis and poor prognosis in a small sample of patients and is overexpressed in breast tumors [97]. RT-PCR and immunocytochemistry experiments demonstrated that the expression levels of voltage-gated proton pump Hv1 is increased among different breast cancer cell lines [87], indicating that proper maintenance of TMP may be necessary for cellular adhesion and function.

4.4. Abrogation of cancer growth

Manipulation of ITMs to induce changes in TMP is another potential therapy target to prevent the transformation of normal cells into cancer cells [11]. Membrane hyperpolarization leads to a decrease in proliferation by sustaining high levels of K+ and Ca2+, which can inhibit cell cycle progression (Fig. 1B) [95]. Interestingly, tumor-like structures generated in *Xenopus* embryos were later inhibited by the upregulation of the anion channel CLIC1 in the stroma leading to the hyperpolarizion of the tumor-like cells [5,6]. Inhibition of certain voltage gated Na+ channels reduces the metastatic ability of prostate cancer cells in a rat model by abrogating their motility [96,98]. Numerous studies suggest that the pharmacological or genetic inhibition of K+ channels can reduce the proliferation of cancer cells [99–101]. For instance, blocking the Kv10.1 channel causes a cessation of cellular proliferation and migration in several myeloid leukemia cell lines [12].

A negative membrane potential has been associated with ATP induced cell death [102,103]. The microenvironment of cancer cells tend to be hypoxic, resulting in increased K+ efflux in the extracellular space [102,103]. The increase in K+ in the microenvironment can inhibit Pannexin-1, leading to apoptosis via caspase-3 activation [104]. This is supported by the observation that normal concentrations of K+ inside a cell inhibit the activation of the apoptosome by preventing the actions of Apaf-2 [105]. TMP across the mitochondria could also decide whether a cell undergoes apoptosis. Loss of normal mitochondrial TMP triggers the release of cytochrome c, into the cytoplasm, signaling the formation of the apoptosome and the death of the cell [84]. These studies suggest that TMP modulation maybe a potential target for directed-apoptosis and proper understanding of TMP and its effect on cell dynamics will be essential for developing novel cancer therapies.

5. *S. mediterranea* and TMP

Ion transporters and channels serve as excellent targets for cancer therapy because they are present on the surface of cell membranes and many molecular tools are readily available for manipulating them [61,94,95]. Most drugs used to block or enhance ion transporter's activity have been characterized extensively and a large number have FDA approval [79], which offers the possibility of quick translation into therapies. Pharmacological deregulation of ion channels is an effective method for disrupting TMP. It allows for precise control and timed inhibition while delivering a more informative result than a gene knockout method where there could be many complications due to functional compensations [10,14,15]. Dissecting the molecular mechanisms by which biophysical properties regulate tumorigenesis and metastatic processes requires a model system that is tractable to both biophysical/physiological techniques and state-of-the-art molecular genetics [11].

The planarian model organism *S. mediterranea* provides an excellent base of study for understanding bioelectric regulation of tissue regeneration as they possess a simple anatomy along with a remarkable ability to rapidly regenerate [19,106–112]. This regenerative ability extends to healing any part of its body after receiving an injury, including the neural tissue, digestive system, brain, photoreceptors and connective tissue (Fig. 2A) [19,107,109,110]. Its robust regeneration is fueled by an abundant population of adult pluripotent stem cells known as neoblasts that is responsible for cellular turnover as well as tissue regeneration [19, 107–110,113]. The genome of *S. mediterranea* has been sequenced and many of molecular tools have been developed to study genetics, physiology, and biochemistry in this model organism [19,107–110, 113].

Immunohistochemistry and in situ hybridization are often used to visualize cell migration and differentiation patterns in planarians [114]. These techniques can determine anatomical structural differences, neoblast state and abnormalities in tissue patterning (Fig. 3A). Neoblasts in different phases of the cell cycle can be visualized through the use of anti-phospho histone H3 antibody (H3P) and bromodeoxyuridine (BrdU) [115]. Fluorescent activated cell sorting (FACS) is a unique method of isolating planarian neoblast populations. Dyes such as Hoechst 33342 and calcein AM are used to stain live cell DNA content and cytoplasmic activity [116]. FACS allows for the isolation of cell populations enriched in radiation-insensitive differentiated cells (Xins) or radiation-sensitive adult stem cells fractions (X1 and X2) (Fig. 3B) [106,116–119]. Cell cycle analysis is also possible through flow cytometry [120,121].

The adult body of *S. mediterranea* provides unique opportunities to analyze regulation of cell proliferation by TMP [1,13,19,122]. Localized or systemic neoblast proliferation could be altered by metabolic changes (feeding or starvation) and tissue injury [17,108,121]. Furthermore, neoblast overproliferation and tumor formation can be induced by manipulation of well-characterized tumor suppressor genes (e.g. p53, PTEN) (Fig. 2B) [123,124]. The pattern of regeneration of entire body parts is susceptible to molecular manipulation of ion flows, gap junctional communications, and conserved signaling pathways such as Wnt and B-catenin [17,18,107,125,126]. Regeneration in planarians proceeds through activation of cell proliferation and application of bioelectric fields are known to modulate repair and tissue polarity in flatworms [127,128]. Membrane potential across the whole planarian body could be monitored using DiBAC (4) (3) staining, and the newly developed approach termed Planarian Immobilization Chips (PICs) to visualize bioelectrical changes in real time while minimizing tissue damage [13,122,129,130].

The H,K-ATPase is a major player in the regulation of tissue maintenance and regeneration in the planarian model. This ion transporter is essential for both the proper development of organ size during planarian regeneration and the anterior polarity in regenerating worms [13, 122]. Functional disruption of H, K-ATPase by RNA interference (RNAi) leads to failure in tissue remodeling and proportion adjustment of regenerated structures [13]. These results in planarians are consistent with zebrafish studies that found bioelectric signaling regulates fin allometric scaling and coordination of growth [131]. Similarly, ion transporters are required for proper regeneration of lost tissue as well stem cell maintenance in *Xenopus* and mice [132,133]. Together, findings in both vertebrate and invertebrate models demonstrate that TMP and ITMs modulate central issues of regeneration and development, such as cell fate decisions, the establishment and maintenance of tissue proportion, and the growth of complex structures, through well conserved mechanisms.

Furthermore, planarians are also amenable to chemical treatments aimed at targeting ion transporters and recordings of TMP in real time [18,122,125,129]. Drug-induced changes in TMP could be used as a venue to perform gain of function studies in planaria, as there are currently no other means for doing such research in this system. Increased knowledge of bioelectricity in living systems will contribute to our understanding of how ion flows can be used in clinical settings to influence cellular proliferation, migration and differentiation to control tissue function. For instance, modulation of ion transport with chemicals could be a powerful tool to halt cell cycle progression in abnormally proliferating cells [134] or an instrument to prompt cellular division to re-establish form and function to lost or damaged tissues [133]. The molecular basis of these processes could be readily investigated in the planarian model and later validated in more complex systems.

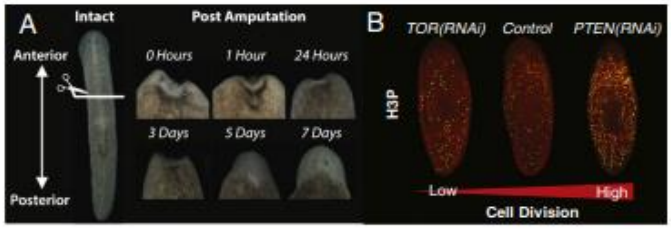

Fig. 2. Planarian tissue regeneration and maintenance. (A) Images of a live worm (left) amputated pre-pharyngeal; images on the right show the regeneration of the anterior portion including the head. Time-lapse images depict proper wound healing response and blastema formation in a regenerating planarian. By Day 7, the fragment has regenerated into a completely functional animal. (B) Image depicts cell division (yellow dots, H3P immunostaining) after RNAi of TOR and PTEN genes in comparison to control (mock-RNAi). TOR(RNAi) reduces mitotic activity while PTEN(RNAi) induce the opposite effect.

6. Concluding remarks

TMP and the many proteins that are involved in its maintenance, are of great importance to the normal cellular function and to a greater extent, the organism. The complex interplay between K+, Na+, Cl− and Ca2+ ions in and out of the cell determines the polarization of TMP at any given moment. Ionic oscillations during the cell cycle are able to control passage of cells through critical checkpoints by regulating key proteins such as Cyclin/CDKs and Rb. The deregulation of a small subset of proteins in this intricate system can lead to abnormal cell behavior, ultimately leading to the onset of tumorigenesis. Most studies that have been performed to explore this phenomenon have been through in vitro methods, however, this only provides a partial view of the bioelectrical phenomena. In order to gain a comprehensive understanding of TMP's role in cellular processes, it is critical to perform in vivo analyses of cell cycle progression and cancer transformation in the adult body and the planarian *S. mediterranea* is a well-suited model organism for this task.

Planarians provide an excellent model for studying mechanisms of bioelectric regulation of cell cycle as they are host to a population of mitotically active, pluripotent stem cells that maintain their high rate of cellular turnover and impressive regenerative capability. They are

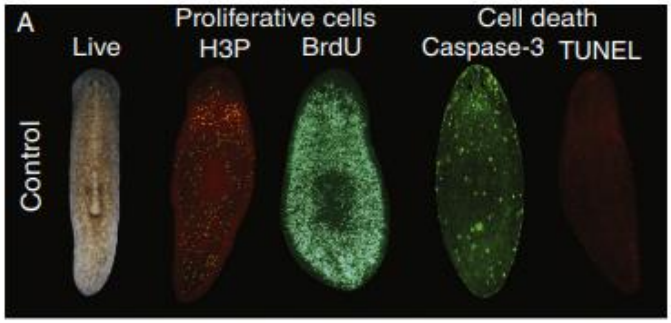

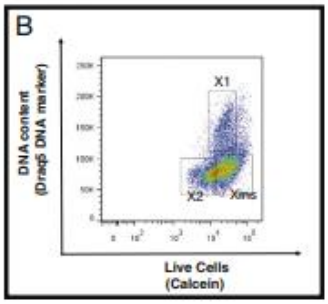

Fig. 3. Planarians allow for analysis of stem cell proliferation, differentiation and cell death in the whole organism. (A) Left to right. Live worm, whole-mount immunohistochemistry (WIHC) to stain cells in different parts of the cell cycle, including mitotic cells alone (H3P), cells entering S phase of the cell cycle (BrdU positive cells, green dots indicate proliferative cells), cell death showing Caspase-3 and TUNEL (fragmented DNA of apoptotic cells) (B) FACS plot shows gates used to isolate irradiation sensitive (X1 and X2) and insensitive (Xins) populations based on DNA content and viability.

amenable to analysis of cellular transformation by chemical treatment or genetic manipulation of tumor suppressor genes. The many tools that have been developed to study these animals will prove useful for manipulating various facets of their internal characteristics and eventually enable us to address how endogenous electric fields contribute to tissue homeostasis and regeneration of the whole organism. Increased efforts in this area will propel the field into creating applications, which can eventually lead to a better understanding of human tissue homeostasis and regeneration.

Conflict of interest

The authors Barghouth et al. declare no conflict of interest.

Acknowledgments

We thank Natasha M. Flores, Devon C. Davidian and T. Harshani Peiris for comments on the manuscript. Research in the Oviedo Lab is supported by grants from the NIH-National Cancer Institute and National Institute of General Medical Sciences, CA176114 and GM109372.

References

[1] M. Levin, Large-scale biophysics: ion flows and regeneration, Trends Cell Biol. 17 (2007) 261–270.
[2] M. Levin, Bioelectric mechanisms in regeneration: unique aspects and future perspectives, Semin. Cell Dev. Biol. 20 (2009) 543–556.
[3] C.D. McCaig, A.M. Rajnicek, B. Song, M. Zhao, Controlling cell behavior electrically: current views and future potential, Physiol. Rev. 85 (2005) 943–978.
[4] S. Sundelacruz, M. Levin, D.L. Kaplan, Role of membrane potential in the regulation of cell proliferation and differentiation, Stem Cell Rev. 5 (2009) 231–246.
[5] B.T. Chernet, M. Levin, Transmembrane voltage potential is an essential cellular parameter for the detection and control of tumor development in a Xenopus model, Dis. Model. Mech. 6 (2013) 595–607.
[6] B.T. Chernet, M. Levin, Transmembrane voltage potential of somatic cells controls oncogene-mediated tumorigenesis at long-range, Oncotarget 5 (2014) 3287–3306.
[7] M. Lobikin, B. Chernet, D. Lobo, M. Levin, Resting potential, oncogene-induced tumorigenesis, and metastasis: the bioelectric basis of cancer in vivo, Phys. Biol. 9 (2012) 065002.
[8] A. Tseng, M. Levin, Cracking the bioelectric code: probing endogenous ionic controls of pattern formation, Commun. Integr. Biol. 6 (2013) e22595.
[9] M. Yang, W.J. Brackenbury, Membrane potential and cancer progression, Front. Physiol. 4 (2013) 185.
[10] M. Levin, Reprogramming cells and tissue patterning via bioelectrical pathways: molecular mechanisms and biomedical opportunities, Wiley Interdiscip. Rev. Syst. Biol. Med. 5 (2013) 657–676.
[11] D.J. Blackiston, K.A. McLaughlin, M. Levin, Bioelectric controls of cell proliferation: ion channels, membrane voltage and the cell cycle, Cell Cycle 8 (2009) 3527–3536.
[12] F. Lang, C. Stournaras, Ion channels in cancer: future perspectives and clinical potential, Philos. Trans. R. Soc. Lond. Ser. B Biol. Sci. 369 (2014) 20130108.
[13] W.S. Beane, J. Morokuma, J.M. Lemire, M. Levin, Bioelectric signaling regulates head and organ size during planarian regeneration, Development 140 (2013) 313–322.
[14] M. Levin, Gap junctional communication in morphogenesis, Prog. Biophys. Mol. Biol. 94 (2007) 186–206.
[15] M. Levin, Molecular bioelectricity in developmental biology: new tools and recent discoveries: control of cell behavior and pattern formation by transmembrane potential gradients, Bioessays 34 (2012) 205–217.
[16] K.R. Robinson, The responses of cells to electrical fields: a review, J. Cell Biol. 101 (1985) 2023–2027.
[17] N.J. Oviedo, M. Levin, smedinx-11 is a planarian stem cell gap junction gene required for regeneration and homeostasis, Development 134 (2007) 3121–3131.
[18] N.J. Oviedo, J. Morokuma, P. Walentek, I.P. Kema, M.B. Gu, J.M. Ahn, J.S. Hwang, T. Gojobori, M. Levin, Long-range neural and gap junction protein-mediated cues control polarity during planarian regeneration, Dev. Biol. 339 (2010) 188–199.
[19] T.H. Peiris, N.J. Oviedo, Gap junction proteins: master regulators of the planarian stem cell response to tissue maintenance and injury, Biochim. Biophys. Acta 1828 (2013) 109–117.
[20] M.B. Djamgoz, R.C. Coombes, A. Schwab, Ion transport and cancer: from initiation to metastasis, Philos. Trans. R. Soc. Lond. Ser. B Biol. Sci. 369 (2014) 20130092.
[21] J. Boonstra, C.L. Mummery, L.G. Tertoolen, P.T. Van Der Saag, S.W. De Laat, Cation transport and growth regulation in neuroblastoma cells. Modulations of K+ transport and electrical membrane properties during the cell cycle, J. Cell. Physiol. 107 (1981) 75–83.
[22] C.D. Cone Jr., Unified theory on the basic mechanism of normal mitotic control and oncogenesis, J. Theor. Biol. 30 (1971) 151–181.
[23] S.W. de Laat, P.T. van der Saag, M. Shinitzky, Microviscosity modulation during the cell cycle of neuroblastoma cells, Proc. Natl. Acad. Sci. U. S. A. 74 (1977) 4458–4461.
[24] M. Petitou, F. Tuy, C. Rosenfeld, Z. Mishal, M. Paintrand, C. Jasnin, G. Mathe, M. Inbar, Decreased microviscosity of membrane lipids in leukemic cells: two possible mechanisms, Proc. Natl. Acad. Sci. U. S. A. 75 (1978) 2306–2310.
[25] W.F. Wonderlin, K.A. Woodfork, J.S. Strobl, Changes in membrane potential during the progression of MCF-7 human mammary tumor cells through the cell cycle, J. Cell. Physiol. 165 (1995) 177–185.
[26] T.L. Baars, S. Petri, C. Peters, A. Mayer, Role of the V-ATPase in regulation of the vacuolar fission–fusion equilibrium, Mol. Biol. Cell 18 (2007) 3873–3882.
[27] E. Gottlieb, S.M. Armour, M.H. Harris, C.B. Thompson, Mitochondrial membrane potential regulates matrix configuration and cytochrome c release during apoptosis, Cell Death Differ. 10 (2003) 709–717.
[28] T.A. Heming, A. Bidani, Effects of plasmalemmal V-ATPase activity on plasma membrane potential of resident alveolar macrophages, Lung 181 (2003) 121–135.
[29] H.G. Sachs, P.J. Stambrook, J.D. Ebert, Changes in membrane potential during the cell cycle, Exp. Cell Res. 83 (1974) 362–366.
[30] W.R. Harvey, H. Wieczorek, Animal plasma membrane energization by chemiosmotic H+ V-ATPases, J. Exp. Biol. 200 (1997) 203–216.
[31] T. Manabe, T. Yoshimori, N. Henomatsu, Y. Tashiro, Inhibitors of vacuolar-type H(+)-ATPase suppresses proliferation of cultured cells, J. Cell. Physiol. 157 (1993) 445–452.
[32] J. Ichikawa, R. Inoue, TRPC6 regulates cell cycle progression by modulating membrane potential in bone marrow stromal cells, Br. J. Pharmacol. 171 (23) (2014) 5280–5294.
[33] M. Forgac, Structure and properties of the vacuolar (H+)-ATPases, J. Biol. Chem. 274 (1999) 12951–12954.
[34] T.J. Jentsch, V. Stein, F. Weinreich, A.A. Zdebik, Molecular structure and physiological function of chloride channels, Physiol. Rev. 82 (2002) 503–568.
[35] M.L. Jennings, J. Cui, Chloride homeostasis in *Saccharomyces cerevisiae*: high affinity influx, V-ATPase-dependent sequestration, and identification of a candidate Cl− sensor, J. Gen. Physiol. 131 (2008) 379–391.
[36] T.K. Klausen, A. Bergdahl, C. Hougaard, P. Christophersen, S.F. Pedersen, E.K. Hoffmann, Cell cycle-dependent activity of the volume- and Ca2+-activated anion currents in Ehrlich lettre ascites cells, J. Cell. Physiol. 210 (2007) 831–842.
[37] M.R. Shen, G. Droogmans, J. Eggermont, T. Voets, J.C. Ellory, B. Nilius, Differential expression of volume-regulated anion channels during cell cycle progression of human cervical cancer cells, J. Physiol. 529 (Pt 2) (2000) 385–394.
[38] L. Munaron, S. Antoniotti, D. Lovisolo, Intracellular calcium signals and control of cell proliferation: how many mechanisms? J. Cell. Mol. Med. 8 (2004) 161–168.
[39] R. Schreiber, Ca2+ signaling, intracellular pH and cell volume in cell proliferation, J. Membr. Biol. 205 (2005) 129–137.
[40] B. Yang, L. Cao, B. Liu, C.D. McCaig, J. Pu, The transition from proliferation to differentiation in colorectal cancer is regulated by the calcium activated chloride channel A1, PLoS ONE 8 (2013) e60861.
[41] J. Mao, L. Chen, B. Xu, L. Wang, W. Wang, M. Li, M. Zheng, H. Li, J. Guo, W. Li, T.J. Jacob, L. Wang, Volume-activated chloride channels contribute to cell-cycle-dependent regulation of HeLa cell migration, Biochem. Pharmacol. 77 (2009) 159–168.
[42] J. Mao, X. Li, W. Chen, B. Xu, H. Zhang, H. Li, L. Wang, X. Jin, J. Zhu, G. Lin, W. Wang, L. Chen, Cell cycle-dependent subcellular distribution of ClC-3 in HeLa cells, Histochem. Cell Biol. 137 (2012) 763–776.
[43] A. Shiozaki, E. Otsuji, Y. Marunaka, Intracellular chloride regulates the G(1)/S cell cycle progression in gastric cancer cells, World J. Gastrointest. Oncol. 3 (2011) 119–122.
[44] B. Nilius, Chloride channels go cell cycling, J. Physiol. 532 (2001) 581.
[45] Z. Qu, W. Yao, R. Yao, X. Liu, K. Yu, C. Hartzell, The Ca(2+)-activated Cl(−) channel, ANO1 (TMEM16A), is a double-edged sword in cell proliferation and tumorigenesis, Cancer Med. 3 (2014) 453–461.
[46] T. Voets, G. Szucs, G. Droogmans, B. Nilius, Blockers of volume-activated Cl− currents inhibit endothelial cell proliferation, Pflugers Arch. 431 (1995) 132–134.
[47] R. Wondergem, W. Gong, S.H. Monen, S.N. Dooley, J.L. Gonce, T.D. Conner, M. Houser, T.W. Ecay, K.E. Ferslew, Blocking swelling-activated chloride current inhibits mouse liver cell proliferation, J. Physiol. 532 (2001) 661–672.
[48] B. Rouzaire-Dubois, M. Malo, J.B. Milandri, J.M. Dubois, Cell size–proliferation relationship in rat glioma cells, Glia 45 (2004) 249–257.
[49] L. Chen, L. Wang, L. Zhu, S. Nie, J. Zhang, P. Zhong, B. Cai, H. Luo, T.J. Jacob, Cell cycle-dependent expression of volume-activated chloride currents in nasopharyngeal carcinoma cells, Am. J. Physiol. Cell Physiol. 283 (2002) C1313–C1323.
[50] S. Aw, D.S. Adams, D. Qiu, M. Levin, H,K-ATPase protein localization and Kir4.1 function reveal concordance of three axes during early determination of left–right asymmetry, Mech. Dev. 125 (2008) 353–372.
[51] J.L. Horng, L.Y. Lin, C.J. Huang, F. Katoh, T. Kaneko, P.P. Hwang, Knockdown of V-ATPase subunit A (atp6v1a) impairs acid secretion and ion balance in zebrafish (*Danio rerio*), Am. J. Physiol. Regul. Integr. Comp. Physiol. 292 (2007) R2068–R2076.
[52] M.S. LaPointe, D.C. Batlle, Na+/H+ exchange and vascular smooth muscle proliferation, Am. J. Med. Sci. 307 (Suppl. 1) (1994) S9–S16.
[53] G.A. Morrill, E. Robbins, Changes in intracellular cations during the cell cycle in HeLa cells, Physiol. Chem. Phys. Med. NMR 16 (1984) 209–219.
[54] C. Galva, P. Artigas, C. Gatto, Nuclear Na+/K +-ATPase plays an active role in nucleoplasmic Ca2+ homeostasis, J. Cell Sci. 125 (2012) 6137–6147.
[55] F. Scamps, S. Valentin, G. Dayanithi, J. Valmier, Calcium channel subtypes responsible for voltage-gated intracellular calcium elevations in embryonic rat motoneurons, Neuroscience 87 (1998) 719–730.
[56] X. Huang, A.M. Dubuc, R. Hashizume, J. Berg, Y. He, J. Wang, C. Chiang, M.K. Cooper, P.A. Northcott, M.D. Taylor, M.J. Barnes, T. Tihan, J. Chen, C.S. Hackett, W.A. Weiss, C.D. James, D.H. Rowitch, M.A. Shuman, Y.N. Jan, L.Y. Jan, Voltage-gated potassium channel EAG2 controls mitotic entry and tumor growth in medulloblastoma via regulating cell volume dynamics, Genes Dev. 26 (2012) 1780–1796.
[57] H. Ouadid-Ahidouch, A. Ahidouch, K(+) channels and cell cycle progression in tumor cells, Front. Physiol. 4 (2013) 220.
[58] C.L. Mummery, J. Boonstra, P.T. van der Saag, S.W. de Laat, Modulations of Na+ transport during the cell cycle of neuroblastoma cells, J. Cell. Physiol. 112 (1982) 27–34.

[59] K.S. Park, M.H. Han, H.K. Jang, K.A. Kim, E.J. Cha, W.J. Kim, Y.H. Choi, Y. Kim, The TREK2 channel is involved in the proliferation of 253 J cell, a human bladder carcinoma cell, Korean J. Physiol. Pharmacol. 17 (2013) 511–516.
[60] J. Wu, D. Zhong, X. Wu, M. Sha, L. Kang, Z. Ding, Voltage-gated potassium channel Kv1.3 is highly expressed in human osteosarcoma and promotes osteosarcoma growth, Int. J. Mol. Sci. 14 (2013) 19245–19256.
[61] A. Arcangeli, Expression and role of hERG channels in cancer cells, Novartis Found. Symp. 266 (2005) 225–232 (discussion 232–224).
[62] C.D. Bortner, J.A. Cidlowski, Ion channels and apoptosis in cancer, Philos. Trans. R. Soc. Lond. Ser. B Biol. Sci. 369 (2014) 20130104.
[63] A. Bordey, S.A. Lyons, J.J. Hablitz, H. Sontheimer, Electrophysiological characteristics of reactive astrocytes in experimental cortical dysplasia, J. Neurophysiol. 85 (2001) 1719–1731.
[64] H. Higashimori, H. Sontheimer, Role of Kir4.1 channels in growth control of glia, Glia 55 (2007) 1668–1679.
[65] F. Lang, M. Foller, K.S. Lang, P.A. Lang, M. Ritter, E. Gulbins, A. Vereninov, S.M. Huber, Ion channels in cell proliferation and apoptotic cell death, J. Membr. Biol. 205 (2005) 147–157.
[66] M. Ritter, E. Woll, S. Waldegger, D. Haussinger, H.J. Lang, W. Scholz, B. Scholkens, F. Lang, Cell shrinkage stimulates bradykinin-induced cell membrane potential oscillations in NIH 3 T3 fibroblasts expressing the ras-oncogene, Pflugers Arch. 423 (1993) 221–224.
[67] E.G. Dora, N. Rudin, J.R. Martell, M.S. Esposito, R.M. Ramirez, RPD3 (REC3) mutations affect mitotic recombination in *Saccharomyces cerevisiae*, Curr. Genet. 35 (1999) 68–76.
[68] M. Classon, E. Harlow, The retinoblastoma tumour suppressor in development and cancer, Nat. Rev. Cancer 2 (2002) 910–917.
[69] N. Takuwa, W. Zhou, Y. Takuwa, Calcium, calmodulin and cell cycle progression, Cell. Signal. 7 (1995) 93–104.
[70] C. Attwooll, E. Lazzerini Denchi, K. Helin, The E2F family: specific functions and overlapping interests, EMBO J. 23 (2004) 4709–4716.
[71] D.L. Burkhart, J. Sage, Cellular mechanisms of tumour suppression by the retinoblastoma gene, Nat. Rev. Cancer 8 (2008) 671–682.
[72] C.R. Kahl, A.R. Means, Regulation of cyclin D1/Cdk4 complexes by calcium/calmodulin-dependent protein kinase I, J. Biol. Chem. 279 (2004) 15411–15419.
[73] A.C. Swann, Free fatty acids and (Na+, K+)-ATPase: effects on cation regulation, enzyme conformation, and interactions with ethanol, Arch. Biochem. Biophys. 233 (1984) 354–361.
[74] E.J. van Zoelen, C.L. Mummery, J. Boonstra, P.T. van der Saag, S.W. de Laat, Membrane regulation of the Na+, K+-ATPase during the neuroblastoma cell cycle: correlation with protein lateral mobility, J. Cell. Biochem. 21 (1983) 77–91.
[75] D. Corda, C. Pasternak, M. Shinitzky, Increase in lipid microviscosity of unilamellar vesicles upon the creation of transmembrane potential, J. Membr. Biol. 65 (1982) 235–242.
[76] G. Berstein, T. Haga, A. Ichiyama, Effect of the lipid environment on the differential affinity of purified cerebral and atrial muscarinic acetylcholine receptors for pirenzepine, Mol. Pharmacol. 36 (1989) 601–607.
[77] P.J. Emmerson, M.J. Clark, F. Medzihradsky, A.E. Remmers, Membrane microviscosity modulates mu-opioid receptor conformational transitions and agonist efficacy, J. Neurochem. 73 (1999) 289–300.
[78] K. Tsuda, I. Nishio, Role of estrogens in the regulation of membrane microviscosity, Circ. Res. 94 (2004) e17.
[79] K.L. Turner, H. Sontheimer, Cl− and K+ channels and their role in primary brain tumour biology, Philos. Trans. R. Soc. Lond. Ser. B Biol. Sci. 369 (2014) 20130095.
[80] A. Fiorio Pla, L. Munaron, Functional properties of ion channels and transporters in tumour vascularization, Philos. Trans. R. Soc. Lond. Ser. B Biol. Sci. 369 (2014) 20130103.
[81] A.P. Andersen, J.M. Moreira, S.F. Pedersen, Interactions of ion transporters and channels with cancer cell metabolism and the tumour microenvironment, Philos. Trans. R. Soc. Lond. Ser. B Biol. Sci. 369 (2014) 20130098.
[82] S.J. Reshkin, M.R. Greco, R.A. Cardone, Role of pHi, and proton transporters in oncogene-driven neoplastic transformation, Philos. Trans. R. Soc. Lond. Ser. B Biol. Sci. 369 (2014) 20130100.
[83] A.A. Marino, I.G. Iliev, M.A. Schwalbe, E. Gonzalez, K.C. Marler, C.A. Flanagan, Association between cell membrane potential and breast cancer, Tumour Biol. 15 (1994) 82–89.
[84] G.J. Thompson, C. Langlais, K. Cain, E.C. Conley, G.M. Cohen, Elevated extracellular [K+] inhibits death-receptor- and chemical-mediated apoptosis prior to caspase activation and cytochrome c release, Biochem. J. 357 (2001) 137–145.
[85] R. Perona, R. Serrano, Increased pH and tumorigenicity of fibroblasts expressing a yeast proton pump, Nature 334 (1988) 438–440.
[86] S.A. Salyer, J.R. Olberding, A.A. Distler, E.D. Lederer, B.J. Clark, N.A. Delamere, S.J. Khundmiri, Vacuolar ATPase driven potassium transport in highly metastatic breast cancer cells, Biochim. Biophys. Acta 1832 (2013) 1734–1743.
[87] Y. Wang, S.J. Li, J. Pan, Y. Che, J. Yin, Q. Zhao, Specific expression of the human voltage-gated proton channel Hv1 in highly metastatic breast cancer cells, promotes tumor progression and metastasis, Biochem. Biophys. Res. Commun. 412 (2011) 353–359.
[88] K. Lansu, S. Gentile, Potassium channel activation inhibits proliferation of breast cancer cells by activating a senescence program, Cell Death Dis. 4 (2013) e652.
[89] P.D. Adams, Healing and hurting: molecular mechanisms, functions, and pathologies of cellular senescence, Mol. Cell 36 (2009) 2–14.
[90] S.H. Alkahtani, The steroidal Na+/K+ ATPase inhibitor 3-[(R)-3-pyrrolidinyl]oxime derivative (3-R-POD) induces potent pro-apoptotic responses in colonic tumor cells, Anticancer Res. 34 (2014) 2967–2971.
[91] C. Liu, Y. Bai, Y. Chen, Y. Wang, Y. Sottejeau, L. Liu, X. Li, J.B. Lingrel, D. Malhotra, C.J. Cooper, J.I. Shapiro, Z.J. Xie, J. Tian, Reduction of Na/K-ATPase potentiates marinobufagenin-induced cardiac dysfunction and myocyte apoptosis, J. Biol. Chem. 287 (2012) 16390–16398.
[92] H. Lallet-Daher, C. Wiel, D. Gitenay, N. Navaratnam, A. Augert, B. Le Calve, S. Verbeke, D. Carling, S. Aubert, D. Vindrieux, D. Bernard, Potassium channel KCNA1 modulates oncogene-induced senescence and transformation, Cancer Res. 73 (2013) 5253–5265.
[93] K. Dezaki, E. Maeno, K. Sato, T. Akita, Y. Okada, Early-phase occurrence of K+ and Cl− efflux in addition to Ca 2+ mobilization is a prerequisite to apoptosis in HeLa cells, Apoptosis 17 (2012) 821–831.
[94] L.A. Pardo, W. Stuhmer, The roles of K(+) channels in cancer, Nat. Rev. Cancer 14 (2014) 39–48.
[95] N. Prevarskaya, R. Skryma, Y. Shuba, Ion channels and the hallmarks of cancer, Trends Mol. Med. 16 (2010) 107–121.
[96] A.A. Chimote, P. Hajdu, V. Kucher, N. Boiko, Z. Kuras, O. Szilagyi, Y.H. Yun, L. Conforti, Selective inhibition of KCa3.1 channels mediates adenosine regulation of the motility of human T cells, J. Immunol. 191 (2013) 6273–6280.
[97] S. Kammerer, A. Sokoloski, H. Hackl, S. Jahn, M. Asslaber, F. Symmans, F. Peintinger, P. Regitnig, W. Scheibmayer, T. Bauernhofer, Overexpression of G protein-activated inward rectifier potassium channel 1 (GIRK1) is associated with lymph node metastasis and poor prognosis in breast cancer, Ann. Oncol. 25 (2014) 8–16.
[98] S. Yildirim, S. Altun, H. Gumushan, A. Patel, M.B. Djamgoz, Voltage-gated sodium channel activity promotes prostate cancer metastasis in vivo, Cancer Lett. 323 (2012) 58–61.
[99] K.W. Chang, T.C. Yuan, K.P. Fang, F.S. Yang, C.J. Liu, C.S. Chang, S.C. Lin, The increase of voltage-gated potassium channel Kv3.4 mRNA expression in oral squamous cell carcinoma, J. Oral Pathol. Med. 32 (2003) 606–611.
[100] S.P. Fraser, J.A. Grimes, M.B. Djamgoz, Effects of voltage-gated ion channel modulators on rat prostatic cancer cell proliferation: comparison of strongly and weakly metastatic cell lines, Prostate 44 (2000) 61–76.
[101] S.T. Menendez, J.P. Rodrigo, S. Alvarez-Teijeiro, M.A. Villaronga, E. Allonca, A. Vallina, A. Astudillo, F. Barros, C. Suarez, J.M. Garcia-Pedrero, Role of HERG1 potassium channel in both malignant transformation and disease progression in head and neck carcinomas, Mod. Pathol. 25 (2012) 1069–1078.
[102] F. Di Virgilio, P. Pizzo, P. Zanovello, V. Bronte, D. Collavo, Extracellular ATP as a possible mediator of cell-mediated cytotoxicity, Immunol. Today 11 (1990) 274–277.
[103] L.M. Zheng, A. Zychlinsky, C.C. Liu, D.M. Ojcius, J.D. Young, Extracellular ATP as a trigger for apoptosis or programmed cell death, J. Cell Biol. 112 (1991) 279–288.
[104] D.G. Jackson, J. Wang, R.W. Keane, E. Scemes, G. Dahl, ATP and potassium ions: a deadly combination for astrocytes, Sci. Rep. 4 (2014) 4576.
[105] K. Cain, C. Langlais, X.M. Sun, D.G. Brown, G.M. Cohen, Physiological concentrations of K+ inhibit cytochrome c-dependent formation of the apoptosome, J. Biol. Chem. 276 (2001) 41985–41990.
[106] P.W. Reddien, Specialized progenitors and regeneration, Development 140 (2013) 951–957.
[107] A.A. Aboobaker, Planarian stem cells: a simple paradigm for regeneration, Trends Cell Biol. 21 (2011) 304–311.
[108] D. Wenemoser, P.W. Reddien, Planarian regeneration involves distinct stem cell responses to wounds and tissue absence, Dev. Biol. 344 (2010) 979–991.
[109] P.W. Reddien, A. Sanchez Alvarado, Fundamentals of planarian regeneration, Annu. Rev. Cell Dev. Biol. 20 (2004) 725–757.
[110] J.C. Rink, Stem cell systems and regeneration in planaria, Dev. Genes Evol. 223 (2013) 67–84.
[111] P.A. Newmark, A. Sanchez Alvarado, Not your father's planarian: a classic model enters the era of functional genomics, Nat. Rev. Genet. 3 (2002) 210–219.
[112] E. Salo, J.F. Abril, T. Adell, F. Cebria, K. Eckelt, E. Fernandez-Taboada, M. Handberg-Thorsager, M. Iglesias, M.D. Molina, G. Rodriguez-Esteban, Planarian regeneration: achievements and future directions after 20 years of research, Int. J. Dev. Biol. 53 (2009) 1317–1327.
[113] J. Pellettieri, A. Sanchez Alvarado, Cell turnover and adult tissue homeostasis: from humans to planarians, Annu. Rev. Genet. 41 (2007) 83–105.
[114] B.J. Pearson, G.T. Eisenhoffer, K.A. Gurley, J.C. Rink, D.E. Miller, A. Sanchez Alvarado, Formaldehyde-based whole-mount in situ hybridization method for planarians, Dev. Dyn. 238 (2009) 443–450.
[115] P.A. Newmark, A. Sanchez Alvarado, Bromodeoxyuridine specifically labels the regenerative stem cells of planarians, Dev. Biol. 220 (2000) 142–153.
[116] T. Hayashi, M. Asami, S. Higuchi, N. Shibata, K. Agata, Isolation of planarian X-ray-sensitive stem cells by fluorescence-activated cell sorting, Dev. Growth Differ. 48 (2006) 371–380.
[117] T. Hayashi, K. Agata, A unique FACS method to isolate stem cells in planarian, Methods Mol. Biol. 879 (2012) 29–37.
[118] S. Moritz, F. Stockle, C. Ortmeier, H. Schmitz, G. Rodriguez-Esteban, G. Key, L. Gentile, Heterogeneity of planarian stem cells in the S/G2/M phase, Int. J. Dev. Biol. 56 (2012) 117–125.
[119] B.T. Romero, D.J. Evans, A.A. Aboobaker, FACS analysis of the planarian stem cell compartment as a tool to understand regenerative mechanisms, Methods Mol. Biol. 916 (2012) 167–179.
[120] H. Kang, A. Sanchez Alvarado, Flow cytometry methods for the study of cell-cycle parameters of planarian stem cells, Dev. Dyn. 238 (2009) 1111–1117.
[121] T.H. Peiris, F. Weckerle, E. Ozamoto, D. Ramirez, D. Davidian, M.E. Garcia-Ojeda, N.J. Oviedo, TOR signaling regulates planarian stem cells and controls localized and organismal growth, J. Cell Sci. 125 (2012) 1657–1665.
[122] W.S. Beane, J. Morokuma, D.S. Adams, M. Levin, A chemical genetics approach reveals H,K-ATPase-mediated membrane voltage is required for planarian head regeneration, Chem. Biol. 18 (2011) 77–89.

[123] N.J. Oviedo, B.J. Pearson, M. Levin, A. Sánchez Alvarado, Planarian PTEN homologs regulate stem cells and regeneration through TOR signaling, Dis. Model. Mech. 1 (2008) 131–143.
[124] B.J. Pearson, A. Sanchez Alvarado, Regeneration, stem cells, and the evolution of tumor suppression, Cold Spring Harb. Symp. Quant. Biol. 73 (2008) 565–572.
[125] T. Nogi, M. Levin, Characterization of innexin gene expression and functional roles of gap-junctional communication in planarian regeneration, Dev. Biol. 287 (2005) 314–335.
[126] P.W. Reddien, Constitutive gene expression and the specification of tissue identity in adult planarian biology, Trends Genet. 27 (2011) 277–285.
[127] S.M. Rose, The correlation between bioelectrical and morphogenetic polarity during regeneration in Tubularia, Dev. Biol. 28 (1972) 274–279.
[128] G. Marsh, H.W. Beams, Electrical control of morphogenesis in regenerating Dugesia tigrina. I. Relation of axial polarity to field strength, J. Cell. Physiol. 39 (1952) 191–213.
[129] N.J. Oviedo, C.L. Nicolas, D.S. Adams, M. Levin, Live imaging of planarian membrane potential using DiBAC4(3), CSH Protoc. 2008 (2008) (pdb prot5055).
[130] J.P. Dexter, M.B. Tamme, C.H. Lind, E.M. Collins, On-chip immobilization of planarians for in vivo imaging, Sci. Rep. 4 (2014) 6388.
[131] S. Perathoner, J.M. Daane, U. Henrion, G. Seebohm, C.W. Higdon, S.L. Johnson, C. Nusslein-Volhard, M.P. Harris, Bioelectric signaling regulates size in zebrafish fins, PLoS Genet. 10 (2014) e1004080.
[132] C. Lange, S. Prenninger, P. Knuckles, V. Taylor, M. Levin, F. Calegari, The H(+) vacuolar ATPase maintains neural stem cells in the developing mouse cortex, Stem Cells Dev. 20 (2011) 843–850.
[133] D.S. Adams, A. Masi, M. Levin, H+ pump-dependent changes in membrane voltage are an early mechanism necessary and sufficient to induce Xenopus tail regeneration, Development 134 (2007) 1323–1335.
[134] N. Villalonga, J.C. Ferreres, J.M. Argiles, E. Condom, A. Felipe, Potassium channels are a new target field in anticancer drug design, Recent Pat. Anticancer Drug Discov. 2 (2007) 212–223.

Appendix II

© 2016. Published by The Company of Biologists Ltd | Development (2016) 143, 1697-1709 doi:10.1242/dev.131318

Regional signals in the planarian body guide stem cell fate in the presence of genomic instability

T. Harshani Peiris[1,2], Daniel Ramirez[1,2], Paul G. Barghouth[1,2], Udokanma Ofoha[1,2], Devon Davidian[1,2], Frank Weckerle[1] and Néstor J. Oviedo[1,2,3,*]

ABSTRACT

Cellular fate decisions are influenced by their topographical location in the adult body. For instance, tissue repair and neoplastic growth are greater in anterior than in posterior regions of adult animals. However, the molecular underpinnings of these regional differences are unknown. We identified a regional switch in the adult planarian body upon systemic disruption of homologous recombination with RNA-interference of *Rad51*. *Rad51* knockdown increases DNA double-strand breaks (DSBs) throughout the body, but stem cells react differently depending on their location along the anteroposterior axis. In the presence of extensive DSBs, cells in the anterior part of the body resist death, whereas cells in the posterior region undergo apoptosis. Furthermore, we found that proliferation of cells with DNA damage is induced in the presence of brain tissue and that the retinoblastoma pathway enables overproliferation of cells with DSBs while attending to the demands of tissue growth and repair. Our results implicate both autonomous and non-autonomous mechanisms as key mediators of regional cell behavior and cellular transformation in the adult body.

KEY WORDS: Stem cells, DNA damage, Planarian, Neoblast, Rad51

INTRODUCTION

The proliferative response of normal and neoplastic cells is influenced by their topographical location along the anteroposterior axis (Auerbach and Auerbach, 1982). In mice, cellular proliferation and engraftment responses are superior in the anterior region of the body (i.e. head and thoracic cavity) to those in posterior areas (Auerbach and Auerbach, 1982; Kobayashi, 1977). Likewise, the effects of carcinogens and the growth of transplanted tumor cells are more aggressive in the anterior than in the posterior regions (Auerbach and Auerbach, 1982; Auerbach et al., 1978; Dispersio, 1981; Kubai and Auerbach, 1980). In humans, survival rates of cutaneous melanoma are attributed to location, with head and neck melanomas presenting the poorest outcomes relative to melanomas in other parts of the body (Lachiewicz et al., 2008; Tseng and Martinez, 2011). Despite these clear observations, the mechanisms underlying regional differences in the growth of normal and neoplastic cells in the adult body are unknown.

Planarians allow for the analysis of cell proliferation during tissue renewal and in response to stress and/or injury in the whole adult organism, providing a paradigm to further study regional regulation of cell proliferation in the adult body. Similar to mice and humans, regional differences in cellular proliferation also exist in the planarian flatworm (Baguñà, 1976; Brøndsted, 1969; Oviedo and Levin, 2007). The neoblast, or planarian stem cell, is the only cell with proliferative capacity within the entire organism, which continuously divides to support the renewal and repair of adult tissues. Uninjured planarians contain larger pools of dividing neoblasts in the anterior region than in the posterior; additionally, regeneration of the head occurs faster than the tail (Baguñà, 1976; Brøndsted, 1969; Oviedo and Levin, 2007; Oviedo et al., 2010). Interestingly, disruption of the tumor suppressor PTEN triggers neoblast hyperproliferation and tissue colonization by abnormal cells. These abnormally proliferative cells are first noted in the anterior part of the planarian (Oviedo et al., 2008c). These results suggest that regional signals along the planarian anteroposterior axis might influence the neoblast's decision to proliferate during cellular turnover, injury repair and cellular transformation.

DNA replication stress is one of the earliest manifestations of cellular transformation (Bartkova et al., 2006; Halazonetis et al., 2008; Macheret and Halazonetis, 2015). Furthermore, DNA damage response, particularly the repair of DNA double-strand breaks (DSBs), serves as an early anti-cancer barrier (Bartkova et al., 2006). Investigating the role of DNA repair mechanisms as key effectors of cell fate along the anteroposterior axis might provide molecular insights about regional regulation of neoblast proliferation. The Rad51 protein is an essential component for homologous recombination, genomic stability and repair of DSBs (Klein, 2008). We identified that systemic disruption of Rad51 via RNA-interference (RNAi) increases DSBs throughout the whole planarian. Strikingly, the cellular response to DSBs depended on the topographical location along the anteroposterior axis. In the presence of DSBs, cells in the anterior region resisted cell death, whereas cells in the posterior underwent apoptosis. We further discovered that this asymmetric topographical response might be established by cues derived from the central nervous system and the retinoblastoma pathway, enabling the survival and proliferation of cells with DSBs in the anterior region of the organism. These experiments reveal newly discovered regulators of cell fate decisions in the adult body and suggest that regional signals modulate tumor suppressor genes during adult tissue renewal. Our data indicate that both cellular location along the anteroposterior axis (non-cell autonomous) and intrinsic cellular properties (cell-autonomous) modulate fate choices in the presence of DNA damage.

RESULTS AND DISCUSSION

Smed-Rad51 is ubiquitously expressed and is essential to maintain DNA integrity

The planarian homolog of *Rad51-A* (*Smed-Rad51*) is expressed throughout the body and is strongly downregulated by lethal doses

[1]Department of Molecular and Cell Biology, School of Natural Sciences, University of California, Merced, CA 95343, USA. [2]Quantitative and Systems Biology Graduate Program, University of California, Merced, CA 95343, USA. [3]Health Sciences Research Institute, University of California, Merced, CA 95343, USA.

*Author for correspondence (noviedo2@ucmerced.edu)

N.J.O., 0000-0002-0213-9781

Received 26 September 2015; Accepted 10 March 2016

Development (2016) 143, 1697-1709 doi:10.1242/dev.131318

of γ-irradiation (Onal et al., 2012; Solana et al., 2012). To discern endogenous topographical differences in *Smed-Rad51* expression, we began by analyzing FACS-isolated cell populations extracted from both the anterior and posterior regions of the body and confirmed *Smed-Rad51* is widely expressed along the anteroposterior axis. Our analysis of FACS-sorted cells revealed that proliferating, irradiation-sensitive neoblasts (X1 cells) express increased levels of *Smed-Rad51* mRNA compared to both early postmitotic (X2 cells) and differentiated cell (Xins) populations (Fig. 1A). The enrichment of Rad51 expression in neoblasts is consistent with its functions during meiosis and germ cells across planarian species (Chinone and Matsumoto, 2014; Xiang et al., 2014). Nonetheless, the role of Rad51 signaling during cellular turnover and repair of adult tissues, which largely relies on the mitotic activity of somatic stem cells, still requires further investigation. This gap in knowledge might be attributed to the fact that homozygous *Rad51* mutations lead to early embryonic lethality and non-viable embryonic stem cells in mice (Lim and Hasty, 1996; Tsuzuki et al., 1996).

To assess the possible roles of Rad51 during cellular turnover, we functionally disrupted *Smed-Rad51* via RNAi [*Rad51(RNAi)*]. This analysis revealed that systemic inhibition of Rad51 leads to a fully penetrant phenotype (100/100 animals) characterized by the progressive loss of tissue in the posterior region and lethality >40 days post-RNAi treatment (Fig. 1B and data not shown). The specific loss of the posterior tissue is an uncommon RNAi phenotype in planarians, thus we assessed whether the efficiency of our RNAi protocol was limited or restricted to a particular region of the animal. Tissues from both the anterior and posterior regions were processed separately to evaluate *Smed-Rad51* mRNA expression and whole animal protein extracts were obtained to assess protein levels after 35 days of *Rad51(RNAi)* treatment. These experiments revealed that after 35 days, the RNAi protocol dramatically reduced Rad51 gene and protein expression throughout the whole animal (Fig. 1C,D). Additionally, we utilized different strategies to functionally downregulate *Smed-Rad51* with double-stranded-RNA (dsRNA) incorporated by feeding (Rouhana et al., 2013) or microinjections specifically

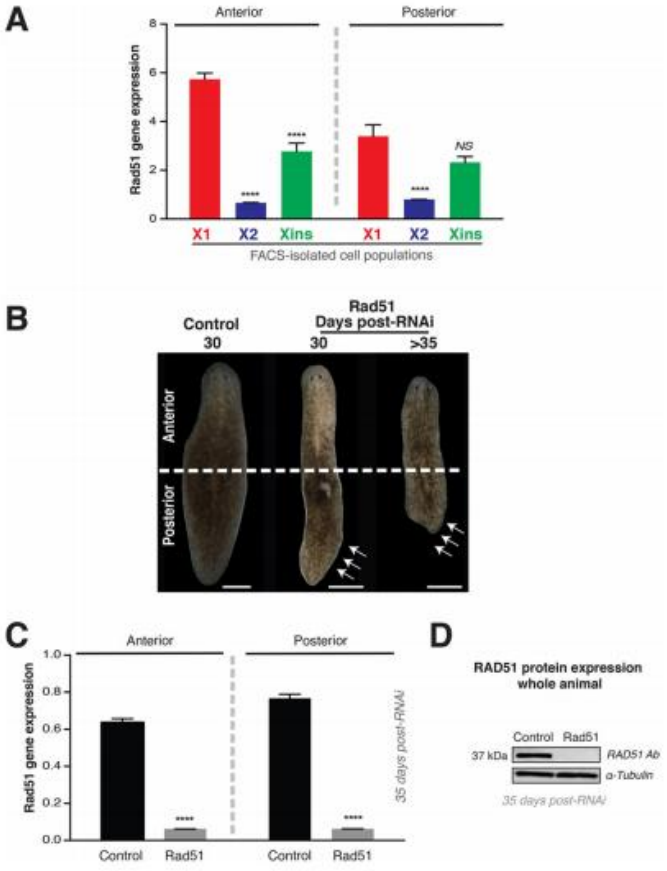

Fig. 1. Rad51 is expressed in neoblasts and differentiated cells and its expression can be downregulated throughout the body. (A) *Smed-Rad51* gene expression levels in FACS-isolated cells (X1, X2 and Xins) measured by qPCR. (B) Representative images of control and *Rad51(RNAi)* animals. The progressive deterioration and tissue lost from posterior body parts are indicated with arrows. (C) *Rad51(RNAi)* reduces expression of *Smed-Rad51* uniformly throughout the body. (D) SMED-RAD51 protein expression is strongly downregulated in the whole organism by *Rad51(RNAi)*. SMED-RAD51 was detected with anti-human RAD51 antibody and alpha tubulin was used as an internal loading control. In A,C, gene expression values represent mean±s.e.m. of triplicates per experiment of at least two biological replicates, each condition was generated by extracting RNA from $n>10$ animals per experiment. The internal control is the ubiquitously expressed clone *H.55.12e*. ****$P<0.0001$; NS, no significance; Tukey's multiple comparisons test.

Development (2016) 143, 1697-1709 doi:10.1242/dev.131318

targeting the anterior or posterior regions of the animal (Oviedo and Levin, 2007). Consistently, we were able to reduce Rad51 expression throughout the animal, leading to the loss of posterior tissue (Fig. S1; data not shown). These findings imply that the phenotype reflects a specific response upon the abrogation of *Smed-Rad51*.

Smed-Rad51 shares a high level of molecular conservation with its homologous counterpart in mammals (Fig. S2), which is crucial for homologous recombination, genomic stability and repair of DNA DSBs (Klein, 2008). To test whether Rad51 is functionally conserved in planarians, we performed *Rad51(RNAi)* treatment and assessed both DNA stability in cells using the Comet assay and chromosomal integrity via karyotyping (Fig. 2A,B). The Comet assay was optimized to detect DSBs and a standard scale was built by using sub-lethal doses of γ-irradiation (1200 rad), which are known to induce DNA damage that is repaired over time (Fig. S3). The RNAi studies revealed that *Smed-Rad51* is essential in maintaining both DNA and chromosomal integrity throughout the whole animal (Fig. 2A,B). Systemic DNA abnormalities in *Rad51 (RNAi)* animals are consistent with the functional conservation of Rad51 in planarians and its distribution along the anteroposterior axis.

To further investigate the function of *Smed-Rad51* in DNA repair, we exposed whole planarians to a single sub-lethal dose of γ-irradiation (1200 rad) that caused DSBs and transiently abrogated neoblast division (Wagner et al., 2011). Specifically, two aspects were analyzed; Rad51 gene and protein levels, and cytoplasmic versus nuclear localization of SMED-RAD51 after γ-irradiation. Both gene and protein expression were downregulated during the first three days post-irradiation, consistent with the disappearance of mitotic activity. Expression peaked at day five and then returned to pre-irradiation levels by day seven. This behavior coincided with the recovery of mitotic activity (Fig. 2C,D and data not shown). Furthermore, analysis of SMED-RAD51 expression in dissociated cells from whole planarians showed that Rad51 protein signal switched from the cytoplasm to the nucleus by day five post-irradiation, implying active DNA repair (Fig. 2E,F). These findings are consistent with a recent report suggesting Rad51 plays roles in DSB repair based on changes in expression pattern during meiosis and after irradiation (Xiang et al., 2014).

Smed-Rad51 is required for proper regulation of cell proliferation and cell death during cellular turnover

The process of cellular turnover depends on a specific balance between cell proliferation and cell death. Thus, we assessed the effects of *Rad51(RNAi)* on cell division and cell death in the adult planarian body that continually undergoes cellular turnover. *Rad51 (RNAi)* reduces neoblast mitotic activity throughout the body. However, this reduction is more pronounced in the posterior area of the planarian, compared with the anterior region in which some cells still divide (Fig. 3A,B; Fig. S1). Intriguingly, suppression of mitosis was accompanied by massive cell death and tissue loss in the posterior area, indicating that it is possible to induce selective elimination of cells and tissues depending on their location along the anteroposterior axis (Fig. 3C-E).

The systemic effects of *Smed-Rad51* downregulation with RNAi are characterized by a dramatic decrease in cell division and a regional specific increase of cell death in the posterior area of the planarian (Fig. 3A-E). To gain insights on the mechanisms regulating cellular decisions upon *Rad51(RNAi)* treatment, we analyzed cells from both the anterior and posterior areas by flow cytometry (Hayashi et al., 2006; Peiris et al., 2016). We found that *Rad51(RNAi)* leads to a ~50% systemic reduction in the number of proliferative cells (e.g. X1 subpopulation, Fig. S4A). This finding is consistent with a restricted number of cells transitioning into the G2/M phase of the cell cycle (Fig. 3A,B). Furthermore, gene expression analysis of *Smed-cyclin B*, which is needed for the progression of neoblasts into the M phase of the cell cycle, revealed a strong downregulation throughout the animal. However, the reduction in gene expression is accentuated in the posterior compared with the anterior region (Fig. 3F,G). Additionally, regional changes in the expression of neoblast markers and the cellular division progeny were also observed after *Rad51(RNAi)* treatment (Fig. S4B,C). These results suggest that despite a severe reduction of neoblasts in *Rad51(RNAi)* animals, the asymmetric distribution of proliferative cells is sustained.

Cell cycle transition between the S and G2/M phases can be visualized throughout the planarian body by double labeling with the thymidine analogue bromodeoxyuridine (BrdU) and anti-histone-3-phosphorylated (H3P) antibody (Newmark and Sanchez Alvarado, 2000). BrdU is incorporated during the S phase, whereas the H3P antibody labels neoblasts in the G2/M phase. After *Rad51 (RNAi)* treatment, BrdU incorporation was severely reduced but the proliferative asymmetry was maintained as demonstrated by the distribution of $BrdU^+$ and $H3P^+$ cells along the anteroposterior axis (Fig. 3H,I; Fig. S5). Quantification of double $BrdU^+$ and $H3P^+$ cells revealed that 60-70% of cells continuing through the cell cycle are positive for both BrdU and H3P, indicating that the remaining cells in *Rad51(RNAi)* animals transition from the S phase to the M phase with similar dynamics to the control group (Fig. 3J). This result implies that regional asymmetry in the progression through the S/G2/M phases of the cell cycle is still preserved despite fewer neoblasts in *Rad51(RNAi)* animals. Additional experiments are required to address the mechanisms influencing regional levels of cell death in the absence of Rad51. Nonetheless, the whole-body Rad51-silencing strategy we applied reveals unappreciated aspects of regional regulation of cell fate in the presence of DNA damage.

Homologous recombination is required to repair DNA after ionizing irradiation and to maintain DNA integrity along the anteroposterior axis

Unrepaired DSBs pose a great risk for cell survival and malignancy. An extensive number of neoblasts and differentiated cells undergo apoptosis in the posterior region, unlike the anterior region (Fig. 3C-E). Nonetheless, the presence of cell division in *Rad51 (RNAi)* animals suggests that either some cells maintain DNA integrity through a Rad51-independent mechanism, or mitosis occurs despite DNA damage. DSB repair proceeds predominantly through two mechanisms; homologous recombination and Ku-dependent non-homologous end joining (NHEJ) (Lord and Ashworth, 2012). We identified in the *Schmidtea mediterranea* genome components associated with NHEJ such as Ku, MRE11 and ATM (ataxia telangiectasia mutated). RNAi knockout of *Smed-Ku70*, *Smed-MRE11* and *Smed-ATM* reduced neoblast division and was further reduced with simultaneous downregulation of *Smed-Rad51*with *Rad51(RNAi)* (Fig. 4A,B). These results suggest that cell division after *Rad51(RNAi)* proceeds without intervention of the NHEJ DNA repair mechanisms, which is consistent with the levels of DSBs present throughout the experimental group. This also implies that after *Smed-Rad51* knockdown, neoblasts with genomic instability are prone to proliferate, a pervasive feature of tumor cells (Halazonetis et al., 2008).

To further understand the mechanisms planarians use to repair damaged DNA, we tested both the roles of homologous

Development (2016) 143, 1697-1709 doi:10.1242/dev.131318

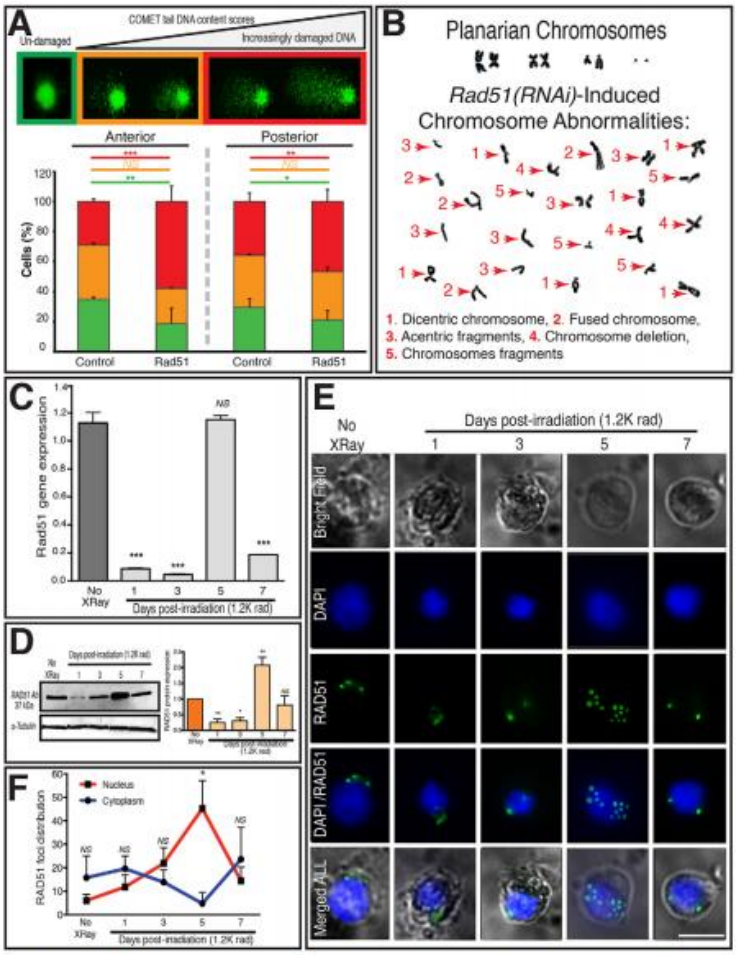

Fig. 2. Rad51 maintains genomic stability and its expression is regulated by gamma irradiation-induced DNA damage. (A) DNA damage in anterior and posterior specific regions were assessed by the Comet assay, gel electrophoresis under alkaline conditions. Visual scoring was used to quantify DNA damage, color-coded key at top represents undamaged (green), moderate damage (orange) and extremely damaged DNA (red) shown in either anterior or posterior regions. (B) Mitotic metaphase spread from whole animals shows multiple chromosome abnormalities after *Rad51(RNAi)*. (C) *Smed-Rad51* mRNA levels from whole animals measured with qPCR over one week post-irradiation. (D) SMED-RAD51 changes after sub-lethal irradiation were measured by western blot using protein extracts from whole animals at each time point. Quantification for each respective time point is shown to the right (bar graph). SMED-RAD51 was detected with anti-human RAD51 antibody and alpha tubulin was used as an internal loading control. (E) Spatial distribution of SMED-RAD51 immunostaining (green) in reference to the cell nucleus (stained with DAPI, blue). Notice SMED-RAD51 signal is mostly perinuclear but at day five after sub-lethal irradiation the signal is closely associated with the cell nucleus. Overlay between bright field and fluorescent images was used to evaluate SMED-RAD51 spatial location (bottom row). The images were obtained from whole animal dissociation. Scale bar: 10 µm. (F) Percentage of SMED-RAD51 foci distribution after sub-lethal irradiation. In A-D,F, analyses were performed using animals ~30 days after first dsRNA injection. Values represent mean±s.e.m. of at least three biological replicates and each condition was generated with 10-20 animals per experiment. *P<0.01, **P<0.005, ***P<0.0005; NS, not significant; Tukey's multiple comparison test.

recombination and NHEJ after a sub-lethal dose of γ-irradiation (1200 rad). Sub-lethally irradiated *Rad51(RNAi)*-treated animals did not recover cell division and died soon after, whereas RNAi of *Smed-Ku70*, *Smed-MRE11* or *Smed-ATM* and the untreated control group, recovered mitotic activity 7 days post-irradiation (Fig. 4C). Rad51 function is facilitated by the breast cancer type 2 susceptibility protein (BRCA2) (Lord and Ashworth, 2012) and RNAi of its planarian homolog *Smed-BRCA2* (Pearson and Sanchez

Development (2016) 143, 1697-1709 doi:10.1242/dev.131318

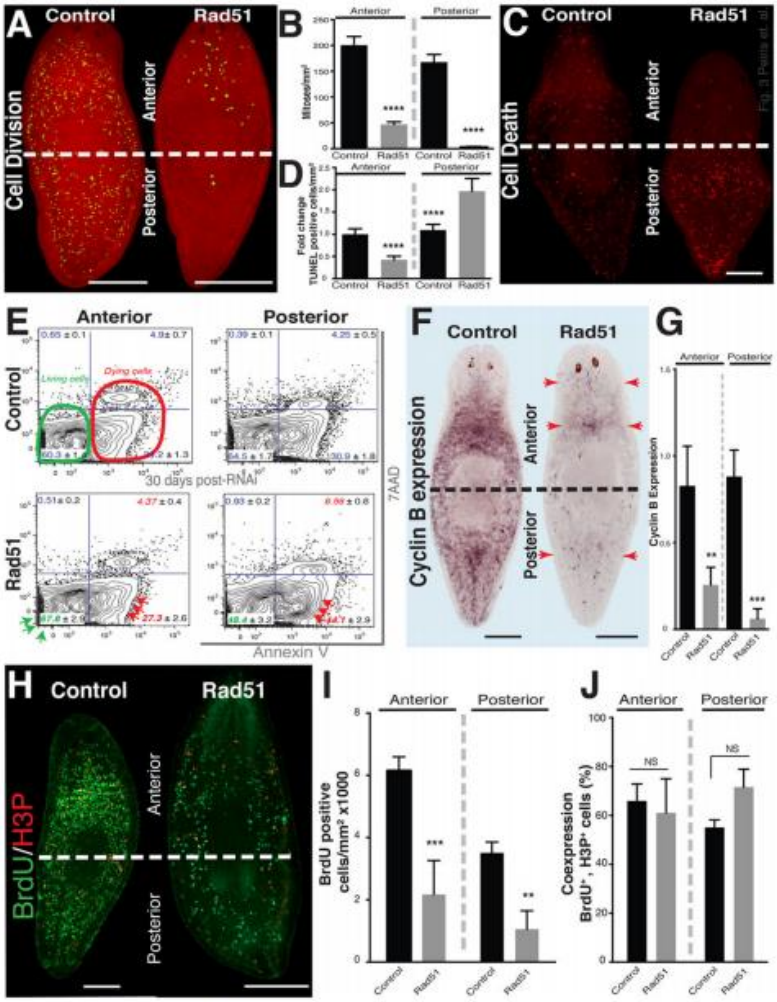

Fig. 3. *Rad51(RNAi)* alters cell proliferation and cell death during systemic cellular turnover in adult planarians. (A) Representative images of mitoses by whole-mount immunostaining with anti-H3P antibody (yellow dots). Dotted line indicates the limits between anterior and posterior areas. (B) Quantification of mitotic cells in the anterior and posterior regions, $n>25$ animals per condition. Cell division disappears over time and animals die after day 40-45 post-*Rad51 (RNAi)* treatment (20 out of 20 animals, data not shown). (C) Whole-mount immunostaining labeling TUNEL-positive nuclei (cell death, red dots) along the anteroposterior axis. (D) Quantification of TUNEL-positive nuclei (cell death levels) in the anterior and posterior regions, $n>10$ animals per condition. (E) The frequency distribution between viable and dead cells visualized with Annexin V and 7 AAD staining in different regions of the animal. Annexin V−/7 AAD− quadrant includes viable cells (outlined green). Annexin V+/7 AAD− and Annexin V+/7 AAD+ indicate cells that are in early and late (necrotic) stages of cell death, respectively (outlined red). The numbers in each quadrant indicate the percentage of cells with that staining profile. (F,G) Expression levels for *Smed-cyclin-B* spatial distribution determined by whole-mount ISH (F) and gene expression levels determined by quantitative PCR (G) in both anterior and posterior regions. Reduction in *Smed-cyclin-B* ISH expression is indicated by red arrows. Gene expression levels are relative to the ubiquitously expressed clone *H.55.12e*. (H) Representative images of whole-mount immunostaining with BrdU and anti-H3P antibody. Green signal corresponds to BrdU incorporated after an 8-10 h pulse, red signal represents cells undergoing mitoses and orange signal represents co-expression in both control and *Rad51(RNAi)* animals. (I) Quantification of cells that incorporated BrdU along the anteroposterior axis. (J) Percentage of cells double-positive (co-expressing) for BrdU and H3P along the anteroposterior axis. In B,D,G,I,J values represent mean±s.e.m. of at least two to three biological replicates and each condition was processed with 10-20 animals per experiment. $^{**}P<0.005$, $^{***}P<0.0005$, $^{****}P<0.0001$; NS, no significance; two-way ANOVA. Scale bars: 200 µm.

Development (2016) 143, 1697-1709 doi:10.1242/dev.131318

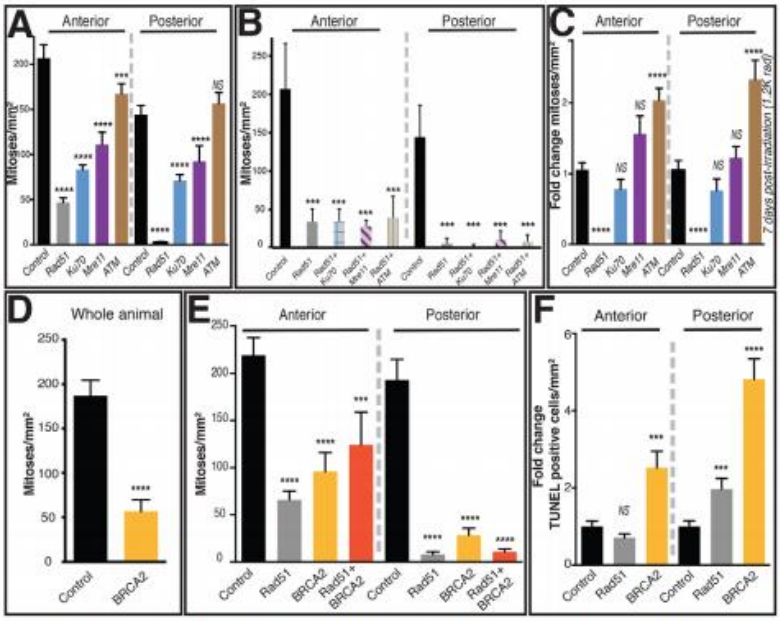

Fig. 4. Homologous recombination and non-homologous end joining (NHEJ) regulate cell division in planarians. (A,B) Levels of mitoses along the anteroposterior axis after individual or simultaneous downregulation of molecules associated with homologous recombination (*Rad51*) and NHEJ (*Ku70*, *Mre11*, *ATM*). (C) Mitotic activity seven days after sublethal doses of gamma irradiation (1200 rad) on animals subjected to downregulation of molecules associated with homologous recombination and NHEJ. Notice *Rad51(RNAi)* sub-lethally irradiated animals fail to recover mitotic activity. (D-F) Mitotic levels after downregulation of BRCA2, a component of homologous recombination, resembles the *Rad51(RNAi)* phenotype, including increased cell death in the posterior region (F). In A-F, all analyses were performed on intact animals ~30 days after first dsRNA and graphs represents mean±s.e.m. of at least two biological replicates with $n>10$ animals in each experiment. ***$P<0.0005$, ****$P<0.0001$; NS, not significant; Tukey's multiple comparison test.

Alvarado, 2010) reproduced the Rad51 phenotype (Fig. 4D,E). This demonstrates both components of the homologous recombination pathway reduce cell proliferation and alter patterns of cell death along the anteroposterior axis (Fig. 4D-F). Taken together, these data suggest that in *S. mediterranea* homologous recombination is the main pathway to: (1) repair DNA after ionizing irradiation and (2) maintain genomic integrity along the anteroposterior axis.

The retinoblastoma pathway mediates cell cycle progression in the presence of DSBs

The anterior region of *Rad51(RNAi)* animals displayed extensive DNA damage and unexpectedly low levels of cell death compared with controls (Figs 2, 3). This is a consistent feature observed in cells with genomic instability that resist undergoing cell death. The establishment and maintenance of cell survival in the presence of DNA damage converge into two pathways controlled by the tumor suppressors p53 and retinoblastoma (Rb) (Campisi, 2005). To assess mechanisms controlling cell fate decisions upon DNA damage, we optimized an RNAi strategy to simultaneously downregulate p53, Rb and Rad51 (Fig. S6), and evaluated cell division along the planarian anteroposterior axis (Fig. 5A,B). In order to downregulate these genes, all of which are required for neoblast maintenance, we developed a dsRNA injection schedule that avoided the depletion of mitotic activity before fixation. Specifically, two variables were considered: (1) the time of mitotic depletion after the first dsRNA injection of each individual gene (i.e.: *Rad51*>40 days; *Rb*>20 days and *p53*>30 days) and (2) the pattern in which mitotic activity vanishes along the anteroposterior axis upon RNAi treatment. For example, mitotic activity progressively diminished from the posterior to the anterior region after injection with *Rad51-RNAi*, whereas *Rb*- and *p53-RNAi*-depleted mitotic activity started in the anterior region, progressing to the posterior region. Therefore, dsRNA injections involving Rb started at day 17 after the initiation of *Rad51(RNAi)* treatment so that by the day of fixation, the Rb phenotype was 13 days after the first injection and still contained dividing cells (Fig. 5A,B).

The tumor suppressor p53 is a crucial downstream component of the DNA damage response (DDR) (Halazonetis et al., 2008). Double RNAi knockdown of p53 and Rad51 resulted in a noticeable increase in mitoses in both anterior and posterior regions when compared with *Rad51(RNAi)* alone. *p53(RNAi)* restricts cell division over time, which is consistent with its role in neoblast maintenance (Pearson and Sanchez Alvarado, 2010). Nonetheless, dividing cells were still present in both the anterior and posterior regions when p53 RNAi knockdown was done individually or combined with knockdown of Rad51 or Rb (Fig. 5A,B). This finding indicates that p53 restricts mitosis in the Rad51 phenotype and confirms that its functions in DDR are

Development (2016) 143, 1697-1709 doi:10.1242/dev.131318

A Percentage of cell division

CONDITION	ANTERIOR	POSTERIOR
Control	100 ± 11.7	100 ± 12.3
Rad51	11.2 ± 4.8****	0.7 ± 0.5****
p53	246 ± 25.4****	176.4 ± 27.9**
Rb	25.4 ± 7.2****	82 ± 18.24NS
p53 + Rb	55.9 ± 9.6**	88.7 ± 5.1NS
Rad51 + p53	33.2 ± 5.6****	11.9 ± 3.6****
Rad51 + Rb	6 ± 3.3****	0.4 ± 0.4****
Rad51 + p53 + Rb	3.5 ± 2.3****	1.1 ± 0.7****

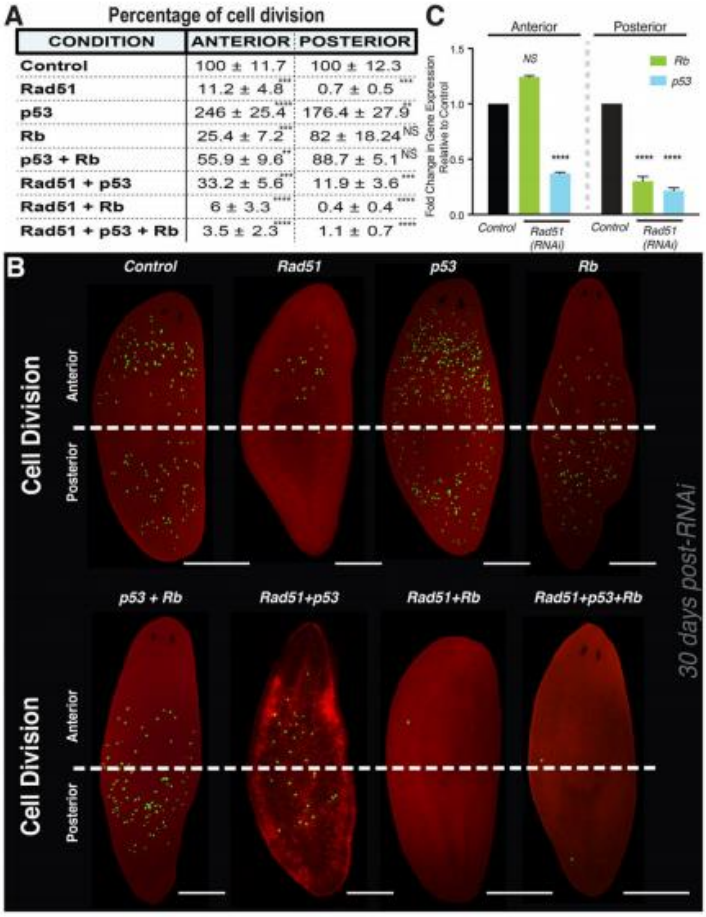

Fig. 5. The retinoblastoma (Rb) pathway mediates cell division after *Rad51(RNAi)*. (A) Percentage of cell division in anterior and posterior regions in single, double and triple RNAi treatment involving *Rad51* and the tumor suppressors *p53* and retinoblastoma (*Rb*). Simultaneous RNAi knockdown of *Rad51* and *Rb* abolish cell division in both anterior and posterior regions. (B) Representative whole-mount immunostaining images with the mitotic marker anti-H3P (green dots). Simultaneous downregulation of *p53* and *Rb* tends to concentrate cell division towards the posterior region of the animal as does *Rb(RNAi)* alone. However, *Rad51(RNAi)+Rb(RNAi)* largely reduces cell division throughout the body, even when *p53* is downregulated in triple RNAi. Each image consists of multiple focal planes stacked together to represent the entire animal (*z*-axis). Scale bars: 200 µm. (C) qPCR analysis from anterior and posterior regions to determine fold-change in *Rb* and *p53* gene expression levels in *Rad51(RNAi)* relative to control. Gene expression values were calculated relative to the ubiquitously expressed clone *H.55.12e*. In A,C, all data represent mean±s.e.m. of at least three biological replicates consisting of 10-20 animals per experiment. ****P<0.0001; NS, not significant; two-way ANOVA.

conserved in planarians (Pearson and Sanchez Alvarado, 2010). Increased mitotic activity in animals subjected to double p53 +Rad51 RNAi revealed cells with the potential to divide in spite of a dysfunctional homologous recombination and further established that cell division in *Rad51(RNAi)* animals occurs independently of p53. However, double Rad51+Rb RNAi knockdown abrogated cell division even when p53 was downregulated, implying that Rb is required for cell cycle progression to G2/M phase in *Rad51(RNAi)* animals (Fig. 5A,B). Interestingly, *Rad51(RNAi)* induced a strong downregulation of p53 throughout the animal accompanied by selective suppression of Rb expression in the posterior region, whereas its levels in the anterior remained stable despite high levels of DNA damage (Fig. 5C). It is possible that p53 downregulation results from the elimination of cells that are more susceptible to loss of Rad51 function, but further experiments are required to test this hypothesis. Posterior-specific levels of cell death in *Rad51(RNAi)* animals might result from the simultaneous downregulation of both p53 and Rb, which has been implicated as a driver of apoptosis in human embryonic stem cells (Conklin et al., 2012). Conversely, the presence of DNA damage and resistance to apoptosis have been suggested as an Rb-mediated mechanism of some tumor cells in response to chemotherapy (Ianari et al., 2009). Thus, it is possible that sustained levels of Rb expression in the anterior region promotes cellular survival, but more importantly, enables the proliferation of cells with damaged DNA. Future experiments assaying Rb phosphorylation as well as the activation and/or repression of components of the Rb regulatory network might lead to insights on Rb-mediated cell fate in the presence of DNA damage in adult stem cells (Sage, 2012). Taken together, our findings suggest that in the presence of genomic instability, the Rb pathway might modulate cellular fate decisions asymmetrically throughout the adult body. Similarly, these results also suggest that non-cell autonomous mechanisms operate along the anteroposterior axis to regulate Rb function.

Development (2016) 143, 1697-1709 doi:10.1242/dev.131318

Tissue-specific signals from the nervous system influence cellular behavior along the anteroposterior axis

The Rad51 phenotype is characterized by the survival of cells with DSBs in the anterior half of the animal. To address whether asymmetric cell behavior is influenced by tissue-specific signals, we produced animals with bipolar heads or tails resulting from perturbation of Wnt signaling (Reddien, 2011) (Fig. S7A-C). Furthermore, we downregulated Rad51 expression in these animals to assess levels of cell division and cell death (Fig. 6A-C). Double-headed planarians are organisms constituted by tissue from the anterior region, lacking posteriorized tissue. Double-headed animals subjected to *Rad51(RNAi)* displayed a reduction in both mitoses and cell death, and cell division was dispersed throughout the anteriorized body (Fig. 6A,B). Conversely, *Rad51(RNAi)* in double-tailed planarians (i.e. organisms lacking anterior tissue) led to a dramatic decrease of mitotic cells, accompanied by an increase in cell death (Fig. 6A,C), which was proportional to the levels of cell death found in the posterior region of *Rad51(RNAi)* animals with normal anteroposterior polarity (Fig. 3D). These results suggest tissue-specific signals in the anterior region promote cell survival in *Rad51(RNAi)* animals.

The planarian brain is located in the anterior part of the animal and occupies most of the head region (Fig. S7A). Therefore, we tested whether the presence of brain tissue might influence the proliferation of cells with DNA damage in Rad51-deficient animals. Double-tailed animals are completely posteriorized and do not possess brain-specific tissue. Thus, we ectopically induced brain formation in these organisms by disrupting the fibroblast growth factor receptor-like molecule gene *nou-darake* (*ndk*) (Iglesias et al., 2011). Double-tailed animals with ectopic brain were subjected to *Rad51(RNAi)* and evaluated for levels of cell division. We observed that the number of dividing cells increased but only in the proximity of ectopic brain tissue. Other parts of the animal that retained tail identity (i.e. devoid of brain) displayed lower levels of cellular proliferation (Fig. 6D,E; Fig. S7D,E). These results suggest: (1) the presence of anterior-specific nervous tissue in a posteriorized environment is capable of altering cell fate decisions to promote proliferation of cells with DNA damage, and (2) the central nervous system, specifically the brain, acts as a regional regulator of cell behavior in the adult planarian. The specific mechanisms need to be further investigated, but our findings suggest that non-cell autonomous signals from the cellular microenvironment might influence cell division in *Rad51(RNAi)* animals.

Cells with DNA damage overproliferate in the presence of nutrients and tissue repair demands

We sought to better understand the influence of the microenvironment on the mitotic response after *Rad51(RNAi)* treatment. Neoblasts are known to mount stereotypical waves of proliferation in response to feeding and injury (Kang and Sanchez Alvarado, 2009; Wenemoser and Reddien, 2010). Therefore, we assessed whether mitotic activity in *Rad51(RNAi)* animals could be altered by an increase in the availability of nutrients and the demands of tissue repair. Feeding triggers an increase in neoblast mitotic activity that is detected as early as 6 h post-feeding and is expected to return to pre-feeding levels by 72 h post-feeding. We found that 6 h post-feeding, cell division in *Rad51(RNAi)* animals increased ~fivefold in both the anterior and posterior regions. However, the increase in neoblast division did not return to pre-feeding levels by 72 h post-feeding (Fig. 7A), but it was sustained and also triggered animal death >35 days post-RNAi treatment (20/20 animals, data not shown). Lethality was preceded by loss of tissue in the anterior tip of the animal, also known as 'head regression', which is characteristic of dysfunctional neoblasts and a lack of cellular turnover (Reddien et al., 2005b).

To evaluate the mitotic response upon injury, we analyzed: (1) regenerating trunk fragments after the removal of anterior and posterior tissues, and (2) tissue transplantation and the engraftment process. Amputation triggers two waves of mitotic activity (at ~6 h and 48 h post-amputation) that are followed by cellular differentiation and formation of the regenerative blastema (Wenemoser and Reddien, 2010). Amputation of *Rad51(RNAi)* animals triggered a neoblast mitotic peak after 6 h post-amputation, which returned to pre-injury levels after 30 h. However, seven days post-amputation, levels of cell division were unexpectedly high in the absence of a regenerative blastema (Fig. 7B). The increase in cell division at seven days post-amputation and the absence of a blastema suggests that in *Rad51 (RNAi)* animals, neoblasts are unable to properly regulate cell division and their division progeny is incompetent to support post-mitotic events associated with tissue regeneration.

Tissue transplantation experiments were designed to assess the mitotic response during engraftment of tissue plugs into an orthotopic (similar) region of a host animal (Fig. 7C). This procedure allowed us to evaluate injury-induced mitotic response during tissue engraftment and regulation of cell division in the entire host animal without the formation of a regenerative blastema. We transplanted tissue plugs from both RNAi and control donors and evaluated cell division within both the host animal and within the transplanted tissue plug itself (experimental scheme is illustrated in Fig. 7C). A tissue plug from the anterior region of a donor animal was transplanted to the anterior region of a host animal. Both control and *Rad51(RNAi)* animals served as either a tissue plug donor and/or engraftment host. In all cases, levels of cell division were analyzed one week post-transplantation, at which point they would be expected to rebound to levels of uninjured animals (Fig. 7C-G).

To evaluate whether mitotic activity in the host animal returns to pre-injury levels, we first transplanted tissue plugs from the anterior donor region into the anterior region of the host (Fig. 7C). The mitotic response was quantified within the host animal excluding the transplanted tissue (i.e. outside the transplant; Fig. 7D,E). We found that tissue plugs from control donors re-established cell division in the *Rad51(RNAi)* hosts and after one week post-transplantation, levels of cell division were comparable with the control group. This suggests that transplanted cells from the donor control were able to regulate mitotic activity after engraftment in a homologous recombination-deficient host (Fig. 7E). Conversely, transplantation of *Rad51(RNAi)* donor tissue into either control or *Rad51(RNAi)* hosts elicited hyperproliferation throughout the animal (Fig. 7E; Fig. S8). These results suggest that neoblasts from *Rad51 (RNAi)* donors sense and respond to injury but are unable to regulate levels of proliferation after the completion of tissue engraftment, which is consistent with the increase of neoblast proliferation during blastema-mediated tissue regeneration (Fig. 7B).

Furthermore, we evaluated the source of abnormally proliferating cells by quantifying mitoses exclusively inside the transplanted donor plugs (i.e. excluding cellular proliferation in the rest of the host animal; Fig. 7F,G). As expected, levels of cell division in tissue plugs from control donors reverted back to the levels of uninjured animals (i.e. ~150-200 mitoses/mm^2). However, cell division within the *Rad51(RNAi)* donor plug increased 16-fold in comparison with uninjured *Rad51(RNAi)* animals (Fig. 3B, Fig. 7G). To assess if this response is specific to homologous recombination deficiency, we also engrafted tissue plugs from NHEJ-deficient donors [*Smed-Ku70(RNAi)*] into control hosts. Mitotic activity inside the transplanted tissue plug and within the

Development (2016) 143, 1697-1709 doi:10.1242/dev.131318

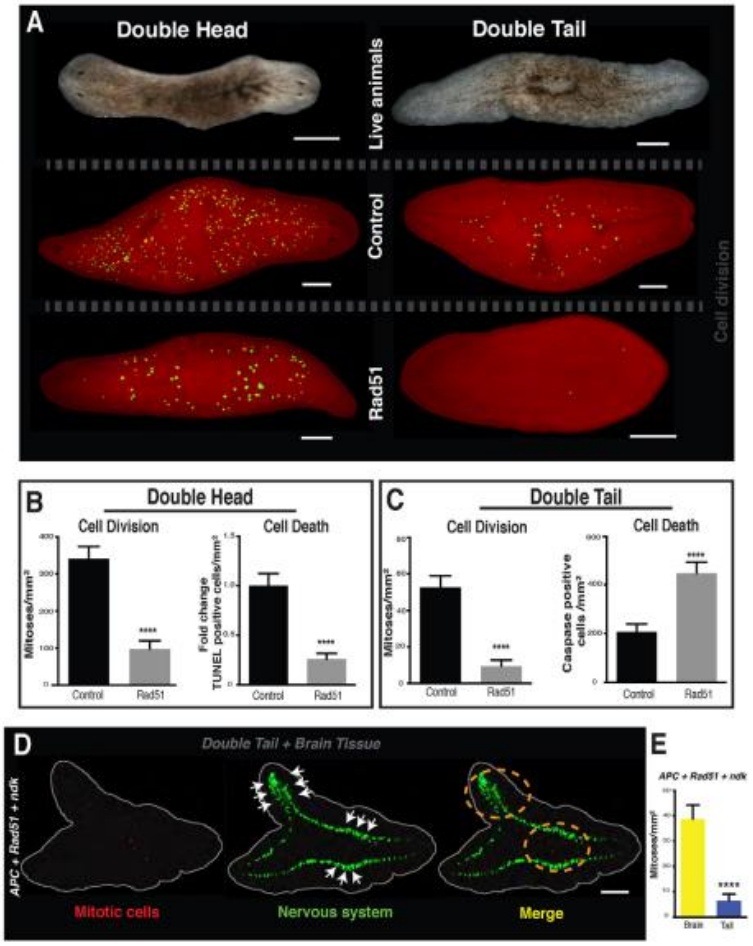

Fig. 6. Anterior-specific nervous tissue modulates cell division in posteriorized animals. (A) Downregulation of *beta-catenin* and *APC* lead to animals with bipolar heads or tails, respectively. The spatial distribution of mitotic cells (yellow dots) labelled with anti-H3P antibody is shown. (B,C) Quantification of mitoses (left) and levels of cell death (right) in double-headed (B) and double-tailed (C) animals treated with *Rad51(RNAi)*. (D,E) Cell division levels in double-tailed animals subjected to double RNAi with *nou-darake* and *Rad51* knockdown. Brain tissue (arrows) and ventral nerve cords were labeled with anti-synapsin staining (green signal). The dotted orange line illustrates an area contiguous to the ectopic brain, including mitotic cells (red dots). Brain tissue was identified by visual thickening of the ventral nerve cords. Scale bars: 200 µm. In B,C,E, data represent mean±s.e.m. of at least three biological replicates with *n*>5-10 animals per experiment. ****P<0.0001 one-way ANOVA.

host was similar to that of the control group after one week post-transplantation (data not shown). These results imply that neoblast hyperproliferation upon injury and/or engraftment is not a result of off-target RNAi effects, but is a specific feature of homologous recombination-deficient cells. Taken together, our findings confirm that in the presence of injury, neoblasts from *Rad51(RNAi)* animals intensify their proliferation capabilities, probably through cell-autonomous mechanisms, but are unable to return to uninjured levels once tissue repair is completed. We also demonstrate that despite high levels of DNA damage, neoblasts sense environmental cues triggered by metabolic and tissue repair signals that override cellular fate decisions imposed by DNA damage (Fig. 7A,B).

We hypothesize that the hyperproliferative state of these cells could be triggered by a defective response that circumvents a block in cell cycle progression in favor of tissue renewal and repair (Bartkova et al., 2006). Moreover, gene expression analysis revealed that markers of the zeta class of neoblasts (van Wolfswinkel et al., 2014) were the least downregulated in the anterior part of *Rad51(RNAi)* animals,

Development (2016) 143, 1697-1709 doi:10.1242/dev.131318

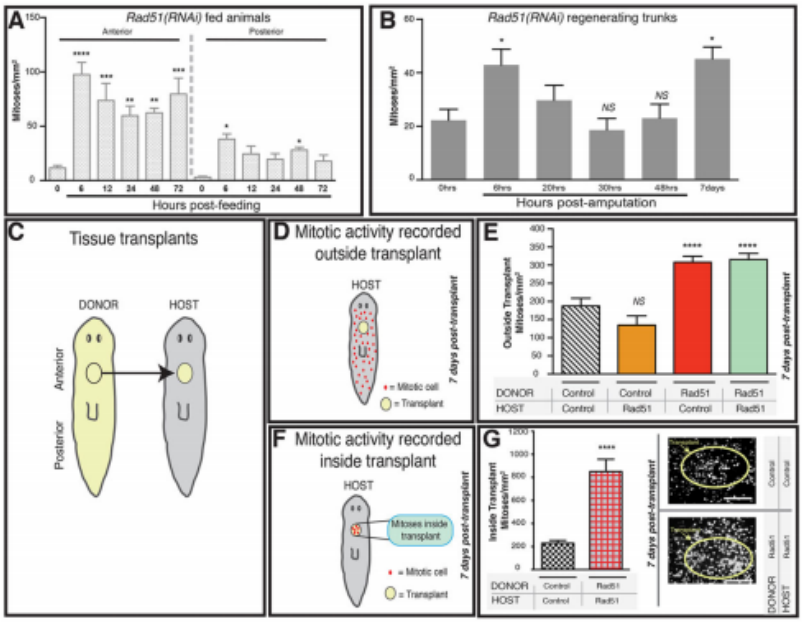

Fig. 7. Metabolic signals and demands for tissue repair trigger neoblast hyperproliferation. (A,B) Mitotic activity increases 6 h after feeding (A) or amputation (B) in *Rad51(RNAi)* animals. Mitotic cells were recorded in both anterior and posterior regions after feeding, whereas in amputated animals the overall number of cells was obtained from regenerating trunk fragments. (C) Schematic representation of tissue plug transplants from the anterior region of donor animals into host animals (arrow). (D) Schematic representation to evaluate mitotic activity (red dots) in the host animal excluding the transplanted tissue plug (yellow circle). (E) Levels of mitotic activity outside of the transplanted plug. Control and *Rad51(RNAi)* animals serve as either tissue plug donor and/or engraftment host. Notice the increased cell division when donor tissue comes from *Rad51(RNAi)* animals. (F) Donor tissue from the anterior region was transplanted into an orthotopic region in host animals and was used to determine levels of cell division inside the transplant. (G) Quantification of mitotic activity inside the transplanted plug, one week after engraftment (left panel). Representative pictures showing mitotic activity inside the transplant (right panel; yellow circles represent the transplant border). Mitotic activity was recorded 7 days after transplantation, when they are expected to be back to levels of uninjured animals. Scale bar: 250 µm. In A,B,E,G, data represent mean±s.e.m. of at least three biological replicates with n>5-10 animals per time point. *P<0.01, **P<0.005, ***P<0.0005. ****P<0.0001; NS, not significant; Tukey's multiple comparison test.

suggesting the phenotype is not homogeneously distributed among neoblast subpopulations (Fig. S9). However, additional experiments are required to rule out whether the hyperproliferative state in *Rad51 (RNAi)* animals is related to a particular neoblast subpopulation. Additional experiments on the Rad51 phenotype in *S. mediterranea* would facilitate the identification and characterization of molecular mechanisms mediating cell division in the presence of DNA damage (Campisi, 2005).

Concluding remarks

The DNA damage response is a potent regulator of cellular behavior that influences decisions about proliferation and apoptosis (Halazonetis et al., 2008; Lord and Ashworth, 2012). The Rad51 phenotype establishes a predictable model where cells with genomic instability undergo collective elimination by apoptosis, alter cell cycle patterns, or bypass surveillance mechanisms to divide and even hyperproliferate. Our results indicate that both cellular location along the anteroposterior axis (non-autonomous) and intrinsic cellular (cell-autonomous) properties modulate cellular fate choices in the presence of DNA damage.

Injury-induced cell proliferation is still activated after downregulation of Rad51, but subsequent mechanisms regulating proliferation fail to return or maintain basal mitotic levels (i.e. cell division to support homeostatic tissue renewal). Consequently, cells with damaged DNA divide abnormally following both cell autonomous and non-autonomous cues. Our results present novel insights into the effects of system-wide Rad51 downregulation in adult tissue maintenance. Thus, we anticipate that further research in the Rad51 phenotype in *S. mediterranea* would facilitate opportunities to analyze *in situ* DNA damage-induced tumor suppression, mechanisms regulating proliferation of cells with genomic instability, and the provocative idea of nervous signals controlling tumor suppressor regulatory networks in specific regions of the adult body.

MATERIALS AND METHODS

Identification of homologs and phylogenetic analysis

Components of the DNA repair and other signaling pathways were identified using the *S. mediterranea* genome database SmedGD (http://smedgd.stowers.org) and other planarian genomic resources (Adamidi et al.,

Development (2016) 143, 1697-1709 doi:10.1242/dev.131318

2011; Labbe et al., 2012; Robb et al., 2008; Sandmann et al., 2011; Zhu and Pearson, 2013). NCBI accession numbers KT375434 (*Smed-ku70*), KT375435 (*Smed-BRCA2*), KT375436 (*Smed-Mre11*) and SmedGD references mk4.001927.02.01, mk4.001165.06.01 (SmedGD v.3.1) are linked to sequences reported in the manuscript. Identified sequences were translated using the Pfam protein domain families database (http://pfam.xfam.org/) and subsequently analyzed using HMMER search to confirm conservation (https://www.ebi.ac.uk/Tools/hmmer/). The sequences were further confirmed by Blastn, blastx, blastp and alignment tools (http://blast.ncbi.nlm.nih.gov/Blast.cgi). The identified sequences were aligned by CLUSTALW or T-Coffee software with sequences obtained using HomoloGene (http://www.ncbi.nlm.nih.gov/homologene). A predictive evolutionary model and phylogenetic tree was built using MEGA software (www.megasoftware.net).

Planarian culture

The planarian species used in these experiments was *Schmidtea mediterranea* CIW4. *S. mediterranea* culture was maintained as previously described (Oviedo et al., 2008a).

RNAi experiments

The synthesis of dsRNA was performed *in vitro* followed by microinjections as previously described (Oviedo and Levin, 2007; Oviedo et al., 2008b). A total of five microinjections over four weeks were initially administered over three consecutive days and then one every 10 days. Alternatively, *in vitro* synthesized dsRNA was also administered by feeding to functionally disrupt genes by RNAi as described (Rouhana et al., 2013). Briefly, 1 µg of the *Smed-Rad51*-specific dsRNA was mixed with 30 µl of planaria food and was fed 3× times per week for 30 days. Although RNAi by feeding or microinjection in different areas of the body both efficiently reduced Rad51 expression, the experiments presented throughout the manuscript involved dsRNA microinjections in the anterior area unless otherwise noted. Under this protocol 100% of the animals showed the phenotype between 20-30 days after first dsRNA microinjection. All analyses were carried out a minimum of four days after the last microinjection. To produce animals with double head or tails, planaria were fed bacteria with engineered vectors as previously described (Reddien et al., 2005a). Briefly, downregulation of APC and β-catenin by RNAi was performed using 4-6 feedings before amputation. After 14 days of regeneration bipolar headed/tailed animals were injected with the desired dsRNA as described in Fig. S10. Dr C. Petersen (Northwestern University, Evanston, IL, USA) and Dr P. Reddien (MIT, Cambridge, MA, USA) kindly provided β-catenin and APC plasmids. Double and triple RNAi experiments were analyzed 30 days after the first *Rad51* dsRNA microinjection as shown in Fig. S10.

Whole-mount immunofluorescence

Planarians were fixed and immunostained as previously described (Peiris et al., 2012). The following primary antibodies were used: anti-H3p (1:250; Millipore, 05-817R), anti-synapsin (1:100; Developmental Studies Hybridoma Bank) and anti-activated caspase-3 (1:500; Abcam, ab13847). Secondary antibodies were: goat anti-mouse Alexa Fluor 488 (1:800; Invitrogen, 673781) for anti-synapsin, anti-arrestin, anti-acetylated tubulin, goat anti-rabbit Alexa Fluor 568 (1:800; Invitrogen, 11036) for anti-H3P, HRP-conjugated goat anti-rabbit antibody (1:2000; Millipore, 12-348) with TSA-Alexa Fluor 488 anti-HRP (ThermoFisher, A-21370) for anti-caspase-3. All images were visualized and the mitotic cells (H3P-positive) and apoptotic cells (caspase-positive) were counted and normalized to the area (mm^2) using NIS element software (Nikon).

BrdU staining

BrdU staining was performed as previously described (Cowles et al., 2012). Double staining with H3P and BrdU was performed as previously described (Newmark and Sanchez Alvarado, 2000).

Sub-cloning of candidate genes

Our sub-cloning strategy was similar to that previously described (Peiris et al., 2012). Briefly, sets of primers were designed to amplify a 400-650 bp region of each candidate gene. Total RNA from asexual *S. mediterranea* was used to synthesize cDNA using Thermo Scientific Verso cDNA kit. The amplified regions were cloned and transformed following the manufacturer's instructions (Qiagen). PCR products were used to synthesize dsRNA or ISH probes as previously described (Oviedo et al., 2008b; Peiris et al., 2012). Primers sequences are listed in Table S1.

Planaria dissociation and cell collection

Planarians were dissociated as previously described with slight modifications (Hayashi et al., 2006; Peiris et al., 2016; Reddien et al., 2005b). Planarians were amputated into small pieces in cold calcium/magnesium-free (CMF) medium and then placed on a rocker for 30 min to 1 h at 4°C. Cells were filtered using a 20 µm filter and centrifuged at 239 ***g*** followed by resuspension in 1 ml of CMF media before cell counting (Peiris et al., 2016).

Fixation and immunostaining of dissociated cells

Fixation and staining protocol were as previously described (Oviedo and Levin, 2007; Peiris et al., 2012). Dissociated cells were washed twice with 1× PBS and then fixed onto cover slips using Carnoy's fixation for 2 h on ice, incubated with 100% methanol for 1 h at −20°C. Samples were rehydrated using mixtures of 75%, 50% and 25% methanol in PBSTx (1×PBS+0.3% Triton X-100). After final rehydration with 100% PBSTx, the cells were blocked in PBSTB [1×PBS+0.3% Triton X-100 containing 0.25% bovine albumin serum (BSA)] for 4 h at room temperature and primary anti-Rad51 (1:500; Abcam, ab109107) antibody added overnight. Cells were then washed six times, 10 min each in PBSTB and then stained with HRP-conjugated goat anti-rabbit secondary antibody (1:500; Millipore, 12-348) overnight. Cells were then washed again, and incubated with 1:1000 TSA-Alexa Fluor 488 in PBSTI (PBST×+10 mM imidazole) for 20 min, followed by a further six 10 min washes in PBSTB. After the final wash, cells were incubated with DAPI (0.1 µg/1 ml) for 15 min and mounted using VECTASHIELD Mounting Medium (Vector Laboratories). Additional details can be found in our previous publication (Oviedo and Levin, 2007; Peiris et al., 2012).

Protein extraction

Animals were dissociated until no tissue fragments were visible and incubated in 1× RIPA buffer (Cell Signaling Technologies, 9806) with protease inhibitors (Roche Complete Mini Protease Inhibitor Cocktail, 04693124001; 1 mM PMSF; 1 mM DTT) for 30 min on ice. Volume-to-mass ratio for this was as follows: 10 large dissociated planaria were incubated in 300 µl of 1× RIPA and protease cocktail mixture. Samples were spun at 20,817 ***g*** for 15 min at 4°C. The supernatant was transferred to a new tube and immediately placed on ice. A 25 µl aliquot of the supernatant was used to measure protein concentration. The remaining solution was mixed with equal volumes of 2× Laemmli buffer (4% SDS, 10% 2-mercaptoethanol, 20% glycerol, 0.004% bromophenol blue, 0.125 M Tris-HCl) and incubated at 95°C for 5 min (or boiled at 100°C) to denature and reduce. Protein lysates were stored at −20°C. A Bio-Rad protein assay was used to determine protein concentration.

Western blot

Protein lysate aliquots of 40 µg were heated at 80°C for 5 min and loaded in 12.5-15% SDS-PAGE gel along with a molecular weight marker (Bio-Rad, 1610375). Samples were transferred to a 30 s methanol-activated PVDF membrane (Bio-Rad, 162-0175) overnight in 1× Tris-glycine transfer buffer [25 mM Tris base, 192 mM glycine, 10% (v/v) methanol, pH 8.3] at 4°C. The membrane was blocked with 5% milk for 1 h and incubated in the primary antibodies overnight at 4°C on a rocker. Primary antibodies: anti-tubulin (1:500; Sigma, 081M4861), anti-Rad51 (1:5000; Abcam, ab109107) and anti-caspase (1:5000; Abcam, ab13847). The membrane was washed three times for 30 min prior to the addition of the secondary antibodies: HRP-conjugated goat anti-rabbit antibody (1:2000; Millipore, 12-348) for anti-Rad51 and anti-caspase, HRP-conjugated goat anti-mouse antibody (1:2000; Invitrogen, G21040) for anti-tubulin. The membrane was washed three times for 30 min and developed using Luminata Forte Western HRP substrate (Millipore, WBLUF0100).

Development (2016) 143, 1697-1709 doi:10.1242/dev.131318

Flow cytometry analysis

Flow cytometry experiments were performed as previously described (Hayashi et al., 2006; Peiris et al., 2016, 2012). Briefly, 1×10^6 cells from dissociated planaria were stained with DNA marker Draq5 (eBioscience, 65-0880-96) at a 1:500 dilution in CMF media for 30 min at room temperature in the dark. Incubation with calcein (Invitrogen, C3100MP) diluted 1:500 in CMF medium for 10 min at room temperature was sufficient to stain live cells. BD FACSDiva software was used for initial gating and samples were either analyzed using a LSRII flow cytometer (BD Biosciences) or sorted using an ARIAII flow cytometer (BD Biosciences). Lethally irradiated planaria were used to approximate the gates for X1 and X2 populations and/or gated as previously described (Eissenhoffer et al., 2008). Final gating of cell populations was performed using FlowJo software (www.flowjo.com) (Peiris et al., 2016).

Cell cycle analysis was performed using either Draq5 (1:500 diluted in CMF media) or DAPI (0.1 µg/ml). Draq5-stained populations were gated for cell cycle using live Draq5-positive populations and FlowJo software. Staining of apoptotic cells was performed using 1×10^5 cells from dissociated planaria immersed in 100 µl binding buffer (BioLegend, 422201) and stained with 5 µl Annexin V (Pacific Blue; BioLegend, 640918) and 5 µl 7-AAD Viability Staining Solution (PECy5; BioLegend, 420404). Labeled cells were incubated at room temperature for 15 min. The samples were immediately analyzed using an LSRII flow cytometer (BD Biosciences). Further details can be found in Peiris et al. (2016).

TUNEL assay

TUNEL assay was performed as previously described (Pellettieri et al., 2010).

Quantification of mitotic activity and image processing

Mitotic cells labeled with fluorescent anti-H3P were counted either manually or with NIS Elements (Nikon). Area measurements for the anterior and posterior regions in each sample were obtained with NIS Elements (Nikon). All fluorescence images consisted of multiple captions at different focal planes (z-axis) and stacked together into a single image to represent the whole animal. Cellular counts or fluorescence signal from images at different magnifications were corrected by area to determine the specific number/mm^2. The analysis of anterior and posterior regions was paired to its respective counterpart (i.e. control anterior versus experimental anterior; control posterior versus experimental posterior) and pooled numbers were plotted separately. Additional details on the procedure and image processing were as previously described (Peiris et al., 2012).

Quantitative RT-PCR

Quantitative RT-PCR (qPCR) was performed as previously described (Peiris et al., 2012). In all cases gene expression is relative to the ubiquitously expressed clone *H.55.12e*. Each individual experiment consisted of triplicates per condition and experiments were independently repeated at least twice. qPCR from sorted cells was obtained by dissociating >20 animals per condition to extract RNA and prepare cDNA as described before. qPCR from anterior and posterior regions was prepared from half body parts of more than 10 animals per condition. Gene expression up- or downregulation levels were also represented with heat maps in reference to the corresponding control. Gene expression corresponds to the mean of triplicated samples of at least two independent experiments with pooled RNA extraction of >20 animals each.

In situ hybridization (ISH)

ISH on isolated cells and quantification were performed as previously described (Oviedo and Levin, 2007; Oviedo et al., 2008c). Whole-mount ISH (WISH) and fluorescent *in situ* hybridization were performed as previously described (Pearson et al., 2009).

Comet assay

Dr Dave Alexander and Dr Manel Camps from University of California Santa Cruz kindly provided the comet assay protocol and Elyse Ozamoto (University of California, Merced, USA) performed the initial adaptations to the planarian model. Frosted microscope slides were coated with 1% normal melting point agarose (NMPA) in 10× PBS and dried overnight. Dissociated cells were resuspended in 10 ml CMF followed by incubation at 37°C for 2 hours. Cells were centrifuged at 664 ***g*** for 2 min and resuspended in 100 µl of 0.5% low melting point agarose (LMPA) made in 10× PBS per 50,000 cells. The mixture was loaded onto coated 1% NMPA dried slides and allowed to dry at 4°C until the agarose solidified. Slides were incubated overnight in a Coplin jar at 4°C with 89% lysing solution (2.5 M NaCl, 100 mM EDTA, 10 mM Trizma base, 8 g pelletized NaOH in dH_2O; filtered and pH 10.0), 10% DMSO and 1% Triton X-100. Medium was then replaced with neutralization buffer (0.4 M Tris base in dH_2O, pH to 7.5) for 5 min and kept at 4°C. The neutralization buffer was then removed and slides were placed into an electrophoresis chamber at 4°C filled with 1× electrophoresis buffer (10 N NaOH and 200 mM EDTA in dH_2O, pH 13) and the sample was allowed to equilibrate for 15 min. The current was adjusted to 12 V for 30 min at 4°C. Next, slides were transferred back into the Coplin jar and equilibrated for 5 min in neutralization buffer. Samples were fixed with cold 100% ethanol for 5 min and stained with a 1:10 ratio of SYBR gold into 1× TE buffer (10 mM Tris-HCl and 1 mM EDTA, pH 7.5). A standard 'DNA damage scale' was built as reference based on different doses of gamma irradiation on whole worms. The scoring scheme is based on a rank from 0 to 2, where a score of 0 showed little DNA damage and 2 is visualized as a disbursed tail, indicating extensive DNA damage (Sinha et al., 2014).

Karyotyping assay and tissue transplantation experiments

Karyotyping and tissue transplants were performed as previously described (Guedelhoefer and Sanchez Alvarado, 2012). The worms for transplantation experiments were grown at 10°C to obtain larger animals more amenable for transplantation. Similar sizes of the transplanted tissue and the opening in the host animals were obtained by using the tip of 10 µl pipettes. Animals that served as donors or hosts were used after 30 days of the first dsRNA microinjection.

Statistical analysis

Data are expressed as mean±s.e.m. unless otherwise noted. The statistical analyses were performed in Prism, GraphPad Software (http://www.graphpad.com).

Acknowledgements

We thank Edelweiss Pfister for technical assistance, members of the planarian community for reagents, and Drs Manel Camps and David Alexander for advice with comet assay. N.J.O. also thanks Drs Julien Sage, Aaron Hemday, Ramen Saha, Kirk Jensen, Jennifer Manilay, Michael Cleary, Michael Umer, and members of the Oviedo Lab for comments on the manuscript.

Competing interests

The authors declare no competing or financial interests.

Author contributions

T.H.P., D.R., P.G.B., U.O., D.D., F.W. and N.J.O. performed the research and analyzed data. N.J.O. conceived the project and wrote the manuscript with P.G.B. All authors read the manuscript and provided comments.

Funding

We acknowledge support from University of California Merced, University of California Cancer Research Coordinating Committee, Health Sciences Research Institute at University of California, Merced and awards from Jane Vilas and the Hellman Fellows Fund. This research was supported by the National Cancer Institute and National Institute of General Medical Sciences of the National Institutes of Health [CA176114 and GM109372 to N.J.O.]. Deposited in PMC for release after 12 months.

Supplementary information

Supplementary information available online at
http://dev.biologists.org/lookup/suppl/doi:10.1242/dev.131318/-/DC1

References

Adamidi, C., Wang, Y., Gruen, D., Mastrobuoni, G., You, X., Tolle, D., Dodt, M., Mackowiak, S. D., Gogol-Doering, A., Oenal, P. et al. (2011). De novo assembly and validation of planaria transcriptome by massive parallel sequencing and shotgun proteomics. *Genome Res.* **21**, 1193-1200.

Auerbach, R. and Auerbach, W. (1982). Regional differences in the growth of normal and neoplastic cells. *Science* **215**, 127-134.
Auerbach, R., Morrissey, L. W. and Sidky, Y. A. (1978). Regional differences in the incidence and growth of mouse tumors following intradermal or subcutaneous inoculation. *Cancer Res.* **38**, 1739-1744.
Baguñà, J. (1976). Mitosis in the intact and regenerating planarian *Dugesia mediterranea* n.sp. I. Mitotic studies during growth, feeding and starvation. *J. Exp. Zool.* **195**, 53-64.
Bartkova, J., Rezaei, N., Liontos, M., Karakaidos, P., Kletsas, D., Issaeva, N., Vassiliou, L.-V., Kolettas, E., Niforou, K., Zoumpourlis, V. C. et al. (2006). Oncogene-induced senescence is part of the tumorigenesis barrier imposed by DNA damage checkpoints. *Nature* **444**, 633-637.
Brøndsted, H. V. (1969). *Planarian Regeneration*, 1st edn. London: Pergamon Press.
Campisi, J. (2005). Senescent cells, tumor suppression, and organismal aging: good citizens, bad neighbors. *Cell* **120**, 513-522.
Chinone, A. and Matsumoto, M. (2014). DrRad51 is required for chiasmata formation in meiosis in planarian Dugesia ryukyuensis. *Mol. Reprod. Dev.* **81**, 409-421.
Conklin, J. F., Baker, J. and Sage, J. (2012). The RB family is required for the self-renewal and survival of human embryonic stem cells. *Nat. Commun.* **3**, 1244.
Cowles, M. W., Hubert, A. and Zayas, R. M. (2012). A Lissencephaly-1 homologue is essential for mitotic progression in the planarian *Schmidtea mediterranea*. *Dev. Dyn.* **241**, 901-910.
Dispersio, L. P. (1981). Regional growth differences of human tumor xenografts in nude mice. *Lab. Anim.* **15**, 179-180.
Eisenhoffer, G. T., Kang, H. Sánchez Alvarado, A., (2008). Molecular analysis of stem cells and their descendants during cell turnover and regeneration in the planarian Schmidtea mediterranea. *Cell Stem Cell* **11**, 327-339.
Guedelhoefer, O. C., IV and Sanchez Alvarado, A. (2012). Amputation induces stem cell mobilization to sites of injury during planarian regeneration. *Development* **139**, 3510-3520.
Halazonetis, T. D., Gorgoulis, V. G. and Bartek, J. (2008). An oncogene-induced DNA damage model for cancer development. *Science* **319**, 1352-1355.
Hayashi, T., Asami, M., Higuchi, S., Shibata, N. and Agata, K. (2006). Isolation of planarian X-ray-sensitive stem cells by fluorescence-activated cell sorting. *Dev. Growth Differ.* **48**, 371-380.
Ianari, A., Natale, T., Calo, E., Ferretti, E., Alesse, E., Screpanti, I., Haigis, K., Gulino, A. and Lees, J. A. (2009). Proapoptotic function of the retinoblastoma tumor suppressor protein. *Cancer Cell* **15**, 184-194.
Iglesias, M., Almuedo-Castillo, M., Aboobaker, A. A. and Saló, E. (2011). Early planarian brain regeneration is independent of blastema polarity mediated by the Wnt/beta-catenin pathway. *Dev. Biol.* **358**, 68-78.
Kang, H. and Sanchez Alvarado, A. (2009). Flow cytometry methods for the study of cell-cycle parameters of planarian stem cells. *Dev. Dyn.* **238**, 1111-1117.
Klein, H. L. (2008). The consequences of Rad51 overexpression for normal and tumor cells. *DNA Repair* **7**, 686-693.
Kobayashi, K. (1977). Effects of whole-body and partial-body X irradiation upon epidermal mitotic activity during wound healing in mouse skin. *Radiat. Res.* **69**, 513-529.
Kubai, L. and Auerbach, R. (1980). Regional differences in the growth of skin transplants. *Transplantation* **30**, 128-131.
Labbe, R. M., Irimia, M., Currie, K. W., Lin, A., Zhu, S. J., Brown, D. D. R., Ross, E. J., Voisin, V., Bader, G. D., Blencowe, B. J. et al. (2012). A comparative transcriptomic analysis reveals conserved features of stem cell pluripotency in planarians and mammals. *Stem Cells* **30**, 1734-1745.
Lachiewicz, A. M., Berwick, M., Wiggins, C. L. and Thomas, N. E. (2008). Survival differences between patients with scalp or neck melanoma and those with melanoma of other sites in the Surveillance, Epidemiology, and End Results (SEER) program. *Arch. Dermatol.* **144**, 515-521.
Lim, D. S. and Hasty, P. (1996). A mutation in mouse rad51 results in an early embryonic lethal that is suppressed by a mutation in p53. *Mol. Cell. Biol.* **16**, 7133-7143.
Lord, C. J. and Ashworth, A. (2012). The DNA damage response and cancer therapy. *Nature* **481**, 287-294.
Macheret, M. and Halazonetis, T. D. (2015). DNA replication stress as a hallmark of cancer. *Annu. Rev. Pathol.* **10**, 425-448.
Newmark, P. A. and Sanchez Alvarado, A. (2000). Bromodeoxyuridine specifically labels the regenerative stem cells of planarians. *Dev. Biol.* **220**, 142-153.
Onal, P., Grun, D., Adamidi, C., Rybak, A., Solana, J., Mastrobuoni, G., Wang, Y., Rahn, H.-P., Chen, W., Kempa, S. et al. (2012). Gene expression of pluripotency determinants is conserved between mammalian and planarian stem cells. *EMBO J.* **31**, 2755-2769.
Oviedo, N. J. and Levin, M. (2007). smedinx-11 is a planarian stem cell gap junction gene required for regeneration and homeostasis. *Development* **134**, 3121-3131.
Oviedo, N. J., Nicolas, C. L., Adams, D. S. and Levin, M. (2008a). Establishing and maintaining a colony of planarians. *CSH Protoc.* **2008**, pdb prot5053.
Oviedo, N. J., Nicolas, C. L., Adams, D. S. and Levin, M. (2008b). Gene knockdown in planarians using RNA interference. *CSH Protoc.* **2008**, pdb prot5054.
Oviedo, N. J., Pearson, B. J., Levin, M. and Sánchez Alvarado, A. (2008c). Planarian PTEN homologs regulate stem cells and regeneration through TOR signaling. *Dis. Model. Mech.* **1**, 131-143.
Oviedo, N. J., Morokuma, J., Walentek, P., Kema, I. P., Gu, M. B., Ahn, J.-M., Hwang, J. S., Gojobori, T. and Levin, M. (2010). Long-range neural and gap junction protein-mediated cues control polarity during planarian regeneration. *Dev. Biol.* **339**, 188-199.
Pearson, B. J. and Sanchez Alvarado, A. (2010). A planarian p53 homolog regulates proliferation and self-renewal in adult stem cell lineages. *Development* **137**, 213-221.
Pearson, B. J., Eisenhoffer, G. T., Gurley, K. A., Rink, J. C., Miller, D. E. and Sanchez Alvarado, A. (2009). Formaldehyde-based whole-mount in situ hybridization method for planarians. *Dev. Dyn.* **238**, 443-450.
Peiris, T. H., Weckerle, F., Ozamoto, E., Ramirez, D., Davidian, D., Garcia-Ojeda, M. E. and Oviedo, N. J. (2012). TOR signaling regulates planarian stem cells and controls localized and organismal growth. *J. Cell Sci.* **125**, 1657-1665.
Peiris, T. H., Garcia-Ojeda, M. E. and Oviedo, N. J. (2016). Alternative flow cytometry strategies to analyze stem cells and cell death in planarians. *Regeneration* [Epub ahead of print] .
Pellettieri, J., Fitzgerald, P., Watanabe, S., Mancuso, J., Green, D. R. and Sanchez Alvarado, A. (2010). Cell death and tissue remodeling in planarian regeneration. *Dev. Biol.* **338**, 76-85.
Reddien, P. W. (2011). Constitutive gene expression and the specification of tissue identity in adult planarian biology. *Trends Genet.* **27**, 277-285.
Reddien, P. W., Bermange, A. L., Murfitt, K. J., Jennings, J. R. and Sanchez Alvarado, A. (2005a). Identification of genes needed for regeneration, stem cell function, and tissue homeostasis by systematic gene perturbation in planaria. *Dev. Cell* **8**, 635-649.
Reddien, P. W., Oviedo, N. J., Jennings, J. R., Jenkin, J. C. and Sanchez Alvarado, A. (2005b). SMEDWI-2 is a PIWI-like protein that regulates planarian stem cells. *Science* **310**, 1327-1330.
Robb, S. M. C., Ross, E. and Sanchez Alvarado, A. (2008). SmedGD: the *Schmidtea mediterranea* genome database. *Nucleic Acids Res.* **36**, D599-D606.
Rouhana, L., Weiss, J. A., Forsthoefel, D. J., Lee, H., King, R. S., Inoue, T., Shibata, N., Agata, K. and Newmark, P. A. (2013). RNA interference by feeding in vitro-synthesized double-stranded RNA to planarians: methodology and dynamics. *Dev. Dyn.* **242**, 718-730.
Sage, J. (2012). The retinoblastoma tumor suppressor and stem cell biology. *Genes Dev.* **26**, 1409-1420.
Sandmann, T., Vogg, M. C., Owlarn, S., Boutros, M. and Bartscherer, K. (2011). The head-regeneration transcriptome of the planarian *Schmidtea mediterranea*. *Genome Biol.* **12**, R76.
Sinha, M., Jang, Y. C., Oh, J., Khong, D., Wu, E. Y., Manohar, R., Miller, C., Regalado, S. G., Loffredo, F. S., Pancoast, J. R. et al. (2014). Restoring systemic GDF11 levels reverses age-related dysfunction in mouse skeletal muscle. *Science* **344**, 649-652.
Solana, J., Kao, D., Mihaylova, Y., Jaber-Hijazi, F., Malla, S., Wilson, R. and Aboobaker, A. (2012). Defining the molecular profile of planarian pluripotent stem cells using a combinatorial RNAseq, RNA interference and irradiation approach. *Genome Biol.* **13**, R19.
Tseng, W. H. and Martinez, S. R. (2011). Tumor location predicts survival in cutaneous head and neck melanoma. *J. Surg. Res.* **167**, 192-198.
Tsuzuki, T., Fujii, Y., Sakumi, K., Tominaga, Y., Nakao, K., Sekiguchi, M., Matsushiro, A., Yoshimura, Y. and Morita, T. Y. (1996). Targeted disruption of the Rad51 gene leads to lethality in embryonic mice. *Proc. Natl. Acad. Sci. USA* **93**, 6236-6240.
van Wolfswinkel, J. C., Wagner, D. E. and Reddien, P. W. (2014). Single-cell analysis reveals functionally distinct classes within the planarian stem cell compartment. *Cell Stem Cell* **15**, 326-339.
Wagner, D. E., Wang, I. E. and Reddien, P. W. (2011). Clonogenic neoblasts are pluripotent adult stem cells that underlie planarian regeneration. *Science* **332**, 811-816.
Wenemoser, D. and Reddien, P. W. (2010). Planarian regeneration involves distinct stem cell responses to wounds and tissue absence. *Dev. Biol.* **344**, 979-991.
Xiang, Y., Miller, D. E., Ross, E. J., Sanchez Alvarado, A. and Hawley, R. S. (2014). Synaptonemal complex extension from clustered telomeres mediates full-length chromosome pairing in *Schmidtea mediterranea*. *Proc. Natl. Acad. Sci. USA* **111**, E5159-E5168.
Zhu, S. J. and Pearson, B. J. (2013). The Retinoblastoma pathway regulates stem cell proliferation in freshwater planarians. *Dev. Biol.* **373**, 442-452.

Appendix III

Peiris et al. BMC Developmental Biology (2016) 16:7
DOI 10.1186/s12861-016-0107-z

BMC Developmental Biology

RESEARCH ARTICLE Open Access

The Akt signaling pathway is required for tissue maintenance and regeneration in planarians

T. Harshani Peiris[1,2†], Daniel Ramirez[1,2†], Paul G. Barghouth[1,2†] and Néstor J. Oviedo[1,2,3*]

Abstract

Background: Akt (PKB) is a serine threonine protein kinase downstream of the phosphoinositide 3-kinase (PI3K) pathway. In mammals, Akt is ubiquitously expressed and is associated with regulation of cellular proliferation, metabolism, cell growth and cell death. Akt has been widely studied for its central role in physiology and disease, in particular cancer where it has become an attractive pharmacological target. However, the mechanisms by which Akt signaling regulates stem cell behavior in the complexity of the whole body are poorly understood. Planarians are flatworms with large populations of stem cells capable of dividing to support adult tissue renewal and regeneration. The planarian ortholog *Smed-Akt* is molecularly conserved providing unique opportunities to analyze the function of Akt during cellular turnover and repair of adult tissues.

Results: Our findings abrogating *Smed-Akt* with RNA-interference in the planarian *Schmidtea mediterranea* led to a gradual decrease in stem cell (neoblasts) numbers. The reduced neoblast numbers largely affected the maintenance of adult tissues including the nervous and excretory systems and ciliated structures in the ventral epithelia, which impaired planarian locomotion. Downregulation of *Smed-Akt* function also resulted in an increase of cell death throughout the animal. However, in response to amputation, levels of cell death were decreased and failed to localize near the injury site. Interestingly, the neoblast mitotic response was increased around the amputation area but the regenerative blastema failed to form.

Conclusions: We demonstrate Akt signaling is essential for organismal physiology and in late stages of the Akt phenotype the reduction in neoblast numbers may impair regeneration in planarians. Functional disruption of *Smed-Akt* alters the balance between cell proliferation and cell death leading to systemic impairment of adult tissue renewal. Our results also reveal novel roles for Akt signaling during regeneration, specifically for the timely localization of cell death near the injury site. Thus, Akt signaling regulates neoblast biology and mediates in the distribution of injury-mediated cell death during tissue repair in planarians.

Keywords: Planarians, Regeneration, Akt, Stem cells

Background

The protein kinase Akt also known as PKB, regulates multiple cellular functions including proliferation, survival, and growth during embryonic development and adult tissue homeostasis [1–5]. In mammals, Akt expression is widely distributed across the body and includes three isoforms, Akt-1-3 (PKBα, ß, and δ, respectively) [1–3]. Akt is evolutionary conserved in both its molecular structure and function among vertebrate and invertebrate organisms [4–7]. Across metazoans, Akt signaling integrates local and systemic information central to cellular and organismal physiology.

Akt regulates adult stem cell proliferation, migration and apoptosis and its deregulation has been implicated in the progression of cancer, diabetes, and aging [1–4, 8–10]. Conditional deletions and transgenic approaches have revealed key aspects of Akt signaling in hematopoietic,

* Correspondence: noviedo2@ucmerced.edu
†Equal contributors
[1]Department of Molecular and Cell Biology, School of Natural Sciences, University of California, 5200 North Lake Road, Merced, CA 95343, USA
[2]Quantitative and Systems Biology Graduate Program, University of California, Merced, CA 95343, USA
Full list of author information is available at the end of the article

epithelial, neural and other tissues [2, 3, 11–14]. Nonetheless, there is limited understanding of how Akt signaling controls the response of stem cells during cellular turnover and tissue injury in the complexity of the whole organism. This paucity is likely due to the ubiquitous nature of this signaling pathway and the difficulty of analyzing stem cells in their natural environment during physiological cell turnover and regeneration in conventional animal models [15–17].

Thus, we sought to investigate Akt function during cellular turnover and injury using the planarian flatworm *Schmidtea mediterranea*. This organism is well known for its stem cell-based regenerative capability. Planarians contain an abundant and accessible population of somatic adult stem cells called neoblasts [18–21]. The neoblasts are the only dividing cells in planarians and constantly proliferate to repair tissues and support systemic cellular turnover [21]. Recently, we described that the genome of *S. mediterranea* contains a single Akt ortholog termed *Smed-Akt*, which affects cell division and impairs planarian locomotion [22]. This study defined the role of *Smed-Akt* in abnormal cell proliferation triggered by the abrogation of the phosphatase PTEN, an upstream component of the Akt signaling pathway, which is highly mutated in human cancers.

Here we report on an extended RNA-interference (RNAi) strategy that disrupts *Smed-Akt* in the whole organism, to analyze its function on the response of neoblasts during systemic cell turnover and tissue repair. Our results show, *Smed-Akt* abrogation leads to a gradual decline in the number of neoblasts, accompanied by massive cell death that affects cellular turnover and maintenance of adult tissues. We also found that impaired locomotion in the *Smed-Akt* phenotype is due to the disruption of cilia maintenance in the ventral epithelium. Intriguingly, large-scale tissue injury is capable of reducing the high levels of *Smed-Akt(RNAi)*-induced levels of cell death, while increasing neoblast proliferation near the wound site however, animals failed to complete the formation of the regenerative blastema. Thus, our results reveal novel roles for Akt signaling during systemic cell turnover and large-scale regeneration of adult tissues.

Results

Smed-Akt is Required for Proper Neoblast Function

Our previous studies identified in the planarian *Schmidtea mediterranea* genome a single Akt ortholog (*Smed-Akt*) to the mammalian Akt2/PKB-ß [22]. *Smed-Akt* is widely expressed in neoblasts and differentiated cells and functional downregulation with RNA-interference [*Smed-Akt(RNAi)*] led to the reduction of neoblast numbers and loss of planarian locomotion [22]. To test whether Akt signaling plays additional roles in the regulation of cellular turnover and tissue regeneration in the adult body, we designed an RNAi protocol consisting of six dsRNA microinjections that effectively downregulated (8.4 folds) *Smed-Akt* expression over the span of 30 days (Fig. 1a).

Neoblast division was visualized through whole-mount immunostaining against the α–phosphorylated histone-3 (H3P) antibody, which labels cells in G2/M phase of the cell cycle (observed as yellow dots in Fig. 1b). Animals subjected to *Smed-Akt(RNAi)* initially displayed an important increase in neoblast division (~0.75 fold) 10 days post RNAi initiation, which was followed by a gradual decline in mitoses, reaching ~ five-fold decrease by day 30, when compared to control (Fig. 1b, c). Importantly, all samples were processed either before or a few days after injection to avoid the possibility of injury-induced increase in mitotic activity. To further characterize the effects of Akt downregulation on the cell cycle dynamics, we evaluated the incorporation of the bromodeoxyuridine analog (BrdU) every ten days for one month (Fig. 1d). BrdU is incorporated during the S phase of the cell cycle and remains in the cell through multiple rounds of cell division, albeit at lower concentrations in each successive cell generation. Control and *Smed-Akt(RNAi)* animals were exposed to a single BrdU pulse at different time points after the first dsRNA injection (i.e. 10, 20, and 30 days) and after 12 h samples were processed as previously described [23]. Consistent with the mitotic counts, BrdU positive cells increased in the first 10 days after *Smed-Akt(RNAi)* and gradually decrease to almost undetectable levels after one month of RNAi treatment (Fig. 1d). We also found a consistent trend in the expression of genes associated with cell cycle regulation (i.e. *cyclin A*, *cyclin B*, *CDK1*, *CDK2*, and *CDK4*), which showed general increase during the first 10 days and dramatically decreases in the successive days, further confirming our observations in mitotic activity and BrdU labeling upon *Smed-Akt(RNAi)* (Fig. 1e). The early increase in gene expression and proliferative cells upon *Smed-Akt* downregulation implies that the phenotype most likely starts before day 10. Our results suggest that *Smed-Akt* is essential to maintain the appropriate number of proliferating neoblast during tissue renewal in adult planarians.

To assess whether the effects of *Smed-Akt(RNAi)* are restricted to cell cycle events, we analyzed the expression of markers associated with neoblasts and the early and late division progeny (e.g. *smedwi-1*, *Prog-1, and Agat-1*, respectively). This analysis revealed a dramatic decrease in the expression of markers associated with neoblasts and their progeny (Fig. 2a). Interestingly, the pattern of expression for *smedwi*-1 and *Agat*-1 were similar to that previous observed in cell cycle genes, while the marker for the early neoblast progeny (*prog-1*) followed a somewhat different pattern, characterized by a strong

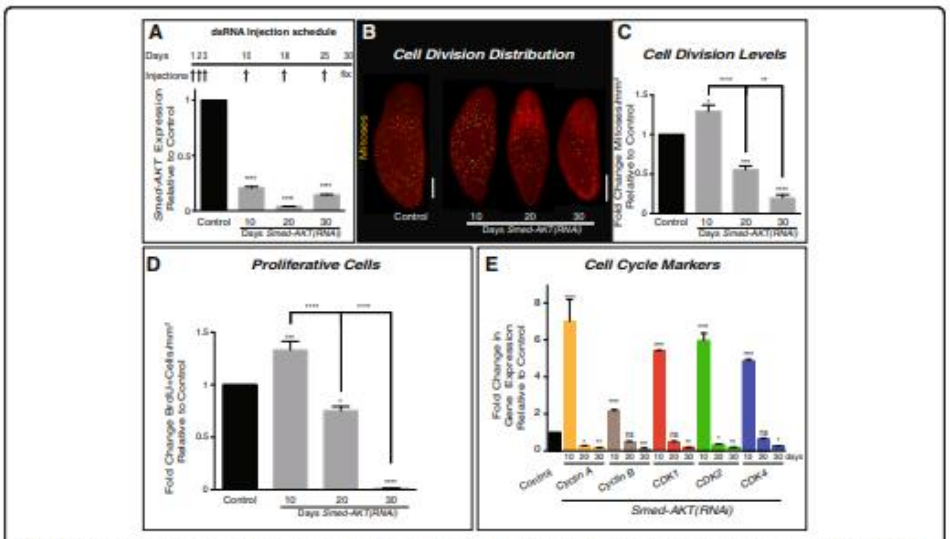

Fig. 1 Downregulation of *Smed-Akt(RNAi)* reduces neoblast proliferation. **a** The dsRNA microinjection schedule is depicted on top. A total of 6 injections (arrows) were performed during a 30 day (black line) period. The RNAi efficiency of the dsRNA microinjections was tested with quantitative PCR(qPCR) on days 10, 20 and 30 after the first dsRNA injection, showing significant down-regulation relative to control. **b** Whole-mount immunostaining of control and *Smed-AKT(RNAi)* worms, using anti-phosphorylated histone H3 (H3P) antibody to label the distribution of cell division at days 10, 20 and 30 after first dsRNA injection. Yellow dots represent mitotic cells. Scale bar 200μm. **c** H3P-signal quantification, represents fold change of cell division (mitoses per mm^2) relative to the control at days 10, 20 and 30 after *Smed-AKT(RNAi)*. A significant increase in cell division was observed 10 days post first injection, which dramatically diminishes by day 30. **d** Quantification of fold change in bromodeoxyuridine (BrdU) positive cells relative to the control at days 10, 20 and 30 after first injection. **e** Relative levels of gene expression, fold change, of cell cycle markers 10, 20 and 30 days after first *Smed-AKT(RNAi)* injection. All analyses were performed using two or more experimental sets with 10 or more animals per experiment at various time points after first dsRNA injection. For qPCR analysis, gene expressions are relative to the ubiquitously expressed clone *H.55.12e*. Graphs represent mean ± s.e.m. of three of more independent experiments. *P* values *** < 0.005 and **** < 0.0001, were calculated by two way ANOVA

downregulation from the beginning of *Smed-Akt(RNAi)*. Whole mount fluorescent in situ hybridization (FISH) with markers of neoblasts and the post-mitotic progeny one month after *Smed-Akt(RNAi)* further confirmed the quantitative PCR (qPCR) results and showed a generalized reduction in gene expression throughout the body, after *Smed-Akt(RNAi)* (Additional file 1).

Proliferative neoblasts are contained within the irradiation sensitive X1 population and can be isolated via flow cytometry cell sorting (FACS) [24]. Recently, cells within the X1 population were classified into two functionally distinct subclasses, the zeta- and sigma-neoblasts [25]. FACS was used to isolate equal number of X1 cells from both control and *Smed-Akt(RNAi)* animals after one month of RNAi. We used a larger number of experimental animals to obtain comparable amount of FACS-isolated cells between both groups. The total RNA extracted was processed to evaluate levels of expression of markers of the sigma and zeta populations (Fig. 2b). Markers of the sigma neoblast subpopulations tend to increase upon *Smed-Akt(RNAi)*, while there little to no change in the zeta subclass, suggesting the effect of *Smed-Akt(RNAi)* is not homogeneously distributed among the neoblasts. Thus, additional experiments are required to further define the differences between gene expression in the neoblast subclasses and to understand these implications. Altogether, our results indicate that *Smed-Akt* is essential for the appropriate expression of neoblast and progeny markers and suggests that a gradual depletion in the number of neoblasts takes place after *Smed-Akt(RNAi)*.

Smed-Akt is a Critical Regulator of Cell Death in Planarians

A fine balance between stem cell proliferation and programmed cell death enables physiological cellular turnover that supports maintenance and growth of adult tissues [26]. Over a 40 days starvation period, animals subjected to *Smed-Akt(RNAi)* exhibited a ~3 fold reduction in

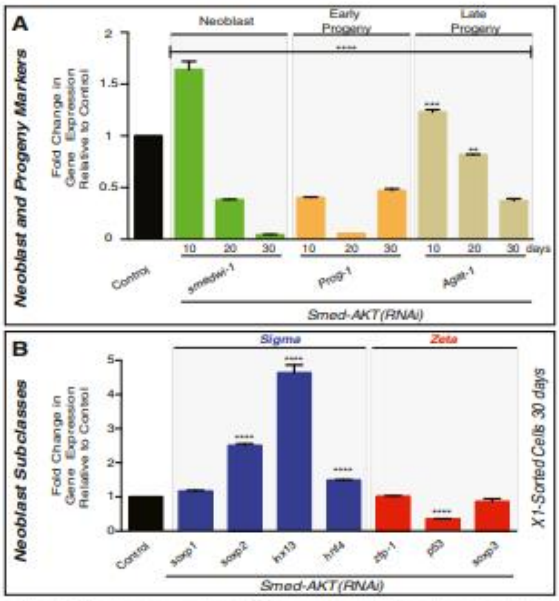

Fig. 2 Akt regulates expression of neoblast and progeny markers. **a** Gene expression levels for markers of neoblasts (*smedwi-1*) and neoblast early (*Prog-1*) and late (*AGAT-1*) progeny were evaluated with qPCR at days 10, 20 and 30 after first dsRNA injection and represented in fold change relative to each sample's individual control. **b** Fold change in gene expression levels involving markers of neoblast subpopulations sigma (blue) and zeta (red). The mRNA levels were measured in X1 sorted cells at day 30 after first injection was used to determine gene expression of *Smed-AKT(RNAi)* animals. All values are relative to equal number (~20,000) of X1 cells sorted from control-water injected animals at 30 days. Gene expressions are all relative to the internal control, the ubiquitously expressed clone *H.55.12e*. Graphs represent mean ± s.e.m. of triplicated samples of two or more biological replicates with at least ten animals per experiment. *P* values ** < 0.001, *** < 0.0005 and **** < 0.0001, were calculated by two way ANOVA

surface area compared to the control group (0.23 ± 0.08 vs 0.72 ± 0.07 mm^2, respectively) (Fig. 3a). These results together with the reduction in neoblast proliferation suggests that the *Smed-Akt(RNAi)* phenotype may be accompanied by increased levels of cell death, contributing to an accelerated reduction in animal size over time, and death by ~45 days after the first injection.

Akt function has been implicated in cellular pro-survival mechanisms [14, 27–29]. Thus, we examined possible roles of *Smed-Akt* as regulator of cell death in planarians by analyzing levels of cell death after RNAi treatment. First, spatial distribution of cell death in the whole body was evaluated using the terminal deoxynucleotidyl transferase dUTP nick end-labeling (TUNEL) assay [30]. These experiments revealed that *Smed-Akt (RNAi)* double the number of TUNEL positive cells, 15 days after the first dsRNA injection and it gradually increase to about threefold by day 30 of the RNAi treatment (Fig. 3b). Despite a slight increase in TUNEL positive cells by day 10 of *Smed-Akt(RNAi)* (data not shown), the predominant increase in cell death was observed around day 15 after the first dsRNA injection. TUNEL positive cells appeared indistinctively scattered along the planarian body at all times, suggesting this is a generalized event, most likely involving both neoblasts and differentiated cells (Fig. 3c). Next, we performed flow cytometry analysis using Annexin V and 7AAD staining [31, 32]. This experiment confirmed the high levels of cell death induced by *Smed-Akt(RNAi)* may involve apoptosis and necrosis (Fig. 3d). The increased levels of cell death in *Smed-Akt (RNAi)* together with the overall animal size reduction indicates that Akt is an important regulator of cellular turnover. The mechanisms are not entirely clear however, it is possible that the impairment in tissue renewal may result from either (1) an initial reduction in neoblast numbers that fail to support homeostasis or (2) generalized cell death events that impact both neoblasts and differentiated cells alike.

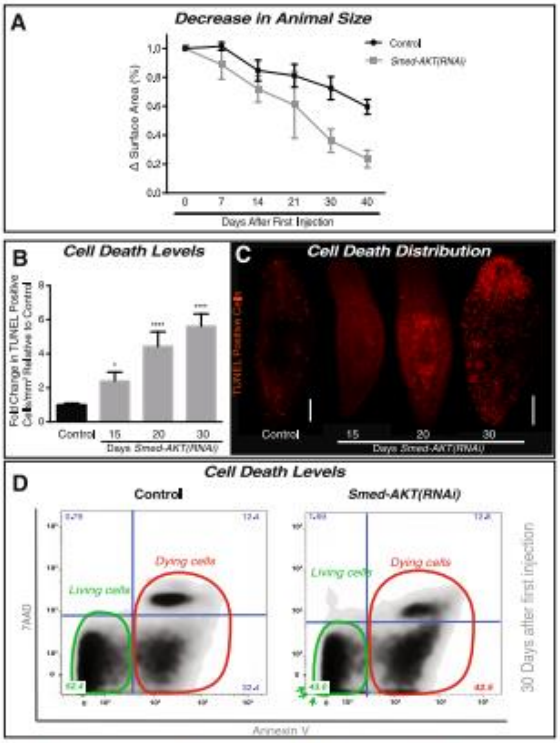

Fig. 3 The impairment of Akt leads to increased cell death in *S. mediterranea*. **a** The reduction in animal size over time was recorded as the difference in surface area (whole animal) expressed in percentage. Surface area measurements were followed for over 40 days of starvation in both the control and *Smed-AKT (RNAi)* animal groups. Graph represent the mean ± s.e.m of five independent time courses with ten or more animals per experiment. **b** Quantification of TUNEL-positive nuclei reveals a gradual increase in cell death from day 15 (~2.5 fold) to 30 days (~6 fold) post first injection relative to its individual control. Graph represent mean ± s.e.m of three biological replicates consisting of five or more animals per experiment. *P*-value * <0.05 and **** <0.0001, by one way-ANOVA. **c** Whole-mount immunostaining labeling TUNEL-positive nuclei (cell death) with control on the left and *Smed-AKT(RNAi)* days 15, 20 and 30 on the right. Each time point consisted of at least two biological replicates with 5 or more animals each. Scale bar 200μm. **d** Flow cytometry analysis of Annexin V and 7 AAD expression, reveals the frequency distribution between living and dead cells. Annexin V-7 AAD quadrant indicates live cells (green circle). Annexin V + 7 AAD and Annexin V + 7 AAD+ indicates cells that are in early and late stages of cell death, respectively (red circle). The numbers in each quadrant indicate the percentage of cells with that staining profile. All experiments were independently repeated three times with at least ten animals each time

Smed-Akt Regulates the Maintenance of Differentiated Tissues

A distinctive macroscopic feature of the *Smed-Akt (RNAi)* phenotype is the impairment of locomotion accompanied by the elongation of the whole body, which are initiated as early as day 15 and progress for over 35 days after the first dsRNA injection (Additional file 2). Planarian gliding is mediated by synchronized cilia movement on the ventral epithelial surface of the animal [33]. Since locomotion is impaired in *Smed-Akt(RNAi)* animals, we therefore evaluated the status of cilia through the expression levels of genes specifically corresponding to intraflagellar transport machinery and flagellar beating (*IFT88, IC2, LC1, LRRC50* and *DNAHβ-1*) [34, 35]. First, we observed through qPCR, a dramatic reduction in the expression of cilia markers required for the structural and mechanical integrity of cilia [34, 36] (Fig. 4a). The reduction in gene expression of cilia markers is detected as early as 10 days after *Smed-Akt (RNAi)* and their expression continues to reduce over time. Second, whole-mount staining with anti-α-Ac-tubulin antibody allowed us to visualize the integrity of ciliated

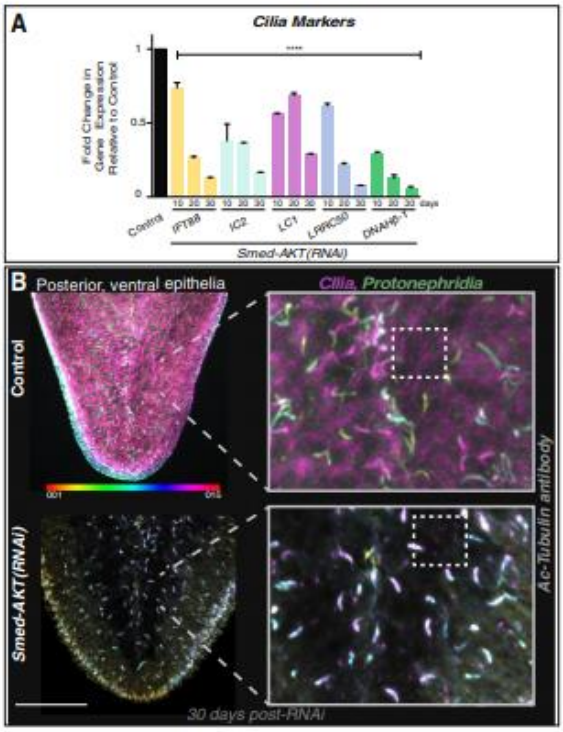

Fig. 4 Akt is required for the maintenance of cilia in the ventral epithelia. **a** Gene expression levels of cilia specific markers at days 10, 20 and 30 after *Smed-AKT(RNAi)* relative to the control. Analysis of markers corresponding to intraflagellar transport machinery (IFT88) and flagellar beating (IC2, LC1, DNAHβ-1 and LRRC50) reveal a marked reduction of gene expression as early as day 10 and it is further reduced by day 30 after first injection in *Smed-AKT(RNAi)* animals. Gene expressions are all relative to the internal control, the ubiquitously expressed clone *H.55.12e*. Graphs represent mean ± s.e.m. of triplicated samples of two or more biological replicates with at least ten animals per experiment. Significance **** <0.0001 is determined through two way-ANOVA. **b** Images show control (top) and *Smed-Akt (RNAi)* (bottom) at day 30 after first dsRNA injection. Images represent depth-coded maximum projections of confocal z-sections in the posterior specific ventral cilia and proximal structures stained with Ac-Tubulin antibody. Superficial structures were labeled in magenta and structures near the dorsal epithelial layer appear in orange (color code scale on the left). Magnified images (on the right) display the effects of *Smed-AKT(RNAi)* on ciliated structures (cilia in ventral epithelia is represented in magenta and sections of the protonephridia in green and blue). Box with dotted lines outline regions of cilia in ventral epithelia, notice the scattered magenta signal in the experimental group. Confocal z-sections were taken on three or more animals of two independent experiments. Depth-coded projections were obtained using ImageJ software. Scale bar 100μm

structures in the ventral epithelia, including parts of the excretory system (e.g. proximal tubules and flame cells in protonephridia) [22, 33–37]. We noted that one month after *Smed-Akt(RNAi)*, the anti-α-Ac-tubulin antibody signal is nearly absent in the areas corresponding to ventral cilia, while control animals showed dense coverage by cilia (magenta signal in Fig. 4b). The confocal stacks, 30 days after *Smed-Akt(RNAi)*, showed a marked reduction of ventral cilia, making the proximal tubules and flame cells of the excretory system readily evident (Fig. 4b). Together, the results obtained through gene and protein expression demonstrates that *Smed-Akt* is required for the structural integrity of cilia and its maintenance. Additionally, our findings suggest that the impaired locomotion in the Akt phenotype is most likely a consequence of inadequate cilia density in the ventral epithelia.

We next sought to evaluate whether the *Smed-Akt (RNAi)* effects are specific to the ventral epithelia or if they extend to other tissues. The excretory system in planarians consists of protonephridial tubules including both ciliated and non-ciliated structures that could be labeled with anti-α-Ac-tubulin antibody and the *Smed-CAVII-1*

gene, respectively [36–38]. Additional markers to each portion of the protonephridial tubules were recently mapped [36], thus providing better opportunities to analyze effects on the excretory system. Specifically, we evaluated the expression of solute carrier transporters (slc) family of genes expressed along the proximal and distal tubules, and the collecting ducts of the protonephridia [36]. We further extended the analysis to include planarian homologs of nephrocystins known to regulate excretory functions and upon their downregulation, lead to cyst-like disease in *S. mediterranea* [36]. The results provided evidence of a generalized reduction in gene expression throughout the protonephridial structures and the nephrocystin markers (NPHP5, 6 and 8) (Fig. 5a, b). The striking reduction in gene expression in the protonephridial structures is evident as early as 10 days after *Akt* disruption. However, macroscopic signs of excretory system defects such as edema and clearing of body pigmentation are evident in *Smed-Akt (RNAi)* animals (30/30) during advanced stages of the phenotype, i.e. ≥ 30 days after the first dsRNA injection

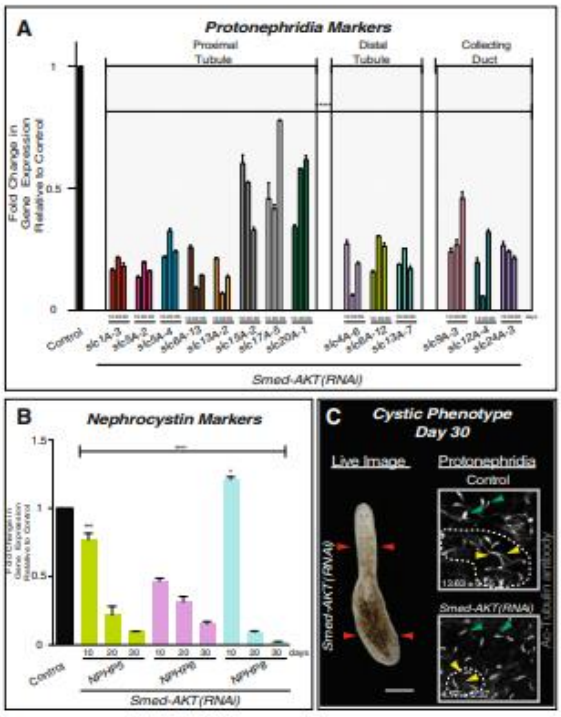

Fig. 5 Down-regulation of Akt leads to a delayed onset of a cystic phenotype. **a** Levels of expression of solute carrier (slc) genes expressed along the planarian protonephridia tubules (proximal and distal) and collecting ducts. There is a striking reduction in expression of all slc genes evident as early as day 10 and is sustained through day 30 after *Smed-AKT(RNAi)*. Each individual sample was analyzed relative to its individual control. **b** Expression levels of nephrocystin markers (NPHP5, 6 and 8) at different time points after RNAi. Levels of expression for each gene are relative to individual controls. All NPHP genes showed markedly reduction in gene expression across 30 days after the first dsRNA injection. In all cases, gene expressions are relative to the internal control, the ubiquitously expressed clone *H.55.12e*. Graphs represent mean ± s.e.m. of triplicated samples of two biological replicates consisting of at least ten animals per experiment. Significance **** <0.0001 is determined through two way-ANOVA. **c** Cystic phenotype is seen in *Smed-AKT(RNAi)* animals by day ≥30 after first dsRNA injection ($N = 30/30$). In the live image, seen on the left, the features of a cystic phenotype (elongation of the head and bloating of the tail) are highlighted by red arrows. Confocal z-stack images on the right, control (top) and *Smed-AKT(RNAi)* (bottom), highlight protonephridial clusters (dotted lines)using Ac-Tubulin staining in the posterior ventral surface at day 30. Protonephridial clusters contain tubules (yellow arrows) and flame cells (green arrows). The number of flame cells per proximal unit are strongly reduced (**** $P < 0.0001$, student *t*-test) in *Smed-AKT(RNAi)* animals 4.77 ± 0.72 vs 13.63 ± 0.55 in control. Flame cell counts were obtained from 5 or more animals, totaling N=30 or more clusters analyzed per condition

(Additional file 3A). Formation of the edema phenotype is consistent with the markedly downregulation of nephrocystin genes, and structural alterations in the proximal structures of the protonephridia (Fig. 5c). Particularly, *Smed-Akt(RNAi)* lead to a generalized decrease in both (13.63 ± 0.55 vs 4.77 ± 0.37) and proximal tubules per protonephridial unit (protonephridial unit is outlined in Fig. 5c), when compared to control. This structural disruption is consistent with the manifestation of edema in planarians [36–38], further validating the reduced integrity of the excretory system during the advanced stages of the *Smed-Akt(RNAi)* phenotype.

To determine whether *Smed-Akt(RNAi)* also affects other organs within planarians, we set out to explore gene and protein expression of markers in terminally differentiated tissues [21, 23, 39–43]. Specifically, mRNA levels of genes associated with the nervous and digestive system, connective and muscle tissues. The results from these experiments demonstrated that most of the genes screened (i.e. 8/10) tend to gradually deplete after *Smed-Akt(RNAi)*, but at least two of the markers including the choline acetyltransferase *ChAT* (neurons) and *tropomyosin* (muscle) followed a different pattern characterized by an increase in expression one month after Akt downregulation (Fig. 6a). Staining with the monoclonal antibody Smed-6G10 (6G10) that labels different muscle fibers in the planarian body [44], revealed the disruption of the Akt signaling affects planarian musculature. Specifically, we observed the disorganization of circular and diagonal muscle fibers and the absence of signal in some areas, suggesting alterations in the normal tissue architecture (arrows in head and pharynx, Fig. 6b). The structural changes in musculature may also explain the incapability to ingest food after 20 days of Akt-RNAi (data not shown) but also the animal's ability to slightly maneuver through peristaltic muscle contractions [34]. ISH experiments also confirmed the widespread reduction in expression of markers of the excretory (*Smed-CAVII-1*), and the nervous (*Smed-PC2*) system, further supporting the notion that disruption of tissue integrity is not restricted to one tissue in particular but rather a more generalized event after downregulation of Akt function (Additional files 3B, and 4). Future experiments are needed to determine whether particular cell types are more susceptible to structural alterations after Akt systemic inhibition. Nonetheless, these results together demonstrate *Smed-Akt* is essential for the maintenance of tissues in planarians.

Smed-Akt(RNAi) Leads to Regeneration Defects

Tissue amputation triggers well-coordinated waves of apoptosis and cellular proliferation aimed at recreating missing tissues and organs within the regenerative blastema. The *Smed-Akt* phenotype is characterized by a reduction in neoblast numbers and increased cell death, affecting the maintenance of differentiated tissues. Thus, we assessed how an unbalance in cell death and proliferation affects large-scale injury-induced regeneration in *S. mediterranea*. We performed planarian head decapitations after 30 days post-RNAi initiation and followed macroscopic and microscopic responses in regenerative body trunks (Fig. 7). One week after amputation control animals formed head blastemas with photoreceptor pigmentation, whereas *Smed-Akt(RNAi)* animals only formed a marginal blastema with limited eye pigmentation (Fig. 7a). Further experiments with antibodies that recognize brain structures and visual neurons (i.e. anti-SYNORF1, anti-VC1), revealed *Smed-Akt(RNAi)* animals failed to regenerate brain and visual neuronal connections (Figs. 7b, c). Likewise, animals with tail amputation also fail to regenerate during the advanced phenotype, suggesting that the reduced number of neoblasts may affect both anterior and posterior regeneration in *Smed-Akt(RNAi)* animals (data not shown). These results also imply that injury-mediated cell differentiation is active despite the initial high levels of cell death and low levels of cellular proliferation.

Previous studies in *S. mediterranea* have shown that localized waves of cell death concentrate to the injury site and a systemic spike of neoblast division take place within the first six hours post-amputation [30, 43]. We followed both cell death and the mitotic response post amputation for seven days and observed cell death is suppressed over time, whereas cell division is increased in *Smed-Akt(RNAi)* animals when compared to the initial time point (Figs. 7d-g). Moreover, cell death not only reduced in *Smed-Akt(RNAi)* animals but it also failed to localize to the injury site as is expected in the first six hours post-amputation (Fig. 7d, e and Additional file 4A, B). The system wide cell death expected was also absent even after more than 2 days of amputation (Additional file 5A-C). Instead, TUNEL positive cells were slightly accumulated to the uninjured, opposite end of the regenerating trunk (n = 10/10). Intriguingly, amputation in the *Smed-Akt(RNAi)* group elicited a system-wide increase in cell division that peaked at six hours post-amputation and was sustained during the first week post-amputation (Fig. 7f, g). Additionally, the experimental group was incapable of producing a timely and localized mitotic response at the injury site, as seen in the control animals 2 days post amputation. However, *Smed-Akt(RNAi)* animals exhibited a delayed localization of cell division (i.e. 4 days post amputation), which persisted through 7 days post amputation (Additional file 6A-C). We propose *Smed-Akt* functions as regulator of cell death and proliferation, during large-scale tissue regeneration in planarians.

Discussion

Maintenance of adult tissues proceeds through a fine balance between cell death and cell division. Our results

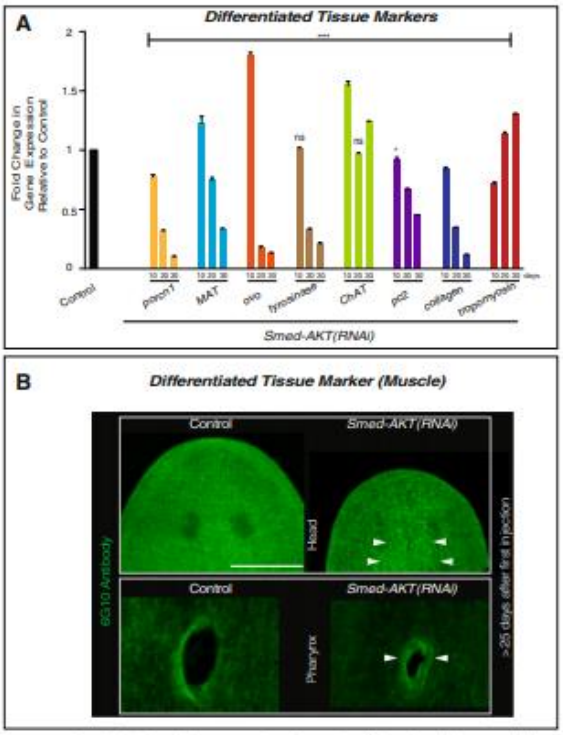

Fig. 6 *Smed-AKT(RNAi)* leads to a generalized reduction in the expression of genes in differentiated tissues and alterations in muscle fibers. **a** Gene expression analysis of differentiated tissue markers at days 10, 20 and 30 after first dsRNA injection. All measurements are relative to the their respective control. Analysis of genes related to the differentiated tissues: intestinal (*porcn-1 and MAT*), photoreceptors (*ovo and tyrosinase*), central nervous system (*ChAT and pc2*), and connective and muscle tissues (*collagen and tropomyosin, respectively*). *Smed-AKT(RNAi)* strongly reduce the expression of most markers except for *ChAT* and *tropomyosin* that are elevated by day 30 after RNAi. Gene expressions are all relative to the internal control, the ubiquitously expressed clone *H.55.12e*. Graphs represent mean ± s.e.m. of triplicated samples of two or more independent experiments with at least ten animals per experiment. Significance (*P<0.05 and ****P<0.0001) was determined with two way-ANOVA. **b** Whole-mount immunostaining of intact control and *Smed-AKT(RNAi)* planarians at >day 25 post RNAi initiation with SMED-6G10 (muscle tissue) antibody. SMED-6G10 antibody specifically labels the circular and diagonal muscle fibers throughout the animal. When compared to the control, *Smed-AKT(RNAi)* showed disarray in the muscle fibers in both the head (top images) and pharyngeal (bottom images) muscular structures (arrowheads). The images are representative of an experiment with five animals in one biological replicate. Scale bar 200 μm

implicate *Smed-Akt* as a critical regulator of cellular turnover, adult tissue maintenance, and regeneration. Disrupting *Smed-Akt* signaling affects the number of proliferative neoblasts during cellular turnover and alters integrity and function of differentiated tissues. Strikingly, tissue injury is capable of altering patterns of cell death and cell proliferation after Akt downregulation.

The *Smed-Akt* phenotype is characterized by an initial increase in cell division that is followed by a gradual depletion in the number of proliferative neoblasts. The nature of the signals triggering cell proliferation in the first 10 days of the phenotype are not clear, but it might involve a compensatory response to overcome deficiencies in cellular turnover due to abnormalities in ciliogenesis [45–48]. Interestingly, even at late stages of the Akt phenotype some neoblasts continue dividing probably to self-renew and/or to continue supporting tissue turnover to some extent as animals subjected to *Smed-Akt(RNAi)* survive for over one month. Two non-exclusive scenarios may explain the presence of dividing neoblasts after *Smed-Akt(RNAi)*: (1) residual Akt expression after RNAi, due to incomplete abrogation. Our qPCR analyses

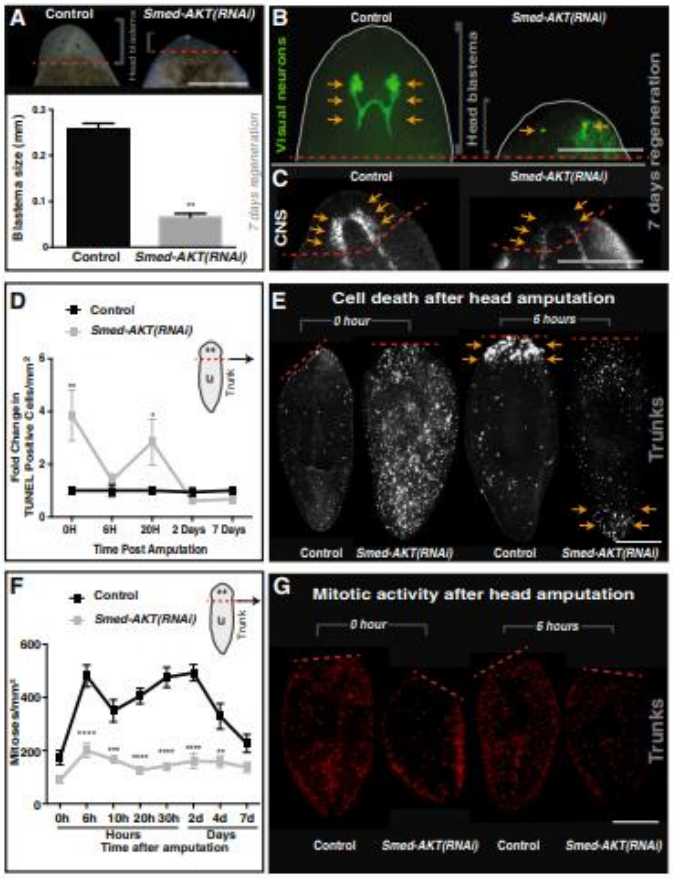

Fig. 7 Akt is required for tissue regeneration. **a** Live images of control and *Smed-Akt (RNAi)* head blastema formation seven days post amputation. Dashed red line represents the amputation plane. Scale bar 100μm. **b** Immunostaining labeling the visual neurons (anti-VC-1 antibody) and (**c**) central nervous system (anti-SYNORF1 antibody) seven days post amputation. Arrows highlight these structures in both the control and *Smed-Akt (RNAi)* animals and red dotted lines represent the plane of amputation. Scale bar 100μm. **d** TUNEL-positive nuclei post amputation, represented in fold change compared to the control. Note that cell death decrease over time, a four fold difference in *Smed-Akt (RNAi)*. **e** Immunostaining of TUNEL-positive nuclei of trunk fragments 0 and 6 h post amputation. Scale bar 200 μm. **f** Levels of H3P positive cells over time post amputation in control and *Smed-Akt (RNAi)*. The quantification was performed on the regenerating trunk fragment. **g** Representative images showing mitotic activity (red dots) after head amputation at 0 and 6 h in trunk fragments. All images are representative of two or more biological replicates consisting of five animals or more per experiment. Scale bar 200 μm. Graphs represent mean ± s.e.m. of two or more biological replicates and *P* values *<0.01, **<0.001, ***<0.0005 and ****<0.0001 were obtained with Wilcoxon test or two way ANOVA

demonstrated that *Smed-Akt* expression is strongly downregulated after RNAi, however, additional experiments involving specific antibody against SMED-AKT protein may be needed to rule out whether AKT protein is still present and active, and (2) intrinsic differences among neoblast populations may confer survival properties to a select group of stem cells when Akt is downregulated. This possibility is supported by the differential expression displayed by neoblast subclasses after *Smed-Akt(RNAi)* (Fig. 2b). Recent progress to unravel the diversity of neoblast sub-populations suggest planarian stem cells are more complex than previously anticipated [25, 49].

Therefore, we envision future experiments would evaluate individual neoblast subpopulations to identify whether some neoblast subtypes are more susceptible to Akt downregulation [3, 9, 10, 50, 51].

The increased amount of cell death in *Smed-Akt (RNAi)* suggests this is a rather generalized event involving both neoblasts and differentiated cells. Our findings implicate decisions of cellular survival greatly depend on *Akt* signaling, but future experiments are required to discern whether apoptosis and/or necrosis initially target neoblasts. This possibility may, in fact, reduce the number of neoblasts making them unable to efficiently support demands of cellular turnover, leading to generic tissue defects. We did not address the mechanism of cell death in the *Smed-Akt* phenotype but since the mitochondrial pathway of apoptosis is remarkably conserved in planarians; it may serve, as in vertebrates, as the favored mechanism for *Akt*-mediated cell death [2, 13, 30, 31, 52, 53].

Studies in mammals show that not all tissues respond homogeneously in response to Akt deficiency, while some do not show measurable changes (e.g. bone marrow and pancreas), others undergo apoptosis (e.g. testes and thymus) [52]. A fine balance between stem cell proliferation and programmed cell death enables physiological cellular turnover to support adult tissue maintenance. Tissue renewal is seen to be altered in *Smed-Akt(RNAi)* animals, most likely due to the increased levels of cell death, which reduce the number of proliferating neoblasts. Our findings indicate that *Smed-Akt(RNAi)* lead to a heterogeneous gene expression response and mixed effects on the architecture of differentiated tissues. This differential sensitivity to *Smed-Akt* deficiency is observed early with alteration of cilia-mediated locomotion and the late onset of a cystic phenotype defined by a malfunctioning excretory system. The effects of abrogated *Smed-Akt* in differentiated tissues may depend on tissue-specific turnover rates but more experiments are needed to better understand the phenotype at systemic level.

The mechanisms by which cilia is strongly reduced after *Smed-Akt(RNAi)* is unclear but our findings indicating severe downregulation in IFT88 may suggest, as in other systems [45–47, 54, 55], that phosphorylated Akt fail to localize to the cilium at the cilliary base leading to disruption of the apical cellular projections. An intriguing finding of the *Smed-Akt(RNAi)* phenotype is the disruption of ciliated structures within the epithelium and excretory system (e.g. flame cells and proximal tubules), which is being recently introduced as an alternative model for cystic kidney disease [36]. Our results showed a significant reduction in gene expression correlating to ciliated structures, protonephridia and nephrocystins within the first 10 days of RNAi initiation that persisted to decrease by day 30. Interestingly, impaired locomotion in *Smed-Akt(RNAi)* animals became slightly evident by day 15 after RNAi treatment, which was exacerbated over time, and the delayed onset of the edema phenotype that correlated with a dysfunctional excretory system. Planarian studies have shown functional downregulation of genes correlating to ciliated structures and nephrocystins led to a rapid edema phenotype by 9–15 days post RNAi treatment [36–38]. These results imply that Akt activity may facilitate the assembly of ciliated structures by regulating gene and protein expression required for maintenance of these structures (e.g. IFT88, NPHPs and SCL family of genes). It is also possible that during the initial part of the Akt phenotype, functional protonephridial units balance electrolyte and carry on waste excretion to compensate the reduction in the number of flame cells and proximal tubules. However, as the phenotype progresses it become unsustainable deriving in extensive damage, leading to the collapse of the excretory system. Further experiments will be required to discriminate how Akt signaling regulates the delayed onset of cyst-like formations. Nonetheless, these results are also significant because Akt signaling and cilia are emerging as possible therapeutic target in leukemia and polycystic disease [56–59]. Altogether, these findings highlight the convenience of the planarian model for analyzing Akt signaling dysfunction in the whole adult organism.

Akt has been studied extensively in the context of cancer and as a regulator of cellular functions, but its participation in large-scale regeneration remains poorly understood. Our findings reveal that Akt plays critical roles during planarian regeneration. Specifically, disruption of Akt impairs the process of blastema formation but does not prevent the initial peaks of cell proliferation upon amputation. In response to amputation, some cells migrate and differentiate to form an incipient blastema, which is discontinued probably due to the lack of timely localization of cell death near the wounded area. The mechanisms by which cell death regulates the process of regeneration still remains poorly understood [60]. Nonetheless, the Akt phenotype presents unique opportunities to address whether a particular signaling pathway and/or cell type that plays major role in guiding injury-induced apoptosis. We propose that Akt signaling serves as mediator of localized cell death events during planarian regeneration.

The intriguing finding that injury-induced repair signals in *Smed-Akt(RNAi)* is capable of reducing cell death is exciting and it reveals a novel role for Akt in large-scale tissue regeneration. Uninjured animals subjected to *Smed-Akt(RNAi)* show high levels of cell death and restricted neoblast division, but within a few hours after amputation, levels of apoptosis dramatically reduce while cellular proliferation increase in the absence of functional Akt. While future experiments will be required to investigate the mechanisms contributing to injury-mediated cellular death, these results imply tissue

damage and repair may alter cellular decisions imposed by a dysfunctional Akt pathway.

Conclusions

Our results demonstrate that Akt forms part of an ancient signaling pathway controlling cellular fate decisions in members of the lophotrocozoans. Thus, we introduce *S. mediterranea* as a valuable model system to dissect Akt function in stem cell-based cellular turnover and repair of adult tissues. The mechanisms controlling the molecular cascade guiding large-scale tissue regeneration are poorly understood however, our analysis identified that Akt is necessary for events related with cell death during regeneration. Future experiments are needed to address the injury-mediated signals capable of reverting levels of cell death and proliferation in the absence of Akt signaling.

Methods

Planarian Culture

The clonal lines of the Planarian strain, *Schmidtea mediterranea* CIW4 was used for all experimental procedures and were cultured as previously described [61].

RNAi Experiments

The synthesis of dsRNA was carried out as previously described in [62] and microinjection experiments were carried out following the schedule in Fig. 1a. Following this injection schedule, phenotype was accomplished by 25–30 days post first injection. All experiments were conducted 5 days after last injection.

Fixation and Whole Mount Immunofluoresence

Animals were fixed using the Carnoys fixation protocol [63] unless otherwise stated. Primary antibody concentrations were used as follows: α -H3P 1:250 (Millipore Cat# 05-817R); α -VC1 1:10,000 (Kind gift of K. Watanabe); anti-α-Ac-Tubulin 1:500 (Sigma, clone 6-11B-1), Smed-6G10 1:1000; SYNORF1 1:100 (Developmental Studies Hybridoma Bank). Secondary antibody concentrations were: Alexa488 (1:400) goat anti-mouse (Invitrogen Cat# 673781), goat-anti-mouse HRP IgG 1:1000 (Life Technologies), and Alexa568 (1:800) goat anti-rabbit (Invitrogen Cat# 11036).

BrdU Staining

Single staining of BrdU staining was performed as previously described [23, 64].

Flow Cytometry Analysis and Cell Sorting

Planarians were dissociated as previously described [24, 32]. Brielfy, $1X10^6$ cells from dissociated planaria were stained with DNA marker Draq5 (eBioscience Cat # 65-0880-96) at a 1:500 dilution in CMF media for 30 min at RT in the dark. Incubation with calcein (Invitrogen Cat # C3100MP) 1:500 diluted in CMF media for 10 min at RT was sufficient to stain live cells. BD *FACSDiva™* software was used for initial gating and samples were either analyzed using LSRII flow cytometer (BD Biosciences) or sorted using ARIAII flow cytometer (BD Biosciences). Apoptotic cells were identified with Annexin V (Pacific Blue) and 7-AAD (PECy5) staining according the manufacturer's instructions (eBiosence) and additional modifications found in our protocol [32]. Flow cytometry analyses were performed with FlowJo software (version 8). Further details on this protocol can be found in our previous publication [63].

TUNEL Assay

Cell death was measured, using the TUNEL assay that labels double stranded DNA breaks with fluorescent tags. Further details on this protocol can be found elsewhere [30]. Animals were mounted and fluorescent images were captured and evaluated with Nikon AZ-100 multizoom microscope and NIS Elements software.

Quantification of Cellular Events, Planarian Measurements and Imaging Processing

Nikon AZ-100 multizoom microscope and NIS Elements (Nikon) AR 3.2 software was used to record animal behavior and digital images of planarian and/or cellular events within the animal. Whole animal measurements were calculated using the number of cellular events (eg. H3P or TUNEL- positive foci) per millimeter square. Area measurement of planarian size decreases was conducted by using 6 or more independent experiment containing 20 or more animals per experiment. Both the control and *Smed-AKT(RNAi)* animals were photographed using the same magnification and area measurements (per mm) were calculated along the 40 day time course. All areas were averaged across experiments. Average areas taken at the site of amputation were confined to a consistent area with a width of 161.05 pixels and a height of 146.939pixels. Fold change representations were determined by dividing experimental/control conditions. Additional details can be found as previously described [63]. Nikon Eclipse Ti confocal microscope and E Z-C1 software were used to obtain Z-stack images using 20X objective. Z-stacks containing 20 sections at 2-1μm intervals were processed using Image J (1.48v). For all images, Adobe Photoshop and Adobe Illustrator were used to adjust color and brightness.

Quantitative RT-PCR

RNA extraction and quantitative real-time PCR (RT-PCR) reactions were preformed as previously described [63]. RT-PCR from sorted cells was obtained by dissociating >20 animals per condition to extract RNA and prepare cDNA as described before [63]. Equal amount of cells were sorted from both control and experimental

conditions, which in some cases required extra animals in experimental groups to achieve the desired target number of cells. In all cases, gene expressions are relative to the ubiquitously expressed clone H.55.12e [24, 63]. Gene expression corresponds to the mean of triplicated samples of at least two independent experiments with pooled RNA extraction of >20 animals each. Fold change represents standardized expression levels of *Smed-Akt(RNAi)*/Control. Each RNAi time point had its own corresponding control RNA extract.

Whole Mount In Situ Hybridization (WISH)

WISH and fluorescent in situ hybridization were performed on animals fixed in 5% N-acteyl cistein (NAC) solution. Riboprobes were synthesized using T3 and T7 polymerase and digoxigenin-labeled ribonucletide mix with specific PCR templates as previously described [24, 63]. Further details about WISH protocols are found as previously described [65].

Statistical Analysis

All graphs are expressed as mean ± s.e.m. Statistical analyses were performed with GraphPad Prism software. *P* value less than 0.05 were considered statistically significant.

Availability of Data and Materials

The datasets supporting the conclusions of this article are included within the article and its Additional files 1, 2, 3, 4, 5 and 6.

Ethics approval and consent to participate

The study does not involve human data or vertebrate animals.

Additional files

Additional file 1: *Smed-Akt(RNAi)* abrogates the expression of markers of neoblast and their postmitotic progeny. Representative images of fluorescent in situ hybridization of *smedwi-1* (neoblast marker), *Smed-Prog-1* (early neoblast progeny marker) and *Smed-AGAT-1* (late division progeny marker) reveals an important reduction upon *Smed-Akt(RNAi)*. Animals were fixed 30 days post first injection. Experiments were repeated at least twice with ten animals per experiment. Scale bar 200μm. (PDF 433 kb)

Additional file 2: The *Smed-Akt(RNAi)* phenotype exhibits a progressive inhibition of locomotion. (A-D) Videos of live planarian under (A) 15 day, (B) 20 days, (C) 25 days and (D) 30 days after first dsRNA injection. As time progresses, the phenotype exacerbates. All videos were taken under the same brightfield magnification. (PDF 199 MB)

Additional file 3: *Smed-Akt(RNAi)* leads to down regulation of genes expressed in the excretory system and cyst-like phenotype. (A) Representative live images taken along the time course post *Smed-Akt(RNAi)*. The control is seen on the top and live images of days 15, 25 and 35 post RNAi initiation show the progression of a cyst-like phenotype (30/30) (elongation of the head and bloating of the tail). Notice at 15 days post RNAi treatment, the planarian is thinned and stretched when compared to the control (50/50). (B) Fluorescent in situ hybridization of *Smed-CAVII-1* (excretory system). The signal for *Smed-CAVII-1* is less intense in experimental than in control, indicated with arrows in the posterior part of the animals upon *Smed-Akt (RNAi)* 30 days after first dsRNA injection. Experiments were repeated at least twice with ten animals per experiment. Scale bar 200μm. (C) Fold change in *Smed-CAVII-1* gene expression relative to the control over the course of 10, 20 and 30 days post first dsRNA injection. Gene expressions are all relative to the internal control, the ubiquitously expressed clone H.55.12e. Graphs represent mean ± s.e.m. of triplicated samples of two biological replicates with at least ten animals per experiment. Significance (*** < 0.0005 and **** < 0.0001) was determined with one way-ANOVA. (PDF 544 kb)

Additional file 4: *Smed-Akt(RNAi)* reduces the expression of CNS marker. (Left) Representative images of fluorescent in situ hybridization of *Smed-PC2* (central nervous system) expression depicts a reduction (yellow arrows) upon *Smed-Akt(RNAi)*. Animals were fixed 30 days after first dsRNA injection. Experiments consisted of two biological replicates with ten animals per experiment. Scale bar 200μm. (Middle) Heat map depicting the intensity of signal generated by *Smed-PC2* expression. For intensity images and graph, low levels of expression are seen in purple and high levels of intensity are seen in red. Reduced *Smed-PC2* expression is also indicated via yellow arrows. (Right) The graph on the right represent the distribution of intensities from the pictures in the middle featuring anterior to the posterior region of the animal (control in orange and experimental in gray). The intensity measurement was obtained from the center of the anterior to the center of the posterior (white line in the middle) vertical line by using Image J software. Scale bar 200μm. (PDF 357 kb)

Additional file 5: *Smed-Akt(RNAi)* animals fails to induce local and system-wide cell death response during regeneration. (A) Quantification of the TUNEL-positive nuclei at the site of amputation at various time points in regeneration, the control (black) and the experimental group (grey). (B) Heat map depicting the intensity of signal generated by TUNEL-positive cells 6 h post amputation at the site of head regeneration (red line depicts amputation plane). For intensity images and graph, low levels of expression are seen in purple and high levels of intensity in TUNEL-positive cells are seen in yellow/red. The graphs on the right represent the distribution of these intensities from the anterior to the posterior region of the amputation site (control in orange and experimental in gray). The intensity measurement was obtained from the area covered by the semi-transparent vertical line by using Image J software. Scale bar 100μm. (C) Immunostaining of TUNEL-positive nuclei of trunk fragments for both the control and experimental group at 6 h (localized cell death response), 2 days (system-wide cell death response) and 7 days (blastema formation) post amputation. Arrows indicate cell death dynamics, proper dynamics (control) and improper dynamics (*Smed-Akt(RNAi)*). Yellow brackets denote the formation of the blastema and its relative size. Scale bar 200μm. All images are representative of two or more biological replicates consisting of five animals or more per experiment. Graphs represent mean ± s.e.m. of two or more biological replicates and *P* values * < 0.01, ** < 0.001, *** < 0.0005 and **** < 0.0001 were obtained with two way ANOVA. (PDF 391 kb)

Additional file 6: Delayed mitotic response upon amputation in *Smed-Akt(RNAi)* animals. (A) Mitotic activity at the site of amputation at various time points during regeneration, control (black) and *Smed-Akt(RNAi)* in grey. (B) Heat map depicting the intensity of signal generated by H3P-positive cells 4 days post amputation at the site of head regeneration. For intensity images and graph, low levels of expression are seen in purple and high levels of intensity in H3P -positive cells are seen in red. The graphs on the right represent the distribution of these intensities from the anterior to the posterior region of the amputation site (control in orange and experimental in gray). The intensity measurement was obtained from the area covered by the semi-transparent vertical line by using Image J software. Scale bar 100μm. (C) Whole-mount immunostaining of H3P-positive cells on trunk fragments for both the control and experimental group from 0 to 6 h (system-wide mitotic response), 2 to 4 days (localized mitotic response) and 7 days (blastema formation) post amputation. Arrows indicate cell proliferation dynamics during regeneration, proper dynamics (control) and improper dynamics (*Smed-Akt(RNAi)*). Yellow brackets denote the formation of the blastema and its size. Notice, at 4 and 7 days, mitotic activity is localized to the site of amputation. Scale bar 200μm. All images are representative of two or more biological replicates consisting of five animals or more per experiment. Graphs represent mean ± s.e.m. of two or more biological replicates and *P* values * < 0.01, ** < 0.001, *** < 0.0005 and **** < 0.0001 were obtained with two way ANOVA. (PDF 282 kb)

Abbreviations
RNAi: RNA-interference; dsRNA: Double-stranded RNA; PI3K: Phosphoinositide 3-kinase; *Smed-Akt*: The planarian Akt ortholog; PTEN: Phosphatase and Tensin homolog; BrdU: Bromodeoxyuridine analog; CDK1-4: Cyclin-Dependent Kinase 1–4; *Prog-1*: Early division progeny −1; *Agat-1*: L-arginine:glycine amidinotransferase marker of the neoblast late division progeny; FACS: Fluorescence-activated cell sorting; anti-α-Ac-tubulin: antibody against α-acetylated tubulin; TUNEL: Terminal deoxynucleotidyl transferase dUTP nick end labeling; *ChAT*: Choline acetyltransferase; SYNORF1: Immunogen sequence against synapsin-1; *VC1*: Visual cells −1; PC2: Prohormone convertase-2; qPCR: Quantitative polymerase chain reaction; H3P: Phospho-Histone H3 (Ser10) Antibody; WISH: Whole-mount in situ hybridization; s.e.m.: Standard error of the mean.

Competing interests
The authors declare that they have no competing interests.

Authors' contributions
THP, DR, PGB, and NJO performed the research and analyzed data. N.J.O. conceived the study, and participated in its design and coordination, and wrote the final manuscript with PGB. All authors read and approved the final manuscript.

Acknowledgments
We thank Edelweiss Pfister, Elyse Ozamoto, and Frank Weckerle for technical assistance, members of the Oviedo lab, and Dr. Katrina Hoyer for comments on the manuscript. We thank Dr. K Watanabe for VC-1 antibody. The Smed-6G10 and SYNORF antibodies developed by Dr. R. Zayas at SDSU and Dr. E. Buchner at the ICNUW were obtained from the Developmental Studies Hybrydoma Bank, created by the NICHD of the NIH and maintained at the University of Iowa, Department of Biology.

Funding
We acknowledge support from UC Merced, UC Cancer Research Coordinating Committee, Health Sciences Research Institute at UCM, and awards from Jane Vilas and the Hellman Fellows Fund. The NCI and NIGMS of the National Institute of Health supported this research, awards CA176114 and GM109372 to NJO.

Author details
[1]Department of Molecular and Cell Biology, School of Natural Sciences, University of California, 5200 North Lake Road, Merced, CA 95343, USA. [2]Quantitative and Systems Biology Graduate Program, University of California, Merced, CA 95343, USA. [3]Health Sciences Research Institute, University of California, Merced, CA 95343, USA.

Received: 23 September 2015 Accepted: 24 March 2016
Published online: 11 April 2016

References
1. Liao Y, Hung MC. Physiological regulation of Akt activity and stability. Am J Trans Res. 2010;2(1):19–42.
2. Luo HR, Hattori H, Hossain MA, Hester L, Huang Y, Lee-Kwon W, Donowitz M, Nagata E, Snyder SH. Akt as a mediator of cell death. Proc Natl Acad Sci U S A. 2003;100(20):11712–7.
3. Hanada M, Feng J, Hemmings BA. Structure, regulation and function of PKB/AKT–a major therapeutic target. Biochim Biophys Acta. 2004;1697(1–2):3–16.
4. Chuang CL, Lu YN, Wang HC, Chang HY. Genetic dissection reveals that Akt is the critical kinase downstream of LRRK2 to phosphorylate and inhibit FOXO1, and promotes neuron survival. Human Mol Genet. 2014;23(21):5649–58.
5. Kandel ES, Hay N. The regulation and activities of the multifunctional serine/threonine kinase Akt/PKB. Exp Cell Res. 1999;253(1):210–29.
6. Gao X, Neufeld TP, Pan D. Drosophila PTEN regulates cell growth and proliferation through PI3K-dependent and -independent pathways. Dev Biol. 2000;221(2):404–18.
7. Goberdhan DC, Paricio N, Goodman EC, Mlodzik M, Wilson C. Drosophila tumor suppressor PTEN controls cell size and number by antagonizing the Chico/PI3-kinase signaling pathway. Gene Dev. 1999;13(24):3244–58.
8. Scheid MP, Woodgett JR. Unravelling the activation mechanisms of protein kinase B/Akt. FEBS letters. 2003;546(1):108–12.
9. Segrelles C, Garcia-Escudero R, Garin MI, Aranda JF, Hernandez P, Ariza JM, Santos M, Paramio JM, Lorz C. Akt signaling leads to stem cell activation and promotes tumor development in epidermis. Stem cells. 2014;32(7):1917–28.
10. Woodgett JR. Recent advances in the protein kinase B signaling pathway. Curr Opin Cell Biol. 2005;17(2):150–7.
11. Bhatt AP, Damania B. AKTivation of PI3K/AKT/mTOR signaling pathway by KSHV. Front Immunol. 2012;3:401.
12. Chen YL, Law PY, Loh HH. Inhibition of akt/protein kinase B signaling by naltrindole in small cell lung cancer cells. Cancer Res. 2004;64(23):8723–30.
13. Fan QW, Cheng C, Hackett C, Feldman M, Houseman BT, Nicolaides T, Haas-Kogan D, James CD, Oakes SA, Debnath J et al. Akt and autophagy cooperate to promote survival of drug-resistant glioma. Sci Signal. 2010;3(147):ra81.
14. Parcellier A, Tintignac LA, Zhuravleva E, Hemmings BA. PKB and the mitochondria: AKTing on apoptosis. Cell Signal. 2008;20(1):21–30.
15. Tanaka EM, Reddien PW. The cellular basis for animal regeneration. Developmental cell. 2011;21(1):172–85.
16. Sanchez Alvarado A, Tsonis PA. Bridging the regeneration gap: genetic insights from diverse animal models. Nat Rev Genet. 2006;7(11):873–84.
17. Poss KD. Advances in understanding tissue regenerative capacity and mechanisms in animals. Nat Rev Genet. 2010;11(10):710–22.
18. Aboobaker AA. Planarian stem cells: a simple paradigm for regeneration. Trends Cell Biol. 2011;21(5):304–11.
19. Reddien PW. Specialized progenitors and regeneration. Development. 2013;140(5):951–7.
20. Rink JC. Stem cell systems and regeneration in planaria. Dev Gene Evol. 2013;223(1–2):67–84.
21. Wagner DE, Wang IE, Reddien PW. Clonogenic neoblasts are pluripotent adult stem cells that underlie planarian regeneration. Science. 2011;332(6031):811–6.
22. Oviedo NJ, Pearson BJ, Levin M, Sánchez Alvarado A. Planarian PTEN homologs regulate stem cells and regeneration through TOR signaling. Dis Model Mech. 2008;1(2–3):131–43.
23. Cowles MW, Brown DD, Nisperos SV, Stanley BN, Pearson BJ, Zayas RM. Genome-wide analysis of the bHLH gene family in planarians identifies factors required for adult neurogenesis and neuronal regeneration. Development. 2013;140(23):4691–702.
24. Reddien PW, Oviedo NJ, Jennings JR, Jenkin JC, Sanchez Alvarado A. SMEDWI-2 is a PIWI-like protein that regulates planarian stem cells. Science. 2005;310(5752):1327–30.
25. van Wolfswinkel JC, Wagner DE, Reddien PW. Single-cell analysis reveals functionally distinct classes within the planarian stem cell compartment. Cell stem cell. 2014;15(3):326–39.
26. Pellettieri J, Sanchez Alvarado A. Cell turnover and adult tissue homeostasis: from humans to planarians. Annu Rev Genet. 2007;41:83–105.
27. Benbrook DM, Masamha CP. The pro-survival function of Akt kinase can be overridden or altered to contribute to induction of apoptosis. Curr Cancer Drug Targets. 2011;11(5):586–99.
28. Zimmermann KC, Bonzon C, Green DR. The machinery of programmed cell death. Pharmacol Ther. 2001;92(1):57–70.
29. Rane MJ, Klein JB. Regulation of neutrophil apoptosis by modulation of PKB/Akt activation. Front Biosci. 2009;14:2400–12.
30. Pellettieri J, Fitzgerald P, Watanabe S, Mancuso J, Green DR, Sanchez Alvarado A. Cell death and tissue remodeling in planarian regeneration. Dev Biol. 2010;338(1):76–85.
31. Bender CE, Fitzgerald P, Tait SW, Llambi F, McStay GP, Tupper DO, Pellettieri J, Sanchez Alvarado A, Salvesen GS, Green DR. Mitochondrial pathway of apoptosis is ancestral in metazoans. Proc Natl Acad Sci USA. 2012;109(13):4904–9.
32. Peiris TH, Garcia-Ojeda ME, Oviedo NJ. Alternative flow cytometry strategies to analyze stem cells and cell death in planarians. Regeneration 2016, In press.
33. Rompolas P, Azimzadeh J, Marshall WF, King SM. Analysis of ciliary assembly and function in planaria. Meth Enzymol. 2013;525:245–64.
34. Rompolas P, Patel-King RS, King SM. An outer arm Dynein conformational switch is required for metachronal synchrony of motile cilia in planaria. Mol Biol Cell. 2010;21(21):3669–79.
35. Sanchez Alvarado A, Newmark PA. Double-stranded RNA specifically disrupts gene expression during planarian regeneration. Proc Natl Acad Sci U S A. 1999;96(9):5049–54.
36. Thi-Kim Vu H, Rink JC, McKinney SA, McClain M, Lakshmanaperumal N, Alexander R, Sanchez Alvarado A. Stem cells and fluid flow drive cyst formation in an invertebrate excretory organ. eLife. 2015;4.

37. Rink JC, Vu HT, Sanchez Alvarado A. The maintenance and regeneration of the planarian excretory system are regulated by EGFR signaling. Development. 2011;138(17):3769–80.
38. Scimone ML, Srivastava M, Bell GW, Reddien PW. A regulatory program for excretory system regeneration in planarians. Development. 2011;138(20):4387–98.
39. Lapan SW, Reddien PW. Transcriptome analysis of the planarian eye identifies ovo as a specific regulator of eye regeneration. Cell reports. 2012;2(2):294–307.
40. Witchley JN, Mayer M, Wagner DE, Owen JH, Reddien PW. Muscle cells provide instructions for planarian regeneration. Cell reports. 2013;4(4):633–41.
41. Gurley KA, Rink JC, Sanchez Alvarado A. Beta-catenin defines head versus tail identity during planarian regeneration and homeostasis. Science. 2008;319(5861):323–7.
42. Lapan SW, Reddien PW. dlx and sp6-9 Control optic cup regeneration in a prototypic eye. PLoS genetics. 2011;7(8), e1002226.
43. Wenemoser D, Reddien PW. Planarian regeneration involves distinct stem cell responses to wounds and tissue absence. Dev Biol. 2010;344(2):979–91.
44. Ross KG, Omuro KC, Taylor MR, Munday RK, Hubert A, King RS, Zayas RM. Novel monoclonal antibodies to study tissue regeneration in planarians. BMC Dev Biol. 2015;15:2.
45. Clement DL, Mally S, Stock C, Lethan M, Satir P, Schwab A, Pedersen SF, Christensen ST. PDGFRalpha signaling in the primary cilium regulates NHE1-dependent fibroblast migration via coordinated differential activity of MEK1/2-ERK1/2-p90RSK and AKT signaling pathways. J Cell Sci. 2013;126(Pt 4):953–65.
46. Higginbotham H, Guo J, Yokota Y, Umberger NL, Su CY, Li J, Verma N, Hirt J, Ghukasyan V, Caspary T, et al. Arl13b-regulated cilia activities are essential for polarized radial glial scaffold formation. Nat Neurosci. 2013;16(8):1000–7.
47. Christensen ST, Clement CA, Satir P, Pedersen LB. Primary cilia and coordination of receptor tyrosine kinase (RTK) signalling. J Pathol. 2012; 226(2):172–84.
48. Jacoby M, Cox JJ, Gayral S, Hampshire DJ, Ayub M, Blockmans M, Pernot E, Kisseleva MV, Compere P, Schiffmann SN, et al. INPP5E mutations cause primary cilium signaling defects, ciliary instability and ciliopathies in human and mouse. Na Genet. 2009;41(9):1027–31.
49. Scimone ML, Kravarik KM, Lapan SW, Reddien PW. Neoblast specialization in regeneration of the planarian Schmidtea mediterranea. Stem cell reports. 2014;3(2):339–52.
50. Bernards R. A missing link in genotype-directed cancer therapy. Cell. 2012;151(3):465–8.
51. Pal SK, Reckamp K, Yu H, Figlin RA. Akt inhibitors in clinical development for the treatment of cancer. Expet Opin Investig Drugs. 2010;19(11):1355–66.
52. Chen WS, Xu PZ, Gottlob K, Chen ML, Sokol K, Shiyanova T, Roninson I, Weng W, Suzuki R, Tobe K, et al. Growth retardation and increased apoptosis in mice with homozygous disruption of the Akt1 gene. Gene Dev. 2001;15(17):2203–8.
53. Pugazhenthi S, Nesterova A, Sable C, Heidenreich KA, Boxer LM, Heasley LE, Reusch JE. Akt/protein kinase B up-regulates Bcl-2 expression through cAMP-response element-binding protein. J Biol Chem. 2000;275(15):10761–6.
54. Schneider L, Clement CA, Teilmann SC, Pazour GJ, Hoffmann EK, Satir P, Christensen ST. PDGFRalphaalpha signaling is regulated through the primary cilium in fibroblasts. Curr Biol. 2005;15(20):1861–6.
55. Zhu D, Shi S, Wang H, Liao K. Growth arrest induces primary-cilium formation and sensitizes IGF-1-receptor signaling during differentiation induction of 3T3-L1 preadipocytes. J Cell Sci. 2009;122(Pt 15):2760–8.
56. Boehlke C, Kotsis F, Patel V, Braeg S, Voelker H, Bredt S, Beyer T, Janusch H, Hamann C, Godel M, et al. Primary cilia regulate mTORC1 activity and cell size through Lkb1. Nat Cell Biol. 2010;12(11):1115–22.
57. Boletta A. Emerging evidence of a link between the polycystins and the mTOR pathways. Pathogenetics. 2009;2(1):6.
58. Dere R, Wilson PD, Sandford RN, Walker CL. Carboxy terminal tail of polycystin-1 regulates localization of TSC2 to repress mTOR. PLoS One. 2010;5(2), e9239.
59. Fischer DC, Jacoby U, Pape L, Ward CJ, Kuwertz-Broeking E, Renken C, Nizze H, Querfeld U, Rudolph B, Mueller-Wiefel DE, et al. Activation of the AKT/mTOR pathway in autosomal recessive polycystic kidney disease (ARPKD). Nephrol Dial Transplant. 2009;24(6):1819–27.
60. Vriz S, Reiter S, Galliot B. Cell death: a program to regenerate. Curr Top Dev Biol. 2014;108:121–51.
61. Oviedo NJ, Levin M. smedinx-11 is a planarian stem cell gap junction gene required for regeneration and homeostasis. Development. 2007;134:3121–31.
62. Oviedo NJ, Nicolas C, Adams DS, Levin M. Gene knockdown in planarians using RNAi interference. Cold Spring Harb Protocols. 2008;3(10):902–6.
63. Peiris TH, Weckerle F, Ozamoto E, Ramirez D, Davidian D, Garcia-Ojeda ME, Oviedo NJ. TOR signaling regulates planarian stem cells and controls localized and organismal growth. J Cell Sci. 2012;125(Pt 7):1657–65.
64. Newmark PA, Sanchez Alvarado A. Bromodeoxyuridine specifically labels the regenerative stem cells of planarians. Dev Biol. 2000;220(2):142–53.
65. Pearson BJ, Eisenhoffer GT, Gurley KA, Rink JC, Miller DE, Sanchez Alvarado A. Formaldehyde-based whole-mount in situ hybridization method for planarians. Dev Dyn. 2009;238(2):443–50.

Appendix IV

Cell. Mol. Life Sci. (2018) 75:1285–1301
https://doi.org/10.1007/s00018-017-2697-4

Cellular and Molecular Life Sciences

ORIGINAL ARTICLE

SUMOylation controls stem cell proliferation and regional cell death through Hedgehog signaling in planarians

Manish Thiruvalluvan[1,2] · Paul G. Barghouth[1,2] · Assaf Tsur[3] · Limor Broday[3] · Néstor J. Oviedo[1,2,4]

Received: 1 September 2017 / Revised: 21 October 2017 / Accepted: 24 October 2017 / Published online: 2 November 2017

Abstract Mechanisms underlying anteroposterior body axis differences during adult tissue maintenance and regeneration are poorly understood. Here, we identify that post-translational modifications through the SUMO (Small Ubiquitin-like Modifier) machinery are evolutionarily conserved in the Lophotrocozoan *Schmidtea mediterranea*. Disruption of SUMOylation in adult animals by RNA-interference of the only SUMO E2 conjugating enzyme *Ubc9* leads to a systemic increase in DNA damage and a remarkable regional defect characterized by increased cell death and loss of the posterior half of the body. We identified that *Ubc9* is mainly expressed in planarian stem cells (neoblasts) but it is also transcribed in differentiated cells including neurons. Regeneration in *Ubc9*(*RNAi*) animals is impaired and associated with low neoblast proliferation. We present evidence indicating that *Ubc9*-induced regional cell death is preceded by alterations in transcription and spatial expression of repressors and activators of the Hedgehog signaling pathway. Our results demonstrate that SUMOylation acts as a regional-specific cue to regulate cell fate during tissue renewal and regeneration.

Keywords Ubc9 · Regeneration · Genomic instability · Rad51 · Patched

Electronic supplementary material The online version of this article (http://doi.org/10.1007/s00018-017-2697-4) contains supplementary material, which is available to authorized users.

✉ Néstor J. Oviedo
noviedo2@ucmerced.edu

[1] Department of Molecular and Cell Biology, University of California, 5200 North Lake Road, Merced, CA 95343, USA

[2] Quantitative and Systems Biology Graduate Program, University of California, Merced, USA

[3] Department of Cell and Developmental Biology, Sackler School of Medicine, Tel Aviv University, Tel Aviv, Israel

[4] Health Sciences Research Institute, University of California, Merced, USA

Introduction

The planarian *Schmidtea mediterranea* provides unique opportunities to dissect mechanisms controlling cellular decisions in the adult body. Signals influencing cellular behavior during adult tissue maintenance, repair, and cancer are evolutionarily conserved between planaria and mammals [2–8]. Systemic disruption of homologous recombination in *S. mediterranea* leads to dramatic increases in DNA double-strand breaks (DSBs) throughout the body [9]. Intriguingly, cells in the anterior region of the body survive and continue dividing with DSBs, while most cells in the posterior region of the planarian body undergo cell death. Brain signals and the retinoblastoma pathway contribute to the survival of cells with DNA damage in the anterior region [9]. However, it remains elusive which mechanisms operate in the posterior region, where cells with DSB are collectively eliminated by apoptosis.

To better understand mechanism(s) leading to collective cellular death, we searched for phenotypes involving regional defects across different animals. Disruption of the SUMOylation pathway during embryonic development in Drosophila and zebrafish lead to AP axis abnormalities and regional defects associated with cell death [10–12]. SUMOylation is an evolutionarily conserved post-translational modification that regulates a myriad of proteins and cellular processes including chromatin organization, transcription, DNA repair, apoptosis, cell

cycle control, protein trafficking, and signal transduction [13–15]. SUMOylation is a highly dynamic and reversible process whereby the small ubiquitin-like modifier (SUMO) is attached to target proteins, acting as a molecular switch that quickly controls protein activity [13]. The SUMOylation cascade requires *Ubc9*, the sole E2 conjugating enzyme necessary for properly attaching SUMO to target proteins [16–20]. Inactivation of *Ubc9* is embryonically lethal, limiting our understanding about the role of SUMOylation in the maintenance and repair of adult tissues [10–12, 21].

Our present findings show that the SUMO pathway is evolutionarily and functionally conserved in the Lophotrocozoan *S. mediterranea*. Disruption of the SUMOylation pathway in planarians with RNA-interference of *Ubc9* lead to regional defects characterized by loss of the posterior half of the body (tail), systemic loss of the adult stem cells and increase in DNA damage, specifically DSBs. In addition, *Ubc9* is required for posterior specific tissue maintenance and regeneration through the regulation of the Hedgehog (Hh) pathway. Altogether, we propose that SUMOylation controls regional fate decisions by balancing activators and repressors of the Hh signaling.

Results

The SUMOylation pathway is conserved in the planarian *Schmidtea mediterranea*

The SUMOylation pathway is cyclic in nature and can be broadly summarized in five steps: SUMO maturation, activation, conjugation, attachment and its removal from the target protein (Fig. 1a). Components of the SUMOylation pathway are evolutionarily conserved from yeast through mammals [13]. The *S. mediterranea* genome includes homologs of all components of the general SUMOylation pathway (Fig. 1b). Interestingly, the two SUMO proteins we identified in planarians are the homologs of SUMO-2/3 and not SUMO-1 (Figure S1A, B). Consistent with other organisms, there is only one homolog for the SUMO E2 conjugating enzyme UBC9 (*Smed-Ubc9*, henceforth *Ubc9*). In most cases, *Ubc9* is known to be the linchpin controlling the SUMOylation pathway and acts as a rate-limiting step for SUMO conjugation [13]. Phylogenetic analysis of UBC9 across different phyla confirms its evolutionary conservation, which in the case of planarians is 73% identical to its human counterpart (Fig. 1c, S1C). These results suggest that the SUMO pathway is evolutionarily conserved in *S. mediterranea*, a Plathyhelmith member of the Lophotrocozoan clade.

SUMOylation is required for regional tissue maintenance

To functionally characterize the role of *Ubc9* in *S. mediterranea*, we performed RNA interference by feeding with dsRNA expressing bacteria mixed with liver six times every three days, and animals were fixed 25 days after the first dsRNA feeding (25 dpf) (Fig. 2a). Animals subjected to *Ubc9*(*RNAi*) exhibited macroscopic signs of tissue degradation, characterized by darkening of the epithelia in the post-pharyngeal region, followed by formation of lesions and complete loss of their tail by day 25 and onward (Fig. 2b). After 25 dpf, the experimental group undergoes rapid tissue deterioration and begins to lyse (Fig. 2c). We noticed that *Ubc9*(*RNAi*) animals have an apparent reduction in size before losing their tail, which was confirmed by the reduction in surface area that started 15 dpf (Fig. 2d). Despite the tissue loss being restricted to the posterior region, qPCR experiments revealed that *Ubc9* gene expression was effectively downregulated throughout the whole organism at 25 dpf (Fig. 2e).

Ubc9 is expressed in neoblasts and post-mitotic cells

To further understand *Ubc9* function in planarians, we characterized its spatial distribution with in situ hybridization and found it is ubiquitously expressed throughout the organism (Fig. 3a). Interestingly, *Ubc9* expression is dramatically reduced 24 h after lethal irradiation (6 k rads), which is known to eliminate planarian stem cells or neoblasts [22], and remains at that level 7 days post-irradiation (dpi) (Fig. 3a). In addition, we detected residual *Ubc9* expression surrounding the pharynx and the periphery of the brain at 7 dpi (Fig. 3a). Distribution of *Ubc9* expression among neoblasts and post-mitotic cells was further confirmed using the single-cell sequencing database [1] (Fig. 3b, c). Furthermore, the single-cell analysis also reveals that *Ubc9* expression is present across all neoblast subclasses and in a subset of differentiated cells including neural, epidermal, and gut (Fig. 3c, S2). Together, these findings suggest that *Ubc9* is mainly expressed in neoblasts but it is also transcribed in post-mitotic cells.

Ubc9 is required for the proper function of stem cells

Neoblasts are the only proliferative cells in planarians, and thus we evaluated mitotic activity by whole-mount immunostaining against phosphorylated histone-3 (H3P) at different time points after *Ubc9*(*RNAi*) (Fig. 3d). These experiments revealed a three-fold reduction in $H3P^{+}$ cells in the experimental group but residual mitotic activity remained (Fig. 3d, e). The macroscopic regional effects are visible by day 15 after *Ubc9*(*RNAi*) (Fig. 2c), but the mitotic decrease

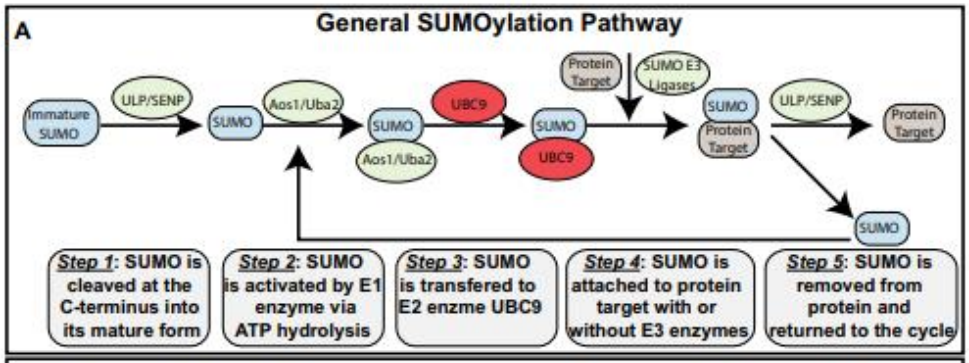

B

	Yeast	Humans	Planarians
Small ubiquitin-related modifiers	Smt3p	SUMO-1, SUMO-2, SUMO-3, SUMO-4	SUMO-2, SUMO-3
Activating enzyme (E1)	Aos1p-ba2p	Aos1 (Sae1)-UBA2 (Sae2)	SAE1, SAE2
Conjugating enzyme (E2)	Ubc9p	UBC9	UBC9
Ligating Enzyme (E3)	Siz1p,Siz2p, Mms21p, Zip3p	PIAS1, PIAS3, PIASxa, PIASxb, PIASy, Mms21	PIAS1, PIAS2
SUMO Protease	Ulp1p, Ulp2p	SENP1-7	ULP1, ULP2, ULP3

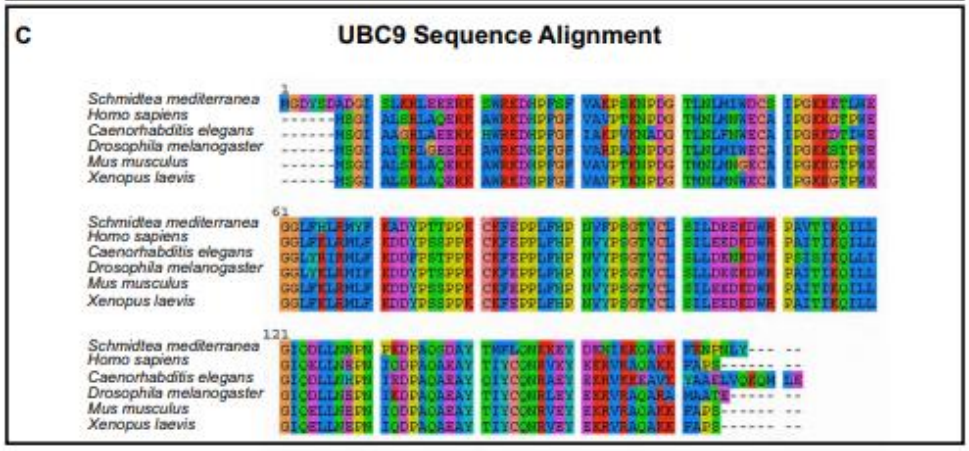

Fig. 1 The SUMOylation pathway is conserved in the planarian *Schmidtea mediterranea*. **a** A general outline of the SUMOylation pathway with the names of enzymes involved and a brief description of major steps in the process. **b** A list of SUMO pathway components found in humans and their homologs in yeast and *S. mediterranea*. **c** Protein alignment of planarian UBC9 and homologs found in humans (NP_003336.1), mice (EDL06246.1), *Drosophila* (NP_476978.1), *C. elegans* (NP_001023158.1) and *Xenopus* (NP_001080758.1). Human and planarian UBC9 protein sequences are 73% identical

is noted by day 20–25 post-RNAi. This suggests that tissue loss precedes effects in neoblast proliferation. To evaluate whether there was a regional reduction in mitotic activity, we separately quantified $H3P^+$ cells in the anterior and posterior regions. Each animal was split into two parts along the AP axis, considering the prepharyngeal as the anterior region and the remaining tissue including the pharynx as the posterior region (Fig. 2e). Such delimitation was made to account for the dramatic reduction in the tail region in the phenotype. This analysis demonstrated that loss of mitotic

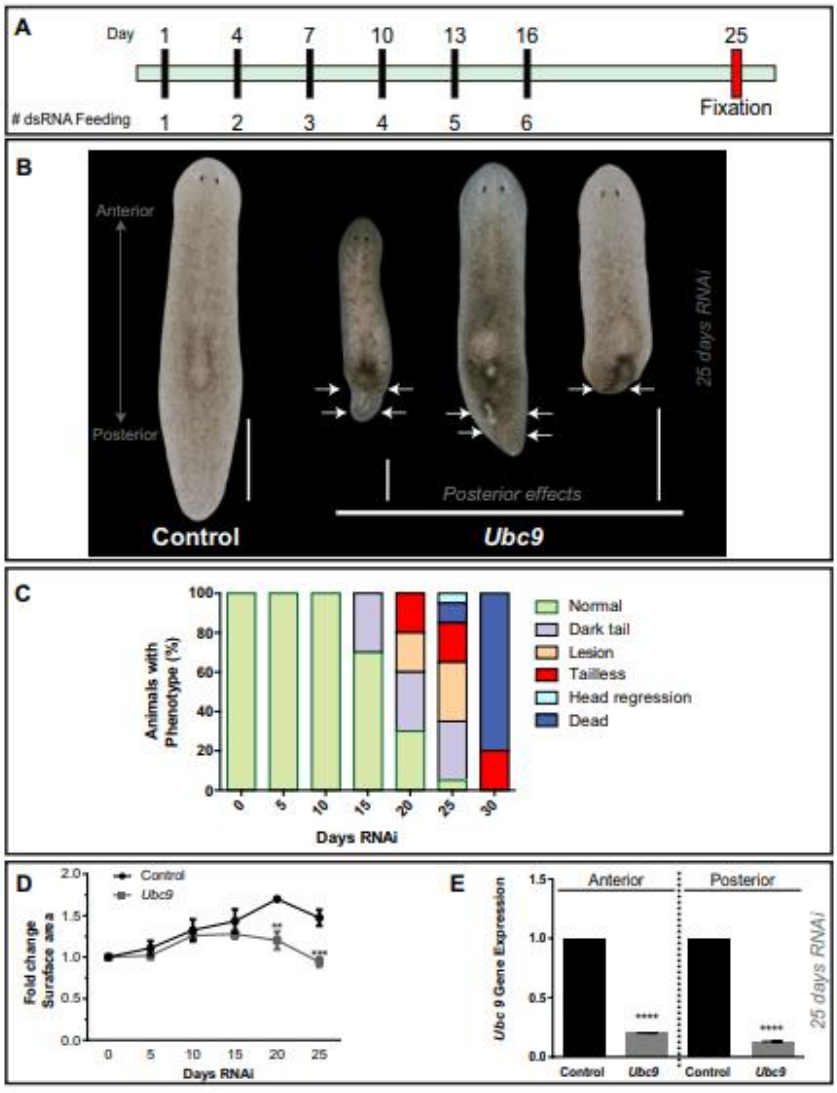

Fig. 2 *Ubc9* is required for regional tissue maintenance. **a** RNAi schedule based on feeding with bacterially expressed dsRNA to knockdown *Ubc9* expression. All controls were fed either *Unc22* or *gfp*. Black bars represent feeding days and red represents fixation. **b** Representative images of control and *Ubc9*(*RNAi*) animals 25 dpf. The arrows indicate different abnormalities including dark tail, lesions, and tail loss. $n = 75$ total animals used in three biological replicates. Scale bar = 200 µm. Note the scale bar on the right applies for the two pictures on the right portion of the figure. **c** Histogram illustrates the progression of the *Ubc9* phenotype based on macroscopic abnormalities observed in "**b**". **d** Change in surface area over the 25-day RNAi time course in controls and *Ubc9*(*RNAi*) animals. The experiment involves 15 animals per time point and three biological replicates. **e** Levels of *Ubc9* expression measured with qPCR. The results show that the RNAi knockdown protocol is effective at reducing transcript levels of *Ubc9* in both anterior and posterior regions. Data obtained from triplicates per experiment of at least two biological replicates. ****$p < 0.0001$; two-way ANOVA

activity was halved along both the anterior and the posterior regions (Fig. 3f).

Next, we analyzed the effects of *Ubc9* downregulation on cell populations and cell cycle dynamics using flow cytometry (FACS) [23]. Pooled cells from anterior and posterior regions were processed separately in both control and *Ubc9*(*RNAi*) animals 25 dpf. First, we examined cellular populations associated with neoblasts (X1) and early and late post-mitotic progeny (X2 and Xins, respectively) [23, 24]. There was an overall reduction in the proliferative X1 population across the AP axis, which was more noticeable (– 4 fold) in the posterior region of the experimental group (Fig. 3g). The decline in the X1 cells is consistent with the reduction in mitotic activity (Fig. 3d–f). However, *Ubc9*(*RNAi*) has an unexpected increase on post-mitotic X2 cells in the anterior region, whereas the posterior region shows the expected decline (Fig. 3g). The mechanism behind this observation remains to be investigated.

Taken together, whole mount in situ hybridization and gene expression levels demonstrate that *Ubc9*(*RNAi*) lead to severe downregulation in markers of X1, X2 and Xins cells (*Smedwi-1*, *Smed-prog-1* and *Smed-AGAT-1*, respectively) (Figure S3A, B). Interestingly, the dramatic reduction in the expression of early progeny marker (*Smed-prog-1*) in the tail region and the persistence of some positive *Smed-prog-1* cells in the anterior region may imply that the enrichment of the X2 fraction is specific to the anterior region of *Ubc9*(*RNAi*) animals. Nonetheless, this finding demonstrates that *Ubc9* is required for the proper function of neoblasts and differentiated cells. Previous studies have shown that blockage in G1 phase of the cell cycle is observed in other organisms after *Ubc9* depletion [25–28]. Consistently, we found in planarians that *Ubc9*(*RNAi*) leads to an increase in G1 phase (74.1 vs 81.1) and a decrease in S and G2/M (13.9 vs 6.02) phases of the cell cycle along the AP axis (Fig. 3h). In addition, the expression levels of genes that are evolutionarily conserved and commonly associated with G1, S and G2/M transitions were significantly decreased ($p < 0.0001$ two-way ANOVA) in *Ubc9*(*RNAi*) animals (Fig. 3i). This is consistent with both a reduction in neoblast numbers and a concomitant reduction in cell cycle as observed in Figs. 3d–h. Together, these results suggest that *Ubc9* is required for maintenance of neoblasts and proper cell cycle transition.

Downregulation of SUMO proteins results in regional defects

We also tested whether RNAi of *S. mediterranea* SUMO proteins lead to gross morphological defects observed with *Ubc9*(*RNAi*). We identified two SUMO homologs in the *S. mediterranea* genome, which we termed *Smed-SUMO2* and *Smed-SUMO3* (Figure S1A, B). Individual RNAi of each component did not lead to behavioral or gross morphological defects, probably due to compensatory roles. However, double RNAi between the small ubiquitin-related modifiers *Smed-SUMO2* and *Smed-SUMO3* did produce regional defects like those noted after *Ubc9*(*RNAi*). Performing *Smed-SUMO2* + *SUMO3*(*RNAi*) led to accelerated tail loss in a fraction of the animals (i.e. 15% animals, 20 dpf) (Figure S4A). The remaining animals gradually underwent regional tissue loss and eventually died. Further evaluation of mitotic activity revealed that simultaneous downregulation of *Smed-SUMO2* + *SUMO3* dramatically reduced the number of proliferative cells across the animal (Figure S4B, C). Analysis of gene expression with markers for neoblasts and post-mitotic cells also demonstrated a dramatic decrease in expression that is consistent with the effects of *Ubc9*(*RNAi*) (Figure S4D). Collectively, these results suggest that regional defects and systemic neoblast dysfunction are specific to the disruption of SUMOylation through RNAi of *Ubc9* and/or *Smed-SUMO2* + *SUMO3*. For simplicity and consistency, we focused on analysis of the SUMO pathway through the downregulation of *Ubc9*.

Ubc9-systemic loss of function leads to regional cell death

To investigate the cause of regional tissue loss after *Ubc9*(*RNAi*), we analyzed cell death through whole-mount immunostaining and FACS [9, 23]. First, immunostaining assay with cell death marker caspase-3; which has been previously characterized in planarians [29], revealed an increase in cell death throughout the animal, with a prominent expression in the posterior region 25 dpf (Fig. 4a). In some instances, cell death signal was associated with cellular clusters, limiting our capacity to manually count dying cells. Instead, we chose to quantify the signal by generating an intensity profile of the fluorescence from anterior to posterior body axis. We found the intensity to be higher in *Ubc9*(*RNAi*), with a four time increase in cell death in the posterior region (Fig. 4b). *Ubc9*(*RNAi*)-induced cell death distribution was further analyzed by FACS using Annexin V, a marker of apoptosis that we have previously characterized in planarians [23]. Anterior and posterior fragments were processed separately and the results show that Annexin V^+cells are markedly increased in the posterior region of the experimental group (Fig. 4c). These results are consistent with regional cell death found in immunostaining using caspase-3 antibody. Furthermore, gene expression of *BCL2*, a survival signal marker [30], is importantly reduced in the posterior region when compared to the anterior region (Fig. 4d). Taken together, our findings demonstrate that *Ubc9* is essential to cellular survival and regional tissue maintenance.

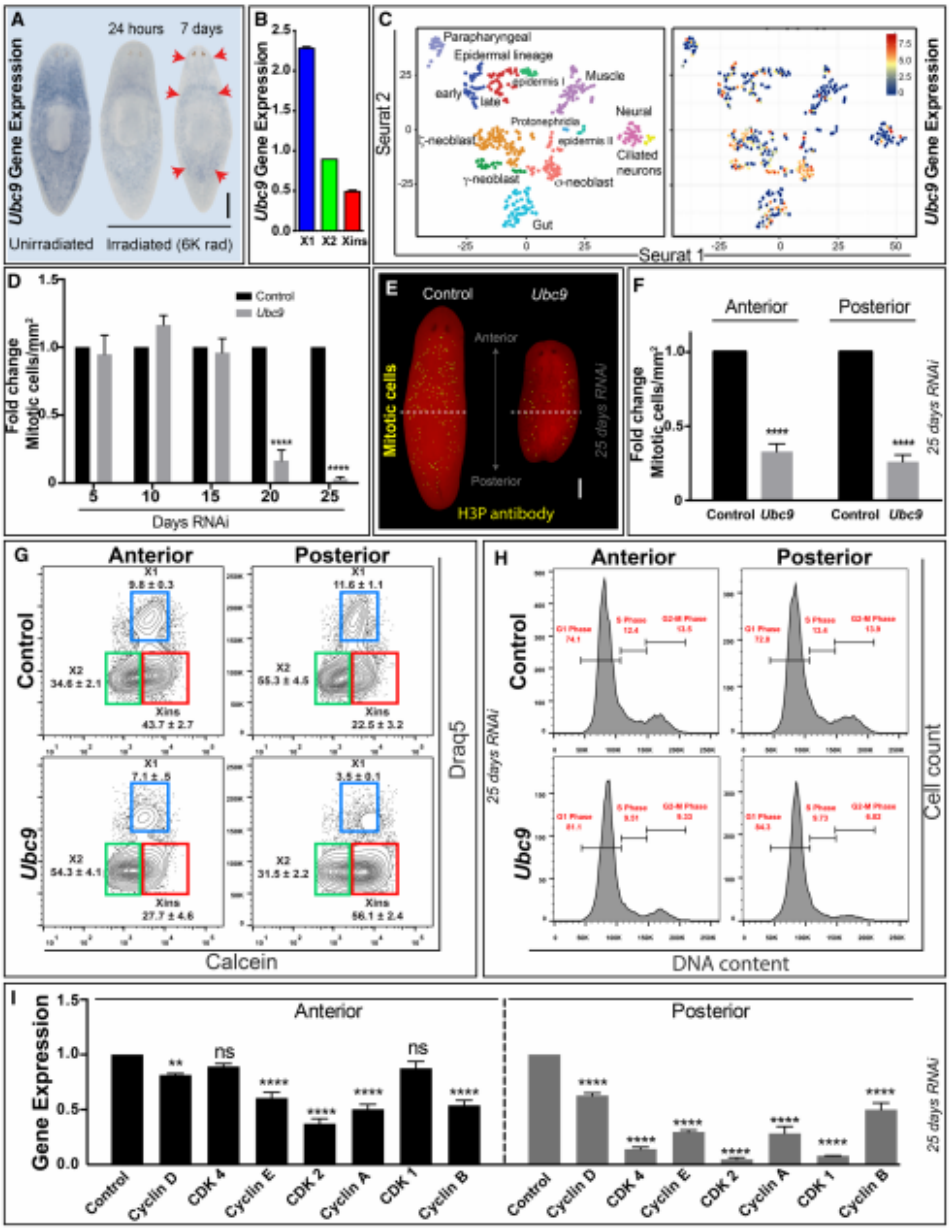
A
24 hours
7 days
Ubc9 Gene Expression
Unirradiated
Irradiated (6K rad)
B
Ubc9 Gene Expression
X1 X2 Xins
C
Parapharyngeal
Epidermal lineage
Muscle
epidermis I
early
late
Protonephridia
Neural
epidermis II
Ciliated neurons
σ-neoblast
γ-neoblast
Gut
Seurat 1
Seurat 2
Ubc9 Gene Expression
D
Control
Ubc9
Fold change Mitotic cells/mm²
Days RNAi
E
Control
Ubc9
Anterior
Posterior
Mitotic cells
25 days RNAi
H3P antibody
F
Anterior
Posterior
Fold change Mitotic cells/mm²
Control Ubc9 Control Ubc9
25 days RNAi
G
Anterior
Posterior
Control
Ubc9
X1
X2
Xins
Draq5
Calcein
H
Anterior
Posterior
Control
Ubc9
25 days RNAi
Cell count
DNA content
I
Anterior
Posterior
Gene Expression
Control
Cyclin D
CDK 4
Cyclin E
CDK 2
Cyclin A
CDK 1
Cyclin B
25 days RNAi

◂**Fig. 3** *Ubc9* is necessary for stem cell function and proper cell cycle transition. **a** Whole mount in situ hybridization using antisense probe against *Ubc9*. Gene expression is found ubiquitously distributed along the AP axis (left) and is dramatically reduced 24 h after lethal exposure to gamma irradiation (6 K rads) and remained at that level for 7 days post-irradiation (red arrows). Experiments involved three biological replicates with 10 animals per experiment. **b** *Ubc9* gene expression levels in different cell populations (X1: proliferative cells, X2: early post-mitotic progeny, and Xins: late post-mitotic progeny). **c** t-SNE plot of single cells displaying clusters of neoblasts and differentiated cells (left), along with the overlaid *Ubc9* expression (right). The respective reference for the level of expression based on the colored gradient scale blue to red (low–high, respectively). The gene expression result for "**b** and **c**" were obtained from the planaria single-cell database hosted by the Reddien Lab at the Whitehead Institute for Biomedical Research (https://radiant.wi.mit.edu/app/) [1]. **d** Time course of mitotic activity along the AP axis, expressed as fold change in reference to the control at each time point. **e** Spatial distribution of mitotic activity in whole mount immunostaining against phospho-histone H3 (Ser10) (H3P) at 25 dpf *Ubc9*(*RNAi*). Dashed line divides anterior and posterior regions of the animal. All scale bars = 200 µm. **f** Fold change mitotic counts obtained independently from the anterior or posterior regions. Mitotic levels involved three biological replicates and more than 40 animals. **g** FACS analysis using DRAQ5, a nuclear dye and Calcein, a live cell marker, in either anterior or posterior regions of control and *Ubc9*(*RNAi*) animals 25 dpf. Blue, green and red squares represent X1, X2 and Xins populations, respectively. **h** Cell cycle analysis using DRAQ5 DNA dye in AP regions of control and *Ubc9*(*RNAi*) animals 25 dpf. Red bars represent percentage of cells at different phases of cell cycle. All FACS analysis performed with more than 10,000 cells and results are representative of three experiments with about 40 animals total. **i** Gene expression levels of various cell cycle markers necessary for proper G1/S and G2/M transition in AP regions of control and *Ubc9*(*RNAi*) animals 25 dpf. Gene expression portrayed as fold change normalized to control. $^{**}p < 0.01$; $^{***}p < 0.001$; $^{****}p < 0.0001$; two-way-ANOVA

Ubc9 is required to maintain genomic integrity along the anteroposterior axis

Ubc9 downregulation in planarians resembles regional features of the *Rad51* phenotype, which is characterized by an increase in DNA double stranded breaks (DSBs) throughout the body [9]. To assess DNA integrity in *Ubc9*(*RNAi*) animals, we collected cells at different dpf and performed (1) COMET assay, (2) karyotyping and (3) immunostaining against markers required for early DNA damage response and repair through homologous recombination (HR). COMET assay was adjusted to detect DSBs [9, 31] and our results confirmed an increase in DNA damage equally distributed along the AP axis and is present as early as 10 dpf (Fig. 5a). The presence of DSBs was accompanied by a two fold increase in chromosomal abnormalities detected by karyotyping (Fig. 5b). Deletions, fusions and dicentric chromosomes characterized the abnormalities that affected all four pairs of chromosomes of the asexual *S. mediterranea* CIW4 strain. The spatial distribution of DNA damage in planarians can be detected with whole mount immunostaining using antibodies against ϒH2Ax (Figure S5) [31] and RAD51 [9, 32]. Our results with these antibodies revealed an increased signal for both in the experimental group (Fig. 5c, d). Interestingly, increase in signal intensities for both antibodies were consistently displayed in clusters in the pre-pharyngeal and post-pharyngeal area for 70% of the animals (Fig. 5c, d). Western blot also confirmed the increase in RAD51 signal after *Ubc9*(*RNAi*) (Fig. 5e, f). Increase in ϒH2Ax and RAD51 levels suggest that the mechanism for sensing DNA damage is active after *Ubc9*(*RNAi*).

To repair DSBs, RAD51 must be translocated from the cytoplasm to the nucleus. Thus, we tested whether RAD51 translocation was compromised in *Ubc9*(*RNAi*) animals. Exposure to gamma irradiation induces DSBs, and RAD51 protein expression and nuclear translocation is at a maximum after 5 days post sub-lethal irradiation (1.25 K rads) [9]. Therefore, control and *Ubc9*(*RNAi*) animals were exposed to sub-lethal irradiation and the cells were harvested after 5 days to evaluate RAD51 sub-cellular location (Fig. 5g). This experiment showed that RAD51 nuclear localization was observed in most of the control cells (~ 80%) whereas smaller fraction of cells (31%) in the experimental group exhibited the same behavior (Fig. 5h). In summary, these data indicate that *Ubc9* functions in maintaining DNA integrity and regulating RAD51 localization are conserved also in *S. mediterranea*.

Regional defects in *Ubc9*(*RNAi*) animals are mediated through modulation of the Hedgehog pathway

Posterior identity in planarians is associated with proper regulation of the evolutionarily conserved Hedgehog (Hh) pathway [16, 33, 34]. Specifically, regional determination of the posterior tissue is established through *Patched* (*Ptc*)-mediated signaling of *Hh* [33, 34]. Hh signaling in planarians is required for ciliogenesis, regeneration [16, 33, 34] and more recently, it has been linked to neural and glial function [17, 35]. However, it is still unknown whether this pathway is necessary for regional information in uninjured animals. Hh signaling activity can be assayed by gene expression analysis of anterior and posterior polarity markers, secreted frizzled protein 1 (*sfrp1*) and frizzled-like protein 4 (*fz4*), respectively [34]. Strikingly, the expression of both *fz4* and *sfrp1* was dramatically altered in uninjured *Ubc9*(*RNAi*) animals, while it remained without change in the control group. The expression of *sfrp1* was elevated and appeared ectopically in the lateral and tail regions at day 10 when compared to control animals (Fig. 6a, red arrows). The pattern and level of expression of *srfp1* decreased to wild-type at day 15. Inversely, *fz4* appeared ectopically in the head and lateral cells at day 10 but was strongly elevated at day 15. Both mRNAs were downregulated when the tail phenotype became obvious (Fig. 6a). This suggests that the

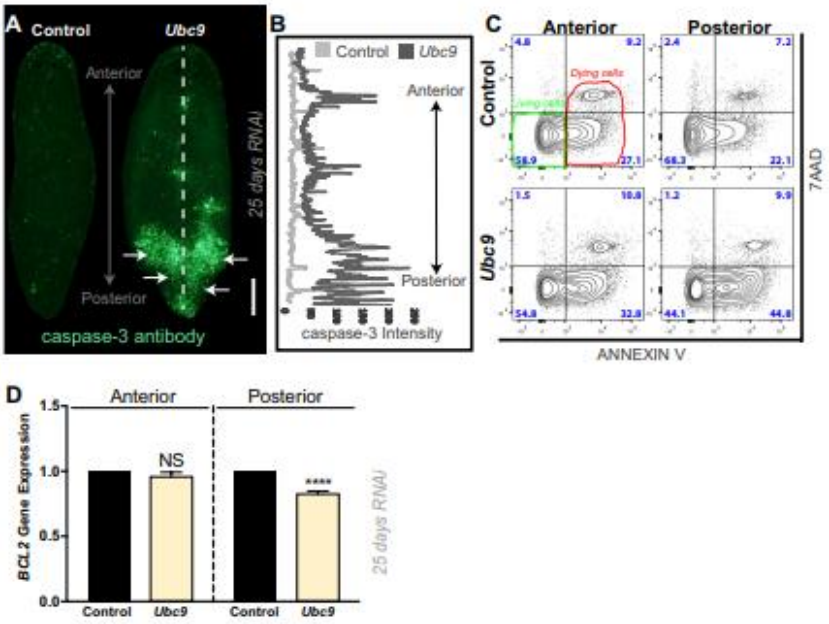

Fig. 4 *Ubc9*-loss of function leads to regional cell death. **a** Whole mount immunostaining against caspase-3, a marker for cell death, in control and *Ubc9*(*RNAi*) animals. About 65% of experimental animals showed similar caspase-3 signal distribution at 25 dpf. Immunostainings involved three biological replicates and more than 40 animals. Scale bars = 200 μm. **b** Intensity of capase-3 signal from anterior to posterior (white line) of control and *Ubc9*(*RNAi*) animals. Intensity signal quantification involved three biological replicates and more than 20 animals. **c** FACS analysis staining against Annexin V, a marker for apoptosis, and 7AAD, a cell viability marker, in AP regions of control and *Ubc9*(*RNAi*) animals 25 dpf. Annexin V-/7 AAD- quadrant includes viable cells (outlined green). Annexin V +/7 AAD– and Annexin V +/7 AAD + indicate cells that are in early and late (necrotic) stages of cell death, respectively (outlined red). Blue numbers in each quadrant indicate the percentage of cells with that staining profile. Data is representative of two experiments with $n > 40$ each. **d** Fold change of *BCL2* gene expression in anterior and posterior regions normalized to control group

downregulation of *Ubc9* may lead to transient ectopic activation of Hh signaling.

We next analyzed the expression of the inhibitor *Ptc* and activators *Hh* and *Smoothened* (*Smo*) at early and late phases of the *Ubc9* phenotype (i.e. 10, 15 and 25 dpf). *Ptc* expression shows a steady increase in days 15–25 that is more than double at late phases of the phenotype (Fig. 6b, c). *Hh* expression decreased at day 10 but increases at day 15 dpf and returned to basal levels at the late stage, while *Smo* expression appears stable. This suggests that depletion of *Ubc9* drives the pathway off equilibrium, leading to abnormal fluctuations in gene expression (Fig. 6b, c). To further examine the importance of the Hh pathway in mediating the loss of posterior homeostasis in *Ubc9*(*RNAi*) animals, we performed double RNAi experiments involving *Ptc*, *Hh*, and *Ubc9*. Different RNAi strategies were assayed and the most consistent results were obtained by first knocking-down either *Ptc* or *Hh* followed by *Ubc9* in a 40 days schedule that included a total of 14 feedings with dsRNA (Fig. 6d). Animals subjected to double RNAi *Ptc* + *Ubc9* displayed similar dynamics as in *Ubc9* alone (Figs. 2c, 6e). However, simultaneous downregulation of *Hh* + *Ubc9* led to more aggressive defects in the posterior region that appeared at day 10 and were lethal for 20% of the animals by day 20 of the *Ubc9*(*RNAi*) (Fig. 6e). The increased regional defects after *Hh* + *Ubc9*(*RNAi*), suggest synergistic/parallel contribution between these factors.

Sumoylation is required for planarian regeneration

We reasoned that if *Ubc9*(*RNAi*) leads to deregulation of the Hh pathway, then amputation would result in deficient tail and brain regeneration [33–35]. Control and *Ubc9*(*RNAi*) animals were amputated pre- and post-pharyngeally at 18

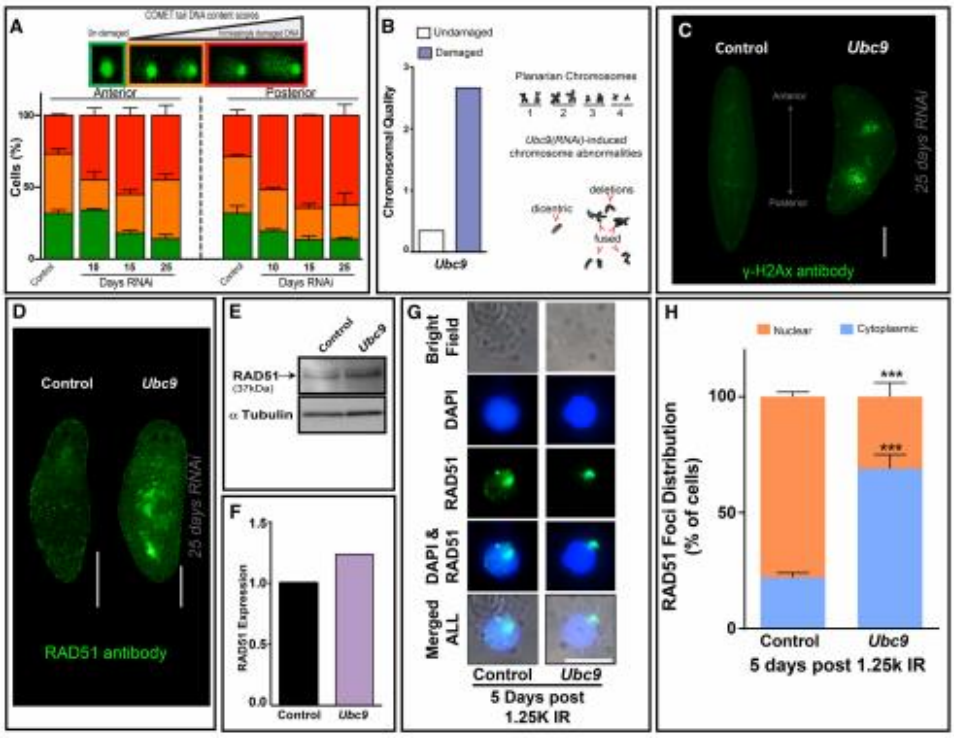

Fig. 5 *Ubc9* is required to maintain genomic integrity along the anteroposterior axis. **a** COMET assay, single gel electrophoresis under alkaline conditions, was performed in AP regions of control and *Ubc9*(*RNAi*) animals at10, 15, and 25 dpf. Visual scoring was used to quantify DNA damage. Color-coded key at bottom represents undamaged (green), moderate damage (orange) and extremely damaged DNA (red) shown in either anterior or posterior regions. DNA damage scale reference is similar to the one used in Peiris et al. 2016b. Downregulation of *Ubc9* leads to systemic accumulation of DNA damage as early as day 10 when compared to controls. Approximately 40 cells were counted for each DNA condition in two biological replicates. **b** Chromosome quality (not damage and damaged) normalized to control in *Ubc9*(*RNAi*) 25 dpf animals. Experiment was repeated twice. **c** Whole mount immunostaining against gamma H2AX antibody in control and *Ubc9*(*RNAi*) animals 25 dpf. Total number of animals was 20 and $n = 2$ biological replicates. **d** Whole mount immunostaining against human RAD51 antibody in control and *Ubc9*(*RNAi*) animals 25 dpf. Total number of animals was 15 and experiment was repeated twice. Scale bars = 200 μm and images are representative of approximately 70% of the animals in each condition. **e**, **f** Western-blot and subsequent quantification for RAD51 in control and *Ubc9*(*RNAi*) animals. Alpha tubulin was used as an internal control. Protein was extracted from $n > 30$ animals. **g** Spatial distribution of RAD51 immunostaining (green) in reference to the cell nucleus (stained with DAPI, blue) in control and *Ubc9*(*RNAi*) 18 dpf and 5 days after sub-lethal irradiation (1.25 k rads). RAD51 subcellular localization to the nucleus is at a maximum at this point in time. Scale bar = 10 μm. **h** Quantification of cells with RAD51 + foci in the nucleus and cytoplasm in control and *Ubc9*(*RNAi*) 18 dpf and 5 days after sub-lethal irradiation (1.25 k rads). Approximately 50 cells were counted for each condition in two biological replicates and all RAD51 stainings were performed with human RAD51 antibody

dpf, which is an early stage of the phenotype where most animals still retain posterior tissue but fluctuations in both *Ptc* expression and the downstream Hh components (*fz4* and *sfrp1*) are detected (Fig. 6b, c). Animals were then allowed to regenerate for 7 days (7 dpa) and blastema formation was evaluated (Fig. 7a). *Ubc9*(*RNAi*) animals formed small anterior blastemas and remarkably, lacked posterior blastema formation (Fig. 7b, c). To further examine the mechanism limiting regeneration, we assayed the mitotic response after amputation and revealed that *Ubc9*(*RNAi*) animals can sense injury, but respond with limited mitotic capability (Fig. 7d). Next, we considered whether regeneration of the nervous system was compromised after *Ubc9*(*RNAi*). Two main observations were made: (1) the size of the regenerated

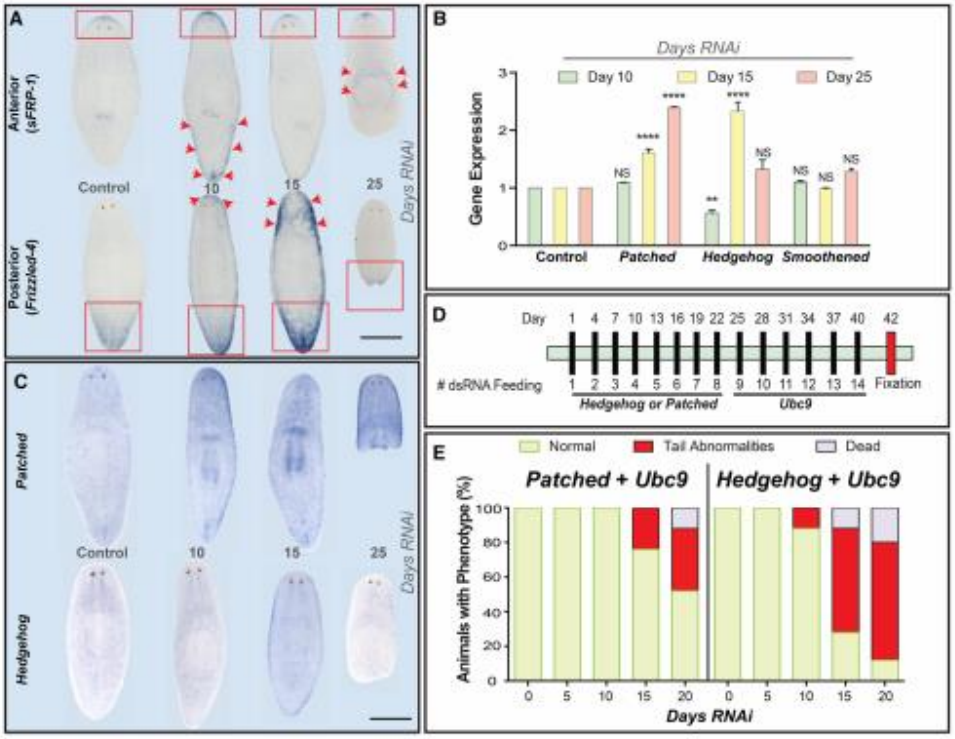

Fig. 6 Regional defects after *Ubc9(RNAi)* are mediated through repression of Hedgehog pathway. **a** Whole mount in situ hybridization expression of *sfrp-1* (anterior polarity marker) and *fz4* (posterior polarity marker) in control and 10, 15 and 25 dpf *Ubc9(RNAi)* animals. Red arrows indicate abnormal gene expression. Scale bars = 200 µm. Note that controls for each time point were executed but no apparent change in gene expression was observed over time –not shown. **b** Gene expression levels of *Patched*, *Hedgehog* and *Smoothened* after *Ubc9(RNAi)* animals at 10, 15 and 25 dpf. Gene expression is given in fold change normalized to control. **c** Whole mount in situ hybridization expression of *Patched* and *Hedgehog* in control and 10, 15 and 25 dpf *Ubc9(RNAi)* animals. Scale bars = 200 µm. **d**. RNAi schedule based on feeding with bacterially expressed dsRNA to perform double knockdown of *Hedgehog* or *Patched* and *Ubc9*. All controls were fed either *Unc22* or *gfp*. Black bars represent feeding days and red represents fixation. **e** Histogram depicts occurrence of tail abnormalities in *Hedgehog* + *Ubc9* and *Patched* + *Ubc9* animals. Data is representative of $n = 30$ animals consisting of three biological replicates

brain was reduced by half, consistent with compromised neurogenesis [35] (Fig. 7e, f) and (2) ventral nerve cords were truncated, likely due to the lack of posterior regeneration (Fig. 7e). Furthermore, we performed similar amputation experiments on double RNAi animals (Fig. 7g) and the regenerative outcome of these double knockdowns between *Ptc*, *Hh*, and *Ubc9* revealed that 100% of animals subjected to double RNAi *Ptc* + *Ubc9* and *Hh* + *Ubc9* presented lack of posterior blastema formation (Fig. 7h). This observation is in accordance with the posterior homeostasis synergistic/parallel effects (Fig. 6e). In addition, during regeneration, the anterior defects were more prevalent in the *Ptc* + *Ubc9(RNAi)* (over 90% of the animals), whereas 35% of the *Hh* + *Ubc9* showed regenerative defects in the anterior end as in single *Ubc9(RNAi)* (Fig. 7b). These results demonstrate that *Ubc9* is required for anterior and posterior blastema formation and organogenesis following injury.

Discussion

Regional signals contribute to cell fate decisions in the adult body. There is a tendency for cells in the anterior part of the body to have a superior proliferative response in health

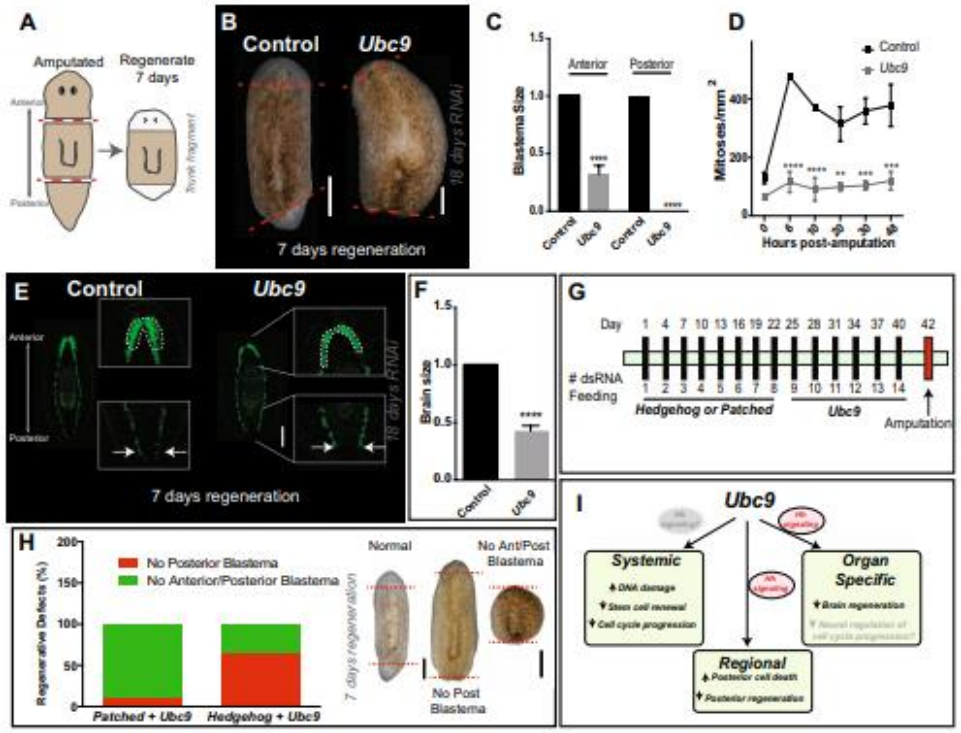

Fig. 7 *Ubc9* is required for proper regeneration. **a** Schematic representation of regeneration experiments on control and *Ubc9*(*RNAi*) animals 18 dpf. **b** Live pictures of control and *Ubc9*(*RNAi*) 18 dpf animals 7 days post amputation (7dpa). **c** Blastema size in control and *Ubc9*(*RNAi*) animals expressed as fold change relative to control. In all experiments used more than 30 animals in three biological replicates. **d** Trunk fragments generated from control and *Ubc9*(*RNAi*) 18dpf animals were fixed at 0, 6, 10, 20, 30 and 48 h post amputation. Mitotic cell numbers were determined via H3P staining and expressed as H3P + foci divided by surface area in mm^2. Three biological replicates with more than 15 animals per time point were used. **e** Whole mount immunostaining against SYNORF-1 (synapsin), a marker for the nervous system, in control and *Ubc9*(*RNAi*) 18 dpf 7DPA. Green signal denotes the planarian central nervous system and insets provide detailed amplification of anterior and posterior ends including brain and tip of the tail, respectively. White dotted lines underscore differences between control and experimental group regarding brain morphology (top) and ventral nerve cords (bottom). More than 20 animals were stained in three biological replicates. **f** Regenerated brain size obtained from determination of surface area in both control and experimental group. Differences in brain size were calculated with Two way-ANOVA. **g** RNAi schedule based on feeding with bacterially expressed dsRNA to perform double knockdown of *Hedgehog* or *Patched* and *Ubc9*. All controls were fed either *Unc22* or *gfp*. Black bars represent feeding days and red represents amputation. **h** Histogram depicts occurrence of regenerative defects in *Patched* + *Ubc9* and *Hedgehog* + *Ubc9* animals 7 days after amputation. Representative images of defects is shown on the right side. **i** Schematic summary representing *Smed-Ubc9* acts as an upstream regulator of different functions in the adult body. At the organismal level, downregulation of *Ubc9* lead to a systemic increase in DNA damage and decrease in in both stem cell renewal and cell cycle progression. However, it remains unclear whether inhibition of Hedgehog (Hh) signaling is associated with any of the systemic effects. Regionally, dysfunctional *Ubc9* triggers collective cell death and posterior specific abrogation of tissue regeneration, which are mediated through Hh signaling. At the organ level, *Ubc9* also regulates proper brain regeneration likely through disruption of Hh signaling that is required for neurogenesis. It is possible that lack of specific neurons in *Ubc9*(*RNAi*) animals also affect neural regulation of cell cycle progression but additional experiments are required. $^{****}p < 0.0001$ and all other statistical comparisons were made with Sidak's multiple comparisons test NS (no significance) $p > 0.05$; $^{**}p < 0.01$; $^{***}p < 0.001$; $^{****}p < 0.0001$. Scale bars = 200 µm

and disease [36]. However, the mechanism underlying this regional difference remains poorly understood. Our results provide critical insight on the regulation of regional cell fate during tissue renewal and regeneration. Specifically, we demonstrate that the sole E2 conjugating enzyme *Ubc9*, an essential component of the SUMOylation pathway, controls cell cycle, stem cell renewal, adult tissue homeostasis and regeneration. In addition, *Ubc9* function is critical for subcellular translocation of RAD51 into the nucleus to repair DNA damage through homologous recombination. Finally, we establish *Ubc9* is an upstream regulator that exerts control over Hedgehog signaling to mediate regional cell fate decisions during tissue homeostasis and regeneration (Fig. 7i).

Post-translational modification (PTMs) with small ubiquitin-like modifier (SUMO) is a key regulator of various cellular processes in metazoans [13, 15]. We establish that SUMOylation is evolutionarily conserved in *S. mediterranea*, a member of the under studied group of Lophotrochozoans. This finding is critical because non-Ecdysozoan protostomes include the largest number of animal phyla across metazoans and the study of members of this group will complement, at the very least, information obtained in more traditional experimental organisms [37–39]. The lack of redundancy of *Ubc9* in the planarian genome recapitulates its evolutionarily conservation in the regulation of the SUMO pathway across eukaryotes. This is further evidenced by the close relationship in the protein sequence between human and planarian UBC9. A major challenge facing the study of *Ubc9* is the fact that its complete abrogation is embryonically lethal, which hampers our capacity to understand the systemic contribution of SUMO pathway at post-embryonic stages [40, 41]. Studies in *S. mediterranea* will provide unique opportunities to analyze PTMs through SUMOylation during simultaneous renewal of many tissues and regeneration in the context of the adult body.

The role of *Ubc9* in regulating stem cells depends on the context and the experimental models in which the studies are performed [42–45]. For example, *Ubc9* function is required for embryonic stem cell survival in vitro and reprogramming of induced pluripotent cells (iPS) but *Ubc9* function is not pertinent to the maintenance of mouse embryonic fibroblasts (MEFs) [46]. Our analysis looks at the function of *Ubc9* in planarians, which contain large pools of adult pluripotent stem cells (neoblasts). *Ubc9*(*RNAi*) led to rapid depletion of neoblasts across the AP body axis. This may be due to its effect on the cell cycle dynamics as knockdown of *Ubc9* causes an accumulation of cells in G1 phase and a reduction in G2/M phase. Previous studies have suggested knockdown of *Ubc9* is a key regulator of G1/S phase transition through various mechanisms of action [25, 28, 42, 44]. Additional findings suggest *Ubc9* knockdown induces DNA damage and chromosomal abnormalities, which would block cells from passing the critical cell cycle checkpoints [21, 47–49]. Therefore, this blockage in G1 phase could also impair the progression of post-mitotic progeny that will negatively impact the maintenance of differentiated tissues. Our findings in planarians are consistent with these observations and support a conserved role for SUMOylation in cell cycle control and adult stem cell maintenance.

Collective regulation of cellular decisions along the AP axis is subject to mechanisms that remain poorly understood. Earlier studies have demonstrated that downregulation of *Ubc9* induces regional cell death that precede lethality during embryonic development in *Drosophila* and zebrafish [10, 11]. In accordance, our results demonstrate consistent regional cell death followed by lethality, supporting functional conservation across metazoans and developmental stages. We propose that *Ubc9* functions as a regulator of regional cell death that prevails during embryonic development and adult stages.

Recently, we reported that loss of function of *Rad51*, a protein required for DNA repair through HR, induces regional defects in planarians [9]. *Ubc9*-mediated regional cell death follows a similar pattern as in *Rad51*(*RNAi*). Double RNAi experiments involving *Rad51* and *Ubc9* demonstrate a synergistic effect in reducing mitotic activity throughout the animal (Figure S6A, B). Furthermore, this complementary effect is also supported by the observation that each gene's expression is reduced but not completely abrogated after *Rad51* or *Ubc9*(*RNAi*) (Figure S6C, D). Taken together, these results suggest that the SUMO pathway overlaps with *Rad51* in some functions as RAD51 is probably also a SUMO target also in planarian, but still exert mitotic control through different mechanisms. For example, signals from the nervous system contribute to maintain mitotic activity in the anterior region of *Rad51*(*RNAi*) animals [9], whereas these neural inputs are limited after *Ubc9*(*RNAi*). It is possible that inhibition of the Hh pathway through *Ubc9* loss of function affects the neuronal subtype(s) [[35] and see discussion below] that send survival signals after abrogation of *Rad51*. However, the specific molecular mechanisms regulating anterior cellular fate in *Ubc9* animals remain to be investigated.

Downregulation of *Ubc9* leads to an increase in DSBs that are similarly distributed along the AP axis. Chromosomal abnormalities were also evident after *Ubc9*(*RNAi*), which is consistent with both defective DNA repair response and chromosomal segregation [21, 47–49]. We also noted that *Ubc9* downregulation leads to DNA damage response that occurs in clusters in both anterior and posterior regions, suggesting there may be focus of cells that are more susceptible to accumulate DSB. Future experiments will address the cause of DNA damage response in clusters after *Ubc9*(*RNAi*). Mechanistically, our results demonstrate that the increase in DSBs after *Ubc9*(*RNAi*) are due to a

disruption in DNA repair through HR. *Ubc9*(*RNAi*) restricts nuclear translocation of RAD51, which is consistent with previous studies showing UBC9 is involved in trafficking of nuclear proteins [21, 50–54]. These data together reveal *Ubc9* is an essential component to maintain genomic integrity during renewal of adult tissues.

The Ubc9 phenotype displays some resemblances in intact and regenerating animals. Specifically, during homeostasis, *Ubc9*(*RNAi*) animals lose their tail and during regeneration, worms are unable to form posterior blastema. In the anterior region, we show (Fig. 2c) that intact animals develop anterior abnormalities over time, which leads to loss of tissue in the anterior region but only at very late stages of the phenotype when they start dying (> 25 days post-RNAi). The regenerating worms also show defective anterior regeneration that is associated with a small blastema and defective neurogenesis and brain formation. These examples demonstrate that anterior and posterior defects are present in both the intact and the regenerating animals. However, differences in the manifestation of these defects are visualized depending on the timeline in which the animals are analyzed (Fig. 2c). Our work suggests that SUMO targets in the posterior regions are more sensitive to changes in their SUMOylation when compared to the anterior counterpart and this is likely the reason for the early posterior defect.

Finally, we provide mechanistic insights behind the cell death-driven regional loss of tissue after *Ubc9*(*RNAi*). Deregulation of Hh pathway by *Ubc9*(*RNAi*) is evident through the steady increase of *Ptc* expression, which is detected early in the phenotype. Previous work has demonstrated that *Ptc* ultimately controls the hedgehog pathway, as high levels of *Ptc* serve to sequester any free Hh and limit the activity of the pathway [55]. Our findings about a role for SUMOylation in regulating Hh signaling are also supported by recent observations in *Drosophila* [56, 57]. Consistently, many members of the Hh pathway are prone to regulation by post-translation modification, such as SUMOylation. For example, Hh stimulates Smo sumoylation by dissociating it from a desumoylation enzyme Ulp1. Sumoylated Smo prevents its ubiquitination and degradation, leading to Smo accumulation on the membrane and elevated Hh pathway activity [56, 57]. Uniquely, our data demonstrate that *Ubc9* is a key regulator of collective cellular decisions such as proliferation and death that are critical for tissue maintenance in the adult body (Fig. 7i). The striking lack of tail regeneration highlights SUMOylation as a region-specific requirement for tissue repair by affecting transcription of Hh genes by regulation of yet to be identified substrate(s). This result is consistent with previous observations in planarians where repression of Hh signaling results in lack of tail regeneration [33, 34]. Nonetheless, it will be interesting to determine whether (1) other mechanisms besides *Ptc* signaling also affect SUMOylation-mediated cell death or (2) if increased *Ptc* expression is involved in regional non-canonical Hh signaling related to cell death. Our findings also highlight the importance of *Ubc9* as an early requirement for neoblasts-driven injury response and suggest that depending on the circumstances SUMOylation may play synergistic/parallel roles or even act as an upstream component of the Hh pathway (Fig. 7i). The *Ubc9* downregulation also extend to *Hh*-mediated impairment of neurogenesis [35], revealing *Ubc9* also controls behavior of neural progenitors and brain function. Hh signaling is also associated with planarian glial cells and future studies will aim to determine whether *Ubc9* loss-of-function affects the function of glial cells through non-canonical Hh signaling. Altogether, our results demonstrate that SUMOylation, in the context of the whole adult body, regulates important aspects of cellular proliferation and cell death at regional and systemic levels (Fig. 7i).

Materials and methods

Planarian culture

Planarian species used in these experiments was *Schmidtea mediterranea* CIW4. The culture was maintained as previously described by [2].

Identification of homologs and phylogenetic analysis

Components of the SUMOylation pathway were identified by BLASTing human SUMO protein sequences into available genomic resources for *S. mediterranea* [58, 59]. Identified sequences underwent a six-frame translation using PFAM and conservation was further confirmed with UNIPROT. The sequences were further verified by Blastn and Blastp in NCBI. The identified sequences were aligned by CLUSTALW with sequences obtained using HomoloGene (http://www.ncbi.nlm.nih.gov/homologene).

Phylogenetic tree for *Ubc9* was constructed using 30 sequences from 30 metazoans and for the SUMO tree we used 31 sequences from 22 metazoans. The sequences were aligned using MAFFT L-INS-I http://mafft.cbrc.jp/alignment/server/ [14]. The alignment was manually adjusted to remove large gaps. Phylogenetic analysis was conducted first by determination of the optimal substitution model for each alignment with ProtTest 2.4 [15]. We constructed maximum likelihood trees in RAxML version 7.3.2 [18], with the appropriate model of protein substitution using the RaxML GUI front end. The best tree and bootsrap proportions were determined by 1000 iterations using Maximum likelihood + Slow bootstrap (100 runs), and PROTGAMMA + LG options using empirical frequencies. Tree images were generated using FigTree (http://tree.bio.ed.ac.uk/software/figtree/), which were then processed using

Adobe Photoshop (http://www.adobe.com/products/photoshopfamily.html).

RNAi experiments

Primers with attb flanking sites were generated for the gene of interest [60]. PCR products were generated using cDNA synthesized from RNA of asexual *S. mediterranea* animals. Thermo Scientific VERSO cDNA synthesis kit was used to make cDNA. The gene was cloned into the pPR244 vector using BP Clonase II kit. The newly generated vector was transformed into NEB5a bacteria and then into HT115 bacteria. HT115 bacteria with the vector was grown in 2XYT media until it reached an OD595 of 0.400. 50 µL of 0.1 M IPTG was added and bacteria were incubated for an additional 4 h. The media was pelleted at 5000 rpm for 5 min and mixed with 25 µL of calf liver and fed to planarians. RNAi feeding times were adjusted for each experiment time.

For *Ubc9*(*RNAi*), planarians were fed UBC9 dsRNA expressing bacteria every 3 days for a total of six feedings. All experiments were performed after 25 days of RNAi starting from the first day of feeding. For double knockdown experiments involving hedgehog and patched RNAi alone, animals were fed with the appropriate dsRNA 8 times every 3 days and then with gfp 6 times every 3 days. For *Ubc9* alone, animals were first fed *gfp* 8 times and then *Ubc9* six times. For *Hh* + *Ubc9* or *Ptc* + *Ubc9*(*RNAi*), animals were fed *Hh* or *Ptc* first and then *Ubc9* after. All animals were fixed at the same time. Same steps were taken to generate animals for the regeneration experiments. For double knockdown experiments involving *Sumo2* and *Sumo3*, 5 ml of bacteria for each gene was grown as before and mixed together before centrifugation. This pellet was once again mixed with 25 µL of calf liver and fed to the planarians. For *Rad51* and *Ubc9* double knockdown, a total of three RAD51 microinjections were administered over three consecutive days and then the animals were fed with Ubc9 dsRNA expressing bacteria 4 times every 3 days.

Whole mount immunofluorescence

Planarians were killed in 5.7% 12 N HCl solution and fixed in Carnoys solution for 2 h on ice. Carnoy's solution was replaced with cold 100% MeOH and animals were placed in −20 °C for 1 h. Worms were bleached overnight in 6% H_2O_2 solution. Worms were then rehydrated in series from 100% MeOH to 100% PBSTx and stained as previously described [9]. Primary antibodies: α-H3p 1:250 (Millipore Cat# 05-817R), α-synapsin, 1:100 (Developmental Studies Hybridoma Bank); and activated caspase-3, 1:500 (Abcam ab13847) [29], RAD51, 1:500 (Abcam ab109107) and Phospho-Histone H2AX 1:1000 (ThemoFisher LF-PA0025) [9]. Similar results were obtained after testing side-by-side the SMED-RAD51 antibody [32] kindly provided by the Sánchez Alvarado/Hawley labs and the commercial RAD51 described above. The results in the manuscript involving RAD51 were obtained with the commercial RAD51 antibody. Secondary antibodies include: Goat anti-mouse Alexa488, 1:400 (Invitrogen Cat# 673781) for α-synapsin, α-arrestin, acetylated tubulin, Goat anti-rabbit Alexa568, 1:800 (Invitrogen Cat# 11036) for H3P, HRP-conjugated Goat anti-rabbit antibody (Millipore Cat# 12-348) with TSA-Alexa568 anti-HRP for caspase-3 (1:2000).

In situ hybridization

Riboprobes for in situ hybridization (ISH) were synthesized using T3 or T7 polymerase (Promega) and digoxigenin labeled ribonucleotide mix (Roche) with specific PCR templates as previously described [9]. Whole-mount ISH (WISH) was performed as previously described [61].

Quantitative real-time PCR

Quantitative real time PCR (qPCR) was performed as previously described [9, 62]. The ubiquitously expressed gene H.55.12e was used as the control. Each individual experiment consisted of triplicates per condition and experiments were independently repeated at least twice. RNA was extracted from anterior and posterior region of animals (> 20 per condition) and converted to cDNA using the Verso cDNA synthesis kit. Gene expression is expressed of fold change in comparison to the control.

Protein extraction and Western blot

Protein studies were performed as previously described [9].

Planarian dissociation

Planarians were amputated, whole or A/P, into small pieces using a razor, suspended in cold calcium, magnesium-free (CMF) media and placed on a rocker for 30 min at 4 °C in the dark. Cells were forced through a 20 micron filter and centrifuged at 1500 rpm followed by resuspension in 1 ml of CMF media before cell counting [23].

Fixation and immunostaining of dissociated cells

Dissociated cells were pipetted onto glass slips and left to anneal for 30 min in the dark. After, the slips were transferred to a glass beaker and fixed in Carnoys solution for 2 h on ice. Carnoys solution was replaced with 100% methanol and transferred to − 20 °C for 1 h. Samples were then rehydrated using mixtures of 75, 50 and 25% Methanol in PBSTx. [2]. After final rehydration with 100% PBSTx

(PBS + 0.3% triton), the cells were blocked in PBST containing bovine albumin serum (BSA) for 4 h RT and primary antibody added overnight: α-RAD51 1:500 (Abcam ab109107). Wash 6 × 10 min in PBSTB and replace with secondary antibody overnight: 1:500 HRP-conjugated Goat anti-rabbit antibody (Millipore Cat# 12-348). Wash 6 × 10 min in PBSTB. Add TSA-Alexa488 in PBSTI 1:1000 for 20 min. Wash 6 × 10 min in PBSTB. Add DAPI (0.1 µg/1 mL) for 15 min and mounted using VECTASHIELD® Mounting Medium.

FACS analysis

FACS analyses were performed as previously described [9, 23].

COMET assay and karyotyping

COMET assay was performed as previously described [9] and karyotyping was performed as previously described [63].

Single-cell sequencing (SCS) data

The *Ubc9* SCS expression analysis was obtained from the planaria single-cell database hosted by the Reddien Lab at the Whitehead Institute for Biomedical Research (https://radiant.wi.mit.edu/app/) [1].

Imaging and data processing

Animal behavior was recorded using a Nikon AZ-100 multizoom microscope and NIS Elements AR 3.2 software. Area measurements were calculated with ImageJ and the difference in animal size were determined as fold change in reference to control group at each time point. Digital pictures were collected using a Nikon AZ-100 multizoom microscope and NIS Elements AR 3.2 software. Brightness and contrast were adjusted with Adobe Photoshop. Neoblasts were counted and normalized to the area (mm^2) using ImageJ. Caspase-3 signal was quantified by measuring levels of fluorescence using NIS element software (Nikon).

Statistical analysis

Data are expressed as mean ± standard error of the mean (SEM) or fold change ± SEM. Statistical analyses were performed in Prism, GraphPad software Inc. (http://www.graphpad.com).

Acknowledgements We thank Edelweiss Pfister for technical assistance and members of the Oviedo Lab for comments on the manuscript. We acknowledge Drs. Marcos Garcia-Ojeda and Anna Beaudin for assistance with FACS analysis and comments on the manuscript. Thanks are also extended to Ulrike Abu-Shach for technical assistance cloning *Ubc9*. The SYNORF antibody was obtained from the Developmental Studies Hybridoma Bank, created by the NICHD of the NIH and maintained at the University of Iowa, Department of Biology. We are grateful to Sánchez Alvarado/Hawley labs for providing a sample of the SMED-RAD51 antibody.

Author contribution statement MT, PGB, AT, LB, and NJO performed research and analyzed data. MT, LB, and NJO wrote the manuscript. All authors read the manuscript, provided comments and approved the final version.

Compliance with ethical standards

Conflict of interest The authors declare no competing or financial interest.

Funding We acknowledge support from University of California Merced and the Israel Science Foundation (ISF 1878/15) and the Israel Cancer Research Fund 14-101-PG to LB. This research was funded by the National Cancer Institute and National Institute of General Medical Sciences of the National Institute of Health, awards CA176114 and GM109372 to NJO.

References

1. Wurtzel O, Cote LE, Poirier A, Satija R, Regev A, Reddien PW (2015) A generic and cell-type-specific wound response precedes regeneration in planarians. Dev Cell 35(5):632–645. https://doi.org/10.1016/j.devcel.2015.11.004
2. Oviedo NJ, Pearson BJ, Levin M, Sánchez Alvarado A (2008) Planarian PTEN homologs regulate stem cells and regeneration through TOR signaling. Dis Model Mech 1(2–3):131–143
3. Owlarn S, Bartscherer K (2016) Go ahead, grow a head! A planarian's guide to anterior regeneration. Regeneration 3(3):139–155. https://doi.org/10.1002/reg2.56
4. Pearson BJ, Sanchez Alvarado A (2008) Regeneration, stem cells, and the evolution of tumor suppression. Cold Spring Harb Symp Quant Biol 73:565–572. https://doi.org/10.1101/sqb.2008.73.045
5. Pellettieri J, Sanchez Alvarado A (2007) Cell turnover and adult tissue homeostasis: from humans to planarians. Annu Rev Genet 41:83–105. https://doi.org/10.1146/annurev.genet.41.110306.130244
6. Roberts-Galbraith RH, Newmark PA (2015) On the organ trail: insights into organ regeneration in the planarian. Curr Opin Genet Dev 32:37–46. https://doi.org/10.1016/j.gde.2015.01.009
7. Tanaka EM, Reddien PW (2011) The cellular basis for animal regeneration. Dev Cell 21(1):172–185. https://doi.org/10.1016/j.devcel.2011.06.016
8. Aboobaker AA (2011) Planarian stem cells: a simple paradigm for regeneration. Trends Cell Biol 21(5):304–311. https://doi.org/10.1016/j.tcb.2011.01.005
9. Peiris TH, Ramirez D, Barghouth PG, Ofoha U, Davidian D, Weckerle F, Oviedo NJ (2016) Regional signals in the planarian body guide stem cell fate in the presence of genomic instability. Development 143(10):1697–1709. https://doi.org/10.1242/dev.131318
10. Epps JL, Tanda S (1998) The Drosophila semushi mutation blocks nuclear import of bicoid during embryogenesis. Current biology: CB 8(23):1277–1280

11. Nowak M, Hammerschmidt M (2006) Ubc9 regulates mitosis and cell survival during zebrafish development. Mol Biol Cell 17(12):5324–5336. https://doi.org/10.1091/mbc.E06-05-0413
12. Lomeli H, Vazquez M (2011) Emerging roles of the SUMO pathway in development. Cell Mol Life Sci 68(24):4045–4064. https://doi.org/10.1007/s00018-011-0792-5
13. Flotho A, Melchior F (2013) Sumoylation: a regulatory protein modification in health and disease. Annu Rev Biochem 82:357–385. https://doi.org/10.1146/annurev-biochem-061909-093311
14. Gareau JR, Lima CD (2010) The SUMO pathway: emerging mechanisms that shape specificity, conjugation and recognition. Nat Rev Mol Cell Biol 11(12):861–871. https://doi.org/10.1038/nrm3011
15. Hay RT (2013) Decoding the SUMO signal. Biochem Soc Trans 41(2):463–473. https://doi.org/10.1042/BST20130015
16. Desterro JM, Thomson J, Hay RT (1997) Ubch9 conjugates SUMO but not ubiquitin. FEBS Lett 417(3):297–300
17. Gong L, Kamitani T, Fujise K, Caskey LS, Yeh ET (1997) Preferential interaction of sentrin with a ubiquitin-conjugating enzyme, Ubc9. J Biol Chem 272(45):28198–28201
18. Johnson ES, Blobel G (1997) Ubc9p is the conjugating enzyme for the ubiquitin-like protein Smt3p. J Biol Chem 272(43):26799–26802
19. Saitoh H, Sparrow DB, Shiomi T, Pu RT, Nishimoto T, Mohun TJ, Dasso M (1998) Ubc9p and the conjugation of SUMO-1 to RanGAP1 and RanBP2. Curr Biol 8(2):121–124
20. Schwarz SE, Matuschewski K, Liakopoulos D, Scheffner M, Jentsch S (1998) The ubiquitin-like proteins SMT3 and SUMO-1 are conjugated by the UBC9 E2 enzyme. Proc Natl Acad Sci USA 95(2):560–564
21. Nacerddine K, Lehembre F, Bhaumik M, Artus J, Cohen-Tannoudji M, Babinet C, Pandolfi PP, Dejean A (2005) The SUMO pathway is essential for nuclear integrity and chromosome segregation in mice. Dev Cell 9(6):769–779. https://doi.org/10.1016/j.devcel.2005.10.007
22. Reddien PW, Oviedo NJ, Jennings JR, Jenkin JC, Sanchez Alvarado A (2005) SMEDWI-2 is a PIWI-like protein that regulates planarian stem cells. Science 310(5752):1327–1330. https://doi.org/10.1126/science.1116110
23. Peiris TH, Garcia-Ojeda ME, Oviedo NJ (2016) Alternative flow cytometry strategies to analyze stem cells and cell death in planarians. Regeneration 3(2):123–135. https://doi.org/10.1002/reg2.53
24. Eisenhoffer GT, Kang H, Sánchez Alvarado A (2008) Molecular analysis of stem cells and their descendants during cell turnover and regeneration in the planarian Schmidtea mediterranea. Cell Stem Cell 3(3):327–339. https://doi.org/10.1016/j.stem.2008.07.002
25. Seufert W, Futcher B, Jentsch S (1995) Role of a ubiquitin-conjugating enzyme in degradation of S- and M-phase cyclins. Nature 373(6509):78–81. https://doi.org/10.1038/373078a0
26. al-Khodairy F, Enoch T, Hagan IM, Carr AM (1995) The Schizosaccharomyces pombe hus5 gene encodes a ubiquitin conjugating enzyme required for normal mitosis. J Cell Sci 108(Pt 2):475–486
27. Meng F, Qian J, Yue H, Li X, Xue K (2016) SUMOylation of Rb enhances its binding with CDK2 and phosphorylation at early G1 phase. Cell Cycle 15(13):1724–1732. https://doi.org/10.1080/15384101.2016.1182267
28. Bellail AC, Olson JJ, Hao C (2014) SUMO1 modification stabilizes CDK6 protein and drives the cell cycle and glioblastoma progression. Nat Commun 5:4234. https://doi.org/10.1038/ncomms5234
29. Beane WS, Morokuma J, Lemire JM, Levin M (2013) Bioelectric signaling regulates head and organ size during planarian regeneration. Development 140(2):313–322. https://doi.org/10.1242/dev.086900
30. Bender CE, Fitzgerald P, Tait SW, Llambi F, McStay GP, Tupper DO, Pellettieri J, Sanchez Alvarado A, Salvesen GS, Green DR (2012) Mitochondrial pathway of apoptosis is ancestral in metazoans. Proc Natl Acad Sci USA 109(13):4904–4909. https://doi.org/10.1073/pnas.1120680109
31. Yin S, Huang Y, Zhangfang Y, Zhong X, Li P, Huang J, Liu D, Songyang Z (2016) SmedOB1 is required for planarian homeostasis and regeneration. Sci Reports 6:34013. https://doi.org/10.1038/srep34013
32. Xiang Y, Miller DE, Ross EJ, Sanchez Alvarado A, Hawley RS (2014) Synaptonemal complex extension from clustered telomeres mediates full-length chromosome pairing in *Schmidtea mediterranea*. Proc Natl Acad Sci USA 111(48):E5159–E5168. https://doi.org/10.1073/pnas.1420287111
33. Yazawa S, Umesono Y, Hayashi T, Tarui H, Agata K (2009) Planarian Hedgehog/Patched establishes anterior-posterior polarity by regulating Wnt signaling. Proc Natl Acad Sci USA 106(52):22329–22334. https://doi.org/10.1073/pnas.0907464106
34. Rink JC, Gurley KA, Elliott SA, Sanchez Alvarado A (2009) Planarian Hh signaling regulates regeneration polarity and links Hh pathway evolution to cilia. Science 326(5958):1406–1410. https://doi.org/10.1126/science.1178712
35. Currie KW, Molinaro AM, Pearson BJ (2016) Neuronal sources of hedgehog modulate neurogenesis in the adult planarian brain. eLife. https://doi.org/10.7554/eLife.19735
36. Auerbach R, Auerbach W (1982) Regional differences in the growth of normal and neoplastic cells. Science 215(4529):127–134
37. Giribet G (2008) Assembling the lophotrochozoan (= spiralian) tree of life. Philos Trans R Soc Lond B Biol Sci 363(1496):1513–1522. https://doi.org/10.1098/rstb.2007.2241
38. Gehrke AR, Srivastava M (2016) Neoblasts and the evolution of whole-body regeneration. Curr Opin Genet Dev 40:131–137. https://doi.org/10.1016/j.gde.2016.07.009
39. Currie KW, Brown DD, Zhu S, Xu C, Voisin V, Bader GD, Pearson BJ (2016) HOX gene complement and expression in the planarian *Schmidtea mediterranea*. EvoDevo 7:7. https://doi.org/10.1186/s13227-016-0044-8
40. Yuan H, Zhou J, Deng M, Liu X, Le Bras M, de The H, Chen SJ, Chen Z, Liu TX, Zhu J (2010) Small ubiquitin-related modifier paralogs are indispensable but functionally redundant during early development of zebrafish. Cell Res 20(2):185–196. https://doi.org/10.1038/cr.2009.101
41. Saracco SA, Miller MJ, Kurepa J, Vierstra RD (2007) Genetic analysis of SUMOylation in *Arabidopsis*: conjugation of SUMO1 and SUMO2 to nuclear proteins is essential. Plant Physiol 145(1):119–134. https://doi.org/10.1104/pp.107.102285
42. Hayashi T, Seki M, Maeda D, Wang W, Kawabe Y, Seki T, Saitoh H, Fukagawa T, Yagi H, Enomoto T (2002) Ubc9 is essential for viability of higher eukaryotic cells. Exp Cell Res 280(2):212–221
43. Yukita A, Hosoya A, Ito Y, Katagiri T, Asashima M, Nakamura H (2012) Ubc9 negatively regulates BMP-mediated osteoblastic differentiation in cultured cells. Bone 50(5):1092–1099. https://doi.org/10.1016/j.bone.2012.02.008
44. Myatt SS, Kongsema M, Man CW, Kelly DJ, Gomes AR, Khongkow P, Karunarathna U, Zona S, Langer JK, Dunsby CW, Coombes RC, French PM, Brosens JJ, Lam EW (2014) SUMOylation inhibits FOXM1 activity and delays mitotic transition. Oncogene 33(34):4316–4329. https://doi.org/10.1038/onc.2013.546
45. Lv X, Pan C, Zhang Z, Xia Y, Chen H, Zhang S, Guo T, Han H, Song H, Zhang L, Zhao Y (2016) SUMO regulates somatic cyst stem cell maintenance and directly targets the Hedgehog pathway in adult Drosophila testis. Development 143(10):1655–1662. https://doi.org/10.1242/dev.130773
46. Tahmasebi S, Ghorbani M, Savage P, Gocevski G, Yang XJ (2014) The SUMO conjugating enzyme Ubc9 is required for inducing

and maintaining stem cell pluripotency. Stem cells 32(4):1012–1020. https://doi.org/10.1002/stem.1600
47. Pelisch F, Sonneville R, Pourkarimi E, Agostinho A, Blow JJ, Gartner A, Hay RT (2014) Dynamic SUMO modification regulates mitotic chromosome assembly and cell cycle progression in *Caenorhabditis elegans*. Nature communications 5:5485. https://doi.org/10.1038/ncomms6485
48. Huang C, Cheng J, Bawa-Khalfe T, Yao X, Chin YE, Yeh ET (2016) SUMOylated ORC2 recruits a histone demethylase to regulate centromeric histone modification and genomic stability. Cell Reports 15(1):147–157. https://doi.org/10.1016/j.celrep.2016.02.091
49. Moschos SJ, Mo YY (2006) Role of SUMO/Ubc9 in DNA damage repair and tumorigenesis. J Mol Histol 37(5–7):309–319. https://doi.org/10.1007/s10735-006-9030-0
50. Shima H, Suzuki H, Sun J, Kono K, Shi L, Kinomura A, Horikoshi Y, Ikura T, Ikura M, Kanaar R, Igarashi K, Saitoh H, Kurumizaka H, Tashiro S (2013) Activation of the SUMO modification system is required for the accumulation of RAD51 at sites of DNA damage. J Cell Sci 126(Pt 22):5284–5292. https://doi.org/10.1242/jcs.133744
51. Kurtzman AL, Schechter N (2001) Ubc9 interacts with a nuclear localization signal and mediates nuclear localization of the paired-like homeobox protein Vsx-1 independent of SUMO-1 modification. Proc Natl Acad Sci USA 98(10):5602–5607. https://doi.org/10.1073/pnas.101129698
52. Ross S, Best JL, Zon LI, Gill G (2002) SUMO-1 modification represses Sp3 transcriptional activation and modulates its subnuclear localization. Mol Cell 10(4):831–842
53. Wu CS, Ouyang J, Mori E, Nguyen HD, Marechal A, Hallet A, Chen DJ, Zou L (2014) SUMOylation of ATRIP potentiates DNA damage signaling by boosting multiple protein interactions in the ATR pathway. Genes Dev 28(13):1472–1484. https://doi.org/10.1101/gad.238535.114
54. Bergink S, Ammon T, Kern M, Schermelleh L, Leonhardt H, Jentsch S (2013) Role of Cdc48/p97 as a SUMO-targeted segregase curbing Rad51-Rad52 interaction. Nat Cell Biol 15(5):526–532. https://doi.org/10.1038/ncb2729
55. Chen Y, Struhl G (1996) Dual roles for patched in sequestering and transducing Hedgehog. Cell 87(3):553–563
56. Ma G, Li S, Han Y, Li S, Yue T, Wang B, Jiang J (2016) Regulation of smoothened trafficking and hedgehog signaling by the SUMO pathway. Dev Cell 39(4):438–451. https://doi.org/10.1016/j.devcel.2016.09.014
57. Zhang J, Liu Y, Jiang K, Jia J (2017) SUMO regulates the activity of Smoothened and Costal-2 in Drosophila Hedgehog signaling. Sci Reports 7:42749. https://doi.org/10.1038/srep42749
58. Robb SM, Gotting K, Ross E, Sanchez Alvarado A (2015) SmedGD 2.0: the Schmidtea mediterranea genome database. Genesis 53(8):535–546. https://doi.org/10.1002/dvg.22872
59. Brandl H, Moon H, Vila-Farre M, Liu SY, Henry I, Rink JC (2016) PlanMine–a mineable resource of planarian biology and biodiversity. Nucleic Acids Res 44(D1):D764–D773. https://doi.org/10.1093/nar/gkv1148
60. Reddien PW, Bermange AL, Murfitt KJ, Jennings JR, Sánchez Alvarado A (2005) Identification of genes needed for regeneration, stem cell function, and tissue homeostasis by systematic gene perturbation in planaria. Dev Cell 8(5):635–649
61. Pearson BJ, Eisenhoffer GT, Gurley KA, Rink JC, Miller DE, Sanchez Alvarado A (2009) Formaldehyde-based whole-mount in situ hybridization method for planarians. Dev Dyn 238(2):443–450. https://doi.org/10.1002/dvdy.21849
62. Peiris TH, Ramirez D, Barghouth PG, Oviedo NJ (2016) The Akt signaling pathway is required for tissue maintenance and regeneration in planarians. BMC Dev Biol 16:7. https://doi.org/10.1186/s12861-016-0107-z
63. Guedelhoefer OCT, Sanchez Alvarado A (2012) Amputation induces stem cell mobilization to sites of injury during planarian regeneration. Development 139(19):3510–3520. https://doi.org/10.1242/dev.082099

Appendix V

Seminars in Cell & Developmental Biology 87 (2019) 145–159

Contents lists available at ScienceDirect

Seminars in Cell & Developmental Biology

Journal homepage: www.elsevier.com/locate/semcdb

DNA damage and tissue repair: What we can learn from planaria

Paul G. Barghouth[a,b,c], Manish Thiruvalluvan[a,b,c], Melanie LeGro[a,b,c], Néstor J. Oviedo[a,b,c,*]

[a] Dept. of Molecular & Cell Biology, University of California, Merced, USA
[b] Quantitative and Systems Biology Graduate Program, University of California, Merced, USA
[c] Health Sciences Research Institute, University of California, Merced, USA

ARTICLE INFO

Article history:
Received 30 January 2018
Received in revised form 22 April 2018
Accepted 30 April 2018
Available online 3 May 2018

Keywords:
DNA damage
DNA repair
DNA double strand breaks
Planaria
Neoblasts
Regeneration
Invertebrates
Stem cells

ABSTRACT

Faithful renewal of aging and damaged tissues is central to organismal lifespan. Stem cells (SCs) generate the cellular progeny that replenish adult tissues across the body but this task becomes increasingly compromised over time. The age related decline in SC-mediated tissue maintenance is a multifactorial event that commonly affects genome integrity. The presence of DNA damage in SCs that are under continuous demand to divide poses a great risk for age-related disorders such as cancer. However, performing analysis of SCs with genomic instability and the DNA damage response during tissue renewal present significant challenges. Here we introduce an alternative experimental system based on the planaria flatworm *Schmidtea mediterranea* to address at the organismal level studies intersecting SC-mediated tissue renewal in the presence of genomic instability. Planaria have abundant SCs (neoblasts) that maintain high rates of cellular turnover and a variety of molecular tools have been developed to induce DNA damage and dissect how neoblasts respond to this stressor. *S. mediterranea* displays high evolutionary conservation of DNA repair mechanisms and signaling pathways regulating adult SCs. We describe genetically induced-DNA damage models and highlight body-wide signals affecting cellular decisions such as survival, proliferation, and death in the presence of genomic instability. We also discuss transcriptomic changes in the DNA damage response during injury repair and propose DNA repair as key component of tissue regeneration. Additional studies using planaria will provide insights about mechanisms regulating survival and growth of cells with DNA damage during tissue renewal and regeneration.

Contents

1. Introduction

Preserving genomic integrity is essential to life. However, DNA is under constant threat from multiple sources, which include errors during DNA replication, products of intrinsic cellular reactions (e.g. reactive oxygen species) and environmental factors such as UV

* Corresponding author at: Department of Molecular & Cell Biology, University of California, 5200 North Lake Road, Merced, CA 95343, USA.
E-mail address: noviedo2@ucmerced.edu (N.J. Oviedo).

https://doi.org/10.1016/j.semcdb.2018.04.013
1084-9521/

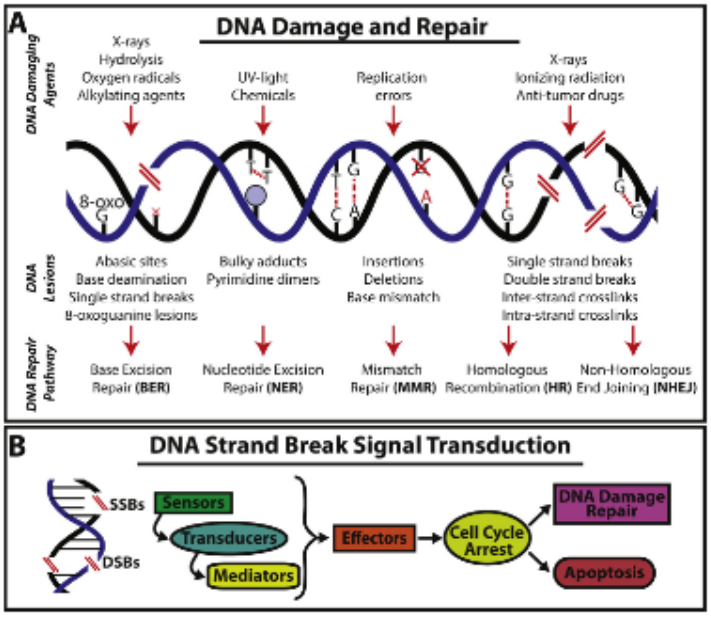

Fig. 1. DNA damage responses and stranded break signal transduction. (A) The illustration summarizes different types of DNA damaging agents, the genomic lession they produce and the specialized DNA repair pathway deployed. For example, expossure to ionizing radiation may lead to DNA single and/or double-stranded breaks and crosslinks that can be repaired through HR or NHEJ (B) Different molecules mediate the repair of DNA strand breaks. Commonly, a signal transduction cascade involving sensors, transducers, mediators, and effector molecules that together influence cellular fate decisions to repair the damage or undergo programmed cell death.

radiation, chemical exposure, *etc.* (Fig. 1A) [1–5]. In humans, for example, these persistent insults generate about 10^5 DNA lesions per cell every 24 h [6–8]. If left unchecked, DNA damage can be transmitted to cellular progeny and potentially compromise tissue integrity and function [3,6,9–14]. Indeed, about 90% of cancer-related deaths worldwide originate from abnormalities in tissues that are constantly renewed by stem cells (SCs) [5,15–17]. Genomic instability (*i.e.* higher rate of genomic changes per cell division) is a major trait in almost all cancers, but the basic mechanisms regulating survival and growth of cells with DNA damage during tissue renewal remain a puzzling biomedical problem.

Exposure to DNA damaging agents generally lead to lesions that are common to all living organisms (Fig. 1A) [6,18,19]. Thus, highly conserved mechanisms of DNA repair have evolved to preserve genetic information and proper cellular function [19–23]. DNA damage response (DDR) sensors and effectors are continuously deployed and are mediated by a specific set of proteins with the goal of re-establishing genomic integrity (Fig. 1B) [19]. Importantly, the timely deployment of DDR is synchronized with cellular responses leading to critical decisions that may involve cell cycle arrest, apoptosis, senescence and DNA repair (Fig. 1B) [18,24]. Altogether, the varying responses to DNA damage aim at preventing exhaustion and abnormal transformation of SC pools while maintaining their ability to mediate tissue homeostasis.

The process of DNA damage and its cellular response have been widely documented by *in vitro* studies and organ specific experimental models. However, the field has benefited less by simultaneous analysis of DNA damage and SC-mediated tissue renewal at the organismal level. We believe that studies merging the cellular response to DNA damage, while attending body demands of cellular turnover may bring important insights about intercellular crosstalk that affects cellular fate decisions in the adult body. For example, there are patterns of regional differences of cell proliferation along the anteroposterior (AP) body axis that affect the fate of SCs and their progeny during tissue renewal, regeneration and carcinogenesis [25–31]. These regional differences are evolutionarily conserved across different species and recent studies have shown that the fate of cells with DNA damage are susceptible to regional signals [22,23]. In an attempt to complement studies of DDR/DNA repair during tissue renewal and cancer formation, we introduce a simplified model system represented by the planaria flatworm. Planaria possess high rates of cellular turnover and tissue regeneration is driven by adult SCs called neoblasts, which facilitate studies about SC-mediated tissue renewal and DNA damage [32–37]. We present a brief description of the DNA lesions and the molecules involved in repair with special emphasis on double-strand breaks (DSBs), the most dangerous form of DNA damage [8,20,38,39]. We highlight the role of DNA damage during tissue renewal and its possible impact in aging and discuss how recent experimental planaria models associated with DNA damage may provide insights about the SC response during adult tissue maintenance and regeneration. In addition, we identify through data mining of various transcriptomic datasets that the DDR is a critical component of the large-scale tissue homeostasis and regeneration in planaria. Ultimately, we propose the use of planaria as a convenient model to address evolutionarily conserved mechanisms of DDR and DNA repair during tissue repair and regeneration in the adult body.

2. Tissue renewal and stem cell response to DNA damage

Organismal lifespan relies on faithful renewal of aging and damaged tissues [40–46]. SCs generate cellular progeny to maintain adult tissues and in humans, this is a daunting process that requires daily demand of billions of cells that could span over a century [47–50]. Tissue renewal is extremely complex, fulfilling different dynamics of cellular turnover that appear unsynchronized among tissues. For example, the small intestinal epithelium is renewed in about 5 days, while epidermal cells in the skin are replaced every 10–30 days, let alone cells within blood tissue have different renewal rates from 1 day to several months [51–54]. Despite its relevance to physiology and disease, it remains poorly understood how this large scale renewal process is coordinated and how it becomes liable as organisms grow older.

Both tissue maintenance and the capacity to preserve genomic integrity decline with age. Intriguingly, there is positive correlation between DNA repair and lifespan in a variety of organisms [40,41,55,56]. For example, longer-lived species such as humans and naked mole rats consistently display higher expression of genes associated with DNA repair, which supports the idea that preservation of genomic integrity is paramount to the longevity of an organism [41]. The mechanistic process by which genome integrity declines with age is not well understood. Nonetheless, several lines

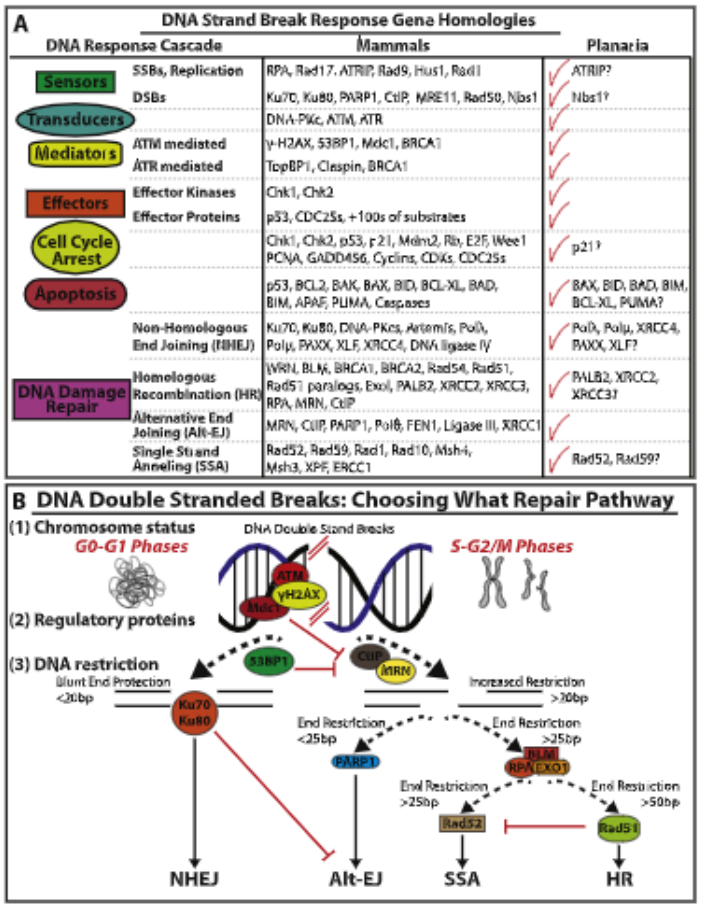

Fig. 2. Planaria display evolutionary conservation of the mechanisms involved in DNA double strand break (DSB). (A) Gene homologies for sequences regulating DDR and signal transduction mechanisms are found in planaria. For simplicity the attention is mostly focused on mediators of DSB. Checkmarks indicate conservation between the planarian species S. mediterranea and humans. However, some genes remain unfound in the planarian genome indicated by a question mark. (B) DSB repair is mediated by four different pathways (*e.g.* NHEJ, Alt-EJ, SSA and HR) however the choice of these pathways are determined by three mechanisms. (1) The status of chromosome homology which is dependent on what phases of the cell cycle DSBs occur (*e.g.* homology during S-G2-M phases which favors HR). (2) The abundance of regulatory proteins in each cell cycle phase. For example, increased expression of ATM, Mdc1 and 53BP1 have been shown to favor NHEJ in the G0/G1 phase of the cell cycle by suppressing MRN and CtIP expression needed for HR-mediated repair. (3) Lastly, the restriction of DNA blunt ends. The length of DSB nucleotide base pairs give rise to blunt end protection or a series of end restrictions. (*e.g.* <20 bp for NHEJ and >50 bp for HR mediated repair).

of evidence imply continued exposure of SCs to DNA damage plays a major role in age-related dysfunctions such as cancer and degenerative diseases [1,3,9,16,57–62]. Eventually, unrepaired genetic lesions may result in SC attrition, cellular transformation and aberrant differentiation that could lead to defective tissue renewal [1,3,9,10,61–63]. It is unclear whether the increased genome alterations are due to individual or combined effects of: (i) impaired DDR, (ii) increased levels of DNA insults, (iii) epigenetic modifications and telomere shortening with age, (iv) higher susceptibility to damaging agents in SC and progenitor populations (*e.g.* quiesent, cycling), and/or (v) defects in cell fate decision mechanisms upon demands of cellular turnover. In reality, this list could be more extensive when cellular turnover is considered in the complexity of the whole organism. Systemic factors associated with inflammation, oxidative stress, metabolism, *etc.*, which also have inputs on decisions of cellular proliferation and apoptosis during tissue turnover [1,3,10,61,63–67]. Collectively, DNA damage greatly influences the ultimate fate of the cell. Nevertheless, it is less clear how cellular decisions are prioritized when physiological demands of tissue turnover are in play and how cancer and degenerative diseases evolve from defects in these cellular decisions.

Increasing evidence demonstrates that preservation of genomic integrity and systemic reduction in DNA damage could be enhanced by physiological or pharmacological manipulations. Specifically, treatments aimed at replenishing the coenzyme NAD^+ (nicotinamide adenine dinucleotide) appear to reduce the decline in adult tissue maintenance with age by enhancing DNA repair in animal models, which altogether lead to improvement in lifespan and healthspan [68–70]. These results strongly suggest that it is possible to alter the fate of both DNA repair and cellular turnover with therapeutic interventions. However, many questions still remain and additional model organisms are needed to simultaneously analyze and integrate process of tissue renewal and DNA repair in the complexity of the whole organism. We believe the planaria model system could provide important insights in this regard.

3. Planaria as a model to study DNA damage and tissue renewal

Planaria are members of the phylum Platyhelminthes (flatworms) and are classically known for their robust regenerative capabilities [71]. Planaria display constant cell renewal and undergo repair upon injury to their tissues and organs (*e.g.* digestive, nervous, muscle, *etc.*) [34]. The planaria *Schmidtea mediterranea*, which is the most common species used worldwide to study aspects of tissue homeostasis, contains a large pool of SCs called neoblasts. Neoblasts are recognized as the only cells with capacity to proliferate in *S. mediterranea* and therefore, serve as the sole source of new cells that support the dozens of different tissues types [32,34,71–73]. The neoblast diversity is only beginning to be elucidated and so far, four subpopulations have been described (*e.g.* Sigma, Gamma, Zeta and Nu) that display restricted potential to generate and maintain tissues [72,74,75]. This diversity within planaria neoblasts allows for the integration of local and environmental stimuli throughout its lifespan to maintain tissue homeostasis.

Similar to SCs in other organisms, neoblasts are in constant crosstalk with their surroundings and are influenced by local and systemic signals involving metabolic status, neural inputs, tissue integrity, *etc.* In the presence of nutrients, planaria increase the body size by incorporation of new cells. Conversely, starvation conditions lead to reduction in animal size by elimination of cells that maintain body proportion [76–78]. Neoblasts also sense and respond to tissue injury by mounting a multi-step proliferative response that mediates the regrowth of missing and damaged parts [79–81].

The capacity to regulate SC division in response to physiological demands and injury has been attributed to the conserved tumor suppressors and oncogenes within the planaria (*e.g.* PTEN, AKT, p53, Rb, SMG) [82–87]. Planaria rarely develop cancer but can be forced to undergo cellular transformation after treatment with carcinogenic compounds or manipulation of tumor suppressor genes [83,87–90]. In line with previously described organisms, preservation of DNA integrity is paramount for tissue homeostasis and extended lifespan in planaria. Recent interest in dissecting mechanisms of DNA repair in planaria revealed the evolutionary conservation of key regulators such as *Rad51*, *p53*, *Rb*, *Ubc9*, *Brca2*, and *Rad54B* that are activated in response to endogenous and exogenous environmental insults [22,23,84,91–93]. Functional studies of DNA repair pathways identified patterns of SC exhaustion and tissue renewal defects similar to those observed in mammals [10]. These planaria features confer unique advantages to analyze critical parameters in response to DNA damage in the context of the whole body. Thus, we propose the use of *S. mediterranea* as a simplified platform to address cell fate decisions in the presence of genomic instability during large-scale SC-mediated cellular turnover and tissue repair.

4. Evolutionarily conserved DNA damage repair mechanisms exist in planaria

Older specimens of *S. mediterranea* are phenotypically indistinguishable from younger ones, which highlight the efficient mechanisms of unlimited cellular renewal in planaria [34]. This also implies that planaria contain efficient DNA repair mechanisms to combat endogenous and exogenous insults that normally deplete SCs in adult tissues, thus preventing aging and cancer-like phenotypes [88]. Indeed, high-throughput query on genomic resources [94,95] have allowed us to identify a wide range of DSB recognition and repair homologs in planaria (Fig. 2A). Specifically, we uncovered components of signaling pathways involved in DNA damage recognition, signaling transduction and effector outcome (*e.g.* cell cycle arrest, cell death and DNA repair).

Though DNA damage can affect cells in numerous ways, DSBs represent the most severe form of DNA damage as they occur when both strands of the DNA double helix are broken in close proximity. Two DSBs within a cell are capable of forming chromosomal translocations and some estimates establish that 10–50 DSBs occur per cell per cycle [8,39,96,97]. Generally, DSBs can be repaired through: non-homologous end joining (NHEJ), homologous recombination (HR) and their alternative pathways: alternative end joining (alt-EJ) and single strand annealing (SSA) (Fig. 2B). The selection of DSB repair pathways is determined by three independent variables: cell cycle phase (*e.g.* chromosome status), the abundance of regulatory proteins in each cell cycle phase and the resection of DNA blunt ends (Fig. 2B). These mechanisms of DSBs repair have been extensively reviewed elsewhere [3,5,20,97–100].

Detailed evaluation of the planaria genome revealed an important molecular conservation of the DDR mediator γ-H2AX and DSB repair protein RAD51 (*e.g.* ~65% and ~81%, respectively) (Fig. 3A, B). Further analysis also showed the presence of key signatures of their phosphorylation sites (*e.g.* S-Q motif the signature for γ-H2AX) or binding domain activity (*e.g.* Rad51's Walker A/B, L1/2 and BRC domains) (Fig. 3A, B). The molecular conservation of these molecules in planaria also facilitates the possibility of using commercial antibodies to evaluate the spatial distribution of DDR proteins at cellular and organismal levels (Fig. 3C) [22,23,101]. DSBs can be induced in planaria through ionizing radiation (IR), RNA

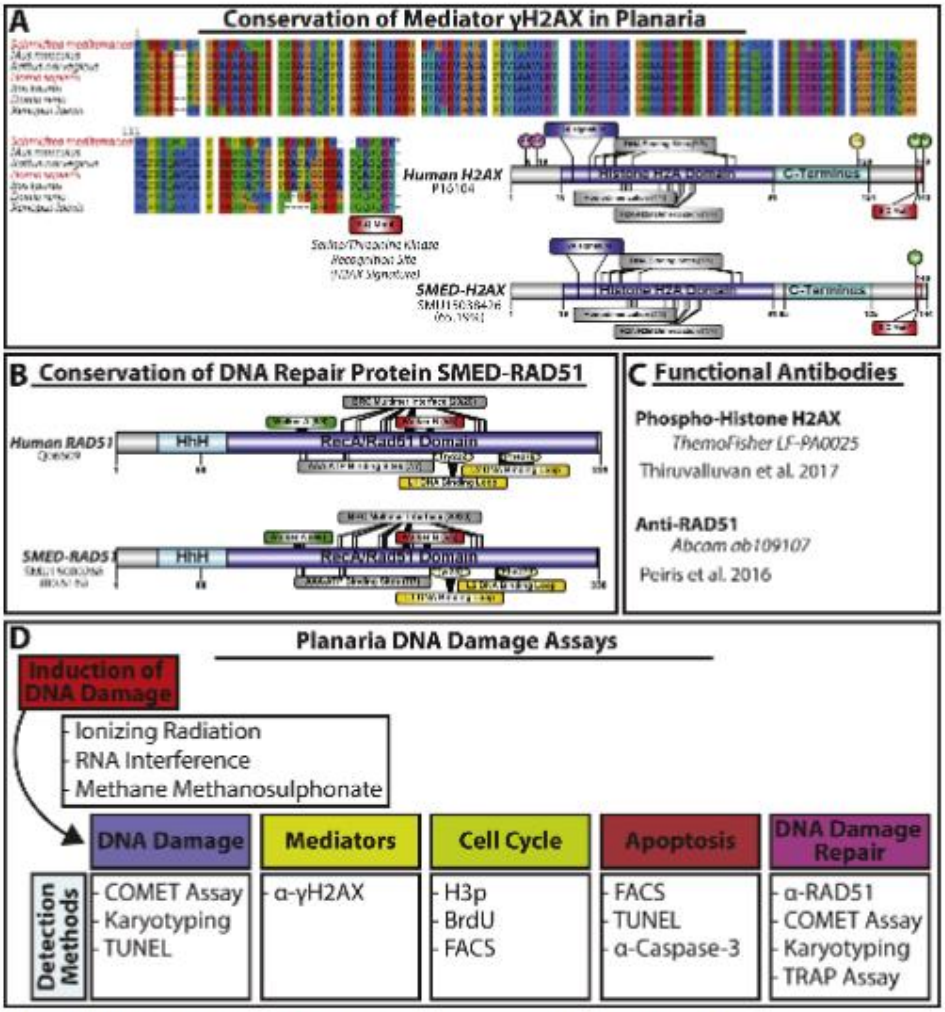

Fig. 3. Molecular conservation of key proteins regulating DNA double strand break repair and DNA damage assays in planaria. (A) Protein alignment of planaria γH2AX and homologs indicate conservation of γH2AX 's S-Q motif among species The *S. mediterranea* mediator γH2AX scores 65.19% similar to the human homolog. Sequence alignment was obtained by CLUSTALW. Using Illustrator for biological sequences (IBS version 1.0) we were able to create diagrams for both human and SMED-γH2AX protein sequences. Human protein length is 143 amino acids (aa) *versus* 144aa in SMED-γH2AX. Within this protein both the planaria and human sequences contain Histone H2A domain (dark blue, 73aa long) and a C-terminus (light blue, 30aa long). Within the Histone H2A domain both contain the H2A signature (6aa long), DNA binding sites (7/7 sites) homodimerization sites (4/4 sites) and H2A-H2B dimerization sites (7/7 sites). Importantly, both contain the S-Q motif (red domain) phosphorylation on Ser-139 site in the S-Q motif. However, Human γH2AX contains acetylation sites (6aa and 10aa), ubiquination site at 120aa and another phosphorylation site at 143aa. (B) The *S. mediterranea* RAD51 sequence shares 80.61% similarity with the human homolog and contains all the documented characteristic binding domains. Both contain a helix-hairpin-helix (HhH) motif (light blue, 48aa long) with a large RecA/Rad51 domain (dark blue, 277aa long). Within the RecA/Rad51 domain there two key features Walker A (green and 8/8 sites) and Walker B (red, 5/5 sites) binding regions. Other features of the protein are the BRC multimer interface (20/20 sites), (AAA-ATP binding sites (7/7 sites), L1/L2 DNA binding loops (yellow) which contain a Tyr 232 and Phe 279, respectively. (C) Details of commercial antibodies that recognize the *S. mediterranea* RAD51 and γH2AX homologs. SMED-RAD51 antibody generated by the Sánchez-Alvarado/Hawley labs (Xiang et al. [92]) recognizes similar peptide size as the commercial human RAD51 (Thiruvalluvan et al. [23]). (D) General assays and detection methods for inducing and quantifying the response and outcome of DNA damage in native stem cells in the planarian model.

interference (RNAi) and through drug exposure such as methyl methanesulfonate (MMS) [22,23,90]. In order to gauge the effects of these DSB inducing strategies, three key strategies have been optimized (*e.g.* TUNEL, COMET assay and karyotyping) [22,23]. The COMET assay, under alkaline conditions (pH> 13), is commonly used to monitor DNA integrity with focus on DSBs. In addition, karyotyping protocols have been optimized to assay abnormalities found in neoblast-specific chromosomes [22,102]. FACS protocols

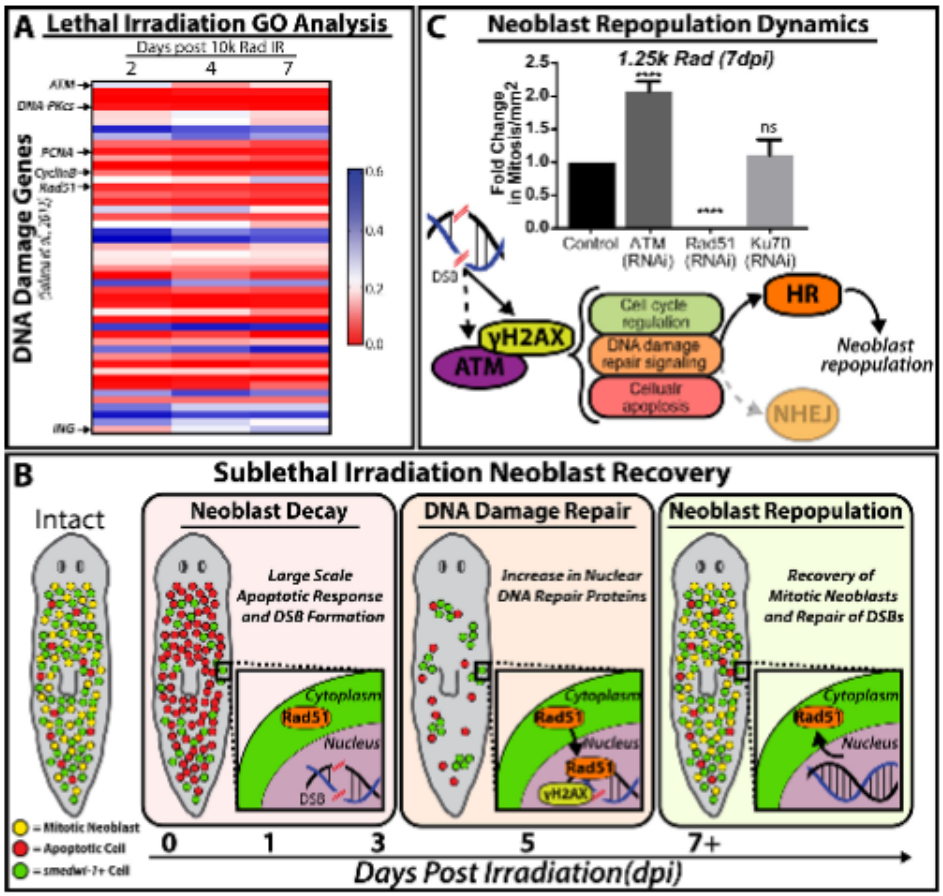

Fig. 4. Neoblast response and repopulation post irradiation is attributed to functional DNA damage detection and repair. (A) Lethal irradiation of planaria (10k rad) irreversibly depletes neoblast populations. Upon analysis of GO term annotations published by Solana et al. [111], genes involved in DDR and repair along a 7 day time course were selected. The heat map shows changes in gene expression at different times post-irradiation with color red indicating reduction and blue increase in gene expression (scale bar to the right). DNA damage response triggers upregulation of ATM gene expression accompanied by a decrease in cell cycle and DNA repair gene expression (*e.g. PCNA, CyclinB* and *Rad51*, respectively). Note that the inhibitor of growth (ING) gene expression is upregulated after 2 hpi. (B) Cartoon depiction of neoblast response to sublethal irradiation. Upon sublethal irradiation, 1–3 dpi, neoblast decay arises from a large scale apoptotic response and a lack of RAD51 nuclear translocation accompanies increases of DSBs. Secondly, the remainder of *smedwi-1+* neoblast clusters begin to slowly expand and cells exhibit a peak of DDR and DNA repair proteins at 5dpi (*e.g.* γH2AX and RAD51, respectively); marking the DNA damage repair response. Lastly, neoblast repopulation occurs 7 + dpi with increases of *smedwi-1+* cells, recovery of mitotic neoblasts and a decrease in DSBs. Cellular events are depicted by the following: mitotic neoblasts (yellow), apoptotic cells (red) and *smedwi-1+* cells (green) (C) Fold change in mitosis in RNAi and mock control animals is quantified 7dpi after 1.25k rad (sub-lethal dose). Notice the increase in mitotic events upon *ATM(RNAi)* and the inability for neoblasts to recover post *Rad51(RNAi)*. Underneath, proposed mechanism of neoblast repopulation post sublethal IR show a possible role of *Smed-ATM* functioning as a transducer of DSB signal in tandem with γH2AX phosphorylation. Further, this model implies that HR signaling is a key player in neoblast repopulation as RNAi of NHEJ did not affect neoblast repopulation. Dotted arrows and shaded colors imply uncertainties within the model and further experiments are required to validate these assumptions and interactions. ****$p < 0.0001$; one-way-ANOVA.

have been implemented to monitor neoblast populations, cell cycle progression and cellular apoptosis [103–106] (Fig. 3D).

Planaria tolerate relatively high doses of IR, far surpassing the thresholds of exposure that are known to be lethal in mammals [107,108]. Thus, the DDR in planaria can be analyzed by exposing animals to IR. For example, exposing planaria to IR above 3000 rad irreversibly eliminates neoblasts, abolishes regeneration, and leads to animal death in about three weeks [37,71,91,109–111]. Lethal doses of IR has been traditionally used as a tool to identify neoblast-associated markers and mechanisms of neoblast repopulation during tissue transplantation and irradiation [37,71,91,109–111]. However, data mining of recent transcriptional data involving samples from a seven day time course upon lethal IR [112] revealed a persistent upregulation of genes involved in DNA damage sensing and signal transduction of DSBs throughout the time course. Interestingly, there was high expression of ATM but reduced gene

expression of DNA-PKcs, required for NHEJ, throughout the time course (Fig. 4A). Similar effects are observed in primary human fibroblasts cell lines during chronic exposure to IR [113]. Because lethal IR exposure irreversibly eliminates neoblasts, the results confirmed that key regulators of cell cycle progression and markers of proliferating neoblasts were nearly abolished upon IR (*e.g. PCNA* and *cyclinB*). Furthermore, the irreversible elimination of neoblasts may also result from a gradual increase in the expression of the inhibitor of growth protein (ING) (Fig. 4A). Members of the ING family have been found to negatively regulate EGFR/PI3K/Akt signaling pathway, which is central to planaria neoblast re-population post IR [91,114]. Thus, the increased amount of IR-induced DNA damage together with upregulation of ING expression may act together to eliminate neoblast and prevent residual cell proliferation post-IR. These findings also indicate that most components of the DDR are associated with neoblasts.

Exposure to sub-lethal doses of IR (*i.e.* 1000–1750 rad) leads to a partial elimination of neoblasts, which allow for studies of DDR, SC repopulation and recovery during adult tissue renewal [91,115] (Fig. 4B). The re-establishment of mitotic activity post sub-lethal IR has been attributed to EGF signaling and active DNA repair mechanisms (*e.g* Rad51 and Rad54B) [91,116]. Sub-lethal IR depletes neoblast mitotic activity within 24 h, accompanied by a significant spike in apoptosis and DSBs. There is a gradual increase in DSB repair that peaks at five days post IR as determined by RAD51 gene/protein expression and RAD51 nuclear translocation (Fig. 4B). Neoblasts uniquely express the gene *smedwt-1* (*ptwt-1*, henceforth) [37,75,117]. *ptwt-1* expression is currently used as the gold standard to recognize the presence of neoblasts and their distribution. *ptwt-1*+ cells clusters are severely reduced during the first 7 days post-irradiation (dpi, 1250 rad) and begin to expand after 9 dpi [91,115]. However, mitotic activity is detectable after 7 dpi (Fig. 4B). Neoblast repopulation depends on EGF signaling that requires active DNA repair mediated by ATM, Rad51, Ku70 and Rad54B [91,116]. Interestingly, functional disruption of ATM with RNA-interference (RNAi) leads to an accelerated re-establishment of mitotic activity 7dpi [116] (Fig. 4C). ATM is an important player of the DDR that influences cellular decisions upon IR through reg-

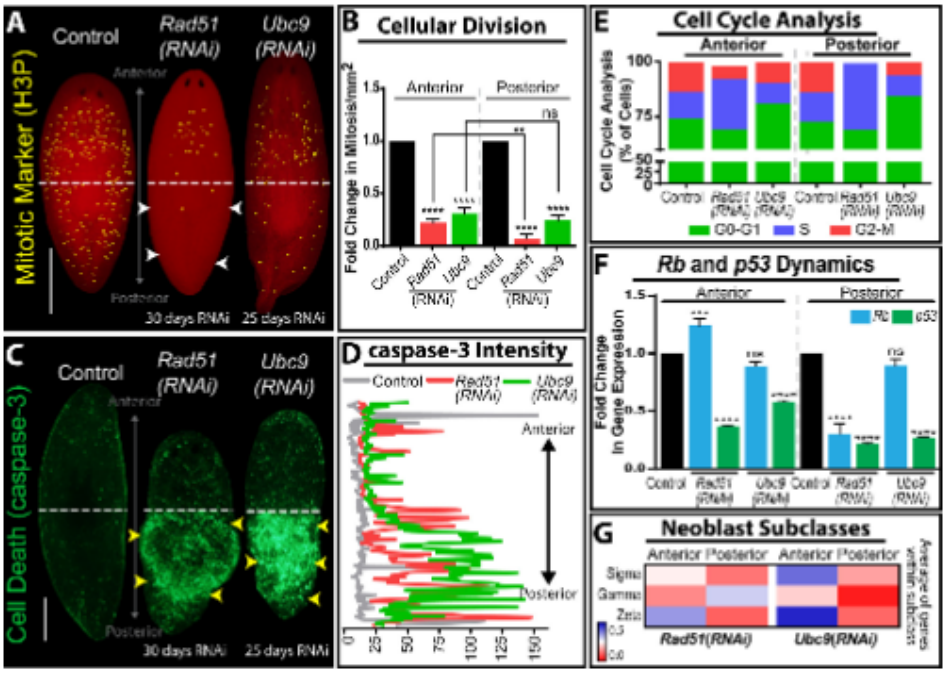

Fig. 5. *Rad51* and *Ubc9* inhibition in planaria yields high levels of DSB and region-specific neoblast responses (A) Whole mount immunostaining of mitotic neoblasts marked by Histone3 phosphorylated (H3P) in mock control, *Rad51(RNAi)* and *Ubc9(RNAi)* models. Note the difference in mitotic cells along the anteroposterior axis in the *Rad51(RNAi)* group; white arrow heads indicate a severe decrease in mitosis in the posterior versus the anterior. (B) Levels of mitotic cells across the anteroposterior axis, confirms the asymmetric distribution of mitoses is specific to *Rad51(RNAi)* but not to animals subjected to *Ubc9(RNAi)*. (C) Whole mount immunostaining of cell death marked by the caspase-3 antibody. Note the increase of apoptotic events (green signal) is concentrated in the posterior region of both *Rad51(RNAi)* and *Ubc9(RNAi)* animals (yellow arroheads). (D) Quantification of the fluorescent intensity signal from caspase-3 stained *Rad51(RNAi)* and *Ubc9(RNAi)* animals confirming the increased cell death in the posterior regions compared to the anterior and control (yellow arrowheads coincide with the increase in cell death). Intensity readings were obtained by tracing a line in the middle of the animal from the anterior to the posterior region using ImageJ software. (E) Cell cycle analysis using flow cytometry in cells dissociated from the anterior and posterior regions in animals subjected to *Rad51(RNAi)* and *Ubc9(RNAi)*. Different phases of the cell cycle are color coded and show that *Rad51(RNAi)* and *Ubc9(RNAi)* animals display different effects on cell cycle repsented by important reduction in M-phase in the posterior region of *Rad51(RNAi)*, while *Ubc9(RNAi)* animals tend to halt cell cycle in G0/G1 phases but some cells still continue to divide. (F) Fold change in gene expression of *Rb* and p53 relative to the control. Rb expression is asymmetrically upregulated in the anterior of *Rad51(RNAi)* but it does not appear affected in the same manner after *Ubc9(RNAi)*. (G) Heat map, representing fold change in the average of gene expression of neoblast subclass (sigma, gamma, zeta) markers in the anterior and posterior regions. Red indicates diminished gene expression and blue increased gene expression. **p < 0.01; ***p < 0.001; ****p < 0.0001; two-way-ANOVA. Scale bars: 200 μm.

ulation of p53/p21 axis to facilitate cell cycle checkpoint arrest [113,118]. Thus, we can postulate that *Smed-ATM* may be key to facilitating an appropriate cellular response to DSBs (*e.g.* detection and cell cycle arrest). Further experiments will be required to identify the role of *Smed-ATM* upon IR in cell cycle regulation and determine if *Smed-ATM(RNAi)* hyper-proliferative neoblasts are gnomically stable; altogether validating the conservation of this protein in planaria. The interplay of DNA repair and neoblast repopulation is only beginning to be understood but the recent evidence suggest that mechanisms of HR are the predominant repair pathway in planaria [23,91,116]. This is further supported by results demonstrating that RNAi of *Rad51* and *Rad54B* in sub-lethally irradiated animals fail to repopulate *ptwt-1+* cells and mitotic activity, resulting in lethality. Conversely, dynamics of mitotic repopulation in *Ku70(RNAi)* sub-lethally irradiated animals are indistinguishable from untreated control group [22] (Fig. 4C). All together, these results imply that *Smed-ATM* is a key upstream regulator of cell fate in response to IR-induced DSBs and HR is the dominant pathway used in repairing damaged DNA in planaria.

5. Genetic models of DNA damage in *S. mediterranea*

Two independent DNA damage models have been developed in planaria by disrupting gene function *via* RNAi of *Rad51* and *Ubc9* [22,23]. Planaria homologs of *Rad51* and *Ubc9* show high evolutionary conservation with higher organisms and their disturbance revealed important patterns of regional defects along the AP axis (Fig. 5A–D). Furthermore, RNAi of *Rad51* and *Ubc9* display loss of genomic integrity, specifically by the accumulation of DSB throughout the planaria body [22,23].

Rad51 is required for nucleofilament formation and without functional RAD51 protein the HR repair complex cannot form [20,119,120]. Full knockout of *Rad51* results in embryonic lethality in mammals [121,122]. Nonetheless, it is possible to knockdown the HR pathway but it is challenging to evaluate organismal SC response and track their progeny in an environment of genomic instability. Thus, the planaria model system offers unique opportunities to overcome these limitations by enabling the possibility of disrupting HR while SC attend systemic demands of cellular turnover and repair. On the other hand, SUMOylation is a dynamic and reversible post-translational modification that requires the cooperation of a host of proteins [123]. Critical to this pathway is UBC9, which determines protein SUMOylation [123]. SUMO attachment regulates protein function as it can affect protein localization, stability, protein–protein interaction, cause conformational changes or act as a hub to form multi-protein complexes [124]. Mounting evidence suggests SUMOylation plays a critical role in the regulation of DSB repair [125–129]. It does so in three ways: (1) regulates protein stability, DNA binding ability and localization of sensors and effectors of DSB repair, including both NHEJ and HR; (2) leads to creation of an open chromatin state more amenable to repair by controlling epigenetic modification through modulation of various methylases and acetylases; (3) orchestrates successful DDR response by coordinating multiple types of post-translational modifications, most notably stubl-mediated ubiquitination [130–139].

5.1. Functional disruption of Rad51 and Ubc9 affects tissue homeostasis in planaria

The unique feature of the *Rad51* and *Ubc9* knockdown models is the prevalence of DNA damage, especially DSBs that is present throughout the planaria body [22,23]. Molecular analysis in both models revealed a transient presence of DNA DSBs and chromosomal abnormalities that progressively increased over time. This is consistent with the role *Rad51* plays in DSBs repair through HR. However, the mechanism driving this phenomenon in the *Ubc9* phenotype was less evident. Two observations were critical to relate SUMOylation to DNA damage: (i) the regional defects in animals subjected to *Ubc9(RNAi)* were similar to those observed in *Rad51* phenotype and (ii) late stages of the *Ubc9* phenotype display increase in RAD51 and γ-H2AX protein expression, which appeared in clusters along the AP axis. Additional analysis revealed that DNA damage in *Ubc9(RNAi)* is due to the inability of RAD51 to translocate from the cytoplasm to the nucleus to repair DSBs [23]. This finding links the two models together and additionally explains phenotypic similarities, which altogether supports the idea that HR is the prominent pathway for repair of DSBs in planaria.

The induction of DNA damage after *Ubc9* and *Rad51(RNAi)* results in a cascade of cell fate decisions led by cell cycle arrest [22,23]. Cell cycle analysis revealed that while most cells in the *Rad51(RNAi)* were arrested in S phase, cells in *Ubc9(RNAi)* animals were primarily arrested in the G1 phase (Fig. 5E). *p53* and *Rb* commonly regulate neoblast fate decisions (*i.e.* apoptosis, proliferation andcell cycle arrest) during tissue renewal and regeneration. This is also the case in the presence of DNA damage in planaria but intriguingly; we found that *p53* gene expression is downregulated across the AP axis in both RNAi groups (Fig. 5F). However, there were stark differences in *Rb* expression. Specifically, there is an increase in *Rb* expression in the anterior region of *Rad51(RNAi)* animals whereas there is no significant change in *Ubc9(RNAi)* group (Fig. 5F). Although our knowledge of *Rb* dynamics relies on gene expression data, it is tempting to link increased *Rb* expression with cell cycle arrest. Canonically, *Rb* is thought to be an important regulator of the G1/S checkpoint and studies suggest that overexpression of *Rb* can increase rates of cellular survival and predispose cells to become more cancerous [140,141]. Furthermore, the genomic instability driven cell cycle arrest in both lead to interesting changes in tissue homeostasis and cellular turnover, specifically in terms of cell survival and death [22,23]. While both models coincide in a significant decrease in the cycling neoblasts, the *Rad51* model reveals a remarkably difference across the AP axis, specifically loss of survival in the posterior region. This is likely due to the differential expression of cell fate regulators *p53* and *Rb*. On the other hand, both models show a massive increase in cell death in the tail region with significantly less cells dying in the anterior. It is possible that *Rb* is acting as switch for allowing cell survival in the anterior but not the posterior. Another explanation as derived from experimentation in the *Ubc9(RNAi)* model, where the cell death is partially attributed to attenuation of Hedgehog signaling, which is known to be an important regulator of posterior polarity in planaria. Whether the same mechanism is driving cellular decisions in the *Rad51* phenotype requires further experimentation.

A remarkable finding from these studies is that some SCs in the anterior region are able to overcome surveillance mechanisms and continue proliferating with genomic instability [22,23]. In the *Rad51(RNAi)*, this is in part due to increased expression of *Rb* and neural inputs in the anterior region. Ectopic introduction of brain tissue in the posterior region, induce neoblast proliferation with DSB. These findings highlight the possibility of intercellular effects, whereby neural signals alter fate decisions of neoblasts with DSBs. Likewise, these results also prompt future studies about possible neural regulation of *Rb* signaling that facilitate proliferation of neoblasts with DSBs. Alternatively, it is possible that a subset of neoblasts is endowed with proliferative capacity to give rise to cancer-like cells in the anterior. Multiple neoblast subtypes have been characterized [72,74,75]. We found that gene expression of markers associated with zeta neoblasts are increased in the anterior for both *Ubc9* and *Rad51(RNAi)* animals (Fig. 5G). Recent research demonstrates the intriguing possibility that inhibition of Hippo signaling trigger dedifferentiation of postmitotic progenitors in pla-

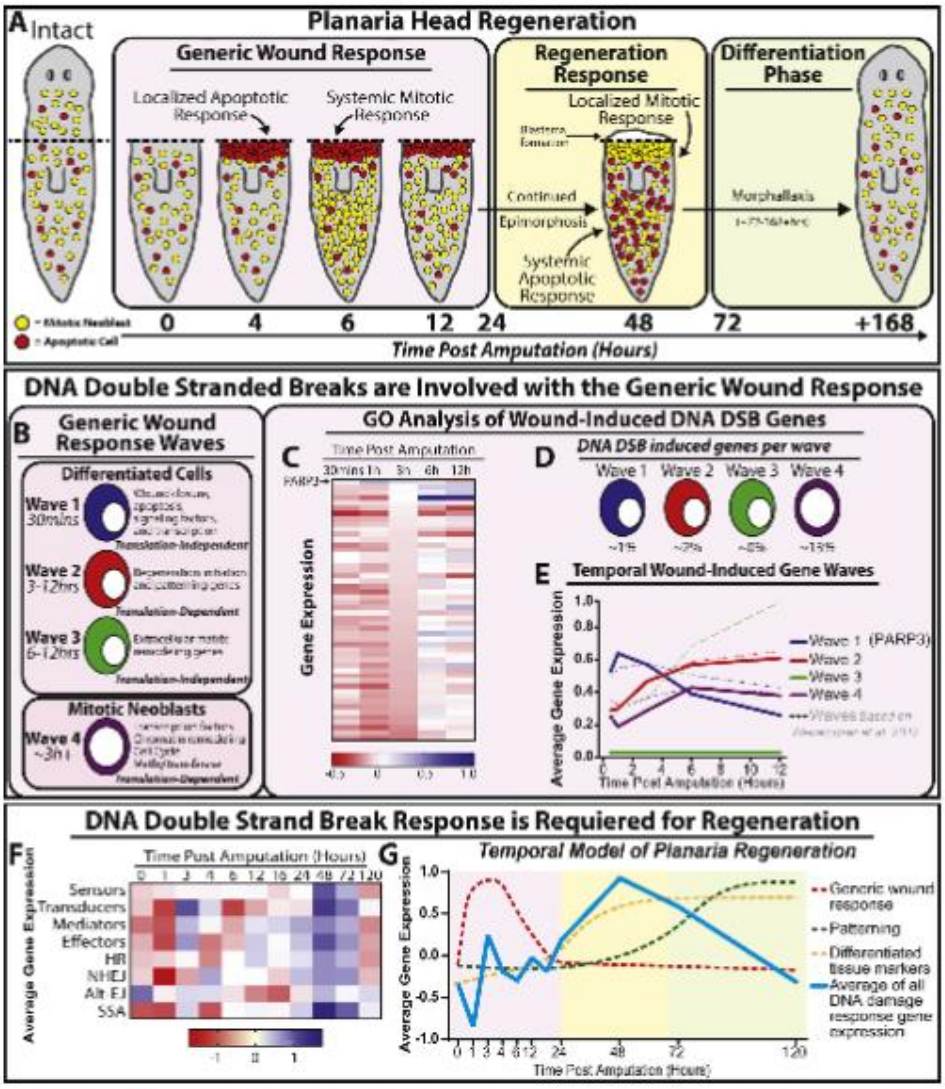

Fig. 6. DNA damage repair (DDR) is activated during the initiation of tissue regeneration (A) Schematic representation of the general cellular events taking place during the first week post-amputation (hpa) of the anterior region in planaria (color coded boxes). During the generic wound response, a localized apoptotic response occurs ~4 hpa, accompanied by a systemic burst of mitotic neoblasts at 6 hpa that gradually reduces ~12 hpa. Next, the regeneration response is followed by a localized increase in cell proliferation and a systemic wave of death. After 72 hpa the tissue will continue restructuring newly formed tissue through differentiation of stem cells and progenitors. (B) Waves of gene expression found in the generic wound response within the first 12 hpa. (C) Heat map representing GO term analysis of wound induced DDR gene expression derived from Wenemoser et al. [79]. (D) Percent of DNA damage genes associated within each wave. (E) Temporal wound-induced gene expression waves. Solid lines indicate averages of DDR specific wave response and dotted lines indicate waves according to Wenemoser et al. [79]. (F) Heat map of average DDR gene expression post amputation. At 48 hpa the average expression of all DDR genes is upregulated following wounding. (G) Graph depicts the temporal model of planaria regeneration including the average expression for genes involved in the DDR. The average of all DNA damage gene expression was obtained from the heat map in (F), (blue line) is plotted against the established temporal model of regeneration (dotted lines) according to Wenemoser et al. [79] and is color coded as shown in (A).

narians [142]. It is tantalizing to speculate that the increasing load of genomic instability may act as a switch for zeta nebolasts to leave their lineage-restricted state and try to fill the niche left behind by sigma cells that cannot survive increasing DNA damage. It is also possible that persistent demands of cellular turnover override fate decisions to promote exit of cell cycle arrest has been noted

in hematopoietic SCs [63]. Some of these cells may have weaker sensors and effectors of the DDR, allowing them to more easily circumvent these checks and balances and ultimately evolve into cancer-like cells. Additional experiments are required to dissect the actual mechanisms driving cells to withstand excessive DNA damage and continue to proliferate. Nonetheless, the results obtained with *Rad51* and *Ubc9* downregulation supports the notion that cellular decisions in the presence of DNA damage are also influenced by regional signals that may involve crosstalk among tissues and organs. This is an important finding as a more comprehensive focus on the regional signals driving proliferation of cells with genomic instability may help in understand the mechanisms facilitating cancer formation and progression.

5.2. DNA damage and repair are essential components of the regenerative response

Cell death and proliferation are not only instrumental during tissue renewal but also in the process of regenerating missing or injured body parts. Upon amputation, planaria undergo an orchestrated series of localized and systemic cascades of cellular proliferation and programmed cell death (*e.g.* ~4–6 h and ~48 h). Recent research have have greatly furthered our understanding of the genetic and molecular cascades required for tissue repair and regeneration [79,80,143]. The initial peaks of systemic cell division and localized cell death events were found to be accompanied by a genetic response called the generic wound response that happen during the first 24 h post-injury/amputation (hpa). This is followed by a wave of specific gene expression representing the regeneration response (24–70 hpa) that includes the second molecular peak of mitosis and apoptosis. Finally, the differentiation phase is attributed to neoblast progeny mediated differentiation and specialization of the blastema at +70 hpa [79,80] (Fig. 6A).

The ability to adjust cell proliferation during simultaneous demands of tissue renewal and injury highlight the faithful mechanisms used by planaria to regulate cell number. Since injury repair relies on cell proliferation and consequently DNA replication, we argue that the DDR is an active player that preserves genome integrity during regeneration. In other words, an increase in cell division is accompanied by DNA replication that is carefully monitored by DNA repair mechanisms. Indeed, recent studies have demonstrated that key components of DNA replication and repair (*e.g. p53, Rb, Rad51* and *Ubc9*) are critical for the regenerative process and without them; planaria fail to regenerate [23,84,86,116]. In addition, cell death is necessary for proper regeneration. The TUNEL assay, which detects cellular apoptosis induced by DSB-nicked ends, is commonly used to evaluate cell death in planaria [105]. After amputation, two peaks of cell death are known to happen at ~4hrs and ~48 h. However, it remains unclear whether these stereotypical patterns of TUNEL + cells are derived from the stressful environment of regeneration or actual DNA damage, specifically DSBs.

We were prompted to reanalyze the possible role DNA damage response play during the early and late phases of tissue regeneration based on published transcriptomic data [79,80]. Transcriptomic changes during the first half of the generic response in planaria offer an interesting resource to discern the role of DDR [79]. This process involves four waves of gene expression found within differentiated tissues (waves 1–3) and neoblasts (wave 4) (Fig. 6B). Using published RNAseq data from Wenemoser et al. [79], we were able to identify genes involved in DNA damage response by GO term analysis. We found that all waves except wave 3 contained genes involved in DDR (Fig. 6C–E). Interestingly, we found PARP-3 as the only DDR gene involved in wave 1 and the only DDR-specific gene with a peak in gene expression within the first hour post amputation. At the decline of PARP-3 expression at 3 h, both wave 2 and wave 4 DDR specific gene expression increased and peaked at 6 h, which coincide with the system wide mitotic response (Fig. 6C). These results suggest that expression of genes in the DDR follow similar transcriptomic changes of the generic wound response except in wave 3. It also implies that PARP family genes may prime the DDR during early regenerative events (Fig. 6C–E). However, the question still remains whether the first peak of TUNEL + cells starting ~4hrs is linked to DNA damage.

PARP-3 catalyzes post-translational modifications of proteins involved in transcription silencing, cell death and interacts with PARP-1 during DDR to accelerate NHEJ [144–147]. In addition, PARP-3 has been shown to act independently of DNA damage and mediate centrosome stability, G1/S cell cycle progression and telomerase activity [145,148,149]. For instance, PARP-3 expression has an inverse relationship with telomerase activity. Lung cancer cells depleted of PARP-3 displayed an increase in telomerase activity [149]. During planaria regeneration, telomerase activity is upregulated and accompanies neoblast proliferation [150]. Thus, the possible role of PARP-3 expression during the first 3 h of regeneration may be to restrict both neoblast cell cycle progression and telomerase activity. The decline in PARP-3 after 3 h may allow the priming of transcription of both cell cycle and DNA repair proteins that are involved during initial mitotic burst at 6 h. The data analysis shows that the initial localized peak of TUNEL + cells may not be in response to DNA damage but to the harsh environment at the amputation site to facilitate wound closure and there is a possibility that PARP-3 may be mediating the post-translational modifications associated with cell death.

Regenerating planaria exhibit a localized mitotic peak and a systemic increase in TUNEL + cells resulting in the formation of a regenerative blastema starting at 48 h post amputation [79,81,105]. Gene expression levels associated with DNA damage response and repair are relatively low within the first 24 h of regeneration (Fig. 6F). Strikingly, at 48 h, there was a dramatic increase in the expression of genes involved in DNA damage signal transduction and DDR (Fig. 6F). Thus, by plotting the average of DDR gene expression values onto the established temporal model of planaria regeneration [151], we observed that the second wave of DDR is much more significant than that of the generic phase and remains a key feature in the regeneration and early differentiation phases (Fig. 6G). Consistently, our recent work strongly supports the idea that DDR is required for large-scale tissue regeneration. Without key molecules such as *Rad51, BRCA2, Ubc9* animals, fail to regenerate and replace lost tissues [23,116]. Furthermore, according to Wurtzel et al. [80]; expression levels of genes involved in HR (*e.g. Rad51-A,-B,-C* and *BRCA2*) were highly active compared to the decrease in NHEJ (*e.g. Ku70, Ku80*, and *Ligase IV*) related genes. However, gene expression analysis revealed that HR and NHEJ were at their peaks at 48 h post amputation. Delving into the molecular dynamics of mitotic events during regeneration in *Rad51* and *Ubc9(RNAi)* animals, we observe that at 6 h post-amputation both groups respond with a slight increase in mitoses but fail to elicit a second mitotic peak at 48 h [23,116]. These results together provide further evidence that DDR is a crucial component of the overall regenerative response in planaria.

6. Final remarks

Preserving genomic integrity over recurrent tissue renewal is an important challenge that wanes with age. DNA damage and the cellular responses associated with it are at the center of efficient cellular turnover. Thus, we advocate for studies of SCs in their natural environment as they attend demands of tissue renewal and repair. The analyses integrating SCs, DNA damage and tissue

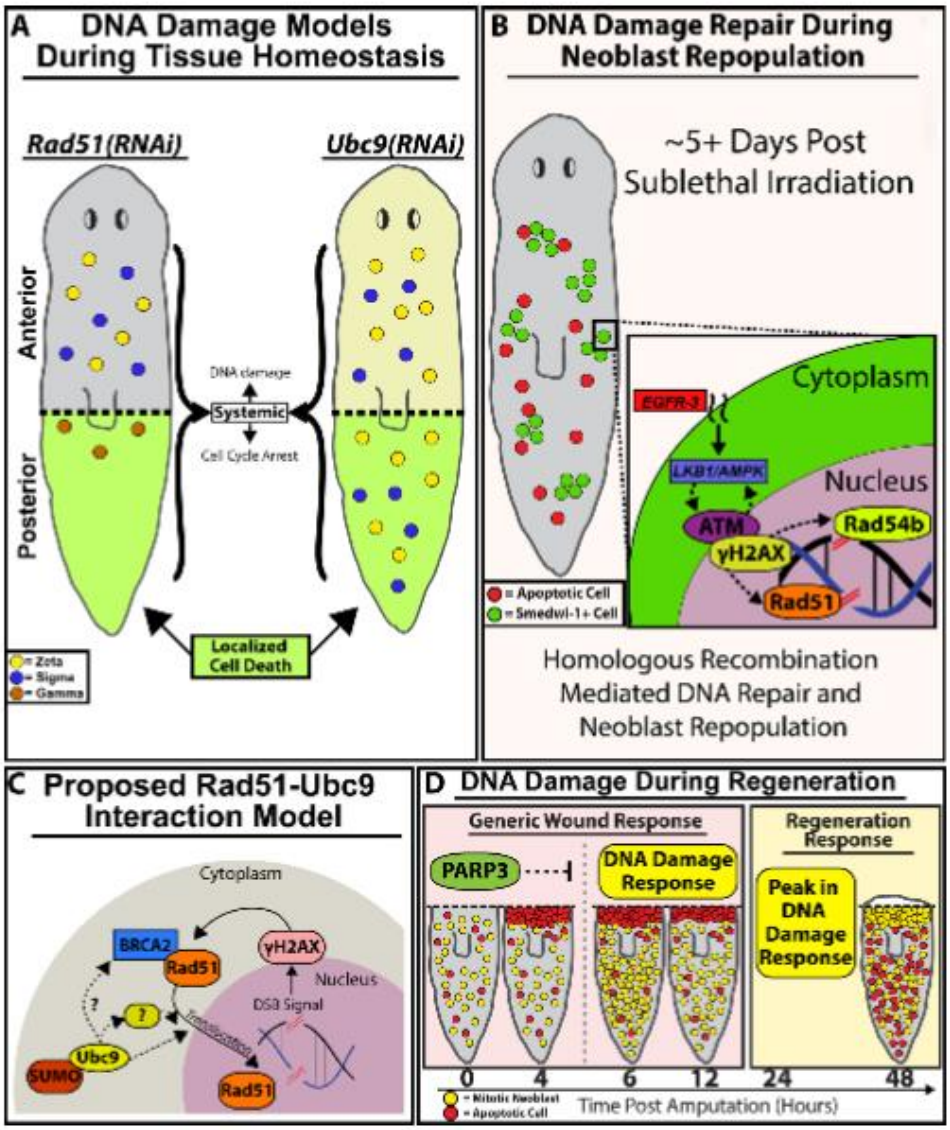

Fig. 7. DNA damage repair (DDR) pathways are critical components of the cell proliferation required for tissue regeneration. (A) *Rad51(RNAi)(gray)* and *Ubc9(RNAi)* (light-yellow) planaria share similar increases in DNA damage along the AP axis accompanied by varying levels of cell cycle arrest. Localized cell death (green) is observed in the posterior region of both RNAi conditions. Survival of neoblasts/sub-types were determined from gene expression data from Fig. 5G; neoblast subtypes: zeta (yellow), sigma (blue) and gamma (brown). (B) 5 days post sublethal irradiation, remaining neoblasts will repair DSBs by homologous recombination and neoblasts will repopulate the entire animal. We propose a hypothetical model whereby EGFR signaling integrates with DDR to facilitate neoblast repopulation post-irradiation (indicated with dotted lines). (C) Proposed RAD51-UBC9 interaction model. Presence of DNA DSB breaks triggers upregulation of RAD51 and γ-H2AX that together participate in DNA repair. However, after *Ubc9(RNAi)* the RAD51 protein accumulates in the cytoplasm as SUMOylation is required for RAD51 translocation to the nucleus. We propose that *Ubc9* may interact with intermediate regulators of Rad51 for DDR. (D) Model of DNA damage during large-scale tissue regeneration. PARP3 expression peaks during the first 4 hpa and may be suppressing DDR gene expression within that timeframe. Upon the decline of PARP3 expression, DDR expression at +6 hpa is observed. A substantial peak in DDR observed in parallel with the regeneration responses that begins +24 hpa. The robust responses of DDR pathways during wound repair could be necessary to drive DNA repair during neoblast proliferation that is required in tissue regeneration.

renewal in the complexity of the whole body present fresh opportunities to the field and has the potential to inform about cellular crosstalk and regulation of signaling pathways (e.g. tumor suppressors, oncogenes) that control cellular decisions in the face of DNA damage (Fig. 7A). The evolutionary and functional conservation of the DDR and mechanisms of SC function in planaria offers a simplified paradigm, in which pharmacological or genetic screens can be performed rapidly and cost-effectively.

The capacity to induce different levels/types of DNA damage with pharmacological compounds, IR and genetic manipulations paves the way for additional studies aimed at understanding the biology of the DDR and possible alternatives for therapeutic applications (Fig. 7B). The genetic models using loss of function of *Rad51* and *Ubc9* enable *in situ* analysis of tissue renewal in response to DNA damage that uniquely allow us to address the molecular basis controlling regional differences in the adult body (Fig. 7A). Furthermore, the activation of regional cell survival and death in response to the systemic presence of DSBs is a great resource to address mechanisms of SC survival with defective DNA. This example prompts the possibility of studying intrinsic and extrinsic cues that may favor or restrict the growth of cancer initiating cells (Fig. 7C, D). What are the signals facilitating survival of SCs with DSB in the anterior, whereas in the posterior surveillance mechanisms remain active and effectively eliminate damaged cells? Our results suggest that neural inputs may influence dynamics of cell cycle in neoblasts carrying DSBs. Thus, future experiments will address the source and the molecules mediating nervous signals that facilitate cell survival in an environment of genomic instability. Since neoblasts in the anterior region tend to survive with DSBs, it brings interesting opportunities to dissect potential differences among SCs and their susceptibility and advantages to DNA damage. Likewise, future studies will also integrate positional cues along the AP axis [152,153] with DNA repair to inform about potential interactions that can enhance or reduce the integrity of the genome. Answering these fundamental questions will enable the field to identify early markers of cellular transformation, mechanisms regulating tumor suppressors, and to define means by which transformed cells survive and form tumors. Finally, we believe that planaria traditionally recognized as model for tissue regeneration, may also represent a fresh alternative to understand and manipulate DNA damage and its effects in the adult body.

Funding

We acknowledge support from the University of California Cancer Research Coordinating Committee (award CRR-18-525108), the National Cancer Institute and National Institute of General Medical Sciences of the National Institute of Health, awards CA176114 and GM109372 to NJO.

Competing interest

The authors declare no competing or financial interest.

Acknowledgements

We thank members of the Oviedo Lab for discussion and comments on the manuscript.

References

[1] S.P. Jackson, J. Bartek, The DNA-damage response in human biology and disease, Nature 461 (7267) (2009).
[2] A. Sancar, L.A. Lindsey-Boltz, K. Unsal-Kaçmaz, S. Linn, Molecular mechanisms of mammalian DNA repair and the DNA damage checkpoints, Annu. Rev. Biochem. 73 (2004) 39–85.
[3] L. Vitale, G. Manic, R. Maria, G. Kroemer, L. Galluzzi, DNA damage in stem cells, Mol. Cell 66 (3) (2017).
[4] J.E. Haber, DNA recombination: the replication connection, Trends Biochem. Sci. 24 (7) (1999) 271–275.
[5] C.J. Lord, A. Ashworth, The DNA damage response and cancer therapy, Nature 481 (7381) (2012) 287–294.
[6] T. Lindahl, Instability and decay of the primary structure of DNA, Nature 362 (6422) (1993) 709–715.
[7] J. Nakamura, V.E. Walker, P.B. Upton, S.Y. Chiang, Y.W. Kow, J.A. Swenberg, Highly sensitive apurinic/apyrimidinic site assay can detect spontaneous and chemically induced depurination under physiological conditions, Cancer Res. 58 (2) (1998) 222–225.
[8] R.L. Saul, B.N. Ames, Background levels of DNA damage in the population, Basic Life Sci. 38 (1986) 529–535.
[9] P.D. Adams, H. Jasper, L.K. Rudolph, Aging-induced stem cell mutations as drivers for disease and cancer, Cell Stem Cell 16 (6) (2015) 601–612.
[10] N.E. Sharpless, R.A. DePinho, How stem cells age and why this makes us grow old, Nat. Rev. Mol. Cell Biol. 8 (9) (2007) 703–713.
[11] D.J. Rossi, C.H. Jamieson, I.L. Weissman, Stems cells and the pathways to aging and cancer, Cell 132 (4) (2008) 681–696.
[12] E.J. Fox, M.J. Prindle, L.A. Loeb, Do mutator mutations fuel tumorigenesis? Cancer Metastasis Rev. 32 (3–4) (2013) 353–361.
[13] R. Hakem, DNA-damage repair; the good, the bad, and the ugly, EMBO J. 27 (4) (2008) 589–605.
[14] P.A. Jeggo, M. Lobrich, How cancer cells hijack DNA double-strand break repair pathways to gain genomic instability, Biochem. J. 471 (1) (2015) 1–11.
[15] J. Ferlay, H.R. Shin, F. Bray, D. Forman, C. Mathers, D.M. Parkin, Estimates of worldwide burden of cancer in 2008: GLOBOCAN 2008, Int. J. Cancer 127 (12) (2010) 2893–2917.
[16] C. Tomasetti, B. Vogelstein, G. Parmigiani, Half or more of the somatic mutations in cancers of self-renewing tissues originate prior to tumor initiation, Proc. Natl. Acad. Sci. U. S. A. 110 (6) (2013) 1999–2004.
[17] A.C. Society, Cancer Facts & Figures, 2013, 2013 http://www.cancer.org/research/cancerfactsfigures/cancerfactsfigures/cancer-facts-figures-2013.
[18] T. Iyama, D.M. Wilson 3rd, DNA repair mechanisms in dividing and non-dividing cells, DNA Repair (Amst) 12 (8) (2013) 620–636.
[19] A. Sancar, L.A. Lindsey-Boltz, K. Unsal-Kacmaz, S. Linn, Molecular mechanisms of mammalian DNA repair and the DNA damage checkpoints, Annu. Rev. Biochem. 73 (2004) 39–85.
[20] J.E. Haber, A life investigating pathways that repair broken chromosomes, Annu. Rev. Genet. 50 (2016) 1–28.
[21] D.B. Lombard, K.F. Chua, R. Mostoslavsky, S. Franco, M. Gostissa, F.W. Alt, DNA repair, genome stability, and aging, Cell 120 (4) (2005) 497–512.
[22] T.H. Peiris, D. Ramirez, P.G. Barghouth, U. Ofoha, D. Davidian, F. Weckerle, N.J. Oviedo, Regional signals in the planarian body guide stem cell fate in the presence of genomic instability, Development 143 (10) (2016) 1697–1709.
[23] M. Thiruvalluvan, P.G. Barghouth, A. Tsur, L. Broday, N.J. Oviedo, SUMOylation controls stem cell proliferation and regional cell death through hedgehog signaling in planarians, Cell. Mol. Life Sci. 75 (2018) 1285–1301.
[24] W.K. Kaufmann, Cell cycle checkpoints and DNA repair preserve the stability of the human genome, Cancer Metastasis Rev. 14 (1) (1995) 31–41.
[25] R. Auerbach, W. Auerbach, Regional differences in the growth of normal and neoplastic cells, Science 215 (4529) (1982) 127–134.
[26] R. Auerbach, L.W. Morrissey, L. Kubai, Y.A. Sidky, Regional differences in tumor growth: studies of the vascular system, Int. J. Cancer 22 (1) (1978) 40–46.
[27] R. Auerbach, L.W. Morrissey, Y.A. Sidky, Regional differences in the incidence and growth of mouse tumors following intradermal or subcutaneous inoculation, Cancer Res. 38 (6) (1978) 1739–1744.
[28] R. Auerbach, L.W. Morrissey, Y.A. Sidky, Gradients in tumour growth, Nature 274 (5672) (1978) 697–699.
[29] L. Dispersio, Regional growth differences of human tumor xenografts in nude mice, Lab. Anim. 15 (1981) 179–180.
[30] L. Kubai, R. Auerbach, Regional differences in the growth of skin transplants, Transplantation 30 (2) (1980) 128–131.
[31] R.T. Prehn, V. Kamik, Differential susceptibility of the axilla and groin of the mouse to chemical oncogenesis, Nature 279 (5712) (1979) 431–433.
[32] A.A. Aboobaker, Planarian stem cells: a simple paradigm for regeneration, Trends Cell Biol. 21 (5) (2011) 304–311.
[33] R.S. King, P.A. Newmark, The cell biology of regeneration, J. Cell Biol. 196 (5) (2012) 553–562.
[34] J. Pellettieri, A. Sanchez Alvarado, Cell turnover and adult tissue homeostasis: from humans to planarians, Annu. Rev. Genet. 41 (2007) 83–105.
[35] P.W. Reddien, A. Sánchez Alvarado, Fundamentals of planarian regeneration, Annu. Rev. Cell Dev. Biol. 20 (2004) 725–757.
[36] A. Sánchez Alvarado, Planarian regeneration: its end is its beginning, Cell 124 (2) (2006) 241–245.
[37] P.W. Reddien, N.J. Oviedo, J.R. Jennings, J.C. Jenkin, A. Sánchez Alvarado, SMEDWI-2 is a PIWI-like protein that regulates planarian stem cells, Science 310 (2005) 1327–1330.
[38] M.R. Lieber, The mechanism of double-strand DNA break repair by the nonhomologous DNA end-joining pathway, Annu. Rev. Biochem. 79 (2010) 181–211.

[39] C. Richardson, M. Jasin, Frequent chromosomal translocations induced by DNA double-strand breaks, Nature 405 (6787) (2000) 697–700.
[40] R.W. Hart, R.B. Setlow, Correlation between deoxyribonucleic acid excision-repair and life-span in a number of mammalian species, Proc. Natl. Acad. Sci. U. S. A. 71 (6) (1974) 2169–2173.
[41] S.L. MacRae, M. Croken, R.B. Calder, A. Aliper, B. Milholland, R.R. White, A. Zhavoronkov, V.N. Gladyshev, A. Seluanov, V. Gorbunova, Z.D. Zhang, J. Vijg, DNA repair in species with extreme lifespan differences, Aging 7 (12) (2015) 1171–1182.
[42] N.A. Bishop, T. Lu, B.A. Yankner, Neural mechanisms of ageing and cognitive decline, Nature 464 (7288) (2010) 529–535.
[43] M.G. Kapetanaki, A.L. Mora, M. Rojas, Influence of age on wound healing and fibrosis, J. Pathol. 229 (2) (2013) 310–322.
[44] T. Lang, T. Streeper, P. Cawthon, K. Baldwin, D.R. Taaffe, T.B. Harris, Sarcopenia: etiology, clinical consequences, intervention, and assessment, Osteoporos Int. 21 (4) (2010) 543–559.
[45] C. Lopez-Otin, M.A. Blasco, L. Partridge, M. Serrano, G. Kroemer, The hallmarks of aging, Cell 153 (6) (2013) 1194–1217.
[46] E.K. Nishimura, S.R. Granter, D.E. Fisher, Mechanisms of hair graying: incomplete melanocyte stem cell maintenance in the niche, Science 307 (5710) (2005) 720–724.
[47] J.C. Reed, Dysregulation of apoptosis in cancer, J. Clin. Oncol. 17 (9) (1999) 2941–2953.
[48] B.D. Simons, H. Clevers, Strategies for homeostatic stem cell self-renewal in adult tissues, Cell 145 (6) (2011) 851–862.
[49] K.W. Oeford, D.T. Scadden, Deconstructing stem cell self-renewal: genetic insights into cell-cycle regulation, nature reviews, Genetics 9 (2) (2008) 115–128.
[50] C.H. Hsu, T. Stedeford, E. Okochi-Takada, T. Ushijima, H. Noguchi, C. Muro-Cacho, J.W. Holder, M. Banasik, Framework analysis for the carcinogenic mode of action of nitrobenzene, J. Environ. Sci. Health Part C 25 (2) (2007) 155–184.
[51] L.G. van der Flier, H. Clevers, Stem cells, self-renewal, and differentiation in the intestinal epithelium, Annu. Rev. Physiol. 71 (2009) 241–260.
[52] K.A.U. Gonzales, E. Fuchs, Skin and its regenerative powers: an alliance between stem cells and their niche, Dev. Cell 43 (4) (2017) 387–401.
[53] E. Fuchs, Epithelial skin biology: Three decades of developmental biology, a hundred questions answered and a thousand New ones to address, Curr. Top. Dev. Biol. 116 (2016) 357–374.
[54] W.W. Pang, S.L. Schrier, I.L. Weissman, Age-associated changes in human hematopoietic stem cells, Semin. Hematol. 54 (1) (2017) 39–42.
[55] M. Hyun, J. Lee, K. Lee, A. May, V.A. Bohr, B. Ahn, Longevity and resistance to stress correlate with DNA repair capacity in Caenorhabditis elegans, Nucleic Acids Res. 36 (4) (2008) 1380–1389.
[56] H. Lans, J.M. Lindvall, K. Thijssen, A.E. Karambelas, D. Cupac, Ø. Fensgård, G. Jansen, J.H.J. Hoeijmakers, H. Nilsen, W. Vermeulen, DNA damage leads to progressive replicative decline but extends the life span of long-lived mutant animals, Cell Death Differ. 20 (12) (2013).
[57] R. Signer, S.J. Morrison, Mechanisms that regulate stem cell aging and life span, Cell Stem Cell 12 (2) (2013) 152–165.
[58] C. Tomasetti, L. Li, B. Vogelstein, Stem cell divisions, somatic mutations, cancer etiology, and cancer prevention, Science 355 (6331) (2017) 1330–1334.
[59] S. Landais, C. D'Alterio, D.L. Jones, Persistent replicative stress alters polycomb phenotypes and tissue homeostasis in Drosophila melanogaster, Cell. Rep. 7 (3) (2014) 859–870.
[60] D.L. Jones, T.A. Rando, Emerging models and paradigms for stem cell ageing, Nat. Cell Biol. 13 (5) (2011) 506–512.
[61] R.M. Brosh Jr, M. Bellani, Y. Liu, M.M. Seidman, Fanconi anemia: a DNA repair disorder characterized by accelerated decline of the hematopoietic stem cell compartment and other features of aging, Ageing Res. Rev. 33 (2017) 67–75.
[62] J. Campisi, F. d'Adda di Fagagna, Cellular senescence: when bad things happen to good cells, Nat. Rev. Mol. Cell Biol. 8 (9) (2007) 729–740.
[63] D. Walter, A. Lier, A. Geiselhart, F.B. Thalheimer, S. Huntscha, M.C. Sobotta, B. Moehrle, D. Brocks, I. Bayindir, P. Kaschutnig, K. Muedder, C. Klein, A. Jauch, T. Schroeder, H. Geiger, T.P. Dick, T. Holland-Letz, P. Schmezer, S.W. Lane, M.A. Rieger, M.A.G. Essers, D.A. Williams, A. Trumpp, M.D. Milsom, Exit from dormancy provokes DNA-damage-induced attrition in haematopoietic stem cells, Nature 520 (7548) (2015) 549–552.
[64] I. Zlatanova, C. Pinto, J.S. Silvestre, Immune modulation of cardiac repair and regeneration: the art of mending broken hearts, Front. Cardiovasc. Med. 3 (2016) 40.
[65] M. Yanada, N. Fujino, M. Ichinose, Inflammatory responses in the initiation of lung repair and regeneration: their role in stimulating lung resident stem cells, Inflamm. Regener. 36 (2016) 15.
[66] H. Jasper, D.L. Jones, Metabolic regulation of stem cell behavior and implications for aging, Cell Metab. 12 (6) (2010) 561–565.
[67] B.J. Houston, B. Nixon, J.H. Martin, G. Iuliis, E.G. Bromfield, K.E. McEwen, R.J. Aitkena, Heat exposure induces oxidative stress and DNA damage in the male germ line, Biol. Reprod. (2018).
[68] E.F. Fang, S. Lautrup, Y. Hou, T.G. Demarest, D.L. Croteau, M.P. Mattson, V.A. Bohr, NAD + in aging: molecular mechanisms and translational implications, Trends Mol. Med. 23 (10) (2017) 899–916.
[69] J. Li, M.S. Bonkowski, S. Moniot, D. Zhang, B.P. Hubbard, A.J.Y. Ling, L.A. Rajman, B. Qin, Z. Lou, V. Gorbunova, L. Aravind, C. Steegborn, D.A. Sinclair, A conserved NAD + binding pocket that regulates protein-protein interactions during aging, Science 355 (6331) (2017) 1312–1317.
[70] J. Yoshino, J.A. Baur, S.I. Imai, NAD(+) intermediates: the biology and therapeutic potential of NMN and NR, Cell Metab. 27 (2018) 513–528.
[71] P.W. Reddien, A. Sánchez Alvarado, Fundamentals of planarian regeneration, Annu. Rev. Cell Dev. Biol. 20 (2004) 725–757.
[72] S.J. Zhu, B.J. Pearson, (Neo)blast from the past: new insights into planarian stem cell lineages, Curr. Opin. Genet. Dev. 40 (2016) 74–80.
[73] J.C. Rink, Stem cell systems and regeneration in planaria, Dev. Genes Evol. 223 (1–2) (2013) 67–84.
[74] A.M. Molinaro, B.J. Pearson, In silico lineage tracing through single cell transcriptomics identifies a neural stem cell population in planarians, Genome Biol. 17 (2016) 87.
[75] J.C. van Wolfswinkel, D.E. Wagner, P.W. Reddien, Single-cell analysis reveals functionally distinct classes within the planarian stem cell compartment, Cell Stem Cell 15 (3) (2014) 326–339.
[76] C. González-Estévez, D.A. Felix, G. Rodriguez-Esteban, A.A. Aboobaker, Decreased neoblast progeny and increased cell death during starvation-induced planarian degrowth, Int. J. Dev. Biol. 56 (1–3) (2012) 83–91.
[77] N.J. Oviedo, P.A. Newmark, A. Sanchez Alvarado, Allometric scaling and proportion regulation in the freshwater planarian Schmidtea mediterranea, Dev. Dyn. 226 (2) (2003) 326–333.
[78] P.A. Newmark, A.S. Alvarado, Not your father's planarian: a classic model enters the era of functional genomics, Nat. Rev. Genet. 3 (3) (2002) 210–219.
[79] D. Wenemoser, S.W. Lapan, A.W. Wilkinson, G.W. Bell, P.W. Reddien, A molecular wound response program associated with regeneration initiation in planarians, Gene Dev. 26 (9) (2012) 988–1002.
[80] O. Wurtzel, L.E. Cote, A. Poirier, R. Satija, A. Regev, P.W. Reddien, A generic and cell-type-specific wound response precedes regeneration in planarians, Dev. Cell 35 (5) (2015) 632–645.
[81] D. Wenemoser, P.W. Reddien, Planarian regeneration involves distinct stem cell responses to wounds and tissue absence, Dev. Biol. 344 (2) (2010) 979–991.
[82] N.J. Oviedo, B.J. Pearson, M. Levin, A. Sánchez Alvarado, Planarian PTEN homologs regulate stem cells and regeneration through TOR signaling, Dis. Models Mech. 1 (2–3) (2008) 131–143.
[83] B.J. Pearson, A. Sanchez Alvarado, Regeneration, stem cells, and the evolution of tumor suppression, Cold Spring Harb. Symp. Quant. Biol. 73 (2008) 565–572.
[84] B.J. Pearson, A. Sánchez Alvarado, A planarian p53 homolog regulates proliferation and self-renewal in adult stem cell lineages, Development (Camb., Engl.) 137 (2) (2010) 213–221.
[85] T.H. Peiris, D. Ramirez, P.G. Barghouth, N.J. Oviedo, The Akt signaling pathway is required for tissue maintenance and regeneration in planarians, BMC Dev. Biol. 16 (2016) 7.
[86] S.J. Zhu, B.J. Pearson, The Retinoblastoma pathway regulates stem cell proliferation in freshwater planarians, Dev. Biol. 373 (2) (2013) 442–452.
[87] C. Gonzalez-Estevez, D.A. Felix, M.D. Smith, J. Paps, S.J. Morley, V. James, T.V. Sharp, A.A. Aboobaker, SMG-1 and mTORC1 act antagonistically to regulate response to injury and growth in planarians, PLoS Genet. 8 (2012) e1002619.
[88] N.J. Oviedo, W.S. Beane, Regeneration: the origin of cancer or a possible cure? Semin Cell Dev. Biol. 20 (5) (2009) 557–564.
[89] N.J. Oviedo, B.J. Pearson, M. Levin, A. Sánchez Alvarado, Planarian PTEN homologs regulate stem cells and regeneration through TOR signaling, Dis. Models Mech. 1 (2–3) (2008) 131–143, discussion 141.
[90] A.S. Stevens, A. Wouters, J.P. Ploem, N. Pirotte, A. Van Roten, M. Willems, N. Hellings, C. Franken, G. Koppen, T. Artois, et al., Planarians customize their stem cell responses following genotoxic stress as a function of exposure time and regenerative state, Toxicol. Sci. 162 (2018) 251–263.
[91] K. Lei, H. Thi-Kim Vu, R.D. Mohan, S.A. McKinney, C.W. Seidel, R. Alexander, K. Gotting, J.L. Workman, A. Sánchez Alvarado, Egf signaling directs neoblast repopulation by regulating asymmetric cell division in planarians, Dev. Cell 38 (4) (2016) 413–429.
[92] A. Chinone, M. Matsumoto, DrRad51 is required for chiasmata formation in meiosis in planarian Dugesia ryukyuensis, Mol. Reprod. Dev. 81 (5) (2014) 409–421.
[93] Y. Xiang, D.E. Miller, E.J. Ross, A. Sanchez Alvarado, R.S. Hawley, Synaptonemal complex extension from clustered telomeres mediates full-length chromosome pairing in Schmidtea mediterranea, Proc. Natl. Acad. Sci. U. S. A. 111 (48) (2014) E5159–68.
[94] H. Brandl, H. Moon, M. Vila-Farre, S.Y. Liu, I. Henry, J.C. Rink, PlanMine–a mineable resource of planarian biology and biodiversity, Nucleic Acids Res. 44 (D1) (2016) D764–73.
[95] S.M.C. Robb, K. Gotting, E. Ross, A. Sánchez Alvarado, SmedGD 2.0: the schmidtea mediterranea genome database, Genesis (New York, N.Y.: 2000) 53 (8) (2015) 535–546.
[96] M.M. Vilenchik, A.G. Knudson, Endogenous DNA double-strand breaks: production, fidelity of repair, and induction of cancer, Proc. Natl. Acad. Sci. U. S. A. 100 (22) (2003) 12871–12876.
[97] M.R. Lieber, The mechanism of double-strand DNA break repair by the nonhomologous DNA end-joining pathway, Annu. Rev. Biochem. 79 (2010) 181–211.
[98] R. Ceccaldi, B. Rondinelli, A.D. D'Andrea, Repair pathway choices and consequences at the double-strand break, Trends Cell Biol. 26 (1) (2016) 52–64.

[99] P. Baumann, S.C. West, Role of the human RAD51 protein in homologous recombination and double-stranded-break repair, Trends Biochem. Sci. 23 (7) (1998) 247–251.
[100] A. Shibata, Regulation of repair pathway choice at two-ended DNA double-strand breaks, Mutat. Res. 803–805 (2017) 51–55.
[101] S. Yin, Y. Huang, Y. Zhangfang, X. Zhong, P. Li, J. Huang, D. Liu, Z. Songyang, Smed0081 is required for planarian homeostasis and regeneration, Sci. Rep. 6 (2016) 34013.
[102] L. Guo, A. Accorsi, S. He, C. Guerrero-Hernandez, S. Sivagnanam, S. McKinney, M. Gibson, A. Sanchez Alvarado, An adaptable chromosome preparation methodology for use in invertebrate research organisms, BMC Biol. 16 (1) (2018) 25.
[103] T.H. Peiris, M.E. Garcia-Ojeda, N.J. Oviedo, Alternative flow cytometry strategies to analyze stem cells and cell death in planarians, Regeneration 3 (2) (2016) 123–135.
[104] T. Hayashi, M. Asami, S. Higuchi, N. Shibata, K. Agata, Isolation of planarian X-ray-sensitive stem cells by fluorescence-activated cell sorting, Dev. Growth Differ. 48 (6) (2006) 371–380.
[105] J. Pellettieri, P. Fitzgerald, S. Watanabe, J. Mancuso, D.R. Green, A. Sánchez Alvarado, Cell death and tissue remodeling in planarian regeneration, Dev. Biol. 338 (1) (2010) 76–85.
[106] C.E. Bender, P. Fitzgerald, S.W. Tait, F. Llambi, G.P. McStay, D.O. Tupper, J. Pellettieri, A. Sanchez Alvarado, G.S. Salvesen, D.R. Green, Mitochondrial pathway of apoptosis is ancestral in metazoans, Proc. Natl. Acad. Sci. U. S. A. 109 (13) (2012) 4904–4909.
[107] E. Seung, N. Iwakoshi, B.A. Woda, T.G. Markees, J.P. Mordes, A.A. Rossini, D.L. Greiner, Allogeneic hematopoietic chimerism in mice treated with sublethal myeloablation and anti-CD154 antibody: absence of graft-versus-host disease, induction of skin allograft tolerance, and prevention of recurrent autoimmunity in islet-allografted NOD/Lt mice, Blood 95 (6) (2000) 2175–2182.
[108] R.H. Mole, The LD50 for uniform low LET irradiation of man, Br. J. Radiol. 57 (677) (1984) 355–369.
[109] C.R. Bardeen, F.H. Baetjer, The inhibitive action of the roentgen rays on regeneration in planarians, J. Exp. Zool. 1 (1904) 191–195.
[110] O.C. Guedelhoefer, A. Sánchez Alvarado, Amputation induces stem cell mobilization to sites of injury during planarian regeneration, Development (Camb., Engl.) 139 (19) (2012) 3510–3520.
[111] P. Abeuave, E. Aboukhatwa, N. Kosaka, J. Thompson, M.A. Hill, A.A. Aboobaker, Epithelial-mesenchymal transition transcription factors control pluripotent adult stem cell migration in vivo in planarians, Development 144 (19) (2017) 3440–3453.
[112] J. Solana, D. Kao, Y. Mihaylova, F. Jaber-Hijazi, S. Malla, R. Wilson, A. Aboobaker, Defining the molecular profile of planarian pluripotent stem cells using a combinatorial RNAseq, RNA interference and irradiation approach, Genome Biol. 13 (3) (2012) R19.
[113] L. Cao, H. Kawai, M. Sasatani, D. Iizuka, Y. Masuda, T. Inaba, K. Suzuki, A. Ootsuyama, T. Umata, K. Kamiya, F. Suzuki, A novel ATM/TP53/p21-mediated checkpoint only activated by chronic γ-irradiation, PLoS One 9 (8) (2014) e104279.
[114] X.-L. Liu, X.-T. Zhang, J. Meng, H.-F. Zhang, Y. Zhao, C. Li, Y. Sun, Q.-B. Mei, F. Zhang, T. Zhang, ING5 knockdown enhances migration and invasion of lung cancer cells by inducing EMT via EGFR/PI3K/Akt and IL-6/STAT3 signaling pathways, Oncotarget 8 (33) (2017) 54265–54276.
[115] D.E. Wagner, I.E. Wang, P.W. Reddien, Clonogenic neoblasts are pluripotent adult stem cells that underlie planarian regeneration, Science (New York, N.Y.) 332 (6031) (2011) 811–816.
[116] T.H. Peiris, D. Ramirez, P.G. Barghouth, U. Ofoha, D. Davidian, F. Weckerle, N.J. Oviedo, Regional signals in the planarian body guide stem cell fate in the presence of genomic instability, Development (Camb., Engl.) 143 (10) (2016) 1697–1709.
[117] D.E. Wagner, I.E. Wang, P.W. Reddien, Clonogenic neoblasts are pluripotent adult stem cells that underlie planarian regeneration, Science 332 (6031) (2011) 811–816.
[118] K.H. Herzog, M.J. Chong, M. Kapsetaki, J.J. Morgan, P.J. McKinnon, Requirement for Atm in ionizing radiation-induced cell death in the developing central nervous system, Science (New York, N.Y.) 280 (5366) (1998) 1089–1091.
[119] M.R.G. Taylor, M. Spírek, K.R. Chaurasiya, J.D. Ward, R. Carzaniga, X. Yu, E.H. Egelman, L.M. Collinson, D. Rueda, L. Krejci, S.J. Boulton, Rad51 paralogs remodel pre-synaptic Rad51 filaments to stimulate homologous recombination, Cell 162 (2) (2015) 271–286.
[120] J. Liu, T. Doty, B. Gibson, W.D. Heyer, Human BRCA2 protein promotes RAD51 filament formation on RPA-covered single-stranded DNA, Nat. Struct. Mol. Biol. 17 (10) (2010) 1260–1262.
[121] T. Tsuzuki, Y. Fujii, K. Sakumi, Y. Tominaga, K. Nakao, M. Sekiguchi, A. Matsushiro, Y. Yoshimura, MoritaT, Targeted disruption of the Rad51 gene leads to lethality in embryonic mice, Proc. Natl. Acad. Sci. U. S. A. 93 (13) (1996) 6236–6240.
[122] D.S. Lim, P. Hasty, A mutation in mouse rad51 results in an early embryonic lethal that is suppressed by a mutation in p53, Mol. Cell. Biol. 16 (12) (1996) 7133–7143.
[123] A. Flotho, F. Melchior, Sumoylation: a regulatory protein modification in health and disease, Annu. Rev. Biochem. 82 (2013) 357–385.
[124] A. Pichler, C. Fatouros, H. Lee, N. Eisenhardt, SUMO conjugation – a mechanistic view, Biomol. Concepts 8 (1) (2017) 13–36.
[125] A.J. Garvin, J.R. Morris, SUMO, a small, but powerful, regulator of double-strand break repair, Philos. Trans. R. Soc. Lond. B Biol. Sci. (1731) (2017) 372.
[126] J.R. Morris, A.J. Garvin, SUMO in the DNA double-stranded break response: similarities, differences, and cooperation with ubiquitin, J. Mol. Biol. 429 (22) (2017) 3376–3387.
[127] M. Nie, M.N. Boddy, Cooperativity of the SUMO and ubiquitin pathways in genome stability, Biomolecules 6 (1) (2016).
[128] P. Sarangi, X. Zhao, SUMO-mediated regulation of DNA damage repair and responses, Trends Biochem. Sci. 40 (4) (2015) 233–242.
[129] Z. Wang, W.-G. Zhu, X. Xu, Ubiquitin-like modifications in the DNA damage response, Mutat. Res. 803–805 (2017) 56–75.
[130] S. Bologna, V. Altmannova, E. Valtorta, C. Koenig, P. Liberali, C. Gentili, D. Anrather, G. Ammerer, L. Pelkmans, L. Krejci, S. Ferrari, Sumoylation regulates EXO1 stability and processing of DNA damage, Cell Cycle (Georget., Tex.) 14 (15) (2015) 2439–2450.
[131] I.A. Hendriks, L.W. Treffers, M. Verlaan-de Vries, J.V. Olsen, A.C. Vertegaal, SUMO-2 Orchestrates Chromatin Modifiers in Response to DNA Damage, Cell Rep. (2015), 2015 Mar 10. pii: S2211-1247(15)00179-5.
[132] I.A. Hendriks, A.C.O. Vertegaal, SUMO in the DNA damage response, Oncotarget 6 (18) (2015) 15734–15735.
[133] C. Huang, J. Cheng, T. Bawa-Khalfe, X. Yao, Y.E. Chin, E.T. Yeh, SUMOylated OBC2 recruits a histone demethylase to regulate centromeric histone modification and genomic stability, Cell Rep. 15 (1) (2016) 147–157.
[134] C.-S. Wu, J. Ouyang, E. Mori, H.D. Nguyen, A. Maréchal, A. Hallet, D.J. Chen, L. Zou, SUMOylation of ATRIP potentiates DNA damage signaling by boosting multiple protein interactions in the ATR pathway, Gene Dev. 28 (13) (2014) 1472–1484.
[135] S.P. Jackson, D. Durocher, Regulation of DNA damage responses by ubiquitin and SUMO, Mol. Cell 49 (5) (2013) 795–807.
[136] B. Lee, M.T. Muller, SUMOylation enhances DNA methyltransferase 1 activity, Biochem. J. 421 (3) (2009) 449–461.
[137] Y. Qin, J. Xu, K. Aysola, N. Begum, V. Reddy, Y. Chai, W.E. Grizzle, E.E. Partridge, E.S.P. Reddy, V.N. Rao, Ubc9 mediates nuclear localization and growth suppression of BRCA1 and BRCA1a proteins, J. Cell. Physiol. 226 (12) (2011) 3355–3367.
[138] H. Shima, H. Suzuki, J. Sun, K. Kono, L. Shi, A. Kinomura, Y. Horikoshi, T. Ikura, M. Ikura, R. Kanaar, K. Igarashi, H. Saitoh, H. Kurumizaka, S. Tashiro, Activation of the SUMO modification system is required for the accumulation of RAD51 at sites of DNA damage, J. Cell Sci. 126 (Pt. 22) (2013) 5284–5292.
[139] R. Vyas, R. Kumar, F. Clermont, A. Helfricht, P. Kalev, P. Sotiropoulou, I.A. Hendriks, E. Radaelli, T. Hochepied, C. Blanpain, A. Sablina, H. van Attikum, J.V. Olsen, A.G. Jochemsen, A.C.O. Vertegaal, J.C. Marine, RNF4 is required for DNA double-strand break repair in vivo, Cell Death Differ. 20 (3) (2013) 490–502.
[140] J.N. Davis, M.T. McCabe, S.W. Hayward, J.M. Park, M.L. Day, Disruption of Rb/E2F pathway results in increased cyclooxygenase-2 expression and activity in prostate epithelial cells, Cancer Res. 65 (9) (2005) 3633–3642.
[141] S. Thomas, A. Balan, P. Balaram, The expression of retinoblastoma tumor suppressor protein in oral cancers and precancers: a clinicopathological study, Dental Res. J. 12 (4) (2015) 307–314.
[142] N. de Sousa, G. Rodriguez-Esteban, J.I. Rojo-Laguna, E. Salo, T. Adell, Hippo signaling controls cell cycle and restricts cell plasticity in planarians, PLoS Biol. 16 (1) (2018) e2002399.
[143] S. Owlarn, F. Klenner, D. Schmidt, F. Rabert, A. Tomasso, H. Reuter, M.A. Mulaw, S. Moritz, L. Gentile, G. Weidinger, K. Bartscherer, Generic wound signals initiate regeneration in missing-tissue contexts, Nat. Commun. 8 (1) (2017) 2282.
[144] M. Altmeyer, S. Messner, P.O. Hassa, M. Fey, M.O. Hottiger, Molecular mechanism of poly(ADP-ribosyl)ation by PARP1 and identification of lysine residues as ADP-ribose acceptor sites, Nucleic Acids Res. 37 (11) (2009) 3723–3738.
[145] C. Boehler, L.R. Gauthier, O. Mortusewicz, D.S. Biard, J.-M. Saliou, A. Bresson, S. Sanglier-Cianferani, S. Smith, V. Schreiber, F. Boussin, F. Dantzer, Poly(ADP-ribose) polymerase 3 (PARP3), a newcomer in cellular response to DNA damage and mitotic progression, Proc. Natl. Acad. Sci. U. S. A. 108 (7) (2011) 2783–2788.
[146] M. Rouleau, D. McDonald, P. Gagné, M.E. Ouellet, A. Droit, J.M. Hunter, S. Dutertre, C. Prigent, M.J. Hendzel, G.G. Poirier, PARP-3 associates with polycomb group bodies and with components of the DNA damage repair machinery, J. Cell. Biochem. 100 (2) (2007) 385–401.
[147] S.L. Rulten, A.E.O. Fisher, I. Robert, M.C. Zuma, M. Rouleau, L. Ju, G. Poirier, B. Reina-San-Martin, K.W. Caldecott, PARP-3 and APLF function together to accelerate nonhomologous end-joining, Mol. Cell 41 (1) (2011) 33–45.
[148] A. Augustin, C. Spenlehauer, H. Dumond, J. Ménissier-De Murcia, M. Piel, A.-C. Schmit, F. Apiou, J.-L. Vonesch, M. Kock, M. Bornens, G. De Murcia, PARP-3 localizes preferentially to the daughter centriole and interferes with the G1/S cell cycle progression, J. Cell. Sci. 116 (Pt. 8) (2003) 1551–1562.
[149] T. Fernández-Marcelo, C. Frías, I. Pascua, C. de Juan, J. Head, A. Gómez, F. Hernando, J.-R. Jarabo, E. Díaz-Rubio, A.-J. Torres, M. Rouleau, M. Benito, P. Iniesta, Poly (ADP-ribose) polymerase 3 (PARP3), a potential repressor of telomerase activity, J. Exp. Clin. Cancer Res. 33 (2014) 19.
[150] T.C.J. Tan, R. Rahman, F. Jaber-Hijazi, D.A. Felix, C. Chen, E.J. Louis, A. Aboobaker, Telomere maintenance and telomerase activity are differentially

regulated in asexual and sexual worms, Proc. Natl. Acad. Sci. U. S. A. 109 (2012) 4209–4214.
[151] O. Wurtzel, L.E. Cote, A. Poirier, R. Satija, A. Regev, P.W. Reddien, A generic and cell-type-specific wound response precedes regeneration in planarians, Dev. Cell 35 (5) (2015) 632–645.
[152] T. Stuckemann, J.P. Cleland, S. Werner, H. Thi-Kim Vu, R. Bayersdorf, S.Y. Liu, B. Friedrich, F. Julicher, J.C. Rink, Antagonistic self-organizing patterning systems control maintenance and regeneration of the anteroposterior axis in planarians, Dev. Cell 40 (3) (2017) 248–263 e4.
[153] O. Wurtzel, I.M. Oderberg, P.W. Reddien, Planarian epidermal stem cells respond to positional cues to promote cell-type diversity, Dev. Cell 40 (5) (2017) 491–504 e5.

Appendix VI

Developmental and Comparative Immunology 93 (2019) 18–27

Contents lists available at ScienceDirect

Developmental and Comparative Immunology

journal homepage: www.elsevier.com/locate/devcompimm

The planarian *Schmidtea mediterranea* is a new model to study host-pathogen interactions during fungal infections

Eli Isael Maciel[a,b], Cen Jiang[a,c], Paul G. Barghouth[a,b], Clarissa J. Nobile[a,d,*], Néstor J. Oviedo[a,d,*]

[a] Department of Molecular & Cell Biology, University of California, Merced, USA
[b] Quantitative and Systems Biology Graduate Program, University of California, Merced, USA
[c] Department of Laboratory Medicine, Ruijin Hospital, Shanghai Jiaotong University School of Medicine, Shanghai, China
[d] Health Sciences Research Institute, University of California, Merced, USA

ARTICLE INFO

Keywords:
Innate immunity
Planarians
Platyhelminthes
Invertebrates
Candida albicans
Pathogenic fungi
Clearance
Infection
Neoblasts
Stem cells

ABSTRACT

Candida albicans is one of the most common fungal pathogens of humans. Currently, there are limitations in the evaluation of *C. albicans* infection in existing animal models, especially in terms of understanding the influence of specific infectious stages of the fungal pathogen on the host. We show that *C. albicans* infects, grows and invades tissues in the planarian flatworm *Schmidtea mediterranea*, and that the planarian responds to infection by activating components of the host innate immune system to clear and repair host tissues. We study different stages of *C. albicans* infection and demonstrate that planarian stem cells increase division in response to fungal infection, a process that is likely evolutionarily conserved in metazoans. Our results implicate MORN2 and TAK1/p38 signaling pathways as possible mediators of the host innate immune response to fungal infection. We propose the use of planarians as a model system to investigate host-pathogen interactions during fungal infections.

1. Introduction

Fungal infections rank among the top ten causes of human death, with over 1 billion people currently infected with a fungal disease worldwide (WHO, 2018). Together with the increase in antifungal drug resistance emerging in recent years, pathogenic fungi represent a notable global threat to human health (Fisher et al., 2012, 2018). *Candida albicans* can lead to infections that range from superficial cutaneous and mucosal infections to severe systemic and invasive infections resulting in over 40% human mortality (Bongomin et al., 2017; Brown et al., 2012). The current gold-standard in the field to study *C. albicans* virulence is the mouse tail-vein injection model, where *C. albicans* is injected directly into the host bloodstream (Clancy et al., 2009). This model, however, only captures the late stages of *C. albicans* infection in humans, once the fungus has breached the host defenses to enter the bloodstream. Therefore, there is a need to understand the earlier stages of infection, such as how *C. albicans* breaches host barriers and defends against the host innate immune system.

C. albicans is a polymorphic fungal pathogen that has the ability to change morphologies depending on its environment. For example, *C. albicans* can reversibly switch between round yeast form cells to elongated filamentous cells (hyphae and pseudohyphae) in response to specific environmental cues, which is an important virulence factor for *C. albicans* host infection (Braun and Johnson, 1997; Saville et al., 2003). The yeast to hyphal transition is important for *C. albicans* infection, colonization, and evasion of the host immune system; the yeast form cells facilitate dissemination through the blood stream, while the hyphal cells cause tissue damage and invasion as well as aid in the escape out of phagocytic cells. In fact, it is well-established that *C. albicans* strains genetically modified to remain "locked" in the yeast or filamentous forms are unable to undergo the yeast to hyphal transition, resulting in highly attenuated conditions for virulence in mouse models of infection (Lo et al., 1997; Saville et al., 2003).

Planarians are flatworms (Platyhelminthes) with high rates of cellular turnover and an extraordinary capacity to regenerate, both processes of which are based on adult stem cells (SCs) called neoblasts (Aboobaker, 2011; King and Newmark, 2012; Pellettieri and Sanchez Alvarado, 2007; Reddien and Sánchez Alvarado, 2004; Wagner et al., 2011). The immune system of planaria has a high degree of evolutionary conservation to the innate immune system of humans (Abnave and Ghigo, 2018; Li et al., 2018; Lu et al., 2017; Maciel and Oviedo, 2018; Peiris et al., 2014; Tsoumtsa et al., 2018). Additionally, similar to humans, planarians are able to distinguish between commensal and pathogenic bacteria (Abnave et al., 2014; Arnold et al., 2016; Keating

* Corresponding authors. Department of Molecular & Cell Biology, University of California, Merced. 5200 North Lake Road, Merced, CA, 95343, USA.
E-mail addresses: cnobile@ucmerced.edu (C.J. Nobile), noviedo2@ucmerced.edu (N.J. Oviedo).

https://doi.org/10.1016/j.dci.2018.12.005
Received 21 September 2018; Received in revised form 7 November 2018; Accepted 11 December 2018
Available online 17 December 2018
0145-305X/

et al., 2017; Torre et al., 2017b). In fact, it takes only a few days for planaria to eliminate infections of a wide range of pathogenic Gram-negative and Gram-positive bacteria, as well as mycobacteria (e.g. *L. pneumophila*, *S. aureus*, and *M. tuberculosis*, respectively) (Abnave et al., 2014). Thus, previous analyses of the planaria innate immune system during bacterial infection has provided useful information about host response strategies aimed at clearance of bacterial pathogens (Abnave and Ghigo, 2018; Abnave et al., 2014; Arnold et al., 2016; Gao et al., 2017; Hammoudi et al., 2018; Li et al., 2018; Lu et al., 2017; Pang et al., 2016; Torre et al., 2017a; Tsoumtsa et al., 2017, 2018). Indeed, the function of the gene encoding the human homolog of Membrane Occupation and Recognition Nexus repeat containing-2 (MORN2) was unknown until a screen in planarians allowed for the identification of its function in phagocytosis and clearance of bacterial infections (Abnave et al., 2014). Interestingly, MORN2 is conserved in planarians and humans, but it is not present in other invertebrate models namely *D. melanogaster* or *C. elegans* (Abnave et al., 2014), and thus its identification would have been missed using other invertebrate infection models.

The study of vertebrate and invertebrate in vivo models of candidiasis to date has provided important insights into the pathogenesis of fungal infections (Bergeron et al., 2017; Chamilos et al., 2007; Fuchs et al., 2010; Glittenberg et al., 2011; Gratacap et al., 2017; Mallick et al., 2016; Mylonakis, 2008; Mylonakis et al., 2007; Peterson and Pukkila-Worley, 2018; Pukkila-Worley et al., 2009a; Segal and Frenkel, 2018). However, there are still existing limitations in analyzing host-pathogen interactions in the context of the adult body and the stem cell response. For example, although mammalian models such as the rat, mouse, and rabbit are the closest species used to mimic human infections, their use is limited by sample size, handling, and cost. On the other hand, invertebrate models, including *Drosophila melanogaster*, *Caenorhabditis elegans* and *Galleria mellonella*, although cost-effective, are limited in their use to analyze embryonic stages, infection methodology (e.g. injections cause injury), and evolutionary divergence from humans, among other limitations. Here, we introduce the use of the planarian *Schmidtea mediterranea* as an alternative invertebrate model to study different stages of fungal infection with *C. albicans*. The simplified anatomy of adult planarians enables an in-depth analysis of fungal infections and the effects they may have on signaling pathways regulating the crosstalk between stem cells and various differentiated tissues. We developed a fungal infection strategy using *C. albicans* as the pathogen and the planaria *S. mediterranea* as the host. We established protocols to visualize *C. albicans* distribution during infection of planarian tissues. These analyses determined that fungi rapidly infect and grow inside planaria causing damage to superficial and deep tissues. Despite this aggressive pathogen invasion, it only takes a few days for *S. mediterranea* to halt *C. albicans* growth and clear the infection while reestablishing form and function of damaged tissues. Furthermore, we find that fungal infection activates neoblast proliferation and increases the expression of highly conserved host molecular cascades such as MORN2 and TAK1/p38.

2. Methods

2.1. Planarian culture

The asexual strain CIW4 of planaria species *Schmidtea mediterranea* was used for all assays. The planaria culture was maintained as previously described (Oviedo et al., 2008).

2.2. Microorganisms

Candida albicans strain SN250 was used as the wild-type control strain, and hyper-filamentous strain TF125 (*nrg1/nrg1*) (Homann et al., 2009), and non-filamentous strain TF156 (*efg1/efg1*) (Homann et al., 2009) were used to assess the effects of filamentation on the infection assays. Strains were grown on yeast peptone dextrose (YPD) agar plates for 2 day at 30 °C, and single colonies were selected and cultured in YPD liquid medium overnight at 30 °C to obtain cultures for infection assays.

2.3. S. mediterranea challenge/infection assay

About ten planarians were kept in plastic wells containing 3 mL of water to which specific concentrations of *C. albicans* cells were added and the total volume was adjusted to 4 mL. The animals were kept in the infected media for three days. After this initial three-day exposure, the planaria were washed daily with fresh water and observed under the microscope to record any behavioral or macroscopic defects for the next seven days. All procedures before, during and after infection with *C. albicans* were performed in water at room temperature, which is the ideal medium and temperature for planaria. Under these conditions, *C. albicans* are not actively dividing in the media, and thus the infection period was extended to three days.

2.4. CFU counting

Planaria were collected after three days of infection as well as at other indicated time points. The animals were homogenized in 1 mL of 1xPBS. The homogenate was further diluted into 10 mL of 1xPBS, and 250 µL of the homogenate was then plated onto YPD media agar plates containing ampicillin (1 µg/mL). After an overnight incubation at 30 °C, *C. albicans* colonies were counted.

2.5. Whole mount immunofluorescence

Planarians were sacrificed by placing them in 5.7% of 12N HCL solution for 5 min and fixing them in Carnoys solution for 2 h on ice. After this, planarians were stored in methanol at −20 °C for at least an hour and then bleached overnight in 6% H_2O_2 solution. Animals were rehydrated in dilutions of Methanol:PBSTx and stained as previously described (Thiruvalluvan et al., 2018). Primary antibodies: α-H3p, 1:250 (Millipore Cat# 05-817R) and caspase-3, 1:500 (Abcam ab13847). Secondary antibodies: Goat anti-rabbit Alexa568, 1:800 (Invitrogen Cat# 11036) for H3P, HRP-conjugated goat anti-rabbit antibody (Millipore Cat# 12-348) with TSA-Alexa568 anti-HRP for caspase-3, 1:2000.

For *C. albicans* staining and p-38 staining in the planaria whole mounts, animals were sacrificed in 10% NAC diluted in PBS. The animals were then fixed in 4% formaldehyde in 0.3% PBSTx and permeabilized with 1% SDS. Animals were then bleached in 6% H_2O_2 in 1xPBS. Primary antibodies: Anti-*Candida*, 1:500 (ThermoFisher Cat# PA1-27158) and anti-phospho p38, 1:800 (Cell Signaling Technologies CAT# 9211).

2.6. TUNEL assay

Worms were prepared for TUNEL or immunostaining identically to those prepared for *C. albicans* staining. TUNEL was then performed as previously described (Pellettieri et al., 2010). During the double staining, the animals were fixed in preparation for TUNEL staining. The double stained always started with TUNEL stain followed by blocking with PSTB for 4 h before the caspase stain.

2.7. Imaging and data processing

Area measurements were calculated using ImageJ software bundled with Java 1.8.0_172 (Schneider et al., 2012) and the differences in animal sizes were determined as fold change in reference relative to control group at each time point. Digital pictures were collected using a Nikon AZ-100 multizoom microscope and NIS Elements AR 3.2 software (Nikon). Brightness and contrast were adjusted using Adobe Photoshop. Neoblasts were counted and normalized to the area using

ImageJ. Caspase-3 signal was quantified by measuring levels of fluorescence using NIS element software (Nikon) as previously described (Thiruvalluvan et al., 2018).

2.8. Gene expression analysis

RNA was extracted with Trizol from control and infected animals at all three time points. The qPCR reactions were performed using SYBR Green Master Mix in a 7500 Fast Real Time PCR cycler (Applied Biosystems). Each of the reactions were performed in triplicate using the median cycle threshold value for analysis and normalized to the ubiquitously expressed clone *H.55.12e*, as described previously (Peiris et al., 2016).

3. Results

3.1. Effects of Candida albicans infection in planarians

We developed a fungal infection strategy in which *C. albicans* was introduced to liquid (water) media containing planaria. After three days of incubation at room temperature (i.e. days post-infection-dpi), the media was replaced daily with fresh water and worms were evaluated under the microscope for seven days to record any macroscopic or behavioral changes (Fig. 1A). Three strains of *C. albicans* were used: wild type/WT (SN250), non-filamentous (TF156, an *efg1/efg1* mutant), and hyper-filamentous (TF125, an *nrg1/nrg1* mutant). In a mouse model of *C. albicans* bloodstream infection, the non-filamentous *efg1/efg1* mutant strain was found to be attenuated for virulence, and in a *C. elegans* infection model, the hyper-filamentous *nrg1/nrg1* mutant strain was highly invasive and virulent (Lo et al., 1997; Pukkila-Worley et al., 2009b). Overall, three days of exposure to *C. albicans* was generally lethal to planarians (Fig. 1B). However, planarian survival rate was lower when exposed to the hyper-filamentous *C. albicans* strain, requiring 4-8 times the concentration of wild-type and non-filamentous strains to kill 50% of the worms 3 dpi (Fig. 1B). Planarian exposure to *C. albicans* for three days demonstrated a dual host response characterized by either survival or death of the planarians. To better understand the mechanisms guiding survival in the presence of *C. albicans*, we focused our analysis on animals that survived after 3 dpi. To that end, we established an effective infection concentration of *C. albicans* in the planarian model at 5 million cells/mL for the hyper-filamentous and 15 million cells/mL for the WT and non-filamentous strains. Next, we determined the capacity of planaria to clear *C. albicans* from their body by macerating individual worms at different time points of infection and plating the content on fungal-selective medium to determine CFUs. Strikingly, the hyper-filamentous strain grew fewer colonies than the WT and the non-filamentous strains; and at 10 dpi, all *C. albicans* strains were eliminated from the planaria (Fig. 1C).

Soaking planarians in media containing the different strains of *C. albicans* (7.5×10^6 cells/mL) for three days led to morphological defects including epithelial lesions, tissue loss (e.g. head regression), partial body lysing and lethality (Fig. 1D and E). Live images were taken after the 3rd day of the infection right after the daily rinse with fresh water. The hyper-filamentous strain was the most virulent leading to over 50% of animal death and the remainder of the animals experienced phenotypes of tissue lesion and lysing that affected ~90% of

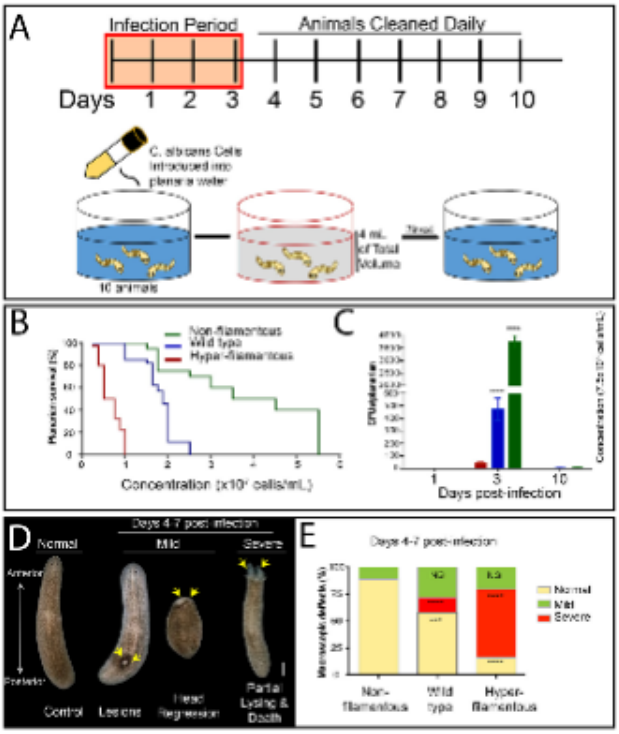

Fig. 1. Infection protocol with *C. albicans* leads to tissue damage in *S. mediterranea*.
A) Graphical illustration of the planaria infection timeline with *C. albicans*. Planaria were placed in small wells with 4 mL of water that was inoculated with *C. albicans* (0.5×10^7 to 6×10^7 cells/mL) and incubated for three days in the dark at room temperature. After the third day liquid was removed and planarians rinsed with freshwater daily for seven days. ***B)*** Planarian survival under different concentrations of three strains of *C. albicans* at the third day of infection. ***C)*** Number of *C. albicans* cells (three different strains) in planarians during the course of infection expressed as colony forming units (CFUs) over time. Note that *C. albicans* growth peaks during the first few days of incubation but by day 10 post-infection the presence of fungi is dramatically reduced. The experiment was replicated three times with 10 animals per experiment. The *C. albicans* concentration is 7.5×10^6 cells/mL for each condition. Two-Way ANOVA, ****P < 0.0001. ***D)*** Representative images and percentage of morphological defects observed after incubating planarians with the different *C. albicans* strains at 7.5×10^6 cells/mL between 4 and 7 days post-infection. Arrows point toward macroscopic lesions in the dorsal side of planarians. ***E)*** Percentage of macroscopic defects associated with the different growth forms at 7.5×10^6 cells/mL between 4 and 7 days post-infection. Scale bar is 200 μm. Two independent replicates were performed with 20 animals each and statistical analyses were based on comparison against the non-filamentous strain. Two-Way ANOVA, ***P < 0.001; ****P < 0.0001, NS = no significant (C, E).

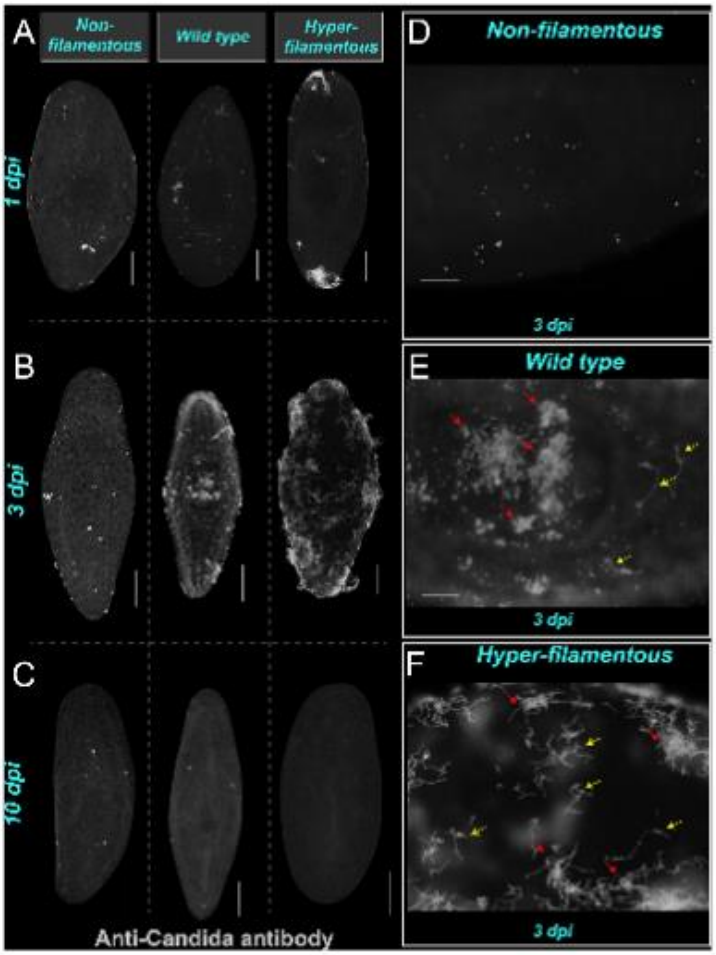

Fig. 2. Visualization of *C. albicans* during and after infection.
A-C) Representative images of whole-mount anti-*Candida* antibody stain during infection days 1, 3 and 10. The images show the presence of *C. albicans* cells on the most superficial layer of planaria tissue. Animals were infected with 2×10^7 cells/mL for the non-filamentous, 1.5×10^7 cells/mL for the wild type and 5×10^6 cells/mL for the hyper-filamentous *C. albicans* strains. ***D-F)*** High magnification images of planarian tissue with anti-*Candida* antibody stain at day 3 post-infection with the non-filamentous, wild type and hyper-filamentous strains, respectively. The yellow arrows indicate the presence of hyphae in tissue infected with the wild type strain. The red arrows point towards clusters of *C. albicans* cells. Scale bar is 200 μm. Five independent replicates were performed using 10 animals each. (For interpretation of the references to colour in this figure legend, the reader is referred to the Web version of this article.)

the animals (Fig. 1E). Exposure to the WT strain led to lesions, head regression and death that affected 45% of the animals, while the non-filamentous strain affected only 10% of the planarian exposed (Fig. 1E). These results demonstrate that the hyper-filamentous strain renders the most aggressive form of infection in *S. mediterranea*. Moreover, we noticed that at 10 dpi, lesions were completely healed in the surviving animals and their behavior was indistinguishable from the untreated animals.

3.2. Visualizing *Candida albicans* infection in planarians

To assess the effects and the spatiotemporal distribution of *C. albicans* in planaria, we used the anti-*Candida* antibody (Abcam, #ab53891) at different time points after infection with each *C. albicans* strain (Fig. 2). This approach allowed us to distinguish the distinct morphological forms of *C. albicans* in whole-mount and in tissue sections, and determine their locations and qualitatively analyze their abundance throughout the planarian body (Figs. 2 and 3). Generally, *C. albicans* cells were detected on planarian tissues from day 1 and the concentration gradually increased and peaked by 3 dpi. Interestingly, at 10 dpi *C. albicans* cells from all strains were dramatically reduced or absent from the planarian body with all three strains (Fig. 2). Overall, the infection with the WT and hyper-filamentous strains were more prolific and aggressive by 3 dpi relative to the non-filamentous strain. No obvious tissue tropism was observed as *C. albicans* cells were observed throughout the planaria body, including within dorsal and ventral surfaces and in deep tissues (Fig. 2B).

In addition, to the general distribution of *C. albicans* in the animal, we also noted the tendency of *C. albicans* to form clusters as the infection progressed (e.g. 3 dpi). The nature of these clusters is unclear but may be suggestive of biofilm development, which is a common *C. albicans* virulence strategy (Lohse et al., 2018; Nobile and Johnson,

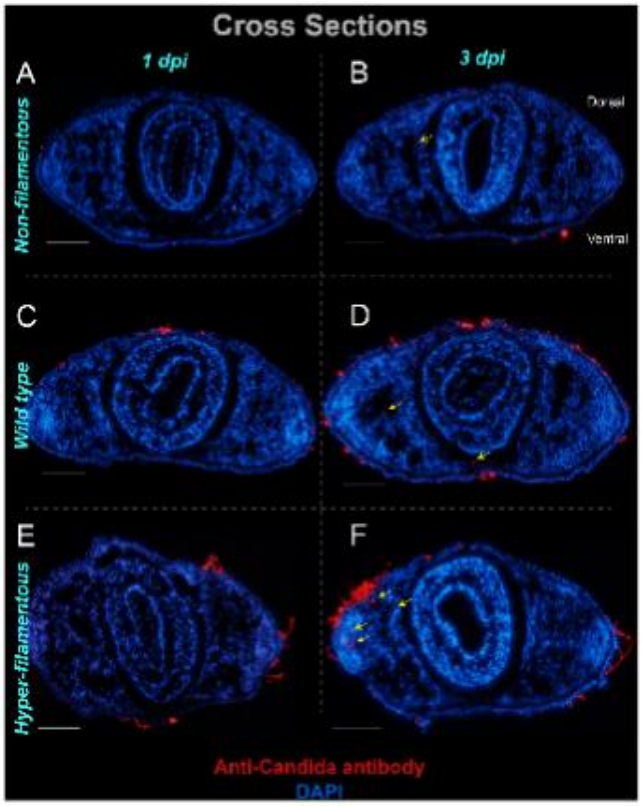

Fig. 3. *C. albicans* invades epithelium and deeper tissues in *S. mediterranea*.
A, B) Transverse cross-section images from the middle part of the planarian body exposed to *C. albicans* strains (red signal) at days 1 and 3 post-infection. The pharynx is the circular structure in the middle of the section. The planaria tissue is counterstained with DAPI (blue). Animals were infected with 2×10^7 cells/mL for the non-filamentous, 1.5×10^7 cells/mL for the wild type and 5×10^6 cells/mL for the hyper-filamentous *C. albicans* strains. The thickness of the sections was 10 μm and dorsal is shown at the top and ventral at the bottom. (For interpretation of the references to colour in this figure legend, the reader is referred to the Web version of this article.)

2015). Close up microscopic observations revealed that hyphal cells were present at 3 dpi in planaria infected with the WT strain (Fig. 2E), indicating the growth of the tissue invasive morphological form at this time point. We also noted that infection with the hyper-filamentous strain typically started at either the anterior or the posterior end of the animal (head or tail) but by 3 dpi the antibody signal was spread throughout the animal (Fig. 2F).

We performed cross sections at different time points post-infection to visualize the distribution of *C. albicans* cells in superficial and deeper planarian tissues. For simplicity, we display representative images of the cross sections taken at the middle part of the body where the pharynx is located (Fig. 3). All three strains were observed to localize to the epithelial layer by 1 dpi, and as the infection progressed *C. albicans* cells were found in deeper tissues (parenchyma) and the amount of pathogen present was strain-dependent (Fig. 3). Specifically, the hyper-filamentous and the WT strains had the largest presence in both the epithelia and parenchyma (Fig. 3C–F). Despite the massive growth of *C. albicans* in the planaria, the fungus became undetectable by 10 dpi, consistent with the CFUs results in Fig. 1C. These results demonstrate that fungi are able to attach, penetrate and grow inside planarian tissues, and that planaria subsequently respond to the infection by recognizing and clearing the pathogen.

3.3. *Candida albicans* infection triggers neoblast division and cell death

To learn about the planaria host response to *C. albicans* infection, we first observed the cellular changes taking place. Neoblasts are the only cells with the capacity to divide in planaria (Bardeen and Baetjer, 1904; Newmark and Sánchez Alvarado, 2000; Reddien et al., 2005; van Wolfswinkel et al., 2014; Wagner et al., 2011; Zeng et al., 2018). Thus, neoblast division provides the cellular progeny required to renew and repair all planarian tissues. Mitotic neoblasts are recognized with anti-histone-3 phosphorylated antibody (H3P) (Newmark and Sánchez Alvarado, 2000). We found that infection with the hyper-filamentous strain was accompanied with an increase in neoblast division during the first 3 dpi, while the WT strain only increased mitotic activity on the first day of infection (Fig. 4A–D). Remarkably, mitotic levels returned to basal levels by 10 dpi in all groups (Fig. 4D). Furthermore, we also found that the expression of the pan-neoblast marker *smedwi-1* displayed significant changes during infection. Specifically, *smedwi-1* expression levels increased at 1 dpi with the hyper-filamentous strain and unexpectedly also increased at 10 dpi with the WT strain (Fig. 4E). Interestingly, there was a dramatic decrease in *smedwi-1* expression at 3 dpi with the WT and non-filamentous *C. albicans* strains, while the group exposed to the hyper-filamentous strain display similar levels of expression as the uninfected control (Fig. 4E). Although the changes in gene expression associated with this neoblast marker are not

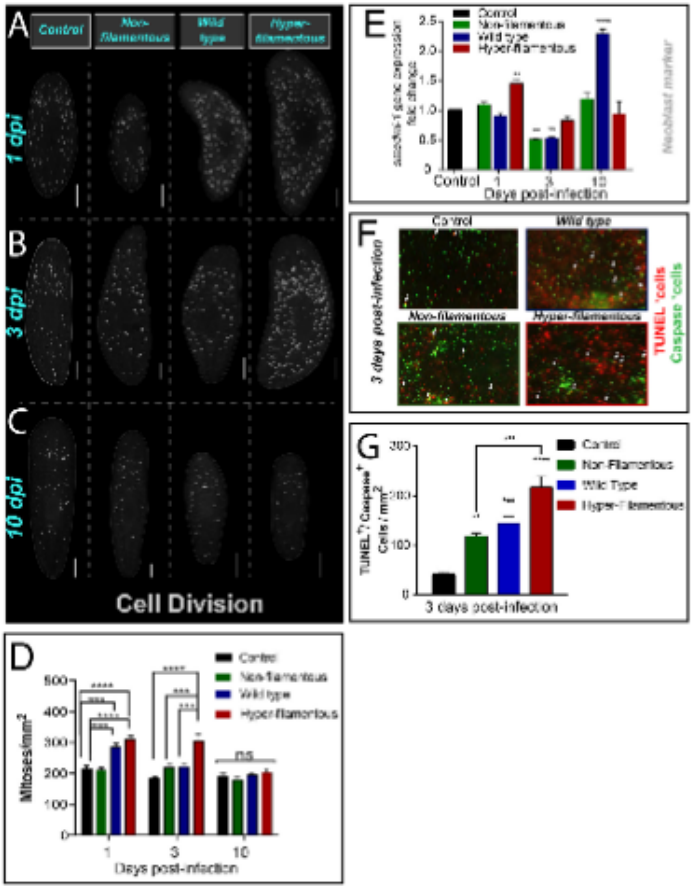

Fig. 4. *C. albicans* infection induces hyper-proliferation and cell death in planaria.
A-C) Whole-mount immunostaining with anti-phospho-histone H3 (Ser10) antibody, which labels mitotic cells (yellow dots) at different times of infection with *C. albicans* strains: non-filamentous (2×10^9 cells/mL), wild type (1.5×10^7 cells/mL) and hyper-filamentous (5×10^6 cells/mL). ***D)*** Number of mitoses at different times of infection with *C. albicans* strains and the non-infected control. ***E)*** Levels of *smedwi-1* gene expression at different times of infection with *C. albicans* strains. The expression of *smedwi-1* is normalized against a non-infected control. The internal reference is based on the ubiquitously expressed clone *H.55.12e*. ***F)*** Double staining with anti-caspase-3 antibody (green signal) and TUNEL positive cells (red signal) in planarian tissue at day 3 post-infection with *C. albicans* strains (7.5×10^6 cells/mL). In all cases the control sample corresponds to un-infected animal. ***G)*** Levels of double positive cells for caspase+/TUNEL+ in planarian tissue at day 3 post-infection with *C. albicans* strains (7.5×10^6 cells/mL). Cell division experiments consisted of three biological replicates using 10 animals each. Cell death experiments consisted of two biological replicates using 4 animals each. All graphs represent mean ± SEM. All statistical comparisons are against control unless noted with bars. Scale bar is 200 μm. Two-Way-ANOVA, $^{*}P < 0.01$; $^{***}P < 0.001$; $^{****}P < 0.0001$ and ns = no significant. (For interpretation of the references to colour in this figure legend, the reader is referred to the Web version of this article.)

mechanistically clear, these findings suggest that neoblasts may form part of the host response to counteract the effects of *C. albicans* infection.

Simultaneous whole-mount immunostaining with the TUNEL (terminal deoxynucletidyl transferase dUTP nick end labeling) assay and anti-caspase-3 antibody were performed to determine whether *C. albicans* infection affects cell death in the host (Fig. 4F and G). Since the TUNEL assay also labels cell death in *C. albicans* and caspase-3 is specific to the planarian, we co-labeled planarian tissue with both TUNEL and the caspase-3 antibody to quantify double positive cells. These experiments revealed that all three *C. albicans* strains triggered an increase in cell death, although the infection with the hyper-filamentous strain displayed four-fold the amount of cell death compared to the control (uninfected sample) (Fig. 4F and G). Taken together, these data demonstrate that the hyper-filamentous *C. albicans* strain triggers the most dramatic changes in the host involving cell death and cell division.

3.4. MORN2 and TAK1/p38 signaling pathways May facilitate efficient clearance of C. albicans infection

To further understand the mechanisms of the innate immune system activated during planarian clearance of *C. albicans* infection, we focused on pattern recognition receptors (PRRs) that are frequently involved in the recognition of fungi during an infection (Drummond and Brown, 2013; Goyal et al., 2018; Tang et al., 2018). Specifically, we performed gene expression analyses of components associated with C-type lectin receptors (CTLs) and Toll like receptors (TLRs) upon infection with different strains of *C. albicans* (Gao et al., 2017; Tsoumtsa et al., 2018). Components of the CTL and TLR pathways are depicted in Fig. 5A. To assess the involvement of the CTL pathway post-infection, we measured the expression of the upstream component, SYK, which encodes an adaptor protein, and the downstream component, TAK1, which encodes a signaling kinase. To evaluate the TLR pathway, we measured MyD88, which encodes an adaptor protein of TLRs that is known to play important roles during *C. albicans* infection and is present in the planarian genome (Roeder et al., 2004; Tsoumtsa et al., 2018). Two other genes MORN2 and Tyrosinase were also selected for expression measurements

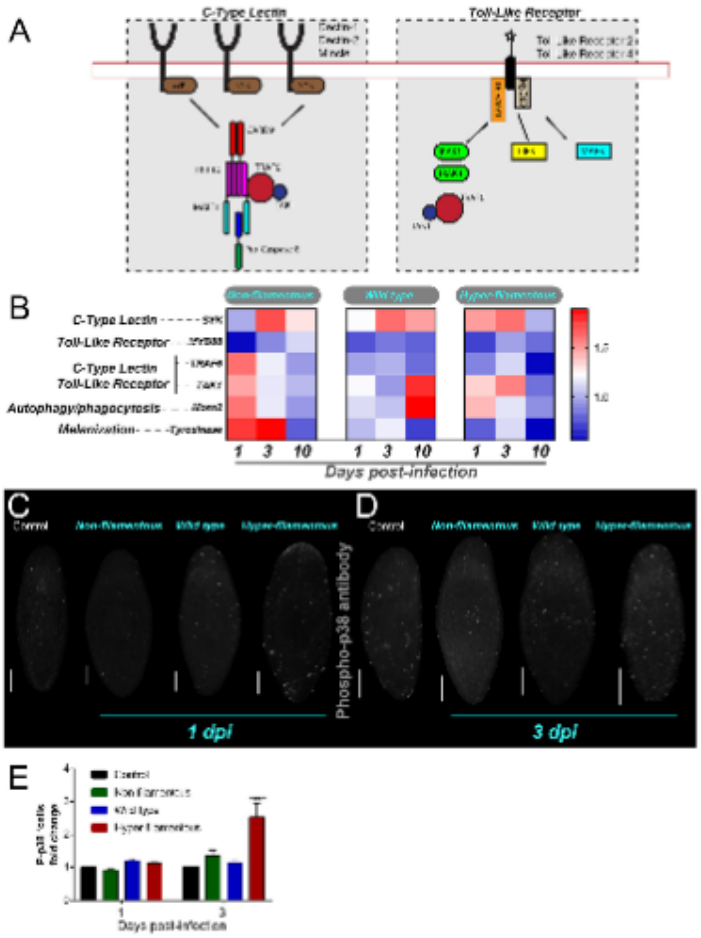

Fig. 5. Downstream effectors of C Type Lectins are upregulated during *C. albicans* infection.
A) Graphical representation of the canonical signaling cascade activated by two particular pattern recognition receptors, C-type lectins (CTLs) and Toll like receptors (TLRs). The left side of the illustration depicts three of the most commonly known C type lectin pattern recognition receptors in response to *C. albicans* infection in mammals. The right side of the illustration shows two of the common toll like receptors that recognize *C. albicans* along with its downstream effectors. ***B)*** Gene expression levels of different components associated with CTL and TLR pathways during time course of infection with *C. albicans* strains. Levels are shown in a heat map and the scale bar displayed indicates red is upregulation and blue is downregulation. Gene expression values represent mean ± SEM of triplicate samples; each condition was generated by extracting RNA from 10 animals. The internal control is the ubiquitously expressed clone *H.55.12e*. ***C, D)*** Whole-mount immunostaining with anti-phosphorylated p38 antibody (P-p38, white dots) at different time points of infection with *C. albicans* strains: non-filamentous (2×10^7 cells/mL), wild type (1.5×10^7 cells/mL) and hyper-filamentous (5×10^6 cells/mL). ***E)*** Number of P-p38 $^+$cells at different time points of infection with *C. albicans* strains and the non-infected control. Experiments consisted of two biological replicates with 10 animals each. All graphs represents mean ± SEM. All statistical comparisons are against control unless noted with bars. Scale bar is 200 μm. Two-Way-ANOVA, $^*p < 0.01$; $^{***}p < 0.001$; $^{****}p < 0.0001$ and ns = no significant. (For interpretation of the references to colour in this figure legend, the reader is referred to the Web version of this article.)

due to their known roles in clearing other microbial pathogens (Abnave et al., 2014; Cerenius et al., 2008). The gene expression measurements during the infection time course revealed that MYD88 was not upregulated during any of the infections or time points while TRAF6 only showed increased expression for the non-filamentous strain in day 1 (Fig. 5B). Conversely, SYK and TAK1 were upregulated in the planaria at different days depending on the strain of *C. albicans*. The non-filamentous and hyper-filamentous strains upregulated most of the selected genes during day 1 and 3, which was different from what was observed for the WT strain, where WT upregulated most genes at day 10 (Fig. 5B). Since the overall upregulation of the CTL effector genes was observed during the infection for all three *C. albicans* strains, we proceeded to look further into the CTL pathway. Recent studies revealed that bacterial infection triggers phosphorylation of p38 MAPK through activation of TAK1, which in turn leads to responses mediated by NF-kB (Arnold et al., 2016). To test whether planarians clear *C. albicans* infection through activation of phospho-p38 MAPK we used the P-p38 human antibody at different time points of infection. The results showed that by day 3, the signal for P-p38 was increased compared to the control (uninfected planaria) and compared to planaria infected with the other two strains of *C. albicans* (Fig. 5C and D). These results suggest that MORN2 and TAK1/p38 signaling pathways may facilitate efficient clearance of *C. albicans* infection.

4. Discussion

Our results demonstrate that the fungal pathogen *C. albicans* can infect planarians, and that this flatworm is capable of recognizing and effectively eliminating *C. albicans* in a relatively short period of time. Here, we introduce a new invertebrate and low-cost model system to enable studies of host-pathogen interactions at different stages of fungal infection. Our findings also provide unique opportunities to analyze the activation of the host innate immune response independently of the adaptive immune response and underscore the privileged evolutionary position of flatworms and their biology that closely relate to human health.

We developed a highly reproducible infection protocol based on soaking planarians in a solution containing *C. albicans*. This cost-effective strategy allows for the visualization of the initial *C. albicans* contact with host tissues, as well as its successive interactions to penetrate and invade deeper within tissues and organs throughout the host. We noticed that although some planaria succumb to fungal infection, some survive, and additional experimentation involving the use of different methods of exposure (e.g. injection and feeding), will be required to understand the underlying basis leading to this differential behavior. Although infecting planarians by feeding has been used before for bacterial infections (Abnave et al., 2014; Arnold et al., 2016), our method of infection through soaking offers several advantages. First, it allows for the control of both the concentration of pathogens exposed to the host as well as for the easy and rapid removal of those pathogens in the media through washes. Second, this novel model is also useful to study mechanisms of host-pathogen epithelial infections by fungi. Third, our protocol is time-effective, taking only a few days from initial exposure to clearance of the infection. Finally, our methods can be easily scaled up to perform high-throughput screens to identify mutants with virulence defects and or antimicrobial compounds that are effective against *C. albicans* infection.

Exposure to three different morphological strains of *C. albicans* (WT, non-filamentous (*efg1/efg1*) and hyper-filamentous (*nrg1/nrg1*)) revealed that filamentation is an important virulent factor that affects planarian tissue. These findings also demonstrate that, similar to vertebrate animal models, the amount of tissue damage and the number of *C. albicans* cells penetrating deeper organs is dependent on the ability of *C. albicans* to undergo the yeast to hyphal transition. Interestingly, all tested *C. albicans* strains were able to adhere to the planarian epithelial cells, but the non-filamentous strain was less efficient at disseminating to internal tissues. This dissemination defect of the non-filamentous strain is likely due to the inability of this strain to cause tissue damage, and thus preventing penetration into the deeper tissues of the planarians. This non-filamentous strain is also likely to be eliminated more easily through phagocytosis. Wild-type *C. albicans* cells can adhere and transition to invasive forms in planarian tissue, and thus this new model can be used to gain mechanistic insights into virulence and possibly biofilm formation during fungal infection. Future studies will address the specific mechanisms used by pathogenic fungi to penetrate and invade host planarian tissues, and will provide deeper mechanistic insights into the host response and whether phagocytosis plays a central role in *C. albicans* clearance. Nonetheless, the current results provide opportunities to analyze direct early interactions between *C. albicans* and epithelial surfaces in the host. We propose that this infection strategy has some resemblance to mucosal infections in vertebrate models, and is consistent with the ability of fungal filamentation to facilitate tissue invasion, biofilm formation, and evasion of host macrophages (Cleary et al., 2016; Fuchs et al., 2010; Kadosh and Lopez-Ribot, 2013; Lo et al., 1997; Mitchell, 1998).

Stem cells in mammals constantly renew tissues that are targeted by microbial infections (e.g. epithelial surfaces). *C. albicans* infection is known to activate the proliferation of mesenchymal and hematopoietic SCs leading to an increase in lineage-restricted cells necessary to fight pathogenic fungi (Megías et al., 2012, 2016; Yáñez et al., 2009, 2011; Yang et al., 2012). Planarians constantly renew tissues from stem cell division and we show here that neoblast proliferation is increased when planarians are exposed to invasive forms of *C. albicans*, which potentially suggests that the stem cell response to fight fungal infection is evolutionarily conserved in metazoans. This claim is also supported by recent findings that associate neoblasts with the ability of the host to combat *Staphylococcus aureus* infection (Keating et al., 2017; Torre et al., 2017b). Future experiments will determine whether the increase in neoblast division upon *C. albicans* infection is directed toward a specific lineage such as the reticular cells, which are known to mediate the planarian innate immune response (Morita, 1991, 1995). Our focus at the organismal level also enables access to the host response involving crosstalk between SCs, differentiated tissues and the innate immune system responding to fungal infection. This comprehensive approach has the potential to identify novel molecular players involved in the rapid clearance of pathogenic fungi.

Our results demonstrating an increase in the gene expression of TAK1 and SYK imply that the planarian response to *C. albicans* infection is mediated by the CTL receptors, which are also activated to eliminate pathogenic bacteria (Abnave et al., 2014; Arnold et al., 2016; Gao et al., 2017). The findings presented here, lead us to propose that *C. albicans* infection elicits innate immune responses in the host involving multiple mechanisms encompassing traceable cellular (i.e. neoblast proliferation) and humoral (e.g. MORN2, TAK1/p38 signaling) activity to efficiently clear infection by pathogenic fungi. This cellular and humoral strategy is also effective to combat bacterial infection and allow for the innate immune system to adapt to recurrent infection (Abnave et al., 2014; Arnold et al., 2016; Torre et al., 2017a). Our results are consistent with the possibilities that other signaling pathways may also become activated during infection and/or that their mechanistic activation may take place at different times. For example, TAK1 and SYK are expressed at different time points when planaria are infected with the different *C. albicans* strains. One possible explanation for this observation is that the WT strain may be capable of masking specific fungal cell wall components that are recognized by the PRRs (McKenzie et al., 2010). Most CTL receptors detect either β-glucans or α-mannans, which are two major components of the *C. albicans* cell wall (Netea et al., 2006). We speculate that the predicted pattern recognition receptor mediating the innate immune response against *C. albicans* is likely to be a CTL receptor, which will activate the SYK protein, and proceed to activate a complex that contains BCL and CARD proteins (Li et al., 2018; Maciel and Oviedo, 2018). This is also consistent with the idea that TAK1 is also active during this process, and interacts with P38 and other MAP kinase cascades that eventually end in the activation of the transcription factor NF-kβ (Arnold et al., 2016; Torre et al., 2017a; Tzoumtsa et al., 2017). Additional insights about the genetic network activated in the host will be obtained in future studies using genome-wide transcriptomic analyses during a time course of infection with *C. albicans*. Nonetheless, our work extends previous analyses of host-pathogen interactions in planaria (Abnave and Ghigo, 2018; Abnave et al., 2014; Arnold et al., 2016; Gao et al., 2017; Hammoudi et al., 2018; Li et al., 2018; Lu et al., 2017; Pang et al., 2016; Torre et al., 2017a; Tzoumtsa et al., 2017, 2018) and introduces a simplified platform to study evolutionarily conserved mechanisms to overcome infections by pathogenic fungi.

5. Conclusion

Collectively, our work introduces planarian flatworms as a low-cost and time efficient model organism to dissect basic mechanisms of host-pathogen responses during fungal infection.

Funding

This work was supported by the National Science Foundation graduate fellowship award 1744620 to EIM, and the University of California Cancer Research Coordinating Committee (Award# CRR-18-525108) and the National Institutes of Health National Cancer Institute and National Institute of General Medical Sciences awards R21CA176114 and R15GM109372 to NJO, and the NIH National Institute of Allergy and Infectious Diseases (NIAID) and NIGMS awards R21AI125801 and R35GM124594 to CJN.

Conflicts of interest

The authors declare no competing or financial interest.

Acknowledgements

We thank Edelweiss Pfister for lab managing and planarian maintenance, and members of the Oviedo and Nobile labs for insightful discussions and comments on the manuscript.

References

Abnave, P., Ghigo, E., 2018. Role of the immune system in regeneration and its dynamic interplay with adult stem cells. Semin. Cell Dev. Biol. https://doi.org/10.1016/j.semcdb.2018.04.002. [Epub ahead of print] Review, PMID: 29635020.

Abnave, P., Mottola, G., Gimenez, G., Boucherit, N., Trouplin, V., Torre, C., Conti, F., Ben Amara, A., Lepolard, C., Djian, B., Hamaoui, D., Mcktouchi, A., Kumar, A., Pagnotta, S., Bonatti, S., Lepidi, H., Salvetti, A., Abi-Rached, L., Lemichez, E., Meye, J.-L., Ghigo, E., 2014. Screening in planarians identifies MORN2 as a key component in LC3-associated phagocytosis and resistance to bacterial infection. Cell Host Microbe 16, 338–350.

Aboobaker, A.A., 2011. Planarian stem cells: a simple paradigm for regeneration. Trends Cell Biol. 21, 304–311.

Arnold, C.P., Merryman, M.S., Harris-Arnold, A., McKinney, S.A., Seidel, C.W., Loethen, S., Proctor, K.N., Guo, L., Sánchez Alvarado, A., 2016. Pathogenic Shifts in Endogenous Microbiota Impede Tissue Regeneration via Distinct Activation of TAK1/MEK/p38. eLife 5.

Bardeen, C.R., Baetjer, F.H., 1904. The inhibitive action of the Roentgen rays on regeneration in planarians. J. Exp. Zool. 1, 191–195.

Bergeron, A.C., Barker, S.E., Brothers, K.M., Prasad, B.C., Wheeler, R.T., 2017. Polyclonal anti-Candida antibody improves phagocytosis and overall outcome in zebrafish model of disseminated candidiasis. Dev. Comp. Immunol. 68, 69–78.

Bongomin, F., Gago, S., Oladele, R., Denning, D., 2017. Global and multi-national prevalence of fungal diseases—estimate precision. J. Fungi 3, 57.

Braun, B.R., Johnson, A.D., 1997. Control of filament formation in Candida albicans by the transcriptional repressor TUP1. Science 277, 105–109.

Brown, G.D., Denning, D.W., Gow, N.A.R., Levitz, S.M., Netea, M.G., White, T.C., 2012. Hidden killers: human fungal infections. Sci. Transl. Med. 4.

Cerenius, L., Lee, B.L., Soderhall, K., 2008. The proPO-system: pros and cons for its role in invertebrate immunity. Trends Immunol. 29, 263–271.

Chamilos, G., Lewis, R.E., Albert, N., Kontoyiannis, D.P., 2007. Paradoxical effect of Echinocandins across Candida species in vitro: evidence for echinocandin-specific and candida species-related differences. Antimicrob. Agents Chemother. 51, 2257–2259.

Clancy, C.J., Cheng, S., Nguyen, M., 2009. Methods in Molecular Biology, vol. 499. springer, pp. 65–76.

Cleary, I.A., Reinhard, S.M., Lazzell, A.L., Monteagudo, C., Thomas, D.P., Lopez-Ribot, J.L., Saville, S.P., 2016. Examination of the pathogenic potential of Candida albicans filamentous cells in an animal model of haematogenously disseminated candidiasis. FEMS Yeast Res. 16.

Drummond, R.A., Brown, G.D., 2013. Signalling C-type lectins in antimicrobial immunity. PLoS Pathog. 9, e1003417.

Fisher, M.C., Hawkins, N.J., Sanglard, D., Gurr, S.J., 2018. Worldwide emergence of resistance to antifungal drugs challenges human health and food security. Science 360, 739–742.

Fisher, M.C., Henk, D.A., Briggs, C.J., Brownstein, J.S., Madoff, L.C., McCraw, S.L., Gurr, S.J., 2012. Emerging fungal threats to animal, plant and ecosystem health. Nature 484, 186.

Fuchs, B., Eby, J., Nobile, C.J., Khoury, J.B., Mitchell, A.P., Mylonakis, E., 2010. Role of filamentation in Galleria mellonella killing by Candida albicans. Microb. Infect. 12, 488–496.

Gao, L., Hao, Y., Deng, H., Hu, W., Zhen, H., Li, N., Qin, N., Yan, M., Wu, W., Liu, B., Zhao, B., Pang, Q., 2017. The role of a novel C-type lectin-like protein from planarian in innate immunity and regeneration. Dev. Comp. Immunol. 67, 413–426.

Glittenberg, M.T., Silas, S., MacCallum, D.M., Gow, N.A., Ligoxygakis, P., 2011. Wild-type Drosophila melanogaster as an alternative model system for investigating the pathogenicity of Candida albicans. Dis. Model. Mech. 4, 504–514.

Goyal, S., Castrillon-Betancur, J.C., Klaile, E., Slevogt, H., 2018. The interaction of human pathogenic fungi with C-type lectin receptors. Front. Immunol. 9, 1261.

Gratacap, R.L., Scherer, A.K., Seman, B.G., Wheeler, R.T., 2017 Jun 12. Control of mucosal candidiasis in the zebrafish swimbladder depends on neutrophils that block filament invasion and drive extracellular trap production. Infect. Immun. https://doi.org/10.1128/IAI.00276-17. pii: IAI.00276-17. [Epub ahead of print], PMID: 28607100.

Hammoudi, N., Torre, C., Ghigo, E., Drancourt, M., 2018. Temperature affects the biology of Schmidtea mediterranea. Sci. Rep. 8, 14934.

Homann, O.R., Dea, J., Noble, S.M., Johnson, A.D., 2009. A phenotypic profile of the Candida albicans regulatory network. PLoS Genet. 5.

Kadosh, D., Lopez-Ribot, J.L., 2013. Candida albicans: adapting to succeed. Cell Host Microbe 14, 483–485.

Keating, S.T., Riksen, N.P., Netea, M.G., 2017. Planarians SET new paths for innate immune memory. EBioMedicine 20, 7–8.

King, R.S., Newmark, P.A., 2012. The cell biology of regeneration. J. Cell Biol. 196, 553–562.

Li, N., Li, A., Zheng, K., Liu, X., Gao, L., Liu, D., Deng, H., Wu, W., Liu, B., Zhao, B., Pang, Q., 2018. Identification and characterization of an atypical RIG-I encoded by planarian Dugesia japonica and its essential role in the immune response. Dev. Comp. Immunol. 91, 72–84.

Lo, H.-J., Köhler, J.R., DiDomenico, B., Loebenberg, D., Cacciapuoti, A., Fink, G.R., 1997. Nonfilamentous C. Albicans mutants are avirulent. Cell 90, 939–949.

Lohse, M.B., Gulati, M., Johnson, A.D., Nobile, C.J., 2018. Development and regulation of single- and multi-species Candida albicans biofilms. Nat. Rev. Microbiol. 16, 19–31.

Lu, Q., Wu, S., Zhen, H., Deng, H., Song, Q., Ma, K., Cao, Z., Pang, Q., Zhao, B., 2017. 14-3-3 alpha and 14-3-3 zeta contribute to immune responses in planarian Dugesia japonica. Gene 615, 25–34.

Maciel, E.L., Oviedo, N.J., 2018. Platyhelminthes: molecular dissection of the planarian innate immune system. In: In: Cooper, E.L. (Ed.), Advances in Comparative Immunology, vol. X. Springer International Publishing, pp. 1107.

Mallick, E.M., Bergeron, A.C., Jones Jr., S.K., Newman, Z.R., Brothers, K.M., Cretton, R., Wheeler, R.T., Bennett, R.J., 2016. Phenotypic plasticity regulates Candida albicans interactions and virulence in the vertebrate host. Front. Microbiol. 7, 780.

McKenzie, C.G., Koser, U., Lewis, L.E., Bain, J.M., Mora-Montes, H.M., Barker, R.N., Gow, N.A., Erwig, L.P., 2010. Contribution of Candida albicans cell wall components to recognition by and escape from murine macrophages. Infect. Immun. 78, 1650–1658.

Mejías, J., Martínez, A., Yáñez, A., Goodridge, H.S., Gozalbo, D., Gil, M.L., 2016. TLR2, TLR4 and Dectin-1 signalling in hematopoietic stem and progenitor cells determines the antifungal phenotype of the macrophages they produce. Microb. Infect. 18, 354–363.

Mejías, J., Yáñez, A., Moriano, S., O'Connor, J.E., Gozalbo, D., Gil, M.L., 2012. Direct toll-like receptor-mediated stimulation of hematopoietic stem and progenitor cells occurs in vivo and promotes differentiation toward macrophages. Stem Cell. 30, 1486–1495.

Mitchell, A.P., 1998. Dimorphism and virulence in Candida albicans. Curr. Opin. Microbiol. 1, 687–692.

Morita, M., 1991. Phagocytic response of planarian reticular cells to heat-killed bacteria. Hydrobiologia 227, 193–199.

Morita, M., 1995. Structure and function of the reticular cell in the planarian Dugesia dorotocephala. In: Cannon, L. (Ed.), Biology of Turbellaria and Some Related Flatworms. Springer, Abo/Turku, Finland, pp. 189–196.

Mylonakis, E., 2008. Galleria mellonella and the study of fungal pathogenesis: making the case for another genetically tractable model host. Mycopathologia 165, 1–3.

Mylonakis, E., Casadevall, A., Ausubel, F.M., 2007. Exploiting amoeboid and non-vertebrate animal model systems to study the virulence of human pathogenic fungi. PLoS Pathog. 3, e101.

Netea, M.G., Gow, N.A., Munro, C.A., Bates, S., Collins, C., Ferwerda, G., Hobson, R.P., Bertram, G., Hughes, H.B., Jansen, T., Jacobs, L., Buurman, E.T., Gijzen, K., Williams, D.L., Torensma, R., McKinnon, A., MacCallum, D.M., Odds, F.C., Van der Meer, J.W., Brown, A.J., Kullberg, B.J., 2006. Immune sensing of Candida albicans requires cooperative recognition of mannans and glucans by lectin and Toll-like receptors. J. Clin. Invest. 116, 1642–1650.

Newmark, P., Sánchez Alvarado, A., 2000. Bromodeoxyuridine specifically labels the regenerative stem cells of planarians. Dev. Biol. 220, 142–153.

Nobile, C.J., Johnson, A.D., 2015. Candida albicans biofilms and human disease. Annu. Rev. Microbiol. 69, 71–92.

Oviedo, N.J., Nicolas, C.L., Adams, D.S., Levin, M., 2008. Establishing and Maintaining a Colony of Planarians. CSH protocols 2008, pdb prot5053.

Pang, Q., Gao, L., Hu, W., An, Y., Deng, H., Zhang, Y., Sun, X., Zhu, G., Liu, B., Zhao, B., 2016. De novo transcriptome analysis provides insights into immune related genes and the RIG-I-like receptor signaling pathway in the freshwater planarian (dugesia japonica). PLoS One 11, e0151597.

Peiris, T.H., Hoyer, K.K., Oviedo, N.J., 2014. Innate immune system and tissue regeneration in planarians: an area ripe for exploration. Semin. Immunol. 26, 295–302.

Peiris, T.H., Ramirez, D., Barghouth, P.G., Ofoha, U., Davidian, D., Weckerle, F., Oviedo, N.J., 2016. Regional signals in the planarian body guide stem cell fate in the presence of genomic instability. Development 143, 1697–1709.

Pellettieri, J., Fitzgerald, P., Watanabe, S., Mancuso, J., Green, D.R., Sanchez Alvarado, A., 2010. Cell death and tissue remodeling in planarian regeneration. Dev. Biol. 338, 76–85.

Pellettieri, J., Sanchez Alvarado, A., 2007. Cell turnover and adult tissue homeostasis: from humans to planarians. Annu. Rev. Genet. 41, 83–105.

Peterson, N.D., Pukkila-Worley, R., 2018. Caenorhabditis elegans in high-throughput screens for anti-infective compounds. Curr. Opin. Immunol. 54, 59–65.

Pukkila-Worley, R., Holson, E., Wagner, F., Mylonakis, E., 2009a. Antifungal drug discovery through the study of invertebrate model hosts. Curr. Med. Chem. 16, 1588–1595.

Pukkila-Worley, R., Peleg, A.Y., Tampakakis, E., Mylonakis, E., 2009b. Candida albicans hyphal formation and virulence: assessed using a Caenorhabditis elegans infection model. Eukaryot. Cell 8, 1750–1758.

Reddien, P.W., Oviedo, N.J., Jennings, J.R., Jenkin, J.C., Sánchez Alvarado, A., 2005. SMEDWI-2 is a PIWI-like protein that regulates planarian stem cells. Science 310, 1327–1330.

Reddien, P.W., Sánchez Alvarado, A., 2004. Fundamentals of planarian regeneration. Annu. Rev. Cell Dev. Biol. 20, 725–757.

Roeder, A., Kirschning, C.J., Rupec, R.A., Schaller, M., Korting, H.C., 2004. Toll-like receptors and innate antifungal responses. Trends Microbiol. 12, 44–49.

Saville, S.P., Lazzell, A.L., Monteagudo, C., Lopez-Ribot, J.L., 2003. Engineered control of cell morphology in vivo reveals distinct roles for yeast and filamentous forms of Candida albicans during infection. Eukaryot. Cell 2, 1053–1060.

Schneider, C.A., Rasband, W.S., Eliceiri, K.W., 2012. NIH Image to ImageJ: 25 years of image analysis. Nat. Methods 9, 671–675.

Segal, E., Frenkel, M., 2018. Experimental in vivo models of candidiasis. J. Fungi 4.

Tang, J., Lin, G., Langdon, W.Y., Tao, L., Zhang, J., 2018. Regulation of C-type lectin receptor-mediated antifungal immunity. Front. Immunol. 9, 123.

Thiruvalluvan, M., Berghouth, P.G., Taur, A., Brodey, L., Oviedo, N.J., 2018. SUMOylation controls stem cell proliferation and regional cell death through Hedgehog signaling in planarians. Cell. Mol. Life Sci. : CMLS 75, 1285–1301.
Torre, C., Abnave, P., Tsoumtsa, L., Mottola, G., Lepolard, C., Trouplin, V., Gimenez, G., Desnoues, J., Gempp, S., Levasseur, A., Padovani, L., Lemichez, E., Ghigo, E., 2017a. Staphylococcus aureus promotes smed-PGRP-2/smed-setd8-1 methyltransferase signalling in planarian neoblasts to sensitize anti-bacterial gene responses during Re-infection. EBioMedicine 20, 150–160.
Torre, C., Abnave, P., Tsoumtsa, L.L., Mottola, G., Lepolard, C., Trouplin, V., Gimenez, G., Desnoues, J., Gempp, S., Levasseur, A., Padovani, L., Lemichez, E., Ghigo, E., 2017b. Staphylococcus aureus promotes smed-PGRP-2/smed-setd8-1 methyltransferase signalling in planarian neoblasts to sensitize anti-bacterial gene responses during Re-infection. EBioMedicine 20, 150–160.
Tsoumtsa, L.L., Sougoufara, S., Torre, C., Lemichez, E., Pontarotti, P., Ghigo, E., 2018. In silico analysis of Schmidtea mediterranea Tlr domain-containing proteins. Dev. Comp. Immunol. 86, 214–218.
Tsoumtsa, L.L., Torre, C., Trouplin, V., Coiffard, B., Gimenez, G., Mege, J.-L., Ghigo, E., 2017. Antimicrobial capacity of the freshwater planarians against S. aureus is under the control of Timeless. Virulence: 8, 1160–1169.
van Wolfswinkel, J.C., Wagner, D.E., Reddien, P.W., 2014. Single-cell analysis reveals functionally distinct classes within the planarian stem cell compartment. Cell Stem Cell 15, 326–339.
Wagner, D.E., Wang, I.E., Reddien, P.W., 2011. Clonogenic neoblasts are pluripotent adult stem cells that underlie planarian regeneration. Science 332, 811–816.
WHO, 2018. The Top Ten Causes of Death. World Health Organization.
Yáñez, A., Megías, J., O'Connor, J.-E., Gozalbo, D., Gil, L.M., 2011. Candida albicans induces selective development of macrophages and monocyte derived dendritic cells by a TLR2 dependent signalling. PLoS One: 6.
Yáñez, A., Murciano, C., O'Connor, J.-E., Gozalbo, D., Gil, L.M., 2009. Candida albicans triggers proliferation and differentiation of hematopoietic stem and progenitor cells by a MyD88-dependent signaling. Microb. Infect. 11, 531–535.
Yang, R., Liu, Y., Kelk, P., Qu, C., Akiyama, K., Chen, C., Atsuta, I., Chen, W., Zhou, Y., Shi, S., 2012. A subset of IL-17 + mesenchymal stem cells possesses anti-Candida albicans effect. Cell Res. 23.
Zeng, A., Li, H., Guo, L., Gao, X., McKinney, S., Wang, Y., Yu, Z., Park, J., Semerad, C., Ross, E., Cheng, L.-C., Davies, E., Lei, K., Wang, W., Perera, A., Hall, K., Peak, A., Box, A., Alvarado, A., 2018. Prospectively isolated Tetraspanin + neoblasts are adult pluripotent stem cells underlying planaria regeneration. Cell 173 1593-1606632960.